Design, Synthesis and Activation of Ruthenium Arene Anticancer Complexes

A Thesis Submitted for the Degree of

Doctor of Philosophy

by

Soledad Betanzos Lara, *M.Sc.*
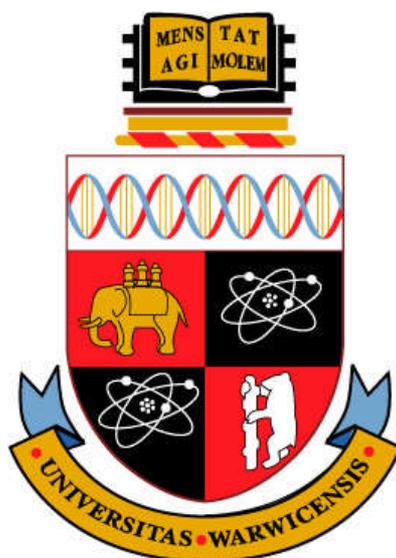
University of Warwick

Department of Chemistry

September 2010

Para mi Mamá, mi Compañerita.

Te amo infinitamente.

Contents

Acknowledgements

I would like to thank Professor Peter J. Sadler for giving me the opportunity to come to the U.K. to be part of the PJS research group. I am very grateful for his supervision and support. I have really enjoyed the experience of working in his group.

A very big and special GRACIAS goes to my dearest friend Dr Abraha Habtemariam for always being there for me and for sharing his knowledge and professional supervision, without which I would have not come this far. Gracias (especially) for your infinite patience, guidance, and advice throughout all my "*amargada*" periods. The best memories I will be taken with me, are for sure those of our every-day time in (and outside) the labs together. I will miss our chats in spanish and having someone to complain to about everything. You have a very special place in my heart!

A very big GRACIAS goes to Dr Sarah J. Farley (MFPPitWW). All I can say is that you are a ZEN and that ILY (NLT). Without you I would have never got the chance to meet the Chemistry security guards (including Playa Muuuujeres), I would have not known what it is to snooze in the office or wear my swimming costume while NMRing in Siberia. Mi Pepe, I raccooooon that you are in every single nice memory I have of my time at Warwick and I am going to miss you a lot! I am so very grateful of having had the chance to have you as a friend.

A very big GRACIAS also goes to Pepe Khatija (my personal fashion adviser). I am very glad we got to know each other and grow an endurable and special friendship. Thanks for introducing me to Topshop online. Oh Pepe, I am definitely going to miss you!

Thanks to Pepe Julie Ann, Pepe Evyenia, Pepe Sabine and Bloody Gamberro (Joan)! Nothing would have been the same without you *people, people*!!

Pasta la Pasta to everyone!

Declaration

I hereby declare that except where specific reference is made to other sources, the work contained in this Thesis is the original work of the author. It has been composed by myself and has not been submitted, in whole or in part, for any other degree, diploma, or other qualification.

Some of the work presented in this Thesis has been published:

1. "Di-μ-Chloro(ethylbenzoate)diruthenium(II): $[(\eta^6\text{-etb})RuCl_2]_2$"

   Habtemariam, A.; Betanzos-Lara, S.; Sadler, P. J. *Inorg. Synth.*, **2010**, *36*, accepted for publication (in press).

2. "Photocontrolled nucleobase binding to an organometallic Ru^{II} arene complex"

   Betanzos-Lara, S.; Salassa, L.; Habtemariam, A.; Sadler, P. J. *Chem. Commun.*, **2009**, 6622–6624.

Soledad Betanzos Lara

September 2010

Abstract

The synthesis and characterisation of Ru^{II} complexes of the form $[(\eta^6\text{-arene})Ru(N,N')X]^+$ (where N,N' is a bidentate chelating ligand and X is a halogen) are described; including the X-ray crystal structures of four of these complexes. The hydrolysis rates at 310 K of the complexes vary over many orders of magnitude and in some cases are followed by partial arene loss. Density Functional Theory (DFT) calculations suggest that the aquation mechanism occurs via a more associative pathway. The significant cytotoxic activity towards A2780 human ovarian cancer cells of some of the complexes is found to be dependent on the chelating ligand. Selective binding to 9-ethylguanine (9-EtG) but not to 9-ethyladenine (9-EtA) is observed in aqueous solution at 310 K in all cases. The X-ray crystal structure of a Ru^{II} arene 9-EtG adduct is also described. DFT calculations show that the 9-EtG nucleobase adducts of all complexes are thermodynamically preferred compared to those of 9-EtA. Preliminary CT-DNA studies in cell-free media suggest that some of these complexes can interact with DNA.

A family of piano-stool Ru^{II} arene complexes of the form $[(\eta^6\text{-arene})Ru(N,N')(L)]^{2+}$ (where N,N' is a chelating ligand and L is a pyridine or a pyridine-derivative), that can selectively photodissociate the monodentate ligand (L) when excited with UVA or visible light is described. The X-ray crystal structures of five of these complexes are also discussed. Their photoactivation allows the formation of a reactive aqua species that otherwise would not form in the dark. Results from TD-DFT calculations suggest that all the Ru^{II} pyridine complexes follow a relatively similar L-ligand photodissociation mechanism, likely to occur from a series of ^3MC triplet states. It is shown how light activation can be used to phototrigger binding of these complexes to nucleobases with specific preference towards 9-EtG over 9-EtA. CT-DNA studies suggest that photoirradiated complexes interact with DNA *via* a combined coordinative, intercalative, and monofunctional binding mode. Some of the complexes are also cytotoxic against A2780 human ovarian cancer cell line in the absence of irradiation.

The possibility of photo(triggering) hydride-transfer reactions using Ru^{II} arene complexes, NAD^+, and formate as the hydride source under biologically relevant conditions is shown. The reactions occur either upon the spontaneous hydrolysis of a Ru–Cl bond in complexes of the form $[(\eta^6\text{-arene})Ru(N,N')Cl]^+$ (where N,N' is a bidentate chelating ligand) or upon the photolysis of a $Ru–N_{(Py)}$ bond in $[(\eta^6\text{-arene})Ru(N,N')Py]^{2+}$ (Py is pyridine). A mechanism involving the formation of a stable formate adduct followed by a hydrogen β-elimination is proposed. It is also demonstrated how a hydride-transfer from 1,4-NADH to some Ru^{II} arene chlorido complexes can occur in aqueous solution.

Neutral Ru^{II} arene complexes of the form $[(\eta^6\text{-arene})Ru(NH_3)Cl_2]$ which are constitutional analogues of cisplatin were synthesised by a novel synthetic method. These analogues display extensive H-bond interactions in the solid state as shown by X-ray crystal structures determination and their biexponential hydrolysis rates at 310 K vary over many orders of magnitude. The complexes are found to readily form mono- and di-guanine adducts upon hydrolysis but are not cytotoxic against the A2780 human ovarian cancer cell line up to the maximum concentration tested (100 μM).

Abbreviations

3-AcOPy	3-acetatepyridine
3-AcPy	3-acetylpyridine
4,4'-bpy	4,4'-bipyridine
4-BzPy	4-benzylpyridine
9-EtA	9-ethyladenine
9-EtG	9-ethylguanine
4,4'-Me$_2$-bpy	4,4'-dimethyl-2,2'-bipyridine
4-MePy	4-methylpyridine
4-MeOPy	4-methoxypyridine
4-PhPy	4-phenylpyridine
Å	Angstrom
A	Absorbance
A	Adenine
acac	Acetylacetonate
ADF	Amsterdam Density Functional
Arg	Arginine
azpy	Arylazopyridine
bathophen	4,7-diphenyl-1,10-phenanthroline
bip	Biphenyl
bp	Base pairs
bpm	2,2'-bipyrimidine
bpy	2,2'-bipyridine
bz	Benzyl
C	Cytosine
°C	Centigrade degree
ca.	*circa*
CBA	Cytometric Bead Array
CD	Circular Dichroism
CDCl$_3$	Deuterated chloroform-*d$_3$*
cisPt	*cis*-diamminedichloroplatinum (II)

COSMO	Conductor-like Screening Model
COSY	Correlation Spectroscopy
Cp	Cyclopentadiene
CT	Calf Thymus
δ	Chemical shift
D	Deuterium
d	Doublet
dab	1,2-diaminobenzene
dd	Doublet of doublets
DEPT	Distortionless Enhancement by Polarization Transfer
DFT	Density Functional Theory
dha	9,10-dihydroanthracene
dienPt	Dichloro(ethylenediamine)platinum (II)
dmba	N,N'-dimethylbenzylamine
(dmba-H)$^+$	N,N'-dimethylbenzylammonium
DMEM	Dubecco's Modified Eagle's medium
DMSO	Dimethyl sulfoxide
DNA	Deoxyribonucleic acid
D_2O	Deuterated water-d_2
dpp	2,3-bis(2-pyridyl)pyrazine
dpq	Dipyrido[3,2-d:2',3'-f]quinoxaline
dppz	Dipyrido[3,2-d:2',3'-c]phenazine
dsDNA	Double-stranded DNA
ε	Extinction coefficient
EAS	Electron Absorption Spectroscopy
ECACC	European Collection of Animal Cell Cultures
EDDM	Electron Density Difference Map
EDTA	Ethylenediaminetetraacetic acid
en	Ethylenediamine
ESI-MS	Electrospray Ionisation Mass Spectrometry
etb	Ethylbenzoate
EtBr	Ethidium bromide
Et_2O	Diethyl ether

Φ_L	Quantum yield
FAAS	Flameless Atomic Absorption Spectroscopy
FCS	Foetal Calf Serum
FDA	Food and Drug Administration
G	Guanine
GABA	γ-aminobutiric acid
GGA	Perdew-Wang Gradient-Corrected functional
GMP	Guanosine-5'-monophosphate
GSH	Glutathione
h	Hour
hat	1,4,5,8,9,12-hexaazatriphenylene
HIV	Human Immunodeficiency Virus
hmb	Hexamethylbenzene
HMGB1	High-Mobility Group protein B1
HOMO	Highest Occupied Molecular Orbital
HPLC	High Performance Liquid Chromatography
HR-MS	High Resolution Mass Spectrometry
IC_{50}	50% inhibitory concentration
ICD	Induced Circular Dichroism
IL	Interligand
ind	Indane
indz	Indazole
imid	Imidazole
J	Coupling constant
K	Kelvin
k	Rate constant
λ	Wavelength
L-alaMe	L-alanine methyl ester
LC	Ligand-centred
LD	Flow Linear Dichroism
LMCT	Ligand-to-Metal Charge Transfer
LUMO	Lowest Unoccupied Molecular Orbital
m	Multiplet

MC	Metal-centred
MeOD	Deuterated methanol-d_4
MLCT	Metal-to-ligand charge transfer
MP	6-mercaptopurine
MRI	Magnetic Resonance Imaging
m/z	Mass-to-charge ratio
NADP$^+$	β-Nicotinamide Adenine Dinucleotide Phosphate
NADPH	Reduced β-Nicotinamide Adenine Dinucleotide Phosphate
NA	Nicotinamide
NAD$^+$	β-Nicotinamide Adenine Dinucleotide
NADH	Reduced β-Nicotinamide Adenine Dinucleotide
NIR	Near Infrared
NMR	Nuclear Magnetic Resonance
NOESY	Nuclear Overhauser Effect Spectroscopy
OC	Nicked plasmid
Φ	Unwinding angle
PACT	Photodynamic Antimicrobial Chemotherapy
PBS	Phosphate Buffered Saline
p-cym	*para*-cymene
PDT	Photodynamic Therapy
ph	Phenyl
phen	1,10-phenanthroline
phendio	1,10-phenanthroline-5,6-dione
por	Porphyrinato
ppm	Parts per million
PS	Photosensitiser
pta	1,3,5-triaza-7-phospha-tricyclo-[3.3.1.1]decane
Py	Pyridine
RNA	Ribonucleic acid
RPMI	Roswell Park Memorial Institute medium
S0	Ground state
s	Singlet
s	Second

SAR	Structure Activity Relationship
SC	Supercoiled plasmid
SCF	Self-Consistent Field
sep	Septet
SOMO	Single Occupied Molecular Orbital
SRB	Sulforhodamine B
T0	Lowest-lying triplet state
TAE	Tris-aceate/EDTA
TCA	Trichloroacetic acid
TFA	Trifluoroacetic acid
TD-DFT	Time-Dependent Density Functional Theory
$t_{1/2}$	Half-life
t	time
t	triplet
tap	1,4,5,8-tetraazaphenanthrene
t_m	Melting temperature
TMEDA	Tetramethylethylenediamine
tha	1,4,9,10-tetrahydroanthracene
thn	1,2,3,4-tetrahydronaphthalene
TOCSY	Total Correlation Spectroscopy
transPt	*trans*-diamminedichloroplatinum (II)
TZP	triple-ζ plus polarization
tris	Tris(hydroxomethyl)aminoethane
trz	1,2,4-triazole
uip	2-(5-uracil)-1H-imidazo[4,5-f][1,10]phenanthroline
UVA	Ultraviolet A
UV-vis	Ultraviolet visible
ZORA	Zero-Order Regular Approximation

Chapter 1

Introduction

Chapter 1
Introduction

The aim of this Chapter is to introduce briefly the field of metallodrugs with particular emphasis on metal complexes as anticancer agents; a more detailed description of the cytotoxic properties of Ru^{II} arene complexes is included. The subsequent sections focus on the advantageous photochemical properties of Ru^{II} (poly)pyridyl complexes for their potential use in biological applications. Finally, the involvement of Ru^{II} complexes in biologically relevant hydride-transfer reactions is described.

1.1   Metal-Based Therapeutics

Metal ions are required for many critical functions in living organisms. In humans, scarcity of some of them can lead to disease states; well-known examples include pernicious anaemia resulting from iron deficiency,[1] growth retardation arising from insufficient dietary zinc,[2] and heart disease in infants owing to copper deficiency.[3] Less well-known than the fact that metal ions are required in biology, is their role as pharmaceuticals. The use of metals in medicine traces back to antiquity with various elements such as arsenic, gold, and iron being used to treat different ailments.[4] The first metal-based drug in modern times used in medicine, an arsenical formulation (arsphenamine) commercially known as *Salvarsan* or *Ehrlich 606*, was used for the treatment of syphilis.[5,6] However, with the later discovery of the better antibiotic activity of penicillin, the use of the arsenic drug was discontinued. More recent examples of metals in medicine include the use of lithium salts for neurological disorders,[7] gold drugs for treating rheumatoid and psoriatic arthiritis,[8] and vanadium compounds being studied as insulin-metabolism mimetic agents in the treatment of

diabetes.[9] It is known that the efficacy of the various organic therapeutic agents can often be enhanced upon coordination with a suitable metal ion;[10] a key concept in the design of metal complexes is the tuning and optimisation of the chemical reactivity to promote possible interactions with the target site yet avoiding side-reactions.[11] By rational ligand design it has been possible for example, to control the toxicity of Gd[III] complexes so that they can be safely injected as Magnetic Resonance Imaging (MRI) contrast agents or to enable the targeting of radiodiagnostic and radiotherapeutic isotopes such as ^{99m}Tc and [186]Re, respectively to the desired organs.[12]

1.1.1 Metal Complexes in Cancer Chemotherapy

Each year, approximately 12.7 million people worldwide are diagnosed with cancer and 7.5 million people die from it; the five most common types of diagnosed cancers are breast, colorectum, stomach, prostate, and lung.[13] The main widely used drugs for treatment of various types of cancers are platinum-based complexes. More than 3000 of these compounds have been synthesised and tested for biological activity;[14] four of them are nowadays registered globally as marketed drugs: cisplatin, carboplatin, oxaliplatin, and nedaplatin, Figure 1.1.
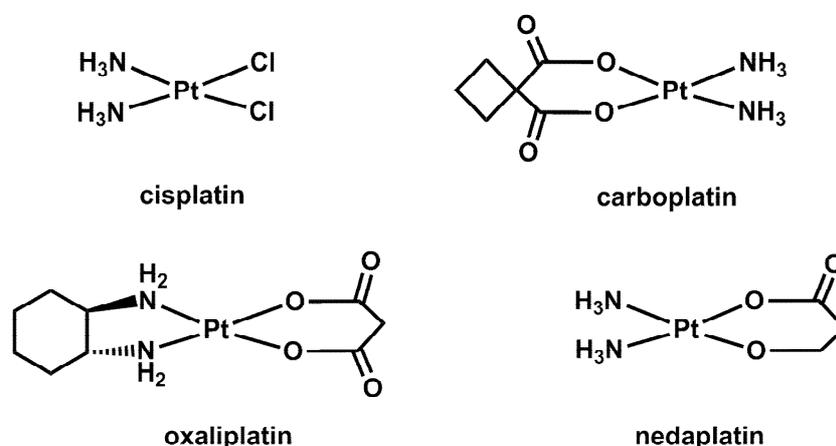
Figure 1.1. Structures of marketed platinum anticancer drugs.

Oxaliplatin is the only of these drugs that has been yet approved by the Food and Drug Administration (FDA) for colorectal cancer.[15,29] Cisplatin, discovered in the 1960s,[16,17,18] is extensively used and effects cures in >80% of cases of testicular cancer.[19] It is also highly efficient against ovarian cancer and contributes to the treatment of head, neck, and bladder cancer, as well as lymphomas,[20] melanomas, and breast cancer.[21] Investigations into the activity of cisplatin at the biomolecular level indicate that genomic DNA is the primary target.[75c] Its anticancer activity comes from its capability to form bifunctional DNA cross-links (after activation by hydrolysis) through binding to adjacent purine bases,[22] predominantly with *N7* of guanine (G). This site is known to be the most electron-rich on DNA and it is believed to be easily accessible for cisplatin in the major groove of B-DNA. Other binding sites include *N7* of adenine (A) and *N3* of cytosine (C).[23] Figure 1.2 shows the structures and numbering scheme for the four DNA nucleobases.
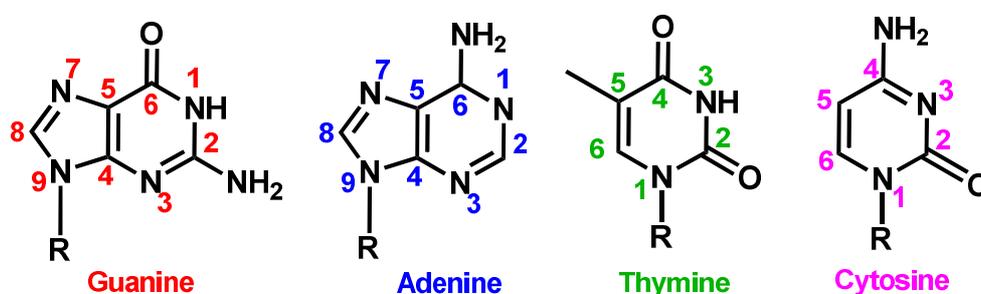
Figure 1.2. Structures and numbering schemes for the four DNA nucleobases. R represents the deoxyribose phosphate backbone.

1,2-Intrastrand cross-links that involve guanine and sometimes adenine, are known to be the most common platinated adducts of DNA in cancer cells treated with cisplatin.[23] In this GG intrastrand cross-linking pathway, activation by hydrolysis is followed by monofunctional binding (causing ring closure) to give the bifunctional GG macrochelate. It is also known that hydrogen-bonding formation between NH

protons of cisplatin and the phosphate backbone or C6O of G nucleobase can play a role in stabilising such cross-links.[24] GG coordination results in distortion of the B-DNA helix towards the major groove[25] (by about 35–40°) followed by unwinding of the DNA. This bend is recognised by the so called High-Mobility Group (HMG) proteins which are believed to strongly bind to bent platinated DNA,[26] Figure 1.3. Finally, the cells undergo apoptosis due to unsuccessful DNA repair.[27]
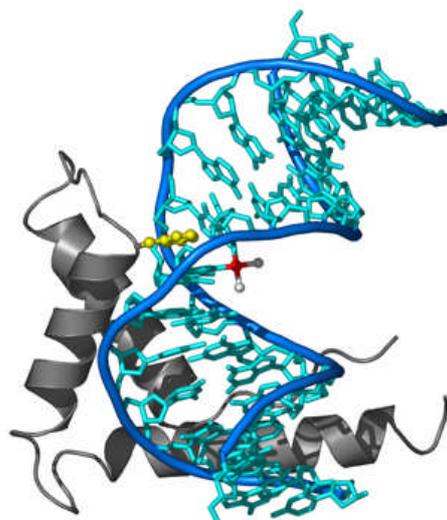
Figure 1.3. A DNA-cisplatin adduct bound to the nonsequence-specific domain A of the High-Mobility Group protein B1 (HMGB1). Pt(NH$_3$)$_2$ shown as red and white spheres, DNA blue, HMBG1 grey cartoon with intercalated phenylalanine as yellow spheres.[28]

A search for related complexes with similar or better activity than cisplatin is being currently carried out. It has become fundamental not only to circumvent the resistance (both natural or acquired) of many tumours to cisplatin, but also to find compounds that would have less toxic side effects, such as nephrotoxicity, neurotoxicity and emetogenesis, as well as a broader spectrum of activity.[29] The Ti^{IV} complex *Budotitane*, Figure 1.4 was the first non-platinum complex to be approved for clinical trials as a potential anticancer drug. Its poor solubility and instability in aqueous solution hampered its formulation even when used in combination with micelles.[30]
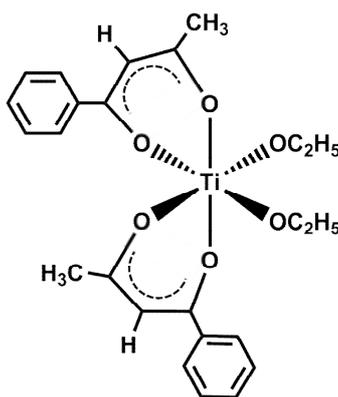
Figure 1.4. Structure of the Ti^{IV} anticancer complex, *Budotitane*.

Au^{I} and Au^{III} complexes have also been tested for anticancer activity in different cell lines, displaying good activity but cardiovascular toxicity.[8] More recently, the anticancer properties of a family of [Au(por)]$^{+}$ (por = porphyrinato ligand) have been reported. Their cytotoxic IC$_{50}$ values (0.033–100 μM) correlate well with their lipophilicity and cellular uptake. Some of them induce apoptosis and display preferential cytotoxicity towards cancer cells than to normal noncancerous cells.[31] The Ru^{III} complexes Na[*trans*-RuCl$_4$(DMSO)(imid)] (**NAMI**), its imidazolium analogue [imidH][*trans*-RuCl$_4$(DMSO)(imid)] (**NAMI-A**), and the indazole compound [indzH][*trans*-RuCl$_4$(indz)$_2$] (**KP1019**), Figure 1.5 are the most prominent examples of ruthenium-based anticancer drugs. Complex **NAMI** was not sufficiently stable in solution for clinical applications[32] whereas compound **NAMI-A** showed high selectivity for solid tumour metastases[33] along with low toxicity at pharmacologically active doses[34] and successfully completed phase I clinical trials.[35] Compound **KP1019** successfully completed phase I clinical trials in 2005.[36]
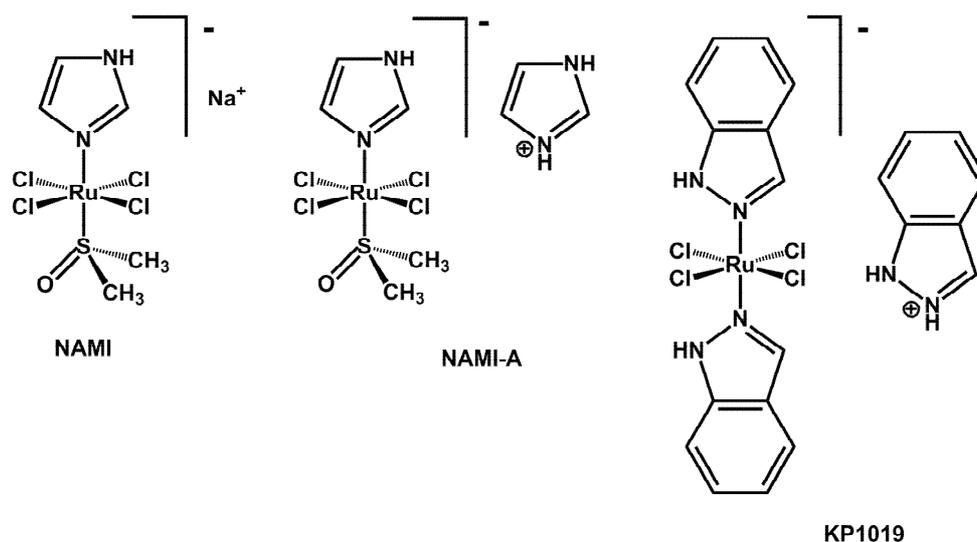
Figure 1.5. Structures of the Ru^{III} anticancer complexes NAMI, NAMI-A and KP1019.

It has been suggested that Ru^{III} complexes are activated by reduction *in vivo* to Ru^{II},[52] form in which they are more reactive due to the increased lability of Ru^{II}–Cl bonds.[37] The reduction of Ru^{III} to Ru^{II} is believed to occur *in vivo* by single-electron transfer reactions from proteins belonging to the mitochondrial electron-transfer chain or from proteins within microsomal electron-transfer systems; the latter ones are believed to be more efficient.[38]

1.1.2 Organometallic Complexes as Anticancer Agents

Organometallic compounds exhibit different ligand exchange kinetics in solution to those observed for other coordination complexes;[39] this feature has shown to be useful in drug design. For example, the organometallic complex titanocene dichloride, Cp_2TiCl_2 was found to exhibit significant activity against lung, breast, and gastrointestinal cancers in mice. It was originally believed to react with DNA to form bifunctional cross-links through the *cis*-$TiCl_2$ motif, in a similar fashion as cisplatin, but surprisingly, it was found to bind more strongly to the DNA phosphate

backbone.[40] Due to hydrolysis of the Ti–Cl and Ti–Cp bonds and formation of hydroxido- and oxido-bridged species, it was finally ruled out from clinical trials.[41,42] In the search for an improved hydrolytic stability, recent studies report on the synthesis of titanocene derivatives[43,44,45] with bridged-cyclopentadienyls (*ansa*-titanocenes) and non-bridged organotitanium titanocenes[46] which have shown *in vivo* activity against A431 and PC-3 xenografts, models for epidermoid and human prostate cancer, respectively, similar to cisplatin. Although a change on the metal centre in the sandwich complexes for V, Nb, or Mo did not alter the cytotoxic activity exhibited *in vitro*,[47] none of these metallocenes have reached clinical trials. Further attempts with the corresponding metallocenes of Zr and Hf have proved to be unfruitful too.[48,49] More recently, a series of ferrrocenyl derivatives of the breast cancer drug tamoxifen, commonly named *ferrocifens*, have proved to be active against both estrogen-dependent and estrogen-independent breast cancer cells.[50] *Ferrocifens* are believed to act against estrogen-independent breast cancer cells by causing oxidative damage to DNA *via* oxidation of the ferrocenyl group in the cells. Furthermore, several studies on the cytotoxicity, hydrophobicity (Log P), cellular uptake, aqueous solution reactivity, and/or extent of DNA adduct formation in several human cancer cell lines have been reported for organometallic Os^{II} arene complexes.[51]

1.1.3   Cytotoxic Ru^{II} Arene Complexes

The use of Ru^{II} arene complexes as potential anticancer agents has been explored given that they often possess good aqueous solubility and the arene ligand is relatively inert towards displacement under physiological conditions.[52] Ru^{II} arene complexes were first shown to form adducts with nucleosides and nucleotides, forming mononuclear[53] or di-, tri-, and tetranuclear complexes.[54] In particular, the discovery of

the biological activity of organoruthenium complexes of the type $[(\eta^6\text{-}$arene$)Ru(X)(Y)(Z)]^{n+}$ (where X and Y are either monodentate ligands or if they are linked, XY represents a chelating ligand; and Z is a leaving group) has opened up a new route towards the design and synthesis of novel anticancer agents.[55,56] Although their mode of action is not yet completely understood, recent results suggest that DNA might be an important target.[55] It is believed that the aquation, particularly if chloride is the leaving group, is largely suppressed in extracellular fluids where high chloride concentrations are found (100 mM), whereas in the cell cytoplasm and nucleus where the chloride concentrations are lower (25 and 4 mM, respectively), the complex is predominantly in the reactive aqua form.[56] Within the cell nucleus it is believed that these complexes bind to DNA forming monofunctional adducts with a high affinity for *N7* of guanine bases (G), as opposed to the bifunctional adducts formed by cisplatin.

1.1.3.1 *Structural Features of Ru^{II} Arene Complexes for Anticancer Activity*

A particularly attractive feature of Ru^{II} arene anticancer complexes is the possibility of modifying their basic structural framework, Figure 1.6.
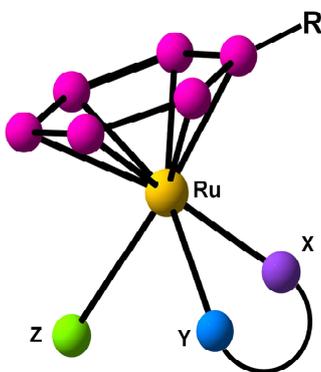
Figure 1.6. Typical structure of a half-sandwich Ru^{II} arene complex $[(\eta^6\text{-}$arene$)Ru(X)(Y)(Z)]^{n+}$ where X and Y can be either monodentate ligands or if linked, XY represents a chelating ligand; Z is a leaving group.

This provides considerable scope for the optimisation of their design in terms of mechanisms of action, selection of target sites, and modulation of possible side-effects.[40,55,56,57,58,60]

1.1.3.1.1   The Arene

It has been found that the arene in organometallic complexes of the general formula $[(\eta^6\text{-arene})Ru(X)(Y)(Z)]^{n+}$ can stabilise Ru in its 2+ oxidation state. The nature of the arene can also help to influence cell uptake and interactions with potential targets.[57] For example, it is believed that the more extended coordinated arenes such as biphenyl (bip) or tetrahydroanthracene (tha), could provide a hydrophobic face that might assist the passage of the Ru^{II} drug across cell membranes.[58] It has also been observed that the cytotoxic activity of Ru^{II} arene complexes appears to increase with the size of the coordinated arene.[55] When tested against the human ovarian cancer cell line (A2780), the 50% inhibitory concentrations (IC_{50} values) of a series of Ru^{II} arene ethylenediamine (en) complexes were found to decrease in the order: benzene (bz, 17 μM) > *para*-cymene (*p*-cym, 10 μM) > biphenyl (bip, 5 μM) > dihydroanthracene (dha, 2 μM) > tetrahydroanthracene (tha, 0.5 μM).[68] The increased cytotoxic potency in these (and other related Ru^{II} extended arene complexes) is assumed to arise from the ability of such arenes to intercalate into DNA, thus generating medium-to-strong π-stacking interactions that cause a significant distortion of the structure of DNA, Figure 1.7.[58,59] Intramolecular π-π arene-nucleobase stacking has also been observed in the crystal structure of $[(\eta^6\text{-bip})Ru(en)(9\text{-EtG-}N7)][PF_6]_2$.[70] Recently, the effect on cytotoxicity and DNA binding of Ru^{II} arene en complexes of structural isomers of the terphenyl ligand (*para*-, *meta*-, and *ortho*-terphenyl)[60] have been explored, Figure 1.8.
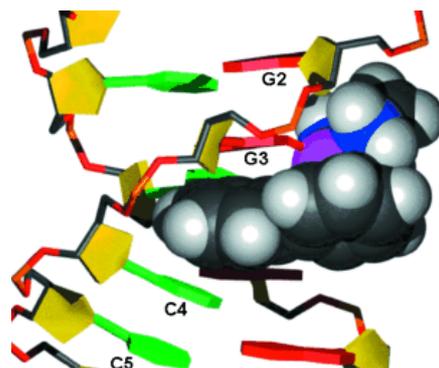
Figure 1.7. Schematic representation of a Ru[II] extended arene complex intercalating between DNA bases.[58] Ru[II] atom shown as a purple sphere, bip arene shown as grey and white spheres, en chelating ligand shown as blue and white spheres, and guanine bases in red.

para-**terphenyl**   *meta*-**terphenyl**   *ortho*-**terphenyl**
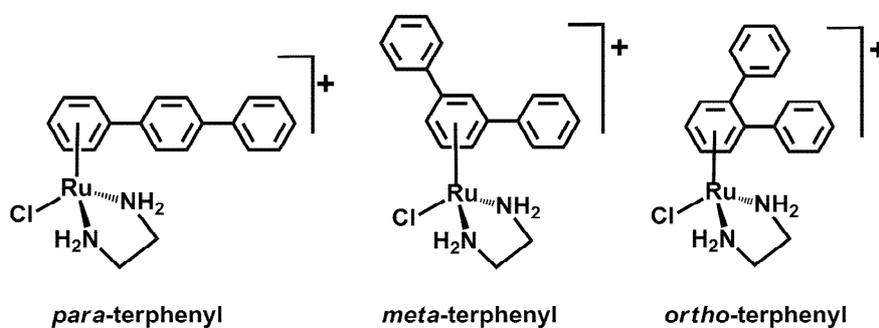
Figure 1.8. Structures of $[(\eta^6\text{-arene})Ru(en)Cl]^+$ complexes where arene is *para-, meta-,* or *ortho*-terphenyl.[60]

The complex containing *para*-terphenyl as the arene ligand, exhibits increased cytotoxicity in several human tumour cell lines, including those resistant to cisplatin. In contrast, complexes containing *meta*- or *ortho*-terphenyl are comparatively less cytotoxic. The results also revealed that in agreement with the relatively high cytotoxicity of the Ru[II] *para*-terphenyl complex, its DNA-binding mode involves combined non-coordinative intercalative and monofunctional coordination binding modes. In contrast, the *ortho*-terphenyl complex was found to bind to DNA only through monofunctional coordination to DNA bases.

1.1.3.1.2   The X and Y Monodentate Ligands

Introducing bifunctional reactivity into Ru^{II} arene complexes can be achieved by synthesising derivatives of the form $[(\eta^6\text{-arene})Ru(X)(Y)(Z)]^{n+}$ where X, Y, and Z are all monodentate ligands. The use of this approach should in theory increase interactions with potential targets such as DNA, in a comparable way to cisplatin. The synthesis and properties of the novel Ru^{II} arene complex $[(\eta^6\text{-}p\text{-cym})Ru(NH_3)_2Cl]^+$ have been recently described.[61] Despite its constitutional similarity to cisplatin, the complex displays an IC_{50} value *ca.* 500 times larger than that of the platinum drug under the same conditions. It is probable that the lack of activity arises from its instability in aqueous (and organic) solutions. The substitution of at least one of the NH_3 groups for a sterically more demanding ligand, usually a heterocyclic amine, a pyridine[62] or phosphine,[63] has also been tried. For example, the complex $[(\eta^6\text{-}p\text{-cym})Ru(P\text{-pta})Cl_2]$ where pta is 1,3,5-triaza-7-phospha-tricyclo-[3.3.1.1]decane (**RAPTA-C**),[64] exhibits only a low activity *in vitro* but it is active *in vivo*, where it inhibits lung metastases in Cytometric Bead Array (CBA) mice, analogously to **NAMI-A**.[65] Aquation seems to be the activating step in its cytotoxic mechanism,[66] Figure 1.9 upon which is believed to induce a local kink in double-stranded DNA (dsDNA) via intrastrand cross-linking of adjacent guanine bases (1,2-GG).[67]
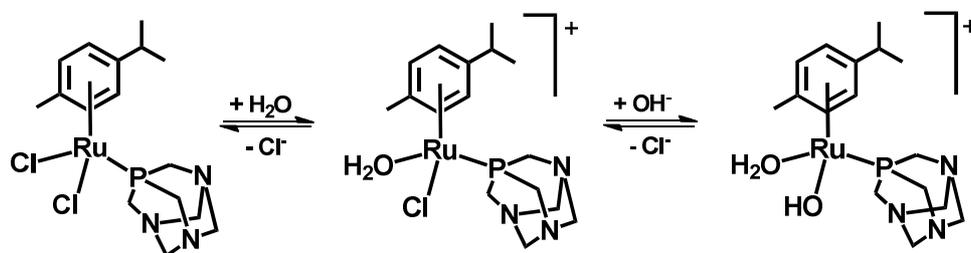
Figure 1.9. Hydrolysis of **RAPTA-C** in water.

1.1.3.1.3 The XY Chelating Ligand

It seems to be highly advantageous for anticancer activity and aqueous solution stability of $[(\eta^6\text{-arene})Ru(X)(Y)(Z)]^{n+}$ complexes, that the monodentate X and Y ligands are replaced by a bidentate chelating group, usually represented as XY. Generally, complexes containing chelating ligands tend to be more active than those containing only monodentate ligands.[68] Several studies on structure activity relationships (SARs) with regard to changes in the nature of the donor atoms in the XY chelating ligand have been done. When XY is changed from ethylenediamine (en) to the anionic acetylacetonate (acac), the rate and extent of the hydrolysis of the leaving group (Z) are considerably increased.[69] The chelate ligand is also known to determine the rate of binding to DNA nucleobases and more dramatically, to change the selectivity for them. This feature is believed to be directly related to the ability to inhibit cancer cell growth *in vitro*. For example, when the chelating ligand is the hydrogen bond acceptor acac, the overall affinity for adenine bases (A) appears to be greater than that for guanine (G) bases,[70] as opposed to the affinity for G when the chelating ligand is en. The evidence points towards the crucial role that N–H groups play in the stabilisation of adducts with G bases via H-bonding,[71] just as the oxygen atoms (in acac) can form favourable H-bonds (Figure 1.10) with the C_6NH_2 group of A bases. Such H-bonding is also thought to play a role in the recognition of DNA by cisplatin.[72] Moreover, SARs reported for Ru^{II} arene complexes containing N,N' chelating ligands have shown that whereas the species containing en showed an increased cytotoxic potency, complexes containing tetramethylethylenediamine (TMEDA) were inactive.[69] Steric effects of the methyl groups as well as lack of H-bonding capability may contribute to the loss of activity of the TMEDA derivative.
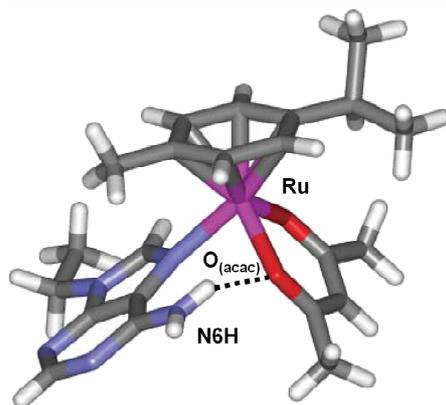
Figure 1.10. Molecular model of [(η[6]-*p*-cym)Ru(acac)(9-EtA-*N7*)][+].[63] The hydrogen bond between acac O and A N6H is represented by a dashed line.[73]

In general, good cytotoxic activity is observed when en is replaced by aromatic amines such as 1,2-diaminobenzene (dab); the IC_{50} values determined for a series of Ru[II] complexes were in the range between 7 and 32 μM.[69] Furthermore, other non-amine N,N'-chelating ligands have also been investigated and the results show that 2,2'-bipyridine (bpy) complexes tend to be non-cytotoxic towards A2780 cells.[69] A similar behaviour was observed for some 1,10-phenanthroline (phen) complexes (with either neutral or negatively charged substitutents), which showed either poor or no activity. This evidence points to the important roles that N–H groups on the bound N atoms of the chelated ligand can play.

1.1.3.1.4 The Z Leaving Group

The leaving group (Z), which is typically a halogen, plays a crucial role in the control of the activation of Ru[II] arene complexes given that with its release from the metal centre, a vacant site for coordinating potential biomolecules is readily made available. Initial studies showed that the substitution of the chloride leaving group by other halides, such as iodide, seemed to have only a small effect on the cytotoxicity.[68] However, recent reports have discussed the correlation between the rate (and extent) of hydrolysis and the cytotoxicity of Ru[II] arene complexes with various chelating

ligands.[74] The evidence suggests that a combination of fast hydrolysis rates and high reactivity usually leads to non-cytotoxic complexes, similarly very slow hydrolysis rates and chemical inertness leads to low *in vitro* cytotoxicity.[75] An exception to this observation was found when the leaving group is not a halide but a thiophenolate.[74] This compound was found active, displaying an IC_{50} value of 23 µM against A2780 human ovarian cancer cells, despite its inertness towards hydrolysis. It was then suggested that the mechanism of action could probably involve the oxidation of the thiolate group, followed by the hydrolysis of the sulfenato thus formed.

1.2   Photochemistry in Medicine

Modern phototherapy involves the use of specific wavelengths of light, both for the treatment of diseases and/or as diagnostic tools.[76] If light therapy is combined with the effect of a drug for the treatment of a disease, it is then commonly known as photochemotherapy. Historically, the concept of combining radiation with a chemical agent dates back to 3000 years ago when the therapeutic effect of sunlight activation of chromophore-containing plants was used for repigmentation of vitiligo in both ancient Egypt and India.[77] Nowadays, the most commonly known form of photochemotherapy is photodynamic therapy (PDT). It involves a tumour-localised photosensitiser (PS) which when appropriately irradiated by visible light, converts triplet oxygen ($^3O_2$) into cytotoxic reactive singlet oxygen species ($^1O_2$). This latter are known to attack key structural entities within the targeted cells and ultimately resulting in necrosis or apoptosis.[78] Typically employed photosensitisers are porphyrins or porphyrin-like molecules.[79] *Photofrin*, the first approved photosensitiser, is a mixture of haematoporphyrin derivatives of varying linkages, lengths, and stereochemistries with an absorption maximum around 630 nm. *Foscan*,

a photofrin derivative, requires a lower light dose to achieve similar responses and has a shorter retention time in the body,[80] Figure 1.11. The lanthanide complex lutetium texaphryn, *Lutrin*, has also been approved for use in cervical, prostate, and brain tumours along with other several potential new photosensitisers now in clinical trials.[76]
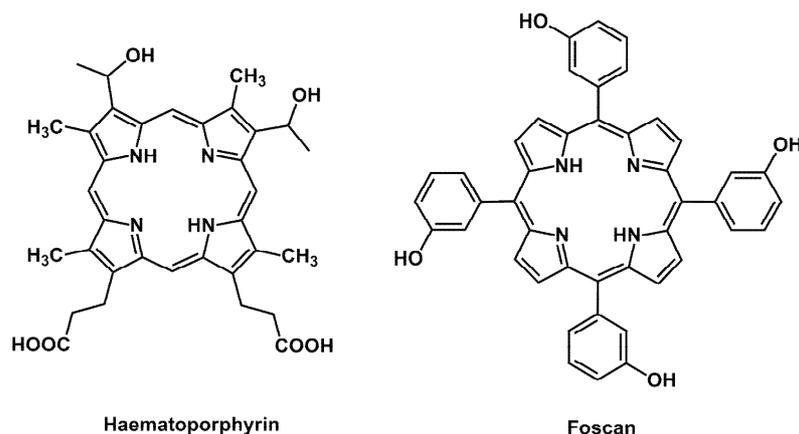
Figure 1.11. Two porphyrin-based drugs in clinical use for photodynamic therapy (PDT).

While using photochemistry in medicine, there are practical considerations to take into account. Whilst irradiation of the skin is easily achievable, internal organs are less accessible. Recent advances in laser technology have helped to overcome this limitation;[81] and it is now possible to irradiate various organs such as lungs, cervix, colon and oesophagus. The rapid development in sophisticated fibre optic technologies[82] could soon allow difficult areas of the body to be reached. Additionally, a large difference between the therapeutic effect of the drug in the presence and in absence of irradiation is desirable, mainly (but not only) to limit unwanted side-effects. The energy of activation should ideally lie within a phototherapeutic window of 620–850 nm[83] and preferably would also be in the range needed to achieve the optimal quantum yield or efficiency of the photochemical process. Short wavelength irradiation such as UVA (λ = 320–400 nm) and UVB (λ =

290–320 nm) are not recommended for therapeutic uses, not only because of their poor penetration through mammalian tissues,[84] Figure 1.12 but mainly because they induce extensive damage to tissues, DNA, and proteins.[85,86] Higher wavelengths are less damaging but penetration through tissues is poor below 600 nm (as a result of absorption by biomolecules such as haemoglobin, cytochromes, and melanin as well as scattering from organelles).[84]
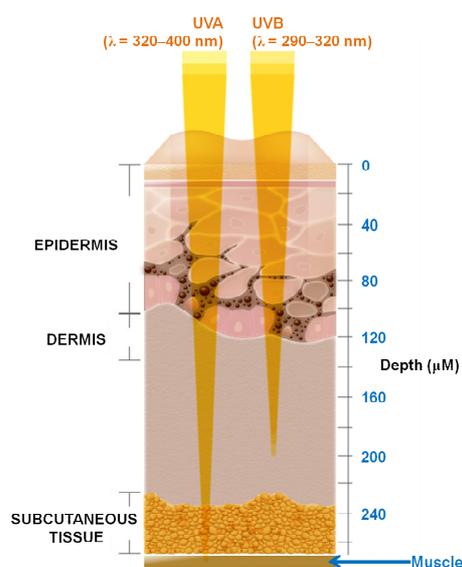
Figure 1.12. The skin penetration depths of UVA (λ = 320–400 nm) and UVB (λ = 290–320 nm) irradiation.[87]

1.2.1   Photoactive Metal Complexes for Biological Applications

In the development of metal complexes as anticancer agents, one design concept receiving increasing interest in recent years is that of photoactivation. For example, titanium dioxide (TiO_2) has been studied extensively for its photochemical properties[88] and it has been reported that it can kill cancer cells when irradiated by UVA.[89] It was recently shown how a mononuclear citrate Ti^{IV} complex is able to undergo photoreduction (with UVA irradiation) to Ti^{III}; this species is a strong reductant which can initiate free radical reactions in cells.[90] Vandium complexes are also being investigated for their potential use as PDT agents.[91] For example, oxo-

vanadium(IV) complexes containing the heterocyclic bases dpq where dpq is dipyrido[3,2-*d*:2',3'-*f*]quinoxaline and dppz is dipyrido[3,2-*d*:2',3'-*c*]phenazine, Figure 1.13 have been shown to exhibit DNA cleavage mechanisms involving both singlet oxygen and hydroxyl radicals when activated at 365 nm, with only the OH˙ radical mechanism operating when irradiated with near-infrared (NIR) light.[92]
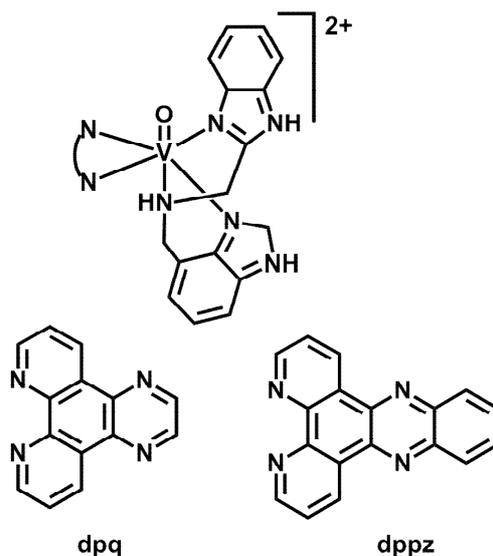
Figure 1.13. Structures of oxovanadium(IV) complexes containing the heterocyclic bases dpq (dipyrido[3,2-*d*:2',3'-*f*]quinoxaline) and dppz (dipyrido[3,2-*d*:2',3'-*c*]phenazine) which can photocleave DNA.[92]

The photochemistry of complexes of the type [M(CO)$_4$(α-diimine)] where M = Cr, Mo, and W has also been investigated.[93] They undergo photochemical substitution of an axial CO ligand when irradiated with UV or visible light. Although such studies have not yet targeted medical applications, controlled CO release can be an efficient and advantageous way of promoting cell death.[94] Furthermore, it has also been shown how UVA and blue light can be successfully employed to activate Pt azide complexes[95] and produce highly cytotoxic compounds which, in contrast, are inactive in the dark. More recently, a novel *trans*-diimine diazido platinum(IV) complex, *trans,trans,trans*-[Pt(N$_3$)$_2$(OH)$_2$(Py)$_2$] where Py is pyridine, which is potently

cytotoxic towards cancer cells using low doses of visible light, has been reported.[96] The results also suggest that the presence of planar σ-donor/π-acceptor pyridine ligands in the system can have a critical effect not only on the photoactivation pathways, but also on the biological activity.

1.2.2   Photoactivatable Ru^{II} (poly)Pyridyl Complexes

The fact that photochemical activation is a very attractive way to achieve precise spatial and temporal control of the biological action of transition metal complexes that behave as inactive drugs in the dark[97] has been recently coupled to the tremendous potential of Ru^{II} (poly)pyridyl complexes as diagnostic and therapeutic agents.[98,99,100] The basic approach involves the modification of the Ru^{II} molecules by introducing a group that can be selectively cleaved by the absorption of light, thus releasing it. The strategy requires breaking of a bond by the use of either high energy UVA ($\lambda \approx 300$ nm) or visible ($\lambda \approx 400$ nm) photons. Ru^{II} (poly)pyridyl complexes present a strong metal-to-ligand charge transfer (MLCT) band in the visible region.[101] It has been shown that light absorption can populate the triplet state that is thermally activated to a dissociative d−d state, which usually leads to photoproducts with very fast kinetics.[102,103] The photochemistry of the bis-arene species such as [(η^6-C$_6$H$_6$)Ru(η^5-C$_5$H$_5$)]$^+$ has been investigated.[104] It was found that photosubstitution of the arene is the dominant reaction pathway where benzene is released. Irradiation in aqueous solution of the Ru^{II} complexes of the form [(η^6-arene)Ru(L)$_3$]$^{2+}$ where arene = benzene, toluene, or isopropyltoluene; and L = NH$_3$ or H$_2$O, was found to lead in each case to the aquation of the arene as the only observable photoreaction to produce [Ru(OH$_2$)$_3$L$_3$]$^{2+}$ plus the corresponding free arene.[105] Other investigations have reported that [(η^6-arene)Ru(P(n-Bu)$_3$)Cl$_2$] dissolved in another arene undergoes

exchange of coordinated and solvent arenes when irradiated with UVA.[106] A few

dinuclear complexes based on the typical half-sandwich motif have been also studied.

Amongst them, the complex $[\{(\eta^6\text{-ind})Ru(Cl)\}_2(\mu\text{-2,3-dpp})_2]^{2+}$ where dpp is 2,3-

bis(2-pyridyl)pyrazine, Figure 1.14 was found to bind to DNA in the dark, *via* a

hydrolysis pathway that generates a reactive aqua intermediate (as observed in

analogous mononuclear Ru^{II} arene complexes).[107]
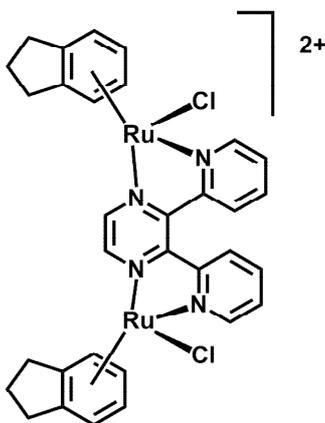
Figure 1.14. Structure of the cation in the photoactivatable dinuclear Ru^{II} arene complex $[\{(\eta^6\text{-ind})Ru(Cl)\}_2(\mu\text{-2,3-dpp})_2][PF_6]_2$.[107]

In vitro DNA transcription experiments on $[\{(\eta^6\text{-ind})Ru(Cl)\}_2(\mu\text{-2,3-dpp})_2]^{2+}$ suggest

that the adduct formed in the dark inhibits RNA synthesis by a RNA polymerase only

to a small extent. In contrast, the adduct formed between DNA and the *pre-irradiated*

complex inhibits the DNA transcription more efficiently, attributed to interstrand

crosslinkings. Interestingly, enhanced interstrand crosslinkings were also observed

with subsequent irradiation of DNA modified by the dinuclear complex in the dark.

The increased reactivity has been attributed to the indane (ind) arene loss upon

irradiation. Moreover, a number of biologically relevant biomolecules have also been

coupled to non-arene Ru^{II} metal complexes to produce species that can be

phototriggered and exert their effect when free. This general principle has been

applied in the development of Ru^{II} (poly)pyridyl complexes as inorganic photolabile

caging groups for several amine-containing neurotransmitters.[108,109,110] In one of these systems, two molecules of γ-aminobutyric acid (GABA) are coordinated to a Ru^{II} centre supported by two 2,2'-bipyridine (bpy) ligands to form the caged complex $[Ru(bpy)_2L_2]^{2+}$ where L is GABA, Figure 1.15, or also one of several amine compounds including serotonin, tryptamine, butylamine, and tyramine.
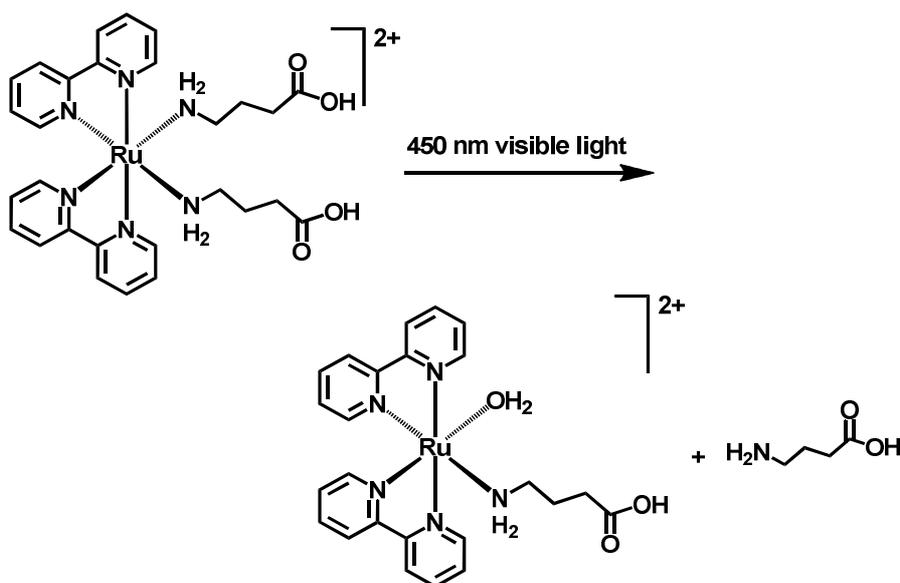
Figure 1.15. Selective photorealese of a γ-aminobutiric acid (GABA) molecule from a Ru^{II} (poly)pyridyl complex with visible light.[108,109,110]

Other examples also include the photoactivation of Ru^{II} complexes with highly π-deficient (poly)azaaromatic ligands like 1,4,5,8-tetraazaphenanthrene (tap) or 1,4,5,8,9,12-hexaazatriphenylene (hat). These complexes led to covalent adducts with functional groups on DNA model nucleobases.[111] Similar photoactivatable Ru^{II} (poly)pyridyl complexes are also able to form covalent adducts with nucleobases upon irradiation.[111]

1.3 Ru^{II} Arene Complexes as Catalytic Agents

Aqueous-phase organometallic catalysis has attracted much recent interest due to the relatively easy recycling of water-soluble catalysts in aqueous-organic biphasic reaction mixtures.[112] Some initial studies have focussed on the catalytic properties of the various cluster species obtained from organometallic Ru^{II} species such as $[(\eta^6\text{-arene})\text{RuCl}_2]_2$ under elevated H_2 pressure.[113] More recently, Ru^{II} arene complexes are finding increasing application in organic synthesis[114] either as catalysts, or as catalyst precursors.[115] Some Ru^{II} arene complexes with bidentate N,N' donor ligands are known to catalyse transfer hydrogenation reactions of ketones and imines;[116,117] they are active in Lewis acid-catalysed Diels–Alder reactions,[118] and some are even active catalysts for the isomerisation of allylic alcohols.[119] The chemistry of transition metal compounds containing the formato ligand bonded in a monodentate fashion is of considerable interest. They offer the potential of participating in the catalysis of both the water-gas shift reaction and the conversion of CO_2 into formic acid.[120] These formato species also participate in the decomposition of formic acid to hydrogen and carbon dioxide[121] and can be usually prepared by reaction of CO_2 into a transition metal-hydrogen bond (a type of reaction showing some similarity to olefin insertion, Eq. 1). Some transition metal-formato complexes have also been obtained previously by metathesis involving formate ion, Eq. 2.[122,123,124]

$$\text{MH} + CO_2 \rightleftharpoons \text{MOCOH} \qquad \text{(Eq. 1)}$$

$$\text{MX} + \text{OCHO}^- \rightleftharpoons \text{MOCHO} + X^- \quad \text{(Eq. 2)}$$

The reverse reaction in Eq. 1, $\text{MOCOH} \rightleftharpoons \text{MH} + CO_2$, is of interest because hydrido species can be obtained by CO_2 elimination from Ru^{II} arene formato complexes.[125,126] One of the critical steps in such mechanisms is believed to involve progressive

coordination mode of the arene ligand from η^6 to η^4 to η^2, and complete loss of the arene ligand in some cases[127] (which may be an unwanted process). Of currently prime importance in the field of biocatalysis, is the increasing demand for enantiopure biologically active compounds and their precursors.[128,129] One example is the (re)generation of the coenzyme 1,4-NADH, which is the reduced form of nicotinamide adenine dinucleotide (NAD^+), Figure 1.16.
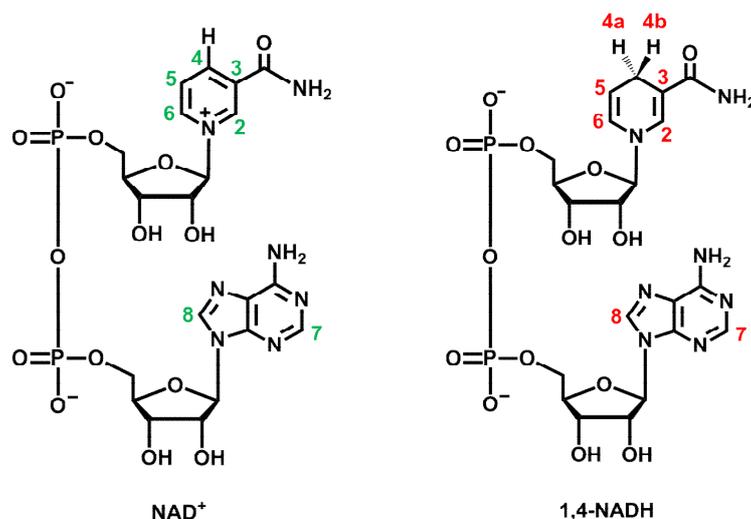
Figure 1.16. Nicotinamide adenine dinucleotide (NAD^+) and the reduced form of the coenzyme 1,4-NADH.

Current interest is also generated by the observation that NAD^+ content in cancer cells is equal or higher than in normal cells.[130] An interference with this distribution could lead to either cell death or a stimulated cell growth. In living cells, NAD^+ and its phosphorylated and reduced forms (NADP, $NADP^+$, NADH and NADPH) have central roles in cellular metabolism and energy production as hydride-accepting and hydride-donating coenzymes.[131] In glucose fermentation for instance, NAD^+ functions as the hydride acceptor in a step catalysed by glyceraldehyde 3-phosphate dehydrogenase, producing NADH and diphosphoglycerate. Similarly, NADH functions as the hydride donor for alcohol dehydrogenase,[132,133] which is required for

the reduction of acetaldehyde to ethanol, regenerating NAD$^+$.[134] Conversion of NAD$^+$ to NADH by enzymatic,[135] photo- or electrochemical[136] methods has been extensively studied. Various transition metal hydrides have been studied as catalysts for the regioselective reduction of NAD$^+$ and NAD$^+$-models to the corresponding 1,4-NADH derivatives.[137] Some Rh^{III} pentamethylcyclopentadienyl complexes[138] and Ru^{II} arene complexes have shown to catalyse the reduction of NAD$^+$ in the presence of formate as the hydride source.[139] This reduction is regioselective, giving the biologically relevant 1,4-NADH isomer.[140]

1.4 Aims

The general aim of this Thesis is concerned with the rational design, synthesis and characterisation of three new families of half-sandwich Ru^{II} arene anticancer complexes which can be activated by different modes. The individual aims can be rationalised as follows.

a) To gain an understanding of the aqueous solution chemistry and ability to kill cancer cells of a series of Ru^{II} arene halido complexes in relation to their chemical structures.

b) To investigate the wavelength-dependent (photo)chemical reactivity of a series of Ru^{II} arene pyridine or pyridine-derivative complexes as novel types of photoactivatable anticancer drugs.

c) To explore the possibility of (photo)triggering hydride-transfer reactions using biologically-relevant substrates and Ru^{II} arene halido complexes or photoactivatable Ru^{II} arene pyridine or pyridine-derivative complexes.

d) To investigate the potential of bifunctional Ru^{II} arene complexes with constitutional similarity to cisplatin as cytotoxic agents.

1.5   References

[1]. Brown, D. A. in *Metal Ions Biol. Syst.*, Siegel, H. (Ed.), **1982**, *14*, p 125.

[2]. (a) Phipps, D. A. *Metals and Metabolism*, Oxford University Press, Oxford, **1976**, p 63; (b) Brewer, G. J. in *Metal Ions Biol. Syst.*, Siegel, H. (Ed.), **1982**, *14*, p 57.

[3]. Sorenson, J. R. J. in *Metal Ions Biol. Syst.*, Siegel, H. (Ed.), **1982**, *14*, p 77.

[4]. Gielen, M.; Tiekink, R. T. (Eds.), *Metallotheurapeutic drugs and metal-based diagnostic agents*, **2005**, John Wiley and Sons, Inc., England.

[5]. Ehrlich, P. *Wiener Medizin. Woch.*, **1922**, *61*, 14–19.

[6]. Orvig, C.; Abrams, M. J. *Chem. Rev.*, **1999**, *99*, 2201–2203.

[7]. Yung, C. Y. *Pharmacol. Biochem. Behav.*, **1984**, *21 Suppl. 1*, 41–47.

[8]. Shaw, C. F. III *Chem. Rev.*, **1999**, *99*, 2589–2600.

[9]. Thompson, K. H.; McNeill, J. H.; Orvig, C. *Chem. Rev.*, **1999**, *99*, 2561–2571.

[10]. Goldstein, M.; Barton, J. K.; Goldberg, J. M.; Kumar, C. V.; Turro, N. J. *J. Am. Chem. Soc.*, **1986**, *108*, 2081–2088.

[11]. Guo, Z.; Sadler, P. J. *Adv. Inorg. Chem.*, **1999**, *49*, 183–306.

[12]. Guo, Z.; Sadler, P. J. *Angew. Chem. Int. Ed.*, **1999**, *38*, 1512–1531.

[13]. Figures taken from the website of the International Agency for Research on Cancer of the World Health Organisation, Project GLOBOCAN 2008, *Cancer Incidence and Mortality Worldwide in 2008*, http://globocan.iarc.fr/; accessed September 2010.

[14]. Weiss, R. B.; Christian, M. C. *Drugs*, **1993**, *46*, 360–377.

[15]. (a) Fuertes, M. A.; Alonso, C.; Pérez, J. *M. Chem. Rev.*, **2003**, *103*, 645–662; (b) Kelland, L. R.; Sharp, S. Y.; O'Neill, C. F.; Raynaud, F. I.; Beale, P. J.; Judson, I. R. *J. Inorg. Biochem.*, **1999**, *77*, 111–115.

[16]. Rosenberg, B.; Camp, L. V. *Nature*, **1965**, *205*, 698–699.

[17]. Rosenberg, B.; Camp, L. V.; Trosko, J. E.; Mansour, V. H. *Nature*, **1969**, *222*, 385–386.

[18]. Rosenberg, B.; Camp, L. V. *Cancer Res*., **1970**, *30*, 1799–1802.

[19]. Jung, Y.; Lippard, S. J. *Chem. Rev*., **2007**, *107*, 1387–1407.

[20]. Cai, S.; Xie, Y.; Davies, N. M.; Cohen, M. S.; Forrest, M. L. *Therapeutic Delivery*, **2010**, *1*, 237–245; (b) Weiss, R. B.; Christian, M. C. *Drugs*, **1993**, *46*, 360–377.

[21]. Chew, H. K.; Doroshow, J. H.; Frankel, P.; Margolin, K. A.; Somlo, G.; Lenz, H.-J.; Gordon, M.; Zhang, W.; Yang, D.; Russell, C.; Spicer, D.; Synold, T.; Bayer, R.; Hantel, A.; Stiff, P. J.; Tetef, M. L.; Gandara, D. R.; Albain, K. S. J. *Clin. Oncology*, **2009**, *27*, 2163–2169.

[22]. (a) Fichtinger-Schepman, A. M. J.; van der Veer, J. L.; den Hartog, J. H. J.; Lohman, P. H. M.; Reedijk, J. *Biochemistry*, **1985**, *24*, 707−713; (b) Pelmenschikov, A.; Zilberberg, I.; Leszczynski, J.; Famulari, A.; Sironi, M.; Raimondi, M. *Chem. Phys. Letters*, **1999**, *314*, 496−500.

[23]. Caradonna, J. P.; Lippard, S. J.; Gait, M. J.; Singh, M. *J. Am. Chem. Soc*., **1982**, *104*, 5793−5975.

[24]. Hambley, T. W. *Drug Des. Deliv*., **1998**, *3*, 153−158.

[25]. (a) Silverman, A. P.; Bu, W.; Cohen, S. M.; Lippard, S. J. *J. Biol. Chem.*, **2002**, *277*, 49743–49749; (b) Ohndorf, U.-M.; Rould, M. A.; He, Q.; Pabo, C. O.; Lippard, S. J. *Nature*, **1999**, *399*, 708–712.

[26]. Huang, J. C.; Zamble, D. B.; Reardon, J. T.; Lippard, S. J.; Sancar, A. *Proc. Natl. Acad. Sci. U.S.A.*, **1994**, *91*, 10394−10398.

[27]. Zamble, D. B.; Jacks, T.; Lippard, S. J. *Proc. Natl. Acad. Sci. U. S. A.*, **1998**, *95*,

6163−6168.

[28]. Image taken from Prof Lippard's Lab Research Gallery, http://web.mit.edu/lippardlab/gallery.html; accessed September 2010.

[29]. Wong, E.; Giandomenico, C. M. *Chem. Rev.*, **1999**, *99*, 2451−2466.

[30]. Pieper, T.; Borsky, K.; Keppler, B. K. in *Topics in Biological Inorganic Chemistry, Vol. 1*, M. J. Clarke; Sadler, P. J. (Eds.), Springer Verlag, Berlin, **1999**, p 171.

[31]. Sun, R. W.-Y.; Li, C. K.-L.; Ma, D. K.; Yan, J. J.; Lok, C. N.; Leung, C. H.; Zhu, N.; Che, C.-M. *Chem. Eur. J.*, **2010**, *16*, 3097–3113.

[32]. Sava, G.; Gagliardi, R.; Cocchietto, M.; Clerici, K.; Marrella, I.; Alessio, E.; Mestroni, G.; Milanino, R. *Pathol. Oncol. Res.*, **1998**, *4*, 30−36.

[33]. (a) Cocchietto, M.; Sava, G. *Pharmacol. Toxicol.* **2000**, *87*, 193−197.; (b) Zorzet, S.; Sorc, A.; Casarsa, C.; Cocchietto, M.; Sava, G. *Met.-Based Drugs*, **2001**, *8*, 1−7.

[34]. (a) Sava, G.; Bergamo, A. *Int. J. Oncol.*, **2000**, *17*, 353−365; (b) Gagliardi, R.; Sava, G.; Pacor, S.; Mestroni, G.; Alessio, E. *Clin. Exp. Metastasis*, **1994**, *12*, 93−100; (c) Magnarin, M.; Bergamo, A.; Carotenuto, M. E.; Zorzet, S.; Sava, G. *Anticancer Res.*, **2000**, *20*, 2939−2944.

[35]. Rademaker-Lakhai, J. M.; Van den Bongard, D.; Pluim, D.; Beijnen, J. H.; Schellens, J. H. *Clin. Cancer Res.*, **2004**, *10*, 3717−3727.

[36]. Jakupec, M. A.; Arion, V. B.; Kapitza, S.; Reisner, E.; Eichinger, A.; Pongratz, M.; Marian, B.; Graf von Keyserlingk, N.; Keppler, B. K. *Int. J. Clin. Pharmacol. Ther.*, **2005**, *43*, 595−596.

[37]. Kelman, A. D.; Clarke, M. J.; Edmonds, S. D.; Peresie, H. J. *J. Clin. Hematol. Onc.*, **1977**, *7*, 274−288.

[38]. Clarke, M. J.; Bitler, S.; Rennert, D.; Buchbinder, M.; Kelman, A. D. *J. Inorg. Biochem.*, **1980**, *12*, 79−87.

[39]. Crabtree, R. H. *The Organometallic Chemistry of Transition Metals*, 4th. Ed., **2005**, John Wiley and Sons. Inc., Hoboken, N.J., U.S.A.

[40]. Guo, M.; Guo, Z.; Sadler, P. J. *J. Biol. Inorg. Chem.*, **2001**, *6*, 698−707.

[41]. Kröger, N.; Kleeberg, U. R.; Mross, K.; Edler, L.; Saß, G.; Hossfeld, D. K. *Onkologie*, **2000**, *23*, 60−62.

[42]. Mross, K.; Robben-Bathe, P.; Edler, L.; Baumgart, J.; Berdel, W. E.; Fiebig, H.; Unger, C. *Onkologie*, **2000**, *23*, 576−579.

[43]. Claffey, J.; Hogan, M.; Muller-Bunz, H.; Pampillon, C.; Tacke, M.; *Chem. Med. Chem.*, **2008**, *3*, 729−731.

[44]. Fichtner, I.; Behrens, D.; Claffey, J.; Gleeson, B.; Hogan, M.; Wallis, D.; Weber, H.; Tacke, M. *Lett. Drug Des. Discovery*, **2008**, *5*, 489−493.

[45]. Allen, O. R.; Gott, A. L.; Hartley, J. A.; Hartley, J. M.; Knox, R. J.; McGowan, P. C. *Dalton Trans.*, **2007**, 5082−5090.

[46]. (a) Sweeney, N. J.; Mendoza, O.; Mueller-Bunz, H.; Pampillon, C.; Rehmann, F.-J. K.; Strohfeldt, K.; Tacke, M. *J. Organomet. Chem.*, **2005**, *690*, 4537−4544; (b) Kelter, G.; Sweeney, N. J.; Strohfeldt, K.; Fiebig, H.-H.; Tacke, M. *Anti-Cancer Drugs*, **2005**, *16*, 1091−1098.

[47]. Köpf-Maier, P.; Köpf, H. *Metal Compounds in Cancer Therapy*, S. P. Fricker (Ed.); Chapman and Hall, London, **1994**, p 109.

[48]. Köpf-Maier, P.; Köpf, H. *Chem. Rev.*, **1987**, *87*, 1137−1152.

[49]. Köpf-Maier, P.; Köpf, H. *Struct. Bond.*, **1988**, *70*, 103−194.

[50]. Top, S.; Vessieres, A.; Leclercq, G.; Quivy, J.; Tang, J.; Vaisserman, J.; Huche, M.; Jaouen, G. *Chem. Eur. J.*, **2003**, *9*, 5223−5236.

[51]. (a) van Rijt, S. H.; Mukherjee, A.; Pizarro, A. M.; Sadler, Peter J. *J. Med. Chem.*, **2010**, *53*, 840−849; (b) Peacock, A. F. A.; Habtemariam, A.; Moggach, S. A.; Prescimone, A.; Parsons, S.; Sadler, P. J. *Inorg. Chem.*, **2007**, *46*, 4049−4059; (c) Hanif, M.; Nazarov, A. A.; Hartinger, C. G.; Kandioller, W.; Jakupec, M. A.; Arion, V. B.; Dyson, P. J.; Keppler, B. K. *Dalton Trans.*, **2010**, *39*, 7345−7352.

[52]. Clarke, M. J. *Metal Complexes in Cancer Chemotherapy*, **1993**, (Keppler, B. K., Ed.), VCH Verlagsgesellschaft, Weinheim, and VCH Publishers, New York, p 129.

[53]. Sheldrick,W. S.; Heeb, S. *Inorg. Chim. Acta*, **1990**, 168, 93−100.

[54]. (a) Sheldrick, W. S.; Hagen-Eckhard, H. S.; Heeb, S. *Inorg. Chim. Acta*, **1993**, *206*, 15−21; (b) Korn, S.; Sheldrick, W. S. *Inorg. Chim. Acta*, **1997**, 254 , 85−91; (c) Korn, S.; Sheldrick, W. S. *J. Chem. Soc. Dalton Trans.*, **1997**, 2191−2199; (d) Annen, P.; Schildberg, S.; Sheldrick, W. S. *Inorg. Chim. Acta*, **2000**, *307*, 115−124.

[55]. Wang, F.; Habtemariam, A.; van der Geer, E. P. L.; Fernández, R.; Melchart, M.; Deeth, R. J.; Aird, R.; Guichard, S.; Fabbiani, F. P. A.; Lozano-Casal, P.; Oswald, I. D. H.; Jodrell, D. I.; Parsons, S.; Sadler, P. J. *Proc. Natl. Acad. Sci. U.S.A.*, **2005**, *102*, 18269–18274.

[56]. Wang, F.; Chen, H. M.; Parsons, S.; Oswald, L. D. H.; Davidson, J. E.; Sadler, P. J. *Chem. Eur. J.*, **2003**, *9*, 5810–5820.

[57]. Yan, Y. K.; Melchart, M.; Habtemariam, A.; Sadler, P. J. *Chem. Commun.*, **2005**, 4764–4776.

[58]. Liu, H. K.; Wang, F. Y.; Parkinson, J. A.; Bella, J.; Sadler, P. J. *Chem. Eur. J.*, **2006**, *12*, 6151−6165.

[59]. (a) Nováková, O.; Nazarov, A. A.; Hartinger, C. G.; Keppler, B. K.; Brabec, V. *Biochem. Pharmacol.*, **2009**, *77*, 364−374; (b) Nováková, O.; Malina, J.; Suchankova,

T.; Kasparkova, J.; Bugarcic, T.; Sadler, P. J.; Brabec, V. *Chem. Eur. J.*, **2010**, *16*, 5744−5754.

[60]. Bugarcic, T.; Nováková, O.; Halamikova, A.; Zerzankova, L.; Vrana, O.; Kasparkova, J.; Habtemariam, A.; Parsons, S.; Sadler, P. J.; Brabec, V. *J. Med. Chem.*, **2008**, *51*, 5310–5319.

[61]. Grguric-Sipka, S.; Stepanenko, I. N.; Lazic, J. M.; Bartel, C.; Jakupec, M. A.; Arion, V. B.; Keppler, B. K. *Dalton Trans.*, **2009**, 3334–3339.

[62]. Chen, Y.; Guo, Z. J.; Parsons, S.; Sadler, P. J. *Chem. Eur. J.*, **1998**, *4*, 672–676.

[63]. Scolaro, C.; Bergamo, A.; Brescacin, L.; Delfino, R.; Cocchietto, M.; Laurenczy, G.; Geldbach, T. J.; Sava, G.; Dyson, P. J. *J. Med. Chem.*, **2005**, *48*, 4164–4171.

[64]. Süss-Fink, G. *Dalton Trans.*, **2010**, *39*, 1673−1688.

[65]. Dyson, P. J *Chimia*, **2007**, *61*, 698−703.

[66]. Scolaro, C.; Hartinger, C. G.; Allardyce, C. S.; Keppler, B. K.; Dyson, P. J. *J. Inorg. Biochem.*, **2008**, *102*, 1743–11748.

[67]. Gossens, C.; Tavernelli, I.; Rothlisberger, U. *J. Am. Chem. Soc.*, **2008**, *130*, 10921−10928.

[68]. Aird, R.E.; Cummings, J.; Ritchie, A. A.; Muir, M.; Morris, R.E.; Chen, H., Murdoch, P. S., Sadler, P. J.; Jodrell, D. I. *Br. J. Cancer*, **2002**, *86*, 1652−1657.

[69]. Habtemariam, A.; Melchart, M.; Fernández, R.; Parsons, S.; Oswald, I. D. H.; Parkin, A.; Fabbiani, F. P. A.; Davidson, J. E.; Dawson,A.; Aird, R. E.; Jodrell, D. I.; Sadler, P. J. *J. Med. Chem.*, **2006**, *49*, 6858−6868.

[70]. Chen, H.; Parkinson, J. A.; Morris, R. E.; Sadler, P. J. *J. Am. Chem. Soc.*, **2003**, *125*, 173–186.

[71]. Liu, H. K.; Berners-Price, S. J.; Wang, F. Y.; Parkinson, J. A.; Xu, J.; Bella, J.;

Sadler, P. J. *Angew. Chem.-Int. Ed.*, **2006**, *45*, 8153–8156.

[72]. Reedijk, J. *Chem. Commun.*, **1996**, 801–806.

[73]. Fernández, R.; Melchart, M.; Habtemariam, A.; Parsons, S.; Sadler, P. J. *Chem. Eur. J.*, **2004**, *10*, 5173–5179.

[74]. Wang, F.; Habtemariam, A.; van der Geer, E. P. L.; Fernández, R.; Melchart, M.; Deeth, R. J.; Aird, R.; Guichard, S.; Fabbiani, F. P. A.; Lozano-Casal, P.; Oswald, I. D. H.; Jodrell, D. I.; Parsons, S.; Sadler, P. J. *Proc. Natl. Acad. Sci. U.S.A.*, **2005**, *102*, 18269–18274.

[75]. (a) Peacock, A. F. A.; Sadler, P. J. *Chem. Asian J.*, **2008**, *3*, 1890–1899; (b) Dougan, S. J.; Sadler, P. J. *Chimia*, **2007**, *61*, 704–715; (c) Jamieson, E. R.; Lippard, S. J. *Chem. Rev.*, **1999**, *99*, 2467–2498.

[76]. Farrer, N. J.; Sadler, P. J. *Aust. J. Chem.*, **2008**, *61*, 669–674.

[77]. Fitzpatrick, T. B.; Pathak, M. A. *J. Invest. Dermatol.*, **1959**, *32*, 229–231.

[78]. (a) Dolmans, D. E.; Fukumura, D.; Jain, R. K. *Nat. Rev. Cancer*, **2003**, *3*, 380–387; (b) Dougherty, T. J.; Gomer, C. J.; Henderson, B. W.; Jori, G.; Kessel, D.; Korbelik, M.; Moan, J.; Peng, Q. *J. Natl. Cancer Inst.*, **1998**, *90*, 889–905.

[79]. Josefsen, L. B.; Boyle, R. W. *Metal-Based Drugs*, **2008**, 1–24.

[80]. MacDonald, I. J.; Dougherty, T. J. *J. Porphyrins Phthalocyanines*, **2001**, *5*, 105–129.

[81]. Zovinka, E. P.; Sunseri, D. R. *J. Chem. Educ.*, **2002**, *79*, 1331–1335.

[82]. (a) Celli, J. P.; Spring, B. Q.; Rizvi, I.; Evans, C. L.; Samkoe, K. S.; Verma, S.; Pogue, B. W.; Hasan, T. *Chem. Rev.*, **2010**, *110,* 2795–2838; (b) Martin, M. J.; Wickramasinghe, Y. A. B. D.; Newson, T. P.; Crowe, J. A. *Chem. & Biol. & Eng. Comput.*, **1987**, 25, 597–604; (b) Eipstein, M. *Crit. Rev. Biomed. Eng.*, **1982**, *7*, 79–120.

[83]. Szaciłowski, K.; Macyk, W.; Drzewiecka-Matuszek, A.; Brindell, M.; Stochel, G. *Chem. Rev.*, **2005**, *105*, 2647–2694.

[84]. Wan, S.; Parrish, J. A.; Anderson, R. R.; Madden, M. *Photochem. Photobiol.*, **1981**, *34*, 679–681.

[85]. (a) World Health Organisation, *Ultraviolet Radiation and the INTERSUN Programme*, http://www.who.int/uv/health/en/; (b) Matsumu, Y.; Ananthaswamy, H. N. *Toxicol. Appl. Pharmacol.*, **2004**, *195*, 298–308.

[86]. Salierno, M.; Marceca, E.; Peterka, D. S.; Yuste, R.; Etchenique, R. *J. Inorg. Biochem*, **2010**, *104*, 418−422.

[87]. Image taken (and modified) from http://clinuvel.com/sun-a-skin/sunburn ; accesed September 2010.

[88]. Fujishima, A.; Rao, T. N.; Tryk, D. A. *J. Photochem. Photobiol.*, **2000**, *1*, 1–21.

[89]. (a) Kalbacova, M.; Macak, J. M.; Schmidt-Stein, F.; Mierke, C. T.; Schmuki, P. *Phys. Status Solidi RRL*, **2008**, *2*, 194–196; (b) Xu, J.; Sun, Y.; Zhao, Y. M.; Huang, J. J.; Chen, C. M., Jiang, Z. Y. *Int. J. Photoenergy*, **2007**, *2007*, 1–7.

[90]. Paradies, J.; Crudass, J.; MacKay, F.; Yellowlees, L. J.; Montgomery, J.; Parsons, S.; Oswald, L.; Robertson, N.; Sadler, P. J. *J. Inorg. Biochem.*, **2006**, *100*, 1260–1264.

[91]. Sasmal, P. K.; Saha, S.; Majumdar, R.; Dighe, R. R.; Chakravarty, A. R. *Chem. Commun.*, **2009**, *13*, 1703–1705.

[92]. Sasmal, P. K.; Saha, S.; Majumdar, R.; Dighe, R. R.; Chakravarty, A. R. *Inorg. Chem.*, **2010**, *3*, 849–859.

[93]. Vlcek, A. *Coord. Chem. Rev.*, **2002**, *230*, 225–242.

[94]. Johnson, T. R.; Mann, B. E.; Clark, J. E.; Foresti, R.; Green, C. J.; Motterlini, R. *Angew. Chem.*, *Int. Ed.*, **2003**, *42*, 3722–3729.

[95]. Mackay, F. S.; Woods, J. A.; Heringova, P.; Kasparkova, J.; Pizarro, A. M.; Moggach, S. A.; Parsons, S.; Brabec, V.; Sadler, P. J. *Proc. Natl. Acad. Sci. U.S.A.* **2007**, *52*, 20743–20748.

[96]. Farrer, N. J.; Woods, J. A.; Salassa, L.; Zhao, Y.; Robinson, K. S.; Clarkson, G.; Mackay, F.; Sadler, P. J. *Angew. Chem. Int. Ed.*, **2010**, *49*, 1–5.

[97]. Farrer, N. J.; Salassa, L.; Sadler, P. J. *Dalton Trans.*, **2009**, 10690–10701.

[98]. (a) Sutin, N.; Creutz, C. *Pure. Appl. Chem.*, **1980**, *52*, 2717–2738; (b) Balzani, V.; Moggi, L.; Manfrin, M. F.; Bolletta, F.; Laurence, G. S. *Coord. Chem. Rev.*, **1975**, *15*, 321–433; (c) Hager, G. D.; Crosby, G. A. *J. Am. Chem. Soc.*, **1975**, *97*, 7031–7037.

[99]. (a) Fernández-Moreira, V.; Thorp-Greenwood, F.; Coogan, M. P. *Chem. Commun.*, **2010**, *46*, 186–202; (b) Puckett, C. A.; Barton, J. K. *Biochemistry*, **2008**, *47,* 11711–11716; (c) Zhang, C. X.; Lippard, S. J. *Curr. Opin. Chem. Biol.*, **2003**, *7*, 481–489.

[100]. Cosgrave, L.; Devocelle, M.; Forster, R. J.; Keyes, T. E. *Chem. Commun.*, **2010**, *46*, 103–105.

[101]. (a) Pinnick, D. V.; Durham, B. *Inorg. Chem.*, **1984**, *23*, 1440–1445; (b) Durham, B.; Wilson, S. R.; Hodgson, D. J.; Meyer, T. J. *J. Am. Chem. Soc.*, **1980**, *102*, 600–607; (c) Collin, J. P.; Jouvenot D.; Koizumi, M.; Sauvage, J. P. *Inorg. Chem.*, **2005**, *44*, 4693–4698.

[102]. (a) Campagna, S.; Puntoriero, F.; Nastasi, F.; Bergamini, G.; Balzani, V. *Top. Curr. Chem.*, **2007**, *280*, 117−214; (b) Wallace, W. M.; Hoggard, P. E. *Inorg. Chem.*, **1979**, *18*, 2934–2935.

[103]. (a) Ruiu, T.; Garino, C.; Salassa, L.; Pizarro, A. M.; Nervi, C.; Gobetto, R.; Sadler, P. J. *Eur. J. Inorg. Chem.*, **2010**, *8*, 1186–1195; (b) Salassa, L.; Garino, C.; Salassa, G.; Gobetto, R.; Nervi, C. *J. Am. Chem. Soc.*, **2008**, *130*, 9590–9597.

[104]. (a) Gill, T. P.; Mann, K. R. *Organometallics*, **1982**, *1*, 485−488; (b) Schrenk, J. L.; Palazzotto, M. C.; Mann, K. R. *Inorg. Chem.*, **1983**, *22*, 4047−4049; (c) McNair, A. M.; Schrenk, J. L.; Mann, K. R. *Inorg. Chem.*, **1984**, *23*, 2633−1640.

[105]. Weber, W.; Ford, P. C. *Inorg. Chem.*, **1986**, *25*, 1088−1092.

[106]. Bennett, M. A.; Smith, A. K. *J. Chem. Soc., Dalton Trans.*, **1974**, 233−241.

[107]. Magennis, S. W.; Habtemariam, A.; Nováková, O.; Henry, J. B.; Meier, S.; Parsons, S.; Oswald, I. D. H.; Brabec, V.; Sadler, P. J. *Inorg. Chem.*, **2007**, *46*, 5059−5068.

[108]. Givens, R. S.; Weber, J. F. W.; Conrad, P. G. II; Orosz, G., Donahue, S. L.; Thayer, S. A. *J. Am. Chem. Soc.*, **2000**, *122*, 2687−2697.

[109]. Zayat, L.; Calero, C.; Alborés, P.; Baraldo, L.; Etchenique, R. *J. Am. Chem. Soc.*, **2003**, *125*, 882−883.

[110]. Nikolenko, V.; Yuste, R.; Zayat, L.; Baraldo, L. M.; Etchenique, R. *Chem. Commun.*, **2005**, 1752−1754.

[111]. (a) Moucheron, C. *New J. Chem.,* **2009**, *33*, 235–245; (b) Elias, B.; Kirsch-DeMesmaeker, A. *Coord. Chem. Rev.,* **2006**, *250*, 1627–1641.

[112]. (a) Joó, F. *Aqueous Organometallic Catalysis,* Kluwer, Dordrecht, The Netherlands, **2001**; (b) Cornils, B.; Herrmann, W. A. (Eds.), *Aqueous-Phase Organometallic Catalysis*, Wiley-VCH, Weinheim, Germany, **1998**.

[113]. (a) Süss-Fink, G.; Meister, A.; Meister, G. *Coord. Chem. Rev.*, **1995**, *143*, 97–111; (b) Chérioux, F.; Maisse-Francois, A.; Neels, A.; Stoeckli-Evans, H.; Süss-Fink, G. *J. Chem. Soc., Dalton Trans.*, **2001**, 2184–2187; (c) Süss-Fink, G.; Faure, M.;

Ward, T. R. *Angew. Chem., Int. Ed.*, **2002**, *41*, 99–101.

[114]. Naota, T.; Takaya, H.; Murahashi, S. I. *Chem. Rev.*, **1998**, *98*, 2599–2660.

[115]. Davies, D. L.; Fawcett, J.; Garratt, S. A.; Russell, D. R. *J. Chem. Soc. Chem Commun.*, **1997**, 1351–1352.

[116]. Noyori, R.; Hashiguchi, S. *Acc. Chem. Res.*, **1997**, *30*, 97–102.

[117]. (a) Faller, J.; Parr, J. *Curr. Org. Chem.*, **2006**, *10*, 151–163; (b) Canivet, J.; Karmazin-Brelot, L.; Süss-Fink, G. *J. Organomet. Chem.*, **2005**, 690, 3202–3211.

[118]. (a) Carmona, D.; Vega, C.; García, N.; Lahoz, F. J.; Elipe, S.; Oro, L. A.; Lamata, M. P.; Viguri, F.; Borao, R. *Organometallics*, **2006**, *25*, 1592–1606; (b) Davenport, A. J.; Davies, D. L.; Fawcett, J.; Garratt, S. A.; Russell, D. R. *J. Chem. Soc., Dalton Trans.*, **2000**, 4432–4441; (c) Davies, D. L.; Fawcett, J.; Garratt, S. A.; Russell, D. R. *Organometallics*, **2001**, *20*, 3029–3034.

[119]. (a) Crochet, P.; Diez, J.; Fernández-Zumel, M. A.; Gimeno, J. *Adv. Synth. Catal.*, **2006**, *348*, 93–100; (b) Díaz-Alvarez, A. E.; Crochet, P.; Zablocka, M.; Duhayon, C.; Cadierno, V.; Gimeno, J.; Majoral, J. P. *Adv. Synth. Catal.*, **2006**, *348*, 1671–1679.

[120]. Behr, A. in Keim, W. (Ed.), *Catalysis in C_1 Chemistry*, Reidel, Dordrecht, **1983**, p 169.

[121]. Darensbourg, D. J.; Kudaroski, R. A. *Adv. Organomet. Chem.*, **1983**, *22*, 129–168.

[122]. Carmona, D.; Chaloupka, S.; Jans, J.; Thouvenot, R.; Venanzi, L. M. *J. Organomet. Chem.*, **1984**, *275*, 303–313.

[123]. Crespo, M.; Sales, J. *J. Organomet. Chem.*, **1987**, *322*, 405–411.

[124]. Keim, W.; Becker, J. *J. Organomet. Chem.*, **1989**, *372*, 447–451.

[125]. Darensbourg, D. J.; Fischer, M. B.; Schmidt Jr., R. E.; Baldwin, B. J. *J. Am. Chem. Soc.*, **1981**, *103*, 1297–1298.

[126]. Ogo, S.; Abura, T.; Watanabe, Y. *Organometallics*, **2002**, *21*, 2964–2969.

[127]. Howell, J. A. S.; Ashford, N. F.; Dixon, D. T.; Kola, J. C.; Albright, T. A.; Kang, S. K. *Organometallics*, **1991**, *10*, 1852–1864.

[128]. Holmann, F.; Kleeb, A.; Otto, K.; Schmid, A. *Tetrahedron Asymmetry*, **2005**, *16*, 3512–3519.

[129]. Otten, L. G.; Hollmann, F.; Arends, I. W. C. E. *Trends Biotech.*, **2010**, *28*, 46–54.

[130]. Torabi, F.; Ramanathan, K., Larsson, P. O.; Gorton, L.; Svanberg, K.; Okamoto, Y.; Danielsoon, B.; Khayyami, M. *Talanta*, **1999**, *50*, 787–797.

[131]. Belenky, P.; Bogan, K. L. *Trends Biochem. Sci.*, **2007**, *32*, 9–12.

[132]. (a) Walker, J. E. *Q. Rev. Biophys.*, **1992**, *25*, 253–324; (b) Yagi, T.; Yagi-Matsuno, A. *Biochemistry*, **2003**, *42*, 2266–2274; (c) Hirst, J. *Biochem. Soc. Trans.*, **2005**, *33*, 525–529; (d) Sazanov, L. A. *Biochemistry*, **2007**, *46*, 2275–2288.

[133]. Yakovlev, G.; Hirst, J. *Biochemistry*, **2007**, *46*, 14250–14258.

[134]. (a) Walsh, C. *Enzymatic Reaction Mechanism*, W. H. Freeman and Company, San Francisco, CA, **1979**; (b) Blankenhorn, G. in *Pyridine-Nucleotide-Dependent Dehydrogenases*; Sund, H. (Ed.); Walter de Gruyter, West Berlin, **1977**, p 185.

[135]. Groger, H.; Hummel, W.; Buchholz, S.; Drauz, K.; Van Nguyen, T.; Rollmann, C.; Husken, H.; Abokitse, K. *Org. Lett.*, **2003**, *5*, 173–176.

[136]. (a) Hollmann, F.; Schmid, A. *Biocatal. Biotransform.*, **2004**, *22*, 63–88; (b) Vuorilehto, K.; Lutz, S.; Wandrey, C. *Bioelectrochemistry*, **2004**, *65*, 1–7.

[137]. (a) Ruppert, R.; Herrmann, S.; Steckhan, E. *J. Chem. Soc., Chem. Commun.*, **1988**, 1150–1151; (b) Hembre, R. T.; McQueen, S. *J. Am. Chem. Soc.*, **1994**, *116*,

2141–2142; (c) Collman, J. P.; Wagenknecht, P. S.; Lewis, N. S. *J. Am. Chem. Soc.*, **1992**, *114*, 5665–5673; (d) Collman, J. P. *Nat. Struct. Biol.*, **1996**, *3*, 213–217; (e) Beley, M.; Collin, J.-P. *J. Mol. Catal.*, **1993**, *79*, 133–140.

[138]. Steckhan, E.; Herrmann, S.; Ruppert, R.; Dietz, E.; Frede, M.; Spika, E. *Organometallics*, **1991**, *10*, 1568–1577.

[139]. Yan, Y. K.; Melchart, M.; Habtemariam, A.; Peacock, A. F. A.; Sadler, P. J. *J. Biol. Inorg. Chem.*, **2006**, *11*, 483–488.

[140]. Westerhausen, D.; Herrmann, S.; Hummel, W.; Steckhan, E. *Angew. Chem., Int. Ed. Engl.*, **1992**, *31*, 1529–1531.

Chapter 2

Materials and Methods

Chapter 2

Materials and Methods

In this Chapter the general techniques and instrumentation used are described. More specific methods related to individual experiments are described in the appropriate Chapters. The synthesis and characterisation of the Ru^{II} dimers used for the synthesis of the mononuclear Ru^{II} arene complexes in subsequent sections is also covered here.

2.1 NMR Spectroscopy

^{1}H and ^{13}C NMR spectra were acquired in 5 mm NMR tubes at 298 K (unless otherwise stated) on either a Bruker AV-400, Bruker DRX-500, Bruker AV III 600 or Bruker AV II 700 NMR spectrometers. All data processing was carried out using XWIN-NMR version 3.6 (Bruker U.K. Ltd.). ^{1}H NMR chemical shifts were internally referenced to TMS *via* 1,4-dioxane ($\delta = 3.71$) or residual CHCl$_3$ ($\delta = 7.27$), MeOH ($\delta = 3.31$) or DMSO ($\delta = 2.50$). 1D spectra were recorded using standard pulse sequences. Typically, data were acquired with 128 transients into 16 k data points over a spectral width of 14 ppm (unless otherwise stated). 2D spectra were recorded using standard pulse-pulse sequences. COSY (COrrelation SpectroscopY) or TOCSY (TOtal Correlation SpectroscopY) were used to identify pairs of nuclei which are J-coupled to one another. Typically, data were acquired with 72 transients into 1024 k data points over a spectral width of 14 ppm (unless otherwise stated) using a relaxation delay of 1.5 s and a mixing time of 0.06 s. 2D NOESY (Nuclear Overhauser Effect SpectroscopY) was used to establish structural information resulting from through-space interactions between protons that are close in spatial proximity. Typically, the data were acquired with 72 transients into 2048 k data points

over a spectral width of 14 ppm using a relaxation delay of 1.5 s and a mixing time of

0.4–0.6 s.

2.2 Water Suppression Methods

Many experiments in this work were performed on samples in aqueous solutions

(99.9% D_2O, 5% methanol-d_4/95% D_2O or 90% H_2O/10% D_2O) so as to be of

biological relevance. The use of such aqueous solutions results in a large HOD signal

that can obscure the others in the ^{1}H NMR spectrum. To minimise this, two main

techniques were used: *presaturation* used a weak, continuous wave at the water

resonance whereas *SHAKA excitation sculpting with gradients*[1] saturated the HOD

peak by irradiating the frequency of water in between pulse sequences.

2.3 pH* Measurements

pH values were measured at ambient temperature using a Corning 240 pH meter

equipped with a micro combination KNO_3 (chloride free) electrode calibrated with

Aldrich buffer solutions of pH 4, 7, and 10. The pH* values (pH meter reading

without correction for effects of deuterium (D) on glass electrode) of NMR samples in

D_2O were measured at about 298 K directly in the NMR tube, before and after

recording NMR spectra, using the same method. The pH* values were adjusted with

dilute NaOH or HNO_3 solutions in D_2O.

2.4 Calculation of pK$_a$* Values

For determinations of pK$_a$* values (determined from solutions in D_2O), the pH* values

of the aqua complexes in D_2O were varied from *ca*. pH* 1 to 12 by the addition of

dilute NaOH or HNO_3 solutions in D_2O, and ^{1}H NMR spectra were recorded. The chemical shifts of the arene ring protons were plotted against pH[*] values. The pH[*] titration curves were fitted to the Henderson-Hasselbalch equation using ORIGIN version 8.0, with the assumption that the observed chemical shifts are weighted averages according to the populations of the protonated and deprotonated species. These pK_a^* values can be converted to pK_a values by use of the equation $pK_a = 0.929$ $pK_a^* + 0.42$ as suggested by Krezel and Bal[2] for comparison with related values in the literature.

2.5   X-ray Crystallography

Diffraction data were collected either on an Oxford Diffraction Gemini four-circle system with a Ruby CCD area detector or on a Siemens SMART three-circle system with CCD area detector equipped with an Oxford Cryosystem Cryostream Cooler. Data collection and solution of the structures were carried out by Dr Guy Clarkson from the Department of Chemistry at the University of Warwick. All structures were refined by full-matrix least squares against F^2 using SHELXL 97.[3] Details of the acquisition and solving of the individual crystal structures are explained in the corresponding chapters.

2.6   Elemental Analysis

Elemental analyses were performed by the Warwick Analytical Service which is the analytical division of Exeter Analytical (U.K. Ltd.) using an Exeter Analytical Elemental Analyser (CE440).

2.7 High Resolution Electrospray Ionisation Mass Spectrometry (HR-MS)

The HR-MS data acquisition was carried out by Dr Lijiang Song or Mr Philip Aston from the Department of Chemistry at the University of Warwick. HR-MS data were obtained on a Bruker MaXis UHR-TOF. All the samples were analysed by positive-ion ESI(+) mass spectra. Samples were prepared either in 100% H_2O or 95% MeOH/5% H_2O mixture and typically injected at 2 µL min^{-1}, nebuliser gas (N_2) 0.4 bar, dry gas (N_2) 4 L min^{-1} and dry temp 180 ºC, Funnel RF 200V, Multiple RF 200, quadrupole ion energy 4 eV, collision cell 5 eV, ion cooler RF settings, ramp from 50 to 250 V, unless otherwise stated.

2.8 Low Resolution Electrospray Ionisation Mass Spectrometry (ESI-MS)

Positive-ion ESI(+) mass spectra were obtained either on a Bruker Esquire2000 Ion Trap Spectrometer or a Bruker MicroTOF Spectrometer. Samples were prepared in either 100% H_2O or 95% MeOH/5% H_2O mixture and typically injected at 2 µL min^{-1}, nebuliser gas (N_2) 25 psi, dry gas (N_2) 9 L min^{-1}, dry temp 300 ºC, capillary – 4000 V (+ mode), end plate offset –500 V, capillary exit 70–170 V, and Oct RF 50–400 V pp, unless otherwise stated. Data were processed using DataAnalysis version 3.3 (Bruker Daltonics).

2.9 UV-vis Absorption Spectroscopy

UV-vis absorption spectra were recorded on a Cary 50-Bio spectrophotometer using 1-cm pathlength quartz cuvettes (600 µL) and a PTP1 Peltier temperature controller.

Spectra were recorded at 310 K in deionised water from 200 to 800 nm and were processed using UV-Winlab software for Windows 95.

2.10   Computational Methods

All Density Functional Theory (DFT) calculations for Chapter 3 were carried out in collaboration with Prof Robert J. Deeth from the Department of Chemistry at the University of Warwick. DFT calculations used the Amsterdam Density Functional (ADF)[4] program (version 2009.01). The coordinates of complexes used for the calculations were directly obtained from the X-ray crystal structures. Modifications to the structures were performed in Chemcraft (version 1.6). Further details of the individual calculations are described within Chapter 3.

Calculations in Chapter 4 were performed in collaboration with Dr Luca Salassa from the Department of Chemistry at the University of Warwick. Gaussian 03 (G03) program[5] employing the DFT method, Becke three parameter hybrid functional, and Lee-Yang-Parr's gradient corrected correlation functional (B3LYP)[6] were used. The LanL2DZ basis set[7] and effective core potential were used for the Ru atom and the 6-31G** basis set[8] was used for all other atoms. Geometry optimisations in the ground state (S0) and lowest-lying triplet state (T0) were performed in the gas phase and the nature of all stationary points was confirmed by normal mode analysis. The conductor-like polarisable continuum model method (CPCM)[9] with water as solvent was used to calculate the electronic structure and the excited states in solution. Fifty singlet excited states and the corresponding oscillator strengths were determined with a Time-Dependent Density Functional Theory (TD-DFT)[10] calculation. Eight triplet excited states were calculated by TD-DFT starting both from the ground-state geometry and the lowest-lying triplet state geometry. The electronic distribution and

the localisation of the singlet and triplet excited states were visualized using the electron density difference maps (EDDMs).[11] GaussSum1.05[12] was used for EDDMs calculations and for the electronic spectrum simulation.

2.11   CT-DNA Interactions in Cell-Free Media

These experiments were performed by the author (as a Visiting Researcher) in collaboration with Dr Olga Nováková in the laboratory of Prof Viktor Brabec at the Academy of Sciences of the Czech Republic, Brno as part of COST Action D39 (November−December 2009). Cisplatin was obtained from Sigma-Aldrich (Prague, Czech Republic). Chloridodiethylenetriamineplatinum(II) chloride ([PtCl(dien)]Cl) was a generous gift of Professor Giovanni Natile from the University of Bari. Restriction endonucleases *Nde*I and *Hpa*I were purchased from New England Biolabs. Acrylamide, bis(acrylamide), and ethidium bromide (EtBr) were obtained from Merck KgaA (Darmstadt, Germany). Agarose was purchased from FMC BioProducts (Rockland, ME). Radioactive reagents were obtained from Amersham (Arlington Heights, IL, U.S.A.).

2.11.1 DNA Binding Kinetics

Calf thymus DNA (CT-DNA) and plasmid DNAs were incubated with the Ru^{II} arene complexes or platinum complexes in 10 mM $NaClO_4$ (pH $\approx$ 6) at 310 K for 24 h in the dark, unless otherwise stated. For each individual assay the values of r_b (r_b values are defined as the number of atoms of the metal bound per nucleotide residue) were determined by Flameless Atomic Absorption Spectrometry (FAAS). CT-DNA (42% G + C, mean molecular mass *ca*. 20 000 kD) was prepared and characterised as described previously.[13]

2.11.2 DNA Transcription by RNA Polymerase *In Vitro*

Transcription of the (*Nde*I/*Hpa*I) restriction fragment of pSP73KB DNA with T7 RNA polymerase and electrophoretic analysis of the transcripts were performed according to the protocols recommended by Promega (Promega Protocols and Applications, 43−46 (1989/90)) as previously described.[14] The DNA concentration used was 7.8×10^{-5} M (0.5 μg/20 μL) (related to the monomeric nucleotide content).

2.11.3 Unwinding of Negatively Supercoiled DNA

Unwinding of closed circular supercoiled pUC19 plasmid DNA was assayed by an agarose gel mobility shift assay.[15] The mean unwinding angle can be calculated from the equation $\Phi = -18\sigma/r_b(c)$, where σ is the superhelical density (representing the number of turns added or removed relative to the total number of turns in the relaxed plasmid, indicating the level of supercoiling), and $r_b(c)$ is the r_b value at which the supercoiled and nick forms comigrate.[16] Samples of plasmid DNA at the concentration of 1.0×10^{-4} M (0.5 μg/15 μL) (related to the monomeric nucleotide content) were incubated with the Ru^{II} arene halido complexes (Chapter 3) at 310 K for 24 h. The *pre-irradiated* forms (irradiation for 24 h) of the Ru^{II} arene pyridine complexes were used in Chapter 4. All samples were precipitated by ethanol and redissolved in the TAE (Tris-acetate/EDTA, pH ≈ 8.0) buffer to remove free, unbound Ru^{II} arene complexes. One aliquot of the precipitated sample was subjected to electrophoresis on 1% agarose gels running at 298 K with TAE buffer and the voltage was set at 25 V. The gels were then stained with ethidium bromide (EtBr), followed by photography with a transilluminator. Electron Absorption Spectrometry (EAS) and/or Flameless Atomic Absorption Spectroscopy (FAAS) were used for the determination of r_b values.

2.11.4 DNA Melting Temperature

CT-DNA at the concentration of 32 μg/mL was modified by Ru^{II} arene complexes at various r_b values in 10 mM $NaClO_4$ with 1 mM Tris-HCl/0.1 mM EDTA and pH = 7.4 at 310 K for 24 h. The samples were then dialysed and the r_b was determined by EAS and FAAS. The salt concentration was then further adjusted by the addition of $NaClO_4$ to values in the range of 0.01−0.22 M. The melting curves of CT-DNA were recorded by measuring the absorbance at 260 nm. The value of the melting temperature (t_m) was determined as the temperature corresponding to a maximum on the first-derivative profile of the melting curves. The t_m values could be thus determined with an accuracy of $\pm$ 0.5 °C.

2.11.5 Circular Dichroism (CD)

Isothermal CD spectra of CT-DNA modified by the Ru^{II} arene complexes were recorded at 298 K in 10 mM $NaClO_4$ by using a Jasco J-720 spectropolarimeter equipped with a thermoelectrically controlled cell holder. The cell pathlength was 1 cm. Spectra were recorded in the range of 230−600 nm in 0.5 nm increments with an averaging time of 0.5 s.

2.11.6 Flow Linear Dichroism (LD)

Flow LD spectra were collected by using a flow Couette cell in a Jasco J-720 spectropolarimeter adapted for LD measurements. Long molecules, such as DNA (minimum length of *ca.* 250 bp) can be orientated in a flow Couette cell. The flow cell consists of a fixed outer cylinder and a rotating solid quartz inner cylinder, separated by a gap of 0.5 mm, giving a total pathlength of 1 mm. LD spectra of DNA at the

concentration 2.3×10^{-4} M modified by the Ru^{II} arene complexes were recorded at 298 K in 10 mM $NaClO_4$.

2.11.7 Ethidium Bromide (EtBr) Fluorescence

Measurements were performed on a Varian Cary Eclipse spectrofluorophotometer using a 1-cm pathlength quartz cell. Fluorescence measurements of CT-DNA modified by Ru^{II} arene complexes in the presence of EtBr were performed at an excitation wavelength of 546 nm, and the emitted fluorescence was analysed at 590 nm. The fluorescence intensity was measured at 298 K in 0.4 M NaCl to avoid secondary binding of EtBr to DNA.[17] The concentrations were 0.01 mg/mL for DNA and 0.04 mg/mL for EtBr, which corresponded to the saturation of all intercalation sites for EtBr in DNA.[18]

2.11.8 Other Physical Methods

Absorption spectra were measured with a Beckman DU 7 4000 UV-Vis spectrophotometer equipped with a thermoelectrically controlled cell holder and 1-cm pathlength quartz cells. The FAAS measurements were carried out on a Varian AA240Z Zeeman atomic absorption spectrometer equipped with a GTA 120 graphite tube atomiser. The PAA gels were visualized by using a BAS 2500 FUJIFILM bioimaging analyser, with the AIDA image analyzer software (Raytest, Germany).

2.12   Cancer Cell Growth Inhibition

The following assays were carried out under normal ambient light conditions (i.e. no irradiation provided).

2.12.1 Materials and Maintenance

The A549 human lung, HCT116 human colon, A2780 human ovarian, and A2780cis human ovarian cisplatin resistant cancer cell lines were obtained from the European Collection of Animal Cell Cultures (ECACC). The A549 lung cell line was grown in DMEM (Dulbecco's Modified Eagle's Medium) and A2780 human ovarian and A2780cis human ovarian cisplatin resistant cell lines were grown in RPMI (Roswell Park Memorial Institute) medium. The HCT116 colon cancer cell line was grown in McCoys 5A medium. All media were supplemented with 10% fetal calf serum (FCS), 1% L-glutamine and 1% penicillin/streptomycin. Experiments were performed with cells within 15 passages from each other. All cells were split when around 80–95% confluence was reached using 0.25% trypsin/EDTA.

2.12.2 *In Vitro* Growth Inhibition Assay

IC_{50} values (concentration at which 50% of the cell growth is inhibited) against A549 human lung, HCT116 human colon, A2780 human ovarian, and A2780cis human ovarian cisplatin resistant cancer cell lines were determined. Plates containing 96 wells with 300 μL capacity were used. A2780 and A2780cis cells were plated out at a density of 5000 cells/well whereas A549 and HCT116 cancer cells were plated out at a density of 2000 and 2500 cells/well, respectively. Plated A2780 and A2780cis cells were grown for 48 h, and A549 and HCT116 cells for 24 h at 310 K before addition of the Ru^{II} arene complexes. The Ru^{II} arene test compound (plus a cisplatin control added to the plates to act as a positive and comparative control) was made up in 5% DMSO and saline to give a 1 mM stock solution by initial dissolution in DMSO followed by dilution with saline. Two rows free of drug solution acted as the 100% cell survival control. Sonication was sometimes used to facilitate complete

dissolution. Serial dilutions were carried out to give final screening concentrations of drug of 400, 200 and 20 μM (final concentration of DMSO of 0.5% (v/v)). Aliquots of 50 μL of these solutions were added to the wells (in triplicate) already containing 150 μL of media, so that the final concentrations were 100, 50, and 5 μM (final concentration of DMSO of 0.125% (v/v)). The cells were exposed to the complex for 24 h, which then was removed and the cells washed with 100 μL phosphate buffered saline (PBS) followed by the addition of 200 μL of fresh media. Then the cells were incubated for 72 h of recovery time. The remaining biomass was then estimated by the sulforhodamine B assay (SRB assay, *vide infra*). The three screening concentrations were used in an initial test of activity. The selected complexes were then tested for half maximal inhibitory concentration (IC_{50}) values determination. The previously described assay was then repeated but using six different concentrations of complex instead, ranging from 0.1 to 100 μM. Each assay was done in triplicate. IC_{50} values were obtained from plots of % cell survival against Log of the drug concentration.

2.12.3 Sulforhodamine B (SRB) Assay[19]

SRB is a pink aminoxanthene dye with two sulfonic acid groups, Figure 2.1. Under mildly acidic conditions it binds to basic amino acid residues in proteins and under more basic conditions the dye is liberated and can be quantitatively extracted for measurement of optical density ($\lambda = 568$ nm).
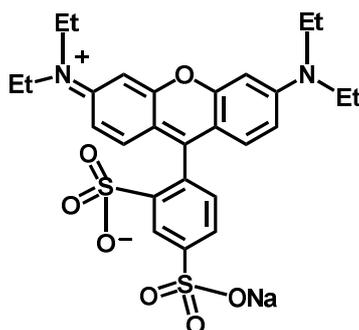
Figure 2.1. Structure of sulforhodamine B sodium salt.

To each well, 50 µL 50% (w/v) of trichloro acetic acid (TCA) was added and the wells were incubated at 277 K for one hour to fix the remaining biomass before washing 10 times with running tap water. Plates were dried with the assistance of a heat-gun until no standing moisture was visible. The TCA-fixed cells were stained with 50 µL 0.4% (w/v) SRB in 1% acetic acid and left to stand for 30 min at ambient temperature. The excess dye was removed with 5 quick rinses of 1% acetic acid and again dried with the assistance of a heat-gun. The cell-bound dye was solubilised by addition of 150 µL of a 10 mM Tris base (tris(hydroxymethyl)aminomethane, pH ≈ 10.5) solution and plates were gently shaken for 15 min and left standing at ambient temperature for 1 h to allow the solutions to become homogeneous. The absorbance was read using a Labsystems Multiscan Ascent354 microplate reader at 590 nm. The absorbance value taken as 100% cell survival was the averaged duplicate absorbance for the control wells. The percentage cell survival relative to this control could then be determined.

2.13 Photocytotoxicity: Cancer Cell Growth Inhibition with UVA Irradiation

These experiments were performed by Mr Aron F. Westendorf in the laboratory of Prof Patrick Bednarski at the Institut für Pharmazie der Ernst-Moritz-Arndt der

Greisfwald Universität in Germany. All stock solutions were prepared in DMSO and were stored at 243 K. Prior to testing, the stock solutions were removed from the freezer and serially diluted in DMSO 2-fold to the desired concentrations, giving series of five dilutions. To investigate the cytotoxic potency of the compounds, six different human cancer cell lines were used: SISO cervical cancer, 5637 and RT-4 bladder cancer, A-427 and LCLC-103H lung cancer, and DAN-nG pancreas carcinoma cell lines. All human cancer cell lines were obtained from the German Collection of Microorganisms and Cell Cultures (DSMZ, Braunschweig), Table 2.1.

Table 2.1 Human cancer cell lines used in the photocytotoxicity test.

Cell line	Patient (sex, age)	Origin	Doubling time (h)
5637	M, 68	Urinary bladder carcinoma	30
A-427	M, 52	Lung carcinoma	38
SISO	F, 67	Cervix adenocarcinoma	48
DAN-G	–	Pancreas carcinoma	42
LCLC-103H	M, 61	Large cell lung cancer	40
RT-4	M, 63	Urinary bladder carcinoma	44

Cells were grown in medium containing 90% RPMI 1640 medium (Sigma, Taufenkirchen, Germany) and 10% Fetal Calf Serum (FCS) (Sigma), supplemented with penicillin G/streptomycin. Cells were kept at 310 K in a water-saturated atmosphere of 5% CO_2 air. Shortly before the cells reached confluence, the cells were passaged.

2.13.1 Screening Method

The cells were seeded out in 96-well microtiter plates in 100 µL medium at a density of 1000 cells/well. The plates were returned to the incubator for 24 h. For the primary screening the stock solutions of the compounds were used. The next day the stock

solutions were directly diluted in medium 500-fold. Medium (100 µL) containing the compounds was added to each well with a maximum DMSO concentration of 0.1 % (v/v). After a preincubation period of 1 h the plates were either irradiated for 30 min with UVA light λ = 366 nm or kept in the dark. Luzchem Expo panels (Luzchem Reasearch Inc., Ontario, Canada) were used for irradiation. The two Expo panels were accommodated with 5 fluorescent lamps each. Lower UV light was cut off by a filter. The light source was positioned 25 cm away from the samples giving an intensity of 0.12 W/cm^2. Medium removal occurred after 6 h. After the complete incubation period of 96 h the medium was discarded and replaced for 25 min with a 1% glutaraldehyde buffer (PBS) solution to fix the cells. The fixing buffer was discarded and the cells were stored under PBS at 269 K until staining. Staining was done with a 0.02% solution of Crystal Violet in water. The dye was added to each well and discarded after 30 min of staining, followed by 15 min washing in water. The cell-bound dye was redissolved in 70% ethanol/water. Optical density was measured at λ = 570 nm with an Anthos 2010 plate reader (Anthos, Salzburg, Austria). The corrected T/C values for the dose-response curves were calculated.

$$\mathrm{T/C_{corr}} = \frac{(OD_{test} - OD_{t=0})}{(OD_{con} - OD_{t=0})} * 100$$

T is the mean optical density of the treated cells and C is the optical density of controls. OD_{test} is the mean optical density of the treated cells after staining, OD_{con} is the mean optical density of the controls and $OD_{t=0}$ is the mean optical density at the time the compounds were added. The IC_{50} values can be calculated by a linear least-squares regression of the T/C_{corr} values versus the logarithm of the added compound concentration and extrapolating to the T/C_{corr} values of 50%.[20]

2.14 Synthesis of Starting Materials

The Ru^{II} arene precursor dimers of the form [(η^6-arene)RuX$_2$]$_2$ where arene is *p*-cym = *para*-cymene, or bip = biphenyl, and X is Cl, Br, or I were synthesised according to a previously reported method[21]; [(η^6-etb)RuCl$_2$]$_2$ where etb = ethylbenzoate was synthesised following published literature.[22] The Ru^{II} arene precursor dimers [(η^6-arene)RuCl$_2$]$_2$ where arene is hmb = hexamethylbenzene, ind = indane, or thn = tetrahydronaphtalene were kindly provided by Dr Abraha Habtemariam and synthesised according to a reported method.[21]

2.14.1 Materials

RuCl$_3$·3H$_2$O was acquired from Precious Metals Online (PMO Pty Ltd) and used as received. The arenes (*p*-cym and bip) were purchased from Sigma-Aldrich. 1,4-dihydrobiphenyl was prepared by a previously reported procedure.[23]

2.14.2 Preparation of Ru^{II} Arene Dimers

[(η^6-*p*-cym)RuCl$_2$]$_2$. To a solution of RuCl$_3$·3H$_2$O (0.15 g, 0.57 mmol) in dry EtOH (reagent grade) (15 mL), a three-fold excess of α-phellandrene (which upon oxidation is to be named *para*-cymene (*p*-cym)) (0.23 g, 1.7 mmol) was added with constant stirring and allowed to react during 18 h. The solvent was then completely removed under vacuum and the remaining solid was washed with portions of EtOH and Et$_2$O (3 × 20 mL) to obtain the corresponding dimer [(η^6-*p*-cym)RuCl$_2$]$_2$ as a red brown solid; yield 85% (3.50 g, 5.71 mmol). Elemental Analysis calc. for C$_{21}$H$_{28}$Cl$_4$Ru$_2$ %C: 39.23, %H: 4.61; found %C: 39.27, %H: 4.51. ^{1}H NMR ((CD$_3$)$_2$SO, 400 MHz) δ_H: 1.28 (12H, d), 2.15 (3H, s), 2.50 (2H, sep), 5.35 (4H, m), 5.52 (4H, m).

[(η⁶-bip)RuCl₂]₂. To a solution of $RuCl_3 \cdot 3H_2O$ (5.0 g, 19.1 mmol) in dry EtOH (15 mL) a three-fold excess of 1,4-dihydrobiphenyl (4.3 g, 27.5 mmol) was added with constant stirring and allowed to react during 18 h. The solvent was then completely removed under vacuum and the remaining solid was washed with portions of EtOH and Et₂O (3 × 20 mL) to obtain the corresponding dimer [(η⁶-bip)RuCl₂]₂ as a red brown solid; yield 43% (5.06 g, 7.76 mmol). Elemental analysis calc. for $C_{24}H_{20}Cl_4Ru_2$ C: 44.19%; H: 3.09%; found: C: 44.18%, H: 3.07%. ¹H NMR ((CD₃)₂SO, 400 MHz) δ_H: 6.08 (6H, m), 6.44 (4H, m), 7.50 (6H, m), 7.82 (4H, m).

2.15   References

[1]. Hwang, T.-L.; Shaka, A. J. *J. Magn. Reson.*, *Series A*, **1995**, *112*, 275–279.

[2]. Krezel, A.; Bal, W. *J. Inorg. Biochem.* **2004**, *98*, 161–166.

[3]. Sheldrick, G. M. SHELXL97, University of Göttingen, Germany, **1997**.

[4]. Te Velde, G.; Bickelhaupt, F. M.; Baerends, E. J.; Fonseca Guerra, C.; Van Gisbergen, S. J. A.; Snijders, J. G.; Ziegler, T. *J. Comp. Chem.*, **2001**, *22*, 931–967.

[5]. Frisch, M. J., et al. *Gaussian 03*, revision D 0.1; Gaussian Inc.: Wallingford CT, **2004**.

[6]. (a) Becke, A. D. *J. Chem. Phys.*, **1993**, *98*, 5648−5652; (b) Lee, C.; Yang, W.; Parr, R. G. *Phys. Rev. B,* **1988**, *37*, 785−789.

[7]. Hay, P. J.; Wadt, W. R. *J. Chem. Phys.*, **1985**, *82*, 270−283.

[8]. McLean, A. D.; Chandler, G. S. *J. Chem. Phys.*, **1980**, *72*, 5639−5648.

[9]. Cossi, M.; Rega, N.; Scalmani, G.; Barone, V. *J. Comput. Chem.*, **2003**, *24*, 669−681.

[10]. (a) Casida, M. E.; Jamorski, C.; Casida, K. C.; Salahub, D. R. *J. Chem. Phys.*, **1998**, *108*, 4439−4449; (b) Stratmann, R. E.; Scuseria, G. E.; Frisch, M. J. *J. Chem. Phys.*, **1998**, *109*, 8218−8224.

[11]. Browne, W. R.; O'Boyle, N. M.; McGarvey, J. J.; Vos, J. G. *Chem. Soc. Rev.*, **2005**, *34*, 641−663.

[12]. O'Boyle, N. M.; Vos, J. G., *GaussSum*, Dublin City University. Available at http://gausssum.sourceforge.net., **2005**.

[13]. (a) Brabec, V.; Palecek, E., *Biophysik*, **1970**, *6*, 290−300; (b) Brabec, V.; Palecek, E., *Biophys. Chem.*, **1976**, *4*, 79−92.

[14]. (a) Brabec, V.; Leng, M. *Proc. Natl. Acad. Sci. U.S.A.,* **1993**, *90*, 5345–5349; (b) Lemaire, M. A.; Schwartz, A.; Rahmouni, A. R.; Leng, M. *Proc. Natl. Acad. Sci. U.S.A.*, **1991**, *88*, 1982–1985.

[15]. Keck, M. V.; Lippard, S. J. *J. Am. Chem. Soc.,* **1992**, *114*, 3386–3390.

[16]. Keck, M. V.; Lippard, S. J. *J. Am. Chem. Soc.*, **1992**, *114*, 3386–3390.

[17]. (a) Butour, J. L.; Macquet, J. P. *Eur. J. Biochem.*, **1977**, *78*, 455–463; (b) Butour, J. L.; Alvinerie, P.; Souchard, J. P.; Colson, P.; Houssier, C.; Johnson, N. P. *Eur. J. Biochem.*, **1991**, *202*, 975−980.

[18]. Butour, J. L.; Macquet, J. P. *Eur. J. Biochem.*, **1977**, *78*, 455–463.

[19]. Skehan, P.; Storeng, R.; Scudiero, D.; Monks, A.; McMahon, J.; Vistica, D.; Warren, J. T.; Bokesch, H.; Kenney, S.; Boyd, M. R. *J. Nat. Cancer Inst.*, **1990**, *82*, 1107–1112.

[20]. Saczewski, F.; Reszka, P.; Gdaniec, M.; Grünert, R.; Bednarski, P. J. *J. Med. Chem.*, **2004**, *47*, 3438−3449.

[21]. (a) Bennet, M. A.; Smith, A. K. *J. Chem. Soc.*, *Dalton Trans.*, **1974**, 233–241; (b) Govindaswamy, P.; Canivet, J.; Therrien, B.; Süss-Fink, G.; Štěpnička, P.; Ludvík, J. *J. Organomet. Chem.*, **2007**, *692*, 3664–3675; (c) Zelonka, R. A.; Baird, M. C. *J. Organomet. Chem.*, **1972**, *35*, C43–C46; (d) Melchart, M.; Habtemariam, A.; Nováková, O.; Moggach, S. A.; Fabbiani, F. P. A.; Parsons, S.; Brabec, V.; Sadler, P. J. *Inorg. Chem.*, **2007**, *46*, 8950–8962.

[22]. Habtemariam, A.; Betanzos-Lara, S.; Sadler, P. J., Di-μ-Chloro(ethylbenzoate)diruthenium(II): [(η^6-etb)RuCl$_2$]$_2$, *Inorg. Synth.*, **2010**, *36*, in press.

[23]. Lindow, D. F.; Cortez, C. N.; Harvey, R. G. *J. Am. Chem. Soc.*, **1972**, *94*, 5406–5412.

Chapter 3

Ru^{II} Arene Halido Complexes
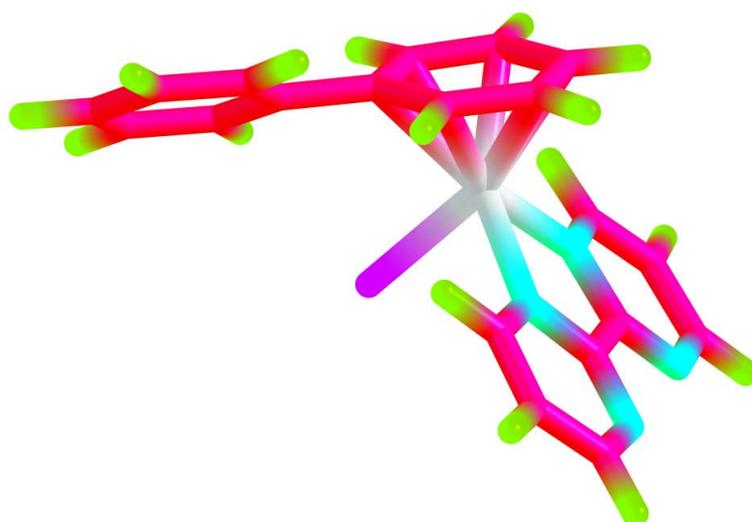
Chapter 3

Ruthenium(II) Arene Halido Complexes

3.1 Introduction

The well-established mechanism of action of the cytotoxic drug cisplatin is the alteration of the secondary structure of DNA *via* coordination to the *N7* atom of a guanine (G) or an adenine (A) base, which requires its prior aquation in the cell to generate the more reactive aqua complexes $[Pt(NH_3)_2(OH_2)Cl]^+$ and $[Pt(NH_3)_2(OH_2)_2]^{2+}$.[1,2] It is believed that one important potential activation mechanism of anticancer metal complexes prior to their interactions with biomolecules could be hydrolysis. It has been shown that certain organometallic Ru^{II} complexes of the type $[(\eta^6\text{-arene})Ru(XY)Z]^{n+}$ where XY is a bidentate chelating ligand and Z is a leaving group, can exhibit promising cytotoxic activity against a variety of cancer cell lines, including cisplatin-resistant cells.[3,4] These studies have shown that the nature of the arene, the chelating ligand, and the leaving group can have a major influence on the rates of activation (towards hydrolysis and/or binding to biomolecules) as well as on the cytotoxic activity.[5] It appears that a more hydrophobic arene ligand along with a single ligand exchange site might be associated with significant anticancer activity. Blockage from further ligand exchange reactions in the remaining two coordination sites can be usually achieved by coordination of a stable bidentate ligand; in this regard, particularly effective are those containing N,N'-heterocyclic groups.[6] For example, Ru^{II} arene complexes with chelating 1,10-phenanthroline (phen), 2,2'-bipyridine (bpy), or arylazopyridine (azpy) ligands have been extensively studied and have been reported to show promising cytotoxicity.[7,8] In the present work, the possibility to tune the chemical reactivity of organometallic Ru^{II} complexes of the

type $[(\eta^6\text{-arene})\text{Ru(N,N')X}][\text{PF}_6]$ by systematically varying the ligands around the metal centre is explored. Ru^{II} arene complexes containing various N,N'-chelating ligands, which all form six-membered chelate rings upon binding, as well as various arenes, and different halides were synthesised and characterised. The aqueous solution chemistry as well as nucleobases binding (to 9-EtG and 9-EtA) were investigated. Their potential as cytotoxic agents was explored not only by determining IC_{50} values against A2780 (human ovarian), A2780cis (human ovarian cisplatin resistant), A549 (human lung) or HCT116 (human colon) cancer cell lines but also by studying preliminary DNA interactions in cell-free media.

3.2 Experimental Section

3.2.1 Materials

$RuCl_3 \cdot 3H_2O$ was acquired from Precious Metals Online (PMO Pty Ltd) and used as received. 2,2'-bipyrimidine (bpm), 1,10-phenanthroline (phen), 1,10-phenanthroline-5,6-dione (phendio), 4,7-diphenyl-1,10-phenanthroline (bathophen), 6-mercaptopurine (MP), 9-ethylguanine (9-EtG), 9-ethyladenine (9-EtA), and KPF_6 were obtained from Sigma-Aldrich. KBr and KI (reagent grade) were obtained from Fisher. The Ru^{II} arene precursor dimers $[(\eta^6\text{-arene})\text{RuX}_2]_2$ where arene is *para*-cymene (*p*-cym), or biphenyl (bip), and X is Cl, Br, or I were synthesised according to a previously reported method[9] as described in Chapter 2. The dimer $[(\eta^6\text{-etb})\text{RuCl}_2]_2$ where etb is ethylbenzoate was synthesised following published literature.[10] $[(\eta^6\text{-arene})\text{RuCl}_2]_2$ precursor dimers where arene is hexamethylbenzene (hmb), indane (ind), or tetrahydronaphthalene (thn) were kindly provided by Dr Abraha Habtemariam from the Department of Chemistry at the University of Warwick and

synthesised according to a published method.[9] The solvents used for UV-vis absorption spectroscopy were dry methanol (reagent grade) and deionised water. For NMR spectroscopy the solvents used were $(CD_3)_2CO$-d_6, DMSO-d_6, MeOD-d_4 and D_2O obtained from Aldrich unless otherwise stated. All chemicals were used without further purification.

3.2.2   Preparation of Ru^{II} Arene Halido Complexes

Complexes of the form [(η^6-arene)Ru(N,N')X][PF$_6$] where arene is *p*-cym, bip, etb, ind, hmb, or thn; N,N' is bpm, phen, phendio, or bathophen; and X is Cl, Br, or I were synthesised as previously described[5b] using a similar procedure. Typically, two mol equiv of the N,N' chelating ligand and two mol equiv of KPF$_6$ were added to a solution of one mol equiv of the appropriate Ru^{II} arene dimer in 20 mL of dry methanol (reagent grade) with constant stirring, and reacted for 48 h upon which the precipitate formed was collected by filtration. The remaining solution was concentrated and portions of Et$_2$O were added to further precipitate the product which was again collected by filtration. Both solids were combined and washed with portions of Et$_2$O and MeOH and dried overnight under vacuum resulting in microcrystalline products. Details of the amounts of reactants, volumes of solvents, colour changes, and nature of the products are described below for the individual reactions, as well as any variations in the synthetic procedure. $^{13}C\{^1H\}$ NMR spectroscopy data are also provided for samples where a satisfactory elemental analysis was not obtained.

[(η^6-*p*-cym)Ru(bpm)Cl][PF$_6$] (1). [(η^6-*p*-cym)RuCl$_2$]$_2$ (0.15 g, 0.24 mmol), 2,2'-bipyrimidine (bpm) (0.08 g, 0.49 mmol) and KPF$_6$ (0.09 g, 0.49 mmol) in dry methanol; the solution turned from red to yellow; a bright yellow solid was obtained;

yield 83% (0.12 g, 0.20 mmol). Elemental analysis calc. for $C_{19}H_{23}ClF_6N_4PRu$ %C: 37.67, %H: 3.51, %N: 9.76; found %C: 36.98, %H: 3.40, %N: 9.44. HR-MS: calc for $C_{18}H_{20}ClN_4Ru$ [M]$^+$ *m/z* 429.0420, found *m/z* 429.0416. ^{1}H NMR (D$_2$O, 700 MHz) δ_H: 1.06 (6H, d, *J* = 7.0), 2.16 (3H, s), 2.68 (1H, sep, *J* = 7.0), 5.97 (2H, d, *J* = 6.4), 6.16 (2H, d, *J* = 6.4), 7.94–7.96 (2H, m), 9.20 (2H, dd, *J* = 1.9, *J* = 4.8), 9.70 (2H, dd, *J* = 2.0, *J* = 5.8).

[(η^6-*p*-cym)Ru(bpm)Br][PF$_6$] (2). [(η^6-*p*-cym)RuBr$_2$]$_2$ (0.15 g, 0.19 mmol), 2,2'-bipyrimidine (bpm) (0.08 g, 0.49 mmol) and KPF$_6$ (0.09 g, 0.49 mmol) in dry methanol; the solution turned from red to yellow; a dark yellow solid was obtained; yield 83% (0.04 g, 0.13 mmol). HR-MS: calc for $C_{18}H_{20}BrN_4Ru$ [M]$^+$ *m/z* 474.9892, found *m/z* 474.9915. ^{1}H NMR (D$_2$O, 700 MHz) δ_H: 1.07 (6H, d, *J* = 7.2), 2.22 (3H, s), 2.74 (1H, sep, *J* = 7.2), 5.94 (2H, d, *J* = 6.4), 6.12 (2H, d, *J* = 6.4), 7.92–7.94 (2H, m), 9.18 (2H, dd, *J* = 1.9, *J* = 4.9), 9.66 (2H, dd, *J* = 1.9, *J* = 5.9). ^{13}C{^{1}H} NMR ((CD$_3$)$_2$CO, 175 MHz) δ_C: 19.1, 22.3, 32.2, 86.6, 86.9, 103.5, 108.6, 125.4, 161.1, 161.3, 164.2.

[(η^6-*p*-cym)Ru(bpm)I][PF$_6$] (3). [(η^6-*p*-cym)RuI$_2$]$_2$ (0.15 g, 0.15 mmol), 2,2'-bipyrimidine (bpm) (0.049 g, 0.30 mmol) and KPF$_6$ (0.06 g, 0.30 mmol) in dry methanol; the solution turned from red to yellow; a bright orange solid was obtained; yield 80% (0.08 g, 0.12 mmol). Suitable crystals for X-ray crystallography were obtained from a saturated acetone-*d$_6$* solution at room temperature. Elemental analysis calc. for $C_{18}H_{20}IF_6N_4PRu$ %C: 32.49, %H: 3.03, %N: 8.42; found %C: 31.81, %H: 2.85, %N: 8.25. HR-MS: calc for $C_{18}H_{20}IN_4Ru$ [M]$^+$ *m/z* 520.9775, found *m/z* 520.9782. ^{1}H NMR (D$_2$O, 700 MHz) δ_H: 1.08 (6H, d, *J* = 7.1), 2.32 (3H, s), 2.84 (1H, sep, *J* = 7.1), 5.92 (2H, d, *J* = 6.4), 6.07 (2H, d, *J* = 6.4), 7.88–7.90 (2H, m), 9.15 (2H, dd, *J* = 1.8, *J* = 4.8), 9.60 (2H, dd, *J* = 2.0, *J* = 5.9).

[(η^6-bip)Ru(bpm)Cl][PF$_6$] (4). [(η^6-bip)RuCl$_2$]$_2$ (0.10 g, 0.15 mmol), 2,2'-bipyrimidine (bpm) (0.05 g, 0.30 mmol) and KPF$_6$ (0.06 g, 0.30 mmol) in dry methanol; the solution turned from brown to dark green; a dark yellow solid was obtained; yield 77% (0.07 g, 0.11 mmol). Suitable crystals for X-ray crystallography were obtained from slow diffusion of Et$_2$O into an acetone saturated solution at 278 K. Elemental analysis calc. for C$_{20}$H$_{16}$ClF$_6$N$_4$PRu·H$_2$O %C: 39.26, %H: 2.97, %N: 9.16; found %C: 38.90, %H: 2.58, %N: 8.64. HR-MS: calc for C$_{20}$H$_{16}$ClN$_4$Ru [M]$^+$ *m/z* 449.0103, found *m/z* 449.0116. ^{1}H NMR ((CD$_3$)$_2$SO, 500 MHz) δ_H: 6.22–6.24 (1H, m,) 6.63–6.64 (2H, m), 6.69–6.70 (2H, m), 7.46–7.48 (2H, m), 7.52–7.53 (1H, m), 7.76–7.77 (2H, m), 7.93–7.95 (2H, m), 9.28–9.29 (2H, m), 9.72–9.73 (m, 2H).

[(η^6-bip)Ru(bpm)Br][PF$_6$] (5). [(η^6-biph)RuBr$_2$]$_2$ (0.13 g, 0.16 mmol), 2,2'-bipyrimidine (bpm) (0.05 g, 0.32 mmol) and KPF$_6$ (0.06 g, 0.32 mmol) in dry methanol; the solution turned from dark red to dark yellow; a green solid was obtained; yield 71% (0.07 g, 0.11 mmol). Elemental analysis calc. for C$_{20}$H$_{16}$BrF$_6$N$_4$PRu·H$_2$O %C: 36.60, %H: 2.76, %N: 8.54; found C: %36.60, %H: 2.46, %N: 8.55. HR-MS: calc for C$_{20}$H$_{16}$BrN$_4$Ru [M]$^+$ *m/z* 492.9596, found *m/z* 492.9637. ^{1}H NMR ((CD$_3$)$_2$SO, 500 MHz) δ_H: 6.25–6.27 (1H, m), 6.62–6.63 (2H, m), 6.69–6.70 (2H, m), 7.45–7.46 (2H, m), 7.51–7.52 (1H, m), 7.72–7.74 (2H, m), 7.90–7.92 (2H, m), 9.26–9.27 (2H, m), 9.68–9.69 (2H, m).

[(η^6-bip)Ru(bpm)I][PF$_6$] (6). [(η^6-biph)RuI$_2$]$_2$ (0.10 g, 0.10 mmol), 2,2'-bipyrimidine (bpm) (0.03 g, 0.20 mmol) and KPF$_6$ (0.04 g, 0.20 mmol) in dry methanol; the solution turned from dark red to dark yellow; a yellow-greenish solid was obtained; yield 73% (0.05 g, 0.07 mmol). Suitable crystals for X-ray crystallography were obtained from a saturated acetone-d_6 solution at room temperature. Elemental analysis calc. for C$_{20}$H$_{16}$F$_6$IN$_4$PRu·2H$_2$O %C: 33.30, %H:

2.79, %N: 7.77; found %C: 33.27, %H: 2.23, %N: 6.37. HR-MS: calc for C$_{20}$H$_{16}$IN$_4$Ru [M]$^+$ *m/z* 540.9463, found *m/z* 540.9481. ^{1}H NMR ((CD$_3$)$_2$SO, 500 MHz) δ_H: 6.11–6.13 (1H, m), 6.65–6.66 (2H, m), 6.72–6.73 (2H, m), 7.40–7.41 (2H, m), 7.48–7.49 (1H, m), 7.66–7.67 (2H, m), 7.85–7.87 (m, 2H), 9.23–9.24 (2H, m), 9.57–9.58 (2H, m).

[(η^6-etb)Ru(bpm)Cl][PF$_6$] (7). [(η^6-etb)RuCl$_2$]$_2$ (0.10 g, 0.16 mmol), 2,2'-bipyrimidine (bpm) (0.06 g, 0.32 mmol) and KPF$_6$ (0.06 g, 0.32 mmol) in dry methanol; the solution turned from red to orange; a bright orange solid was obtained; yield 93% (0.20 g, 0.36 mmol). Suitable crystals for X-ray crystallography were obtained from slow diffusion of Et$_2$O into an acetone saturated solution at 278 K. Elemental analysis calc. for C$_{17}$H$_{16}$ClF$_6$N$_4$O$_2$PRu %C: 34.62, %H: 2.73, %N: 9.50; found %C: 34.54, %H: 2.65, %N: 9.40. HR-MS: calc for C$_{17}$H$_{16}$ClN$_4$O$_2$Ru [M]$^+$ *m/z* 445.0001, found *m/z* 445.0018. ^{1}H NMR ((CD$_3$)$_2$CO, 600 MHz) δ_H: 1.42 (3H, t, *J* = 7.1), 4.52 (2H, q, *J* = 7.1), 6.44–6.47 (2H, m), 6.77–6.80 (1H, m), 7.22 (2H, d, *J* = 6.1), 8.08–8.11 (2H, m), 9.37 (2H, dd, *J* = 2.4, *J* = 4.9), 9.90 (2H, dd, *J* = 1.8, *J* = 5.5).

[(η^6-hmb)Ru(bpm)Cl][PF$_6$] (8). [(η^6-hmb)RuCl$_2$]$_2$ (0.10 g, 0.15 mmol), 2,2'-bipyrimidine (bpm) (0.05 g, 0.29 mmol) and KPF$_6$ (0.02 g, 0.15 mmol) in dry methanol; the solution turned from red to dark yellow; a bright yellow solid was obtained; yield 82% (0.04 g, 0.06 mmol). Elemental analysis calc. for C$_{20}$H$_{24}$ClF$_6$N$_4$PRu·H$_2$O %C: 38.75, %H: 4.23, %N: 9.04; found %C: 38.17, %H: 3.92, %N: 8.76. HR-MS: calc for C$_{20}$H$_{24}$ClN$_4$Ru [M]$^+$ *m/z* 457.0729, found *m/z* 457.0732. ^{1}H NMR ((CD$_3$)$_2$CO, 600 MHz) δ_H: 2.31 (18H, s), 8.06–8.09 (2H, m), 9.31 (2H, dd, *J* = 1.8, *J* = 4.7), 9.47 (2H, dd, *J* = 1.8, *J* = 5.7).

[(η^6-ind)Ru(bpm)Cl][PF$_6$] (9). [(η^6-ind)RuCl$_2$]$_2$ (0.10 g, 0.17 mmol), 2,2'-bipyrimidine (bpm) (0.06 g, 0.34 mmol) and KPF$_6$ (0.03 g, 0.17 mmol) in dry

methanol; the solution turned from red to dark brown; a dark green solid was obtained; yield 79% (0.06 g, 0.11 mmol). Elemental analysis calc. for $C_{17}H_{16}ClF_6N_4PRu \cdot H_2O$ %C: 35.46, %H: 3.15, %N: 9.73; found %C: 35.41, %H: 2.67, %N: 9.67. HR-MS: calc for $C_{17}H_{16}ClN_4Ru$ [M]$^+$ *m/z* 413.0103, found *m/z* 413.0100. ^{1}H NMR (CD$_3$OD, 600 MHz) δ_H: 2.05–2.22 (4H, m), 2.92–3.00 (2H, m), 6.00–6.02 (2H, m), 6.28–6.30 (2H, m), 7.95–7.98 (2H, m), 9.28–9.30 (2H, m), 9.71–9.73 (2H, m).

[(η^6-thn)Ru(bpm)Cl][PF$_6$] (10). [(η^6-thn)RuCl$_2$]$_2$ (0.10 g, 0.17 mmol), 2,2'-bipyrimidine (bpm) (0.06 g, 0.34 mmol) and KPF$_6$ (0.03 g, 0.17 mmol) in dry methanol; the solution turned from red to dark green; a bright yellow solid was obtained; yield 87% (0.08 g, 0.15 mmol). Elemental analysis calc. for $C_{18}H_{18}ClF_6N_4PRu \cdot 2H_2O$ %C: 35.57, %H: 3.65, %N: 9.22; found %C: 35.32, %H: 2.90, %N: 9.23. HR-MS: calc for $C_{17}H_{16}ClN_4Ru$ [M]$^+$ *m/z* 426.8885, found *m/z* 426.0235. ^{1}H NMR (CD$_3$OD, 600 MHz) δ_H: 1.56–1.64 (2H, m), 1.69–1.77 (2H, m), 2.66–2.69 (2H, m), 2.74–2.77 (2H, m), 5.92–5.96 (2H, m), 6.03–6.05 (2H, m), 7.82–7.85 (2H, m), 9.12 (2H, dd, *J* = 2.0, *J* = 4.7), 9.66 (2H, dd, *J* = 2.0, *J* = 5.7)

[(η^6-*p*-cym)Ru(phen)Cl][PF$_6$] (11). [(η^6-*p*-cym)RuCl$_2$]$_2$ (0.10 g, 0.16 mmol), 1,10-phenanthroline (phen) (0.06 g, 0.32 mmol) and KPF$_6$ (0.06 g, 0.32 mmol) in dry methanol; the solution turned from red to bright yellow; a bright yellow solid was obtained; yield 92% (0.17 g, 0.30 mmol). Elemental analysis calc. for $C_{22}H_{22}ClF_6N_2PRu$ %C: 44.34, %H: 3.72, %N: 4.40; found %C: 43.66, %H: 3.63, %N: 4.75. HR-MS: calc for $C_{22}H_{22}ClN_2Ru$ [M]$^+$ *m/z* 451.0512, found *m/z* 451.0530. ^{1}H NMR (D$_2$O, 600 MHz) δ_H: 0.88 (6H, d, *J* = 6.9), 2.19 (3H, s), 2.54 (1H, sep, *J* = 6.9), 5.96 (2H, d, *J* = 6.4), 6.19 (2H, d, *J* = 6.4), 8.7 (2H, dd, *J* = 5.3, *J* = 8.3), 8.16 (2H, s), 8.78 (2H, dd, *J* = 1.0, *J* = 8.3), 9.75 (2H, dd, *J* = 1.0, *J* = 5.3).

[(η^6-*p*-cym)Ru(phendio)Cl][PF$_6$] (12). [(η^6-*p*-cym)RuCl$_2$]$_2$ (0.10 g, 0.16 mmol), 1,10-phenanthroline-5,6-dione (phendio) (0.06 g, 0.32 mmol) and KPF$_6$ (0.06 g, 0.32 mmol) in dry methanol; the solution turned from red to dark green; a bright dark green solid was obtained; yield 93% (0.17 g, 0.30 mmol). HR-MS: calc for C$_{22}$H$_{20}$ClF$_6$N$_2$O$_2$Ru [M]$^+$ *m/z* 481.0254, found *m/z* 481.0261. ^{1}H NMR ((CD$_3$)$_2$CO, 600 MHz) δ_H: 1.14 (6H, d, *J* = 6.9), 2.36 (3H, s), 2.84 (1H, sep, *J* = 6.9), 6.11 (2H, d, *J* = 5.9), 6.37 (2H, d, *J* = 5.9), 8.07–8.10 (2H, m), 8.77–8.79 (2H, m), 9.82–9.83 (2H, m). ^{13}C{^{1}H} NMR ((CH$_3$)$_2$CO, 125 MHz) δ_C: 18.1, 21.4, 31.0, 65.2, 84.5, 86.3, 104.2, 106.1, 128.8, 137.8, 154.1, 159.3, 174.2.

[(η^6-*p*-cym)Ru(bathophen)Cl][PF$_6$] (13). [(η^6-*p*-cym)RuCl$_2$]$_2$ (0.10 g, 0.16 mmol), 4,7-diphenyl-1,10-phenanthroline (bathophen) (0.11 g, 0.32 mmol) and KPF$_6$ (0.06 g, 0.32 mmol) in dry methanol; the solution turned from red to dark green; a bright dark green solid was obtained; yield 88% (0.21 g, 0.29 mmol). Elemental analysis calc. for C$_{34}$H$_{30}$ClF$_6$N$_2$PRu %C: 54.59, %H: 4.04, %N: 3.74; found %C: 54.10, %H: 3.88, %N: 3.71. HR-MS: calc for C$_{34}$H$_{30}$ClN$_2$Ru [M]$^+$ *m/z* 603.1141, found *m/z* 603.1154. ^{1}H NMR ((CD$_3$)$_2$CO, 600 MHz) δ_H: 1.16 (6H, d, *J* = 7.0), 2.36 (3H, s), 2.92 (1H, sep, *J* = 7.0), 6.22 (2H, d, *J* = 6.5), 6.42 (2H, d, *J* = 6.5), 7.69–7.77 (10H, m), 8.15 (2H, d, *J* = 5.5), 8.23 (2H, s), 10.07 (2H, d, *J* = 5.5).

[(η^6-*p*-cym)Ru(MP)Cl][PF$_6$] (14). [(η^6-*p*-cym)RuCl$_2$]$_2$ (0.10 g, 0.16 mmol), 6-mercaptopurine (MP) (0.11 g, 0.32 mmol) and KPF$_6$ (0.06 g, 0.32 mmol) in dry methanol; the solution turned from red to dark yellow; a bright yellow solid was obtained; yield 22% (0.04 g, 0.07 mmol). Elemental analysis calc. for C$_{15}$H$_{18}$ClF$_6$N$_4$PRuS %C: 31.72, %H: 3.19, %N: 9.87; found %C: 31.52, %H: 3.18, %N: 9.41. HR-MS: calc for C$_{15}$H$_{17}$N$_4$RuS [M]$^+$ *m/z* 387.0215, found *m/z* 387.0207. ^{1}H NMR (CD$_3$OD, 600 MHz) δ_H: 1.23 (3H, d, *J* = 6.9), 1.26 (3H, d, *J* = 6.9), 2.25 (3H,

s), 2.84 (1H, sep, J = 6.9), 5.73 (1H, d, J = 5.9), 5.87 (1H, d, J = 6.0), 5.95 (1H, d, J = 6.1), 6.05 (1H, d, J = 5.9), 8.56 (1H, s), 9.21 (1H, s).

[(η^6-*p*-cym)Ru(bpm)(9-EtG-*N7*)][PF$_6$]$_2$ (15). [(η^6-*p*-cym)Ru(bpm)Cl][PF$_6$] (0.10 g, 0.17 mmol), AgNO$_3$ (0.03 g, 0.17 mmol), 9-ethylguanine (9-EtG) (0.10 g, 5.22 mmol) and KPF$_6$ (0.16 g, 0.85 mmol) in 10 mL of a 1:1 mixture of MeOH/H$_2$O; the solution turned from bright to dark yellow; a dark yellow solid was obtained; yield 68% (0.10 g, 0.12 mmol). Suitable crystals for X-ray crystallography were obtained from a saturated water/acetone solution at room temperature. Elemental analysis calc. for C$_{25}$H$_{29}$F$_{12}$N$_9$OP$_2$Ru·2H$_2$O %C: 33.42, %H: 3.70, %N: 14.03; found %C: 33.13, %H: 3.42, %N: 13.67. HR-MS: calc. for C$_{25}$H$_{29}$N$_9$ORu [M]$^{2+}$ *m/z* 286.5767, found *m/z* 286.5774. ^{1}H NMR (D$_2$O, 500 MHz) δ_H: 0.95 (6H, d, J = 7.0), 1.15 (3H, d, J = 7.0), 1.89 (3H, s), 2.46 (1H, sep, J = 7.0), 3.85 (2H, q, J = 7.0), 6.12 (2H, d, J = 7.0), 6.35 (2H, d, J = 6.5), 7.29 (1H, s), 7.99 (2H, t, J = 5.0), 9.19 (2H, dd, J = 2.0, J = 5.0), 10.08 (2H, dd, J = 2.0, J = 6.0).

3.2.3 X-ray Crystallography

The details of the diffraction instrumentation are described in Chapter 2. The X-ray crystal structures discussed in this chapter were determined by Dr Guy Clarkson from the Department of Chemistry at the University of Warwick. The structures of complexes **3**, **4**, **6**, **7** and **15** were solved by direct methods using SHELXS[11] (TREF) with additional light atoms found by Fourier methods. Hydrogen atoms were added at calculated positions and refined using a riding model with freely rotating methyl groups. Anisotropic displacement parameters were used for all non-H atoms; H-atoms were given isotropic displacement parameters equal to 1.2 (or 1.5 for methyl

hydrogen atoms) times the equivalent isotropic displacement parameter of the atom to which the H-atom is attached. Refinement used SHELXL 97.[12]

3.2.4   Aqueous Solution Chemistry

3.2.4.1   *Determination of the Ru−X Bond Hydrolysis*

Hydrolysis of the Ru^{II} arene halido complexes was monitored by UV-vis spectroscopy. The nature of the hydrolysis products as well as the extent of the reactions were verified by ^{1}H NMR spectroscopy or HR-MS. For UV-vis spectroscopy the complexes were dissolved in methanol and diluted with H_2O to give 100 μM solutions (5% MeOH/95% H_2O). The absorbance was recorded at several time intervals at the selected wavelength (at which the maximum changes in absorbance were registered) over *ca.* 8–16 h at 310 K. Plots of the change in absorbance with time were computer-fitted to the pseudo first-order rate equation, A = $C_0 + C_1e^{-kt}$ (where C_0 and C_1 are computer-fitted constants and A is the absorbance corresponding to time) using Origin version 8.0 (Microcal Software Ltd.) to give the half-lives ($t_{1/2}$, min) and rate constant values (k, min^{-1}). For ^{1}H NMR spectroscopy, the complexes were dissolved in MeOD-d_4 and diluted with D_2O to give 100 μM solutions (5% MeOD-d_4/95% D_2O). The spectra were acquired at various time intervals on a Bruker DMX 700 spectrometer ([1]H = 700 MHz) using 5 mm diameter tubes. All data processing was carried out using XWIN NMR version 2.0 (Bruker U.K. Ltd.). ^{1}H NMR signals were referenced to dioxane as an internal reference (δ = 3.71). The relative amounts of Ru^{II} arene halido species or aqua adducts (determined by integration of peaks in ^{1}H NMR spectra) were quantified.

3.2.4.2   *Determination of the Rate of Arene Loss*

The complexes were dissolved in MeOD-*d$_4$* and diluted with D$_2$O to give 100 μM solutions (5% MeOD-*d$_4$*/95% D$_2$O). Arene loss over time was followed by ^{1}H NMR spectroscopy at 310 K for 24 h.

3.2.5   **Interactions with Nucleobases**

The reaction of the Ru^{II} arene halido complexes with 9-ethylguanine (9-EtG) or 9-ethyladenine (9-EtA) was monitored over time. D$_2$O solutions (100 μM) of the Ru^{II} arene complexes were mixed with equimolar amounts of the corresponding nucleobases and the ^{1}H NMR spectra of the resulting solution was recorded at 310 K at various time intervals for 48 h.

3.2.6   **DFT Calculations**

Density functional theory (DFT) calculations were performed using the Amsterdam Density Functional (ADF) program suite (version 2009.01).[13] The conductor-like screening model (COSMO), as implemented in the ADF program, was used to simulate aqueous environments.

3.2.6.1   *Mechanism of Hydrolysis*

Geometries and energies were obtained by using the non-relativistic Perdew/Wang gradient-corrected functional (PW91). The conductor-like screening model (COSMO) as implemented in ADF was used to simulate the aqueous environment with ε = 78.4, probe radius = 1.9 Å, and the ND parameter which controls integration accuracy set to 4 (default 3). The frozen-core approximation[14] was applied with the orbitals up to and

including that labelled in brackets as follows: Ru[3d], O[1s], C[1s], N[1s], Cl[2p], Br[4p], and I[4d]. Basis sets and other details are described in A.3.1.

3.2.6.2 *DFT-Geometry Optimisation of Ru^{II} Arene Nucleobase Adducts*

Geometry optimisations were carried out for the 9-EtG and 9-EtA adducts of [(η^6-*p*-cym)Ru(bpm)(9-EtG-*N7*)]$^{2+}$ (**1-9EtG**), [(η^6-*p*-cym)Ru(bpm)(9-EtA-*N7*)]$^{2+}$ (**1-9EtA**), [(η^6-hmb)Ru(bpm)(9-EtG-*N7*)]$^{2+}$ (**8-EtG**), [(η^6-hmb)Ru(bpm)(9-EtA-*N7*)]$^{2+}$ (**8-EtA**) [(η^6-ind)Ru(bpm)(9-EtG-*N7*)]$^{2+}$ (**9-EtG**), [(η^6-ind)Ru(bpm)(9-EtA-*N7*)]$^{2+}$ (**9-EtA**), [(η^6-thn)Ru(bpm)(9-EtG-*N7*)]$^{2+}$ (**10-EtG-*N7***), [(η^6-thn)Ru(bpm)(9-EtG-*N3*)]$^{2+}$ (**10-EtG-*N3***), [(η^6-thn)Ru(bpm)(9-EtA-*N7*)]$^{2+}$ (**10-EtA**), [(η^6-*p*-cym)Ru(phen)(9-EtG-*N7*)]$^{2+}$ (**11-EtG**), [(η^6-*p*-cym)Ru(phen)(9-EtA-*N7*)]$^{2+}$ (**11-EtA**), [(η^6-*p*-cym)Ru(bathophen)(9-EtG-*N7*)]$^{2+}$ (**13-EtG**), and [(η^6-*p*-cym)Ru(bathophen)(9-EtA-*N7*)]$^{2+}$ (**13-EtA**); for the free 9-ethylguanine and 9-ethyladenine molecules, as well as for the Ru^{II} arene cations without the bound 9-EtG or 9-EtA. The energies of the separate fragments were subtracted from the energy of the entire Ru^{II} arene nucleobase adducts in the optimised geometry calculation to obtain the total binding energy of 9-EtG and 9-EtA in each complex.

3.3   Results

3.3.1   Synthesis and Characterisation

The [(η^6-arene)Ru(N,N')X]$^{n+}$ complexes studied in this work are listed in Table 3.1 and their general structures are shown in Figure 3.1. The monocationic Ru^{II} arene halido complexes **1−14** were synthesised as PF$_6$ salts in good yields (>50% in almost all cases) by the reaction of the corresponding [(η^6-arene)RuX$_2$]$_2$ dimer and an excess of the N,N'/N,S chelating ligand in methanol. The 9-EtG-*N7* complex **15** was synthesised as a PF$_6$ salt in good yield (~68%) by the reaction of [(η^6-*p*-cym)Ru(bpm)Cl][PF$_6$] (**1**) with AgNO$_3$ in a 1:1 mixture of MeOH/H$_2$O to afford the corresponding aqua species [(η^6-*p*-cym)Ru(bpm)(OH$_2$)]$^{2+}$ to which excesses of 9-EtG and KPF$_6$ were added. All the synthesised complexes were fully characterised by 1D and 2D ^{1}H NMR methods as well as 1D ^{13}C{^{1}H} NMR. The ^{1}H NMR resonances of the η^6-coordinated arenes and N,N'/N,S ligands in all the Ru^{II} arene halido complexes are low-field-shifted *ca.* 0.6 ppm compared to the free ligands. In the case of the mercaptopurine complex [(η^6-*p*-cym)Ru(MP)Cl][PF$_6$] (**14**), the four aromatic protons within the *p*-cym ring were observed as a set of four doublets (one doublet per proton), Figure 3.2.
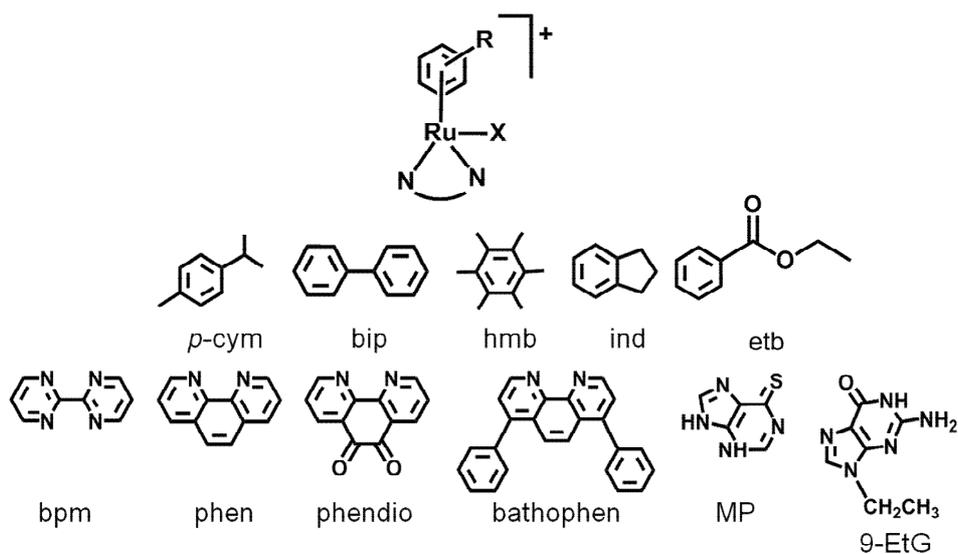
Figure 3.1. General structures of the complexes studied in this work synthesised as PF$_6$ salts.

Table 3.1. [(η^6-arene)Ru(N,N'/N,S)X]$^+$ complexes studied in this work.

Compound	Arene	N,N'/N,S	X
(**1**)	*p*-cym	bpm	Cl
(**2**)	*p*-cym	bpm	Br
(**3**)	*p*-cym	bpm	I
(**4**)	bip	bpm	Cl
(**5**)	bip	bpm	Br
(**6**)	bip	bpm	I
(**7**)	etb	bpm	Cl
(**8**)	hmb	bpm	Cl
(**9**)	ind	bpm	Cl
(**10**)	thn	bpm	Cl
(**11**)	*p*-cym	phen	Cl
(**12**)	*p*-cym	phendio	Cl
(**13**)	*p*-cym	bathophen	Cl
(**14**)	*p*-cym	MP	Cl
(**15**)	*p*-cym	bpm	9-EtG
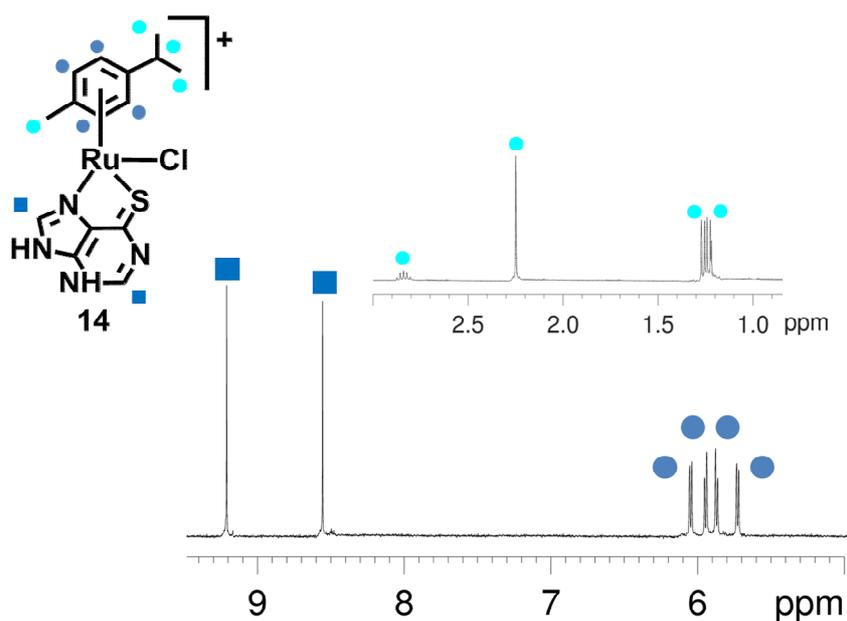
Figure 3.2. ^{1}H NMR spectra of complex [(η^6-*p*-cym)Ru(MP)Cl][PF$_6$] (**14**) in MeOD-d_4 solution. ■ = MP, ● = *p*-cym.

3.3.2 X-ray Crystal Structures

The molecular structures of complexes **3**, **4**, **6**, **7** and **15** were determined by single crystal X-ray diffraction. The molecular structure of complex **1** has been previously published.[9b] Selected bond lengths and angles are given in Table 3.2, the structures with numbering schemes are shown in Figure 3.3 and the crystallographic data are listed in Table A.3.1. Selected H-bond lengths and angles not described herein are shown in Table A.3.2. In all cases, the complexes adopt the familiar pseudo-octahedral three-legged piano stool geometry common to all other Ru^{II} arene structures[15] with the Ru^{II} atom π-bonded to the corresponding arene ligand (*p*-cym in **3** and **15**; bip in **4** and **6**; or etb in **7**), coordinated to a chloride (**4** and **7**), to an iodide (**3** and **6**), or to *N7* of 9-EtG (**15**), and to two nitrogen atoms of the chelating ligand 2,2'-bipyrimidine (bpm) which constitute the three legs of the piano stool.

Table 3.2. Selected bond lengths (Å) and angles ($^{\circ}$) for [(η^6-*p*-cym)Ru(bpm)I][PF$_6$] (**3**), [(η^6-bip)Ru(bpm)Cl][PF$_6$] (**4**), [(η^6-bip)Ru(bpm)I][PF$_6$] (**6**), [(η^6-etb)Ru(bpm)Cl][PF$_6$] (**7**), and [(η^6-*p*-cym)Ru(bpm)(9-EtG-*N7*)][PF$_6$]$_2$ (**15**).

Bond length/angle	(**3**)	(**4**)	(**6**)	(**7**)	(**15**)
Ru−arene$_{(centroid)}$	1.704	1.691	1.693	1.684	1.693
Ru(1)−I(1)	2.706(3)	–	2.70476(16)	–	–
Ru(1)−Cl(1)	–	2.402(8)	–	2.3743(9)	–
Ru(1)−N(13)	–	–	–	–	2.1125(19)
Ru(1)−N(1)	2.091(2)	2.092(2)	2.0901(12)	2.073(3)	2.0972(18)
Ru(1)−N(8)	2.0833(19)	2.093(2)	2.0833(12)	2.081(3)	2.0941(18)
C(6)−C(7)	1.472(4)	1.476(4)	1.477(2)	1.472(5)	1.477(3)
N(8)−Ru(1)−N(1)	76.78(8)	76.72(9)	76.90(5)	77.06(12)	77.05(7)
I(1)−Ru(1)−N(8)	86.38(6)	–	82.60(3)	–	–
Cl(1)−Ru(1)−N(8)	–	83.64(6)	–	83.36(8)	–
I(1)−Ru(1)−N(1)	85.79(6)	–	88.00(3)	–	–
Cl(1)−Ru(1)−N(1)	–	83.00(7)	–	84.67(8)	–
N(13)−Ru(1)−N(8)	–	–	–	–	86.59(7)
N(13)−Ru(1)−N(1)	–	–	–	–	88.64(7)

The Ru^{II} to *p*-cym$_{(centroid)}$ distances (as measured from Mercury version 2.2) do not vary significantly between all the derivatives. Similarly, the Ru−Cl bond lengths in the Ru^{II} arene chlorido complexes are almost the same (~2.4 Å). The Ru(1)−I(1) bond lengths in **3** and **6** are also within the same range (~2.7 Å). The Ru(1)−N(1)$_{(bpm)}$ and Ru(1)−N(8)$_{(bpm)}$ bond lengths in these arene complexes are ~2.09 Å. The N(1)−Ru(1)−N(8) bond angles in complexes **3**, **4**, **6**, **7**, and **15** do not differ significantly from each other. In the case of complex [(η^6-bip)Ru(bpm)Cl][PF$_6$] (**4**), Figure 3.4 the Ru^{II} molecules lay back-to-back with an adjacent complex in an intermolecular π-π stacking interaction. The mean planes, defined by both the bound and the unbound phenyl rings (ph) in the bip arene, are perfectly parallel. The shortest atomic contact C(16)···C(22) is 3.298 Å and the centroid-centroid distance is 4.182 Å. The uncoordinated ph ring is tilted 36.2° relative to the main plane defined by the Ru–coordinated ph ring.
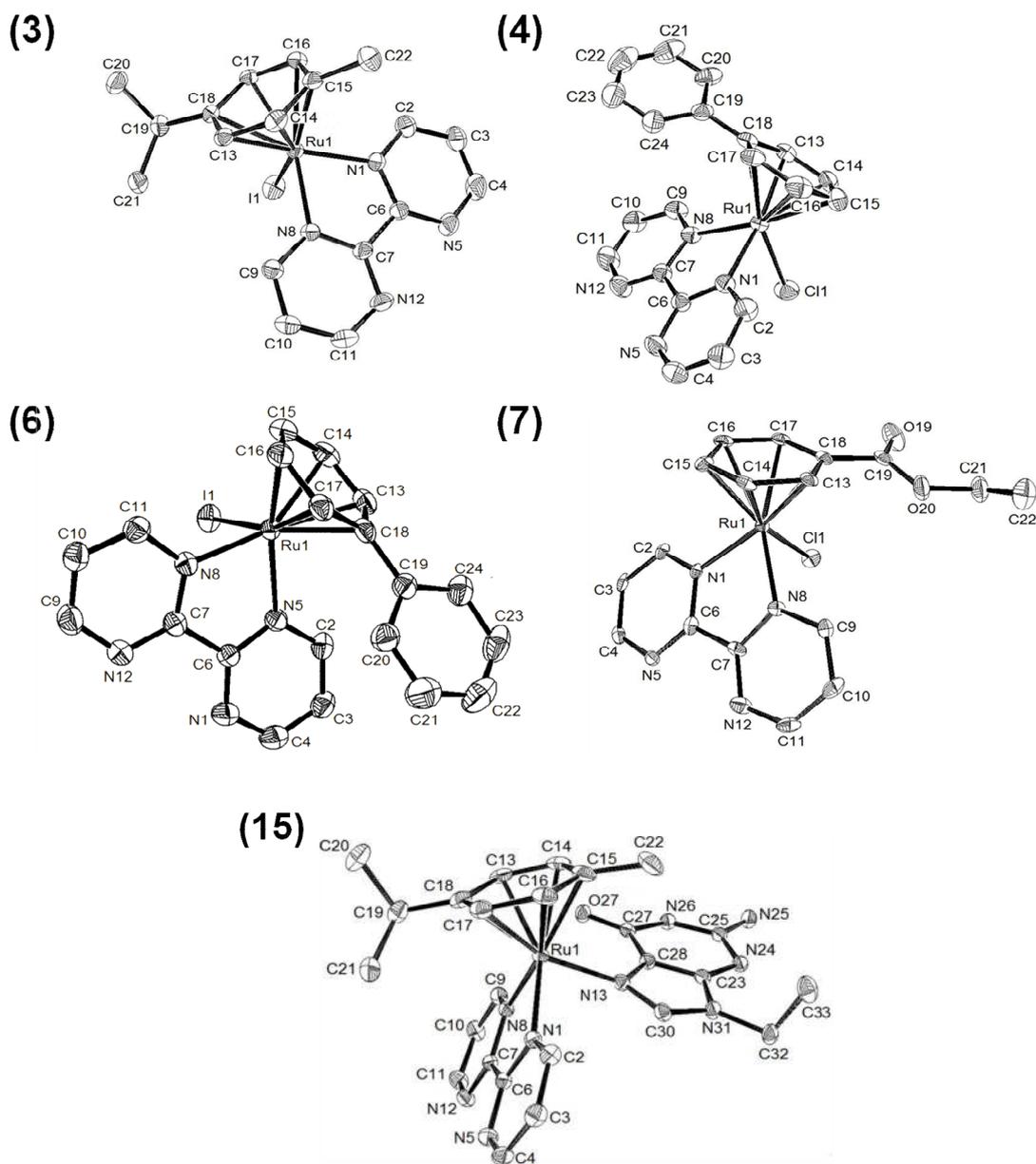
Figure 3.3. X-ray structure of the cations $[(\eta^6\text{-}p\text{-cym})Ru(bpm)I]^+$ (**3**), $[(\eta^6\text{-bip})Ru(bpm)Cl]^+$ (**4**), $[(\eta^6\text{-bip})Ru(bpm)I]^+$ (**6**), $[(\eta^6\text{-etb})Ru(bpm)Cl]^+$ (**7**), and $[(\eta^6\text{-}p\text{-cym})Ru(9\text{-EtG-}N7)]^{2+}$ (**15**). Thermal ellipsoids show 50% probability. The PF_6 anions and hydrogens have been omitted for clarity.

An intramolecular π-π interaction was found in the crystal structure of $[(\eta^6\text{-bip})Ru(bpm)I][PF_6]$ (**6**). The angle between mean planes of the interacting π systems (the uncoordinated ph ring in bip and a pyrazine ring from bpm) is 30.9°, the shortest atomic contact C(19)···C(2) is 3.130 Å, and the centroid-centroid distance is 4.183 Å,

Figure 3.5. The uncoordinated ph ring is tilted 31.48º towards the bpm chelating ligand.
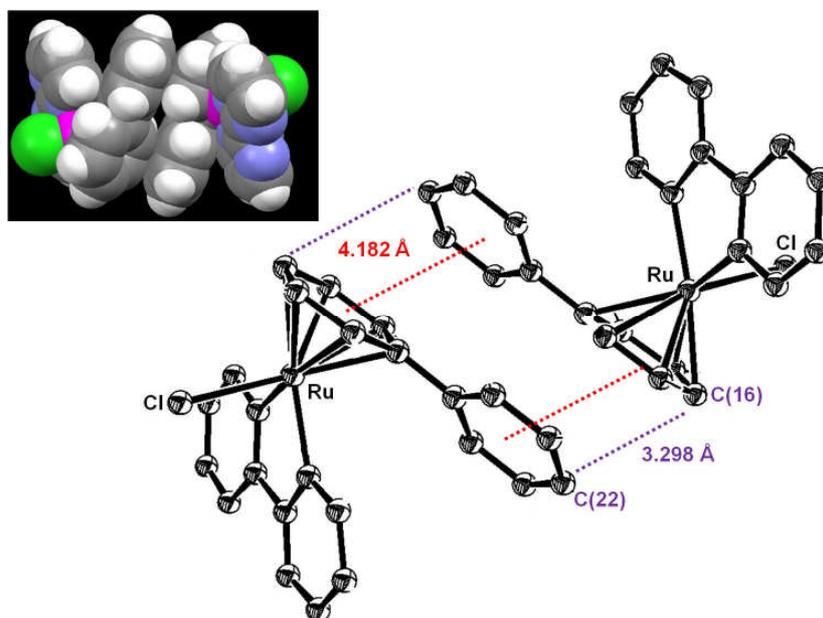
Figure 3.4. X-ray crystal structure of the cation $[(\eta^6\text{-bip})Ru(bpm)Cl]^+$ (**4**) showing π-π stacking through the interacting π systems (bip ligand). Inset: Spacefilling model showing the π-π interaction. The PF_6 anions and hydrogens have been omitted for clarity.
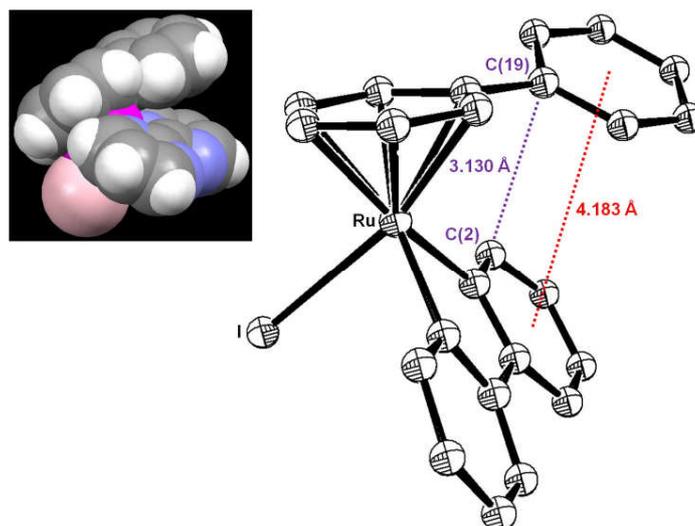
Figure 3.5. X-ray crystal structure of the cation $[(\eta^6\text{-bip})Ru(bpm)I]^+$ (**6**) showing π-π stacking through the π systems in the bip (uncoordinated benzene ring) and the bpm (pyrazine ring). Inset: Spacefilling model showing the π-π stacking. The PF_6 anions and hydrogens have been omitted for clarity.

Molecules in the unit cell of complex [(η^6-etb)Ru(bpm)Cl][PF$_6$] (**7**) lie in perpendicularly arranged pairs establishing a CH-π interaction between the C−H protons of one of the pyrazine rings in the bpm ligand and the centroid of one of the pyrazine rings in the bpm (belonging to the neighbouring molecule) with a C(4)−H(4A)···bpm$_{(centroid)}$ distance of 2.927 Å, Figure 3.6.
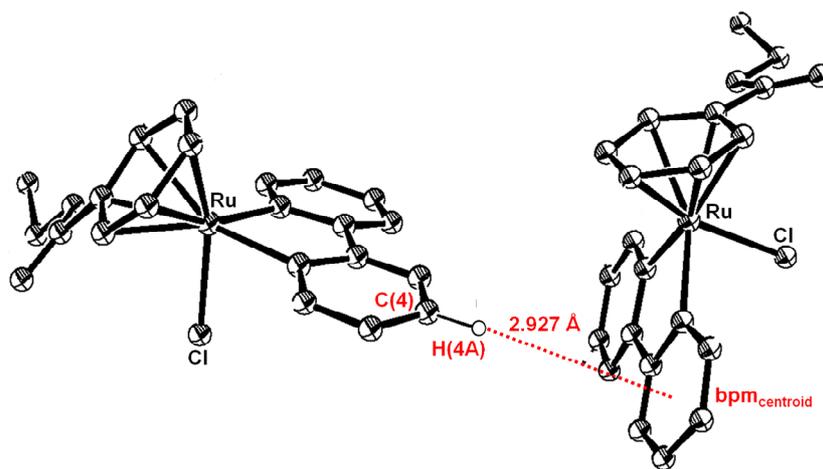
Figure 3.6. X-ray crystal structure of the cation [(η^6-etb)Ru(bpm)Cl]$^+$ (**7**) showing a CH-π interaction. The PF$_6$ anions and other hydrogens have been omitted for clarity.

In the crystal structure of [(η^6-*p*-cym)Ru(bpm)(9-EtG-*N7*)][PF$_6$]$_2$ (**15**), two cationic molecules are interconnected by means of a H-bond interaction in which two water molecules act as bridges (N26−H26···O100$_{(water)}$···H25−N25), Figure 3.7. Additionally, the 9-EtG adduct was also characterised by ^{1}H NMR spectroscopy and Figure 3.8 shows its 2D ^{1}H-^{1}H NOESY spectra. An NOE cross-peak between H8 of bound 9-EtG and the 2,2'-CH in bpm was observed, suggesting that these two atoms are in close proximity (as previously observed in analogous Ru^{II} arene complexes).[16] The twist angles between the aromatic pyrazine rings of the bpm chelating ligand in complexes **3**, **4**, **6**, **7**, and **15** are 4.5°, 4.6°, 9.4°, 10.0° and 4.6°, respectively.
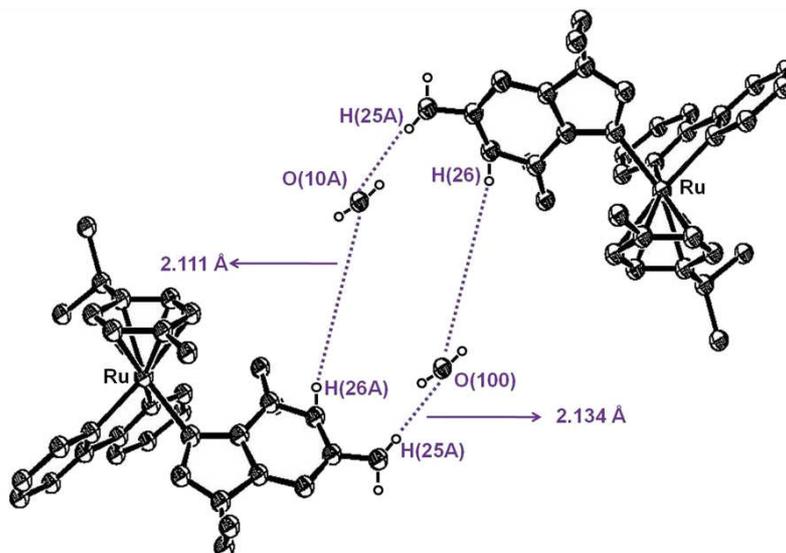
Figure 3.7. Bis-water bridged interaction found in the X-ray crystal structure of the cation [(η^6-*p*-cym)Ru(bpm)(9-EtG-*N7*)]$^{2+}$ (**15**). The PF$_6$ anions and other hydrogens have been omitted for clarity.
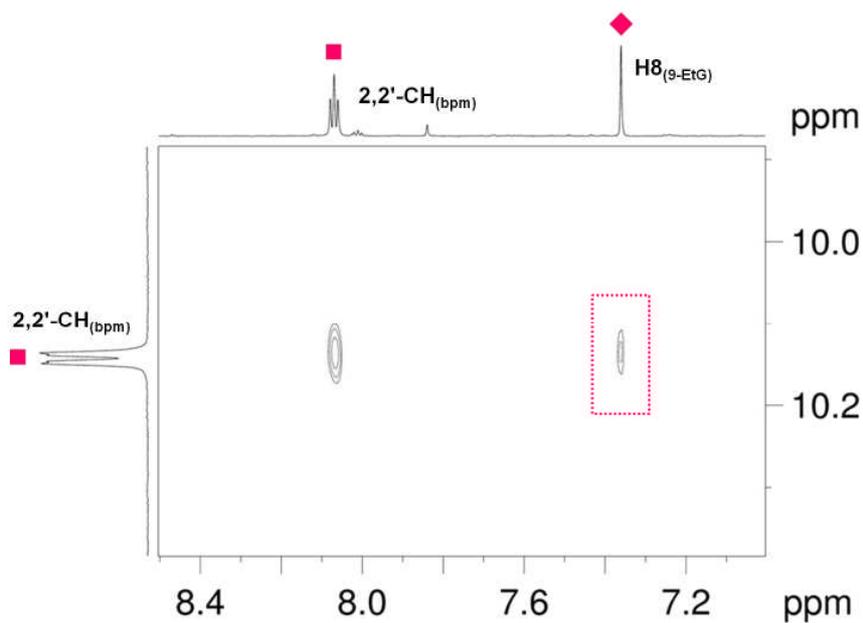
Figure 3.8. ^{1}H-^{1}H NOESY NMR spectrum of [(η^6-*p*-cym)Ru(bpm)(9-EtG-*N7*)]$^{2+}$ (**15**) in D$_2$O (aromatic region only). **Magenta** = [(η^6-*p*-cym)Ru(bpm)(9-EtG-*N7*)]$^{2+}$; ■ = bpm protons, ♦ = H8 of coordinated 9-EtG.

3.3.3   Aqueous Solution Chemistry

The aqueous solution chemistry (with respect to hydrolysis) of the Ru^{II} arene complexes **1−14** was studied at 310 K over *ca*. 8 h–16 h.

3.3.3.1   Hydrolysis Equilibria

In order to characterise the products of hydrolysis and determine the extent of the reactions, freshly-made 100 µM (5% MeOD-d_4/95% D$_2$O) solutions of complexes **1−13** were allowed to equilibrate for 24−48 h at 310 K and were then studied at the same temperature using ^{1}H NMR spectroscopy. Complex **14** was synthesised in low yields and its hydrolysis products were only verified by HR-MS. The ^{1}H NMR spectra of complexes **1−13** initially contained one major set of peaks (halido species) and then a second set of peaks increased in intensity with time. The new set of peaks had the same chemical shifts as those of the aqua adducts under the same conditions (~100 µM solutions, 5% MeOD-d_4/95% D$_2$O) at 310 K; the aqua adducts were separately prepared by treatment of the chlorido complexes with AgNO$_3$ in water at 298 K overnight and removal of AgCl by filtration. The mass-to-charge ratios and isotopic models obtained from HR-MS spectra were consistent with the formation of the aqua adducts as the corresponding products, Table 3.3.

Table 3.4 summarises the percentage of species detected at equilibrium by ^{1}H NMR after 24 h of reaction for complexes **1−11** and **13** followed by ^{1}H NMR. For complexes [(η^6-bip)Ru(bpm)Cl][PF$_6$] (**4**), [(η^6-bip)Ru(bpm)Br][PF$_6$] (**5**), [(η^6-etb)Ru(bpm)Cl][PF$_6$] (**7**), and [(η^6-*p*-cym)Ru(phendio)Cl][PF$_6$] (**12**) a separate set of peaks was also observed for the products which had undergone arene loss during the aquation. In the case of complex **12**, it was observed that it displayed a complicated ^{1}H NMR spectrum upon dissolution in 5% MeOD-d_4/95% D$_2$O at 310 K, suggesting

that besides hydrolysis of the chlorido bond, another reaction(s) (probably on the N,N' chelating ligand, 1,10-phenanthroline-5,6-dione (phendio)) had occurred over time. No further attempts to characterise the reaction products were made.

Table 3.3. Mass-to-charge ratios obtained from HR-MS spectra for the products of hydrolysis of Ru^{II} arene complexes **1−14**.

	Observed peak [M]$^{2+}$	Chemical formula Calc m/z	Found m/z
(**1**)	$[(\eta^6\text{-}p\text{-cym})\text{Ru(bpm)}(\text{OH}_2)]^{2+}$	$C_{18}H_{22}N_4O$ 206.0418	206.0408
(**2**)	$[(\eta^6\text{-bip})\text{Ru(bpm)}(\text{OH}_2)]^{2+}$	$C_{20}H_{18}N_4ORu$ 216.0262	216.0255
(**7**)	$[(\eta^6\text{-etbz})\text{Ru(bpm)}(\text{OH}_2)]^{2+}$	$C_{17}H_{18}N_4O_3Ru$ 214.0208	214.0203
(**8**)	$[(\eta^6\text{-hmb})\text{Ru(bpm)}(\text{OH}_2)]^{2+}$	$C_{20}H_{26}N_4ORu$ 220.0572	220.0567
(**9**)	$[(\eta^6\text{-ind})\text{Ru(bpm)}(\text{OH}_2)]^{2+}$	$C_{17}H_{18}N_4ORu$ 198.0259	198.0254
(**10**)	$[(\eta^6\text{-thn})\text{Ru(bpm)}(\text{OH}_2)]^{2+}$	$C_{17}H_{18}N_4ORu$ 204.7250	204.9615
(**11**)	$[(\eta^6\text{-}p\text{-cym})\text{Ru(phen)}(\text{OH}_2)]^{2+}$	$C_{22}H_{24}N_2ORu$ 217.0466	217.0458
(**12**)	$[(\eta^6\text{-}p\text{-cym})\text{Ru(phendio)}(\text{OH}_2)]^{2+}$	$C_{22}H_{22}N_2O_3Ru$ 232.0337	232.0325
(**13**)	$[(\eta^6\text{-}p\text{-cym})\text{Ru(bathophen)}(\text{OH}_2)]^{2+}$	$C_{34}H_{32}N_2ORu$ 293.0779	293.0665
(**14**)	$[(\eta^6\text{-}p\text{-cym})\text{Ru(MP)}(\text{OH}_2)]^{2+}$	$C_{15}H_{20}N_4OSRu$ 202.7415	202.0207

It can be seen that within the series of complexes having *p*-cym as arene and bpm as chelating ligand, the Cl (**1**) and Br (**2**) complexes hydrolysed to more than *ca.* 75% at equilibrium, but the I (**3**) complex afforded only *ca.* 31% of the aqua adduct. Similarly, in the bip/bpm series it was found that the Cl (**4**) and Br (**5**) complexes hydrolysed to a larger extent than the analogous I (**6**) complex. For complexes **1**, **11**, and **12−14** where *p*-cym (arene) and Cl (leaving group) are constant but the chelating ligand is varied, the amount of aqua adduct determined by ^{1}H NMR at equilibrium increases in the order bathophen (**13**) < phen (**11**) < bpm (**1**). When the chelating

ligand is maintained as bpm and the leaving group as Cl, changing the arene modifies

the extent of hydrolysis in the decreasing order *p*-cym (**1**) > thn (**10**) > ind (**9**) > hmb

(**8**) > etb (**7**) > bip (**4**).

Table 3.4. Percentage of species present at equilibrium after 24 h of the hydrolysis reaction in a 100 μM (5% MeOD-d_4/95% D$_2$O solution) at 310 K of complexes **1**−**11** and **13** followed by ^{1}H NMR.

	Compound	% Ru−X	% Ru−OH$_2$	% Arene loss
(**1**)	[(η^6-*p*-cym)Ru(bpm)Cl][PF$_6$]	21.8	78.2	0.0
(**2**)	[(η^6-*p*-cym)Ru(bpm)Br][PF$_6$]	10.2	89.8	0.0
(**3**)	[(η^6-*p*-cym)Ru(bpm)I][PF$_6$]	68.9	31.1	0.0
(**4**)	[(η^6-bip)Ru(bpm)Cl][PF$_6$]	34.3	17.6	48.1
(**5**)	[(η^6-bip)Ru(bpm)Br][PF$_6$]	18.0	13.7	68.3
(**6**)	[(η^6-bip)Ru(bpm)I][PF$_6$]	95.5	4.5	0.0
(**7**)	[(η^6-etb)Ru(bpm)Cl][PF$_6$]	78.4	18.7	2.9
(**8**)	[(η^6-hmb)Ru(bpm)Cl][PF$_6$]	56.2	43.8	0.0
(**9**)	[(η^6-ind)Ru(bpm)Cl][PF$_6$]	42.1	57.9	0.0
(**10**)	[(η^6-thn)Ru(bpm)Cl][PF$_6$]	24.6	75.4	0.0
(**11**)	[(η^6-*p*-cym)Ru(phen)Cl][PF$_6$]	46.5	53.5	0.0
(**13**)	[(η^6-*p*-cym)Ru(bathophen)Cl][PF$_6$]	49.3	50.7	0.0

3.3.3.2   Kinetics of Hydrolysis

Dissolution of compounds **1**–**14** in 5% MeOH/95% H$_2$O at 310 K gave rise to ligand

exchange reactions as indicated by the concomitant changes in UV-Vis absorption

bands. The time evolution spectra for all the Ru^{II} arene complexes at 310 K are shown

in Figure 3.9. The time dependence of the absorbance of all the complexes at the

selected wavelength followed pseudo first-order kinetics in each case. The

corresponding rate constants and half-life values are listed in Table 3.5. The

dependence of the absorbance at 332 nm over *ca.* 16 h during aquation of [(η^6-*p*-

cym)Ru(bpm)Cl][PF$_6$] (**1**) at 310 K is shown in Figure 3.10.
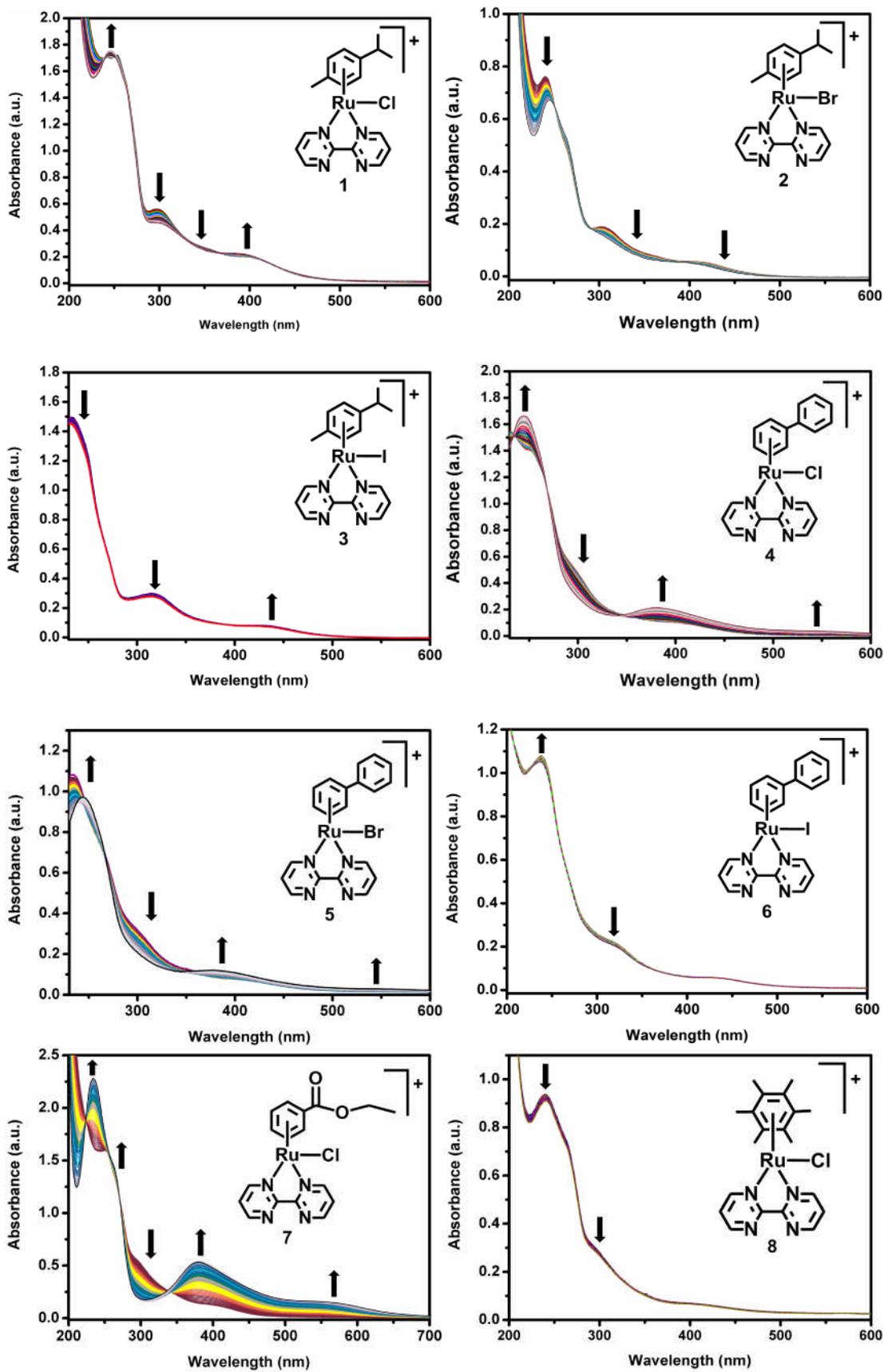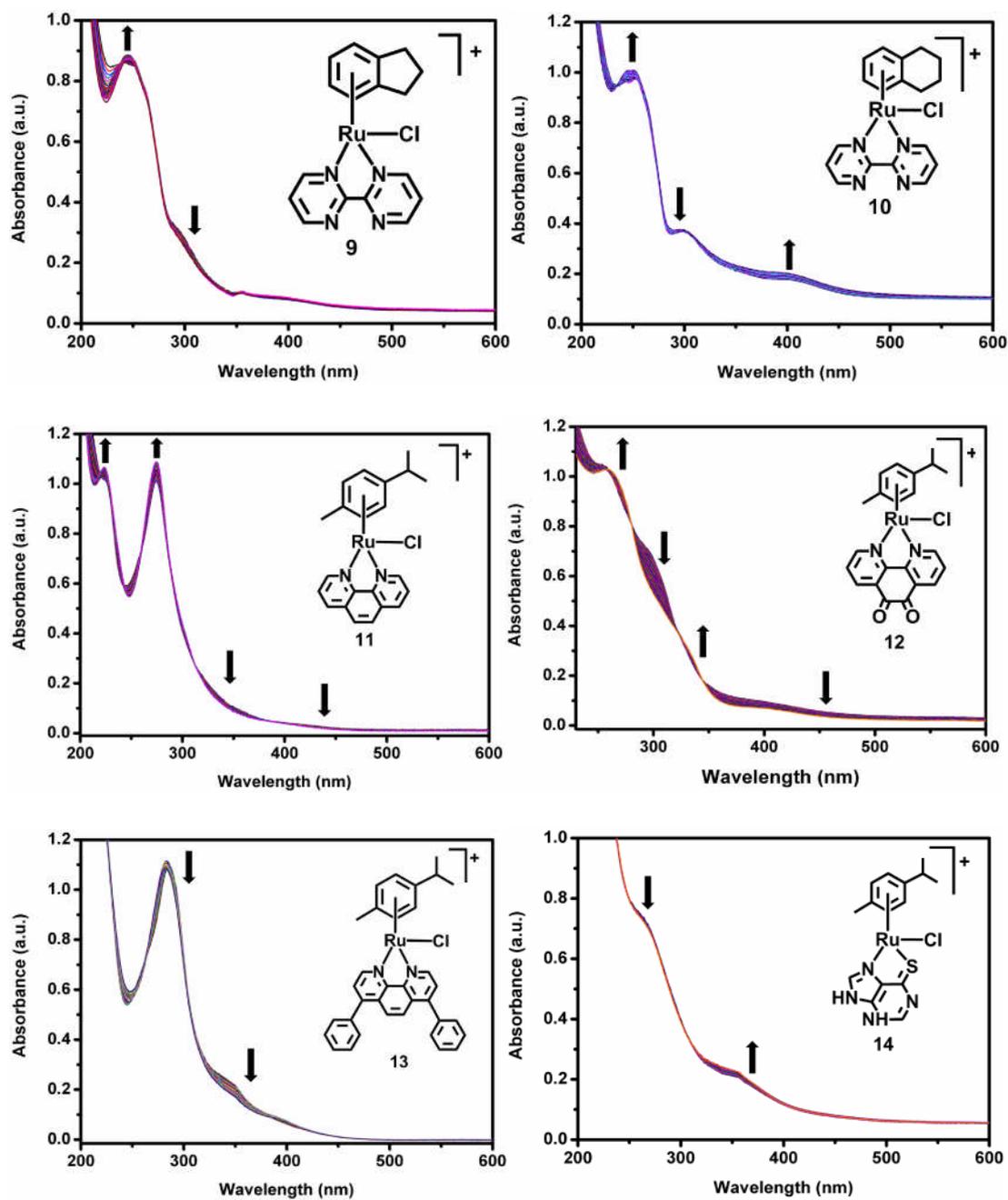
Figure 3.9. Time evolution of the hydrolysis reaction of complexes **1**–**14** in a 100 μM (5% MeOH/95% H$_2$O) solution at 310 K followed by UV-vis spectroscopy.

Table 3.5. Hydrolysis data for complexes **1−14** determined by UV-vis spectroscopy as 100 µM (5% MeOH/95% H$_2$O) solutions at 310 K.

	Compound	t$_{1/2}$ (min)	k $\times$ 10^{-3} (min^{-1})[a]
(**1**)	[(η^6-*p*-cym)Ru(bpm)Cl][PF$_6$]	92.3	7.51 ± 0.07
(**2**)	[(η^6-*p*-cym)Ru(bpm)Br][PF$_6$]	22.4	31.0 ± 0.91
(**3**)	[(η^6-*p*-cym)Ru(bpm)I][PF$_6$]	234.8	2.95 ± 0.08
(**4**)	[(η^6-bip)Ru(bpm)Cl][PF$_6$]^b	175.9	3.94 ± 0.04
(**5**)	[(η^6-bip)Ru(bpm)Br][PF$_6$]^b	39.7	17.0 ± 0.31
(**6**)	[(η^6-bip)Ru(bpm)I][PF$_6$]^b	714.6	0.97 ± 0.04
(**7**)	[(η^6-etb)Ru(bpm)Cl][PF$_6$]^b	14.5	50.0 ± 0.05
(**8**)	[(η^6-hmb)Ru(bpm)Cl][PF$_6$]	40.2	17.2 ± 1.32
(**9**)	[(η^6-ind)Ru(bpm)Cl][PF$_6$]	43.3	16.0 ± 0.15
(**10**)	[(η^6-thn)Ru(bpm)Cl][PF$_6$]	89.9	7.71 ± 0.44
(**11**)	[(η^6-*p*-cym)Ru(phen)Cl][PF$_6$]	22.8	30.5 ± 0.43
(**12**)	[(η^6-*p*-cym)Ru(phendio)Cl][PF$_6$]^b	59.6	11.6 ± 0.10
(**13**)	[(η^6-*p*-cym)Ru(bathophen)Cl][PF$_6$]	16.9	40.8 ± 0.86
(**14**)	[(η^6-*p*-cym)Ru(MP)Cl][PF$_6$]	23.9	29.0 ± 0.81

^{a} The errors quoted are fitting errors
^{b} The rate constants for complexes that underwent arene loss detected by ^{1}H NMR (**4**, **5**, **7**, and **12**) were determined over the period of time before the onset of arene loss
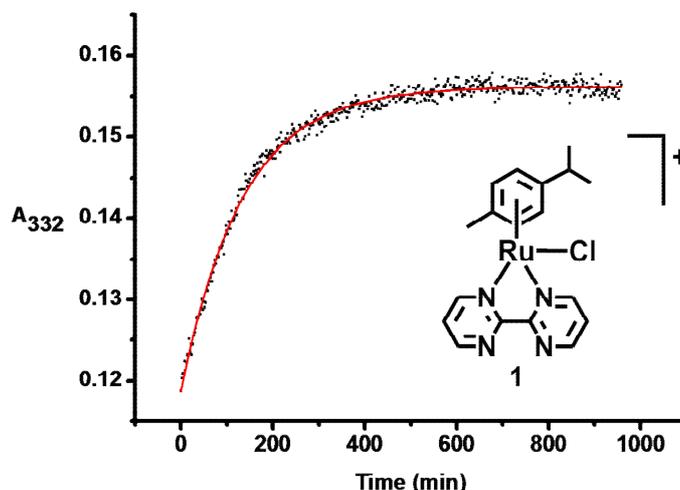
Figure 3.10. Dependence of the absorbance at 332 nm over *ca.* 16 h during aquation of [(η^6-*p*-cym)Ru(bpm)Cl][PF$_6$] (**1**) at 310 K. The red solid line is the best fit to pseudo-first order kinetics.

From Table 3.5 can be seen that within the series of complexes having *p*-cym as arene and bpm as chelating ligand, the hydrolysis rates decrease in the order Br (**2**) > Cl (**1**) > I (**3**). The same observation is found for the bip/bpm series where the corresponding rates decrease in the order Br (**5**) > Cl (**4**) > I (**6**). In the case where *p*-cym (arene) and

Cl (leaving group) are kept constant but the bpm chelating ligand is replaced, the half-life values increase in the order bathophen (**13**) < phen (**11**) < MP (**14**) < phendio (**12**) < bpm (**1**). In the case when the chelating ligand is maintained as bpm and the leaving group as Cl, changing the arene modifies the rate of hydrolysis in the increasing order *p*-cym (**1**) < thn (**10**) < ind (**9**) < hmb (**8**) < etb (**7**).

3.3.3.3 pK$_a$* Determination.

The changes in the ^{1}H NMR chemical shifts of the aromatic protons in either the corresponding arene rings or the corresponding N,N' chelating ligands of the aqua adducts of complexes **1** (*p*-cym/bpm), **8** (hmb/bpm), **9** (ind/bpm), **10** (thn/bpm), **11** (*p*-cym/phen), and **13** (*p*-cym/bathophen) present in an equilibrated 100 μM (D$_2$O) solution at 310 K were followed with change in pH* over the range *ca.* 1 to 12. Figure 3.11 shows how the peaks shift to higher field due to deprotonation of the bound water molecule in the aqua adduct of complex **1**, $[(\eta^6$-*p*-cym)Ru(bpm)(OH$_2$)]$^{2+}$, but do not change in intensity as an indication that no other species are being formed.
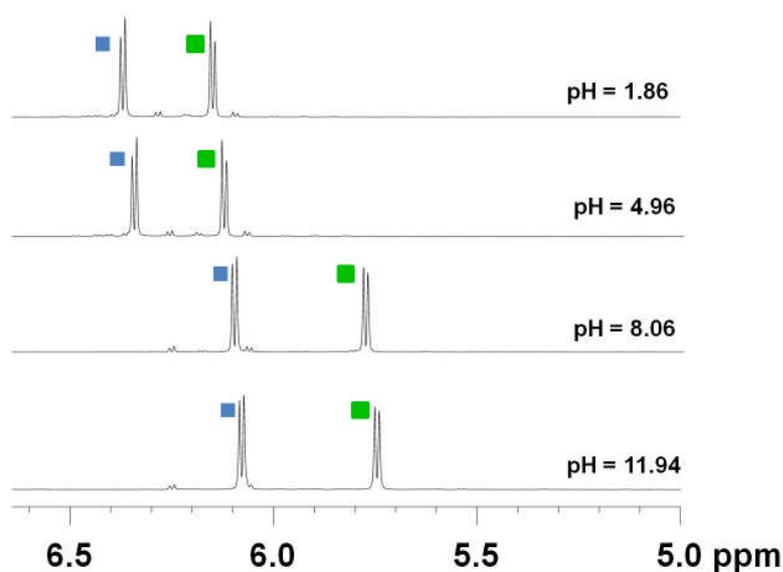
Figure 3.11. ^{1}H NMR spectra recorded during a pH* titration of a solution of the aqua adduct of complex **1**, $[(\eta^6$-*p*-cym)Ru(bpm)(D$_2$O)]$^{2+}$. **Blue** indicates the ortho$_{(methyl)}$ protons and **Green** indicates the metha$_{(methyl)}$ protons on the coordinated *p*-cym ring shifting with a change of pH*.

The data for complexes **1**, **8−11**, and **13** were fitted to the Henderson-Hasselbalch equation which yielded the corresponding pK_a^* values listed in Table 3.6. It can be seen that close to physiological pH values (~7.0) complexes **1**, **8**, **9** and **11** exist as a mixture of their aqua and hydroxido forms. However complexes **10** and **13**, which have higher pK_a^* values (10.12 and 10.84, respectively), exist predominantly as the aqua adducts.

Table 3.6. pK_a^* values for the aqua species of complexes **1**, **8−11**, and **13** at 310 K.

	Compound	pK_a^*
(**1**)	$[(\eta^6\text{-}p\text{-cym})Ru(bpm)(OH_2)]^{2+}$	6.96
(**8**)	$[(\eta^6\text{-hmb})Ru(bpm)(OH_2)]^{2+}$	7.04
(**9**)	$[(\eta^6\text{-ind})Ru(bpm)(OH_2)]^{2+}$	6.91
(**10**)	$[(\eta^6\text{-thn})Ru(bpm)(OH_2)]^{2+}$	10.12
(**11**)	$[(\eta^6\text{-}p\text{-cym})Ru(phen)(OH_2)]^{2+}$	7.32
(**13**)	$[(\eta^6\text{-}p\text{-cym})Ru(bathophen)(OH_2)]^{2+}$	10.84

3.3.4 Mechanism of Hydrolysis: Density Functional Theory (DFT) Approach

Density Functional Theory (DFT) computational methods were employed to obtain information about the influence of the leaving group on the mechanism of hydrolysis for the *p*-cym/bpm series of Ru^{II} arene complexes **1−6**. A test of the structural accuracy of the functional PW91 with COSMO solvation was performed by comparing the fully optimised structures of the cations in complexes **1–6** with the corresponding X-ray crystal structures of **1**,[9b] **3**, **4** and **6**. The functional PW91 was found to overestimate the Ru^{II} bond lengths by *ca.* 0.01−0.04 Å, particularly for the computed Ru−X distances (~2.44 Å) which were ~0.05 Å longer than those found in the solid state. However, the overall agreement with the experimental data was satisfactory. A scheme for the reaction modelled is shown in Figure 3.12.
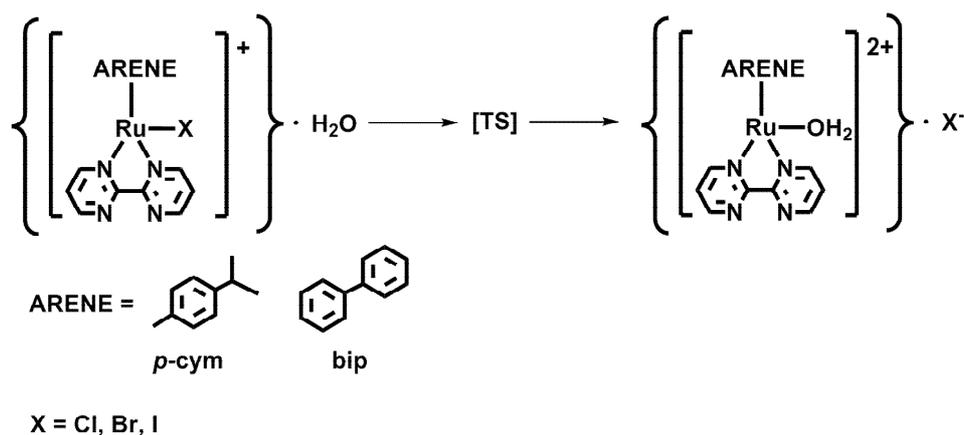
Figure 3.12. Hydrolysis reaction modelled for the cationic Ru^{II} arene complexes $[(\eta^6\text{-}$arene$)Ru(bpm)X]^+$ (**1–6**). [TS] is transition state.

For each of the resting states ([RS] = $\{[(\eta^6\text{-}$arene$)Ru(bpm)X]^+ \cdot H_2O]\}$) and the corresponding products ([P] = $\{[(\eta^6\text{-}$arene$)Ru(bpm)(OH_2)]^{2+} \cdot X^-]\}$), the results from the calculations indicated that the systems retained both the entering (H_2O) and the leaving groups (X^-) within the second coordination sphere of the Ru^{II} centre. Complex **1** was chosen as a *model* system; based on previously reported work[5b] on analogous Ru^{II} arene complexes, a full geometry optimisation of its transition state ([TS]) was performed starting from Ru–Cl and Ru–OH_2 distances of 3.200 Å and 2.899 Å, respectively, in the initial geometry. The optimised structure for the [TS] for the Ru^{II} arene cation $[(\eta^6\text{-}p\text{-cym})Ru(bpm)Cl]^+$ is shown in Figure 3.13. The geometry-optimised structure in the [TS] of the Ru^{II} arene cation in complex **1**, gave Ru–Cl and Ru–OH_2 distances of 3.11 Å and 2.68 Å, respectively. The corresponding energy value determined for the [TS] (–6657.51 kcal mol^{-1}) was found to be 20.09 kcal mol^{-1} larger than that for the reagent in [RS]. Since the hydrolysis reaction could be *a priori* assumed to be either an associative, a dissociative, or a concerted process, a set of frequencies calculation was performed for the [TS] of the Ru^{II} arene cation in complex **1**. Two negative values of frequencies were retrieved from the computation,

–152 and –20 cm^{-1}. The first (and more negative) frequency value (–152 cm^{-1}) was related to the vibrational mode of the system where the entry of the water molecule (H$_2$O) and loss of the halido ligand (Cl$^-$) are a concerted process. The corresponding scaled displacement vectors are shown in Figure 3.14.
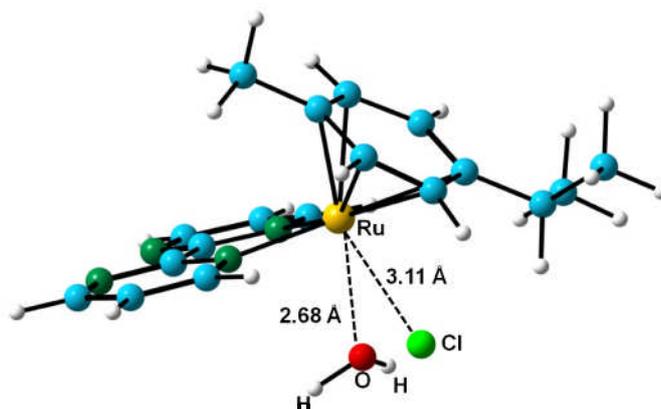
Figure 3.13. DFT-optimised geometry in the transition state [TS] during the hydrolysis reaction of the Ru^{II} arene cation [(η^6-*p*-cym)Ru(bpm)Cl]$^+$ (**1**).

Figure 3.14. DFT-optimised geometry in the transition state [TS] during the hydrolysis reaction of the Ru^{II} arene cation [(η^6-*p*-cym)Ru(bpm)Cl]$^+$ (**1**) showing the scaled displacement vectors.

Under the assumption that the same associative hydrolysis mechanism applies, the effect of varying X and the arene was explored. The results are listed in Table 3.7, from where it can be seen that the corresponding barrier heights do not vary significantly when the arene *p*-cym (in complexes **1**, **2**, and **3**) is substituted by bip (in

complexes **4**, **5**, and **6**). The forward reaction barriers and overall reaction energies for the aquation of the corresponding halido ligand (Cl, Br, or I) follow the increasing order Cl < Br < I and *p*-cym < bip.

Table 3.7. Selected bond lengths, forward reaction barriers, and overall reaction energies from Density Functional Theory (DFT) calculations for $\{[(\eta^6\text{-}p\text{-}cym)$Ru(bpm)X]$^+$·H$_2$O]$\}\rightarrow$[TS]$\rightarrow\{[(\eta^6\text{-}p\text{-}cym)$Ru(bpm)(OH$_2$)]$^{2+}$·Cl$^-$]$\}$.

	Ru–X/Ru–OH$_2$ [RS] (Å)	Ru–X/Ru–OH$_2$ [TS] (Å)	Ru–X/Ru–OH$_2$ [P] (Å)	$\Delta E^{\ddagger}$ (kcal mol^{-1})	ΔE_{reacc} (kcal mol^{-1})
p-cym/bpm					
(**1**) Cl	2.45/3.87	3.11/2.68	4.01/2.17	20.1	5.5
(**2**) Br	2.58/3.93	3.29/2.68	4.14/2.18	21.0	7.3
(**3**) I	2.77/4.09	3.58/2.68	4.43/2.19	22.8	9.6
bip/bpm					
(**4**) Cl	2.47/3.82	3.02/2.72	4.01/2.16	20.0	6.2
(**5**) Br	2.57/3.88	3.19/2.73	4.15/2.17	20.9	7.5
(**6**) I	2.76/4.01	3.45/2.74	4.41/2.17	22.3	10.3

[RS] = Resting state
[TS] = Transition state
[P] = Product
ΔE_{reacc} values relative to reactant species at zero

3.3.5 Interactions with Nucleobases

The possibility that some of the Ru^{II} arene halido complexes studied herein could react directly with nucleobases was investigated. Interactions between 9-ethylguanine (9-EtG), 9-ethyladenine (9-EtA), and complexes **1**, **8**–**11**, and **13** were studied by means of multidimensional ^{1}H NMR spectroscopy and the nature of the products was verified by HR-MS. All the reactions were carried out in an NMR tube in D$_2$O and followed for 48 h at 310 K. Figure 3.15 shows the reaction of complex **11** with 9-EtG as a generic example.
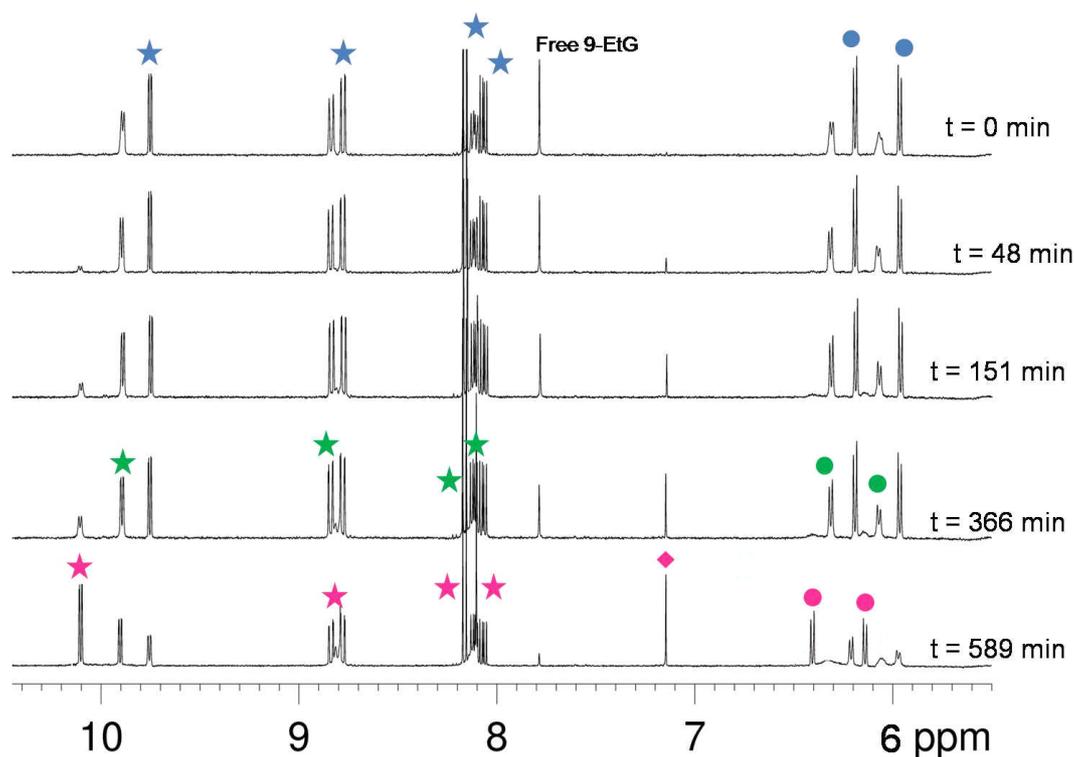
Figure 3.15. Time dependence of the ^{1}H NMR spectra of a 100 µM solution of [(η^6-*p*-cym)Ru(phen)Cl][PF$_6$] (**11**) in D$_2$O at 310 K in the presence of an equimolar amount of 9-EtG. **Blue** = [(η^6-*p*-cym)Ru(phen)Cl]$^+$, **Green** =[(η^6-*p*-cym)Ru(phen)(OH$_2$)]$^{2+}$, **Magenta** = [(η^6-*p*-cym)Ru(phen)(9-EtG-*N7*)]$^{2+}$; ★ = phen, ● = *p*-cym; ♦ = bound 9-EtG-*N7*.

The interactions occur *via* the *in situ* formation of the corresponding reactive aqua adduct for each complex upon hydrolysis, followed by coordination (mainly) to the *N7* position as has been previously observed for similar Ru^{II} arene guanine and adenine adducts.[5a,17] Figure 3.16 shows the numbering scheme for the nucleobases 9-EtG and 9-EtA.
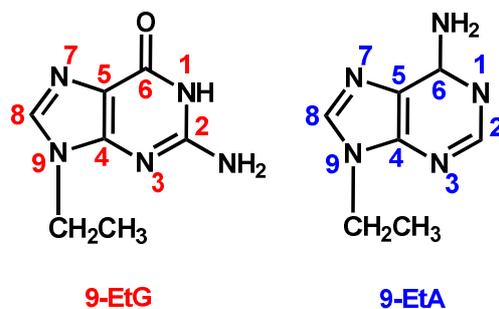
Figure 3.16. Numbering scheme for the nucleobases 9-EtG and 9-EtA.

Peaks assigned to the bound 9-EtG-*N7* in all complexes are shifted to high field in comparison to those of free 9-EtG. The H8 peak in all the Ru^{II} arene guanine adducts has a chemical shift in the range of 7.15–7.60 ppm (free 9-EtG is found at 7.79 ppm under the same conditions). Table 3.8 lists the percentage of species present in solution for the reaction of complexes **1**, **8**–**11**, and **13** with 9-EtG at selected sets of time. The most quantitative reactions with 9-EtG were found for complexes **8**, **9**, and **10**. Interestingly, for complex **10** around 12% of a second guanine-bound species was also detected at equilibrium (*ca*. 510 min), Figure 3.17. A similar experiment was carried out to investigate the possibility of forming 9-ethyladenine (9-EtA) adducts with the Ru^{II} arene complexes **1**, **8**–**11**, and **13**. The addition of an equimolar amount of 9-EtA to freshly prepared 100 μM D$_2$O solutions of the complexes at 310 K resulted in no new species formed even after 48 h of reaction.

Table 3.8. Time dependence and extent of formation of nucleobase adducts for 100 μM aqueous solutions of Ru^{II} arene complexes **1**, **8**–**11**, and **13** determined by ^{1}H NMR spectroscopy at 310 K.

	Compound	Time (min)	% 9-EtG-*N7* adduct	% 9-EtA-*N7* adduct
(**1**)	[(η^6-*p*-cym)Ru(bpm)Cl][PF$_6$]	104[a]	34.1	–
		2880	34.1	0.0
(**8**)	[(η^6-hmb)Ru(bpm)Cl][PF$_6$]	56[a]	80.6	–
		2880	80.6	0.0
(**9**)	[(η^6-ind)Ru(bpm)Cl][PF$_6$]	52[a]	94.3	–
		2880	94.3	0.0
(**10**)	[(η^6-thn)Ru(bpm)Cl][PF$_6$]	510[a]	88.9/11.1[b]	–
		2880	88.9/11.1[b]	0.0
(**11**)	[(η^6-*p*-cym)Ru(phen)Cl][PF$_6$]	589[a]	72.0	–
		2880	72.0	0.0
(**13**)	[(η^6-*p*-cym)Ru(bathophen)Cl][PF$_6$]	1419[a]	40.2	–
		2880	40.2	0.0

[a] Time needed to reach equilibrium
[b] Coordination to form the second 9-EtG adduct occurs presumably *via N3*
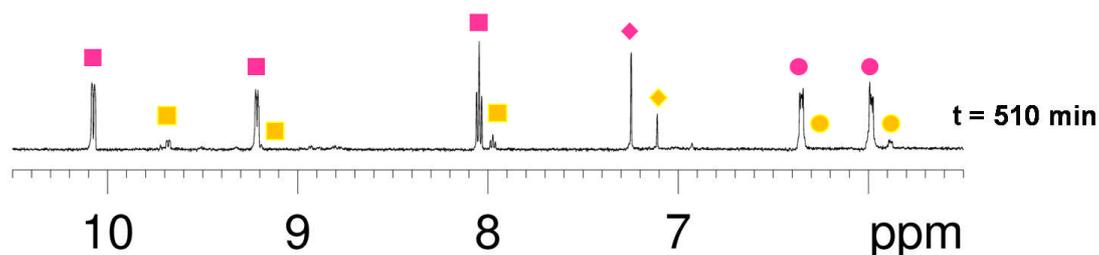
Figure 3.17. ^{1}H NMR spectra of the reaction of a 100 μM solution of $[(\eta^6\text{-thn})\text{Ru(bpm)Cl}][\text{PF}_6]$ (**10**) with equimolar amounts of 9-EtG in D$_2$O at 310 K after 510 min. **Magenta** $= [(\eta^6\text{-thn})\text{Ru(bpm)(9-EtG-}N7)]^{2+}$; **Yellow** $= [(\eta^6\text{-thn})\text{Ru(bpm)(9-EtG-}N3)]^{2+}$; ■ = bpm, ● = *p*-cym; ♦ = bound 9-EtG.

The second H8 peak observed by ^{1}H NMR from the reaction of 9-EtG and complex **10** has a chemical shift of 7.11 ppm and is assumed to arise from the *N3* coordination to the Ru^{II} centre to form $[(\eta^6\text{-thn})\text{Ru(bpm)(9-EtG-}N3)]^{2+}$ (as it has also been suggested for other metal complexes).[17] The mass-to-charge ratios and isotopic models obtained from HR-MS spectra were consistent with the formation of the guanine adducts as the corresponding products of the individual reactions, Table 3.9.

Table 3.9. Mass-to-charge ratios obtained from HR-MS spectra for the products of interactions of Ru^{II} arene complexes **1**, **8**–**11**, and **13** with 9-EtG

	Observed peak $[M]^{2+}$	Chemical formula Calc *m/z*	Found *m/z*
(**1**)	$[(\eta^6\text{-}p\text{-cym})\text{Ru(bpm)(9-EtG-}N7)]^{2+}$	C$_{25}$H$_{29}$N$_9$ORu 286.5767	286.5755
(**8**)	$[(\eta^6\text{-hmb})\text{Ru(bpm)(9-EtG-}N7)]^{2+}$	C$_{27}$H$_{33}$N$_9$ORu 300.5924	300.5916
(**9**)	$[(\eta^6\text{-ind})\text{Ru(bpm)(9-EtG-}N7)]^{2+}$	C$_{24}$H$_{25}$N$_9$ORu 278.5610	278.5601
(**10**)	$[(\eta^6\text{-thn})\text{Ru(bpm)(9-EtG-}N7)]^{2+}$	C$_{25}$H$_{27}$N$_9$ORu 570.6165	570.6155
(**11**)	$[(\eta^6\text{-}p\text{-cym})\text{Ru(phen)(9-EtG-}N7)]^{2+}$	C$_{29}$H$_{31}$N$_7$ORu 297.5815	297.5820
(**13**)	$[(\eta^6\text{-}p\text{-cym})\text{Ru(bathophen)(9-EtG-}N7)]^{2+}$	C$_{41}$H$_{39}$N$_7$ORu 373.6130	373.6127.

3.3.6 DFT-Geometry Optimisation of Ru^{II} Arene Nucleobase Adducts

In order to gain further knowledge on the nature and relative stabilities of the guanine and adenine adducts of the Ru^{II} arene complexes **1**, **8−11**, and **13**, their optimised geometries were obtained using DFT calculations. Their minimum energy structures are shown in Figures 3.18 and 3.19 (for the 9-EtG-*N7* and the 9-EtA-*N7* adducts, respectively). The total binding energies for both nucleobases are shown in Table 3.10.
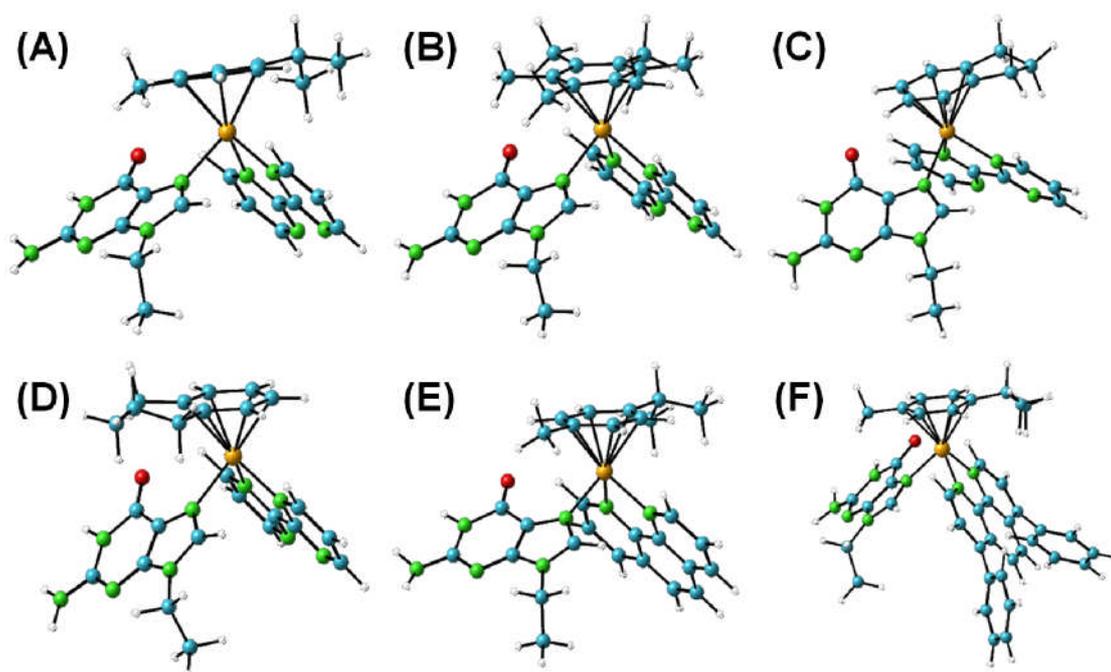
Figure 3.18. Optimised geometries for the guanine adducts (A) [(η^6-*p*-cym)Ru(bpm)(9-EtG-*N7*)]^{2+} (**1-EtG**), (B) [(η^6-hmb)Ru(bpm)(9-EtG-*N7*)]^{2+} (**8-EtG**), (C) [(η^6-ind)Ru(bpm)(9-EtG-*N7*)]^{2+} (**9-EtG**), (D) [(η^6-thn)Ru(bpm)(9-EtG-*N7*)]^{2+} (**10-EtG**), (E) [(η^6-*p*-cym)Ru(phen)(9-EtG-*N7*)]^{2+} (**11-EtG**), and (F) [(η^6-*p*-cym)Ru(bathophen)(9-EtG-*N7*)]^{2+} (**13-EtG**).

The binding energies include a COSMO contribution which simulates an aqueous environment. Under these conditions, the binding of 9-ethylguanine was found to be more favorable than that of 9-ethyladenine by ~10.0 kcal mol^{−1}. Furthermore, the nucleobase 9-ethylguanine shows significant binding energies towards all compounds

($\geq$38.5 kcal mol^{-1}), the largest value being for the adduct [(η^6-thn)Ru(bpm)(9-EtG-*N7*)]$^{2+}$ (**10-9EtG**) with a binding energy of 41.0 kcal mol^{-1}. In the case of 9-ethyladenine, it was found that it has a smaller binding energy value towards all compounds ($\leq$34.4 kcal mol^{-1}); the largest energy was calculated for the adduct [(η^6-thn)Ru(bpm)(9-EtA-*N7*)]$^{2+}$ (**10-9EtA**).
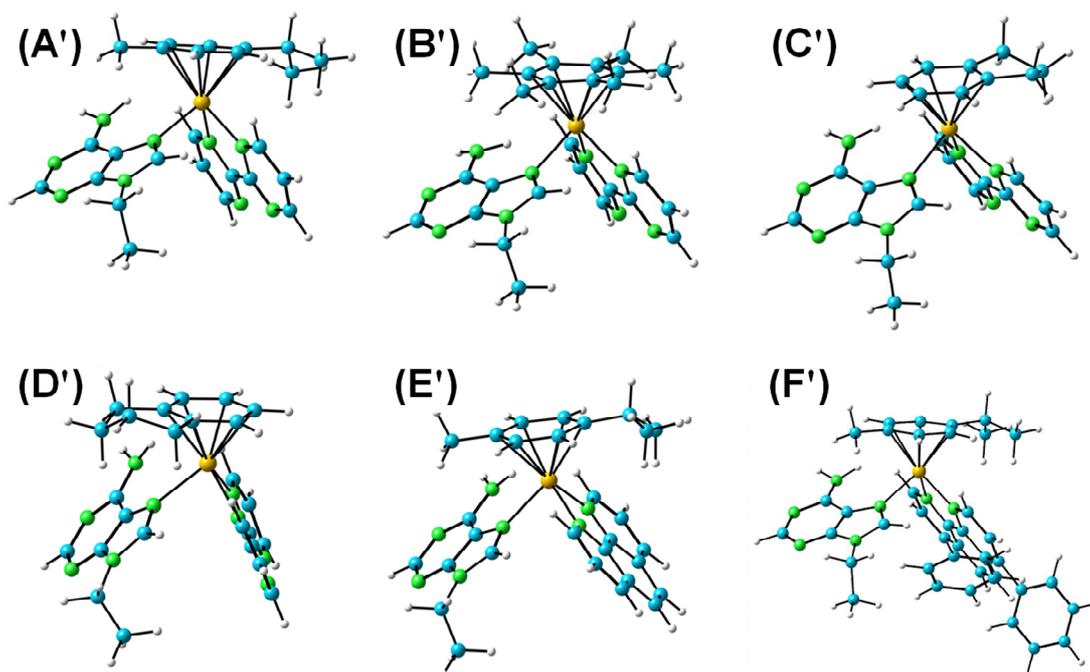
Figure 3.19. Optimised geometries for the adenine adducts (A') [(η^6-*p*-cym)Ru(bpm)(9-EtA-*N7*)]$^{2+}$ (**1-EtA**), (B') [(η^6-hmb)Ru(bpm)(9-EtA-*N7*)]$^{2+}$ (**8-EtA**), (C') [(η^6-ind)Ru(bpm)(9-EtA-*N7*)]$^{2+}$ (**9-EtA**), (D') [(η^6-thn)Ru(bpm)(9-EtA-*N7*)]$^{2+}$ (**10-EtA**), (E') [(η^6-*p*-cym)Ru(phen)(9-EtA-*N7*)]$^{2+}$ (**11-EtA**), and (F') [(η^6-*p*-cym)Ru(bathophen)(9-EtA-*N7*)]$^{2+}$ (**13-EtA**).

Table 3.10. Solution (COSMO) 9-EtG and 9-EtA binding energies for adducts of Ru^{II} arene complexes **1**, **8**–**11**, and **13**.

Compound	9-EtG (kcal mol^{-1})	9-EtA (kcal mol^{-1})
(**1**)	38.5	30.8
(**8**)	39.3	30.3
(**9**)	39.3	32.4
(**10**)	41.0	34.4
(**11**)	39.8	33.7
(**13**)	38.7	32.3

The binding of 9-EtG to the *N3* position in complex **10** was also investigated. The minimum energy structures are shown in Figure 3.20 for both the 9-EtG-*N7* and 9-EtG-*N3* adducts. The calculated total binding energies are 41.0 and 18.5 kcal mol^{-1} for the 9-EtG-*N7* and the 9-EtG-*N3* adduct, respectively.

10-9EtG-*N7*   **10-9EtG-*N3***
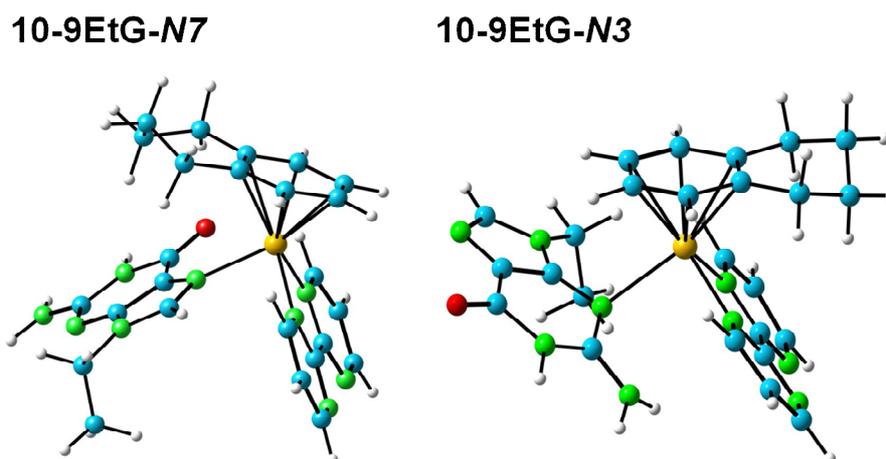
Figure 3.20. DFT-optimised geometries for the guanine adducts [(η^6-thn)Ru(bpm)(9-EtG-*N7*)]$^{2+}$ (**10-EtG-*N7***) and [(η^6-thn)Ru(bpm)(9-EtG-*N3*)]$^{2+}$ (**10-EtG-*N3***).

3.3.7 DNA Interactions in Cell-Free Media

In order to explore the possibility of having DNA as the potential target for this new family of compounds, the complexes [(η^6-*p*-cym)Ru(bpm)Cl]$^+$ (**1**) and [(η^6-*p*-cym)Ru(phen)Cl]$^+$ (**11**) were selected for preliminary studies of CT-DNA interactions in cell-free media.

3.3.7.1 DNA Binding Kinetics

The results of binding experiments are summarised in Table 3.11. The results show that both complexes reacted with CT-DNA to a moderate extent and the reactions were complete after *ca*. 20 h. Complex **11** was found to bind much faster and to a

larger extent than complex **1**. Complex **11** reaches equilibrium within the first 1.5 hours of reaction. After 24 h of reaction both complexes were found to reach the same extent of binding of ~60%, Figure 3.21. The dialysis experiments against two different sodium salts indicate that the coordination of the Ru^{II} arene complexes to CT-DNA is reversible and dependent on the nature of the salt. In the case of [(η^6-p-cym)Ru(phen)(Cl)][PF$_6$] (**11**), dialysis either against 10 mM NaClO$_4$ or 0.1 M of NaCl resulted in a decrease on the percentage of complex bound to DNA (down to ~20.0%). For complex **1**, dialysis against 10 mM NaClO$_4$ did not change the percentage of complex reacted with DNA whereas dialysis against 0.1 M of NaCl reduced the amount to the same extent as found for complex **11** (~20.0%).
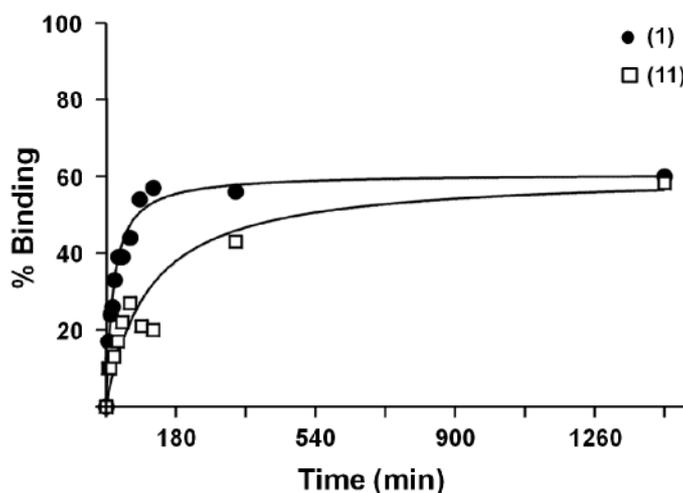
Figure 3.21. Percentage of binding to CT-DNA obtained from the experiment of DNA precipitation by EtOH of complexes [(η^6-p-cym)Ru(bpm)(Cl)][PF$_6$] (**1**) and [(η^6-p-cym)Ru(phen)(Cl)][PF$_6$] (**11**) as a function of time.

Table 3.11. Percentage of binding of complexes **1** and **11** to CT-DNA (1.0×10^{-4} M) in 10 mM NaClO$_4$ at 310 K as determined by FAAS after 24 h.

	% Ru^{II} bound	
Method	(**1**)[a]	(**11**)[a]
DNA precipitation by EtOH	61.0	62.0
Dialysis against 10 mM NaClO$_4$	77.0	19.6
Dialysis against 0.1 M NaCl	21.6	17.3

[a] Data are the average of two independent experiments

3.3.7.2   DNA Transcription by RNA Polymerase In Vitro

Further investigations were aimed at finding the Ru binding sites in natural DNA for the reactions of [(η^6-*p*-cym)Ru(bpm)(Cl)][PF$_6$] (**1**) and [(η^6-*p*-cym)Ru(phen)(Cl)][PF$_6$] (**11**). The autoradiogram of the inhibition of RNA synthesis by T7 RNA polymerase on pSP73KB DNA containing adducts of the Ru^{II} arene complexes or cisplatin is shown in Figure 3.22. The bands corresponding to the transcription of DNA modified by complexes **1** and **11** yielded fragments of newly synthesised RNA of defined sizes, which indicates that RNA synthesis on these templates was prematurely terminated. The major stop sites produced occurred at similar positions in the gel and were solely at guanine residues, Figure 3.23 for both Ru^{II} arene complexes. Both the profiles are similar to that obtained for DNA treated with the anticancer drug cisplatin and also to those reported previously for the Ru^{II} arene compounds, such as [(η^6-arene)Ru(en)Cl]$^+$.[18]
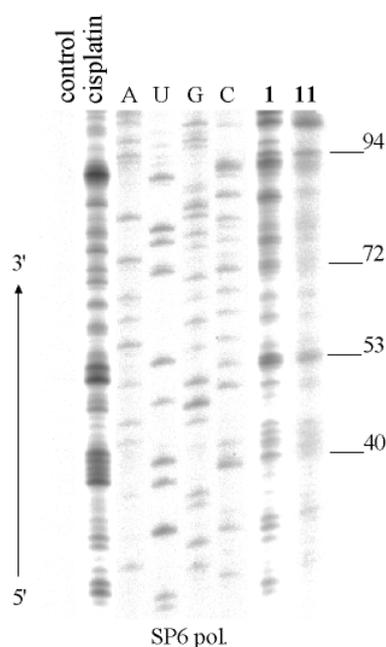
Figure 3.22. Autoradiogram of 6% polyacrylamide/8 M urea sequencing gel showing inhibition of RNA synthesis by T7 RNA polymerase on pSP73KB DNA containing adducts of Ru^{II} arene complexes or cisplatin. Lanes: chain terminated marker RNAs, cisplatin, at $r_b = 0.02$; A, U, G and C, the template modified by Ru^{II} arene compounds **1** and **11**.

```
                                  1
5'     ATTTAGGTGA CACTATAGAA CCAGATCTGA TATCATCGAT
3'     TAAATCCACT GTGATATCTT GGTCTAGACT ATAGTAGCTA
                            SP6

       24
       GAATTCGAGC TCGGATCCTC TAGAGTCGAC CTGCAGGCAT
       CTTAAGCTCG AGCCTAGGAG ATCTCAGCTG GACGTCCGTA
                •   •   •   ••• •       •   •   •   •   •

       64
       GCAAGCTTCA GCTGCTCGAG GCCGGTCTCC CTATA    3'
       CGTTCGAAGT CGACGAGCTC CGGCCAGAGG GATAT    5'
              •      •    •    •    ••      ••  •
```
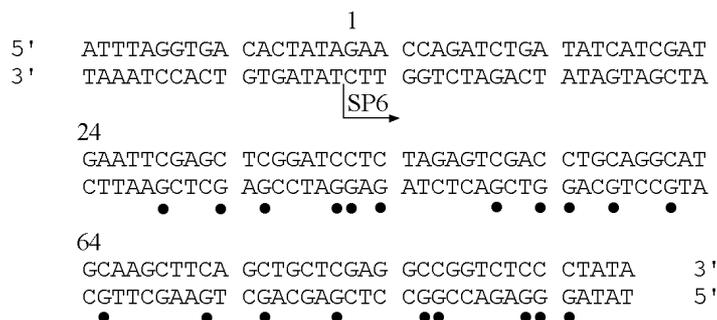
Figure 3.23. Left: Schematic diagram showing the portion of the sequence used to monitor inhibition of RNA synthesis by the Ru^{II} arene complexes **1** and **11**. The arrows indicate the start of the T7 RNA polymerase, which used as template the upper strand of pSP73KB DNA, respectively. The numbers correspond to the nucleotide numbering in the sequence map of pSP73KB plasmid. (●) Indicates major stop sites for DNA modified by ruthenation.

3.3.7.3   Unwinding of Supercoiled pUC19 Plasmid DNA

The native agarose gel resulting from DNA modified by complexes $[(\eta^6\text{-}p\text{-}cym)Ru(bpm)(Cl)][PF_6]$ (**1**) and $[(\eta^6\text{-}p\text{-}cym)Ru(phen)(Cl)][PF_6]$ (**11**) are shown in Figure 3.24. The DNA unwinding angle produced by the adducts of **1** and **11** was determined to be 7.7° and 6.6°, respectively. The comigration point of the modified supercoiled and nicked DNA (r_b(c)) was reached at $r_b = 0.13$ and 0.15 (for **1** and **11**, respectively) as shown in Table 3.12.
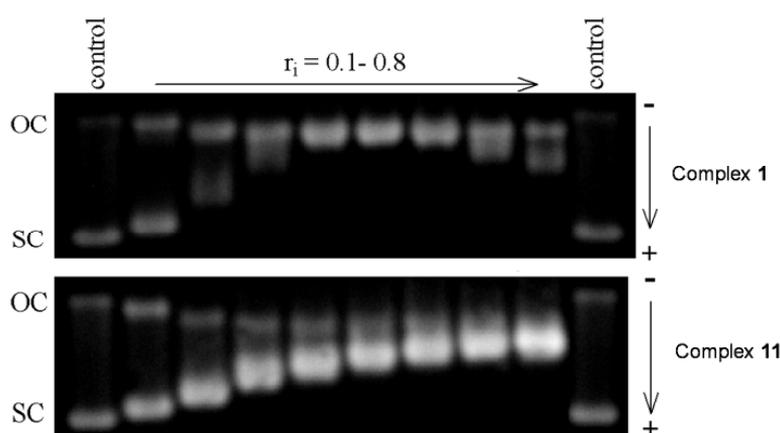
Figure 3.24. The unwinding of supercoiled pUC19 plasmid DNA (1.0×10^{-4} M) by complexes $[(\eta^6\text{-}p\text{-}cym)Ru(bpm)(Cl)][PF_6]$ (**1**) and $[(\eta^6\text{-}p\text{-}cym)Ru(phen)(Cl)][PF_6]$ (**11**). Left and right lanes are controls (unmodified DNA); top bands correspond to the form of nicked plasmid (OC) and the bottom bands to the closed and negatively supercoiled plasmid (SC). r_i is the molar ratio of free Ru complex to nucleotide phosphates at the onset of incubation with DNA.

Table 3.12. Unwinding of supercoiled pUC19 DNA by Ru^{II} arene complexes [(η^6-*p*-cym)Ru(bpm)(Cl)][PF$_6$] (**1**) and [(η^6-*p*-cym)Ru(phen)(Cl)][PF$_6$] (**11**).

	Compound	r_b(c)	Unwinding Angle (°)
(**1**)	[(η^6-*p*-cym)Ru(bpm)(Cl)][PF$_6$]	0.14	7.7±1.7
(**11**)	[(η^6-*p*-cym)Ru(phen) (Cl)][PF$_6$]	0.15	6.6±1.7
Cisplatin		0.08	13.0±0.4

3.3.8 Cancer Cell Growth Inhibition (IC$_{50}$ Values)

The concentrations of complexes at which 50% inhibition of growth of cancer cells is achieved (IC$_{50}$ values) were determined. The halido complexes **1−6** were tested against the A2780 human ovarian, A2780 cisplatin resistant human ovarian, A459 human lung, and HCT116 human colon cancer cell lines whereas the remaining halido complexes **8−11** and **13−14** were tested against the A2780 human ovarian cancer cell line. Complexes **1−6**, **8−10** and **14** displayed IC$_{50}$ values larger than 100 μM against the corresponding cell lines tested (IC$_{50}$ value for cisplatin was 1.0 μM under the same conditions). Complexes **11** and **13** were found to be cytotoxic to the A2780 human ovarian cancer cell line, Table 3.13. Both complexes contain *p*-cym as arene and Cl as leaving group. The most active complex is [(η^6-*p*-cym)Ru(bathophen)Cl][PF$_6$] (**13**) with an IC$_{50}$ value of 0.5 μM, (cisplatin 1.1 μM under the same conditions). The activity of complex [(η^6-*p*-cym)Ru(phen)Cl][PF$_6$] (**11**) against this cancer cell line is IC$_{50}$ 23 μM.

Table 3.13. IC$_{50}$ values for Ru^{II} arene complexes **11** and **13** against the A2780 human ovarian cancer cell line.

	Compound	IC$_{50}$ μM (A2780)[a]
(**11**)	[(η^6-*p*-cym)Ru(phen)Cl][PF$_6$]	22.9
(**13**)	[(η^6-*p*-cym)Ru(bathophen)Cl][PF$_6$]	0.5
	Cisplatin	1.1

[a] Complexes **1−6**, **8−10** and **14** had IC$_{50}$ values larger than 100 μM against the cell lines tested (*vide supra*; cisplatin 1.0 μM under the same conditions)

3.4 Discussion

Thirteen new Ru^{II} arene complexes containing N,N' chelating ligands (**1–13**) and one Ru^{II} arene complex with an N,S chelating ligand (**14**) (Figure 3.1) have been synthesised and fully characterised. The 9-EtG-*N7* adduct of [(η^6-*p*-cym)Ru(bpm)(9-EtG-*N7*)][PF$_6$]$_2$ (**15**) was also synthesised and fully characterised. Their aquation, acidity of their aqua adducts, nucleobase binding, cell-free media DNA interactions and IC$_{50}$ values in relation to the nature of the substituents on the Ru^{II} centre were investigated.

3.4.1   Synthesis and Characterisation

The ^{1}H NMR resonances of the coordinated η^6-arene and N,N'/N,S in all the new Ru^{II} arene halido complexes **1–14** are low-field-shifted *ca.* 0.6 ppm (compared to the free ligands) due to coordination to the Ru^{II} centre. Although work on Co^{III}, Pt^{II}, Rh^{III}, and Ir^{III} complexes with 6-mercaptopurine (MP) has been reported before,[19,20,21] examples of Ru^{II}−MP complexes are not so widespread and in most cases, they are not half-sandwich complexes.[22,23] Therefore, the Ru^{II} arene complex [(η^6-*p*-cym)Ru(MP)Cl]$^+$ (**14**) might be one of the few examples of piano-stool complexes which incorporate MP as a chelating ligand. Given that MP has multiple potential binding sites, its coordination to the Ru^{II} centre was elucidated using ^{1}H NMR spectroscopy. It is assumed that the MP ligand coordinates in a bidentate manner *via* the S and *N7* atoms, to form a five-membered chelate ring as previously observed in analogous complexes.[24] A magnetic inequivalency of the aromatic *p*-cym ring protons on going from the [(η^6-*p*-cym)RuCl$_2$]$_2$ dimer to the [(η^6-*p*-cym)Ru(MP)Cl][PF$_6$] (**14**) monomer was observed in the ^{1}H NMR spectrum of complex **14** in methanol-*d$_4$* solution. This evidence is in agreement with the generation of a Ru chiral centre.

3.4.2 X-ray Crystal Structures

The molecular structures of complexes **3**, **4**, **6**, **7** and **15** were determined by single crystal X-ray diffraction. The values for Ru–arene$_{(centroid)}$ bond lengths are comparable to analogous Ru^{II} arene complexes containing N,N' chelated ligands.[25,29,40,52] Neither the nature of the corresponding N,N' chelating ligand nor the halogen greatly influence the corresponding Ru–arene$_{(centroid)}$ distances (~1.70 Å). The Ru−X distances are not affected either by a change of arene or the N,N' chelating ligand. The corresponding Ru–I bond lengths in **3** and **6** are slightly shorter compared to other Ru^{II} arene complexes containing iodide as a leaving group.[26,27,28] For the four halido complexes, the Ru–N,N' bond lengths are significantly longer than those found in the crystal structures of similar arene Ru^{II} arene bipyridine complexes.[29] The X-ray crystal structures of compounds **3**, **4**, **6** and **7** show an increased number of intra and/or intermolecular π-π stacking interactions, particularly for complexes **4** and **6**, which contain bip as the arene. Their crystal packing also displays strong H-bonding throughout the unit cell, which is a common feature observed in similar Ru^{II} arene complexes containing extended aromatic rings.[30] In the case of complex **7**, particularly interesting is the presence of CH-π interactions between the C−H protons of one of the pyrazine rings in the 2,2'-bipyrimidine (bpm) chelating ligand and the centroid of one of the pyrazine rings in the bpm belonging to the neighbouring molecule. The occurrence of CH-π interactions is now well established[31,29] and the interaction ranges from weak (CH···π centre 2.6–3.0 Å) to very strong (CH···π centre < 2.6 Å).[32] Such interactions can play an important role in protein stability and in recognition processes. The CH···π interactions observed for complex **7** (2.9 Å) are well within the weak-interaction category. The nature of the arene ligand in these complexes seems to exert an important influence on the planarity of the bpm ligand.

The two pyrazine rings in the cation $[(\eta^6\text{-etb})\text{Ru(bpm)Cl}]^+$ (**7**) are considerably more twisted (~10.0º) compared to the chlorido analogue $[(\eta^6\text{-bip})\text{Ru(bpm)Cl}]^+$ (**4**) (~4.6º). This observation is in good agreement with the intramolecular π-π interactions found between the uncoordinated-bip ring and one of the pyrazine rings (assuming that a more planar bpm is needed to enhance such interactions). In contrast, complex **7** displays a more distorted bpm ligand since one of the pyrazine rings is properly spatially placed to promote the CH-π interactions with the neighbouring molecule. The crystal structure of the 9-EtG adduct **15** shows multiple H-bonding interactions throughout the crystal packing. The main fragments involved are bpm, 9-EtG, and the solvent molecules (water). Such aggregations have been observed in a number of Ru^{II} and Pt^{II} crystal structures containing purine derivatives.[33] Water is an important participant in intercalation modes and specific binding of water to DNA complexes can make a significant contribution to the free energy of drug binding.[34] The presence of numerous water molecules together with PF_6 anions contribute to the overall stabilisation of the crystal packing. The average H-bonding distances and angles (~3.0 Å and 160º, respectively) are indicative of their strong nature.

3.4.3   Mechanism of Hydrolysis

The transition state obtained from density functional theory (DFT) calculations, suggested that aquation of the $[(\eta^6\text{-arene})\text{Ru(bpm)X}]^+$ complexes where arene is *p*-cym (**1−3**) or bip (**4−6**) and X is Cl, Br, or I proceeds *via* a concerted interchange associative (I_a) mechanism rather than a stepwise dissociation/coordination process (dissociative, I_d). For the *p*-cym/bpm series of complexes (**1−3**) the reaction does not appear to be strongly associatively nor dissociatively activated, because the corresponding Ru–X bonds at the transition state extend by ~0.66, 0.71, and 0.81 Å

for Cl, Br, and I, respectively relative to the reactant species. In the case of the corresponding Ru–O bonds in the transition state, it was found that they are ~0.50 Å longer than in the aqua products in the three cases. The results for the bip/bpm series of complexes (**4−6**) showed that the hydrolysis might not be strongly associatively nor dissociatively activated either. The corresponding Ru–X bonds at the transition state extend by ~0.58, 0.61, and 0.69 Å for Cl, Br, and I, respectively relative to the reactants, whereas the Ru–O bonds in the transition state were found to be ~0.55 Å longer than in the aqua products. Given that Ru–X bond-breaking alone is not the rate controlling step in the associative pathway (I_a), a heavier (and larger) halide will impede the access of the H_2O molecule to the central Ru^{II} atom in associative states. This hypothesis is in good agreement with the experimental observation that complexes **3** and **6** (bearing I as the leaving group) display the slowest rates of hydrolysis within the corresponding series. This assumption has been also suggested for Ru complexes displaying higher coordination numbers (i.e. seven).[35] The calculated reaction barriers and overall reaction energies for the aquation of the halido complexes **1**–**6** follow the increasing order Cl ≈ Br < I. However, the effect of different halides on the experimental hydrolysis rates of these Ru^{II} arene complexes differs from the calculation and follows the increasing order Br < Cl < I. This trend has been experimentally observed before for platinum compounds of the type $[PtX_n(OH_2)_{4-n}]^{(2-n)+}$, for which Br analogues of Cl complexes hydrolyse faster in all three hydrolysis steps.[28] The calculated higher activation energies might be responsible for the observed slower hydrolysis of the iodido complexes during the associative ligand interchange in each series. The accuracy of the calculation was not able to account for the differences found experimentally in the hydrolysis rates between the Cl and Br complexes.

3.4.4 Aqueous Solution Chemistry

Complexes **2**, **5**, **7−9** and **11−14** undergo relatively fast hydrolysis with half-lives inthe order of minutes (less than 60 min). The reported half-lives of aquation of the previously reported chlorido ethylenediamine (en) Ru^{II} arene complexes, [(η^6-dha)Ru(en)Cl][PF$_6$], [(η^6-tha)Ru(en)Cl][PF$_6$] and [(η^6-bip)Ru(en)Cl][PF$_6$][36] are 10–80 times smaller than those of these complexes under comparable conditions. Within the *p*-cym/Cl series containing various chelating ligands, the presence of a better π-acceptor chelating ligand appears to increase the overall half-lives. By withdrawing electron-density from the Ru^{II} centre, the positive charge on the metal centre might increase making it less favourable for the chlorido ligand to leave thus slowing down the hydrolysis reaction. This argument explains why the rates increase in the order **1** (bpm) < **12** (phendio) < **11** (phen) ≈ **14** (MP) < **13** (bathophen). The fact that the substituent heteroatoms on the chelating ligands (such as the extra pair of nitrogens in 2,2'-bipyrimidine (bpm) or two oxygens in 1,10-phenanthroline-5,6-dione (phendio)) are electron donors[37] and may contribute to stabilise the Ru−Cl bonds by π-back donation. In this respect, previous work[36,38] has shown that an N,N' chelating group such as 2,2'-bipyridine (bpy) slows down substitution of the aqua ligand in [(η^6-C$_6$H$_6$)Ru(bpy)(OH$_2$)]$^{2+}$ just as the replacement of en by acetylacetonate (acac) to give [(η^6-arene)Ru(acac)(OH$_2$)]$^+$ complexes accelerates hydrolysis. Within the Ru^{II} arene bpm/Cl series, it was observed that the incorporation of arenes with either an increased aromatic character or electron withdrawing substituents in the coordinated ring, significantly decreases the rate of the hydrolysis reaction in the order **7** (etb) > **8** (hmb) > **9** (ind) > **10** (thn) > **1** (*p*-cym) > **4** (bip). Bip has a high aromaticity and competes as a π-acceptor[39] with the chelating ligand (bpm) for electron density. This leads to a weakening of the corresponding Ru−arene bonds and consequently to the

complete loss of the bip and etb in the case of complexes **4** and **7**, respectively. No arene loss is observed in the case of the other arenes, all of which have electron donating aliphatic substituents on the ring. The same arene loss was previously observed for other Ru^{II} bip complexes containing phenylazopyridines as π-acceptor ligands.[40] Within this same series of complexes **1**−**6**, it can also be noticed that a combination of a large leaving group (such as I) and a large arene (such as bip) in complexes **3** and **6**, together make the Ru^{II} centre less accessible to an incoming ligand. This effect corresponds to the experimental observation of a very slow hydrolysis rate. The inclusion of a more electronegative halide (like Cl or Br in **1** and **2** or **4** and **5**) leads to an increase in the hydrolysis rate, which is enhanced when the bulky arene is replaced by a less sterically-demanding ligand such as *p*-cym in complexes **1**−**3**. Arene ligands such as benzene (bz) are reported to exhibit a strong *trans*-labilising effect for the aqua ligand in $[(\eta^6\text{-bz})Ru(OH_2)_3]^{2+}$.[41] This class of strong π-acid ligands are able to accept electron density from the central Ru^{II} atom giving rise to a higher charge on the metal. Acidic hydrolysis of Ru^{III} complexes such as $[Ru(NH_3)_4(X)_2]^+$ and $[Ru(NH_3)_5X]^{2+}$ (X is Cl, Br, and I) occurs *via* an associative pathway in which bond-making is more important than bond-breaking. Therefore, the electron-accepting effect of strong π-acid arene ligands might be responsible for the shift toward a more associative pathway in the $I_d \leftrightarrow I_a$ mechanistic continuum for the $[(\eta^6\text{-}p\text{-cym})Ru(N,N')Cl]^+$ complexes studied herein.

For complexes **1** (*p*-cym/bpm), **8** (hmb/bpm), **9** (ind/bpm), and **11** (*p*-cym/phen) the pK_a* values were found to be in the range from 6.91 to 7.32 and are all significantly lower (*ca.* 1.5 units) than those of analogous $[(\eta^6\text{-arene})Ru(OH_2)]^{2+}$ complexes.[5b,42] In the case of complexes **10** (thn/bpm) and **13** (*p*-cym/bathophen), the values are considerably higher (10.12 and 10.84, respectively). Such a decrease in acidity has

been attributed before[46] to an increased electron density on the metal centre (as might be the case for **10** and **13**) favoured by a proper combination of electron donating/π-acceptor−arene/chelating ligands. Therefore, the coordinated aqua ligands of complexes **1**, **8**, **9**, and **11** will therefore undergo a slightly less basic dissociation (than that of complexes **10** and **13**) to give equal amounts of the corresponding aqua and hydroxido adducts at physiological pH (7.2–7.4). However, only the aqua adducts of complexes **10** and **13** will be present at biologically relevant pH. This behaviour could account for the observed extents of reactions with nucleobases (*vide infra*) given that hydroxido species are recognised to be relatively inert to substitution reactions than the corresponding aqua complexes.[43]

3.4.5   Interactions with Nucleobases

Since DNA is known to be a potential target for transition metal anticancer agents,[44] the reaction of complexes **1**, **8**–**11**, and **13** with 9-EtG and 9-EtA were investigated in aqueous solution at 310 K. The ^{1}H NMR peaks corresponding to H8 in all the 9-EtG-*N7* adducts are shifted to high field (~0.5 ppm) relative to free 9-EtG under the same conditions. Usually, metallation at the *N7* site of purine bases produces a low field shift of the H8 resonance by about 0.3–1 ppm.[45,46] This effect has also been observed before for analogous Ru^{II} arene complexes containing bpy[29] or acac[5a] as the chelating ligands. The observation could be attributed to the shielding effect exerted on H8 by a donation of electron density from the Ru^{II}–N$7_{(9\text{-}EtG)}$ bond by the corresponding N,N'-chelating ligands in complexes **1**, **8**–**11**, and **13**. The compounds studied in this work showed significant and rapid binding to 9-EtG-*N7* (detectable after *ca.* 10 min and to *ca.* 34–94% extent). The interactions for complexes [(η^6-*p*-cym)Ru(bpm)Cl)]$^+$ (**1**), [(η^6-thn)Ru(bpm)Cl)]$^+$ (**10**) and [(η^6-*p*-cym)Ru(bathophen)Cl)]$^+$ (**13**) require *ca.* 8 h

to reach equilibrium in each case. However, a different behaviour was observed for complexes [(η^6-hmb)Ru(bpm)Cl)]$^+$ (**8**) and [(η^6-ind)Ru(bpm)Cl)]$^+$ (**9**), whose interactions with 9-EtG showed to be much faster, reaching equilibrium after 56 and 52 min, respectively. The corresponding amounts of 9-EtG-*N7* adducts detected at equilibrium for all complexes did not change over the course of 48 h. The reactions were found to proceed to a wide range of extents and appear to be sensitive to both the nature of the arene and the N,N' chelating ligand. The reactions of complexes **1**, **11** and **13** having *p*-cym as arene but different chelating ligands seem to produce the lesser amounts of 9-EtG-*N7* adducts, increasing in the order **13** (bathophen) < **1** (bpm) < **11** (phen). A change of the arene significantly increases the extent of the reactions; the percentage of guanine adduct detected increases in the order **8** (hmb) < **9** (ind) < **10** (thn). Since nucleobase binding is likely to require initial hydrolysis of the chlorido bonds, the slow aquation rates and reduced extent of hydrolysis reactions determined for these complexes at equilibrium may be in turn one of the factors accounting for the observed extents of nucleobase binding. A second factor which might have an important role in the extent of the nucleobase reactions with the Ru^{II} arene complexes, is the stability of the guanine adduct formed. The calculated binding energies for 9-EtG in the corresponding nucleobase adducts appear to be related to the trend determined for the extent of nucleobase binding (*vide infra*); the more stable adducts are formed from the more quantitative reactions. None of the Ru^{II} arene complexes **1**, **8**–**11**, and **13** showed evidence of binding towards 9-ethyladenine. These complexes display a more discriminating behaviour towards binding to guanine bases when compared to cisplatin, for which binding to adenine is also observed.[47] It has been found that H-bonding from C6O in guanine to N–H protons in the bidentate chelating ligand ethylenediamine (en), is an important factor contributing to the high preference

for binding of {(η^6-arene)Ru(en)}$^{2+}$ to guanine versus adenine. Replacement of en (NH as H-bond donor) by bpm in these series of complexes did not change the selectivity for guanine bases.

3.4.6 DFT-Optimised Geometries for Nucleobase Adducts

Computational methods were used to gain insight into the guanine-specific binding observed for **1**, **8–11**, and **13**. Surprisingly, compounds **1**, **8**, **9**, and **10**, which were found to be non cytotoxic, showed a significant binding energy for 9-EtG-*N7* (~38.8 kcal mol^{-1}). The 9-EtG-*N7* adduct of compound **10** [(η^6-thn)Ru(bpm)(9-EtG-*N7*)]$^{2+}$ (**10-9EtG-*N7***) was found to be the most thermodynamically preferred with 41.0 kcal mol^{-1}. The binding of 9-ethyladenine was found to be less favourable than that of 9-ethylaguanine by ~10.0 kcal mol^{-1} in all cases and again, the highest binding energy value was determined for the 9-EtA-*N7* in [(η^6-thn)Ru(bpm)(9-EtA-*N7*)]$^{2+}$ (**10-9EtA-*N7***). This significant thermodynamic difference may account for the guanine-specific binding observed for the Ru^{II} arene complexes **1**, **8–11**, and **13** in solution. As would be expected, the binding energy of 9-EtG to complex **10** through *N7* is ~20 kcal mol^{-1} more stable than the binding through *N3* (the 9-EtG-*N3* adduct was also detected by ^{1}H NMR). The calculations were also able to reproduce the H-bond distance (CH$_{(N,N'-chelating)}$···O$_{(9-EtG)}$) found in the crystal structure of the 9-EtG adduct, complex **15** within sufficient accuracy. Therefore, it is assumed that the analogous values from the DFT-optimised geometries for the rest of the 9-EtG adducts of complexes **1**, **8–11** and **13** will also be within the expected ranges. The calculations predict CH$_{(N,N'-chelating)}$···O$_{(9-EtG)}$ distances within the range of 2.20–3.11 Å and C–H$_{(N,N'-chelating)}$···O$_{(9-EtG)}$ angles within 114.93–134.97°. Surprisingly, the shortest H-bond distance was found for the

9-EtG adduct of complex **10**, which might explain the high binding energy calculated for this adduct.

3.4.7   DNA Interactions in Cell-Free Media

Two complexes of the form [(η^6-*p*-cym)Ru(N,N')Cl]$^+$ where N,N' is bpm (**1**) or phen (**11**) were selected for preliminary studies with CT-DNA in cell-free media. Upon hydrolysis the two complexes form the corresponding monofunctional reactive aqua species [(η^6-*p*-cym)Ru(N,N')(OH$_2$)]$^{2+}$ to different extents (~22% and 47% for **1** and **11**, respectively). Their effects on DNA differ from each other as revealed by the preliminary DNA binding experiments. The nature of the N,N' chelating ligands was found to play a key role in the mode of interaction of these complexes. The aqua adduct of complex **11** binds faster (within the initial 1.5 h) but to the same extent as the adduct of complex **1**. These results are in good agreement with the hydrolysis rates and half-lifes determined for both complexes by UV-vis absorption spectroscopy in such a way that the time needed to generate the corresponding aqua adducts might be limiting the initial binding of the Ru^{II} arene complexes to DNA. As soon as the maximum conversion is achieved, the final overall extent does not vary significantly. The rate of binding to DNA for complex **1** is slower than that determined for the anticancer drug cisplatin (t$_{1/2}$ *ca.* 2 h under similar conditions),[48] for which DNA binding is thought to be responsible for its cytotoxic properties. Interestingly, the corresponding binding rate for complex **11** was found to be in the same range as that of cisplatin. In contrast, other Ru^{II} arene analogues i.e. [(η^6-bip)Ru(en)Cl]$^+$, which has also been shown to be cytotoxic to cancer cells,[15a,49] react much more rapidly with DNA under similar conditions (t$_{1/2}$ *ca.* 10 min). The results of the transcription mapping experiments suggest that complexes **1** and **11** preferentially form DNA

adducts that represent a rather strong block for RNA polymerase. Binding to DNA, inhibits RNA synthesis in a similar fashion and with similar stopsites to cisplatin and to the Ru^{II} arene complex [(η^6-bip)Ru(en)Cl]$^+$. For both complexes these stopsites were only guanine residues, which agrees well with the nucleobase binding studies (followed by multidimensional ^{1}H NMR spectroscopy) which showed that they bind to 9-EtG but do not bind to 9-EtA. The strong preference for guanine bases may allow these Ru^{II} arene complexes to target selectively G-rich regions of DNA, such as telomeres which play key role in cell division.[50] The binding upon hydrolysis of the Ru^{II} arene complexes **1** and **11** to DNA results in a mild degree of unwinding (7–8°) which is very similar for the two complexes but smaller than that observed for the Ru^{II} arene complex [(η^6-arene)Ru(en)Cl]$^+$ (7–14°).[30] The unwinding angles produced by the adducts of Ru^{II} arene compounds **1** and **11** resemble more those produced by monofunctional cisplatin adducts (6° and 13° for mono or bifunctional adducts, respectively).[51]

3.4.8 Cancer Cell Growth Inhibition (IC$_{50}$ Values)

Complexes containing either 2,2'-bipyrimidine (bpm), 10-phenanthroline-5,6-dione (phendio) or 6-mercaptopurine (MP) as the N,N' or N,S chelating ligand, respectively (**1**–**10**, **12** and **14**) were non cytotoxic against neither A2780, A2780cis, A549 or HCT116 up to the maximum concentration tested (100 μM). A loss of cytotoxicity towards cancer cells has been previously observed for complexes of the type [(η^6-arene)Ru(en)Cl]$^+$ when en, a σ-donor, is replaced by 2,2'-bipyridine,[52] a strong π-acceptors. Two extra pairs of nitrogens in bpm could contribute to make the ligand comparatively an even weaker π-acceptor. Changing the electronic features of the chelating ligands by incorporating electron donating heteroatoms on the 4,4' position

of bpm (such as in the phendio complex **12**) or changing the N,N' for N,S chelation (as in the single MP complex **14**), did not restore the cytotoxic activity. From a structural point of view, loss of activity in these derivatives could arise from the absence of $N_{(sp^3)}H$ groups, which are known to stabilise nucleobase adducts through strong H-bonding between an NH of en and C6O from the guanine (G) nucleobase.[53] The electronic properties of the complexes might also account for the observed loss of activity. The increased back-donation of electron density from Ru^{II} onto bpm, phendio or MP, would in turn make the metal centre more acidic compared to en analogues promoting side-interactions with other biomolecules before reaching the DNA target in cell-containing media, accounting for the preliminary DNA interactions found for complex **1** in cell-free media despite of its low cytotoxicity. The acidic nature of these derivatives is in good agreement with the experimental hydrolysis rates determined for these series of bpm-bearing complexes, where the rate values determined by UV-vis spectroscopy follow the increasing order of **1** (bpm) < **12** (phendio) < **14** (MP). By increasing the aromatic character of the ligand and the incorporation of electron withdrawing substituents on the 4,4' position of bpm in phen complex **11** or bathophen complex **13**, respectively showed a dramatic increase in anticancer activity towards the A2780 human ovarian cancer cell line compared to the other analogues (IC$_{50}$ 22.9 and 0.5 μM, respectively; cisplatin 1.1 μM under the same conditions). Complex **13**, $[(\eta^6$-*p*-cym)Ru(bathophen)Cl][PF$_6$] shows higher activity than cisplatin under these conditions. The different cytotoxicity profiles of these two active compounds indicate that the nature of the N,N' chelating ligand is important in the mechanism of action. The activity of **13** (compared to **11**) is probably enhanced by the presence of a more extended N,N' chelating ligand such as bathophen, which could act as a better DNA intercalator than **11**, contributing to its high cytotoxicity.

3.5 Summary

It is shown herein that incorporation of different motifs surrounding the Ru^{II} centre can lead not only to significant changes in the chemical reactivity of the complexes towards hydrolysis but also in the interaction with biologically relevant molecules such as DNA. The hydrolysis rates of $[(\eta^6\text{-arene})Ru(N,N')X]^+$ complexes vary over many orders of magnitude, from half-lives of minutes (14.5 min for complex $[(\eta^6\text{-etb})Ru(bpm)Cl]^+$ (**7**)) to hours (12 h for complex $[(\eta^6\text{-bip})Ru(bpm)I]^+$ (**6**)) at 310 K. Density functional theory calculations on complexes **1**–**6** suggest that aquation occurs *via* a more associative pathway in an $I_a \leftrightarrow I_d$ mechanistic continuum for which bond-making is of greater importance than bond-breaking. For both *p*-cym and bip complexes **1**–**6**, the calculated reaction barriers and overall reaction energies follow the order I > Br $\approx$ Cl which may be the basis of the explanation for the slow hydrolysis rate determined by UV-vis spectroscopy for I complexes **3** and **6**. The calculation was not able to reproduce the subtle reverse trend between Cl and Br complexes. In general, we were not able to establish an obvious correlation between hydrolysis rates and anticancer activity which implies that the mechanism of action for these series of complexes does not depend solely on this process. It has also been shown that the half-sandwich Ru^{II} arene complexes containing phenanthroline (**11**) or bathophenanthroline (**13**) as N,N'-chelating ligands exhibit increased cytotoxic activity towards A2780 human ovarian cancer cells, in contrast to analogous complexes containing bipyridine previously reported. X-ray crystal structures have shown that bip complexes (**4** and **6**) can form strong inter- and intraligand π-π interactions which enforces planarity on the bpm ligand, particularly in the case of complex **4**. An interesting feature of the structure of complex **7** is the presence of

aromatic CH-π (bpm) interactions. Strong binding to 9-EtG but not to 9-EtA was observed for complexes containing N,N' chelating ligands such as bpm, phen and bathophen as well as different arenes such as *p*-cym, hmb, ind and thn. By the use of DFT calculations, the binding energies for model DNA nucleobases were assessed. DFT calculations show that the 9-EtG nucleobase adducts of all complexes are thermodynamically preferred compared to their 9-EtA adducts by ~10 kcal mol^{-1}, explaining the guanine-specific binding observed experimentally for complexes **1**, **8**–**11** and **13**. Preliminary DNA binding studies show that complexes **1** and **11** bind to DNA, suggesting that it might be an important target for these complexes. Therefore, the reduced cytotoxic potency determined for complexes (**1**, **8**, **9**, and **10**) might not be due to lack of reactivity towards DNA but perhaps due to the occurrence of side reactions with other biomolecules or to a reduced cell uptake. Further studies are needed to identify the mechanism that inactivates some of the complexes suppressing the cytotoxic activity up to the maximum concentration tested (100 µM).

3.6 References

[1]. Jung, Y.; Lippard, S. J. *Chem. Rev.*, **2007**, *107*, 1387–1407.

[2]. van Zutphen, S.; Reedijk, J. *Coord. Chem. Rev.*, **2005**, *249*, 2845–2853.

[3]. Aird, R. E.; Cummings, J.; Ritchie, A. A.; Muir, M.; Morris, R. E.; Chen, H.; Sadler, P. J.; Jodrell, D. I. *Br. J. Cancer*, **2001**, *86*, 1652–1657.

[4]. Yan, Y. K.; Melchart, M.; Habtemariam, A.; Sadler, P. J. *Chem. Commun.*, **2005**, 4764–4776.

[5]. (a) Fernández, R.; Melchart, M.; Habtemariam, A.; Parsons, S.; Sadler, P. J. *Chem. Eur. J.*, **2004**, *10*, 5173–5179; (b) Wang, F.; Habtemariam, A.; van der Geer, E. P. L.; Fernández, R.; Melchart, M.; Deeth, R. J.; Aird, R.; Guichard, S.; Fabbiani,

F. P. A.; Lozano-Casal, P.; Oswald, I. D. H.; Jodrell, D. I.; Parsons, S.; Sadler, P. J. *Proc. Natl. Acad. Sci. U.S.A.*, **2005**, *102*, 18269–18274.

[6]. Bloemink, M. J.; Engelking, H.; Karentzopoulos, S.; Krebs, B.; Reedijk, J. *Inorg. Chem,*. **1996**, *35*, 619–627.

[7]. Nováková, O.; Kasparkova, J.; Vrana, O.; van Vliet, P. M.; Reedijk, J.; Brabec, V. *Biochemistry,* **1995**, *34*, 12369–12378.

[8]. Velders, A. H.; Kooijman, H.; Spek, A. L.; Haasnoot, J. G.; De Vos, D.; Reedijk, J. *Inorg. Chem.,* **2000**, *39*, 2966-2967.

[9]. (a) Bennet, M. A.; Smith, A. K. *J. Chem. Soc.*, *Dalton Trans.*, **1974**, 233–241; (b) Govindaswamy, P.; Canivet, J.; Therrien, B.; Süss-Fink, G.; Štěpnička, P.; Ludvík, J. *J. Organomet. Chem.*, **2007**, *692*, 3664–3675; (c) Zelonka, R. A.; Baird, M. C. *J. Organomet. Chem.,* **1972**, *35*, C43–C46; (d) Melchart, M.; Habtemariam, A.; Nováková, O.; Moggach, S. A.; Fabbiani, F. P. A.; Parsons, S.; Brabec, V.; Sadler, P. J. *Inorg. Chem.*, **2007**, *46*, 8950–8962.

[10]. Habtemariam, A.; Betanzos-Lara, S.; Sadler, P. J. Di-μ-Chloro(ethylbenzoate)diruthenium(II): [(η6-etb)RuCl2]2, *Inorg. Synth.*, **2010**, *36*, in press.

[11]. (a) Sheldrick, G. M. *Acta Cryst.*, **1990**, *A46*, 467−473; (b) Sheldrick, G. M. *Acta Cryst.*, **2008**, *64*, 12−122.

[12]. Sheldrick, G. M. *SHELXL-97*, University of Göttingen: Göttingen, Germany, **1997**.

[13]. Baerends, E. J.; Berces, A.; Bo, C.; Boerrigter, P. M.; Cavallo, L.; Deng, L.; Dickson, R. M.; Ellis, D. E.; Fan, L.; Fischer, T. H. *et. al.* (2000) ADF 2009 (Free University, Amsterdam).

[14]. Baerends, E. J.; Ros, P.; Ellis, D. E. *Theor. Chim. Acta, 1972,* **27**, 339–354.

[15]. (a) Morris, R. E.; Aird, R. E.; del Socorro Murdoch, P.; Chen, H.; Cummings, J.; Hughes, N. D.; Parsons, S.; Parkin, A.; Boyd, G.; Jodrell, D. I.; Sadler, P. J. *J. Med. Chem.*, **2001**, *44*, 3616−3621; (b) Chen, H.; Parkinson, J. A.; Parsons, S.; Coxall, R. A.; Gould, R. O.; Sadler, P. J. *J. Am. Chem. Soc.*, **2002**, *124*, 3064–3082.

[16]. Yan, Y. K.; Melchart, M.; Habtemariam, A.; Sadler, P. J. *Chem. Commun.*, **2005**, 4764−4776.

[17]. (a) Dorcier, A.; Dyson, P. J.; Gossens, C.; Rothlisberger, U.; Scopelliti, R.; Tavernelli, I. *Organometallics* **2005**, *24,* 2114−2123; (b) Reedijk, J. *Chem. Rev.*, **1999**, *99,* 2499−2510.

[18]. Nováková, O.; Chen, H.; Vrana, O.; Rodger, A.; Sadler, P. J.; Brabec, V., *Biochemistry*, **2003**, *42*, 11544–11554.

[19]. Zhou, C.; Xusheng, D.; Hong, L., *Bioelectrochemistry*, **2007**, 70, 446–451.

[20]. (a) Hadjiliadis, N.; Theophanides, T., *Inorg. Chim. Acta,* **1975**, *15,* 167−178; (b) Hadjiliadis, N.; Theophanides, T. *Can. J. Spectrosc.*, **1977**, *22*, 51−56.

[21]. Yamanari, K.; Ito, R.; Yamamoto, S.; Konno, T.; Fuyuhiro, A.; Fujioka, K.; Arakawa, R. *Inorg. Chem.*, **2002**, *41,* 6824−6830.

[22]. Grigoratos, A.; Katsaros, N. *Inorganica Chimica Acta,* **1985**, *108*, 41−45.

[23]. Yamanari, K.; Nozaki, T.; Fuyuhiro, A.; Kaizaki, S. *Bull. Chem. Soc. Jpn.,* **2002**, *75*, 109–110.

[24]. (a) Yamanari, K.; Kida, M.; Yamamoto, M.; Fuyuhiro, A.; Kaizaki, S. *J. Chem. Soc., Dalton Trans*., **1996**, 305−309; (b) Amo-Ochoa, P.; Castillo, O.; Alexandre, S. S.; Welte, L.; de Pablo, P. J.; Rodríguez-Tapiador, M. I.; Gómez-Herrero, J.; Zamora, F. *Inorg. Chem.*, **2009**, *48,* 7931−7936.

[25]. (a) Süss-Fink, G. *Dalton Trans.*, **2010**, *39*, 1673–1688; (b) Singh, A.; Chandra, M.; Sahay, A. N.; Pandey, D. S.; Pandey, K. K.; Mobin, S. M.; Puerta, M. C.; Valerga, P. *J. Organomet. Chem.*, **2004**, *689*, 1821–1834.

[26]. Flower, K. R.; Pritchard, R. G. *J. Organomet. Chem.*, **2001**, *620*, 60–68.

[27]. Gül, N.; Nelson, J. H. *Organometallics*, **1999**, *18*, 709–725.

[28]. Gül, N.; Nelson, J. H. *Polyhedron*, **1999**, *18*, 1835–1843.

[29]. Bugarcic, T.; Habtemariam, A.; Stepankova, J.; Heringova, P.; Kašpárková, J.; Deeth, R. J.; Johnstone, R. D. L.; Prescimone, A.; Parkin, A.; Parsons, S.; Brabec, V.; Sadler, P. J. *Inorg. Chem.*, **2008**, *47*, 11470–11486.

[30]. (a) van Rijt, S. H.; Hebden, A. J.; Amaresekera, T.; Deeth, R. J.; Clarkson, G. J.; Parsons, S.; McGowan, P.; Sadler, P. J. *J. Med. Chem.*, **2009**, *52*, 7753–7764; (b) Bugarcic, T.; Nováková, O.; Halámiková, A.; Zerzánková, L.; Vrána, O.; Kašpárková, J.; Habtemariam, A.; Parsons, S.; Sadler, P. J.; Brabec, V. *J. Med. Chem.*, **2008**, *51*, 5310–5319.

[31]. Brandl, M.; Weiss, M. S.; Jabs, A.; Suhnel, J.; Hilgenfeld, R. *J. Mol. Biol.,* **2001**, *307*, 357–377.

[32]. Bogdanovic, G. A.; Spasojevic-de Bire, A.; Zaric, S. D. *Eur. J. Inorg. Chem.,* **2002**, 1599–1602.

[33]. (a) Dieter-Wurm, I.; Sabat, M.; Lippert, B. *J. Am. Chem. Soc.*, **1992**, *114*, 357–359; (b) Witkowshi, H.; Freisinger, E.; Lippert, B. *J. Chem. Soc., Chem. Commun.*, **1997**, 1315–1316; (c) Sigel, R. K. O.; Freisinger, E.; Metzger, S.; Lippert, B. *J. Am. Chem. Soc.*, **1998**, *120*, 12000–12007.

[34]. Qu, X.; Chaires, J. B. *J. Am. Chem. Soc.*, **2001**, *123*, 1–7.

[35]. (a) Basolo, F.; Pearson, R. G. *Mechanisms of Inorganic Reactions: A Study of Metal Complexes in Solution*, Wiley, New York, 2nd Ed., 1967, p 124; (b) Broomhead, J. A.; Kane-Maguire, L. A. P. *Inorg. Chem.*, **1968**, *7*, 2519–2523.

[36]. Wang, F.; Chen, H.; Parsons, S.; Oswald, I. D. H.; Davidson, J. E.; Sadler, P. J. *Chem. Eur. J.*, **2003**, *9*, 5810–5820.

[37]. Kunkely, H.; Vogler, A. *Inorg. Chim. Acta*, **2003**, *343*, 357–360.

[38]. Dadci, L.; Elias, H.; Frey, U.; Hornig, A.; Koelle, U.; Merbach, A. E.; Paulus, H.; Schneider, J. S. *Inorg. Chem.,* **1995**, *34*, 306–315.

[39]. Koefod, R. S.; Mann, K. R. *J. Am. Chem. Soc.*, **1990**, *112*, 7287–7293.

[40]. Dougan, S. J.; Melchart, M.; Habtemariam, A.; Parsons, S.; Sadler, P. J. *Inorg. Chem.,* **2007**, *46*, 10882–10894.

[41]. Rapaport, I.; Helm, L.; Merbach, A. E.; Bernhard, P.; Ludi, A. *Inorg. Chem.,* **1988**, *27*, 873–879.

[42]. Takeuchi, K. J.; Thompson, M. S.; Pipes, D. W.; Meyer, T. J. *Inorg. Chem.,* **1984**, *23*, 1845−1851.

[43]. Chen, H.; Parkinson, J. A.; Morris, R. E.; Sadler, P. J. *J. Am. Chem. Soc.*, **2003**, *125*, 173–186.

[44]. Zhang, C. X.; Lippard, S. J. *Curr. Opin. Chem. Biol.,* **2003**, *7*, 481–489.

[45]. Scheller, K. H.; Scheller-Krattiger, V.; Martin, R. B. *J. Am. Chem. Soc.,* **1981**, *103*, 6833–6839.

[46]. Peacock, A. F. A.; Habtemariam, A.; Fernández, R.; Walland, V.; Fabbiani Francesca, P. A.; Parsons, S.; Aird, R. E.; Duncan, I. J.; Sadler P. J. *J. Am. Chem. Soc.,* **2006**, *128*, 1739–1748.

[47]. Baik, M.-H.; Friesner, R. A.; Lippard, S. J. *J. Am. Chem. Soc.*, **2003**, *125*, 14082–14092.

[48]. Bancroft, D. P.; Lepre, C. A.; Lippard, S. J. *J. Am. Chem. Soc.*, **1990**, *112*, 6860–6871.

[49]. (a) Aird, R.; Cummings, J.; Ritchie, A.; Muir, M.; Morris, R.; Chen, H.; Sadler, P.; Jodrell, D. *Br. J. Cancer*, **2002**, *86*, 1652–1657; (b) Nováková, O.; Kasparkova, J.; Bursova, V.; Hofr, C.; Vojtiskova, M.; Chen, H.; Sadler, P. J.; Brabec, V. *Chem. Biol.*, **2005**, *12*, 121–129.

[50]. Neidle, S., *Nucleic Acid Structure and Recognition*, Oxford University Press, Oxford, **2002**, p. 76.

[51]. Keck, M. V.; Lippard, S. J. *J. Am. Chem. Soc.*, **1992**, *114*, 3386–3390.

[52]. Habtemariam, A.; Melchart, M.; Fernández, R.; Parsons, S.; Oswald, I. D. H.; Parkin, A.; Fabbiani, F. P. A.; Davidson, J. E.; Dawson, A.; Aird, R. E.; Jodrell, D. I.; Sadler, P. J. *J. Med. Chem.,* **2006**, *49*, 6858–6868.

[53]. Liu, H. K.; Berners-Price, S. J.; Wang, F. Y.; Parkinson, J. A.; Xu, J. J.; Bella, J.; Sadler, P. J. *Angew. Chem., Int. Ed.,* **2006**, *45*, 8153–8156.

Chapter 4

Photoactivatable Ru^{II}
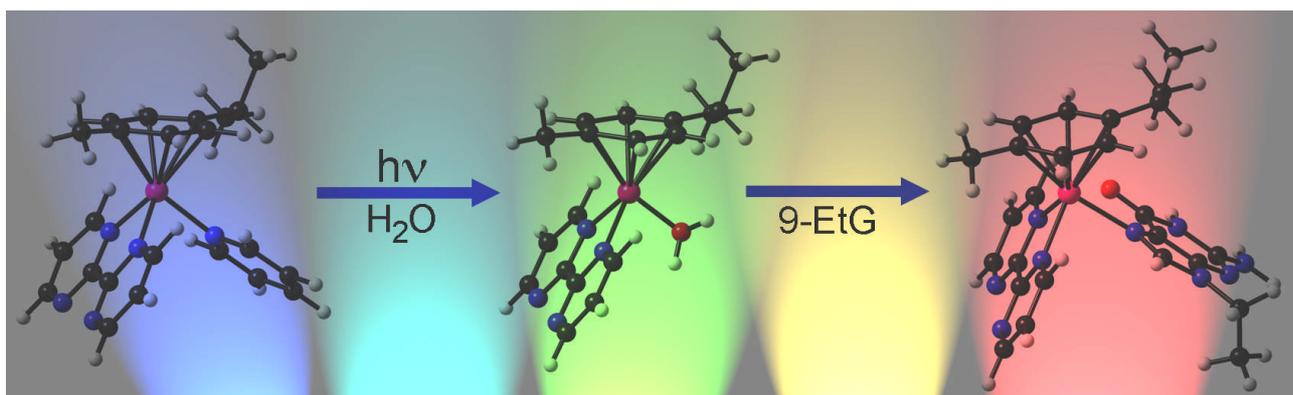
Arene Complexes

Chapter 4

Photoactivatable Ruthenium(II) Arene Complexes Containing Pyridine and Pyridine–Derivative Ligands

4.1 Introduction

Metal coordination compounds as therapeutics for malaria, arthiritis, Human Immunodeficiency Virus (HIV), cancer, and other medicinal applications have been investigated in the last twenty years.[1,2] Apart from cisplatin and some of its derivatives, there are few examples of successful metallopharmaceuticals in (pre)clinical trials for antitumour therapy. In light of this, new metal complexes with novel promising activation properties are starting to evolve and photochemical activation is one of the most important concepts currently exploited;[3] it uses the notion of metal-pro-drug activation specifically triggered by photoirradiation with light. The strategy offers the possibility of controlling the location, timing, and dosage of the therapeutic metal complex. Moreover, Ru^{II} arene complexes of general formula $[(\eta^6\text{-arene})Ru(XY)Z]^{n+}$ where XY is a bidentate chelating ligand and Z is a leaving group (typically an halogen), have been extensively investigated for their promising cytotoxic properties towards various cancer cell lines.[4,5] A crucial step in one mode of activation of these anticancer agents is usually the initial aquation of the Ru–Z bond to form a more reactive aqua species.[6] It has been shown that a combination of fast hydrolysis rates and high reactivity can lead to inactive complexes, similarly very slow hydrolysis rates and chemical inertness often leads to low *in vitro* cytotoxicity.[5,7] One key strategy to increase the potential of this class of complexes is to activate the release of the monodentate ligand Z with visible light or UVA photoirradiation to

promote the formation of the aqua adduct, which otherwise would not form in the dark. The work reported here is concerned with the synthesis and characterisation of a series of organometallic Ru^{II} complexes of the form $[(\eta^6\text{-arene})Ru(N,N')(L)][PF_6]_2$ where N,N' is a bidentate chelating ligand and L is a pyridine or pyridine-derivative ligand that can be selectively dissociated upon photoirradiation. Their behaviour in the dark (ambient light conditions) and under photoirradiation in aqueous solution, as well as in the presence of nucleobases such as 9-ethylguanine (9-EtG) and 9-ethyladenine (9-EtA) was investigated. A description of the excited states for all the Ru^{II} arene complexes was made with the aid of Time-Dependent Density Functional Theory (TD-DFT) calculations. Finally, their potential as cytotoxic agents was also investigated by performing cell growth inhibition assays (IC$_{50}$ values) in various human cancer cell lines and by studying DNA interactions in cell-free media, both in the dark and upon photoirradiation.

4.2   Experimental Section

4.2.1   Materials

RuCl$_3$·3H$_2$O was acquired from Precious Metals Online (PMO Pty Ltd) and used as received. 2,2'-bipyrimidine (bpm), 1,10-phenanthroline (phen), 1,10-phenanthroline-5,6-dione (phendio), 4,7-diphenyl-1,10-phenanthroline (bathophen), pyridine (Py), 4-methylpyridine (4-MePy), 4-methoxypyridine (4-MeOPy), 4,4'-bipyridine (4,4'-bpy), 4-phenylpyridine (4-PhPy), 4-benzylpyridine (4-BzPy), 1,2,4-triazole (trz), 3-acetylpyridine (3-AcPy), nicotinamide (NA), 3-acetatepyridine (3-AcOPy), 9-ethylguanine (9-EtG), 9-ethyladenine (9-EtA) and KPF$_6$ were obtained from Sigma-Aldrich. The Ru^{II} halido mononuclear precursors $[(\eta^6\text{-arene})Ru(N,N')Cl][PF_6]$, where

arene is *para*-cymene (*p*-cym); N,N' is bpm, phen, phendio, bathophen, or bpy were synthesised according to a previously reported method[8] while [(η^6-arene)Ru(bpy)Cl][PF$_6$] where arene is hexamethylbenzene (hmb) or indane (ind) were kindly provided by Dr Abraha Habtemariam and synthesised according to a reported method.[8] The solvents used for photochemistry and UV-vis absorption spectroscopy were dry methanol (reagent grade) and deionised water. For NMR spectroscopy the solvents used were acetone-d_6, DMSO-d_6, methanol-d_4 and D$_2$O obtained from Aldrich unless otherwise stated. All chemicals were used without further purification.

4.2.2 Preparation of Ru^{II} Arene Complexes Containing Pyridine or Pyridine-Derivative Ligands

Complexes of the form [(η^6-arene)Ru(N,N')(L)][PF$_6$]$_2$ where arene is *p*-cym, hmb, or ind; N,N' is bpm, phen, phendio, bathophen, or bpy; and L is Py, 4-MePy, 4-MeOPy, 4,4'-bpy, 4-PhPy, 4-BzPy, trz, 3-AcPy, NA, or 3-AcOPy were synthesised using a similar procedure as previously described.[4] Using an aluminium-foil-covered flask at room temperature the corresponding chlorido complex [(η^6-arene)Ru(N,N')Cl][PF$_6$] and AgNO$_3$ in 10 mL of a 1:1 mixture of MeOH/H$_2$O were refluxed overnight. Precipitated AgCl was then removed by filtration. A large excess of the appropriate ligand L was added, and the mixture was left stirring for 24−48 h. The volume was reduced by rotary evaporation and a two to five mol equiv excess of KPF$_6$ was added. The precipitate that formed was collected by filtration and washed with portions of Et$_2$O/MeOH and dried overnight in vacuum resulting in a microcrystalline product. Details of the amounts of reactants, colour changes, and nature of the products for the individual reactions are described below, as well as any variations in the synthetic

procedure. ^{13}C{^{1}H} NMR spectroscopy data is also provided for samples where a satisfactory elemental analysis was not returned.

[(η^6-*p*-cym)Ru(bpm)(Py)][PF$_6$]$_2$ (1). [(η^6-*p*-cym)Ru(bpm)Cl][PF$_6$] (0.10 g, 0.17 mmol), AgNO$_3$ (0.03 g, 0.17 mmol), pyridine (Py) (0.34 g, 4.35 mmol) and KPF$_6$ (0.16 g, 0.85 mmol) in the solvent mixture; the solution turned from bright to dark yellow; a dark yellow solid was obtained; yield 72% (0.09 g, 0.12 mmol). HR-MS: calc for C$_{23}$H$_{25}$N$_5$Ru [M]$^{2+}$ *m/z* 236.5574, found *m/z* 236.5580. ^{1}H NMR (D$_2$O, 500 MHz) δ_H: 0.94 (6H, d, *J* = 7.0), 1.85 (3H, s), 2.48 (1H, sep, *J* = 7.0), 6.18 (2H, d, *J* = 6.5), 6.49 (2H, d, *J* = 6.5), 7.42–7.45 (2H, m), 7.93–7.95 (1H, m), 8.14–8.16 (2H, m), 8.41 (2H, dd, *J* = 1.3, J = 6.4), 9.29 (dd, 2H, *J* = 1.9, *J* = 4.9), 10.05 (dd, 2H, *J* = 1.9, *J* = 5.9). ^{13}C{^{1}H} NMR ((CH$_3$)$_2$CO, 125 MHz) δ_C: 17.1, 21.5, 30.7, 85.9, 90.6, 107.2, 108.0, 126.1, 127.4, 140.1, 153.8, 154.8, 161.0, 161.4, 163.7.

[(η^6-*p*-cym)Ru(bpm)(4-MePy)][PF$_6$]$_2$ (2). [(η^6-*p*-cym)Ru(bpm)Cl][PF$_6$] (0.10 g, 0.17 mmol), AgNO$_3$ (0.03 g, 0.17 mmol), 4-methylpyridine (4-MePy) (0.40 g, 4.35 mmol) and KPF$_6$ (0.16 g, 0.85 mmol) in the solvent mixture; the solution turned from bright to dark yellow; a dark green solid was obtained; yield 75% (0.10 g, 0.13 mmol). Suitable crystals for X-ray crystallography were obtained from slow diffusion of Et$_2$O into an acetone saturated solution at 278 K. Elemental analysis calc. for C$_{24}$H$_{27}$F$_{12}$N$_5$P$_2$Ru %C: 37.12, %H: 3.50, %N: 9.02; found %C: 36.89, %H: 3.32, %N: 8.95. HR-MS: calc for C$_{24}$H$_{27}$N$_5$Ru [M]$^{2+}$ *m/z* 243.5653, found *m/z* 243.5649. ^{1}H NMR (D$_2$O, 500 MHz) δ_H: 0.91 (6H, d, *J* = 7.0), 1.81 (3H, s), 2.29 (3H, s), 2.44 (1H, sep, *J* = 7.0), 6.13 (2H, d, *J* = 6.5), 6.44 (2H, d, *J* = 6.5), 7.21–7.23 (2H, m), 8.09–8.11 (2H, m), 8.14–8.16 (2H, m), 9.25 (2H, dd, *J* = 2.0, J = 5.0), 10.00 (dd, 2H, *J* = 2.0, *J* = 6.0).

[(η^6-*p*-cym)Ru(bpm)(4-MeOPy)][PF$_6$]$_2$ (3). [(η^6-*p*-cym)Ru(bpm)Cl][PF$_6$] (0.10 g, 0.17 mmol), AgNO$_3$ (0.03 g, 0.17 mmol), 4-methoxypyridine (4-MeOPy) (0.38 g, 3.48 mmol) and KPF$_6$ (0.16 g, 0.85 mmol) in the solvent mixture; the solution turned from bright to dark yellow; a dark green solid was obtained; yield 76% (0.10 g, 0.13 mmol). HR-MS: calc for C$_{24}$H$_{27}$N$_5$ORu [M]$^{2+}$ *m/z* 251.5627, found *m/z* 251.5623. ^{1}H NMR (D$_2$O, 500 MHz) δ_H: 0.91 (6H, d, *J* = 6.9), 1.83 (3H, s), 2.44 (1H, sep, *J* = 6.9), 3.79 (3H, s), 6.13 (2H, d, *J* = 6.2), 6.43 (2H, d, *J* = 6.4), 6.92 (2H, d, *J* = 6.7), 8.10–8.11 (4H, m), 9.25 (dd, 2H, *J* = 1.9, J = 5.0), 10.00 (dd, 2H, *J* = 1.9, *J* = 6.0). ^{13}C{^{1}H} NMR ((CH$_3$)$_2$CO, 125 MHz) δ_C: 17.2, 21.5, 30.7, 56.1, 85.8, 90.4, 107.3, 108.0, 113.6, 126.0, 154.3, 160.9, 161.3, 163.7, 168.4.

[(η^6-*p*-cym)Ru(bpm)(4,4'-bpy)][PF$_6$]$_2$ (4). [(η^6-*p*-cym)Ru(bpm)Cl][PF$_6$] (0.10 g, 0.17 mmol), AgNO$_3$ (0.03 g, 0.17 mmol), 4,4'-bipyridine (4,4'-bpy) (0.37 g, 2.38 mmol) and KPF$_6$ (0.16g, 0.85 mmol) in the solvent mixture; the solution turned from bright to dark yellow; a bright yellow solid was obtained; yield 76% (0.10 g, 0.13 mmol). HR-MS: calc for C$_{28}$H$_{28}$N$_6$Ru [M]$^{2+}$ *m/z* 275.0708, found *m/z* 275.0709. ^{1}H NMR (D$_2$O, 500 MHz) δ_H: 0.92 (6H, d, *J* = 7.0), 1.86 (3H, s), 2.48 (1H, sep, *J* = 7.0), 6.19 (2H, d, *J* = 6.6), 6.50 (2H, d, *J* = 6.4), 7.63 (2H, dd, *J* = 1.8, *J* = 6.3), 7.77 (2H, m), 8.16 (t, 2H, *J* = 5.3), 8.49–8.51 (2H, m), 8.59–8.61 (2H, m), 9.27 (2H, dd, *J* = 2.0, *J* = 4.9), 10.06 (2H, dd, *J* = 1.9, *J* = 5.8). ^{13}C{^{1}H} NMR ((CH$_3$)$_2$CO, 125 MHz) δ_C: 18.1, 22.4, 31.6, 87.0, 91.5, 108.4, 109.0, 122.1, 125.5, 127.0, 143.0, 150.0, 151.6, 155.2, 161.9, 162.3, 164.6.

[(η^6-*p*-cym)Ru(bpm)(4-PhPy)][PF$_6$]$_2$ (5). [(η^6-*p*-cym)Ru(bpm)Cl][PF$_6$] (0.10 g, 0.17 mmol), AgNO$_3$ (0.03 g, 0.17 mmol), 4-phenylpyridine (4-PhPy) (0.28 g, 3.48 mmol) and KPF$_6$ (0.16g, 0.85 mmol) in the solvent mixture; the solution turned from bright to dark yellow; a bright yellow solid was obtained; yield 76% (0.11 g, 0.13 mmol).

Elemental analysis calc. for $C_{29}H_{31}F_{12}N_5OP_2Ru$ %C: 40.66, %H: 3.65, %N: 8.18; found %C: 40.01, %H: 3.32, %N: 7.92. HR-MS: calc for $C_{29}H_{29}N_5Ru$ [M]$^{2+}$ *m/z* 274.5731, found *m/z* 274.5735. ^{1}H NMR (D$_2$O, 500 MHz) δ_H: 0.94 (6H, d, *J* = 6.9), 1.88 (3H, s), 2.49 (1H, sep, *J* = 6.9), 6.20 (2H, d, *J* = 6.4), 7.49–7.50 (3H, m), 7.67 (2H, dd), 7.70–7.71 (3H, m), 8.15 (t, 2H, *J* = 5.3), 8.36–8.37 (2H, m), 8.59–8.60 (2H, m), 9.28 (2H, dd, *J* = 1.9, *J* = 4.9), 10.07 (2H, dd, *J* = 1.9, *J* = 5.8).

[(η^6-*p*-cym)Ru(bpm)(4-BzPy)][PF$_6$]$_2$ (6). [(η^6-*p*-cym)Ru(bpm)Cl][PF$_6$] (0.10 g, 0.17 mmol), AgNO$_3$ (0.03 g, 0.17 mmol), 4-benzylpyridine (4-BzPy) (0.28 g, 3.48 mmol) and KPF$_6$ (0.16g, 0.85 mmol) in the solvent mixture; the solution turned from bright to dark yellow; a bright yellow solid was obtained; yield 73% (0.11 g, 0.12 mmol). Suitable crystals for X-ray crystallography were obtained from slow diffusion of Et$_2$O into an acetone saturated solution at 278 K. Elemental analysis calc. for $C_{30}H_{31}F_{12}N_5P_2Ru \cdot H_2O$ %C: 41.39, %H: 3.82, %N: 8.04; found %C: 41.28, %H: 3.36, %N: 8.21. HR-MS: calc for $C_{30}H_{31}N_5Ru$ [M]$^{2+}$ *m/z* 281.5810, found *m/z* 231.5802. ^{1}H NMR (D$_2$O, 500 MHz) δ_H: 0.90 (6H, d, *J* = 6.9), 1.81 (3H, s), 2.43 (1H, sep, *J* = 6.9), 4.00 (2H, s), 6.16 (2H, d, *J* = 6.5), 6.46, (2H, d, *J* = 6.5), 7.25–7.27 (3H, m), 7.39 (2H, d, *J* = 6.2), 8.12 (2H, t, *J* = 5.3), 8.22 (2H, d, *J* = 6.6), 8.65 (2H, d, *J* = 6.4), 9.27 (2H, dd, *J* = 1.9, *J* = 4.9), 10.02 (2H, dd, *J* = 1.9, *J* = 5.8).

[(η^6-*p*-cym)Ru(bpm)(trz)][PF$_6$]$_2$ (7). [(η^6-*p*-cym)Ru(bpm)Cl][PF$_6$] (0.10 g, 0.17 mmol), AgNO$_3$ (0.03 g, 0.17 mmol), 1,2,4-triazole (trz) (0.24 g, 3.48 mmol) and KPF$_6$ (0.16 g, 0.85 mmol) in the solvent mixture; the solution turned from bright to dark yellow; a pale yellow solid was obtained; yield 23% (0.03 g, 0.04 mmol). Suitable crystals for X-ray crystallography were obtained from a saturated acetone-d_6 at room temperature. HR-MS: calc for $C_{20}H_{23}N_7Ru$ [M]$^{2+}$ *m/z* 231.5526, found *m/z* 231.5518. ^{1}H NMR ((CD$_3$)$_2$CO, 500 MHz) δ_H: 1.14 (6H, d, *J* = 6.9), 2.15 (3H, s), 2.77 (1H, sep,

J = 6.9), 6.48 (2H, d, J = 6.4), 6.71 (2H, d, J = 6.4), 8.12–8.14 (3H, m), 8.57 (1H, s), 9.22 (1H, s), 9.38 (2H, dd, J = 1.9, J = 4.7), 10.16 (2H, dd, J = 1.9, J = 5.8). ^{13}C{^{1}H} NMR ((CH$_3$)$_2$CO, 125 MHz) δ_C: 17.2, 21.4, 30.8, 87.0, 88.9, 105.8, 108.6, 125.2, 143.1, 146.4, 160.9, 163.9.

[(η^6-hmb)Ru(bpm)(Py)][PF$_6$]$_2$ (8). [(η^6-hmb)Ru(bpm)Cl][PF$_6$] (0.10 g, 0.17 mmol), AgNO$_3$ (0.03 g, 0.17 mmol), pyridine (Py) (0.34 g, 4.35 mmol) and KPF$_6$ (0.16 g, 0.85 mmol) in the solvents mixture; the solution turned from bright to dark yellow; a bright yellow solid was obtained; yield 86 % (0.06 g, 0.11 mmol). Elemental analysis calc. for C$_{25}$H$_{29}$F$_{12}$N$_5$P$_2$Ru·2H$_2$O %C: 36.33, %H: 4.02, %N: 8.47; found %C: 36.40, %H: 3.47, %N: 8.49. HR-MS: calc for C$_{25}$H$_{29}$N$_5$Ru [M]$^{2+}$ *m/z* 250.5731, found *m/z* 250.5719. ^{1}H NMR ((CD$_3$)$_2$CO, 500 MHz) δ_H: 2.32 (18H, s), 7.56–7.58 (2H, m), 8.05–8.06 (1H, m), 8.29–8.30 (2H, m), 8.68 (2H, dd, J = 1.3, J = 6.4), 9.41 (2H, dd, J = 1.9, J = 4.8), 9.94 (2H, dd, J = 1.9, J = 5.7).

[(η^6-ind)Ru(bpm)(Py)][PF$_6$]$_2$ (9). [(η^6-ind)Ru(bpm)Cl][PF$_6$] (0.10 g, 0.17 mmol), AgNO$_3$ (0.03 g, 0.17 mmol), pyridine (Py) (0.34 g, 4.35 mmol) and KPF$_6$ (0.16 g, 0.85 mmol) in the solvent mixture; the solution turned from bright to dark yellow; a bright yellow solid was obtained; yield 71 % (0.09 g, 0.13 mmol). Elemental analysis calc. for C$_{22}$H$_{21}$F$_{12}$N$_5$P$_2$Ru·3H$_2$O %C: 33.01, %H: 3.40, %N: 8.75; found %C: 32.41, %H: 3.63, %N: 8.87. HR-MS: calc for C$_{22}$H$_{21}$N$_5$Ru [M]$^{2+}$ *m/z* 228.5415, found *m/z* 228.5418. ^{1}H NMR ((CD$_3$)$_2$CO, 500 MHz) δ_H: 2.80–2.87 (4H, m), 3.00–3.07 (2H, m), 6.46 (2H, dd, J = 2.3, J = 4.5), 7.00 (2H, dd, J = 2.3, J = 4.3), 7.56 (2H, t, J = 7.0), 8.06–8.08 (1H, m), 8.27–8.28 (2H, m), 8.86–8.87 (2H, m), 9.45 (2H, dd, J = 1.8, J = 4.7), 10.44 (2H, dd, J = 1.8, J = 5.8).

[(η^6-p-cym)Ru(phen)(Py)][PF$_6$]$_2$ (10). [(η^6-p-cym)Ru(phen)Cl][PF$_6$] (0.10 g, 0.17 mmol), AgNO$_3$ (0.03 g, 0.17 mmol), pyridine (Py) (0.34 g, 4.35 mmol) and KPF$_6$ (0.16 g, 0.85 mmol) in the solvents mixture; the solution turned from bright to dark yellow; a bright yellow solid was obtained; yield 83% (0.11 g, 0.14 mmol). Suitable crystals for X-ray crystallography were obtained from a saturated acetone solution at room temperature. Elemental analysis calc. for C$_{27}$H$_{27}$F$_{12}$N$_3$P$_2$Ru·2H$_2$O %C: 39.52, %H: 3.81, %N: 5.12; found %C: 38.96, %H: 3.17, %N: 5.46. HR-MS: calc for C$_{27}$H$_{27}$N$_3$Ru [M]$^{2+}$ *m/z* 247.5622, found *m/z* 247.5616. ^{1}H NMR (D$_2$O, 500 MHz) δ_H: 0.75 (6H, d, *J* = 6.9), 1.83 (3H, s), 2.39 (1H, sep, *J* = 6.9), 6.18 (2H, d, *J* = 6.5), 6.55 (2H, d, *J* = 6.5), 7.31 (2H, t, *J* = 7.1), 7.80–7.82 (1H, m), 8.17 (2H, s), 8.26–8.27 (2H, m), 8.40–8.42 (2H, m), 8.90 (2H, dd, *J* = 1.0, *J* = 8.3), 10.09 (2H, dd, *J* = 1.0, *J* = 5.3).

[(η^6-p-cym)Ru(phendio)(Py)][PF$_6$]$_2$ (11). [(η^6-p-cym)Ru(phendio)Cl][PF$_6$] (0.10 g, 0.16 mmol), AgNO$_3$ (0.03 g, 0.16 mmol), pyridine (Py) (0.25 g, 3.2 mmol) and KPF$_6$ (0.16 g, 0.85 mmol) in the solvents mixture; the solution turned from dark green to yellow; a bright yellow solid was obtained; yield 70% (0.09 g, 0.11 mmol). HR-MS: calc for C$_{27}$H$_{25}$N$_3$O$_2$Ru [M]$^{2+}$ *m/z* 262.5493, found *m/z* 262.5498. ^{1}H NMR ((CD$_3$)$_2$CO, 500 MHz) δ_H: 1.06 (6H, d, *J* = 6.9), 2.00 (3H, s), 2.80 (1H, sep, *J* = 6.9), 6.46 (2H, d, *J* = 6.5), 6.92 (2H, d, *J* = 6.6), 7.55–7.56 (2H, m), 8.07–8.08 (1H, m), 8.28–8.29 (2H, m), 8.73 (2H, dd, *J* = 1.4, *J* = 6.5), 8.88 (2H, dd, *J* = 1.2, *J* = 8.0), 10.26 (2H, dd, *J* = 1.3, *J* = 5.6). ^{13}C{^{1}H} NMR ((CH$_3$)$_2$CO, 125 MHz) δ_C: 17.2, 21.6, 30.7, 84.8, 91.7, 127.5, 130.6, 131.2, 139.0, 140.6, 153.4, 159.8, 173.7.

[(η^6-p-cym)Ru(bathophen)(Py)][PF$_6$]$_2$ (12). [(η^6-p-cym)Ru(bathophen)Cl][PF$_6$] (0.10 g, 0.13 mmol), AgNO$_3$ (0.02 g, 0.13 mmol), pyridine (Py) (0.21 g, 2.7 mmol) and KPF$_6$ (0.05 g, 0.26 mmol) in the solvents mixture; the solution turned from dark green to yellow; a bright yellow solid was obtained; yield 89% (0.11 g, 1.2 mmol).

Elemental analysis calc. for $C_{39}H_{35}F_{12}N_3P_2Ru·H_2O$ %C: 49.06, %H: 3.91, %N: 4.40; found %C:48.96, %H: 3.35, %N: 4.28. HR-MS: calc for $C_{39}H_{35}N_3Ru$ [M]$^{2+}$ *m/z* 323.5937, found *m/z* 323.5931. ^{1}H NMR ((CD$_3$)$_2$CO, 500 MHz) δ_H: 0.98 (6H, d, *J* = 7.0), 2.06 (3H, s), 2.72 (1H, sep, *J* = 7.0), 6.61 (2H, d, *J* = 6.5), 6.96 (2H, d, *J* = 6.0), 7.50 (2H, t, *J* = 6.5), 7.70–7.73 (10H, m), 7.99–8.01 (1H, m), 8.24 (2H, s), 8.38 (2H, dd, *J* = 1.0, *J* = 5.5). 8.88 (2H, d, *J* = 6.5), 10.55 (2H, dd, *J* = 1.0, *J* = 5.5).

[(η^6-ind)Ru(bpy)(Py)][PF$_6$]$_2$ (13). [(η^6-ind)Ru(bpy)Cl][PF$_6$] (0.10 g, 0.17 mmol), AgNO$_3$ (0.02 g, 0.17 mmol), pyridine (Py) (0.36 g, 4.5 mmol) and KPF$_6$ (0.06 g, 0.26 mmol) in the solvents mixture; the solution remained bright yellow; a bright yellow solid was obtained; yield 92% (0.11 g, 1.5 mmol). Suitable crystals for X-ray crystallography were obtained from slow diffusion of Et$_2$O into an acetone saturated solution at 278 K. Elemental analysis calc. for $C_{24}H_{23}F_{12}N_3P_2Ru$ %C: 38.72, %H: 3.11, %N: 5.64; found %C: 38.42, %H: 2.99, %N: 5.60. HR-MS: calc for $C_{24}H_{23}N_3Ru^{2+}$ [M]$^{2+}$ *m/z* 227.5465, found *m/z* 227.5461. ^{1}H NMR ((CD$_3$)$_2$CO, 500 MHz) δ_H: 2.60–2.64 (4H, m), 2.91–2.95 (2H, m), 6.39–6.42 (2H, m), 6.91–6.93 (2H, m), 7.51 (2H, t, *J* = 6.6), 8.02–8.04 (1H, m), 8.11–8.13 (2H, m), 8.48–8.50 (2H, m), 8.68 (2H, d, *J* = 8.1), 8.73–8.75 (2H, m), 10.10 (2H, d, *J* = 5.7).

[(η^6-*p*-cym)Ru(bpm)(3-AcPy)][PF$_6$]$_2$ (14). [(η^6-*p*-cym)Ru(bpm)Cl][PF$_6$] (0.10 g, 0.17 mmol), AgNO$_3$ (0.03 g, 0.17 mmol), 3-acetylpyridine (3-AcPy) (0.21 g, 1.74 mmol) and KPF$_6$ (0.16 g, 0.85 mmol) in the solvents mixture; the solution turned from bright to dark yellow; a pale yellow solid was obtained; yield 91% (0.13 g, 0.16 mmol). Elemental analysis calc. for $C_{25}H_{27}F_{12}N_5OP_2Ru·3H_2O$ %C: 34.97, %H: 3.87, %N: 8.16; found %C: 34.31, %H: 3.04, %N: 8.04. HR-MS: calc for $C_{25}H_{27}N_5ORu$ [M]$^{2+}$ *m/z* 257.5627, found *m/z* 257.5630. ^{1}H NMR ((CD$_3$)$_2$CO, 500 MHz) δ_H: 1.05 (6H, d, *J* = 7.0), 2.11, (3H, s), 2.56 (3H, s), 2.76 (1H, sep, *J* = 7.0), 6.56 (2H, d, *J* =

6.5), 6.85 (2H, d, J = 6.5), 7.69–7.71 (1H, m), 8.28–8.30 (2H, m), 8.49–8.51 (1H, m), 8.98–8.99 (1H, m), 9.04 (1H, s), 9.44 (2H, dd, J = 1.9, J = 4.8), 10.48 (2H, dd, J = 1.92, J = 7.75).

[(η^6-p-cym)Ru(bpm)(NA)][PF$_6$]$_2$ (15). [(η^6-p-cym)Ru(bpm)Cl][PF$_6$] (0.10 g, 0.17 mmol), AgNO$_3$ (0.03 g, 0.17 mmol), nicotinamide (0.21 g, 1.74 mmol) and KPF$_6$ (0.16 g, 0.85 mmol) in the solvents mixture; the solution turned from bright to dark yellow; a pale yellow solid was obtained; yield 84% (0.11 g, 0.15 mmol). HR-MS: calc for C$_{24}$H$_{26}$N$_6$ORu [M]$^{2+}$ m/z 258.0603, found m/z 258.0598. ^{1}H NMR ((CD$_3$)$_2$CO, 500 MHz) δ_H: 1.05 (6H, d, J = 6.9), 2.11, (3H, s), 2.76 (1H, sep, J = 6.9), 2.86 (2H, br), 6.57 (2H, d, J = 6.1), 6.85 (2H, d, J = 6.1), 7.64–7.67 (2H, m), 8.25–8.26 (2H, m), 8.43–8.45 (1H, m), 8.72–8.73 (1H, m), 9.12 (1H, s), 9.43–9.44 (2H, m), 10.45–10.46 (2H, m). ^{13}C{^{1}H} NMR ((CH$_3$)$_2$CO, 125 MHz) δ_C: 17.2, 21.5, 30.7, 86.2, 90.5, 107.4, 108.0, 126.2, 127.0, 128.8, 138.7, 153.0, 155.6, 161.0, 161.5, 163.7, 164.0

[(η^6-p-cym)Ru(bpm)(3-AcOPy)][PF$_6$]$_2$ (16). [(η^6-p-cym)Ru(bpm)Cl][PF$_6$] (0.10 g, 0.17 mmol), AgNO$_3$ (0.03 g, 0.17 mmol), 3-acetatepyridine (3-AcOPy) (0.21 g, 1.74 mmol) and KPF$_6$ (0.16 g, 0.85 mmol) in the solvents mixture; the solution turned from bright to dark yellow; a pale yellow solid was obtained; yield 69 % (0.10 g, 0.12 mmol). HR-MS: calc for C$_{25}$H$_{27}$N$_5$ORu [M]$^{2+}$ m/z 265.5602, found m/z 265.5600. ^{1}H NMR ((CD$_3$)$_2$CO, 500 MHz) δ_H: 0.92 (6H, d, J = 7.0), 2.62 (1H, sep, J = 7.0), 2.66 (3H, s), 3.76 (3H, s), 6.46 (2H, d, J = 6.2), 6.72 (2H, d, J = 6.1), 7.57–7.59 (1H, m), 8.18–8.20 (2H, m), 8.34–8.35 (1H, m), 8.90–8.92 (1H, m), 8.98 (1H, s), 9.31–9.33 (2H, m), 10.39–10.40 (2H, m). ^{13}C{^{1}H} NMR ((CH$_3$)$_2$CO, 125 MHz) δ_C: 17.2, 21.5, 30.6, 53.0, 86.6, 90.2, 107.8, 108.2, 126.8, 127.5, 129.6, 140.7, 154.0, 156.9, 160.2, 161.6, 162.9, 164.2.

4.2.3   X-ray Crystallography

The details of the diffraction instrumentation used are described in Chapter 2. X-ray crystal structures discussed in this Chapter were determined by Dr Guy Clarkson from the Department of Chemistry at the University of Warwick. The structures of **2**, **6**, **7**, **10**, and **13** were solved by direct methods using SHELXS[9] (TREF) with additional light atoms found by Fourier methods. Hydrogen atoms were added at calculated positions and refined using a riding model with freely rotating methyl groups. Anisotropic displacement parameters were used for all non-H atoms; H-atoms were given isotropic displacement parameters equal to 1.2 (or 1.5 for methyl hydrogen atoms) times the equivalent isotropic displacement parameter of the atom to which the H-atom is attached. Refinement used SHELXL 97.[10]

4.2.4   Photoirradiation of Ru^{II} Arene Complexes

Aqueous solutions of the Ru^{II} arene complexes were photoirradiated at 310 K using the phtoreactor LZC 4V Illuminator (Luzchem, Canada) with temperature controller and UVA (λ_{irr} = 300−400 nm with a maximum intensity at ~360 nm, 5 mW cm^{-2}) or visible light lamps (λ_{irr} = 400−660 nm providing average light power of 100 mW). Outside the photoreactor, solutions were stored in the dark to minimise unwanted photoreactions between measurements.

4.2.5   Photoirradiation of Ru^{II} Arene Complexes followed by UV-vis Absorption Spectroscopy

UV-vis absorption spectra of 100 µM solutions of the Ru^{II} arene complexes were recorded on a Cary 50-Bio spectrophotometer using a 1-cm pathlength quartz cuvette

(600 µL) and a PTP1 Peltier temperature controller. Spectra were recorded at 310 K in deionised water from 200 to 800 nm at different stages of photoirradiation, and were processed using UV-Winlab software for Windows 95. Solutions were stored in the dark to minimise unwanted photoreactions between measurements.

4.2.6 Photoirradiation of Ru^{II} Arene Complexes followed by ^{1}H NMR Spectroscopy

^{1}H NMR spectra of 300 mM solutions (D$_2$O) of the Ru^{II} arene complexes were acquired at different stages of photoirradiation on a Bruker DMX 500 spectrometer (^{1}H = 500 MHz) using 5 mm diameter NMR tubes. All data processing was carried out using XWIN NMR version 2.0 (Bruker U.K. Ltd.). ^{1}H NMR signals were referenced to dioxane as an internal reference ($\delta = 3.71$).

4.3 Results

4.3.1 Synthesis and Characterisation

The complexes [(η^6-arene)Ru(N,N')(L)]$^{2+}$ studied in this work are listed in Table 4.1 and their general structures are shown in Figure 4.1. The dicationic Ru^{II} arene pyridine or pyridine-derivative ligands complexes **1−16** were synthesised as PF$_6$ salts in good yields (>50% in almost all cases) by the reaction of the corresponding [(η^6-arene)Ru(N,N')Cl][PF$_6$] complex with AgNO$_3$ in a 1:1 mixture of MeOH/H$_2$O to afford the corresponding aqua species [(η^6-arene)Ru(N,N')(OH$_2$)]$^{2+}$, to which excesses of the appropriate ligand L and KPF$_6$ were added. All the synthesised complexes were fully characterised by 1D and 2D ^{1}H NMR methods as well as 1D ^{13}C{^{1}H} NMR.

Table 4.1. $[(\eta^6\text{-arene})Ru(N,N')(L)]^{2+}$ complexes studied in this work.

Compound	Arene	N,N'	L
(**1**)	*p*-cym	bpm	Py
(**2**)	*p*-cym	bpm	4-MePy
(**3**)	*p*-cym	bpm	4-MeOPy
(**4**)	*p*-cym	bpm	4,4'-bpy
(**5**)	*p*-cym	bpm	4-PhPy
(**6**)	*p*-cym	bpm	4-BzPy
(**7**)	*p*-cym	bpm	trz
(**8**)	hmb	bpm	Py
(**9**)	ind	bpm	Py
(**10**)	*p*-cym	phen	Py
(**11**)	*p*-cym	phendio	Py
(**12**)	*p*-cym	bathophen	Py
(**13**)	ind	bpy	Py
(**14**)	*p*-cym	bpm	3-AcPy
(**15**)	*p*-cym	bpm	NA
(**16**)	*p*-cym	bpm	3-AcOPy

Compared to the chlorido analogues, the ^{1}H NMR resonances for all the new Ru^{II} arene complexes are low frequency shifted by *ca*. 0.6 ppm. The binding of the monodentate ligand to the Ru^{II} centre was confirmed by the appearance of a set of new peaks corresponding to the bound form (which appears low shifted compared to the free L ligand). Figure 4.2 shows the ^{1}H NMR spectra in the aromatic region for complex $[(\eta^6\text{-}p\text{-cym})Ru(phendio)(Py)][PF_6]_2$ (**11**) in acetone-d_6 solution as a generic example.
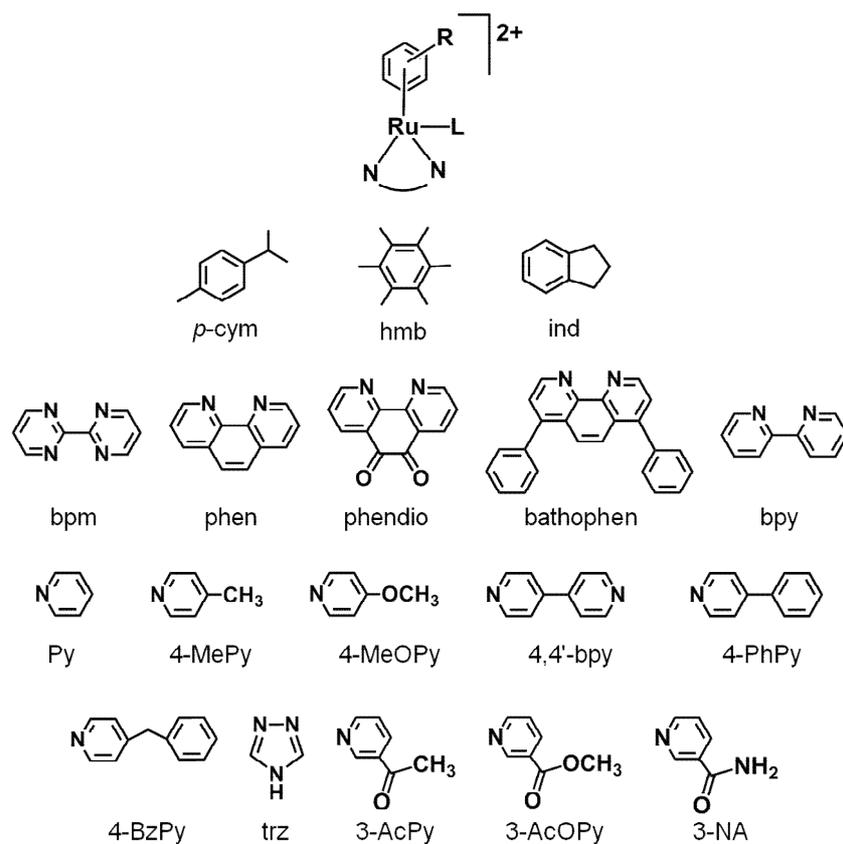
**Figure 4.1.** Structures of the dicationic complexes studied in this work synthesised as PF$_6$ salts.
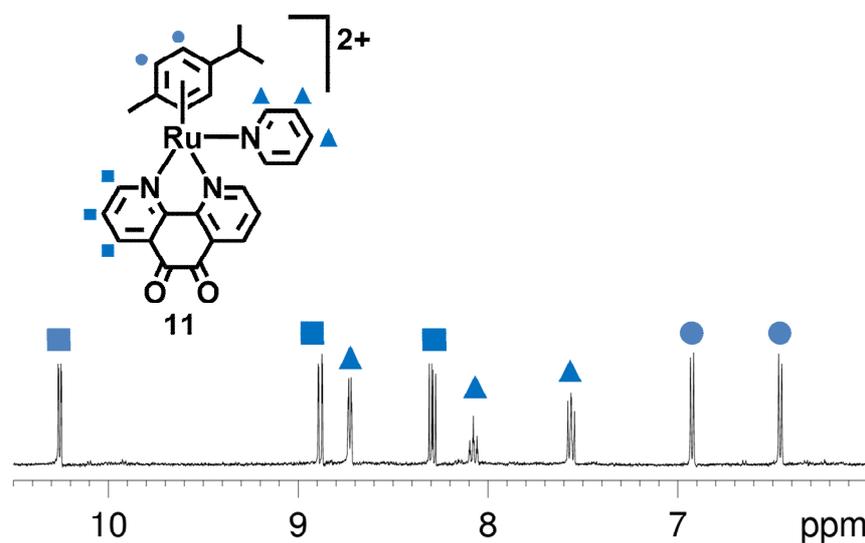
Figure 4.2. ^{1}H NMR spectra in the aromatic region of complex [(η^6-*p*-cym)Ru(phendio)(Py)][PF$_6$]$_2$ (**11**) in acetone-*d$_6$* solution. ■ = phendio, ▲ = Py, ● = *p*-cym.

4.3.2   X-ray Crystal Structures

The molecular structure of complexes **2**, **6**, **7**, **10**, and **13** were determined by single crystal X-ray diffraction. Selected bond lengths and angles are given in Table 4.2, the structures with numbering schemes are shown in Figure 4.3, and the crystallographic data are listed in Table A.4.1. The complexes are found to adopt the familiar pseudo-octahedral three-legged piano stool geometry common to all Ru^{II} arene structures[5] with the Ru atom π-bonded to the arene ligand (*p*-cym in **2**, **6**, **7**, and **10**; ind in **13**), coordinated to a pyridine nitrogen (**2**, **6**, **7**, **10**, and **13**), and to two nitrogen atoms of the chelating ligand (bpm for **2**, **6**, and **7**; phen for **10**; bpy for **13**) which constitute the three legs of the piano stool.

Table 4.2. Selected bond lengths (Å) and angles (°) for [(η^6-*p*-cym)Ru(bpm)(4MePy)][PF$_6$]$_2$ (**2**), [(η^6-*p*-cym)Ru(bpm)(4-BzPy)][PF$_6$]$_2$ (**6**), [(η^6-*p*-cym)Ru(bpm)(trz)][PF$_6$]$_2$ (**7**), [(η^6-*p*-cym)Ru(phen)(Py)][PF$_6$]$_2$ (**10**), and [(η^6-ind)Ru(bpy)(Py)][PF$_6$]$_2$ (**13**).

Bond length/Angle	2	6	7	10	13
Ru−arene$_{(centroid)}$	1.691	1.703	1.699	1.698	1.703
Ru(1)−N(13)	2.110(2)	2.121(2)	2.1041(19)	2.1169(14)	2.1250(14)
Ru(1)−N(1)	2.099(2)	2.090(2)	2.0866(18)	2.0853(13)	2.0877(13)
Ru(1)−N(8)	2.094(2)	2.094(2)	2.0808(18)	2.0970(14)	2.0727(13)
C(6)−C(7)	1.478(4)	1.479(3)	1.493(3)	1.421(2)	1.466(2)
N(8)−Ru(1)−N(1)	76.86(9)	76.93(8)	77.09(7)	78.07(5)	77.23(5)
N(13)−Ru(1)−N(8)	87.40(9)	87.96(8)	85.94(7)	85.36(5)	86.22(5)
N(13)−Ru(1)−N(1)	86.40(9)	87.43(8)	83.94(7)	87.03(5)	87.05(5)

The Ru^{II} to *p*-cym$_{(centroid)}$ distances (as measured from Mercury version 2.2) do not vary significantly between the derivatives. The molecules in complex [(η^6-*p*-cym)Ru(bpm)(4-MePy)][PF$_6$]$_2$ (**2**) lie in a mirror-image fashion opposite to an adjacent complex, giving rise to a π-π stacking interaction. The angle between mean planes in the interacting π systems (within the bpm ligand) is 7.09°, the shortest

atomic contact is C(11)−C(6) 3.492 Å, and the centroid-centroid distance is 4.067 Å,

Figure 4.4. The internal cleft defined by the planes of the 4-MePy and the bpm ligand

is 88.09°.
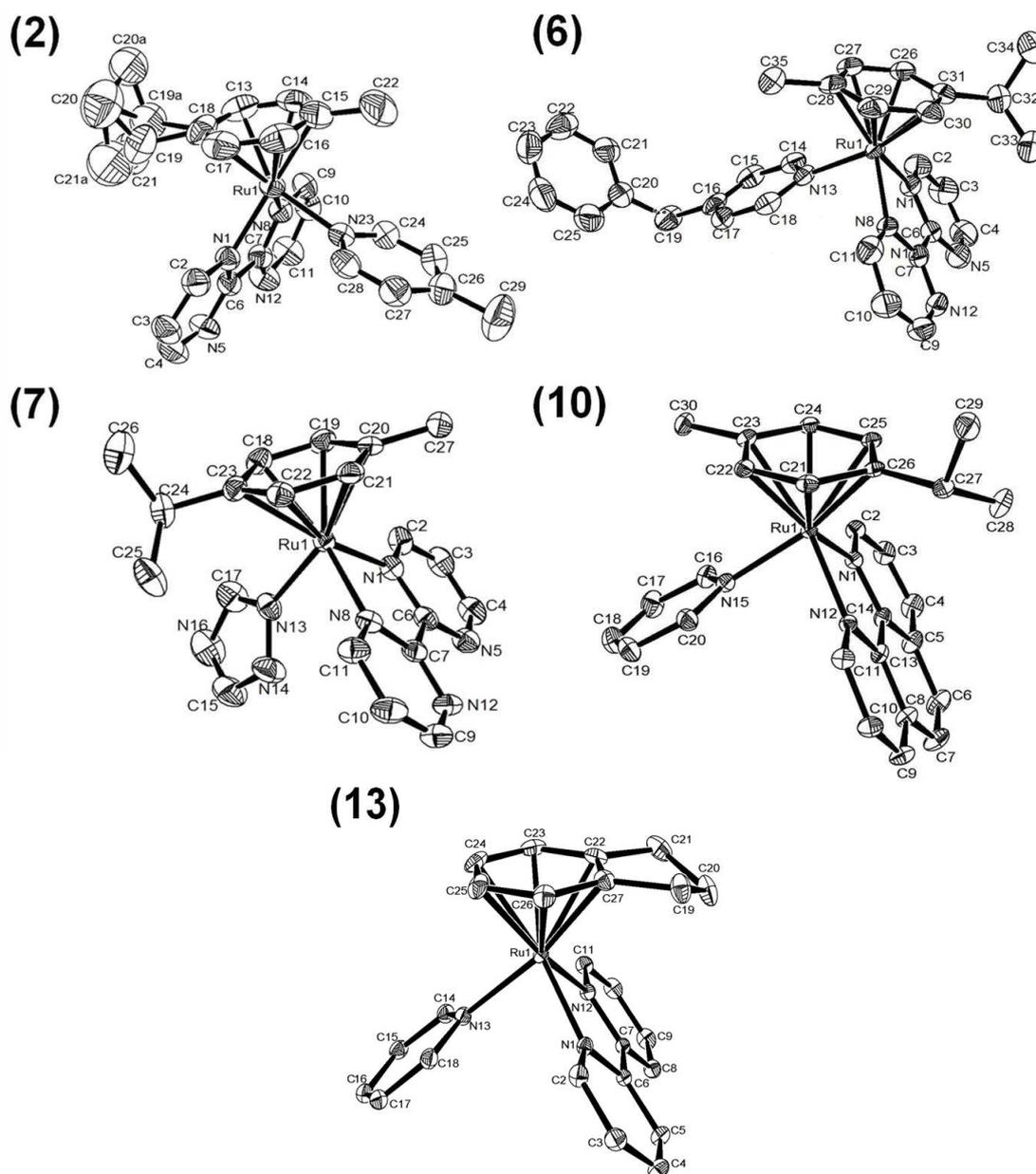
Figure 4.3. X-ray structure of the cations in [(η^6-*p*-cym)Ru(bpm)(4-MePy)][PF$_6$]$_2$ (**2**), [(η^6-*p*-cym)Ru(bpm)(4-BzPy)][PF$_6$]$_2$ (**6**), [(η^6-*p*-cym)Ru(bpm)(trz)][PF$_6$]$_2$ (**7**), [(η^6-*p*-cym)Ru(phen)(Py)][PF$_6$]$_2$ (**10**), and [(η^6-ind)Ru(bpy)(Py)][PF$_6$]$_2$ (**13**). Thermal ellipsoids show 50% probability. The PF$_6$ anions and hydrogens have been omitted for clarity.
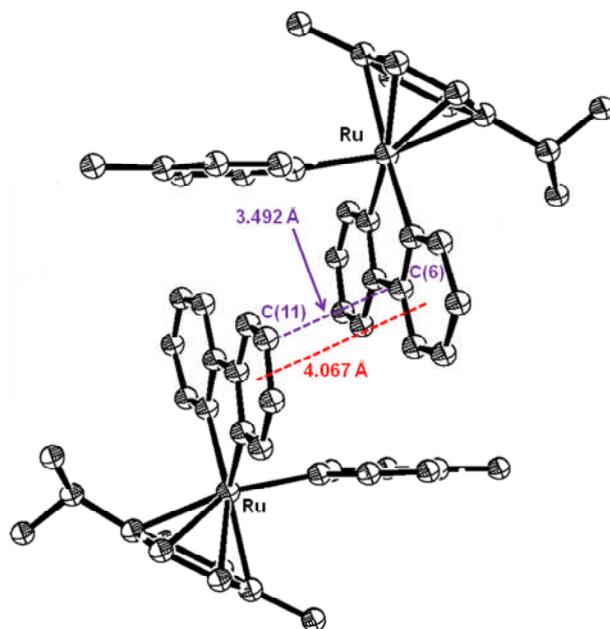
Figure 4.4. X-ray crystal structure of $[(\eta^6\text{-}p\text{-cym})Ru(bpm)(4\text{-MePy})][PF_6]_2$ (**2**) showing a π-π stacking interaction. The PF_6 anions and hydrogens have been omitted for clarity.

In the unit cell of $[(\eta^6\text{-}p\text{-cym})Ru(bpm)(4\text{-BzPy})][PF_6]_2$ (**6**) there is a π-π stacking interaction between the bpm and the benzyl (bz) ring of a neighbouring complex. The closest atomic contact between mean planes is N(5)−C(21) 3.280 Å, and the angle between the bpm chelating ligand and the bz ring is 14.94°, Figure 4.5. The angle between the Py and the bz rings is 71.62°; the internal cleft defined by the planes of the 4-BzPy and the bpm ligand is 84.45°. Several hydrogen bonds and short contacts were found in the unit cell of complex $[(\eta^6\text{-}p\text{-cym})Ru(bpm)(trz)]^{2+}$ (**7**), also involving the methanol solvent molecules, and the PF_6 anions, Figure 4.6. The internal cleft defined by the planes of the trz and the bpm ligand is 83.92°. Selected contact distances not discussed herein are shown in Table A.4.2.
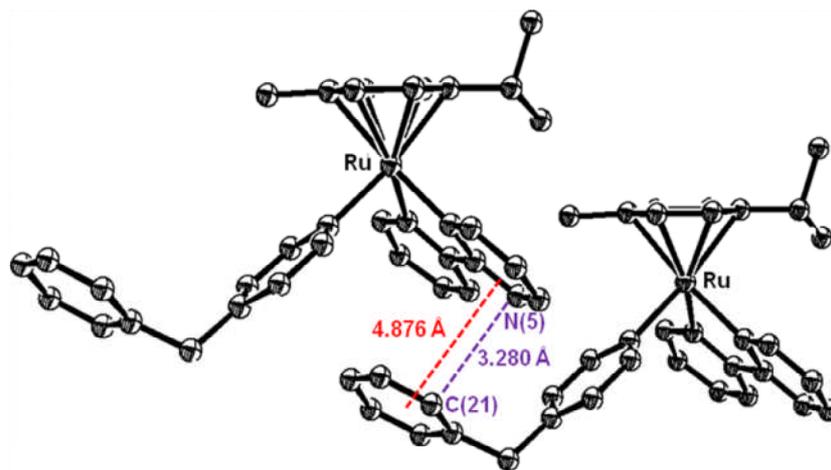
Figure 4.5. X-ray crystal structure of $[(\eta^6\text{-}p\text{-cym})\text{Ru(bpm)(4-BzPh)}][\text{PF}_6]_2$ (**6**) showing a π-π stacking interaction. The PF_6 anions and hydrogens have been omitted for clarity.
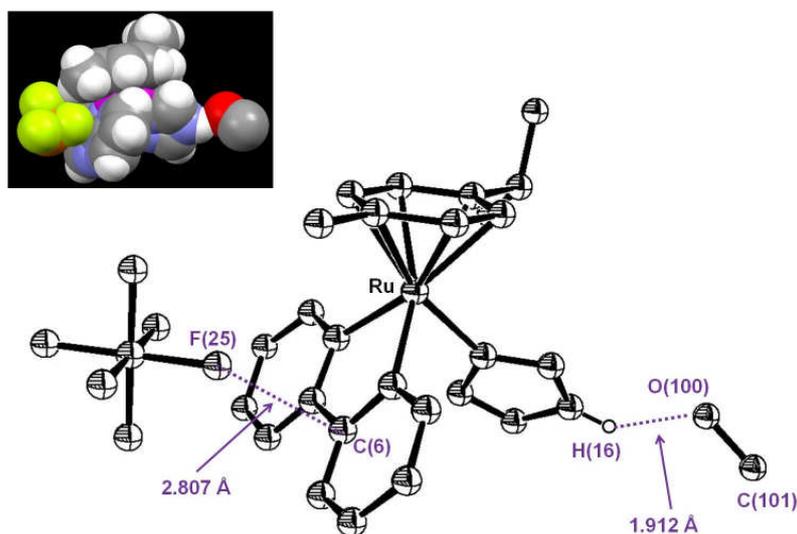
**Figure 4.6.** X-ray structure of the cation $[(\eta^6\text{-}p\text{-cym})\text{Ru(bpm)(trz)}]^{2+}$ (**7**) showing the presence of intermolecular contacts between the Ru^{II} complex, a PF_6 anion, and a methanol solvent molecule. Inset: Spacefilling model of $[(\eta^6\text{-}p\text{-cym})\text{Ru(bpm)(trz)}][\text{PF}_6]_2$ (**7**) showing the intermolecular contacts. The PF_6 anions and other hydrogens have been omitted for clarity.

In the unit cell of $[(\eta^6\text{-}p\text{-cym})\text{Ru(phen)(Py)}][\text{PF}_6]_2$ (**10**), two adjacent molecules lay in an upside-down alternate fashion giving rise to a π-π stacking interaction. The mean planes are defined by the phen chelating ligands of individual molecules and display a distance of 3.374 Å and an angle of 180°. The shortest atomic contact is C(6)−C(7) 3.449 Å and the centroid-centroid distance is 4.850 Å, Figure 4.7.
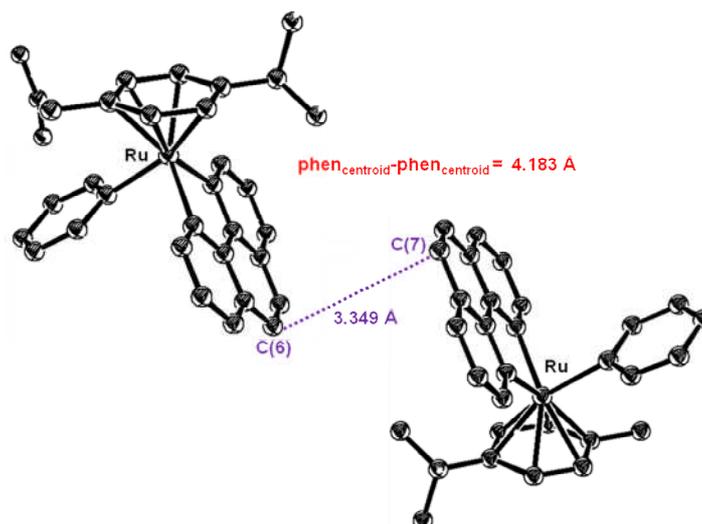
Figure 4.7. X-ray crystal structure of $[(\eta^6$-*p*-cym)Ru(phen)(Py)][PF$_6$]$_2$ (**10**) showing a π-π stacking interaction.

An acetone molecule very close to complex **10** was modelled sitting in a cleft between the pyridine and the phen chelating ligands showing close contacts, Figure 4.8. The spacefilling model shows the presence of intermolecular contacts between C(16) in the phen ligand and O(202a) in the acetone molecule with a C(16)−O(202a) distance of 2.914 Å. The cleft is defined by the planes of the Py and the phen ligand (angle between mean planes 89.21°), a centroid-centroid distance of 4.575 Å, and the shortest atomic contact N(15)−N(12) of 2.857 Å. Selected contact distances not discussed herein are shown in Table A.4.2. In the crystal structure of $[(\eta^6$-ind)Ru(bpy)(Py)][PF$_6$]$_2$ (**13**) there is a weak π-stacking interaction between the bpy chelating ligands of neighbouring complexes. The molecules are related by an inversion centre with the closest atomic contact of 3.539 Å between C(4) and C(8), Figure 4.9. The mean planes through the interacting π systems are parallel. The internal cleft defined by the planes of the Py and the bpy ligand is 89.54°.
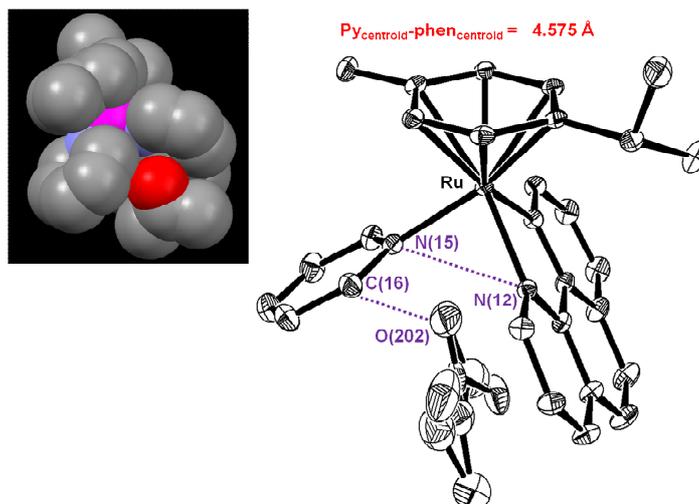
Figure 4.8. X-ray structure of the cation $[(\eta^6$-*p*-cym)Ru(phen)(Py)]$^{2+}$ (**10**) showing a disordered acetone lying in a cleft between the bound phen and the pyridine. Inset: Spacefilling model of $[(\eta^6$-*p*-cym)Ru(phen)(Py)][PF$_6$]$_2$ (**10**) showing the presence of intramolecular contacts. The PF$_6$ anions and hydrogens have been omitted for clarity.
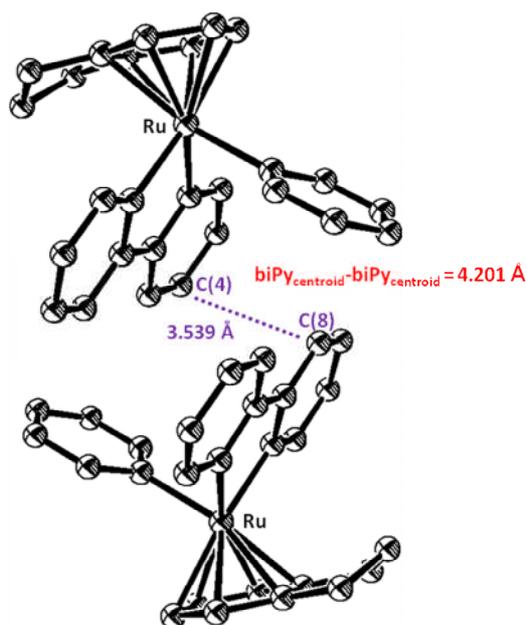

Figure 4.9. X-ray crystal structure of $[(\eta^6$-ind)Ru(bpy)(Py)][PF$_6$]$_2$ (**13**) showing a π-π stacking interaction. The PF$_6$ anions and hydrogens have been omitted for clarity.

The twist angles between the aromatic pyrazine rings of the bpm ligand are 7.09°, 6.80°, 2.21°, and 4.56° in complexes **2**, **6**, and **7**, respectively. The twist angle between the aromatic pyridine rings of the bpy is 3.91° in **13**.

4.3.3   DFT Optimised-Geometry Structures of Ru^{II} Arene Complexes

A geometry optimisation of complexes **1−6** and **8−16** with the general formula $[(\eta^6\text{-}$ arene)Ru(N,N')(L)]$^{2+}$ was performed for both the ground state (S0) and the lowest-lying triplet state (T0), employing the DFT method with the B3LYP functional, as described in the Computation section in Chapter 2. The corresponding bond lengths for each geometry are shown in Tables 4.3 and 4.4.

Table 4.3. Selected calculated bond distances (Å) for Ru^{II} arene complexes **1−6** and **8−16** in the ground state (S0) geometry.

Compound	Ru−N$_{(L)}$	Ru−N,N'	Ru−N,N'	Ru−arene$_{(centroid)}$
(**1**)	2.151	2.117	2.115	1.852
(**2**)	1.940	2.101	2.104	1.811
(**3**)	1.940	2.105	2.100	1.811
(**4**)	2.145	2.118	2.115	1.850
(**5**)	1.940	2.104	2.101	1.810
(**6**)	1.940	2.104	2.101	1.810
(**8**)	2.159	2.124	2.125	1.862
(**9**)	2.150	2.114	2.114	1.850
(**10**)	2.148	2.119	2.121	2.032
(**11**)	2.147	2.119	2.121	1.844
(**12**)	2.148	2.119	2.121	1.844
(**13**)	2.151	2.104	2.104	1.853
(**14**)	2.148	2.118	2.114	1.850
(**15**)	2.146	2.118	2.112	1.853
(**16**)	2.148	2.117	2.114	1.850

Table 4.4. Selected calculated bond distances (Å) for Ru^{II} arene complexes **1−6** and **8−16** in the lowest-lying triplet state (T0) geometry.

Compound	Ru−N$_{(L)}$	Ru−N,N'	Ru−N,N'	Ru−arene$_{(centroid)}$
(**1**)	2.108	2.158	2.452	2.089
(**2**)	2.139	2.404	2.131	2.058
(**3**)	2.140	2.081	2.345	2.625
(**4**)	2.133	2.414	2.129	2.067
(**5**)	2.119	2.132	2.410	2.069
(**6**)	2.133	2.396	2.132	2.058
(**8**)	2.159	2.151	2.466	2.014
(**9**)	2.132	2.134	2.389	2.110
(**10**)	2.479	2.120	2.119	1.844
(**11**)	2.148	2.119	2.119	1.846
(**12**)	2.478	2.100	2.102	2.035
(**13**)	2.137	2.355	2.125	2.108
(**14**)	2.149	2.117	2.114	1.851
(**15**)	2.146	2.116	2.113	1.849
(**16**)	2.146	2.122	2.439	2.078

4.3.3.1 Ground State (S0) Geometry

All the DFT geometry-optimised Ru^{II} arene complexes have a pseudo-octahedral structure in the ground-state (S0). The calculated Ru−N,N'$_{(bpm)}$ distances in the bpm-containing complexes **1−6**, vary around the same value (~2.12 Å). The Ru−N$_{(L)}$ bond lengths in **1−6** are ~1.94 Å, except for complexes **1** and **4** which are slightly larger (2.15 and 2.14 Å, respectively). For complexes **2** and **6**, the computed Ru−N$_{(L)}$ distances are slightly shorter than the ones determined by X-ray diffraction crystallography (2.11 and 2.12 Å, respectively). The experimental evidence that they are almost identical was also reproduced by the computational results. The calculated Ru−*p*-cym$_{(centroid)}$ distances for complexes **1** and **4** have similar values, which are slightly larger (~1.85 Å) when compared to those of complexes **2**, **3**, **5** and **6**. Particularly in the case of complexes **2** and **6**, the computed Ru−*p*-cym$_{(centroid)}$ distances are larger than those found in their X-ray crystal structures (1.69 and 1.70 Å, respectively). The calculated Ru−N,N'$_{(bpm)}$ distances in the bpm−Py containing Ru^{II} arene complexes **1** (*p*-cym), **8** (hmb), and **9** (ind), resulted in almost identical

values, being slightly larger (~0.1 Å) in the case of complex **8** (2.13 Å). The same

trend was observed for its Ru−N$_{(Py)}$ and Ru−hmb$_{(centroid)}$ bond lengths in, which are

both ~0.1 Å longer. The Ru−N,N' and the Ru−N$_{(Py)}$ bond distances in complexes **10**

and **12** (phen and bathophen, respectively) display the same value (~2.12 Å);

however, complex **10** was found to have a longer Ru−*p*-cym$_{(centroid)}$ distance in

comparison to complex **12**. This same bond distance also differs significantly from

that determined by X-ray crystallography for complex **10** (*vide supra*), where the

value predicted is *ca*. 0.4 Å larger. Conversely, the calculated Ru−N$_{(Py)}$ distances in **10**

were found to be in good agreement with those in the X-ray crystal structure.; its

Ru−N,N'$_{(phen)}$ distances are barely longer. The DFT calculations show that the

Ru−N,N'$_{(bpm)}$ distance in complex **9** is *ca*. 0.10 Å shorter than the analogue

Ru−N,N'$_{(bpy)}$ distance found in complex **13**. The Ru−N$_{(Py)}$ and Ru−ind$_{(centroid)}$ distances

in **9** and **13** are practically within the same range. When compared to the X-ray crystal

structure, the calculated Ru−ind$_{(centroid)}$ as well as the Ru−N,N'$_{(bpy)}$ bond length

distances of complex **13** were found to be slightly larger, whereas the corresponding

Ru−N$_{(Py)}$ is in good agreement. Finally, for complexes **14−16**, the calculations show

that the Ru−N,N'$_{(bpm)}$, the Ru−N$_{(L)}$, and the Ru−*p*-cym$_{(centroid)}$ distances are identical in

the three cases (~2.12, 2.15, and 1.85 Å, respectively).

4.3.3.2 *Lowest-Lying Triplet State (T0) Geometry*

The lowest-lying triplet states geometries were also optimised for complexes **1−6** and

8−16, due to the key role that this state can play in their photochemistry. It was found

that the Ru−N$_{(Py)}$ distances are practically within the same range for complexes **1−6**

(~2.14 Å), except for complexes **1** and **4** which display slightly smaller values. All

complexes have similar Ru−N$_{(L)}$ distances, except complexes **1** and **5** which are

slightly shorter, when compared to the ground state (S0). Within this series (**1−6**), one of the Ru−N,N' bond distances in the T0 state is considerably longer than the other, typically 2.18 and 2.40 Å. The Ru−*p*-cym$_{(centroid)}$ distances are in general longer compared to the ground state (~2.06 Å); complex **4** having the largest value (*ca.* 2.26 Å). For complexes **8** and **9**, the corresponding Ru−N$_{(Py)}$ bond lengths are slightly longer, and also remain unchanged compared to those in the ground state. Both of the calculated Ru−N,N'$_{(bpm)}$ distances in each case have two different values, being one of them significantly larger (~2.4 Å). Each of the computed Ru−arene$_{(centroid)}$ distances (hmb for **8** and ind for **9**) are longer than those calculated for the ground state. Complex **11** was found to keep nearly the same geometry as in S0. In the case of complexes **10** and **12**, the estimated Ru−N$_{(Py)}$ distance are considerably elongated (~2.5 Å) whereas the corresponding Ru−N,N' bond lengths are almost identical to the ones observed for S0 and also very similar between them (~2.11 Å). In the same way as observed in the X-ray crystal structure, the computational results show that the calculated Ru−*p*-cym$_{(centroid)}$ distance in complex **10** is shorter than that found in the ground state, whereas the opposite trend is found in the calculation results of complex **12**. Complexes **9** and **13** display similar Ru−N$_{(Py)}$ bond distances as those calculated for their S0. Furthermore, these two complexes follow the common trend of having one Ru−N,N'$_{(bpm)}$ bond length longer than the other, while the Ru−ind$_{(centroid)}$ lengths are in general larger than those in the ground state. Finally, for complexes **14−16**, the calculated Ru−N$_{(L)}$ distances are found to be larger than those computed for complex **1** (and practically for any of all the bpm−*p*-cym containing derivatives). The value resembles more to that obtained for the ground state. In the case of the Ru−N,N'$_{(bpm)}$ distances, while complex **16** follows the common trend of having one Ru−N,N'$_{(bpm)}$ bond length larger than the other, complexes **14** and **15** do not follow it. Both of the

calculated Ru−N,N'$_{(bpm)}$ distances for complexes **14** and **15** are within the same range (~2.11 Å).

4.3.4 Orbital Analysis

The shapes of selected frontier orbitals for the Ru^{II} arene complexes **1−6** and **8−16** in the ground state (S0) were analysed, in particular the Highest Occupied Molecular Orbitals (HOMOs) and the first four Lowest Unoccupied Molecular Orbitals (LUMOs). The Single Occupied Molecular Orbitals (SOMOs) of the lowest-lying triplet state are also described along with their Spin Density Surfaces (total electron density of electrons of one spin (α), minus the total electron density of the electrons of the other spin (β)).[11] Visualisation of the SOMOs and the spin density surface of a metal complex is useful to understand where unpaired electrons of a triplet state are localised.

4.3.4.1 Molecular Orbitals in the Ground State

Complexes [(η^6-*p*-cym)Ru(bpm)(Py)]$^{2+}$ (**1**) and [(η^6-*p*-cym)Ru(bpm)(4-MePy)]$^{2+}$ (**2**) are found to have similar frontier orbitals. The HOMO is delocalised mainly on the Ru−*p*-cym moiety, with some contribution from the bpm chelating ligand. The LUMO is bpm-centred while the LUMO+1 is delocalised around the Ru−*p*-cym bond. The LUMO+1 for complexes **1** (Figure 4.10) and **2** has an important σ*-antibonding character towards the pyridine-derivative ligand (Py and 4-MePy, respectively). The LUMO+2 is mainly bpm-centred, whereas the LUMO+3 resembles the LUMO+1 in character. In the case of [(η^6-*p*-cym)Ru(bpm)(4-MeOPy)]$^{2+}$ (**3**), all the orbitals share similar features to those found for complex **1** and its analogue complex **2**, with the

exception of the HOMO, where a significant delocalisation over the 4-MeOPy was observed. The 4,4'-bpy ligand in complex **4** (Figure 4.10) contributes to the overall character of the LUMO+2 and LUMO+3, evidence which, however, is not observed for the corresponding complexes **1** and **3**. The HOMOs of $[(\eta^6$-p-cym)Ru(bpm)(4-PhPy)]$^{2+}$ (**5**) and $[(\eta^6$-p-cym)Ru(bpm)(4-BzPy)]$^{2+}$ (**6**) are fully centred on the corresponding pyridine-derivative, while the empty orbitals are consistently similar to those found in **1**, as well as for the other derivatives complexes **2**−**4**. A direct orbital comparison between complex **1** and complexes **14**, **15** (Figure 4.10) and **16** reveals that while complexes **15** and **16** maintain the similar features found for complex **1**, complex **14** displays a different character. Its high-energy LUMOs (i.e. LUMO+1, LUMO+2, and LUMO+3) display not only a significant σ*-antibonding character towards the 3-AcPy ligand, but also an important contribution coming from its π orbitals. Additionally, LUMO+3 in complex **14** has a reduced arene$_{(p\text{-cym})}$ character, as well as an increased bpm contribution. The character of both the low- and the high-energy orbitals for complexes **8** and **9** resemble more to those observed for **1**, with the only exception of the LUMO+1 which is observed to have lost the σ*-antibonding character towards the Py ligand. Only small differences were found between complexes **9** and **13** when compared to **1**. The Ru^{II} complex **13** has HOMO, LUMO and LUMO+1 very similar to complex **9**. However, the LUMO+2 has a σ*-antibonding character toward the Py ligand, while the LUMO+3 shares the bpm-centred nature of LUMO+2 found in the other derivatives, along with a considerable contribution from its π orbitals. Finally, complexes **10** and **12** have HOMOs with an increased contribution from the corresponding N,N'-chelating ligand, particularly in the case of **12** (bathophen). Compared to complex **1**, the LUMO+1 and LUMO+2 have reversed characters, so that LUMO+2 and LUMO+3 are more σ*-antibonding in

character. Complex **11** is found to have orbital character similar to complex **1**. A complete representation of the frontier orbitals for complexes **1−6** and **8−16** are reported in the Appendix section.
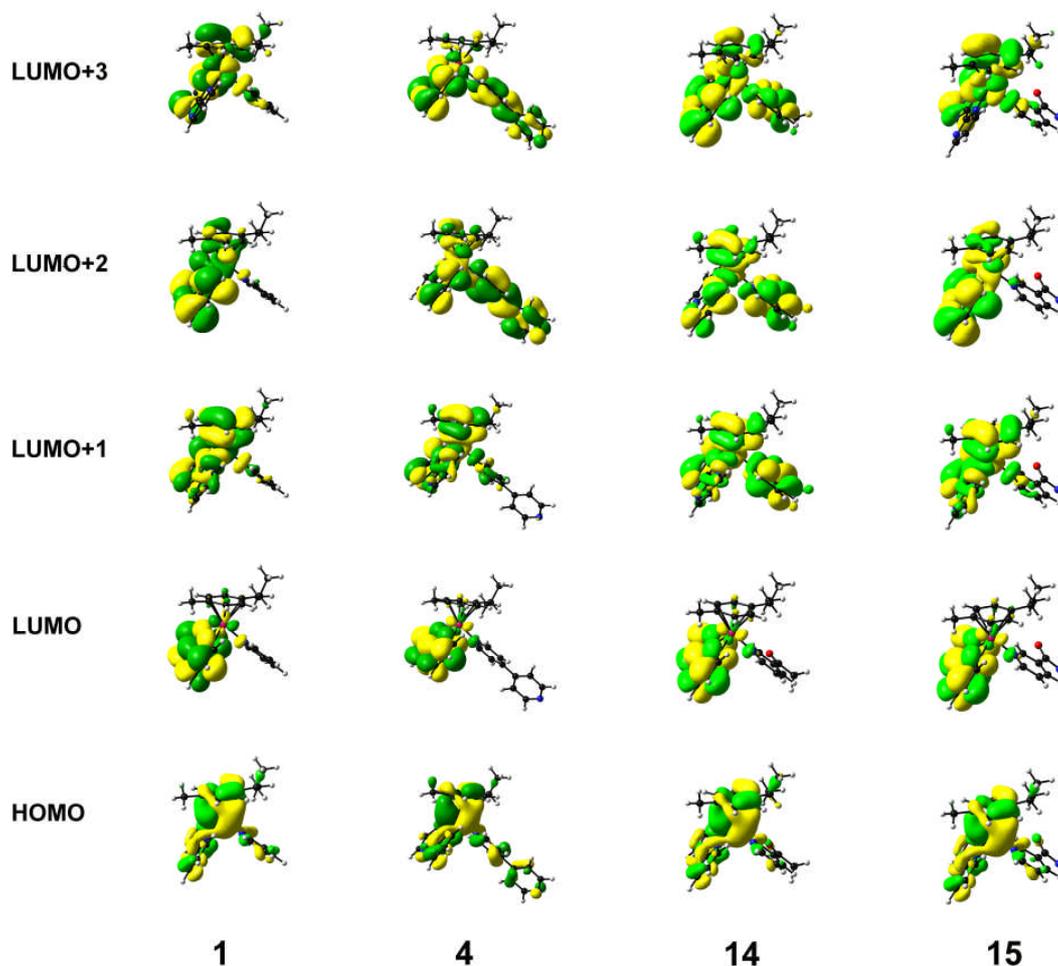

Figure 4.10. Selected frontier orbitals for complexes **1**, **4**, **14**, and **15** in the ground state (S0) geometry.

4.3.4.2 *Molecular Orbitals in the Lowest-Lying Triplet State*

In the case of complex **1**, both the *highest*-SOMO and the *lowest*-SOMO (*h*-SOMO and *l*-SOMO, respectively) are delocalised over the Ru−arene$_{(p\text{-cym})}$ and Ru−N,N'$_{(bpm)}$ bonds, Figure 4.11. In the case of complex **2**, these two orbitals (*h*-SOMO and *l*-SOMO) are in general, similar to those found in complex **1**, only differing in the contribution from the 4-MePy to the *l*-SOMO. For complexes **3** and **4** this same effect

is also observed but rather increased, and the contribution of the 4,4'-bpy in the latter complex comes mainly from the uncoordinated Py ring which contributes to the *l*-SOMO also through the non-coordinated-N-centred σ orbital.

l-SOMO   *h*-SOMO   Spin Density Surface
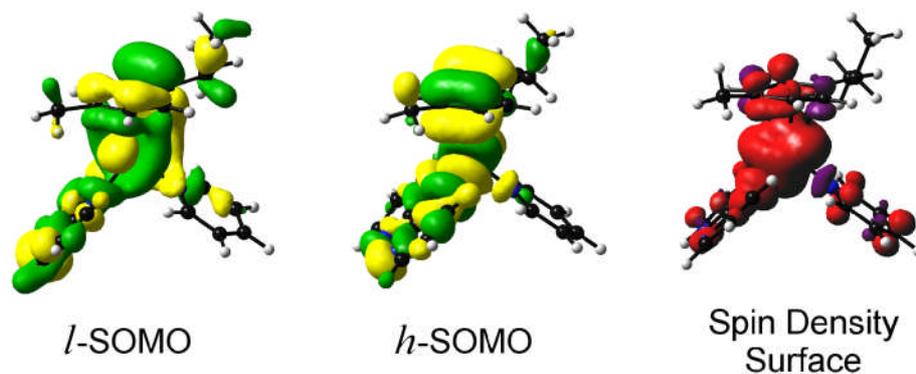
Figure 4.11. Calculated *lowest-* and *highest-* Single Occupied Molecular Orbitals (*h*-SOMO and *l*-SOMO, respectively), and spin density surface for [(η^6-*p*-cym)Ru(bpm)(Py)]$^{2+}$ (**1**).

Complex [(η^6-*p*-cym)Ru(bpm)(4-PhPy)]$^{2+}$ (**5**) is very similar to **1**, where both the *h*-SOMO and the *l*-SOMO are delocalised over the Ru−arene$_{(p\text{-cym})}$ and Ru−N,N'$_{(bpm)}$ bonds. As observed for complex **4**, the *l*-SOMO in **5** is also delocalised on the phenyl ring of the 4-PhPy ligand. Similar features are found for complex [(η^6-*p*-cym)Ru(bpm)(4-BzPy)]$^{2+}$ (**6**), where both the *h*-SOMO and the *l*-SOMO are centred in the benzyl ring of the 4-BzPy ligand. The spin density maps for complexes **1**−**6** show that the nature of these lowest-lying triplet states are mainly Ru−arene$_{(p\text{-cym})}$ centred. Comparison of complex **1** with complexes **14**, **15** and **16**, show that the *l*-SOMO on the two first complexes has the same character as that in complex **1**, whereas the *h*-SOMO is N,N'$_{(bpm)}$ localised and similar to the LUMO in the ground state (S0). In the case of **16**, the *l*-SOMO and the *h*-SOMO lie at inverted energy levels compared to those of complexes **14** and **15**. The spin density maps for complexes **14** and **15** show that the unpaired electrons are mainly localised on the

pyridine-derivative ligand, while for **16** they are centred on the Ru−arene$_{(p\text{-cym})}$ moiety. The *l*-SOMO and the *h*-SOMO of complex **11** are centred on the *p*-cym and the phendio N,N'-chelating ligand, respectively. In the case of complexes **10** (phen) and **12** (bathophen), both the *l*-SOMO and the *h*-SOMO display a σ*-antibonding character towards the Py ligand (particularly the *h*-SOMO). The *l*-SOMO is also more localised on the corresponding N,N' chelating ligand (phen in **10**, and bathophen in **12**), whereas the *h*-SOMO is centred on the Ru-arene$_{(p\text{-cym})}$ fragment. The spin density map of complex **11** is mainly N,N'$_{(phendio)}$ centred, while for **10** and **12** they are delocalised over all the Ru^{II} complex. Complexes $[(\eta^6\text{-hmb})Ru(bpm)(Py)]^{2+}$ (**8**) and $[(\eta^6\text{-ind})Ru(bpm)(Py)]^{2+}$ (**9**) display high similarity when compared to **1**. However, their *h*-SOMOs have some σ*-antibonding character towards the monodentate pyridine ligand. Their spin density maps are mainly Ru−arene centred (only the aromatic ring of the ind arene is involved in the case of **9**). Complex **13** shows a N,N'$_{(bpy)}$-*l*-SOMO localisation as that observed for complex **1**. The spin density maps of complexes **9** and **13** are Ru−arene$_{(ind)}$ centred in both cases.

4.3.5   Electronic Absorption Spectra and Singlet Excited States

The behaviour under visible light and UVA photoirradiation in aqueous solution of complexes **1−6**, **8−10**, and **12−16** was explored. Due to its instability in aqueous solution, photoirradiation experiments of complex **11** were performed in an acetone solution. Complex **7** was not obtained in sufficient yields and therefore was not considered for photochemical studies. The UV-vis absorption spectra of complexes **1−6** and **8−16** were recorded at 310 K as 100 μM solutions in H$_2$O from 200 to 800 nm. In the dark (i.e. no irradiation provided), aqueous solutions of all the complexes

were remarkably stable over a large range of pH* values (pH* = 2–12) and no hydrolysis reaction was observed at room temperature over a period of *ca.* 2 months. Figure 4.12 shows the experimental UV-vis absorption spectra and the calculated electronic transitions for all the complexes. The corresponding maxima of absorption (λ, nm) and extinction coefficients (ε, M^{-1} cm^{-1}) are listed in Table 4.5. A complete set of DFT and TD-DFT calculations was performed with Gaussian 03[12] on complexes **1**−**6** and **8**−**16** at the B3LYP/LanL2Dz/6-31G** level, to characterise the singlet and triplet excited states and to obtain insights into the mechanism of ligand photodissociation. The TD-DFT-calculated singlet transitions of all the derivatives are, in general, in good agreement with the experimental data. For complex **1** and the analogue complexes **2**, **3**, and **4**, the absorbance tail in the 380–420 nm region is assigned to mixed metal centred/metal-to-ligand charge transfer (^{1}MC/^{1}MLCT) transitions. These transitions are partially dissociative; they have significant contributions from Ru−N,N'$_{(bpm)}$ and the corresponding Ru−N$_{(L)}$ σ*-antibonding orbitals that could be populated by light excitation. In the case of complex [(η^6-*p*-cym)Ru(bpm)(4-PhPy)][PF$_6$]$_2$ (**5**) this low-energy absorbance tail, however, displays more ^{1}MLCT character, with contributions from the phenyl ring (within the 4-PhPy). Pure ^{1}MLCT (Ru → bpm) states are found at higher energy (UVA region) for **1**. In the case of complex **2** these transitions are present as a broad shoulder *ca.* 300 nm, along with a maximum at *ca.* 275 nm which can be associated with transitions of mixed character.

Table 4.5. Wavelength of absorption maxima (λ, nm) and extinction coefficients (ε, M^{-1} cm^{-1}) for complexes **1−6** and **8−16**.

| Compound	Wavelength (λ, nm)	Extinction Coefficient $\times 10^3$ (ε, M^{-1} cm^{-1})
(**1**) [(η^6-*p*-cym)Ru(bpm)(Py)][PF$_6$]$_2$	383	2.31
	254	23.1
(**2**) [(η^6-*p*-cym)Ru(bpm)(4-MePy)][PF$_6$]$_2$	374	1.30
	251	45.6
(**3**) [(η^6-*p*-cym)Ru(bpm)(4-MeOPy)][PF$_6$]$_2$	384	1.34
	247	4.85
(**4**) [(η^6-*p*-cym)Ru(bpm)(4,4'-bpy)][PF$_6$]$_2$	382	0.28
	252	3.43
(**5**) [(η^6-*p*-cym)Ru(bpm)(4-PhPy)][PF$_6$]$_2$	373	0.75
	286	8.30
	265	9.10
(**6**) [(η^6-*p*-cym)Ru(bpm)(4-BzPy)][PF$_6$]$_2$	357	0.43
	254	5.69
(**8**) [(η^6-hmb)Ru(bpm)(Py)][PF$_6$]$_2$	382	0.88
	242	12.2
(**9**) [(η^6-ind)Ru(bpm)(Py)][PF$_6$]$_2$	392	0.51
	293	4.93
	249	12.0
(**10**) [(η^6-*p*-cym)Ru(phen)(Py)][PF$_6$]$_2$	362	1.47
	275	11.5
(**11**) [(η^6-*p*-cym)Ru(phendio)(Py)][PF$_6$]$_2$	301	0.76
	275	1.31
(**12**) [(η^6-*p*-cym)Ru(bathophen)(Py)][PF$_6$]$_2$	395	1.21
	289	10.7
(**13**) [(η^6-ind)Ru(bpy)(Py)][PF$_6$]$_2$	348	0.01
	313	0.45
	300	0.54
	255	1.18
(**14**) [(η^6-*p*-cym)Ru(bpm)(3-AcPy)][PF$_6$]$_2$	372	3.29
	250	17.9
(**15**) [(η^6-*p*-cym)Ru(bpm)(3-NA)][PF$_6$]$_2$	366	2.86
	253	15.6
(**16**) [(η^6-*p*-cym)Ru(bpm)(3-AcOPy)][PF$_6$]$_2$	365	2.13
	248	12.5
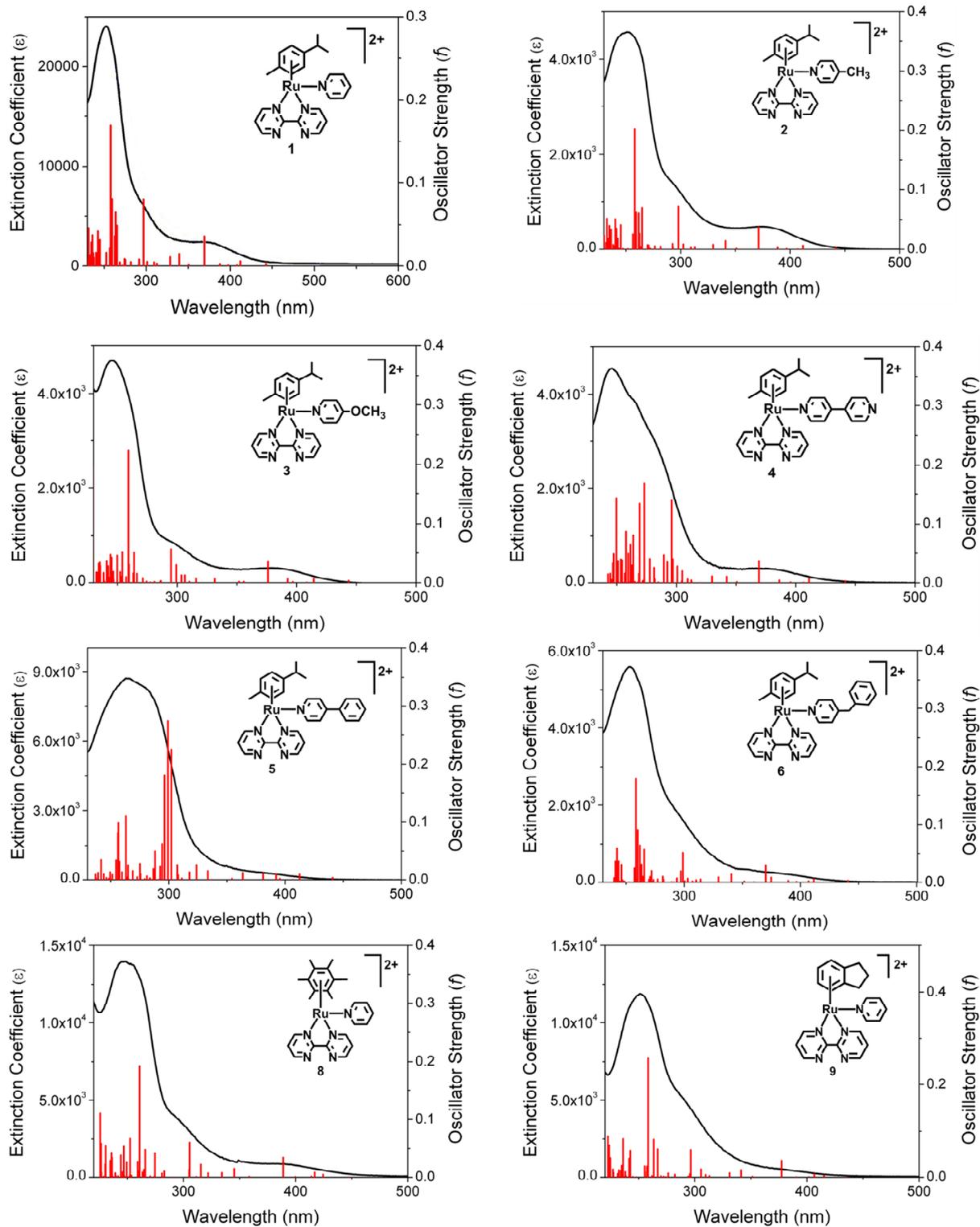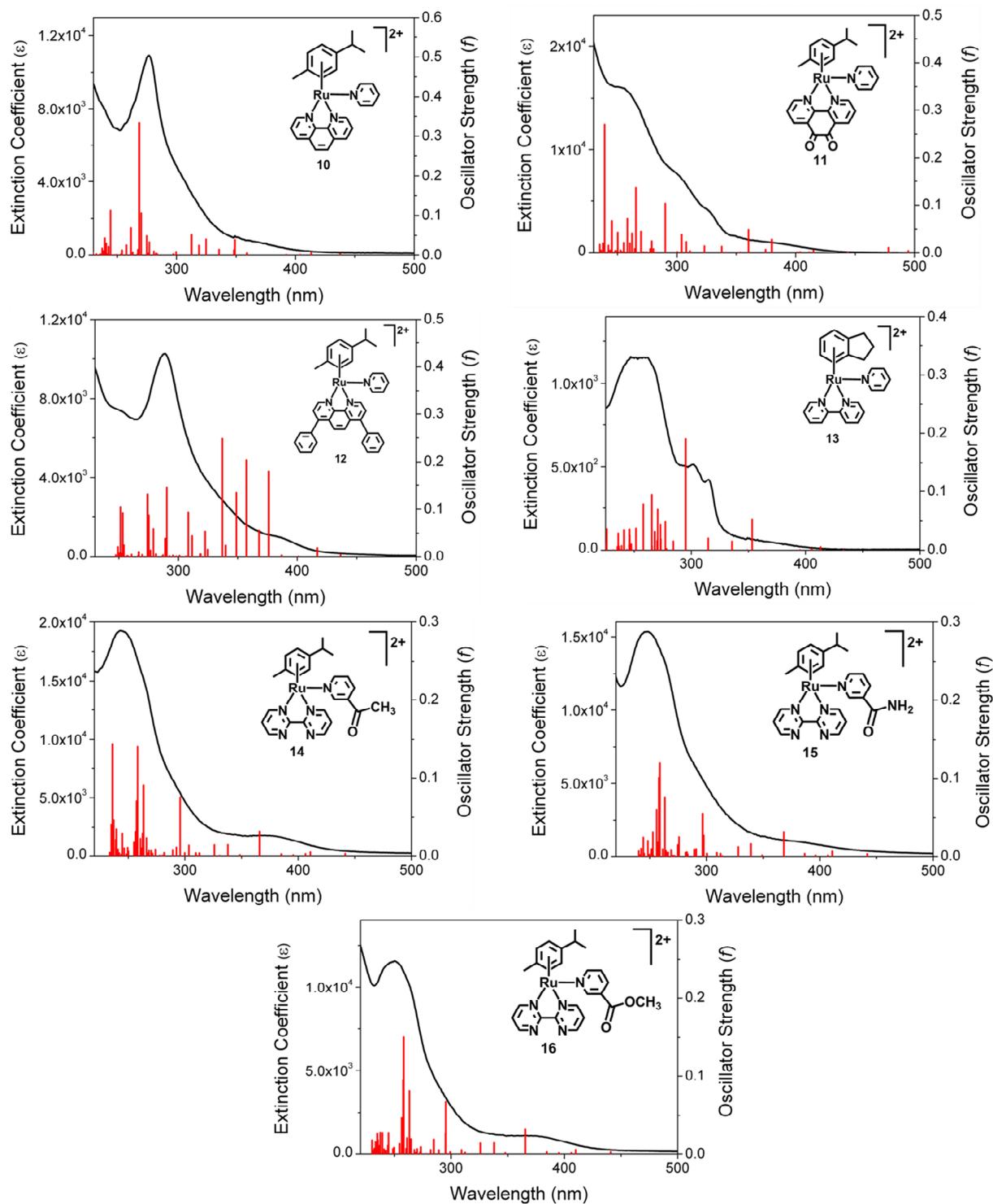
Figure 4.12. Experimental UV-Vis spectrum (black) of the Ru^{II} pyridine or pyridine-derivative complexes **1−6** and **8−16** in aqueous solution at 310 K. The calculated electronic transitions are shown as red vertical bars with heights equal to their oscillator strength.

Selected Electron Density Difference Maps (EDDMs) for complexes **1**, **4**, **14**, and **15** are shown in Figure 4.13. For complex **3**, several transitions around this same region (*ca.* 300 nm) acquire a more pronounced interligand (^{1}IL) character given that the methoxy group (on 4-MeOPy) is involved as an electron-density donor. In the case of complex **4**, within the UV region, the higher energy transitions display a mixed character, whereas the lower energy tend to be more intense (compared to **1**, **2**, or **3**).
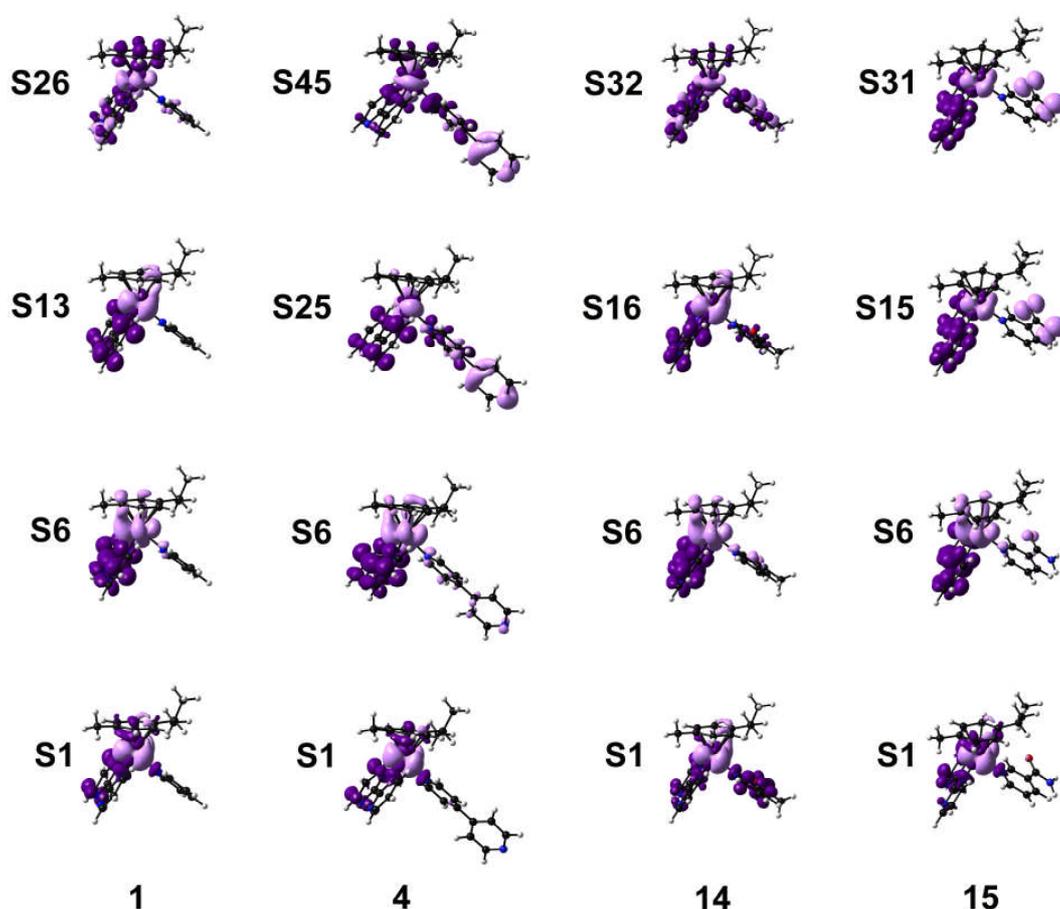
Figure 4.13. Selected electron difference density maps (EDDMs) of singlet excited state transitions for complexes **1**, **4**, **14**, and **15** in H_2O. Light violet indicates a decrease in electron density; dark purple indicates an increase.

Complex **5** displays a different contribution to the overall character of the transitions (highest intensity) at *ca.* 300 nm when compared to the analogue complexes **1**−**4**, being mainly composed by metal-to-ligand charge transfer/ligand centred

(^{1}MLCT/^{1}LC, Ru → bpm/Ph → Py) states. For complex **6**, the maximum of absorbance is around the 250 nm region (as also observed for complexes **1**−**4**) though in this case they are predominantly ^{1}MLCT (Ru → bpm) in character. Its low energy transitions (λ < 370 nm) are similar to the analogue complexes **1**−**4**, with some of them being ^{1}IL (Bz → bpm) based. The UV-vis spectrum of the Ru^{II} ind complexes **8** and **9** is found to keep all the spectroscopic features exhibited by **1**, both in the low and the high-energy regions. Overall, complex **8** displays transitions that are red-shifted, whereas the corresponding for complex **9** are slightly blue-shifted. Complexes **10** and **11** have both lower-energy singlet transitions that are either ^{1}MLCT or ^{1}MC in character, which could have a dissociative nature. The main absorption band in complex **10** is mixed in character, composed by a ^{1}LC transition centred on the phen chelating ligand and a ^{1}MLCT (Ru → *p*-cym, phen) transition, whereas the analogue absorption band on complex **11** is a mixed ^{1}LC on the phendio along with a ^{1}MC. For complex **10**, the calculations predict singlet transitions that are in general slightly blue-shifted, whereas the opposite effect is predicted for complex **11**. Complex **13** shows similar electronic transitions as those found in the analogue complexes **9** and **1**, which are ^{1}MC or ^{1}MLCT in character, the first ones being dissociative (LUMO+2 contribution). An intense transition can be observed around 300 nm that accounts for the pronounced shoulder seen in the experimental spectrum. Such transition is a mixed ^{1}MLCT (Ru → bpm)/^{1}LC. The second maximum of absorption at higher energy (λ = 255 nm) is again of mixed character, with both ^{1}MC/^{1}LC and ^{1}MLCT transitions contributing to it. In the case of complex **12**, as could be expected for molecules with extended and highly conjugated aromatic surfaces, the DFT calculations overestimated its contribution to the transitions at about 370 nm. This is probably due to an error on the computing of the corresponding HOMO−LUMO

energy.[13] However, in a similar fashion as found in the other related complexes, the lower energy transitions are mainly ^{1}MC and ^{1}MLCT (Ru → bpm), while the higher energy tend to be mainly composed of ^{1}MLCT (Ru → bathophen) states. The overall features of the UV-vis absorption spectra of complexes **14**, **15**, and **16**, resemble significantly to those observed for complex **1**. Orbital composition of computed singlet transitions and selected EDDMs for complexes **1−6** and **8−16** are reported in the Appendix section.

4.3.6 Photoirradiation of Ru^{II} Arene Complexes with Visible Light Followed by UV-vis Absorption Spectroscopy

As shown by UV-vis data, if aqueous solutions of complexes **1−6**, **8−10**, and **12−16** are photoirradiated with visible light (λ_{irr} = 400−660 nm, 1 J cm^{-2} h^{-1}) at 310 K, the electronic absorption bands shift and change in intensity, the largest changes being observed around the 200−300 nm region, Figure 4.14. The presence of an isosbestic point at *ca*. 310 nm indicates the formation of a single photoproduct in all cases.
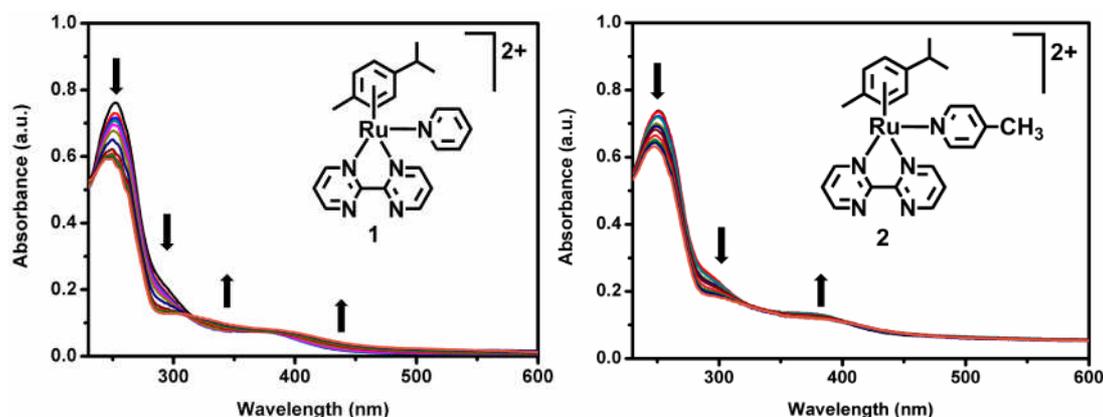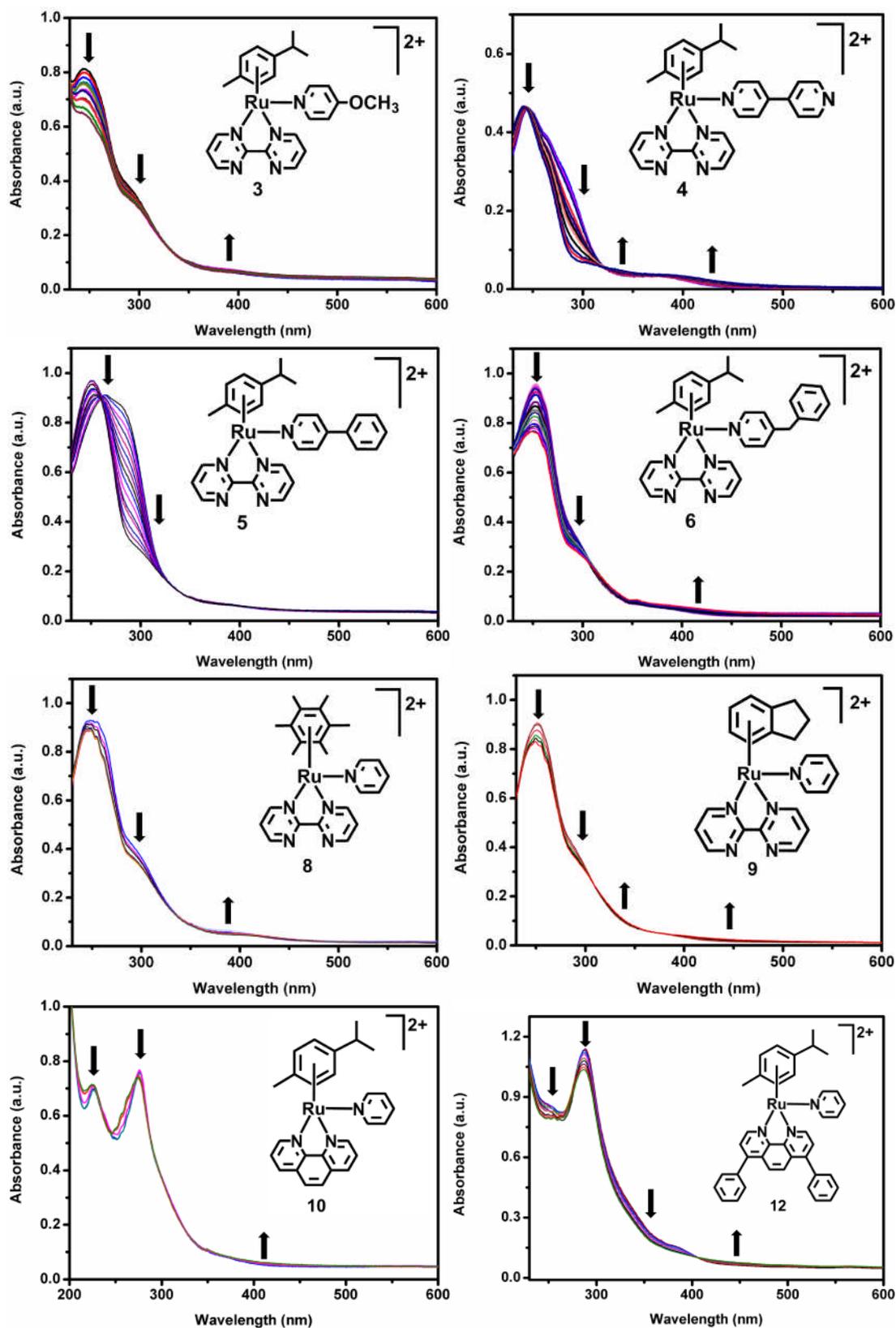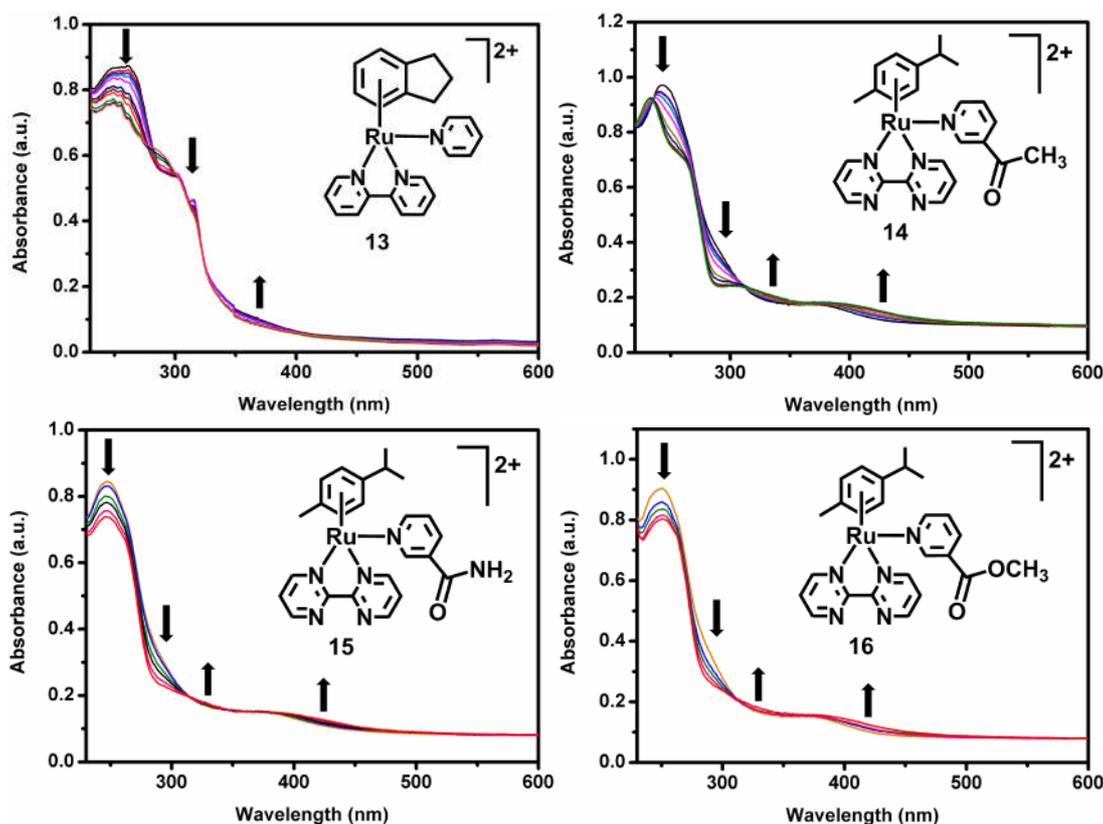
Figure 4.14. Photolysis (λ_{irr} = 400–660 nm) of the Ru^{II} arene pyridine or pyridine-derivative complexex **1−6**, **8−10**, and **12−16** in aqueous solution during *ca.* 10−12 h followed by UV-Vis.

4.3.7   Triplet Excited States

In addition to the singlet excited state calculations described (*vide supra*), triplet excited states were calculated by DFT and TD-DFT for complexes **1−6** and **8−16**. The full set of calculations performed is schematised in Figure 4.15 and described in the computational methods in Chapter 2. Both the ground state (S0) and the lowest-lying triplet state (T0) geometries were employed in the triplet calculations. Eight transitions were calculated in each case. The triplets calculated from the S0 geometry (shown in red in Figure 4.15) describe the triplet excited states formed right after excitation (Franck-Condon) and intersystem crossing (ultrafast ~fs), but before significant structural relaxation[14] (i.e. vibrational relaxation and solvation dynamics); these excited states are reported in the appropriate Appendix section and are not

considered for discussion. In d^6 metal complexes (as those of Ru^{II} studied in this work) the lowest-lying triplet T0 (shown in black in Figure 4.15) is typically the state to which the excited molecules relax after excitation and intersystem crossing, before returning to the ground state. It plays a key role in their photophysical and photochemical properties, and for this reason its characterisation was performed by geometry optimisation (*vide supra*) and spin density surface calculations using TD-DFT methods (T1 shown in green in Figure 4.15). The characterisation of higher energy triplet states (shown in green in Figure 4.15) was obtained as well by TD-DFT. The complete computational results are reported in the appropriate Appendix section. Analysis of the T0 geometry of complexes **1−6** reveals that they have a distorted geometry, highlighting both an elongated Ru−N,N'$_{(bpm)}$ bond (with respect to the ground state), which is typically *ca.* 0.3 Å longer, as well as an elongated Ru−N$_{(L)}$ bond in the case of complexes **2**, **3**, **5**, and **6**. In the case of complexes **1** and **4**, no Ru−N$_{(L)}$ bond elongation is observed. Spin density surfaces (Figure 4.11) show that the nature of the T0 for complexes **1−6** is ^{3}MC, which is consistent with the lack of emission from this family of compounds (altogether with the low energy of this state). A similar T0 is usually found to be in favour of non-emissive deactivation pathways.[15] Significantly, such T0 states do not have a dissociative character towards the L-monodentate ligand, since the SOMOs have no antibonding character with respect to the Ru−N$_{(L)}$ bond (except in the case of complex **1**). In fact, there is not a dramatic increase in the Ru−N$_{(L)}$ bond length for the optimised lowest-lying triplet geometries.

GS (S0): DFT/geom. opt.
T0: DFT/geom. opt. spin density surface
T0 = T0 geom. with spin multiplicity 1
S: TDDFT/S0 geom.
T: TDDFT/S0 geom.
T: TDDFT/T0 geom.
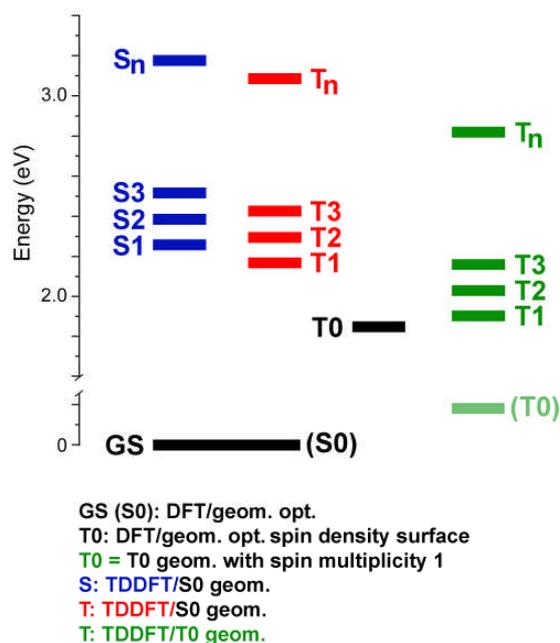
Figure 4.15. Schematic representation of the computational method applied to the study of the singlet and triplet excited states for complexes **1−6** and **8−16**.

The observed increase in the Ru−N,N'$_{(bpm)}$ distance can be ascribed to the population of a Ru−N,N'$_{(bpm)}$ σ*-antibonding *h*-SOMO; this involves only one of the bound-N within the bpm. Dissociation of bpm is prevented by the strong coordination of the other pyrazine ring of the ligand. The ^{3}MC nature of the lowest-lying triplet state for complexes **1−6** was confirmed by the TD-DFT calculations, which provide T1 states that are consistent with their analogue T0. At higher energies, a series of other ^{3}MC states have dissociative character towards L, (see EDDMs). They contain contributions from Ru–N$_{(L)}$ σ*-antibonding orbitals and dissociation of L can occur from these states during the excited state evolution to the ground state. For complexes **1−6**, the first low-energy triplets (T0/T1, T2, and T3) have generally a ^{3}MC character which is not dissociative, whereas only T4−T6 are dissociative towards the corresponding L-monodentate ligand (they involve the LUMO+3, which has a dissociative character), Figure 4.16.

At even higher energy, i.e. T7 and T8 (see Appendix section), ^{3}MLCT of Ru $\rightarrow$ N,N'$_{(bpm)}$ character are present. In the case of complexes **4−6**, the ^{3}MLCT character in the T2−T8 triplet states is more pronounced.
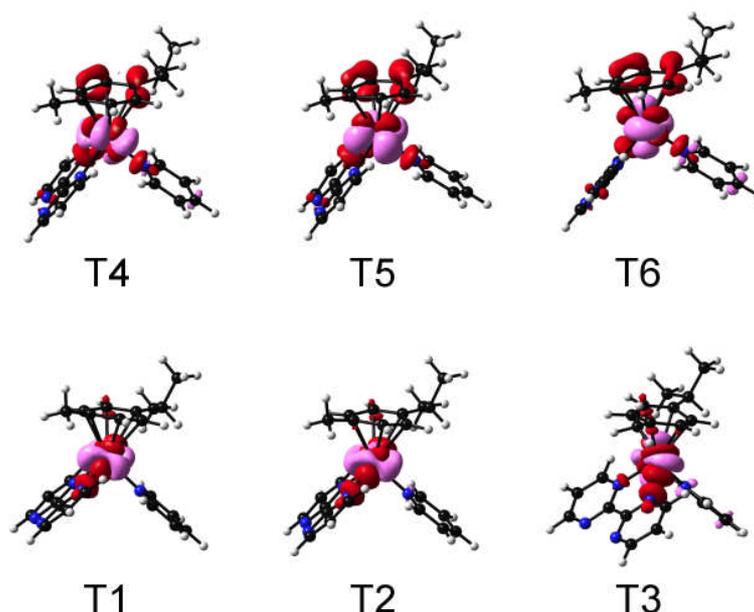

Figure 4.16. Selected electron difference density maps (EDDMs) of triplet excited state transitions for complex **1** in H$_2$O (shown in green in Figure 4.15). Pink indicates a decrease in electron density, while red indicates an increase.

In the case of complexes **8** and **9**, the T0 geometries show elongated Ru−N,N'$_{(bpm)}$ bonds. The spin density surface suggests a lowest-lying triplet state with a ^{3}MC dissociative character towards one of the pyrazine rings in the bpm ligand, due to the *h*-SOMO orbital having a σ*-antibonding nature. Similarly to **1−6**, TD-DFT triplet calculations highlight the presence of dissociative Ru−N$_{(L)}$ ^{3}MC for both complexes **8** and **9** (T4 and T5), confirming as well that the lowest-lying triplet state is not dissociative. The T0 geometries of complexes **10** and **12** have a distorted Ru $\rightarrow$ N$_{(Py)}$ bond. Their spin density surfaces are ^{3}MC and have a Ru−N$_{(L)}$ σ*-antibonding *h*-SOMO. They both behave like their analogue complexes **1–6** and **9**, where the dissociative ^{3}MC states are present above the lowest-lying triplet state. In the case of

11, no distortions are observed when comparing S0 and T0. The TD-DFT calculations show that there is a greater ^{3}MLCT character, with no significant involvement of the σ*-antibonding orbitals and the ^{3}MC states. Complex **13** behaves more similarly to complex **1**. For complexes **14** and **15**, a non-distorted T0 geometry was found, whereas complex **16** displays an elongated Ru−N,N'$_{(bpm)}$ bond, just as observed for the analogue complexes **1−6**. The three complexes **14−16** display Ru−N$_{(L)}$ bond distances similar to the ground state (S0). The spin density surfaces of complexes **14** and **15** are L-centred (where L is 3-AcPy and NA, respectively), while for complex **16** (where L is 3-AcOPy) is ^{3}MC (Ru → arene$_{(p\text{-cym})}$). The SOMOs of complexes **14** and **15** are consistent with a non-dissociative lowest-lying triplet state. Conversely, according to TD-DFT calculations, the T1 state for complexes **14** and **15** has a marked dissociative nature towards the Ru−N$_{(L)}$ bond (contribution from LUMO+1 and LUMO+3).

4.3.8 Photoirradiation of Ru^{II} Arene Complexes with Visible Light followed by ^{1}H NMR Spectroscopy

^{1}H NMR spectra recorded at different stages of photolysis with visible light (λ_{irr} = 400−660 nm) confirm that all the photoirradiated complexes selectively release their pyridine or pyridine-derivative ligand (L) with the subsequent *in situ* formation of the corresponding aqua adduct as the only photoproduct. The spectra for complexes **1** and **10** are shown in Figure 4.17; for the remaining derivatives the observed changes were identical to the ones described as follows.
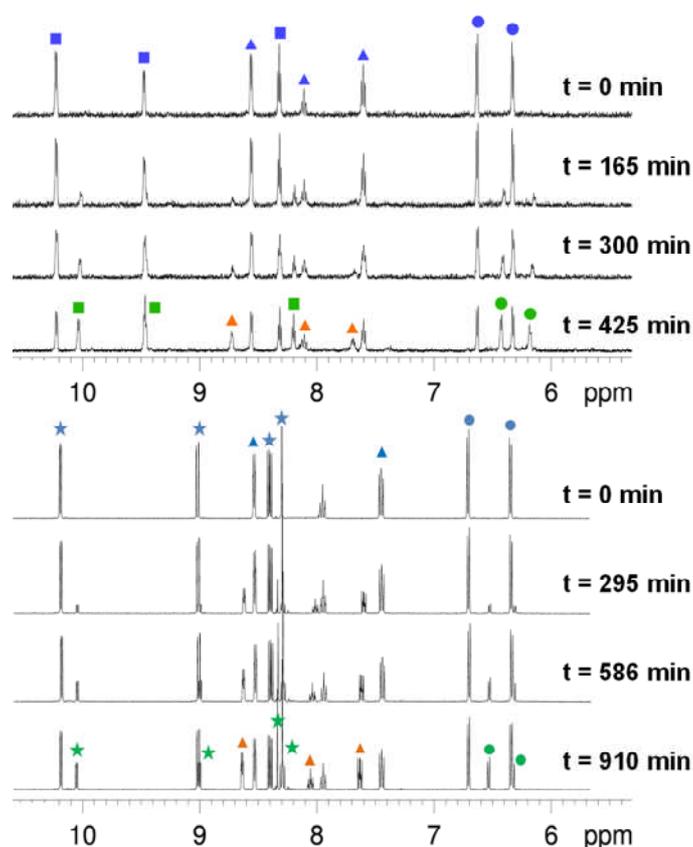
Figure 4.17. Selected ^{1}H NMR spectra of complexes **1** (top) and **10** (bottom) during their aqueous photolysis (λ_{irr} = 400−660 nm). **Blue** = Py complex, **green** = aqua adduct; ■ = bpm, ★ = phen, ▲ = Py, ● = *p*-cym. Free Py is indicated with **orange ▲**.

The spectra of each of the complexes in D$_2$O (or complex **11** in (CD$_3$)$_2$CO) at 310 K initially contained a set of peaks assigned to the original Ru−L complex, [(η^6-arene)Ru(N,N')(L)]$^{2+}$. Further photoirradiation with visible light (λ_{irr} = 400−660 nm) at 310 K produces a second set of peaks which increase in intensity as photoirradiation is maintained. These peaks are assigned to the corresponding aqua species [(η^6-arene)Ru(N,N')(OH$_2$)]$^{2+}$. A third set of peaks attributed to the free pyridine or pyridine-derivative was also detected. Solutions of all the Ru^{II} arene complexes kept in the dark at 310 K for longer than *ca*. 2 months did not show any detectable formation of the aqua adducts. The pH* values of the solutions were determined at the beginning and at the end of each photoirradiation experiment. In

most cases a slight decrease on the values was registered, from an average of ~7.14 at the starting point down to ~6.52 at the final stage. The mass-to-charge ratios and isotopic models obtained from HR-MS spectra were consistent with the formation of the aqua complexes as the corresponding photoproducts, Table 4.6.

Table 4.6. Mass-to-charge ratios obtained from HR-MS spectra for the photolysis products of Ru^{II} arene complexes **1−6**, **8−10**, and **12−16**.

	Observed peak $[M]^{2+}$	Chemical formula Calc m/z	Found m/z
(1)−(6), **(14)−(16)**	$[(\eta^6\text{-}p\text{-cym})Ru(bpm)(OH_2)]^{2+}$	$C_{18}H_{22}N_4O$ 206.0418	206.0408
(8)	$[(\eta^6\text{-hmb})Ru(bpm)(OH_2)]^{2+}$	$C_{20}H_{26}N_4ORu$ 220.0572	220.0567
(9)	$[(\eta^6\text{-ind})Ru(bpm)(OH_2)]^{2+}$	$C_{17}H_{18}N_4ORu$ 198.0259	198.0254
(10)	$[(\eta^6\text{-}p\text{-cym})Ru(phen)(OH_2)]^{2+}$	$C_{22}H_{24}N_2ORu$ 217.0466	217.0458
(11)	$[(\eta^6\text{-}p\text{-cym})Ru(phendio)\{(CH_3)_2CO\}]^{2+}$	$C_{25}H_{26}N_2O_3Ru$ 503.5608	503.5610
(12)	$[(\eta^6\text{-}p\text{-cym})Ru(bathophen)(OH_2)]^{2+}$	$C_{34}H_{32}N_2ORu$ 293.0779	293.0665
(13)	$[(\eta^6\text{-ind})Ru(bpy)(OH_2)]^{2+}$	$C_{19}H_{20}N_2ORu$ 197.0307	197.0304

4.3.9   Structure–Photoactivity Relationship

4.3.9.1   Dependence on the 4-(substituted)pyridine Derivative

Each of the $[(\eta^6\text{-arene})Ru(N,N')(L)]^{2+}$ complexes **1−6** and **8−16** was found to photoconvert to their corresponding aqua adducts to various extents after a given amount of photoirradiation time. Figure 4.18 shows and Table 4.7 lists the percentage of species detected by ^{1}H NMR after *ca.* 10−12 h of continuous visible light photoirradiation (λ_{irr} = 400−660 nm) at 310 K for complexes **1−6** (all of which incorporate bpm, *p*-cym and 4-(substitued)pyridines); complex **1** is also included for comparison. Within this group, complex $[(\eta^6\text{-}p\text{-cym})Ru(bpm)(4,4'\text{-}$

bpy)]$^{2+}$ (**4**) photoconverts at the slowest rate and to the lesser extent. Complexes **1** and **3** where L = Py and 4-MeOPy, respectively were found to convert to a higher extent.
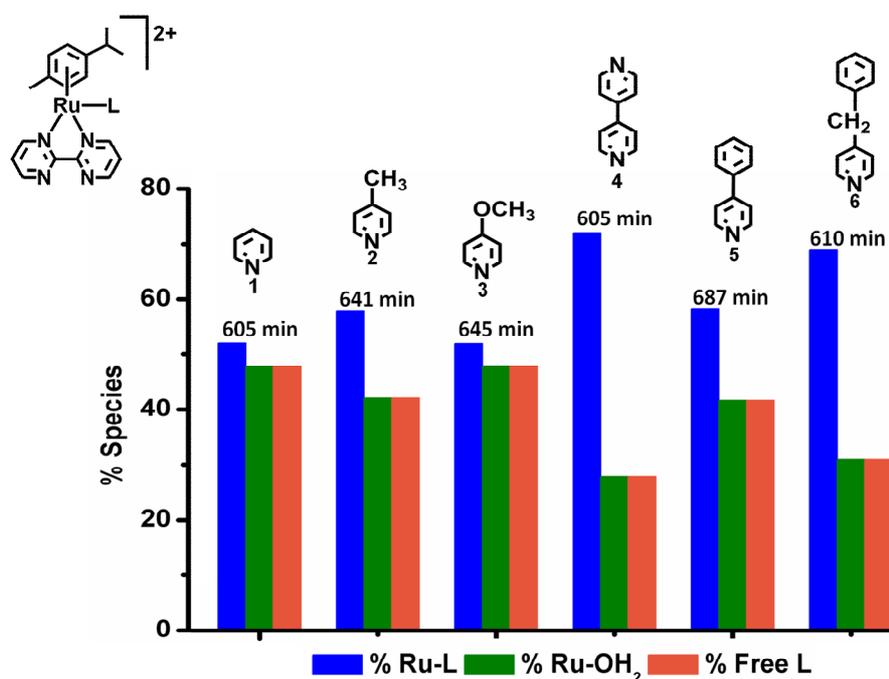

Figure 4.18. Comparison chart showing the percentage of species formed after the photoirradiation of complexes **1−6** in aqueous solution at 310 K with visible light (λ_{irr} = 400−660 nm) followed by ^{1}H NMR. **Blue** = L complex, **green** = aqua adduct; **orange** = free L.

Table 4.7. Percentage of species present after *ca*. 10−12 h of photoirradiation in aqueous solution with visible light (λ_{irr} = 400−660 nm) at 310 K of complexes **1−6** followed by ^{1}H NMR.

Compound	Time (min)	% Species		
		Ru−L	Ru−OH$_2$	Free L
(**1**) [(η^6-*p*-cym)Ru(bpm)(Py)]$^{2+}$	605	52.1	47.9	47.9
(**2**) [(η^6-*p*-cym)Ru(bpm)(4-MePy)]$^{2+}$	641	57.9	42.1	42.1
(**3**) [(η^6-*p*-cym)Ru(bpm)(4-MeOPy)]$^{2+}$	645	52.0	48.0	48.0
(**4**) [(η^6-*p*-cym)Ru(bpm)(4,4'-bpy)]$^{2+}$	605	72.1	27.9	27.9
(**5**) [(η^6-*p*-cym)Ru(bpm)(4-PhPy)]$^{2+}$	687	58.3	41.7	41.7
(**6**) [(η^6-*p*-cym)Ru(bpm)(4-BzPy)]$^{2+}$	610	69.0	31.0	31.0

4.3.9.2   Dependence on the 3-(substituted)pyridine Derivative

When L is 3-acetylpyridine (**14**), nicotinamide (**15**) or 3-acetatepyridine (**16**), the amount of aqua adduct produced is larger after a shorter time of photoirradiation when compared to complex **1**. A full conversion of compound **14** to the aqua adduct before the offset of continuous 10 h of photoirradiation is achieved. Figure 4.19 shows and Table 4.8 lists the percentage of species detected by ^{1}H NMR after *ca.* 10−12 h of continuous visible light photoirradiation at 310 K for complexes **14−16**. It can be seen complex **14** is the most effectively photoactivated complex of the series.
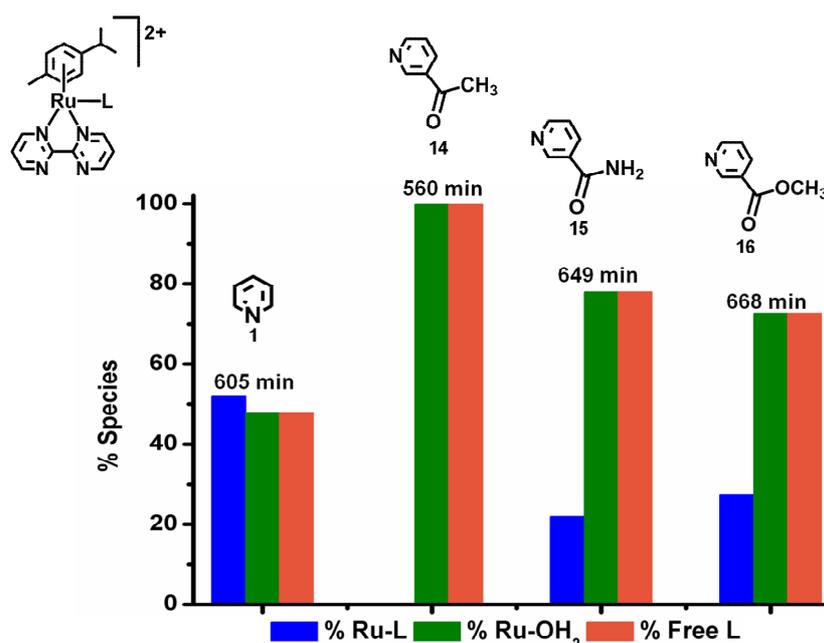
Figure 4.19. Comparison chart showing the percentage of species present after *ca.* 10–12 h of photophotoirradiation in aqueous solution with visible light (λ_{irr} = 400–660 nm) at 310 K for complexes **14**–**16** followed by ^{1}H NMR. **Blue** = L complex, **green** = aqua adduct; **orange** = free L.

Table 4.8. Percentage of species present after *ca.* 10−12 h of photoirradiation in aqueous solution with visible light (λ_{irr} = 400−660 nm) at 310 K for complexes **1**, and **14**−**16** followed by ^{1}H NMR

	Compound	Time (min)	Ru−L	% Species Ru−OH$_2$	Free L
(**1**)	[(η^6-*p*-cym)Ru(bpm)(Py)]$^{2+}$	605	52.1	47.9	47.9
(**14**)	[(η^6-*p*-cym)Ru(bpm)(3-AcPy)]$^{2+}$	560	0	100.0	100.0
(**15**)	[(η^6-*p*-cym)Ru(bpm)(NA)]$^{2+}$	649	22.0	78.0	78.0
(**16**)	[(η^6-*p*-cym)Ru(bpm)(3-AcOPy)]$^{2+}$	668	27.3	72.7	72.7

4.3.9.3 *Dependence on the N,N'-chelating Ligand*

Table 4.9 lists and Figure 4.20 shows the percentage of species detected by ^{1}H NMR after *ca.* 10−12 h of continuous visible light photoirradiation at 310 K for complexes **10** and **12**; complex **1** is also included for comparison. Complex **11** appeared to be unstable in aqueous media and was only considered for photoirradiation in acetone-d_6 solution. It can be seen that after *ca.* 628 and 610 min of photoirradiation, 75% and 60% of complexes **10** and **12**, respectively are still present intact in the solution and *ca.* 25% and 40% of their corresponding aqua adduct has been formed (accompanied by the same percentage of released Py).

Table 4.9. Percentage of species present after *ca.* 10−12 h of photoirradiation in aqueous solution with visible light (λ_{irr} = 400−660 nm) at 310 K for complexes **1**, **11**, and **13** followed by ^{1}H NMR.

	Compound	Time (min)	Ru−L	%Species Ru−OH$_2$/ Ru−Acetone	Free L
(**1**)	[(η^6-*p*-cym)Ru(bpm)(Py)]$^{2+}$	605	52.1	47.9	47.9
(**10**)	[(η^6-*p*-cym)Ru(phen)(Py)]$^{2+}$	628	74.6	25.4	25.4
(**11**)	[(η^6-*p*-cym)Ru(phendio)(Py)]$^{2+}$	402	62.4	37.6[a]	53.9
(**12**)	[(η^6-*p*-cym)Ru(bathophen)(Py)]$^{2+}$	610	60.3	39.7	39.7

[a] The photoirradiation for complex **11** was carried out in acetone-d_6 solution
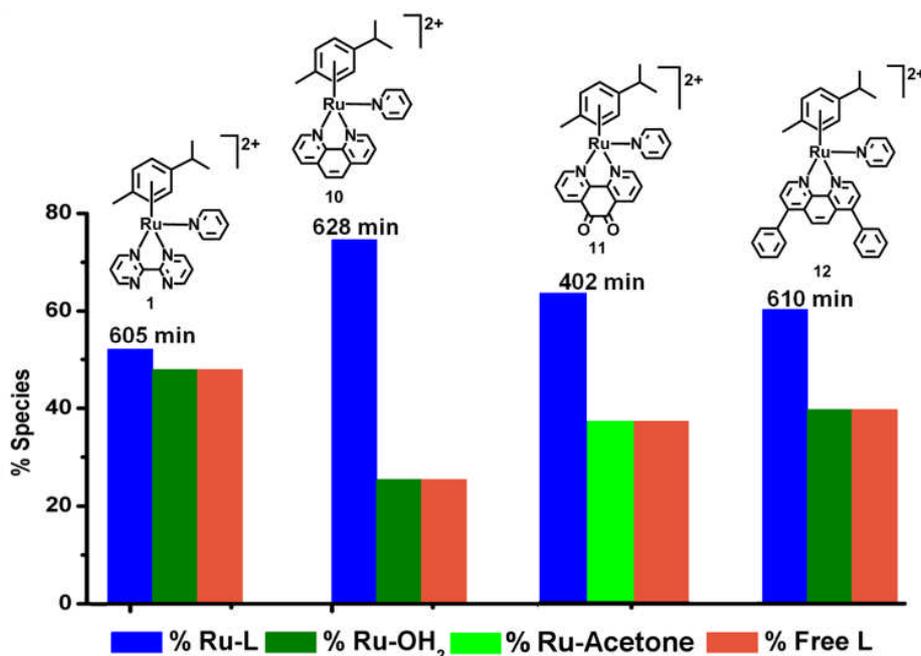
Figure 4.20. Comparison chart showing the percentage of species present after *ca*. 10−12 h of photoirradiation in aqueous solution with visible light (λ_{irr} = 400−660 nm) at 310 K for complexes **1**, **10**, **11** and **12** followed by ^{1}H NMR. **Blue** = L complex, **green** = aqua adduct/**bright green** = acetone adduct; **orange** = free L.

4.3.9.4 *Dependence on the Arene*

Table 4.10 lists and Figure 4.21 shows and the percentage of species detected by ^{1}H NMR after *ca*. 10−12 h of continuous visible light photoirradiation at 310 K for complexes **8** and **9**; complex **1** is also included for comparison. It can be seen that after *ca*. 305 and 425 min of photoirradiation, 100% of complexes **8** and **9** have been photo-converted to their corresponding aqua adduct (accompanied by the same percentage of released Py).

Table 4.10. Percentage of species present after *ca*. 10−12 h of photoirradiation in aqueous solution with visible light (λ_{irr} = 400−660 nm) at 310 K for complexes **1**, **8**, **9**, and **10** followed by ^{1}H NMR.

| Compound	Time (min)	% Species Ru−L	Ru−OH$_2$	Free L
(**1**) [(η^6-*p*-cym)Ru(bpm)(Py)]$^{2+}$	605	52.1	47.9	47.9
(**8**) [(η^6-hmb)Ru(bpm)(Py)]$^{2+}$	305	0	100.0	100.0
(**9**) [(η^6-ind)Ru(bpm)(Py)]$^{2+}$	396	0	100.0	100.0
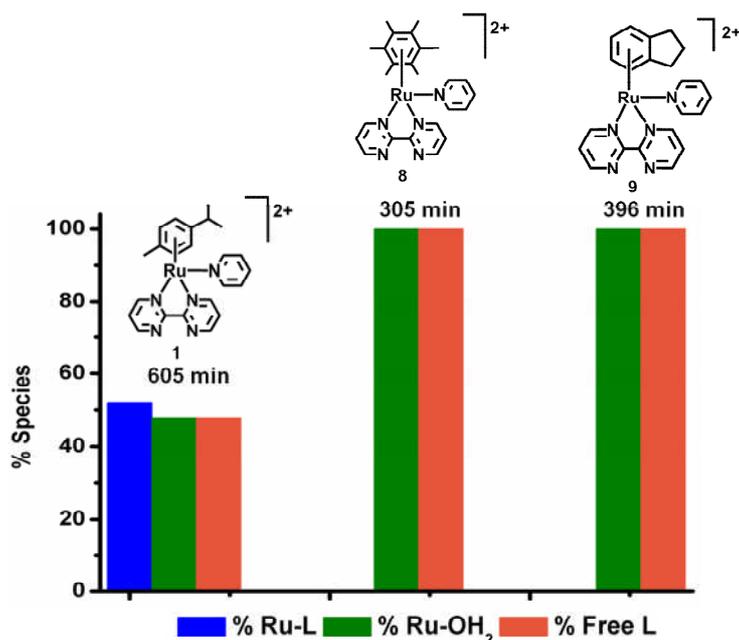
Figure 4.21. Comparison chart showing the percentage of species present after *ca.* 10–12 h of photoirradiation in aqueous solution with visible light (λ_{irr} = 400−660 nm) at 310 K for complexes **1**, **8**, and **9** followed by ^{1}H NMR. **Blue** = L complex, **green** = aqua adduct; **orange** = free L.

Table 4.11 lists and Figure 4.22 shows the percentage of species detected by ^{1}H NMR after *ca.* 10–12 h of continuous visible light photoirradiation at 310 K for complex **13**; complexes **1** and **9** are also included for comparison. It can be seen that after *ca.* 643 min of photoirradiation, 78% of complex **13** is still present intact in the solution.

Table 4.11. Percentage of species present after *ca.* 10−12 h of photoirradiation in aqueous solution with visible light (λ_{irr} = 400−660 nm) at 310 K for complexes **1**, **9**, and **13** by ^{1}H NMR.

|	Compound	Time (min)	% Species Ru−L	Ru−OH$_2$	Free L
(**1**)	[(η^6-*p*-cym)Ru(bpm)(Py)]$^{2+}$	605	52.1	47.9	47.9
(**9**)	[(η^6-ind)Ru(bpm)(Py)]$^{2+}$	425	0	100.0	100.0
(**13**)	[(η^6-ind)Ru(bpy)(Py)]$^{2+}$	643	77.4	22.6	22.6
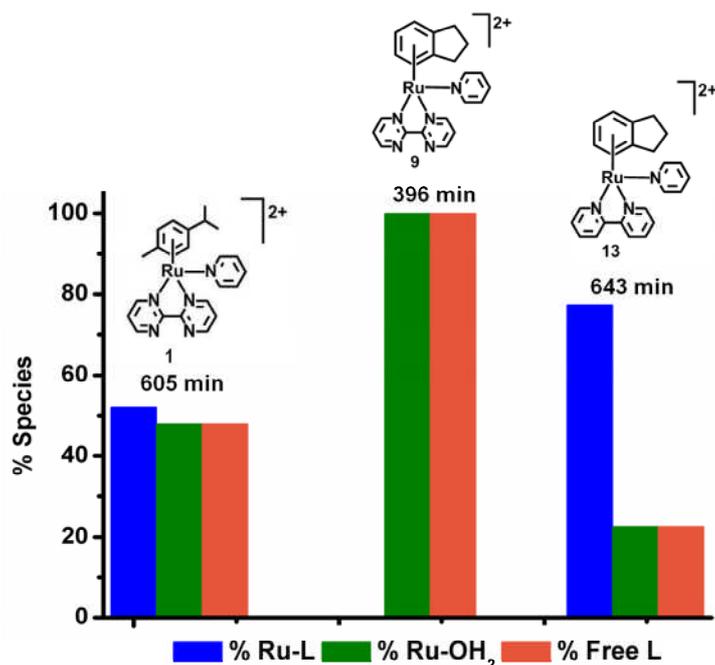
Figure 4.22. Comparison chart showing the percentage of species present after *ca*. 10−12 h of photoirradiation in aqueous solution with visible light (λ_{irr} = 400−660 nm) at 310 K for complexes **1**, **9**, and **13** followed by ^{1}H NMR. **Blue** = L complex, **green = aqua** adduct; **orange** = free L.

4.3.10 Photoirradiation of Ru^{II} Arene Complexes with UVA followed by UV-vis Absorption Spectroscopy

In order to investigate the effect of the wavelength of light on the photolysis process (in addition to visible light), selected Ru^{II} arene complexes (**1**, **8−10**, and **13−16**) were also photoirradiated by UVA (λ_{irr} = 300−400 nm) at 310 K. The photoirradiation was followed by UV-vis absorption spectroscopy and the spectra are shown in Figure 4.23

For the selected Ru^{II} arene complexes (**1**, **8−10**, and **13−16**), photoirradiation with UVA in aqueous solution at 310 K during *ca*. 3−5 h (photoirradiation was terminated when no further changes were observed). Similar spectral changes as when photoirradiated with visible light can be observed, but in half of the photoirradiation time. The electronic absorption spectra exhibit the characteristic shift and change in intensity, with higher and stronger changes being observed around the 200–300 nm

region. The presence of an isosbestic point at *ca*. 310 nm indicates the formation of a single photoproduct. HR-MS spectra were consistent with the formation of the corresponding aqua complexes as the photoproducts.
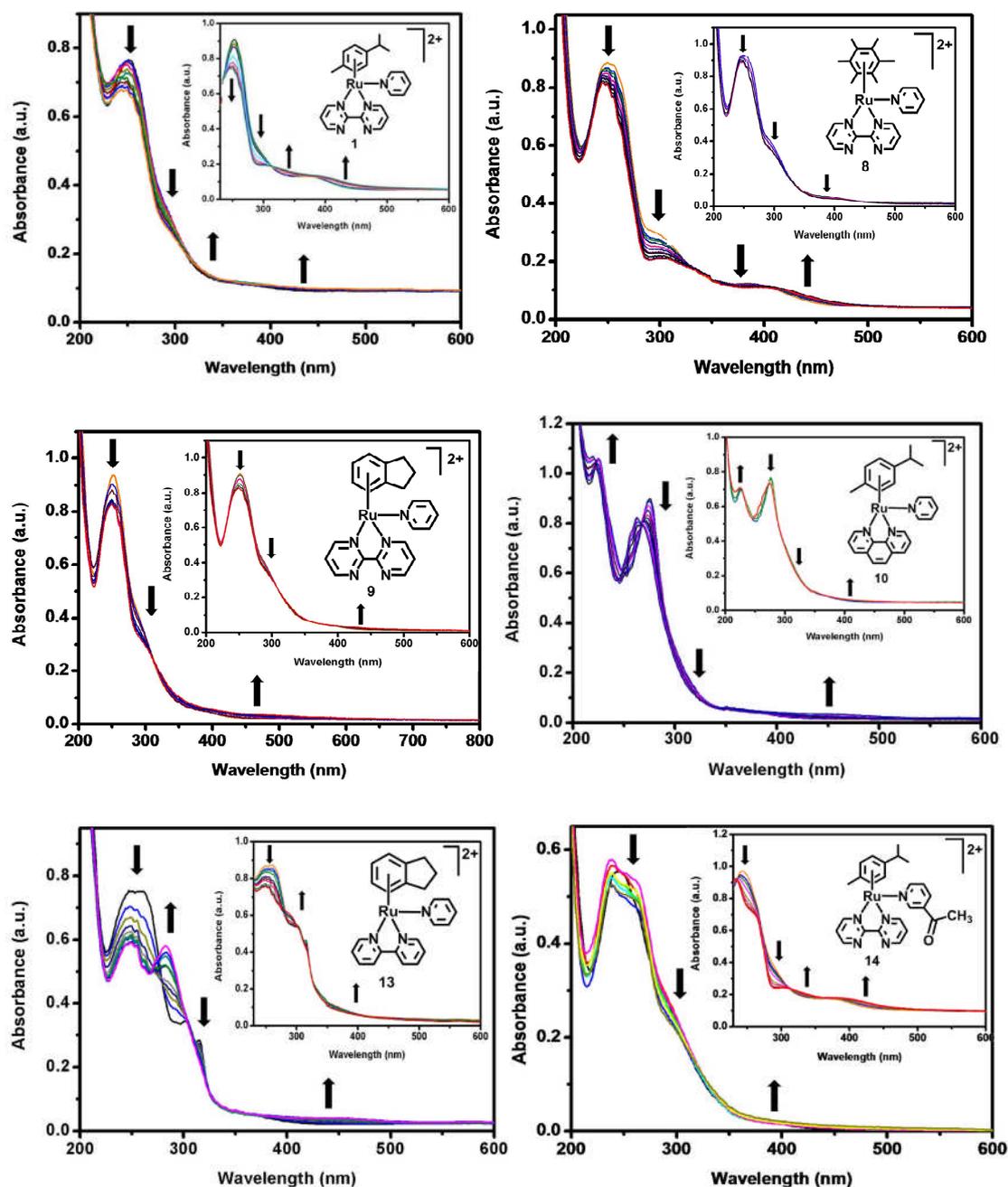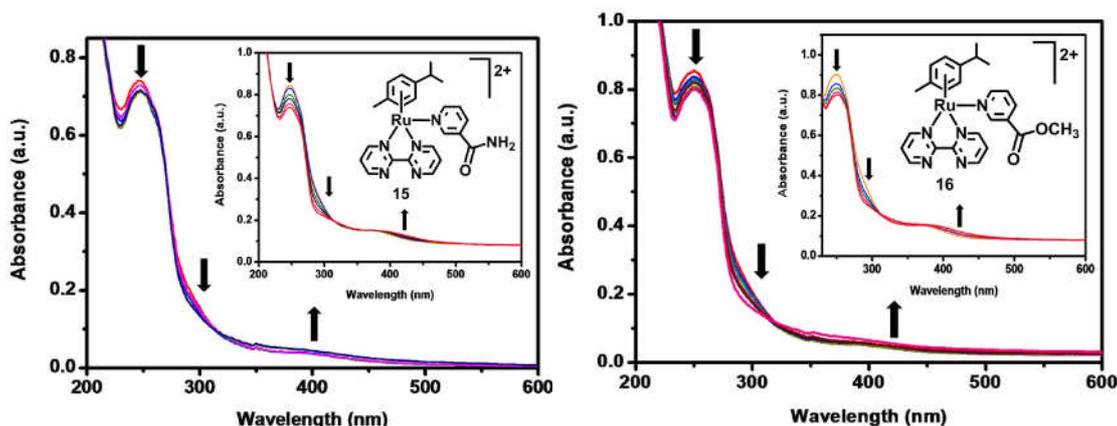
Figure 4.23. UV-vis absorption spectra of the photolysis reaction with UVA photoirradiation (λ_{irr} = 300–400 nm) during *ca*. 3–5 h, of Ru^{II} arene pyridine or pyridine-derivative complexes **1**, **8**–**10**, and **13**–**16** in aqueous solution at 310 K. Inset: UV-vis absorption spectra for the photolysis reaction with visible light (λ_{irr} = 400–660 nm) during *ca*. 10–12 h.

4.3.11 Photoirradiation of Ru^{II} Arene Complexes with UVA followed by ^{1}H NMR Spectroscopy

In order to confirm the nature of the photoproduct produced by the photolysis of the selected Ru^{II} arene complexes (**1**, **8**−**10**, and **13**−**16**) with UVA photoirradiation (λ_{irr} = 300−400 nm), their ^{1}H NMR spectra were recorded at different stages of photoirradiation in D$_2$O at 310 K for *ca*. 3−5 h. In an identical fashion as when using visible light, all the photoirradiated complexes selectively release their pyridine-derivative ligand with the subsequent *in situ* formation of the corresponding aqua complex as the only photoproduct. Spectra for complex **1** are shown in Figure 4.24. When using UVA as the source of photoirradiation, a larger extent of photoconversion of all the selected [(η^6-arene)Ru(N,N')(L)]$^{2+}$ complexes to their corresponding aqua species [(η^6-arene)Ru(N,N')(OH$_2$)]$^{2+}$ can be achieved with less than half the photoirradiation time (i.e. from 425 min to 180 min in the case of **1**). Table 4.12 lists the percentage of species detected by ^{1}H NMR after *ca*. 4−6 h of continuous UVA photoirradiation at 310 K for complexes **1**, **8**−**10**, and **13**−**16**.
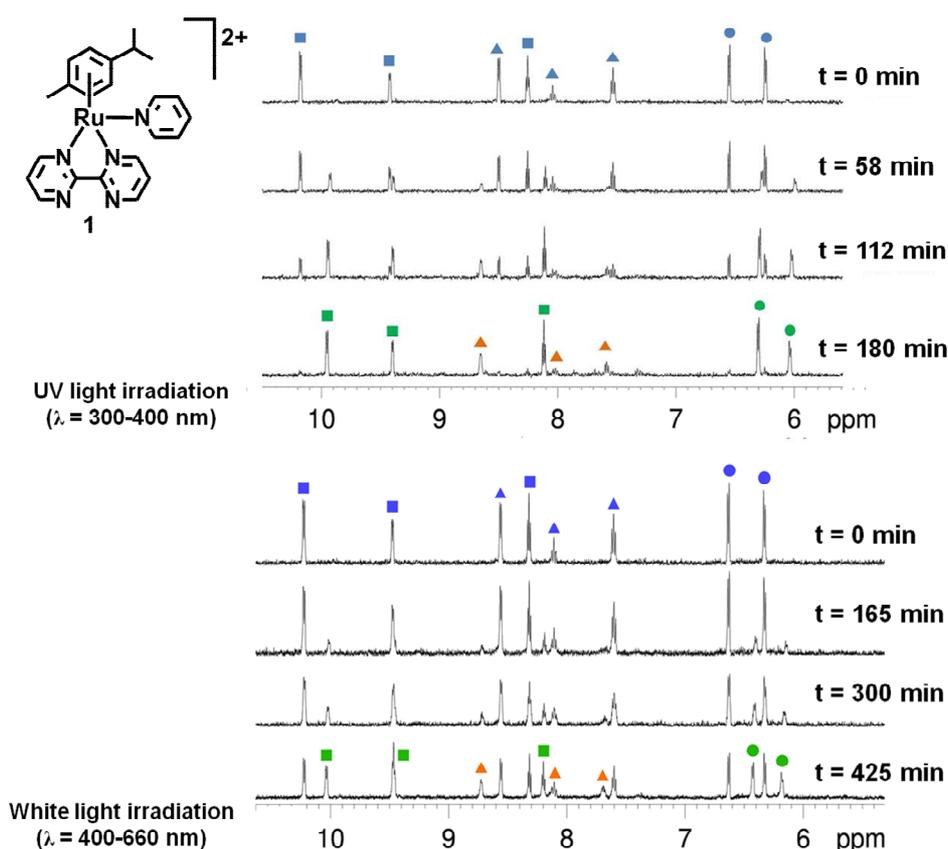
Figure 4.24. ^{1}H NMR spectra of complex **1** during its aqueous photolysis with: (top) UVA photoirradiation (λ_{irr} = 300−400 nm) or (bottom) visible light (λ_{irr} = 400−660 nm) at 310 K. **Blue** = Py complex, **green** = aqua adduct; ■ = bpm, ▲ = Py, ● = p-cym. Free Py is indicated with **orange ▲**.

Table 4.12. Percentage of species present after *ca.* 3−5 h of photoirradiation in aqueous solution with UVA photoirradiation (λ_{irr} = 300−400 nm) at 310 K for complexes **1**, **8**−**10**, and **13**−**16** by ^{1}H NMR.

	Compound	Time (min)	% Species Ru−L	% Species Ru−OH$_2$	% Species Free L
(**1**)	[(η^6-p-cym)Ru(bpm)(Py)]$^{2+}$	180	0	100	100
(**8**)	[(η^6-hmb)Ru(bpm)(Py)]$^{2+}$	138	5.5	94.5	94.5
(**9**)	[(η^6-ind)Ru(bpm)(Py)]$^{2+}$	149	0	100	100
(**10**)	[(η^6-p-cym)Ru(phen)(Py)]$^{2+}$	220	14.1	85.9	85.9
(**13**)	[(η^6-ind)Ru(bpy)(Py)]$^{2+}$	226	46.0	54.0	54.0
(**14**)	[(η^6-p-cym)Ru(bpm)(3-AcPy)]$^{2+}$	189	0	100	100
(**15**)	[(η^6-p-cym)Ru(bpm)(3-NA)]$^{2+}$	204	12.4	87.6	87.6
(**16**)	[(η^6-p-cym)Ru(bpm)(3-AcOPy)]$^{2+}$	210	12.8	87.2	87.2

4.3.12 Photocontrolled Nucleobase Binding

In order to investigate the ability of the $[(\eta^6\text{-arene})Ru(N,N')(L)][PF_6]_2$ complexes to bind to DNA bases, a photoirradiation experiment with visible light ($\lambda_{irr} = 400–660$ nm) at 310 K in the presence of 9-ethylguanine (9-EtG) was performed for complexes **1–6**, **8–10**, and **12–16**. As shown in Figure 4.25 (selected example for complex **1**), photoirradiation of the complexes with visible light at 310 K in D_2O in the presence of 1 mol equiv of 9-EtG resulted in the initial formation of the corresponding aqua adduct $[(\eta^6\text{-arene})Ru(N,N')(OH_2)]^{2+}$ followed by coordination of the nucleobase to the Ru centre to form $[(\eta^6\text{-arene})Ru(N,N')(9\text{-EtG-}N7)]^{2+}$. The binding to 9-EtG is not reversible upon the termination of photoirradiation. Figure 4.26 shows the 2D ^1H-^1H NOESY spectra which was used to assign the proton resonances and to confirm the structure of $[(\eta^6\text{-}p\text{-cym})Ru(bpm)(9\text{-EtG-}N7)]^{2+}$ (**1-EtG**). An NOE cross-peak between H(8) of 9-EtG and the 2,2'-CH of bpm was observed, suggesting coordination of 9-EtG through *N7* as previously observed.[16] The ^1H NMR signals for the 9-EtG adduct of complex **1** have the same chemical shift as the isolated 9-EtG complex **15** described in Chapter 3, as they are the same species. For the rest of the Ru^{II} arene complexes which also selectively photorelease the pyridine or the pyridine-derivative ligands, a similar behaviour was observed when the photoirradiation was carried out in the presence of 9-EtG. The mass-to-charge ratios and isotopic models obtained from HR-MS spectra are consistent with the formation of the corresponding guanine adducts, Table 4.13. A similar photoirradiation experiment was performed in the presence solely of 9-EtA (9-ethyladenine), resulting in that no coordination to the Ru centre of this nucleobase was observed.
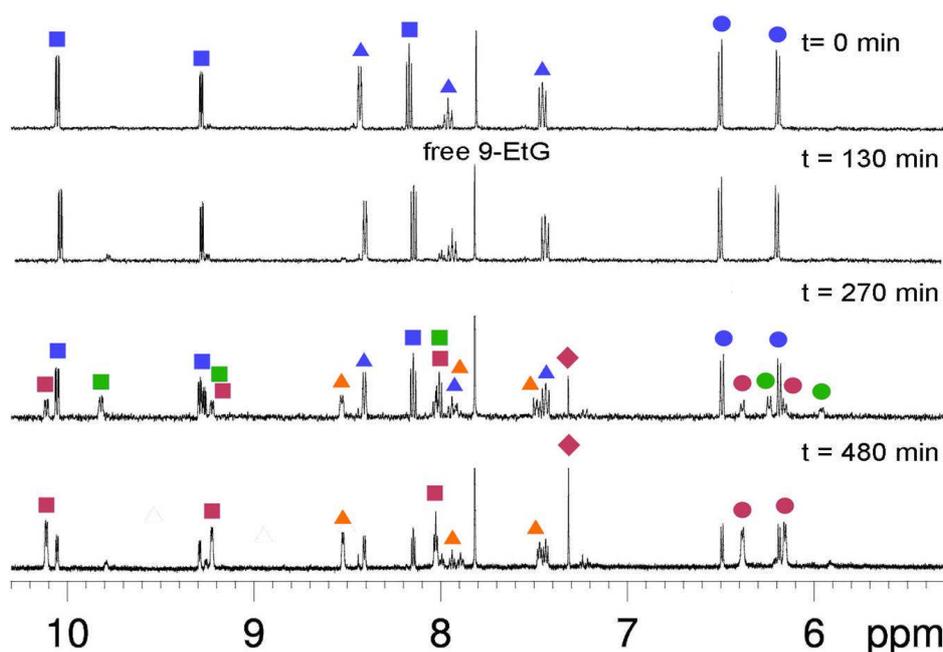
Figure 4.25. ^{1}H NMR spectra during the aqueous photolysis (λ_{irr} = 400−660 nm) of **1** in the presence of 9-EtG. **Blue** = [(η^6-*p*-cym)Ru(bpm)(Py)]$^{2+}$, **green** = [(η^6-*p*-cym)Ru(bpm)(OH$_2$)]$^{2+}$, **magenta** = [(η^6-*p*-cym)Ru(bpm)(9-EtG-*N7*)]$^{2+}$; ■ = bpm, ▲ = Py, ● = *p*-cym. Free Py is indicated with **orange** ▲ and coordinated 9-EtG with **magenta** ♦.
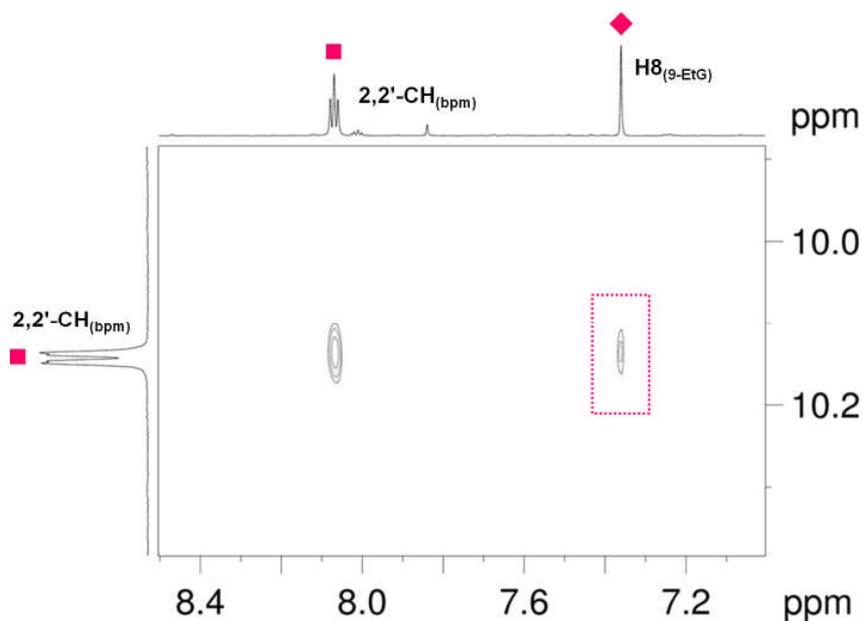
Figure 4.26. ^{1}H-^{1}H NOESY NMR spectrum of [(η^6-*p*-cym)Ru(bpm)(9-EtG-*N7*)]$^{2+}$ (15) in D$_2$O (aromatic region only). Magenta = [(η^6-*p*-cym)Ru(bpm)(9-EtG-*N7*)]$^{2+}$; ■ = bpm protons, ♦ = H8 of coordinated 9-EtG.

Table 4.13. Mass-to-charge ratios obtained from HR-MS spectra for the photolysis products of Ru^{II} arene complexes **1**−**6**, **8**−**10**, and **12**−**16**.in the presence of 9-EtG.

	Observed peak [M]$^{2+}$	Chemical formula Calc *m/z*	Found *m/z*
(**1**)−(**7**), (**14**)−(**17**)	[(η^6-*p*-cym)Ru(bpm)(9-EtG-*N7*)]$^{2+}$	C$_{25}$H$_{29}$N$_9$ORu 286.5767	286.5755
(**8**)	[(η^6-hmb)Ru(bpm)(9-EtG-*N7*)]$^{2+}$	C$_{27}$H$_{33}$N$_9$ORu 300.5924	300.5916
(**9**)	[(η^6-ind)Ru(bpm)(9-EtG-*N7*)]	C$_{24}$H$_{25}$N$_9$ORu 278.5610	278.5601
(**10**)	[(η^6-*p*-cym)Ru(phen)(9-EtG-*N7*)]$^{2+}$	C$_{29}$H$_{31}$N$_7$ORu 297.5815	297.5820
(**13**)	[(η^6-*p*-cym)Ru(bathophen)(9-EtG-*N7*)]$^{2+}$	C$_{41}$H$_{39}$N$_7$ORu 373.6130	373.6127

4.3.13 Photocontrolled CT-DNA Interactions in Cell-Free Media

In order to explore the possibility and nature of the interactions of this new family of photoactivatable compounds with DNA, three complexes (**1**, **4** and **11**) were selected for further studies with CT-DNA in cell-free media.

4.3.13.1 DNA Binding Kinetics

Reaction mixtures of DNA and complexes [(η^6-*p*-cym)Ru(bpm)(Py)]$^{2+}$ (**1**), [(η^6-*p*-cym)Ru(bpm)(4,4'-bpy)]$^{2+}$ (**4**) and [(η^6-*p*-cym)Ru(phen)(Py)]$^{2+}$ (**10**) were prepared in three ways: (A) in the dark (henceforth referred to as *non-irradiated*), (B) following the addition to DNA of (beforehand) irradiated **1**, **4** and **10** (*pre-irradiated*), or (C) by addition of **1**, **4** and **10** to DNA followed by photoirradiation of the resulting mixture (*irradiated*). The samples were photoirradiated with visible light (λ_{irr} = 400−660 nm) at selected photoirradiation times. The binding kinetics experiments with CT-DNA where then performed as described in Chapter 2. The results, summarised in Table 4.14, indicate that the *non-irradiated* forms of **1**, **4**, and **10** are not bound to DNA significantly in 10 mM NaClO$_4$ (less than 5%

for **1** and **10** and *ca.* 20% of **4** after 48 h). *Pre-irradiated* forms of complexes **1**, **4**,

and **10** reacted with DNA in *ca.* 40%, 54%, and 58%, respectively after 24 h; and

irradiated forms of **1**, **4** and **10** reacted in *ca.* 41%, 50%, and 54%, respectively

after 24 h. It can be seen that *pre-irradiated* Ru^{II} arene complexes bind faster but

to the same extent as the *irradiated* DNA mixtures, Figure 4.27.

Table 4.14. Percentage of binding of *non-irradiated*, *pre-irradiated*, or *irradiated* forms of complexes **1**, **4** and **10** to CT-DNA in 1.0 mM NaClO$_4$ as determined by FAAS.

Time (hours)	*Non-irradiated*[a]			*Pre-irradiated*[b]			*Irradiated*[c]		
	1	**4**	**10**	**1**	**4**	**10**	**1**	**4**	**10**
24	3.1	18.7	3.7	40.2	54.5	57.6	41.1	50.3	54.0
48	1.0	17.4	7.9	41.5	62.2	49.7	ND	ND	ND

[a] Incubations with DNA were at 310 K. The concentration of DNA was 50 μg/mL. Data are the average of two independent experiments.
[b] Photoirradiation was carried out in absence of DNA for *24* h, followed by a further incubation with DNA in the dark.
[c] Photoirradiation of was carried out in presence of DNA for *24* h.
[ND] Not determined.
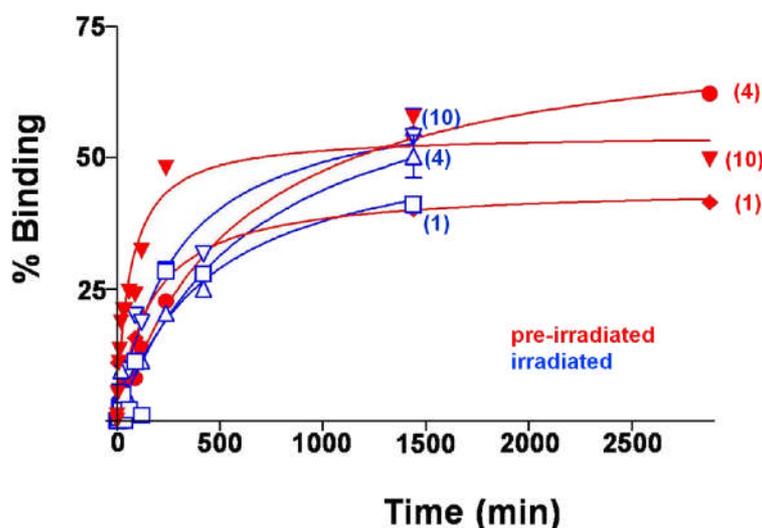
**Figure 4.27.** Percentage of binding to CT-DNA by *pre-irradiated* (red) and *irradiated* (blue) forms of complexes [(η^6-*p*-cym)Ru(bpm)(Py)][PF$_6$]$_2$ (**1**), [(η^6-*p*-cym)Ru(bpm)(4,4'-bpy)][PF$_6$]$_2$ (**4**) and [(η^6-*p*-cym)Ru(phen)(Py)][PF$_6$]$_2$ (**10**) as a function of time.

4.3.13.2 DNA Transcription by RNA Polymerase in Vitro

Cutting of pSP73KB DNA by *Nde*I and *Hpa*I restriction endonucleases yielded a 212-bp fragment. This fragment contained the T7 RNA polymerase promotor. The Ru^{II} arene complexes were tested as their *non-irradiated*, *pre-irradiated* and *irradiated* forms. All samples were precipitated and redissolved after incubation with DNA (7.8×10^{-5} M, 0.5 μg/20 μL) to remove the unbound Ru^{II} arene complexes; r_b of complexes **1**, **4** and **10** was determined using EAS and FAAS. The autoradiogram of the inhibition of RNA synthesis by T7 RNA polymerase on pSP73KB DNA containing adducts of the Ru^{II} arene complexes or cisplatin is shown in Figure 4.28. The bands corresponding to the transcription of DNA modified by the *non-irradiated* forms of complexes **1**, **4**, and **10** are rather faint in intensity indicating that RNA synthesis on the modified fragment do not stop the polymerase, except for complex $[(\eta^6\text{-}p\text{-cym})\text{Ru}(\text{bpm})(4,4'\text{-bpy})][\text{PF}_6]_2$ (**4**), which was found to bind to DNA without photoirradiation (*ca.* 20%). The *pre-irradiated*, and *irradiated* forms of **1**, **4**, and **10** yielded fragments of newly synthesized RNA of defined sizes, which indicates that RNA synthesis on these templates was prematurely terminated. The major stop sites produced occurred at similar positions in the gel and were exclusively at guanine residues, Figure 4.29 and are identical for the three Ru^{II} arene complexes. The total intensity of the bands on the autoradiogram corresponding to transcripts of single-ruthenated DNA fragments (modified to the same level (r_b)) differed. The intensities of those corresponding to the transcription of DNA modified by the *pre-irradiated* forms of complexes **1**, **4** and **10** are slightly stronger than those of those corresponding to the transcription of DNA modified by the *irradiated* forms.

The profiles are similar to that obtained for DNA treated with the anticancer drug cisplatin and also to those reported previously for the Ru^{II} arene compounds, such as $[(\eta^6\text{-arene})Ru(en)Cl]^+$.[17]
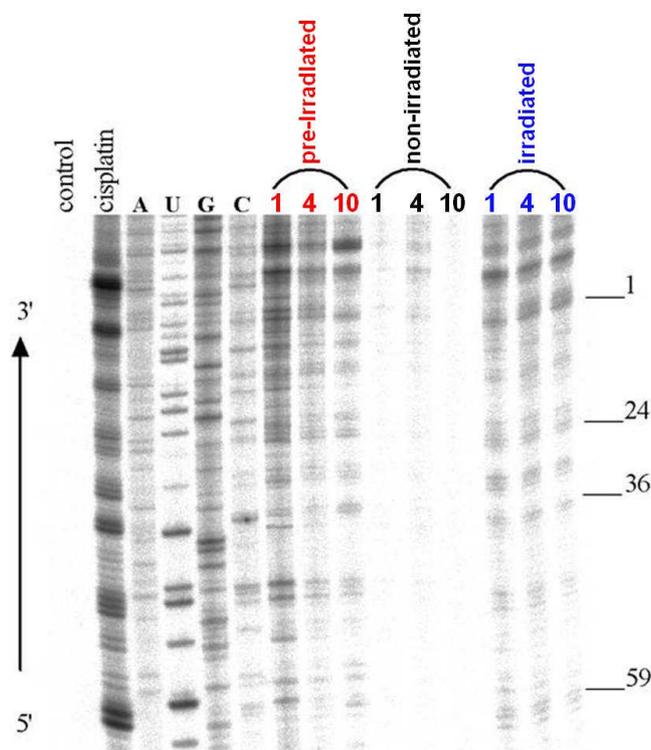

Figure 4.28. Autoradiogram of 6% polyacrylamide/8 M urea sequencing gel showing inhibition of RNA synthesis by T7 RNA polymerase on pSP73KB DNA containing adducts of Ru^{II} arene complexes or cisplatin. Lanes: chain terminated marker RNAs, cisplatin, at $r_b = 0.02$; A, U, G and C, the template modified by Ru^{II} arene compounds.
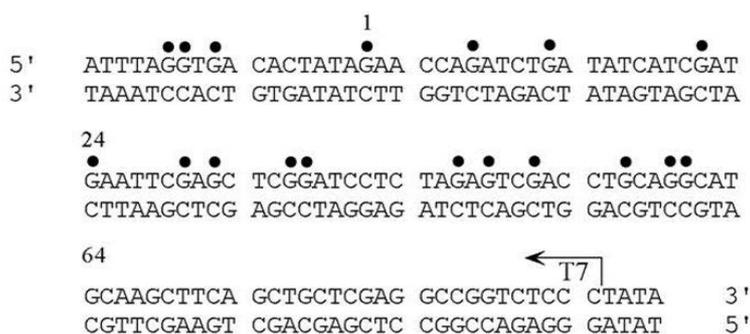
Figure 4.29. Schematic diagram showing the portion of the sequence used to monitor inhibition of RNA synthesis by Ru^{II} arene complexes. The arrows indicate the start of the T7 RNA polymerase, which used as template the upper strand of pSP73KB DNA, respectively. The numbers correspond to the nucleotide numbering in the sequence map of pSP73KB plasmid. (●) Indicates major stop sites for DNA modified by ruthenation.

4.3.13.3 Unwinding of Supercoiled pUC19 Plasmid DNA

The plasmid was incubated with the Ru^{II} arene complexes **1**, **4** and **10** in 10 mM NaClO$_4$, at pH ≈ 6 for 24 h at 310 K in their *pre-irradiated* and *irradiated* forms. All samples were precipitated and redissolved after incubation with DNA to remove free, unbound Ru^{II} species. The r_b(c) value was determined by EAS and FAAS. The native agarose gel resulting from DNA modified by the Ru^{II} arene complexes **1**, **4**, and **10** in their *pre-irradiated* forms are shown in Figure 4.30 and the corresponding *irradiated* forms is shown in Figure 4.31. The DNA unwinding angle produced by the adducts formed by *pre-irradiated* and *irradiated* forms of the Ru^{II} arene complexes **1** and **4**, and **10** was determined to be 6.6±1.7°, 5.2±2.2°, and 6.1±2.2°, respectively using this approach. The commigration point of the modified supercoiled and nicked DNA (r_b(c)) was reached at r_b = 0.16, 0.19 and 0.17 for complexes **1**, **4**, and **10** respectively, Table 4.15. From the autoradiogram it can also be noticed that an increasing amount of nicked (OC) form occurred during photoirradiation of the Ru^{II} arene complexes in the presence of DNA (*irradiated* form), r_b(c) for **1** and **10** is not changed whereas DNA is almost completely nicked with increasing ruthenation in the case of **4**.

Table 4.15. Unwinding of supercoiled pUC19 DNA by Ru^{II} arene complexes **1**, **4** and **11**.

Compound		r_b(c)	Unwinding Angle (°)
(1)	[(η^6-*p*-cym)Ru(bpm)(Py)][PF$_6$]$_2$	0.16±0.03	6.6±1.7
(4)	[(η^6-*p*-cym)Ru(bpm)(4,4'-bpy)][PF$_6$]$_2$	0.19±0.04	5.2±2.2
(10)	[(η^6-*p*-cym)Ru(phen)(Py)][PF$_6$]$_2$	0.17±0.04	6.1±2.0
Cisplatin		0.08	13
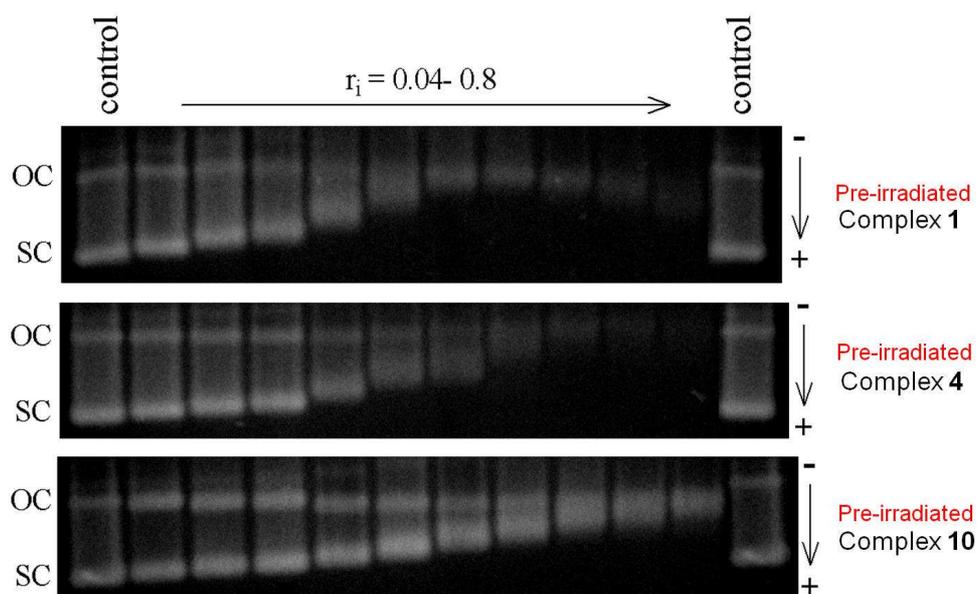
Figure 4.30. The unwinding of supercoiled pUC19 plasmid DNA (1.0×10^{-4} M, 0.5 µg/15 µL) by complexes **1**, **4**, and **10** in their *pre-irradiated* forms. Left and right lanes are controls (unmodified DNA); top bands correspond to the form of nicked plasmid (OC) and the bottom bands to the closed, negatively supercoiled plasmid (SC). r_i values increase on going from left to right lanes (molar ratio of free Ru complex to nucleotide phosphates at the onset of incubation with DNA).
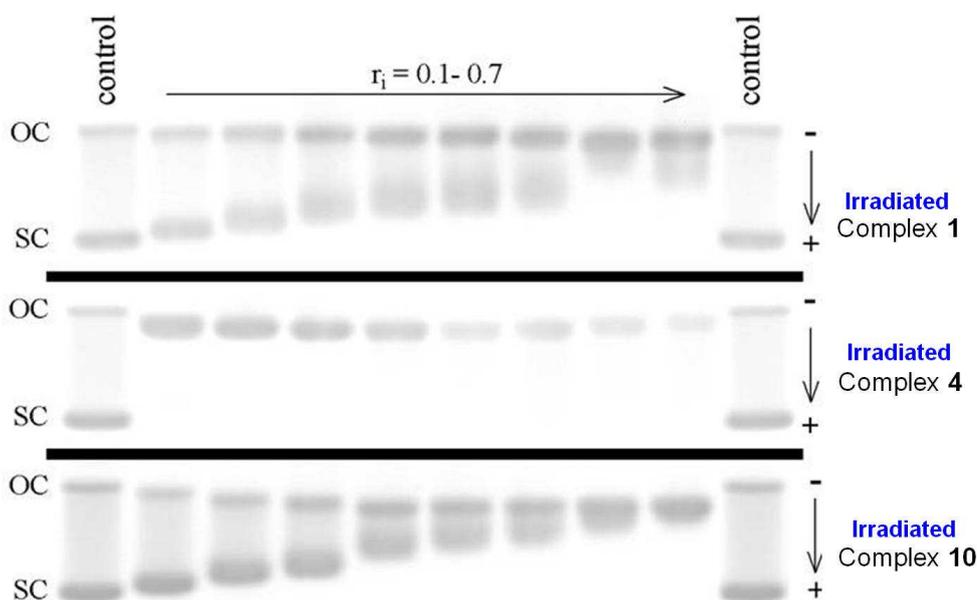

Figure 4.31. The unwinding of supercoiled pUC19 plasmid DNA (1.0×10^{-4} M, 0.5 µg/15 µL) by complexes **1**, **4**, and **10** in their *irradiated* forms. Left and right lanes are controls (unmodified DNA); r_i values increase on going from left to right lanes; top bands correspond to the form of nicked plasmid (OC) and the bottom bands to the closed, negatively supercoiled plasmid (SC).

4.3.13.4 DNA Melting Temperature

CT-DNA was modified by Ru^{II} arene complexes **1**, **4** and **10** in their *irradiated* forms at various r_b values in 10 mM NaClO$_4$ at 310 K for 24 h. The samples were then dialysed and the r_b was determined by EAS and FAAS. The salt concentration was then further adjusted by the addition of NaClO$_4$ to values in the range of 0.01−0.22 M. The DNA melting temperature (t_m) is dependent both on the amount of bound Ru and on the salt concentration. The observed trend for the three complexes **1**, **4** and **10** is a constant oscillation of the t_m values, indicating that the DNA adducts formed are unstable at higher ionic strengths and temperatures, Table A.4.48. The t_m changes are relatively small and a slight stabilisation effect is observed at low ionic strengths. At the highest ionic strength, a tendency for a slight destabilisation was observed.

4.3.13.5 Circular Dichroism (CD)

CD spectra of DNA modified by complexes **1**, **4** and **10** in their *irradiated* forms (at 298 K in 10 mM NaClO$_4$) were also recorded at r_b values in the range of 0.010−0.125. These complexes have no intrinsic CD signals as they are achiral and any CD signal above 300 nm is therefore attributed to the interaction of the complexes with DNA. Below 300 nm any change in the normally found spectrum for DNA in canonical B-conformation (B-DNA) is due either to the DNA induced CD (ICD) of the metal complex or the metal-complex-induced perturbation of the DNA spectrum. As can be seen from Figure 4.32, the conservative CD spectrum transforms at wavelengths below 300 nm upon interaction of the three complexes with CT-DNA. There is a significant increase for complexes **1** and **4** and a decrease for complex **10** in the intensity of the positive band around 280 nm. The signature of complex **4** coordinated

to CT-DNA is a strong positive ICD centered at around 400 nm. The signature of complexes **1** and **10** bound to CT-DNA includes no such ICD. The changes in CD spectra of CT-DNA modified by Ru^{II} arene complexes **1** and **10** complexes (at different r_b values) were monitored at 246 and 278 nm; the changes exerted by complex **4** were also monitored at 400 nm, Figure A.4.48.
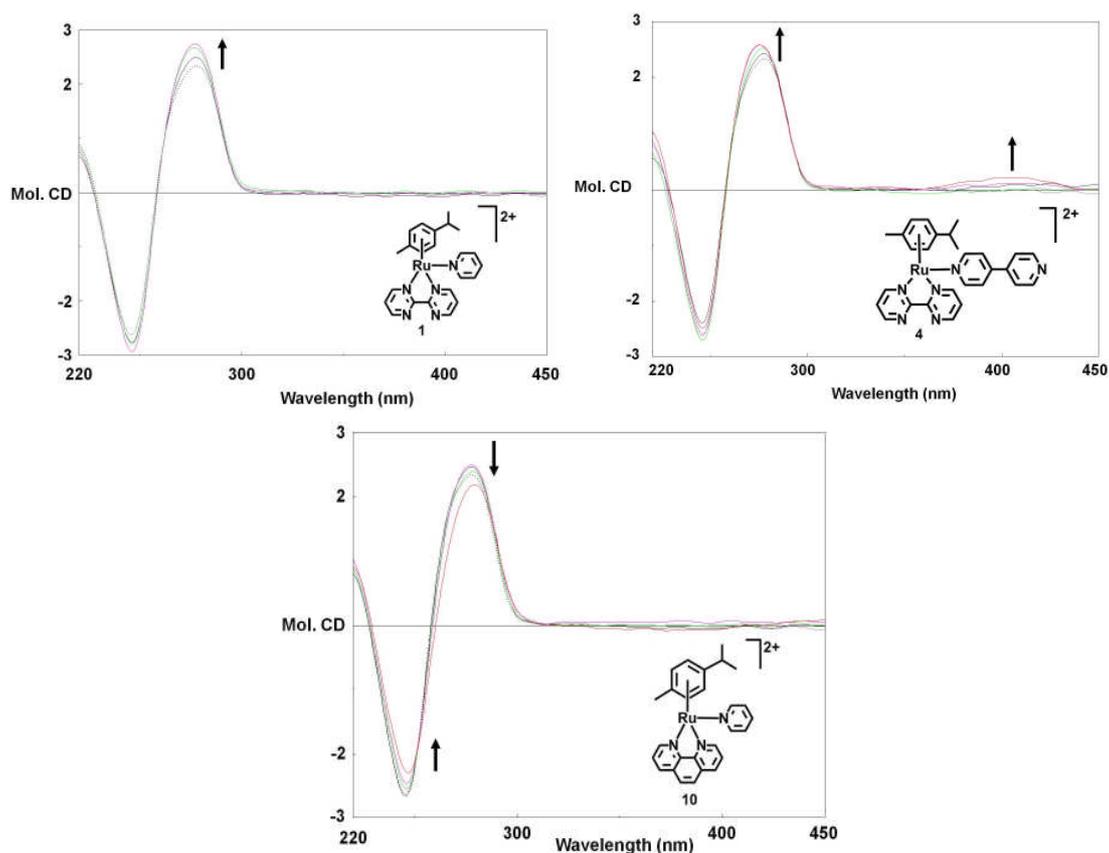

Figure 4.32. Circular dichroism (CD) spectra of CT-DNA (1×10^{-4} M) modified by Ru^{II} arene complexes **1**, **4** and **10** in their *irradiated* forms; the medium was 10 mM NaClO$_4$, pH $\approx$ 6.

4.3.13.6 Flow Linear Dichroism (LD)

Binding of all three Ru^{II} arene complexes to CT-DNA was also monitored by linear dichroism spectroscopy, Figure 4.33. It is well established that the magnitude of the LD signal measured within the DNA absorption band (i.e. at the 258 nm maximum) is a function of its persistence length. It is known that changes in flexibilities, or the

formation of rigid bends or kinks induced by strongly bound compounds, can manifest themselves as decreases in the abilities of the modified DNA molecules to align themselves in the hydrodynamic flow gradient of the LD cell. The magnitudes of the LD signals at 258 nm decrease as a function of r_b for the *irradiated* forms of Ru^{II} arene complexes **1**, **4** and **10**. The changes in the LD spectrum of CT-DNA modified by complexes **1**, **4**, and **10** (at different r_b values) were monitored at 258.5 nm, Figure A.4.49. The largest changes are induced by complex **4.** Complexes **1** and **10** behave similarly and within the same range.
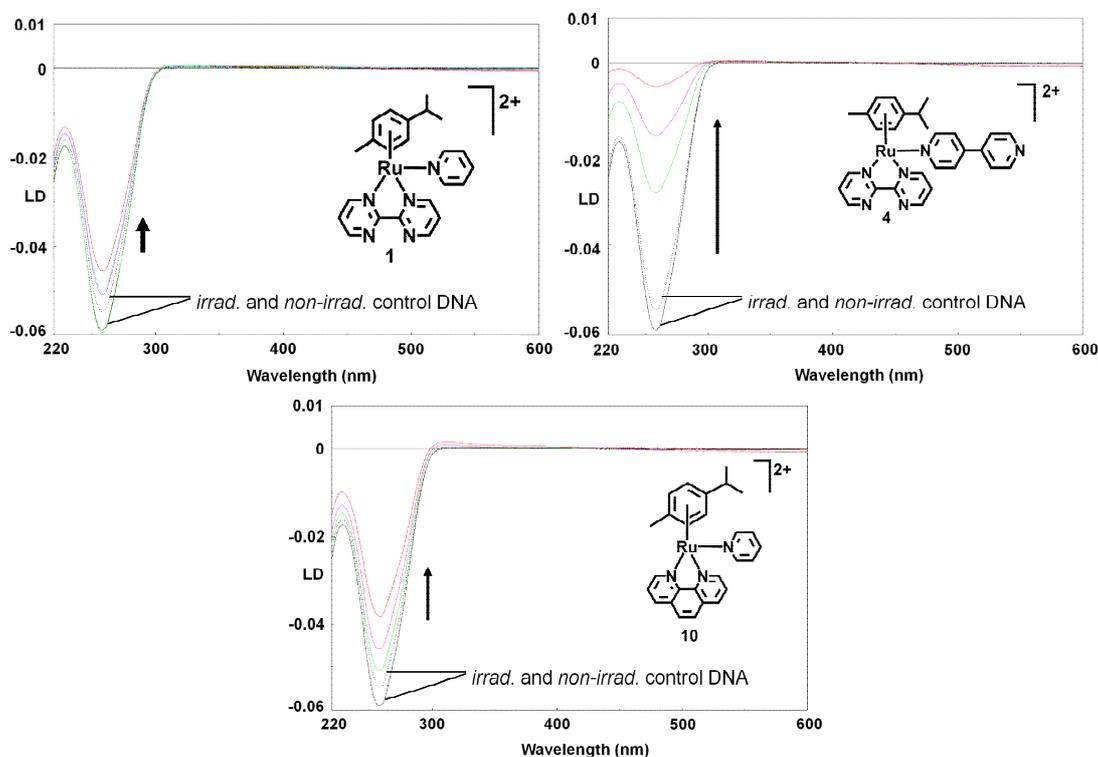

Figure 4.33. Linear dichroism spectra of CT-DNA modified by Ru^{II} arene complexes **1**, **4**, and **10**. LD spectra were recorded for DNA in 10 mM NaClO$_4$. The concentration of DNA was 2.3×10^{-4} M.

4.3.13.7 Ethidium Bromide (EtBr) Fluorescence

The ability of complexes to displace the DNA intercalator EtBr from CT-DNA, was probed by monitoring the relative fluorescence of the EtBr-DNA adduct after treating

the DNA with varying concentrations of the Ru^{II} arene complexes **1**, **4** and **10** in their

irradiated forms. The 24-hour *irradiated* DNA mixtures were dialysed before the

fluorescence measurement and r_b was determined by EAS and FAAS. Figure 4.34

shows a plot of relative fluorescence *versus* r_b for the three Ru^{II} arene complexes

along with cisplatin, transplatin and monofunctional dienPt. All three adducts of the

Ru^{II} arene complexes decreased the EtBr fluorescence.
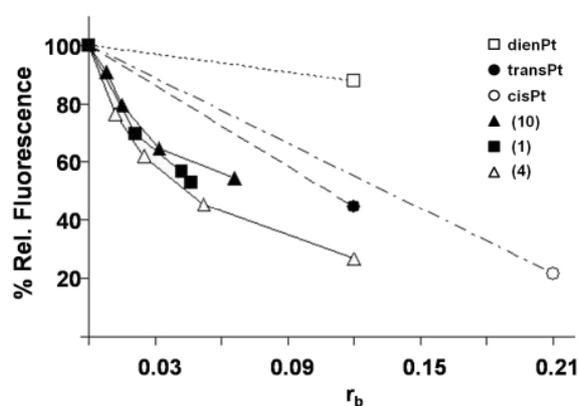
Figure 4.34. EtBr fluorescence *versus* r_b for DNA modified by cisplatin ($\bigcirc$), dienPt ($\square$), transPt ($\bullet$), and Ru^{II} arene complexes **1** ($\blacksquare$), complex **4** ($\triangle$), and complex **10** ($\blacktriangle$) in their *irradiated* forms in 10 mM $NaClO_4$ at 310 K (24h photoirradiation followed by 24 h incubation).

4.3.14 Cancer Cell Growth Inhibition (IC$_{50}$ Values)

The IC$_{50}$ values in ambient light conditions (i.e. no irradiation provided) for the Ru^{II} arene

complexes (**1−6** and **8−16**) against the A2780 human ovarian cancer cell line are

given in Table 4.16. In general, the complexes were moderately active against the

A2780 human ovarian cancer cell line in ambient light conditions and their potencies

vary in several orders of magnitude. The most potent complex [(η^6-p-

cym)Ru(bathophen)(Py)][PF$_6$]$_2$ (**12**) had an IC$_{50}$ value under these conditions of 7.4

µM, comparable to that of cisplatin (2.2 µM) under the same conditions. As a general

trend, the most active complexes against the A2780 human ovarian cancer cell line in

ambient light conditions contain *p*-cym as the arene and bpm as the N,N' chelating ligand. A change in the arene and chelating ligand to ind or hmb and phen in complexes **8**, **9** and **10**, respectively was found to decrease the activity. Within the cytotoxic series of compounds, complexes that displayed activity have either Py or 3-(substituted)Py as the L group, being the Py-bearing complexes the most active.

Table 4.16. IC$_{50}$ values for Ru^{II} arene complexes against the A2780 human ovarian cancer cell line in ambient light conditions.

	Compound	IC$_{50}$ μM
(**1**)	[(η^6-*p*-cym)Ru(bpm)(Py)][PF$_6$]$_2$	9.0
(**3**)	[(η^6-*p*-cym)Ru(bpm)(4-MeOPy)][PF$_6$]$_2$	70.0
(**4**)	[(η^6-*p*-cym)Ru(bpm)(4,4'-bpy)][PF$_6$]$_2$	61.1
(**8**)	[(η^6-hmb)Ru(bpm)(Py)][PF$_6$]$_2$	23.2
(**9**)	[(η^6-ind)Ru(bpm)(Py)][PF$_6$]$_2$	92.0
(**10**)	[(η^6-*p*-cym)Ru(phen)(Py)][PF$_6$]$_2$	25.9
(**12**)	[(η^6-*p*-cym)Ru(bathophen)(Py)][PF$_6$]$_2$	7.4
(**15**)	[(η^6-*p*-cym)Ru(bpm)(NA)][PF$_6$]$_2$	19.0
(**16**)	[(η^6-*p*-cym)Ru(bpm)(3-AcOPy)][PF$_6$]$_2$	9.2
	Cisplatin	1.5

[a] Complexes **2**, **5**, **6**, **13** and **14** had IC$_{50}$ values larger than 100 μM against the cell line tested (*vide supra*).

4.3.15 Photocytotoxicity: Cancer Cell Growth Inhibition upon UVA Photoirradiation

The cytotoxic effects of four Ru^{II} arene complexes, compounds **1**, **2**, **3**, and **4**, with and without UVA photoirradiation were tested. Based on the primary screening protocol selected for the assay, it was observed that they have reduced cytotoxic potency under the tested concentrations and were not chosen for further IC$_{50}$ determination. However, interesting observations can be made from the experiment. Results of the primary screening with UV photoirradiation and in dark conditions are shown in Figure 4.35. The T/C$_{corr}$ values determined highly depend on the cell line used. A427 (human lung carcinoma) and 5637 (human urinary bladder carcinoma)

appear to be more sensitive towards the complexes compared to DAN-g (human pancreas carcinoma). Both in the dark and in light conditions the most cytotoxic compound towards A427 and DAN-g human cancer cell lines is compound **3** whereas complex **2** is towards 5637. Overall, there was no statistical significant difference between the photoirradiated samples and those which were not photoirradiated due to the insufficient activation of the compounds with UVA photoirradiation (as shown by the photoirradiation experiments described previously in this Chapter) and/or to the photodecomposition products having similar cytotoxic effects.
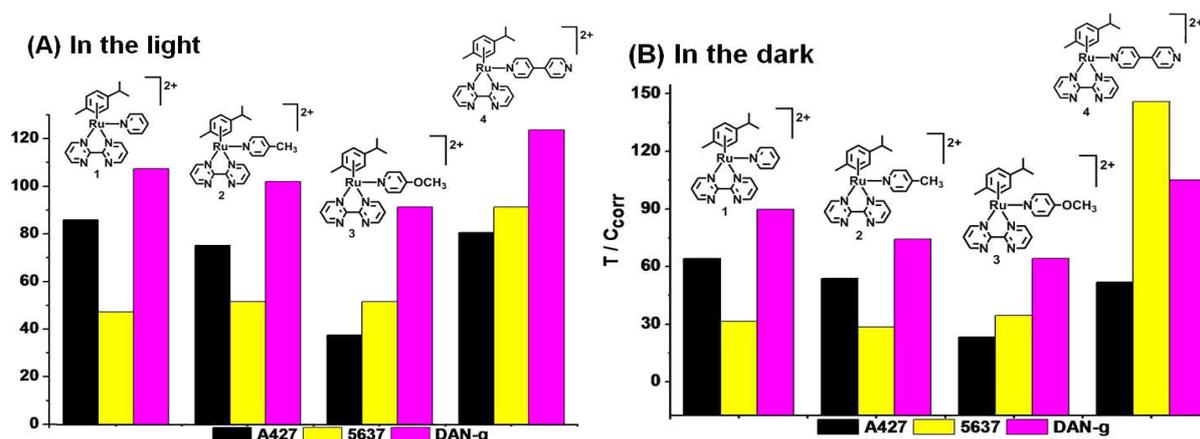

Figure 4.35. Results of the primary screening with (A) UVA photoirradiation and (B) when the plates were kept in the dark. The concentrations used were **1** (61.74 mM), **2** (50.53 mM), **3** (79.25 mM), and **4** (65.53 mM).

4.4 Discussion

4.4.1 X-ray Crystal Structures

To the best of my knowledge, the X-ray crystal structures of **2**, **6**, **7**, **10** and **13** are the first reported examples of $[(\eta^6\text{-arene})Ru(N,N')(L)]^{2+}$ where L is 4-MePy (**2**), 4-BzPy (**6**), trz (**7**), or Py (**10**, **13**). The overall structures of the solved $[(\eta^6\text{-arene})Ru(N,N')(L)]^{2+}$ complexes do not differ greatly from each other and are found

to adopt the familiar pseudo-octahedral three-legged piano stool geometry common to all other Ru^{II} arene structures[5,6] with the Ru atom π-bonded to the arene ligand (*p*-cym in **2**, **6**, **7**, and **10**; ind in **11**), σ-bonded to a pyridine nitrogen (**2**, **6**, **10**, and **11**), a triazole (**7**), and to two nitrogen atoms of the chelating ligand (bpm for **2**, **6**, and **7**; phen for **10**; bpy for **13**) which constitute the three legs of the piano stool. The corresponding bond lengths and angles are comparable to analogous Ru^{II} arene complexes containing N,N' chelated ligands.[21] Neither the nature of the corresponding N,N'-chelating ligand nor the N-σ-donor, have an influence the corresponding Ru^{II}–arene$_{(centroid)}$ distances (~ 1.70 Å). Interestingly, for all the complexes, one of the Ru–N,N' bonds is found to be always longer than the other. A close inspection of the Ru–N$_L$ bond lengths for complexes **2** and **6** reveals no significant difference between them. A larger distortion from planarity on the bpm ligand is found for **2** compared to **6** (7.09°, and 6.80°, respectively). The nature of the arene does not influence significantly the Ru–N,N'$_{(bpm)}$ bond lengths (comparing any of the *p*-cym complexes to ind in compound **10** revealed no major variation). As described in the results section, there are extended short range interactions in the X-ray crystal structures of complexes **2**, **6**, **7**, **10** and **11**; i.e. intermolecular π-π interactions, hydrogen bonds and *pseudo*-trapping of small molecules that involve either the N,N' chelating ligands or the pyridine-derivatives (which could allow intercalation into DNA and therefore contribute to the cytotoxicity of this new class of compounds). The synthesis of complex **7** produced a mixture of products that was difficult to separate. However, through crystallisation complex **7** was obtained but in rather low yields. The synthesis of complex **7** was performed aiming to investigate the photorelease of biological active compounds such as triazoles.[18]

4.4.2 Photochemistry

The photochemistry in aqueous solution at 310 K of the Ru^{II} arene complexes **1−6**, **8−10**, and **12−16** (Table 4.1 and Figure 4.1) of the general formula [(η^6-arene)Ru(N,N')(L)]$^{2+}$ where N,N' is a bidentate chelating ligand and L is a pyridine or pyridine-derivative was investigated under visible (λ$_{irr}$ = 400−660 nm) or UVA photoirradiation (λ$_{irr}$ = 300−400 nm), using both experimental (UV-vis and ^{1}H NMR spectroscopies) as well as theoretical methods (DFT and TD-DFT calculations). The experimental results showed that this family of Ru^{II} arene complexes can selectively and exclusively photodissociate the monodentate ligand (L) when excited with visible (λ$_{irr}$ = 400−660 nm) or UVA photoirradiation (λ$_{irr}$ = 300−400 nm), while the corresponding bound arenes and chelating ligands remain intact. It was observed that with the use of UVA photoirradiation, the formation of the corresponding reactive Ru^{II} arene aqua species can be achieved in a shorter period of time and the process is much more efficient than when visible light is employed. This evidence is in good agreement with the more intense absorption bands in the UV-region of the absorption spectrum displayed by all the Ru^{II} arene complexes studied. The presence of isosbestic points in their UV-vis absorption spectra is also in good agreement with the formation of the single photoproduct in all cases, the reactive aqua adduct Ru−OH$_2$ (and the corresponding free L ligand detected by ^{1}H NMR). It is clear that since the Ru−OH$_2$ species do not form in the dark, the photoactivation of the complexes allows strict control of the Ru−N$_{(L)}$ bond hydrolysis reaction. Their remarkable behaviour contrasts to that observed for the analogous Ru^{II} arene complexes of the form [(η^6-arene)Ru(L)$_3$]$^{2+}$ where arene = benzene, toluene, or isopropyltoluene; and L = NH$_3$ or H$_2$O, for which visible light photoirradiation in aqueous solution leads in each case to the aquation of the arene as the only observable photoreaction (to produce

$[Ru(OH_2)_3L_3]^{2+}$ *plus* the corresponding free arene).[19] As shown by the TD-DFT calculations, the selective photochemical dissociation of the L ligand is consistent with the presence of $Ru-N_{(L)}$ σ^*-antibonding orbitals (typically the LUMO+3) which participate in several singlet and triplet transitions. Furthermore, although in most cases there is one dissociative $Ru-N,N_{(chelating)}$ σ^*-antibonding orbital (LUMO+1, as shown by the calculations), such dissociative nature is only towards one aromatic ring (i.e. one pyrazine ring in bpm in complexes **1–9** and **14–16**). The second aromatic ring in all the chelating ligands remains strongly bound thus preventing their dissociation, providing further photochemical stability to this family of complexes towards light-induced chelating ligand loss. On the basis of the computational work, as well as photochemistry rates and examples reported in the literature, triplets states are believed to play a key role in the ligand photodissociation mechanism of these Ru^{II} arene complexes. In fact, despite the presence of some dissociative singlet excited states, the slow formation of the $Ru-OH_2$ species (more than 10 h of photoirradiation with visible light in some cases) confirms this hypothesis. As in the case of other Ru^{II} (poly)pyridyl complexes, such states can also undergo photochemical reactions due to their distorted geometry[20,21] which yield free ligand molecules and a Ru^{II} (poly)pyridyl residue, generally an aqua or solvento complex. From the computational point of view, it is believed that all the Ru^{II} pyridine complexes studied in this Chapter follow a relatively similar photoinduced ligand dissociation mechanism. It is likely that this dissociation occurs from a series of ^{3}MC triplet states with dissociative character (T4–T5). At lower energy ^{3}MC with non-dissociative character are present (T1–T3). The nature of these low-lying triplet states is also consistent with the absence of fluorescence of the complexes in solution. There is evidence that competitive-radiationless decay processes are much faster than these

potential photochemical processes for some d^6 metal complexes, particularly for Ru[II] (poly)pyridyl complexes.[22] Figure 4.36, shows a summary of the photochemical decomposition mechanisms for the Ru[II] arene complexes based on the computational data. After intersystem crossing promoted by the strong spin-orbital coupling, both ^{3}MC non-dissociative and dissociative triplet states can be populated. The non-dissociative ^{3}MC states are responsible for the return of the excited molecules to the ground state (consistent with the absence of fluorescence). The dissociative ^{3}MCs which can be populated by thermal activation and cause the selective dissociation of the L ligand. An attempt to understand the relationship between the photoactivity and structure of the Ru[II] arene pyridine and pyridine-derivative complexes was also made on the basis of the experimental data. The experimental observations can be summarised as follows,

(a)   Change of the basic Py ring for a 4-substituted Py ring. More electron-donating substituents on the Py ring in the *para*-position moderately increase the extent of the photo-induced hydrolysis, whereas no effect on the rate is observed.

(b)   Change of the basic Py ring for a 3-substituted Py ring. Both the extent and the rate of photo-induced hydrolysis decrease on changing the *meta*-substituent on the Py ring following the order ketone > amide ≈ ester.

(c)   Change of the arene. More electron-donating substituents on the arene ring increase both the extent and the rate of photo-induced hydrolysis.

(d)   Change of the N,N'-chelating ligand. The more aromatic character, the lesser the extent of photo-induced hydrolysis. However, no effect on the rate is observed.

This might be an indication that the corresponding rates and extents of the photolysis reactions could also be related to the formation of the more thermodynamically favoured aqua adducts. Such a hypothesis is further supported by the experimental

observations that showed that the photoactivatable Ru^{II} arene complexes **8** and **9**, displayed the best rates and extent of the photo-induced hydrolysis (i.e. they generate ~100% of their corresponding aqua adduct in the less time of photoirradiation, either with visible or UVA). The presence of a better electron-donating arene (such as hmb in **8** or ind in **9**) stabilises the aqua derivatives to a greater extent than those of the other complexes.
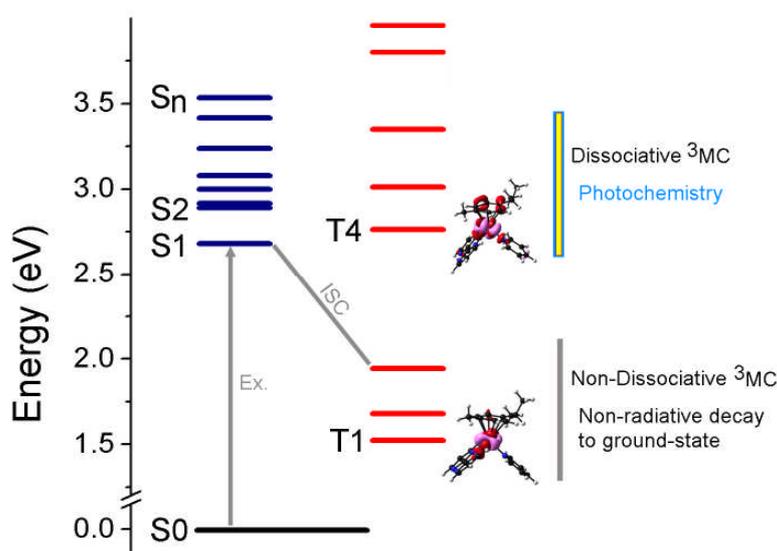

Figure 4.36. Proposed photochemical decomposition mechanisms for the Ru^{II} arene pyridine or pyridine-derivative complexes based on the TD-DFT computational data.

4.4.3   Photocontrolled DNA Interactions in Cell-Free Media

Three complexes of the form $[(\eta^6\text{-}p\text{-cym})Ru(N,N')(L)]^{2+}$ where N,N' is bpm (**1**, **4**) and L is Py (**1**, **10**) or 4,4'-bpy (**4**) were selected for further studies with CT-DNA in cell free media. As it was shown in the results section (*vide supra*), upon photoactivation the three complexes undergo a clean and selective photorelease of the corresponding pyridine (**1**, **10**) or the pyridine-derivative ligand 4,4'-bpy (**4**) to form a monofunctional reactive aqua species $[(\eta^6\text{-}p\text{-cym})Ru(N,N')(OH_2)]^{2+}$. Although the photoactivation of these three Ru–L complexes is very similar, their effects on DNA

differ from each other (both in dark and light conditions) as revealed by their IC$_{50}$ values (in ambient light) and DNA binding experiments, particularly in the case of complex **4**. This evidence suggest that the nature of the pyridine-derivative (both when bound and when photoreleased from the metal centre) as well as the N,N' chelating ligand play a key role on the mode of interaction of these complexes. Incorporating an extended pyridine such as 4,4'-bpy (as in complex **4**) provides already a low *ca*. 20% of interaction of Ru compound with DNA after 48 h in the dark (*non-irradiated* form) which might account for its mild cytotoxicity towards the A2780 human ovarian cancer cell line in ambient light conditions. In comparison, less than 5% of interaction with DNA was determined for **1** and **10** after 48 h, also in the *non-irradiated* forms. Upon photoirradiation, the corresponding monofunctional reactive aqua species $[(\eta^6\text{-}p\text{-cym})Ru(N,N')(OH_2)]^{2+}$ are formed accompanied by the selective release of the corresponding L ligand. All the aqua adducts were found to bind to DNA at varying rates. The *pre-irradiated* forms of Ru complexes bind faster but to the same extent as the *irradiated* forms. These results are in good agreement with the fact that irradiating $[(\eta^6\text{-}p\text{-cym})Ru(N,N')(L)]^{2+}$ is a requirement for the generation of the reactive aqua species. The relatively long photoirradiation times needed to start generating the corresponding aqua adducts limits the initial binding of the Ru complexes to DNA, but as soon as the full photoconversion is achieved, the overall extent does not vary. The rate of binding to DNA, however, is slower than that determined for the anticancer drug cisplatin (t$_{1/2}$ *ca*. 2 h under similar conditions),[23] for which DNA binding is thought to be responsible for its cytotoxic properties. In contrast, another Ru^{II} analogue $[(\eta^6\text{-bip})Ru(en)Cl]^+$, which has also been shown to be cytotoxic to cancer cells,[4] reacts much more rapidly with DNA under similar conditions (t$_{1/2}$ *ca*. 10 min).[17] The relatively small extent of binding of the *non-*

irradiated forms of the Ru complexes along with the slower kinetics of binding to DNA only upon photoirradiation is an advantageous characteristic that may allow more drug to reach its target *in vivo* without being deactivated by reacting with other biological molecules. *In vitro* RNA synthesis by RNA polymerases on DNA templates containing several types of bifunctional adducts of platinum or Ru complexes can be prematurely terminated at the level or in the proximity of DNA adducts. Importantly, monofunctional DNA adducts of several platinum complexes are unable to terminate RNA synthesis.[24] A similar approach was used for these experiments. The results of the transcription mapping experiments suggest that the *non-irradiated* forms of **1**, **4** and **10** bind to DNA only upon photoirradiation, inhibiting RNA synthesis in a similar fashion and with similar stopsites to cisplatin and to the Ru complex [(η^6-bip)Ru(en)Cl]$^+$. For the *pre-irradiated* and *irradiated* forms of complexes **1**, **4**, and **10** the stopsites were only guanine residues, which agrees well with the photocontrolled nucleobase binding studies performed (followed by multidimensional ^{1}H NMR spectroscopy; see results section) which show that these complexes bind importantly to 9-EtG but do not bind to 9-EtA. The strong preference for guanine bases may allow these Ru^{II} arene complexes to target selectively G-rich regions of DNA, such as telomeres which play key role in cell divison.[25] DNA binding upon photoirradiation of Ru^{II} complexes **1**, **4** and **10**, results in a mild degree of unwinding (6–7°) which is very similar for the three complexes but smaller than that observed for the Ru^{II} complexes [(η^6-arene)Ru(en)Cl]$^+$ (7 and 14°).[30] The unwinding angles produced by the adducts of Ru^{II} arene compounds **1**, **4** and **10** resemble more to those produced by monofunctional cisplatin adducts (6° and 13° for mono or bifunctional adducts, respectively).[26] The aromatic ligands such as the corresponding N,N' chelating (bpm or phen) in the DNA adducts of the Ru^{II} arene

compounds, could be geometrically and favourably-positioned to interact with the double helix. This hypothesis is supported by previous reports on the observation that the single ring *p*-cym arene ligand (in contrast to extended aromatic rings) in analogous monofunctional Ru^{II} arene complexes does not intercalate into the DNA base-pair stack.[30] In this respect, and in contrast to cisplatin, potential intercalating ligands such as phen or bpm, might interact with DNA by aromatic π-stacking between base pairs. This type of interaction is known to result in the lengthening, stiffening, and unwinding of the helix.[26] The DNA cleaving ability of phen solely has made it a frequently used reagent in DNA footprint studies[27] whereas bpm has been studied for its tendency to from aggregates *via* stacking between large planar molecules both in the solid state and solution.[28] The binding of the Ru^{II} arene compounds **1**, **4** and **10** to DNA upon photoirradiation may also affect its melting behaviour. Previously,[28] two important factors have been considered to account for the thermal stability of DNA modified by monofunctional Ru^{II} complexes in media of relatively low ionic strength (0.01 M Na$^+$).

1.   A destabilising effect of conformational distortions.

2.   A stabilising effect of the positive charge on the Ru moieties and of noncovalent binding, such as changes in solvent structure and the counterion distribution around the phosphate groups of DNA which may help to overcome unfavourable electrostatics for the hybridisation of the strands of the duplex.[29]

Under the conditions of the experiments, it is assumed that all the Ru^{II} arene complexes have produced monofunctional adducts with DNA upon photoirradiation. It is likely that some conformational distortions due to the formation of the adducts will destabilise the helix, as has been consistently observed in earlier studies with various other Ru and platinum compounds. The t_m changes induced by the Ru^{II} arene

compounds **1**, **4** and **10** in the *irradiated* forms are small, however. It is possible that the fluctuations in the t_m values due to the modification by the Ru^{II} arene compounds **1**, **4** and **10** is a consequence of the DNA adducts being unstable at higher ionic strengths and temperatures which in turn might be associated with the stabilising effect that arises from non-covalent interactions of the aromatic ligands (arene or N,N' chelating) with the duplex inferred from both the DNA unwinding angles (7° is a typical unwinding angle for monofunctional binders) and quenching of EtBr fluorescence, as well as from the overall positive charge on these Ru^{II} arene compounds. The magnitudes of the LD signals at 258 nm decrease as a function of r_b for all Ru^{II} arene complexes in the *irradiated* forms. These results suggest that the formation of DNA adducts might be accompanied by the appearance of flexible hinge joints at the site of the lesion. CD spectra showed that the binding of **1** and **4** to DNA and concomitant release of pyridine or 4,4'-bpy upon photoirradiation results in conformational alterations in double-helical DNA of a non-denaturational character, similar to those induced in DNA by antitumor cisplatin. In contrast, upon photoirradiation, the binding of **10** to DNA accompanied by the photorelease of pyridine results in conformational alterations in DNA of a denaturational character, similar to those induced in DNA by clinically ineffective transplatin. The signature of complex **4** coordinated to CT-DNA is a strong positive ICD centered at around 400 nm. This could imply that the molecule become oriented as a consequence of their noncovalent interactions with DNA. Hence, these results suggest the case for combined coordinative, intercalative, and monofunctional coordination binding modes of complexes **1**, **4** and **10** upon photoirradiation.

4.4.4   Cancer Cell Growth Inhibition (IC$_{50}$ Values)

Complexes **2**, **5**, **6**, **13** and **14** were non cytotoxic against the A2780 human ovarian cancer cell line under ambient light conditions up to the maximum concentration tested (100 μM). It has been previously observed a loss of cytotoxicity in ambient light conditions towards cancer cells for complexes of the type [(η^6-hmb)Ru(en)(X)]$^+$ when X is replaced by Py.[6] The loss of activity in this complex is assumed to arise from its negligible aquation believed to be the first step towards anticancer activity. The discovery of complexes that do not hydrolyse over a large period of time but retain significant cytotoxicity implies a different mechanism of action for complexes **1**, **3**, **4**, **8**, **9**, **10**, **12**, **15**, and **16**. The cytotoxicity of several isomers of [Ru(azpy)$_2$(bipy)]$^{2+}$ incapable of hydrolysis has been reported.[30] Wang *et. al.* reported significant anticancer activity for the complex [(η^6-hmb)Ru(en)(SPh)]$^{2+}$ which does not undergo hydrolysis.[6] Since no spontaneous hydrolysis is observed for complexes **1**, **3**, **4**, **8−9**, **10**, **12**, **15** and **16**, the species responsible for the cytotoxicity could be the intact cation or the corresponding aqua adducts generated by direct displacement of the L ligands by strong nucleophiles within the media or the cell. The intact cations might exert a cytotoxic effect by mechanisms which include modification of mitochondrial membrane permeability (as observed, for example, with lipophilic cations of Au(I) carbene complexes[31]) and/or DNA intercalation by the aromatic ligands as observed in experiments of DNA interactions in cell-free media.

4.5 Summary

This work provides the first example of a family of piano-stool Ru^{II} arene complexes of the form $[(\eta^6\text{-arene})Ru(N,N')(L)]^{2+}$ (where N,N' is a chelating ligand and L is a pyridine or a pyridine-derivative) that can selectively photodissociate the monodentate ligand (L) when excited with UVA or visible light. Such a unique feature allows control of the hydrolysis reaction of the complexes and, therefore, the formation of a reactive aqua species that otherwise would not form in the dark. Their photochemical behaviour was thoroughly explored, not only experimentally but also using TD-DFT calculations. From the computational point of view, it is believed that all the Ru^{II} pyridine complexes follow a relatively similar photochemical-L-ligand-dissociation mechanism. It is likely that photodecomposition occurs from a series of ^{3}MC triplet states with dissociative character (T4–T5). At lower energy, ^{3}MC states with non-dissociative character are present (T1–T3). The nature of these low-lying triplet states is also consistent with the absence of fluorescence of the complexes in solution. The process proved to be much more efficient when UVA-range irradiation was used and a preliminary structure-photoactivity relationship was established. The presence of a better electron-donating arene (such as hmb in **8** or ind in **9**) seems to stabilise the aqua derivatives to a greater extent than those of the other complexes. On the other hand, and as demonstrated from the experiments of interactions with 9-EtG and 9-EtA, light activation can be used to phototrigger binding of these potential anticancer agents with discriminating preference towards 9-EtG. Furthermore, in order to investigate also the possibility of phototriggering the binding to DNA of the Ru^{II} arene pyridine or pyridine-derivative complexes, studies on CT-DNA interactions in cell-free media were carried out. The CT-DNA binding studies show that

complexes **1**, **4** and **10** in the *pre-irradiated* forms are bound faster but to the same extent as the *irradiated* forms. The *non-irradiated* forms, as expected bind negligibly. Further results on DNA interactions in cell-free media strengthen the case for combined coordinative, intercalative, and monofunctional coordination binding modes of complexes **1**, **4** and **10** upon photoirradiation. These combined results suggest that DNA might be an important target for these complexes. Under the premise that hydrolysis is known to be one mechanism which provides a pathway for cytotoxicity, we were not able to establish an obvious mechanism of action which would account for the cytotoxicity of these Ru^{II} arene pyridine or pyridine-derivative complexes in ambient light conditions. The protocol for photocytotoxicity proved to be partially inadequate, since the time of photoirradiation used was not the optimal to produce enough quantities of the corresponding Ru^{II} arene aqua adducts. Therefore, there is the possibility that the intact cations might exert a cytotoxic effect by mechanisms which include modification of mitochondrial membrane permeability (as observed, for example, with lipophilic cations of Au(I) carbene complexes)[31] and/or DNA intercalation by the aromatic ligands (as it was observed from the experiments of DNA interactions in cell-free media). These encouraging results indicate that the photochemistry of these Ru^{II} arene complexes can be exploited to integrate them with the promising biological properties inherent in half-sandwich Ru^{II} complexes, thus increasing their potential as anticancer agents.

4.6 References

[1]. (a) Hartinger, C. G.; Dyson, P. J. *Chem. Soc. Rev.*, **2009**, *38*, 391–401; (b) Clarke, M. J. *Coord. Chem. Rev.*, **2003**, *236*, 209–233.

[2]. Navarro, M. *Coord. Chem. Rev.*, **2009**, *253*, 1619–1626.

[3]. Crespy, D.; Landfester, K.; Schubert, U. S.; Schiller, A. *Chem. Commun.*, **2010**, advance article, doi:10.1039/C0CC01887B.

[4]. (a) Aird, R.; Cummings, J.; Ritchie, A.; Muir, M.; Morris, R.; Chen, H.; Sadler, P.; Jodrell, D. *Br. J. Cancer*, **2002**, *86*, 1652–1657; (b) Morris, R. E.; Aird, R. E.; Murdoch, P. D.; Chen, H. M.; Cummings, J.; Hughes, N. D.; Parsons, S.; Parkin, A.; Boyd, G.; Jodrell, D. I.; Sadler, P. J. *J. Med. Chem.*, **2001**, *44*, 3616–3621; (c) Nováková, O.; Kašpárková, J.; Bursova, V.; Hofr, C.; Vojtiskova, M.; Chen, H.; Sadler, P. J.; Brabec, V. *Chem. Biol.*, **2005**, *12*, 121–129.

[5]. Chen, H.; Parkinson, J. A.; Parsons, S.; Coxall, R. A.; Gould, R. O.; Sadler, P. J. *J. Am. Chem. Soc.*, **2002**, *124*, 3064−3082.

[6]. Wang, F.; Habtemariam, A.; van der Geer, E. P. L.; Fernández, R.; Melchart, M.; Deeth, R. J.; Aird, R.; Guichard, S.; Fabbiani, F. P. A.; Lozano-Casal, P.; Oswald, I. D. H.; Jodrell, D. I.; Parsons, S.; Sadler, P. J. *Proc. Natl. Acad. Sci. U.S.A.*, **2005**, 102, 18269−18274.

[7]. Peacock, A. F. A.; Habtemariam, A.; Moggach, S. A.; Prescimone, A.; Parsons, S.; Sadler, P. J. *Inorg. Chem.*, **2007**, *46*, 4049−4059.

[8]. Govindaswamy, P.; Canivet, J.; Therrien, B.; Süss-Fink, G.; Štěpnička, P.; Ludvík, J. *J. Organomet. Chem.*, **2007**, *692*, 3664−3675.

[9]. (a) Sheldrick, G. M., *Acta Cryst.* **1990**, *A46*, 467−473; (b) Sheldrick, G. M., *Acta*

Cryst. **2008**, *64*, 12−122.

[10]. Sheldrick, G. M. *SHELXL-97*, University of Göttingen: Göttingen, Germany, **1997**.

[11]. (a) Shriver, D. F.; Atkins, P. W. *Inorganic Chemistry*, Oxford University Press, Oxford, **2002**; (b) http://www.iupac.org/goldbook/S05864.pdf.

[12]. Frisch, M. J.; Trucks, G. W.; Schlegel, H. B.; Scuseria, G. E.; Robb, M. A.; Cheeseman, J. R.; Montgomery, J. A. J.; Vreven, T.; Kudin, K. N.; Tomasi, J.; Barone, V.; Mennucci, B.; Cossi, M.; Scalmani, G.; Rega, N.; Pettersson, G. A.; Nakatsuji, H.; Hada, M.; Ehara, M.; Toyota, K.; Fukuda, R.; Hasegawa, J.; Ishida, M.; Nakajima, T.; Honda, Y.; Kitao, O.; Nakai, H.; Klene, M.; Li, X.; Knox, J. E.; Hratchian, H. P.; Cross, J. B.; Bakken, V.; Adamo, C.; Jaramillo, J.; Gomperts, R.; Stratmann, R. E.; Yazyev, O.; Austin, A. J.; Cammi, R.; Pomelli, C.; Ochterski, J. W.; Ayala, P. Y.; Morokuma, K.; Voth, G. A.; Salvador, P.; Dannenberg, J. J.; Zakrzewski, V. G.; Dapprich, S.; Daniels, A. D.; Strain, M. C.; Farkas, O.; Malick, D. K.; Rabuck, A. D.; Raghavachari, K.; Foresman, J. B.; Ortiz, J. V.; Cui, Q.; Baboul, A. G.; Clifford, S.; Cioslowski, J.; Stefanov, B. B.; Liu, G.; Liashenko, A.; Piskorz, P.; Komaromi, I.; Martin, R. L.; Fox, D. L., Keith, T.; Al-Laham, M. A.; Peng, C. Y.; Nanayakkara, A.; Challocombe, M.; Gill, P. M. W.; Johnson, B.; Chen, W.; Wong, M. W.; Gonzalez, C.; Pople, J. A., *Gaussian 03*, (Revision D 0.1); Gaussian Inc.: Wallingford CT, 2004.

[13]. Wang, Y-G.; *J. Phys. Chem. A*, **2009**, *113*, 10867−10872.

[14]. Damrauer, N. H.; Cerullo, G.; Yeh, A.; Boussie, T. R.; Shank, C. V.; McCusker, J.; *Science*, **1997**, *275*, 54−57.

[15]. Mann, K. R.; Blough, A. M.; Schrenk, J. L.; Koefod, R. S.; Freedman, D. A.;

Matachek, J. R., *Pure Appl. Chem.*, **1995**, *67*, 95−101.

[16]. Yan, Y. K.; Melchart, M.; Habtemariam, A.; Sadler, P. J. *Chem. Commun.*, **2005**, 4764−4776.

[17]. Nováková, O.; Chen, H.; Vrana, O.; Rodger, A.; Sadler, P. J.; Brabec, V. *Biochemistry*, **2003**, *42*, 11544–11554.

[18]. (a) Lakomska, I.; Kooijman, H.; Spek, A. L.; Shen, W.-Z.; Reedijk, J. *Dalton Trans.*, **2009**, *48*, 10736−10741; (b) Ferreira, S. B.; Sodero, A. C. R.; Cardoso, M. F. C.; Lima, E. S.; Kaiser, C. R.; Silva, F. P., Jr.; Ferreira, Vitor, F. *J. Med. Chem.*, **2010**, *53*, 2364−2375; (c) Bay, H.; Quaddouri, B.; Guaadaoui, A.; Touzani, R.; Benchat, N.-E.; Hamal, A.; Taleb, M.; Bellaoui, M.; el Kadiri, S. *Lett. Drug Design Discovery*, **2010**, *7*, 41−45; (d) Ovsepyan, T. R.; Melik-Ogandzhanyan, R. G.; Panosyan, G. A.; Arsenyan, F. G.; Garibdzhanyan, B. T. *Pharm. Chem. J.*, **2009**, *43*, 645−648.

[19]. Weber, W.; Ford, P. C. *Inorg. Chem.*, **1986**, *25*, 1088−1092.

[20]. (a) Pinnick, D. V.; Durham, B., *Inorg. Chem.* **1984**, *23*, 1440–1445; (b) Durham, B.; Wilson, S. R.; Hodgson, D. J.; Meyer, T. J. *J. Am. Chem. Soc.*, **1980**, *102*, 600–607; (c) Collin, J. P.; Jouvenot D.; Koizumi, M.; Sauvage, J. P. *Inorg. Chem.*, **2005**, *44*, 4693–4698.

[21]. Moucheron, C.; Kirsch-De Mesmaeker, A.; Kelly, J. M. *J. Photochem. Photobiol. B*, **1997**, *40*, 91–106.

[22]. (a) Pinnick, D. V.; Durham, B. *Inorg. Chem.*, **1984**, *23*, 1440–1445; (b) Durham, B.; Wilson, S. R.; Hodgson, D. J.; Meyer, T. J. *J. Am. Chem. Soc.*, **1980**, *102*, 600–607; (c) Collin, J. P.; Jouvenot D.; Koizumi, M.; Sauvage, J. P. *Inorg. Chem.*, **2005**, *44*, 4693–4698; (d) Watts, R. J., *J. Chem. Educ.* **1983**, *60*, 834–842; (e) Baerends, E. J.; Rosa, A. *Coord. Chem. Rev.*, **1998**, *177*, 97–125; (f) Vos, J. G.; Kelly, J. M. *Dalton*

Trans., **2006**, 4869–4883; (g) Farrer, N. J.; Salassa, L.; Sadler, P. J. *Dalton Trans.*, **2009**, 10690–10701.

[23]. Bancroft, D. P.; Lepre, C. A.; Lippard, S. J. *J. Am. Chem. Soc.*, **1990**, *112*, 6860–6871.

[24]. Lemaire, M. A.; Schwartz, A.; Rahmouni, A. R.; Leng, M. *Proc. Natl. Acad. Sci. U.S.A.*, **1991**, *88*, 1982−1985.

[25]. Neidle, S. *Nucleic Acid Structure and Recognition*, Oxford University Press, Oxford, **2002**, p 76.

[26]. Kemp, S.; Wheate, N. J.; Wang, S.; Collins, J. G.; Ralph, S. F.; Day, A. I.; Higgins, V. J.; Aldrich-Wright, J. R. *J. Biol. Inorg. Chem.*, **2007**, *12*, 969–979.

[27]. (a) Papavassiliou, A. G. *Biochem. J.*, **1995**, *305*, 345–357; (b) Papavassiliou, A. G. *Methods Mol. Biol.*, **1994**, *30*, 43–78.

[28]. (a) Connick, W. B.; Marsh, R. E.; Schaefer, W. P.; Gray, H. B. *Inorg. Chem.*, **1997**, *36*, 913–922; (b) Herber, R. H.; Croft, M.; Coyer, M. J.; Bilash, B.; Sahiner, A. *Inorg. Chem.*, **1994**, *33*, 2422–2426.

[29]. (a) Maeda, Y.; Nunomura, K.; Ohtsubo, E. *J. Mol. Biol.*, **1990**, *215*, 321–329; (b) Bjorndal, M. T.; Fygenson, D. K. *Biopolymers*, **2002**, *65*, 40–44.

[30]. Chen, H. M.; Parkinson, J. A.; Nováková, O.; Bella, J.; Wang, F. Y.; Dawson, A.; Gould, R.; Parsons, S.; Brabec, V.; Sadler, P. J. *Proc. Natl. Acad. Sci. U.S.A.*, **2003**, *100*, 14623–14628.

[31]. Barnard, P. J.; Baker, M. V.; Berners-Price, S. J.; Day, D. D. *J. Inorg.Biol. Chem.*, **2004**, *98*, 1642–1647.

Chapter 5

Hydride-Transfer of

Ru^II Arene Complexes

NAD^+   1,4-NADH
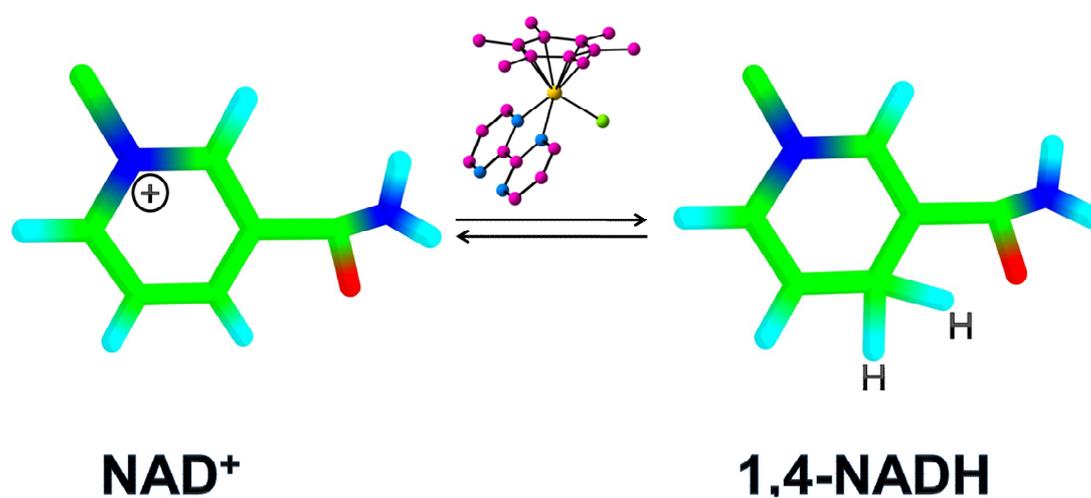
Chapter 5

Hydride-Transfer of Ruthenium(II) Arene Complexes

5.1 Introduction

The observation that some Ru^{II} arene complexes can form stable hydride complexes[1,2,3] in aqueous solution using formate as the hydride donor,[4,11,19] has opened up a path towards water-soluble organometallic complexes for catalysis. This area attracts continuously growing interest because of environmentally friendly processing, simple product separation and pH dependent selectivity in aqueous media.[5,6] For example, the Ru^{II} complexes $[(\eta^6\text{-}C_6Me_6)Ru(bpy)(OH_2)]^{2+}$ and $[(\eta^6\text{-}C_6Me_6)Ru(phen)Cl]^+$ where bpy is 2,2'-bipyridine and phen is 1,10-phenanthroline and other related complexes[7] have been shown to catalyse the reduction of ketones (such as cyclohexanone and acetophenone) to alcohols and imines;[8,9,10] although the conditions for optimum turnover are (usually) not biologically compatible.[11,12] It has been noticed that catalytic activity usually requires the presence of a labile coordination site on the Ru^{II} centre and/or arene displacement;[13,14] it is also believed that the nature of all the coordinated ligands can have a pronounced effect on the catalytic properties of these complexes. This observation has led to the development of a wide range of synthetic routes to complexes as catalytic precursors containing various substituted arenes together with other ligands such as halides, carboxylates, amines, oxygen or nitrogen chelating groups, Schiff bases, carbenes, phosphines, alkyl, and aryl groups.[15,16,17] In the field of biocatalysis, Rh^{III} pentamethylcyclopentadienyl[18,29] and Ru^{II} arene complexes[19] have been shown to catalyse the reduction of β-nicotinamide adenine dinucleotide (NAD$^+$) in the presence of formate as the hydride source. This reduction is regioselective, giving the

biologically relevant 1,4-NADH isomer and in the case of the Rh^{III} derivative, it was further shown how it can drive enzymatic reactions relying on NADH as a cofactor.[20] In the present work, hydride-transfer reactions of a series of Ru^{II} arene halido complexes to regioslectively reduce NAD$^+$ in the presence of formate under biologically relevant conditions are described. It is also shown herein, that this reaction can be specifically phototriggered if an initial Ru^{II} arene pyridine complex is irradiated with UVA (λ_{irr} = 300−400 nm) or visible light (λ_{irr} = 400−660 nm). The reverse metabolic-like reaction (1,4-NADH → NAD$^+$) was also investigated, exploring the hydride-donor potential of 1,4-NADH to Ru^{II} arene complexes. A preliminary elucidation of the mechanism(s) involved is attempted.

5.2 Experimental Section

5.2.1 Materials

β-Nicotinamide adenine dinucleotide hydrate (NAD$^+$), β-nicotinamide adenine dinucleotide reduced dipotassium salt (1,4-NADH), sodium borohydride (NaBH$_4$), sodium formate (NaHCO$_2$), silver nitrate (AgNO$_3$), and potassium hexafluorophosphate (KPF$_6$) were obtained from Sigma-Aldrich. The Ru^{II} arene halido precursors [(η^6-p-cym)Ru(bpm)Cl][PF$_6$], [(η^6-bip)Ru(bpm)Cl][PF$_6$], [(η^6-hmb)Ru(bpm)Cl][PF$_6$], [(η^6-ind)Ru(bpm)Cl][PF$_6$], and [(η^6-p-cym)Ru(phen)Cl)][PF$_6$] were synthesised as described in Chapter 3 following a method previously described.[21] The Ru^{II} arene halido complexes [(η^6-(hmb)Ru(en)Cl][PF$_6$], [(η^6-ind)Ru(bpy)Cl][PF$_6$], [(η^6-ind)Ru(4,4'-Me$_2$-bpy)Cl][PF$_6$], and [(η^6-p-ind)Ru(phen)Cl][PF$_6$] were kindly provided by Dr Abraha Habtemariam from the Department of Chemistry at the University of Warwick and synthesised according to a reported method.[22] The Ru^{II} arene pyridine precursors [(η^6-p-

cym)Ru(bpm)(Py)][PF$_6$]$_2$, [(η^6-hmb)Ru(bpm)(Py)][PF$_6$]$_2$, [(η^6-ind)Ru(bpm)(Py)][PF$_6$]$_2$, [(η^6-*p*-cym)Ru(phen)(Py)][PF$_6$]$_2$, and [(η^6-ind)Ru(bpy)(Py)][PF$_6$]$_2$ were synthesised as described in Chapter 4. The solvent used for UV-vis absorption spectroscopy was deionised water. The solvents used for ^{1}H NMR spectroscopy were methanol-d_4 and D$_2$O from Aldrich unless otherwise stated.

5.2.2 Hydride-Transfer Reactions Using Sodium Borohydride (NaBH$_4$)

The following experiment was carried out under normal ambient light conditions (i.e. no photoirradiation provided). An excess of NaBH$_4$ (2.5 mol equiv) was added to 300 mM solutions of the Ru^{II} arene halido complexes in 90% H$_2$O/10% D$_2$O at room temperature. The ^{1}H NMR spectra of the resulting solutions were recorded at 310 K at various time intervals for 4−6 h.

5.2.3 Interactions of Ru^{II} Arene Complexes with Sodium Formate (NaHCO$_2$)

The following experiment was carried out under normal ambient light conditions (i.e. no photoirradiation provided). An excess of NaHCO$_2$ (25 mol equivalent) was added to 300 mM solutions of the Ru^{II} arene halido complexes in 90% H$_2$O/10% D$_2$O at room temperature. The ^{1}H NMR spectra of the resulting solutions were recorded at 310 K at various time intervals for 24–48 h. The pH* of the solutions was recorded at the beginning and at the end of the experiment.

5.2.4 Interactions of Ru^{II} Arene Complexes with Sodium Formate (NaHCO$_2$) upon Visible Light Photoirradiation

^{1}H NMR spectra of 300 mM (90% H$_2$O/10% D$_2$O) solutions of the Ru^{II} arene pyridine complexes in the presence of an excess of NaHCO$_2$ (25 mol equiv) were acquired at

different stages of photoirradiation with visible light (λ_{irr} = 400−660 nm) at 310 K for 12 h. The pH* of the solutions was recorded at the beginning and at the end of the experiment.

5.2.5   Preparation of a Ru^{II} Arene Formato Complex

The complex [(η^6-*p*-cym)Ru(bpm)(O$_2$CH)][PF$_6$] where *p*-cym = *para*-cymene and bpm = 2,2'-bipyrimidine, was synthesised using a similar procedure previously reported.[23] Using an aluminium-foil-covered flask at room temperature [(η^6-*p*-cym)Ru(bpm)Cl][PF$_6$] and AgNO$_3$ in a 1:1 mixture of MeOH/H$_2$O (10 mL) were refluxed overnight (18 h). Precipitated AgCl was then removed by filtration. A 25 mol equiv excess of sodium formate (NaHCO$_2$) was added and the mixture was left stirring for 30 min at room temperature. The volume was reduced by rotary evaporation and a 2–5 mol equiv of KPF$_6$ was added. The precipitate that formed was collected by filtration and washed with portions of Et$_2$O/MeOH and dried overnight in vacuum resulting in a microcrystalline product. Details of the amounts of reactants, volumes of solvents mixture, colour changes, and nature of the product are described below.

[(η^6-*p*-cym)Ru(bpm)(O$_2$CH)][PF$_6$] (16). [(η^6-*p*-cym)Ru(bpm)Cl][PF$_6$] (0.10 g, 0.17 mmol), AgNO$_3$ (0.03 g, 0.17 mmol), NaHCO$_2$ (0.10 g, 2.94 mmol) and KPF$_6$ (0.16 g, 0.85 mmol); the solution turned from bright yellow to dark green; a dark yellow solid was obtained; yield 64% (0.07 g, 0.11 mmol). Elemental analysis calc. for C$_{19}$H$_{23}$F$_6$N$_4$O$_3$PRu %C: 37.94, %H: 3.85, %N: 9.32; found %C: 37.59, %H: 3.59, %N: 10.09. HR-MS: calc for C$_{19}$H$_{21}$N$_4$O$_2$Ru [M]$^+$ *m/z* 439.0708, found *m/z* 439.011. ^{1}H NMR (D$_2$O, 500 MHz) δ_H: 1.02 (6H, d, *J* = 6.90), 2.08 (3H, s), 2.58 (1H, sep, *J* =

6.90), 6.04 (2H, d, $J = 6.49$), 6.29 (2H, d, $J = 6.49$), 7.66 (1H, s), 7.92–7.94 (2H, m), 9.19 (2H, dd, $J = 1.97$, $J = 4.88$), 9.90 (2H, dd, $J = 1.99$, $J = 5.80$).

5.2.6 Aqueous Solution Chemistry of the Ru^{II} Arene Formato Complex

5.2.6.1 Determination of the Ru$-$O$_2$CH Bond Hydrolysis

The following experiment was carried out under normal ambient light conditions (i.e. no photoirradiation provided). Hydrolysis of the Ru^{II} arene formato complex was monitored by UV-vis spectroscopy. The nature of the hydrolysis products as well as the extent of the reaction were verified by ^{1}H NMR spectroscopy or HR-MS. For UV-vis spectroscopy, the Ru^{II} arene formato complex was dissolved in H$_2$O to give a 100 μM solution. The absorbance was recorded at several time intervals at the selected wavelength (at which the maximum changes in absorbance were registered) at 310 K over 8 h. A plot of the change in absorbance with time was computer-fitted to the pseudo first-order rate equation: $A = C_0 + C_1 e^{-kt}$ (where C_0 and C_1 are computer-fitted constants and A is the absorbance corresponding to time) using Origin version 8.0 (Microcal Software Ltd.) to give the half-life ($t_{1/2}$, min) and rate constant value (k, min^{-1}). For ^{1}H NMR spectroscopy, the Ru^{II} arene formato complex was dissolved in 90% H$_2$O/10% D$_2$O to give a 100 μM solution. The ^{1}H NMR spectra at 310 K were recorded at various time intervals. The relative amounts of Ru^{II} arene formato species or aqua adduct were quantified (determined by integration of peaks in ^{1}H NMR spectra).

5.2.7 Regioselective Reduction of NAD$^+$ by Ru^{II} Arene Complexes in the Presence of Formate

The following experiment was carried out under normal ambient light conditions (i.e. no photoirradiation provided). An equimolar amount of NAD$^+$ was added to an NMR tube containing a 300 mM solution of the Ru^{II} arene halido complexes and an excess of NaHCO$_2$ (25 mol equiv) in 90% H$_2$O/10% D$_2$O at room temperature. The ^{1}H NMR spectra of the resulting solutions were recorded at 310 K at various time intervals for 24–48 h.

5.2.8 Regioselective Reduction of NAD$^+$ by Ru^{II} Arene Complexes in the Presence of Formate upon UVA Photoirradiation

An equimolar amount of NAD$^+$ was added to an NMR tube containing a 300 mM solution of the Ru^{II} arene pyridine complexes and an excess of NaHCO$_2$ (25 mol equiv) in 90% H$_2$O/10% D$_2$O at room temperature. ^{1}H NMR spectra of the resulting solutions were acquired at different stages of photoirradiation with UVA (λ_{irr} = 300−400 nm) at 310 K for 12 h.

5.2.9 Interactions of Ru^{II} Arene Complexes with 1,4-NADH

The following experiment was carried out under normal ambient light conditions (i.e. no photoirradiation provided). An equimolar amount of 1,4-NADH was added to an NMR tube containing a 300 mM solution of the Ru^{II} arene halido complexes in 90% H$_2$O/10% D$_2$O at room temperature. The ^{1}H NMR spectra of the resulting solutions were recorded at 310 K at various time intervals for 24–48 h.

5.2.10 Interactions of Ru^{II} Arene Complexes with 1,4-NADH upon UVA Photoirradiation

An equimolar amount of 1,4-NADH was added to an NMR tube containing a 300 mM solution of the Ru^{II} arene pyridine complex in 90% H$_2$O/10% D$_2$O at room temperature. ^{1}H NMR spectra of the resulting solutions were acquired at different stages of irradiation with UVA (λ_{irr} = 300$-$400 nm) at 310 K for 12 h.

5.2.11 Qualitative Studies of 1,4-NADH upon UVA Photoirradiation

A 100 µM solution of 1,4-NADH in water was irradiated with UVA (λ_{irr} = 300$-$400 nm) at 310 K. The photoreaction was followed by UV-vis spectroscopy at different stages of photoirradiation for 12 h.

5.3 Results

5.3.1 Hydride-Transfer Reactions Using Sodium Borohydride (NaBH$_4$)

The possibility that some of the Ru^{II} arene halido complexes studied in Chapter 3 and other related Ru^{II} arene analogues could react directly with NaBH$_4$ to generate hydride species (Ru–H) was investigated. The [(η^6-arene)Ru(N,N')Cl]$^+$ complexes studied in this section are listed in Table 5.1 and their general structures are shown in Figure 5.1. The attempts to generate Ru–H species upon interaction with NaBH$_4$ were studied by means of ^{1}H NMR spectroscopy. Addition of 2.5 mol equiv of NaBH$_4$ to 300 mM solutions containing complexes **1**–**10** in 90% H$_2$O/10% D$_2$O at 298 K caused a colour change from bright yellow to dark-brown. The ^{1}H NMR spectrum at 310 K of the Ru^{II} arene complexes **1**–**4** acquired after *ca*. 45 min suggested the formation of several Ru–H species in each case, as indicated by the presence of multiple low-intensity singlets in the higher-field region of the spectrum between –6 and –10 ppm.

Table 5.1. [(η^6-arene)Ru(N,N')Cl]$^+$ complexes studied in this section.

Compound	Arene	N,N'
(**1**)	*p*-cym	bpm
(**2**)	*p*-cym	phen
(**3**)	hmb	bpm
(**4**)	ind	bpm
(**5**)	hmb	en
(**6**)	ind	bpy
(**7**)	ind	4,4'-Me$_2$-bpy
(**8**)	ind	phen
(**9**)	thn	bpm
(**10**)	bip	bpm
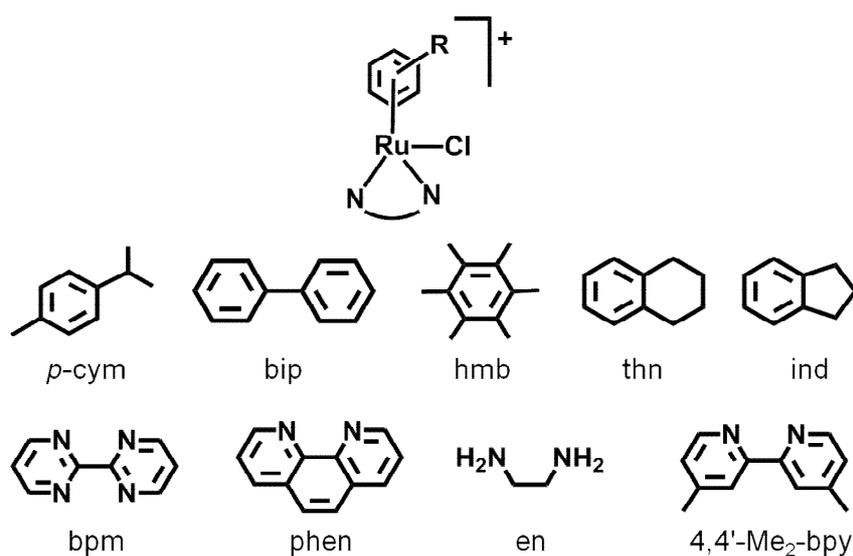
Figure 5.1. Structures of the monocationic complexes studied in this section synthesised as PF$_6$ salts.

The ^{1}H NMR spectrum of the Ru^{II} arene complexes **5**–**9** acquired after *ca*. 30 min suggested the formation of single Ru–H species in each case, as indicated by the presence of medium-to-high-intensity sharp singlets in the higher field region of the spectrum, Figure 5.2. For complexes **5**–**9** the sharp singlets appear at –8.35, –6.20, –6.30, –6.14, and –8.03 ppm, respectively. In the case of complex **10** no reaction was observed after 60 min.
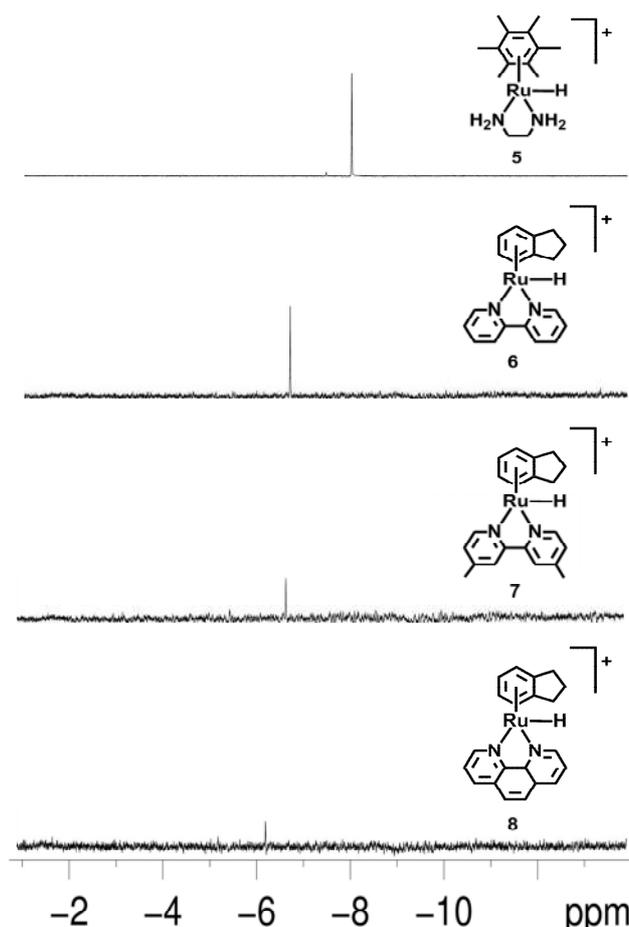
Figure 5.2. High-field region ^{1}H NMR spectra of solutions (300 mM) containing the Ru^{II} arene complexes **5**–**9** and NaBH$_4$ (2.5 mol equiv) in 90% H$_2$O/10% D$_2$O at 310 K after 45 min suggesting the presence of Ru–H species.

5.3.2   Interactions of Ru^{II} Arene Complexes with Sodium Formate (NaHCO$_2$)

Given the evidence that the Ru^{II} arene chlorido complexes **1**–**9** could directly react with NaBH$_4$ to generate Ru–H species in solution, their reaction with sodium formate (as a source of hydride) was investigated. The selected $[(\eta^6$-arene)Ru(N,N')Cl]$^+$ complexes are listed in Table 5.2 and their general structures are shown in Figure 5.3.

Table 5.2. $[(\eta^6$-arene)Ru(N,N')Cl]$^+$ complexes studied in this section.

Compound	Arene	N,N'
(**1**)	*p*-cym	bpm
(**2**)	*p*-cym	phen
(**3**)	hmb	bpm
(**4**)	ind	bpm
(**9**)	thn	bpm

All the reactions were carried out in NMR tubes as 300 mM (90% H$_2$O/10% D$_2$O) solutions and changes in the spectra were followed during 24 h at 310 K. The initial pH* of the Ru^{II} arene complexes solutions in the presence of formate (25 mol equiv) was 6.9–7.2. The ^{1}H NMR spectra of complexes **1−4** and **9** initially contained one major set of peaks assigned to the corresponding chlorido species and then a second set of peaks increased in intensity with time. The new set of peaks has the same chemical shifts as those of the aqua adducts under the same conditions (300 mM solutions in 90% H$_2$O/10% D$_2$O at 310 K; the aqua adducts were separately prepared by treatment of the chlorido complexes with AgNO$_3$ in water at room temperature overnight and removal of AgCl by filtration). A third set of peaks in the ^{1}H NMR spectra was also observed over time and was attributed to the formation of a Ru^{II} formate adduct (Ru–O$_2$CH) in each case. Peaks assigned to the bound formate in all compounds are high-field shifted in comparison to those of free formate (8.40 ppm under the same conditions; 310 K and pH* ≈ 7.0). The O$_2$C–H peak in the formate adduct of complex **1** has a chemical shift of 7.29 ppm whereas in the formate adducts of complexes **2**, **3**, **4**, and **9**, the corresponding singlet is observed at 7.65, 7.68, 7.68, and 7.66 ppm, respectively. The mass-to-charge ratios and isotopic models obtained from HR-MS spectra were consistent with the formation of the formato complexes as the corresponding products in each case, Table 5.3. In most of the cases the reactions reach equilibrium within the first hour after mixing. No further changes in the amount of species present in solution after 24 h were observed, as quantified by integration of the peaks in the ^{1}H NMR spectra. No significant changes in the initial pH* values of solutions of Ru^{II} arene complexes in the presence of formate (25 mol equiv) at the end of the reaction were observed. Figure 5.4 shows the progress of the reaction of [(η^6-hmb)Ru(bpm)Cl]$^+$ (**3**) followed by ^{1}H NMR spectroscopy as a generic example.
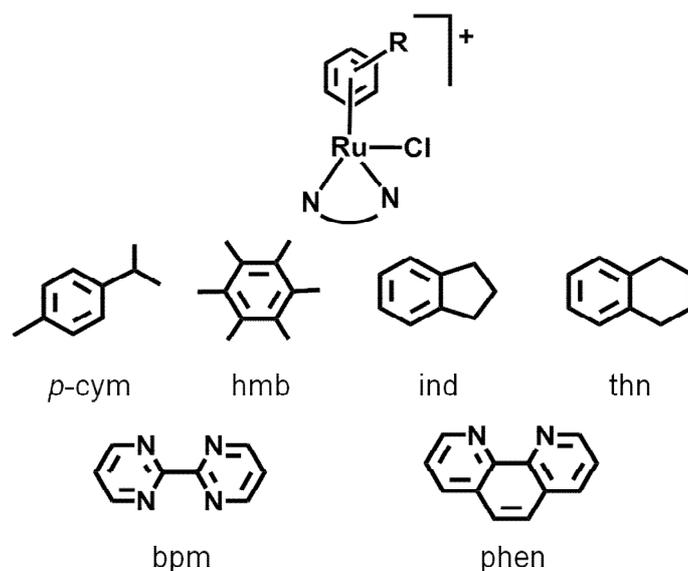
Figure 5.3. Structures of the monocationic complexes studied in this section synthesised as PF_6 salts.

Table 5.3. Mass-to-charge ratios obtained from HR-MS spectra for the products of reaction of a 300 mM solution (90% H_2O/10% D_2O) of Ru^{II} arene complexes **1–4** and **9** with sodium formate (molar ratios 1:25, respectively) at 310 K and pH* ≈ 6.9–7.2.

	Observed peak [M]$^+$	Chemical formula Calc m/z	Found m/z
(**1**)	$[(\eta^6\text{-}p\text{-cym})Ru(bpm)(O_2CH)]^+$	$C_{19}H_{21}N_4O_2Ru$ 439.0708	439.0709
(**2**)	$[(\eta^6\text{-}p\text{-cym})Ru(phen)(O_2CH)]^+$	$C_{21}H_{25}N_4O_2Ru$ 467.1021	467.1015
(**3**)	$[(\eta^6\text{-hmb})Ru(bpm)(O_2CH)]^+$	$C_{17}H_{18}N_4O_2Ru$ 423.0259	423.0254
(**4**)	$[(\eta^6\text{-ind})Ru(bpm)(O_2CH)]^+$	$C_{17}H_{18}N_4O_2Ru$ 204.7250	204.9615
(**9**)	$[(\eta^6\text{-thn})Ru(bpm)(O_2CH)]^+$	$C_{23}H_{23}N_2O_2Ru$ 461.0804	461.0824

The reactions of the Ru^{II} arene complexes **1–4** and **9** with sodium formate were found to display a wide range of rates. It can be seen that for complexes where *p*-cym (arene) is kept constant but the N,N'-chelating ligand is varied, the time needed to reach equilibrium is longer in the case of complex **1** than that for complex **2**, Table 5.4. When the chelating ligand is kept as bpm, changing the arene modifies the rate in the decreasing order ind (**4**) > *p*-cym (**1**) > hmb (**3**) ≈ thn (**9**).
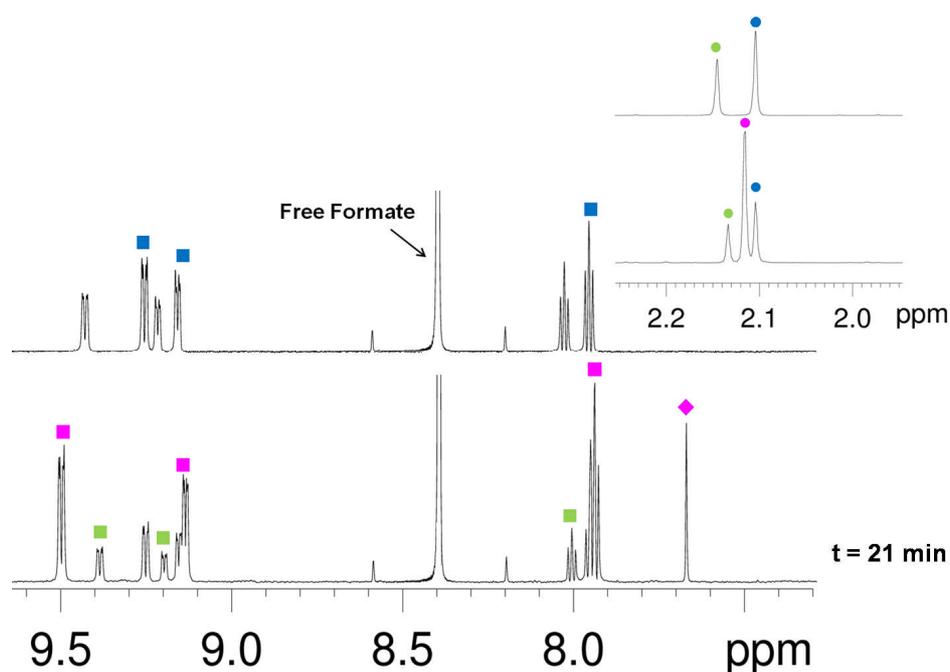
Figure 5.4. ^{1}H NMR spectrum showing the aromatic region just after mixing (top) and after *ca.* 21 min (bottom) of the reaction of a 300 mM solution (90% H$_2$O/10% D$_2$O) of Ru^{II} arene complex [(η^6-hmb)Ru(bpm)(O$_2$CH)]$^+$ (**3**) with sodium formate (molar ratios 1:25, respectively) at 310 K and pH* $\approx$ 6.9. Inset: ^{1}H NMR spectra (aliphatic region) after *ca.* 21 min of reaction. **Blue** = [(η^6-hmb)Ru(bpm)Cl]$^+$; **Green** = [(η^6-hmb)Ru(bpm)(OH$_2$)]$^{2+}$; **Pink** = [(η^6-hmb)Ru(bpm)(O$_2$CH)]$^+$; ■ = bpm, ● = hmb; ♦ = bound HCO$_2$.

Table 5.4. Percentage of species present at equilibrium for the reaction of a 300 mM solution (90% H$_2$O/10% D$_2$O) of Ru^{II} arene complexes **1–4** and **9** with sodium formate (molar ratios 1:25, respectively) at 310 K and pH* $\approx$ 6.9–7.2 followed by ^{1}H NMR.

	Compound	Time (min)[a]	% Species[b] Ru−Cl	Ru−OH$_2$	Ru−O$_2$CH
(**1**)	[(η^6-*p*-cym)Ru(bpm)Cl]$^+$	59	24.1	11.0	64.9
(**2**)	[(η^6-*p*-cym)Ru(phen)Cl]$^+$	17	46.5	3.7	49.7
(**3**)	[(η^6-hmb)Ru(bpm)Cl]$^+$	21	16.5	12.5	71.0
(**4**)	[(η^6-ind)Ru(bpm)Cl]$^+$	81	1.94	13.3	84.7
(**9**)	[(η^6-thn)Ru(bpm)Cl]$^+$	20	19.8	22.4	57.7

[a] Time needed to reach equilibrium.
[b] No changes in the percentage of species were observed after 24 h of reaction.

The reaction of complex **2** was found to give the lowest yield compared to those of the other complexes. The percentage of species present in solution was further monitored after 24 h of incubation at 310 K. In each case, no changes were observed and no evidence of Ru–H species in the high-field region of the spectrum was

detected by ^{1}H NMR. A plausible reduction reaction upon hydride-transfer from the Ru^{II} arene formate adducts to acetone (to generate *iso*-propanol) was assessed by adding 10 mol equiv to the equilibrated solutions. No reaction was observed.

5.3.3   Interactions of Ru^{II} Arene Complexes with Sodium Formate (NaHCO$_2$) upon Visible Light Photoirradiation

The possibility that some of the photoactivatable Ru^{II} arene pyridine complexes studied in Chapter 4 could react directly with formate in solution upon photoirradiation with visible light (λ_{irr} = 400−660 nm) and further generate hydride species (Ru–H) was investigated. The selected [(η^6-arene)Ru(N,N')(Py)]$^{2+}$ complexes are listed in Table 5.5 and their general structures are shown in Figure 5.5.

Table 5.5. [(η^6-arene)Ru(N,N')(Py)]$^{2+}$ complexes studied in this section.

Compound	Arene	N,N'
(**11**)	*p*-cym	bpm
(**12**)	*p*-cym	phen
(**13**)	hmb	bpm
(**14**)	ind	bpm
(**15**)	ind	bpy

All the reactions were carried out in NMR tubes as 300 mM (90% H$_2$O/10% D$_2$O) solutions and followed by ^{1}H NMR spectroscopy at different stages of photoirradiation with visible light (λ_{irr} = 400−660 nm) for 12 h at 310 K. The initial pH* of solutions of Ru^{II} arene pyridine complexes in the presence of sodium formate (25 mol equiv) was in the range of 7.0–7.4. The spectra of each of the complexes initially contained a set of peaks assigned to the original Ru−Py complex.

Further photoirradiation with visible light (λ_{irr} = 400−660 nm) at 310 K produced a second set of peaks which increased in intensity over time and are assigned to the corresponding aqua species (along with the peaks assigned to the released Py ligand as it has been described in Chapter 4).
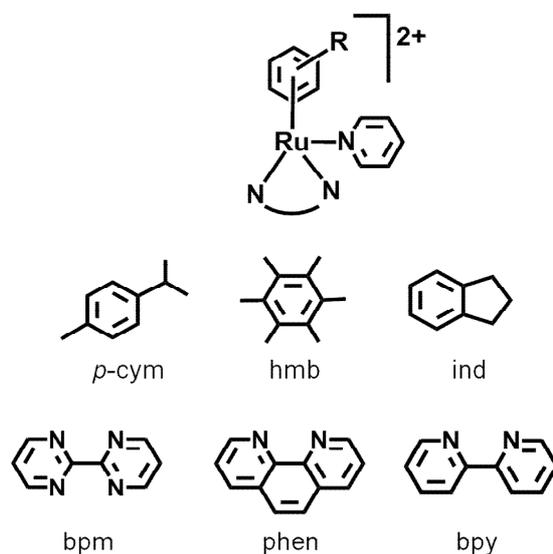
Figure 5.5. Structures of the dicationic complexes studied in this section synthesised as PF$_6$ salts.

An additional set of peaks began to increase in intensity just after the first indication of aqua adducts being formed; this new set of peaks is related to the formation of the corresponding formato complexes (Ru−O$_2$CH) in each case. The pH* of the irradiated solutions at the end of the photoirradiation experiment was *ca.* 7.0 in all cases. Typical spectra recorded during the course of the photoirradiation are shown for [(η^6-*p*-cym)Ru(bpm)(Py)]$^{2+}$ (**11**) in Figure 5.6.
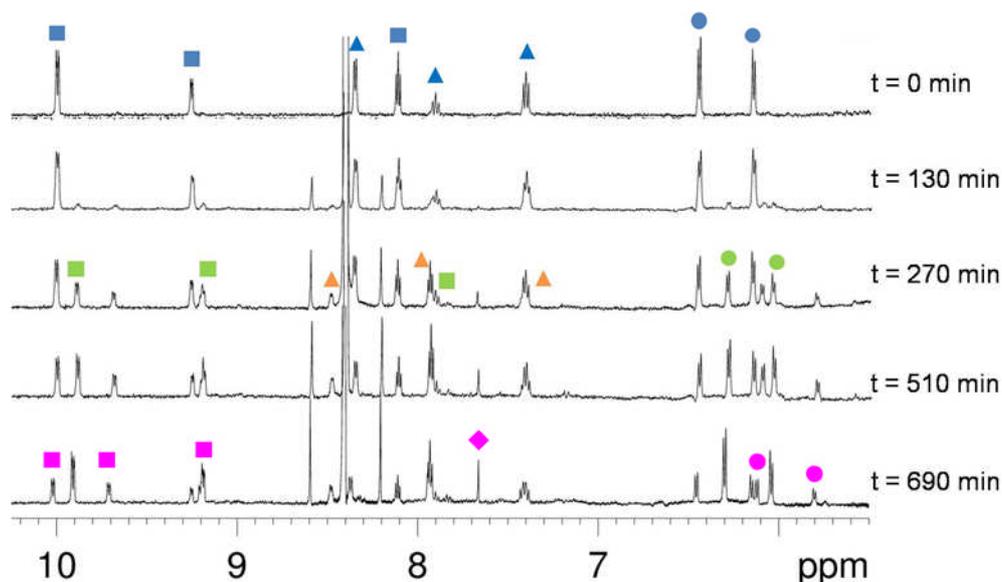
Figure 5.6. ^{1}H NMR spectra during the aqueous photolysis with visible light (λ_{irr} = 400–660 nm) of a 300 mM solution (90% H$_2$O/10% D$_2$O) of [(η^6-*p*-cym)Ru(bpm)(Py)]$^{2+}$ (**11**) in the presence of sodium formate (molar ratios 1:25, respectively) at 310 K and pH* $\approx$ 7.0. **Blue** = [(η^6-*p*-cym)Ru(bpm)(Py)]$^{2+}$; **Green** = [(η^6-*p*-cym)Ru(bpm)(OH$_2$)]$^{2+}$; **Pink** = [(η^6-*p*-cym)Ru(bpm)(O$_2$CH)]$^+$; ■ = bpm, ● = *p*-cym; ♦ = bound HCO$_2$. Free Py is indicated with **Orange ▲**.

Peaks assigned to the formate adducts for all compounds have the same chemical shifts as those of the formate adducts obtained by direct reaction of the chlorido complexes **1**–**4** and **9** with formate in aqueous solution under the same conditions since they are the same species (*vide supra*). The mass-to-charge ratios and isotopic models obtained from HR-MS spectra of the resulting irradiated samples of the Py complexes **11**–**14** are also identical to those of the formate adducts of complexes **1**–**4** (*vide supra*). The HR-MS spectra of the irradiated solution of complex [(η^6-ind)Ru(bpy)(Py)]$^{2+}$ (**15**) (for which no chlorido analogue was investigated) gave the observed peaks: [(η^6-ind)Ru(bpy)(O$_2$CH)]$^+$ calc. for C$_{20}$H$_{19}$N$_2$O$_2$Ru [M]$^+$ *m/z* 421.0490, found *m/z* 421.0490. Table 5.6 lists the percentage of species detected by ^{1}H NMR after 12 h of continuous visible light photoirradiation (λ_{irr} = 400−660 nm) of complexes **11**−**15**.

Table 5.6. Percentage of species present after 4−18 h of photoirradiation with visible light (λ_{irr} = 400−660 nm) for 300 mM solutions (90% H$_2$O/10% D$_2$O) of Ru^{II} arene complexes complexes **11−15** in the presence of sodium formate (molar ratios 1:25, respectively) at 310 K and pH* $\approx$ 7.0−7.4 followed by ^{1}H NMR.

Compound		Irr Time (min)	% Species		
			Ru−Py	Ru−OH$_2$	Ru−O$_2$CH
(**11**)	[(η^6-p-cym)Ru(bpm)(Py)]$^{2+}$	690	46.7	18.0	35.3
(**12**)	[(η^6-p-cym)Ru(phen)(Py)]$^{2+}$	568	61.6	32.0	6.4
(**13**)	[(η^6-hmb)Ru(bpm)(Py)]$^{2+}$	245	14.6	14.4	71.0
(**14**)	[(η^6-ind)Ru(bpm)(Py)]$^{2+}$	336	8.4	4.4	87.2
(**15**)	[(η^6-ind)Ru(bpy)(Py)]$^{2+}$	583	59.3	39.6	1.1

For complexes **11**, **12** and **15** less than *ca.* 50% of the original Ru^{II} arene pyridine complex had been photoconverted to the corresponding aqua adduct after *ca.* 10 h of continuous visible light photoirradiation. A change of arene (i.e. from *p*-cym to hmb) modifies the extent of the photoreaction as well as the time needed to achieve the photoconversion (as described in Chapter 4). In the present experiment, the fastest reactions are those of complexes [(η^6-hmb)Ru(bpm)(Py)]$^{2+}$ (**13**) and [(η^6-ind)Ru(bpm)(Py)]$^{2+}$ (**14**). The aqua adducts generated upon photoirradiation where found to react further with the excess of formate present in the solution, to generate the corresponding formato complexes. A plausible reduction reaction upon hydride-transfer from the Ru^{II} arene formate adducts to acetone (to generate *iso*-propanol) was assessed by adding 10 mol equiv to the equilibrated solutions. No reaction was observed. No binding of formate was observed either for any of the Ru^{II} arene pyridine complexes in the absence of photoirradiation even after 30 days of incubation at 310 K and pH* $\approx$ 7.0−7.4.

5.3.4 Synthesis and Characterisation of a Ru^{II} Arene Formato Complex

The formato complex [(η^6-p-cym)Ru(bpm)(O$_2$CH)][PF$_6$] (**16**), Figure 5.7 was isolated

and characterised in order to study the possibility of generating hydride species (Ru–

H) in solution that could further be used as catalysts for hydride-transfer reactions.

16
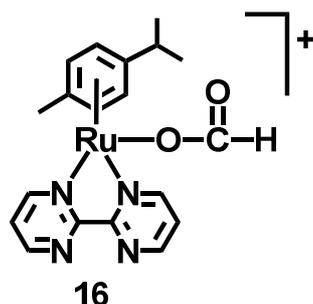
Figure 5.7. Structure of the formato complex [(η^6-p-cym)Ru(bpm)(O$_2$CH)][PF$_6$] (**16**) synthesised as PF$_6$ salt.

Complex **16** was synthesised as PF$_6$ salt in good yields (64%) and was fully

characterised by 1D and 2D ^{1}H NMR methods as well as HR-MS. Compared to its

chlorido analogue (complex **1**), the ^{1}H NMR resonances of complex **16** are high-field-

shifted by *ca*. 0.3 ppm. The binding of the formate ligand to the Ru^{II} centre was

confirmed by the appearance of a sharp singlet at 7.66 ppm (compared to free formate

at 8.40 ppm under the same conditions, 310 K and pH* ≈ 7.2), Figure 5.8.
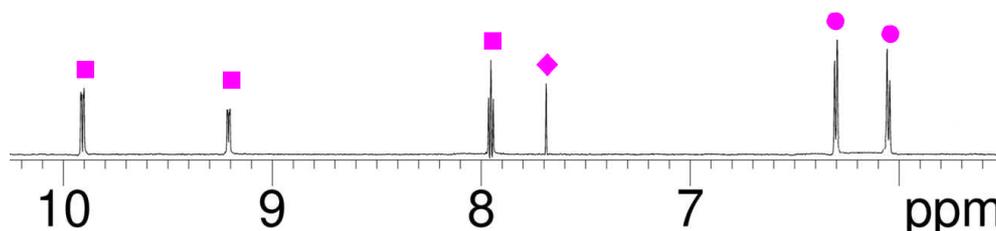
Figure 5.8. ^{1}H NMR spectrum of a 300 mM solution of [(η^6-p-cym)Ru(bpm)(O$_2$CH)][PF$_6$] (**16**) in 90% H$_2$O/10% D$_2$O at 310 K and pH* ≈ 7.2. ■ = bpm, ● = p-cym; ♦ = bound O$_2$CH.

5.3.5 Aqueous Solution Chemistry of the Ru^{II} Arene Formato Complex

The aqueous solution chemistry (with respect to hydrolysis and/or hydride formation) of the Ru^{II} arene complex **16** was studied at 310 K over 8−14 h.

5.3.5.1 *Hydrolysis Equilibria*

In order to characterise the products of hydrolysis, to monitor formation of Ru–H species, and to determine the extent of the reaction of complex **16**, the changes in the ^{1}H NMR spectrum of a freshly-made 100 μM solution (90% H$_2$O/10% D$_2$O) were followed for 24 h at 310 K. The ^{1}H NMR spectrum of complex **16** initially contained one major set of peaks (formato species) and then a second set of peaks increased in intensity over time. The new set of peaks had the same chemical shifts as those of the aqua adduct under the same conditions (100 μM solution in 90% H$_2$O/10% D$_2$O at 310 K and pH* ≈ 7.2). Figure 5.9 shows the changes of the ^{1}H NMR spectrum during the hydrolysis reaction of complex **16**.
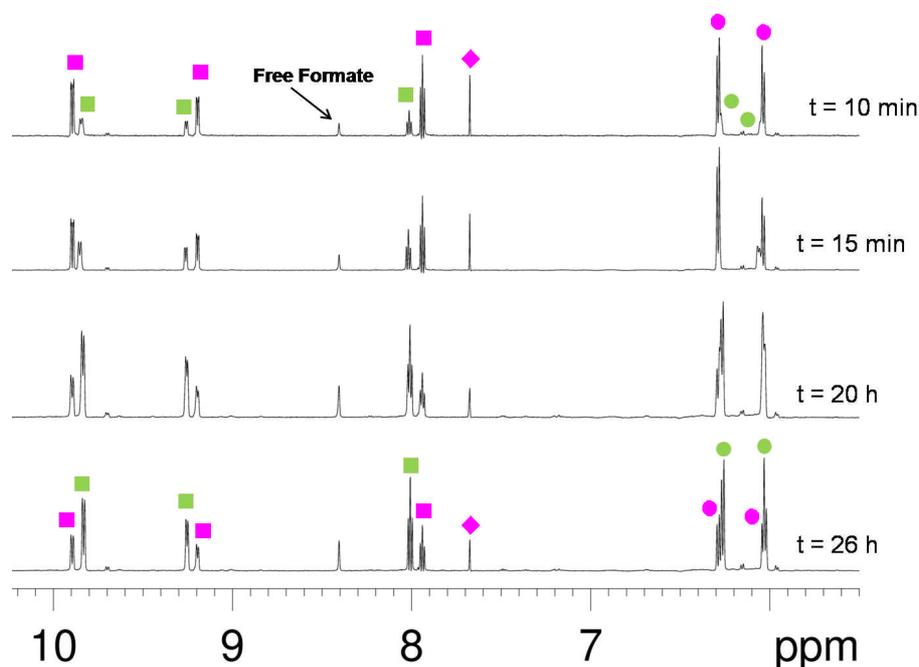
Figure 5.9. ^{1}H NMR spectra recorded during the hydrolysis reaction of a 100 μM solution (90% H$_2$O/10% D$_2$O) of [(η^6-*p*-cym)Ru(bpm)(O$_2$CH)][PF$_6$] (**16**) at 310 K and pH* ≈ 7.2. **Pink** = [(η^6-*p*-cym)Ru(bpm)(O$_2$CH)]$^+$; **Green** = [(η^6-*p*-cym)Ru(bpm)(OH$_2$)]$^{2+}$; ■ = bpm, ● = *p*-cym; ♦ = bound HCO$_2$.

The mass-to-charge ratio and isotopic model obtained from HR-MS spectra were consistent with the formation of the aqua complex as the corresponding product; observed peak: $[(\eta^6\text{-}p\text{-cym})Ru(bpm)(OH_2)]^+$ calc. for $C_{18}H_{22}N_4ORu$ $[M]^{2+}$ *m/z* 206.0418, found *m/z* 206.0408. The hydrolysis reaction for complex **16** reached 68.2% of completion after 24 h. No arene loss (*p*-cym) and no formation of Ru–H species were detected over this period, even after the addition of freshly distilled acetone (10 mol equiv) to promote a possible hydride-transfer reaction (*vide supra*).

5.3.5.2   *Kinetics of Hydrolysis*

Dissolution of compound **16** in H_2O at 310 K gave rise to ligand substitution reactions as indicated by the concomitant changes in the UV-Vis absorption bands. The time evolution spectrum for complex **16** is shown in Figure 5.10.
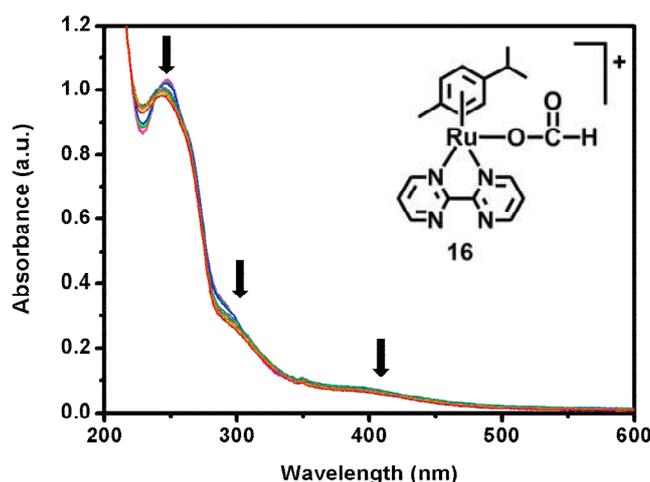
Figure 5.10. Time evolution of the hydrolysis reaction of a 100 μM H_2O solution of complex **16** at 310 K followed by UV-vis spectroscopy for *ca*. 8 h.

The time dependence of the absorbance for complex **16** at the selected wavelength followed pseudo first-order kinetics. Figure 5.11 shows the dependence of the

absorbance at λ = 288 nm over *ca.* 8 h during aquation of [(η^6-*p*-cym)Ru(bpm)(O$_2$CH)][PF$_6$] (**16**) at 310 K. The corresponding rate constant (k × 10^{-3}, min^{-1}) and half-life (t$_{1/2}$, min) are 15.3 ± 0.58 and 45.3, respectively (the errors quoted are fitting errors).
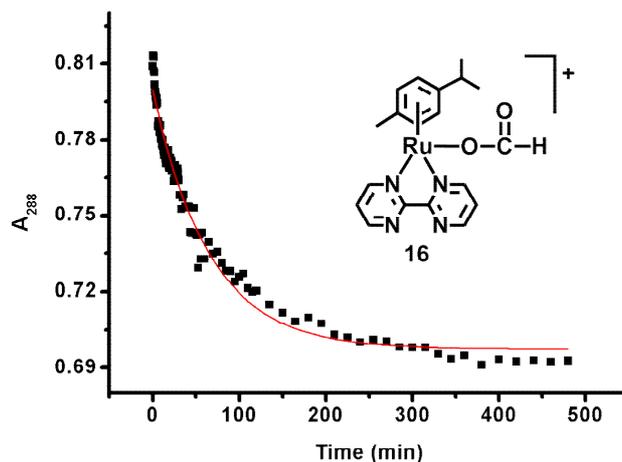
Figure 5.11. Dependence of the absorbance at λ = 288 nm over *ca.* 8 h during aquation of [(η^6-*p*-cym)Ru(bpm)(O$_2$CH)][PF$_6$] (**16**) at 310 K. The red solid line is the best fit to pseudo-first order kinetics.

5.3.6 Regioselective Reduction of NAD$^+$ by Ru^{II} Arene Complexes in the Presence of Formate

The possibility of using selected Ru^{II} arene chlorido complexes as catalytic agents on the regioselective reduction of β-nicotinamide adenine dinucleotide (NAD$^+$) to reduced β-nicotinamide adenine dinucleotide (1,4-NADH) in the presence of sodium formate (as a source of hydride) was investigated. The selected [(η^6-arene)Ru(N,N')Cl]$^+$ complexes are listed in Table 5.7 and their general structures are shown in Figure 5.12. The interactions were studied by means of multidimensional ^{1}H NMR spectroscopy over 24–48 h at 310 K.

Table 5.7. [(η^6-arene)Ru(N,N')Cl]$^+$ complexes studied in this section.

Compound	Arene	N,N'
(**1**)	*p*-cym	bpm
(**3**)	hmb	bpm
(**4**)	ind	bpm
(**9**)	thn	bpm
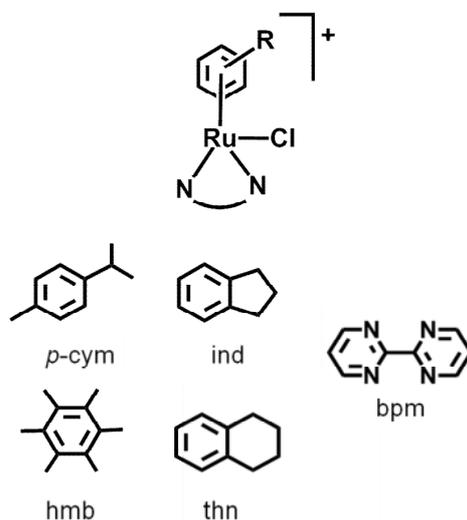
Figure 5.12. Structures of the monocationic complexes studied in this section synthesised as PF$_6$ salts.

The pH* of the Ru^{II} arene chlorido solutions prior to the addition of NAD$^+$ was 6.9–7.2. A decrease of the pH* value to 5.2–5.8 after addition of NAD$^+$ was recorded. Figure 5.13 shows the ^{1}H NMR spectra of [(η^6-hmb)Ru(bpm)Cl]$^+$ (**3**) in 90% H$_2$O/10% D$_2$O (300 mM) at 310 K in the presence of an excess of sodium formate and NAD$^+$ (molar ratios 1:25:1, respectively) after 300 min of reaction as a generic example. The spectrum initially contained three major sets of peaks assigned to the chlorido complex [(η^6-hmb)Ru(bpm)Cl] (**3**), the aqua adduct [(η^6-hmb)Ru(bpm)(OH$_2$)]$^{2+}$, and the formate adduct [(η^6-hmb)Ru(bpm)(O$_2$CH)]$^+$ at equilibrium. Upon addition of NAD$^+$ (1 mol equiv), some changes in the ^{1}H NMR spectrum were noticed within the first 30 min of reaction. The structures and numbering scheme for NAD$^+$, 1,4-NADH and 1,6-NADH are shown in Figure 5.14. The changes suggest the fast regioselective reduction of NAD$^+$ to 1,4-NADH as

indicated by a decrease on the intensity of the signals of free NAD$^+$ (H2 at 9.38 ppm) and the new peaks assignable to 1,4-NADH (H2 at 6.92 ppm and H4a/H4b at 2.70 ppm). The ^{1}H NMR spectra within the first 30 min of reaction, also reveal the emergence of a second singlet around 7.20 ppm that could be tentatively assigned to H2 in 1,6-NADH (as a minor product). It was noticed that after a total of *ca*. 300 min, the initial amount of NAD$^+$ had been fully consumed.
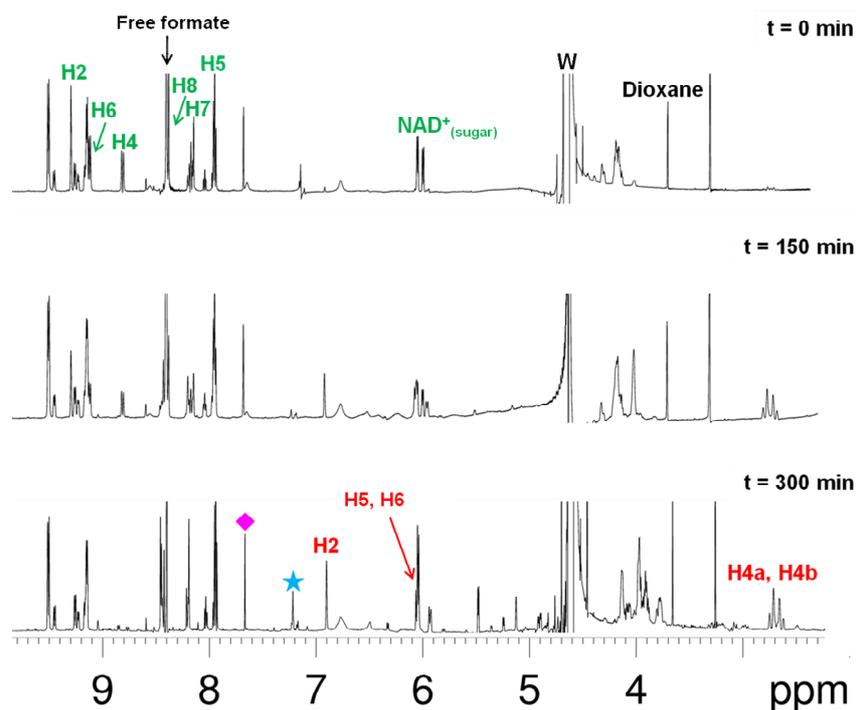
Figure 5.13. ^{1}H NMR spectra during the reaction of a 300 mM solution (90% H$_2$O/10% D$_2$O) of [(η^6-hmb)Ru(bpm)Cl]$^+$ (**3**) in the presence of NaHCO$_2$ and NAD$^+$ (molar ratios 1:25:1, respectively) at 310 K and pH* ≈ 5.2. ♦ **Pink** = [(η^6-hmb)Ru(bpm)(O$_2$CH)]$^+$; ★= 1,6-NADH. **NAD$^+$** is indicated in **dark green** and **1,4-NADH** in **red.**

The progress of the reaction was further monitored for the next 24 h (once the initial amount of NAD$^+$ had been consumed), Figure 5.15. The appearance of a sharp singlet around –7.49 ppm, which increased in intensity over time, occurred simultaneously with an accumulation of 1,4-NADH (t ≈ 400 min) and the appearance of a second signal around –9.92 ppm after *ca*. 480 min. The nature of these high-field sharp

singlets may be related to the formation of Ru–H species. No significant changes in the amount of formate adduct (Ru–O$_2$CH) present in solution during the first 560 min of reaction were observed.
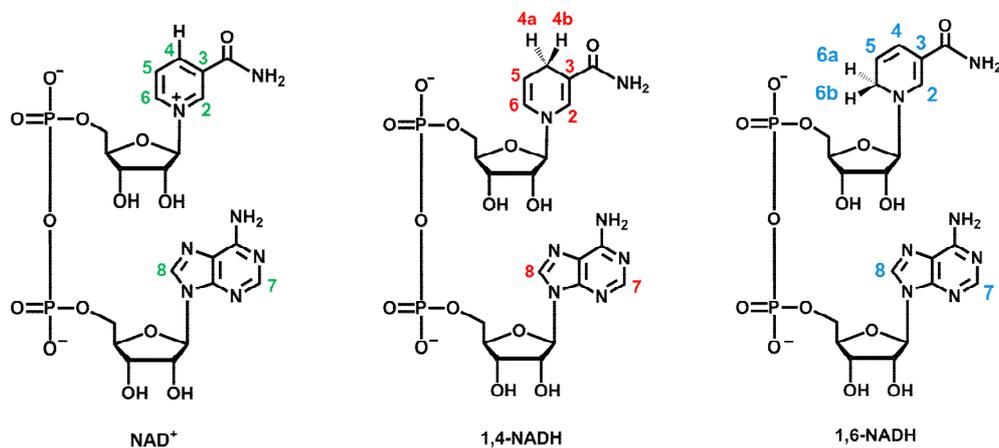
Figure 5.14. Structures and numbering scheme for NAD$^+$, 1,4-NADH and 1,6-NADH.
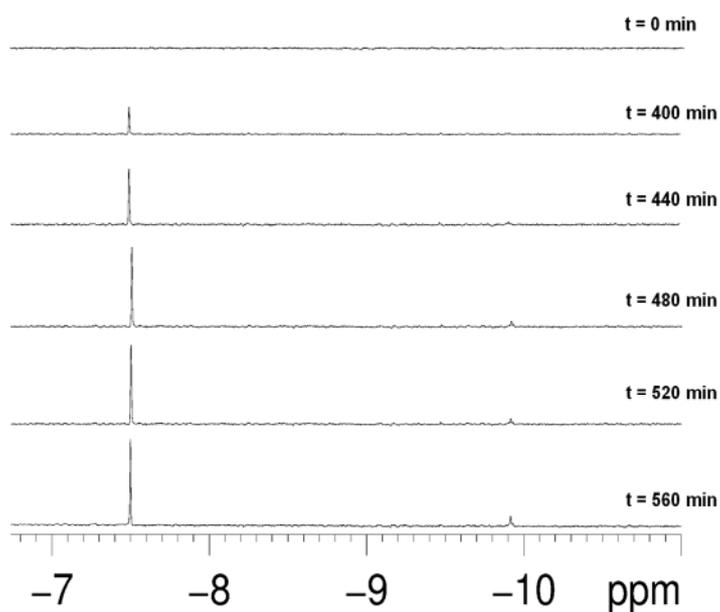
Figure 5.15. ^{1}H NMR spectra in the high-field region during the reaction of a 300 mM solution (90% H$_2$O/10% D$_2$O) of [(η^6-hmb)Ru(bpm)Cl]$^+$ (**3**) in the presence of NaHCO$_2$ and NAD$^+$ (molar ratios 1:25:1, respectively) at 310 K and pH* $\approx$ 5.2.

A slight decrease in the amount of 1,4-NADH (that had been generated during the first 5 h of reaction) was detected just as the maximum intensity of the high-field signals was reached. Since the accumulation of 1,4-NADH seemed to be linked with the formation of Ru–H species, an extra mol equiv of NAD$^+$ was added to the solution at this stage (t $\approx$ 560 min). The ^{1}H NMR spectra after *ca.* 5 min after the addition of a second mol equiv of NAD$^+$ (t' = 0 min), resulted in the immediate disappearance of the Ru–H peaks, Figure 5.16.
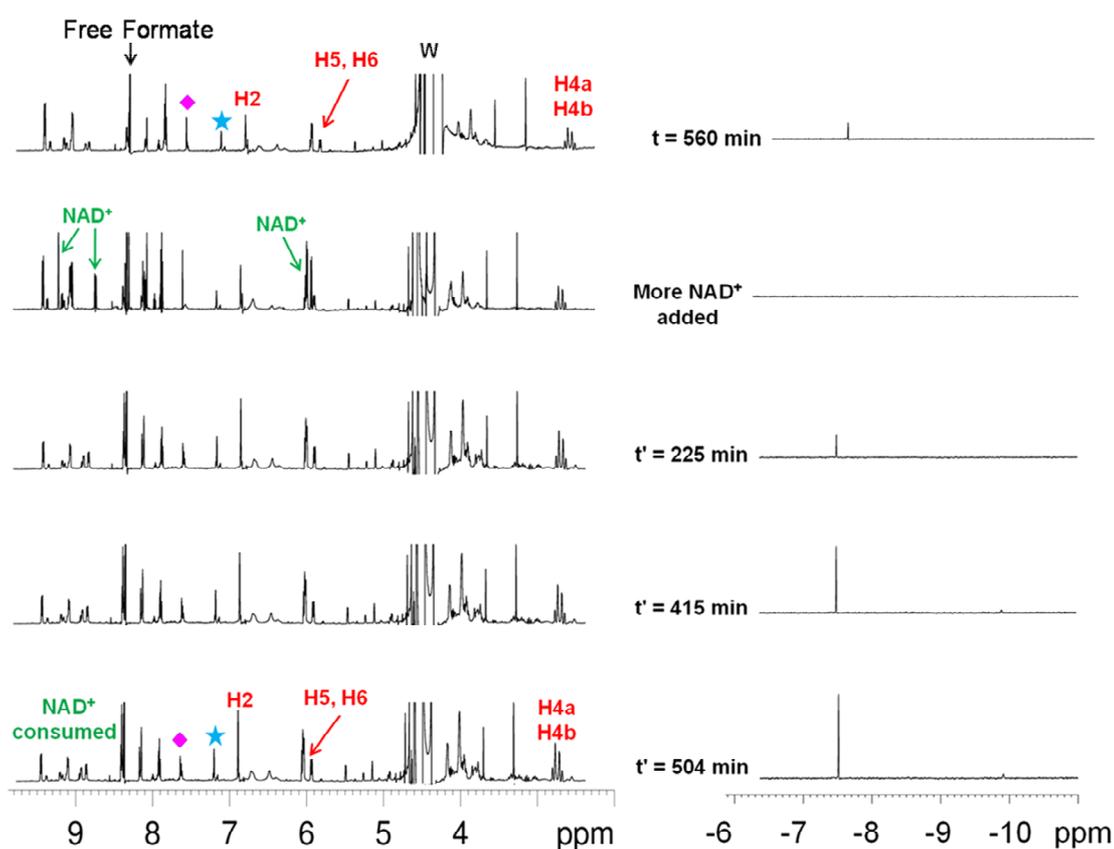
Figure 5.16. ^{1}H NMR spectra recorded during the reaction of a 300 mM solution (90% H$_2$O/10% D$_2$O) of [(η^6-hmb)Ru(bpm)Cl]$^+$ (**3**) in the presence of NaHCO$_2$ and NAD$^+$ (molar ratios 1:25:1, respectively) at 310 K and pH* $\approx$ 5.2. A second mol equiv was added after 560 min of reaction. ♦ **Pink** = [(η^6-hmb)Ru(bpm)(O$_2$CH)]$^+$; ★ = 1,6-NADH. **NAD$^+$** is indicated in **dark green** and **1,4-NADH** in **red**.

As the reaction progressed, an increase on the 1,4-NADH signals and a subsequent decrease in the intensity of those for NAD$^+$ was observed; simultaneously, the signals

of Ru–H species were restored. A decrease in the intensity of the formate adduct signals $[(\eta^6\text{-hmb})Ru(bpm)(O_2CH)]^+$ following the addition of extra amounts of NAD$^+$ was also detected. No changes on the amount of 1,6-NADH were observed.

Around t' = 504 min (after the addition of extra NAD$^+$), the second mol equiv of NAD$^+$ was again fully consumed. The Ru−H signal at −7.49 ppm was restored and reached again a maximum intensity, whereupon it began to decrease and ultimately disappeared (t' = 924 min).The decay in the intensity of this Ru−H signal seems to be accompanied by a simultaneous and fast decrease in intensity of all the signals initially assigned to the Ru^{II} arene species present in solution and of those of 1,4- and 1,6-NADH, Figure 5.17.
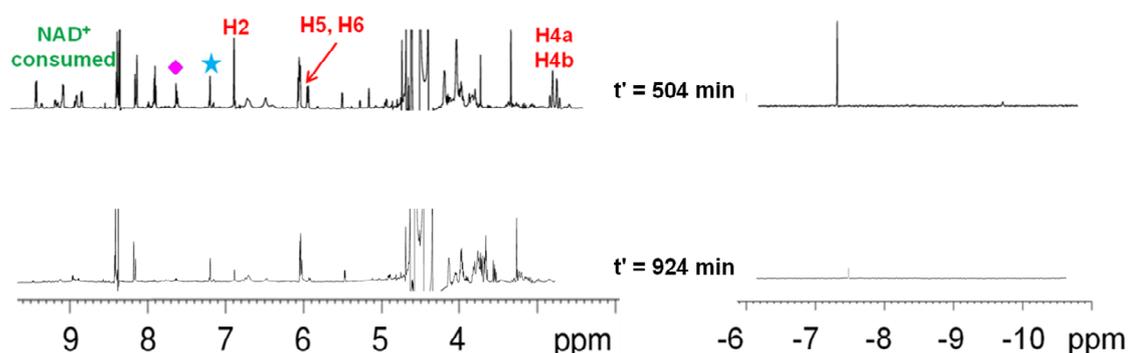
Figure 5.17. ^{1}H NMR spectra recorded *ca*. 924 min after a second mol equiv of NAD$^+$ was added to the reaction of a 300 mM solution (90% H$_2$O/10% D$_2$O) of $[(\eta^6\text{-}$hmb)Ru(bpm)Cl]$^+$ (**3**) in the presence of NaHCO$_2$ and NAD$^+$ (initial molar ratios 1:25:1, respectively) at 310 K and pH* ≈ 5.2. ♦ **Pink** = $[(\eta^6\text{-hmb})Ru(bpm)(O_2CH)]^+$; ★= 1,6-NADH. **NAD$^+$** is indicated in **dark green** and **1,4-NADH** in **red**.

Complex $[(\eta^6\text{-ind})Ru(bpm)Cl]^+$ (**4**) was also found to catalyse the reduction reaction of NAD$^+$ to 1,4-NADH (as observed by ^{1}H NMR spectroscopy) in a similar fashion to complex **3** under the same conditions (310 K and pH* ≈ 5.2). Complexes $[(\eta^6\text{-}p\text{-}$cym)Ru(bpm)Cl]$^+$ (**2**) and $[(\eta^6\text{-thn})Ru(bpm)Cl]^+$ (**9**) did not catalyse the hydride-transfer reaction under these conditions.

5.3.7 Regioselective Reduction of NAD$^+$ by Ru^{II} Arene Complexes in the Presence of Formate upon UVA Photoirradiation

Complex $[(\eta^6\text{-hmb})Ru(bpm)(Py)]^{2+}$ (**13**), Figure 5.18 was selected to explore the possibility of phototriggering the regioselective reduction of NAD$^+$ to 1,4-NADH in the presence of sodium formate. By fast-activating the Ru^{II} arene pyridine complex **13** in aqueous solution with UVA photoirradiation ($\lambda_{irr} = 300-400$ nm), the formation of a reactive aqua species can be achieved in a relatively short period of time (see Chapter 4). If the reaction is performed in the presence of sodium formate (25 mol equiv), a stable formate adduct is formed (*vide supra*). UVA photoirradiation was selected over visible light because the photolysis process of this family of complexes has been shown to be much more efficient than when visible light is employed (see Chapter 4). The interactions were studied by means of multidimensional ^{1}H NMR spectroscopy.

13
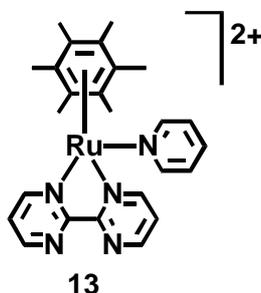
Figure 5.18. Structure of the dicationic complex studied in this section synthesised as PF$_6$ salt.

All the reactions were carried out in an NMR tube in a 90% H$_2$O/10% D$_2$O solution and followed at different stages of photoirradiation with UVA ($\lambda_{irr} = 300-400$ nm) at 310 K. The initial pH* of the solution (prior to the addition of NAD$^+$) was 7.6; once NAD$^+$ was added a decrease to 5.8 was registered. Figure 5.19 shows the progress of the reaction for complex **13** within the first 330 min of photoirradiation. As it has been herein described (*vide supra* and also in Chapter 4), the spectra initially

contained a set of peaks assigned to the original Ru−Py complex, [(η^6-hmb)Ru(bpm)(Py)]^{2+} (**13**). Further photoirradiation with UVA at 310 K produces a second set of peaks which increased in intensity as photoirradiation was continued and are assigned to the corresponding aqua species [(η^6-hmb)Ru(bpm)(OH_2)]^{2+} (along with the peaks assigned to the released Py ligand). An additional set of peaks increased in intensity just after the first indication of aqua adduct being formed was detected; this new set of peaks corresponds to the formation of the formate adduct [(η^6-hmb)Ru(bpm)(O_2CH)]^{+}. The ^1H NMR signals of this formate adduct have the same chemical shift as those observed when the Ru^{II} arene chlorido complex **3** was used as the starting material (since it is the same species).
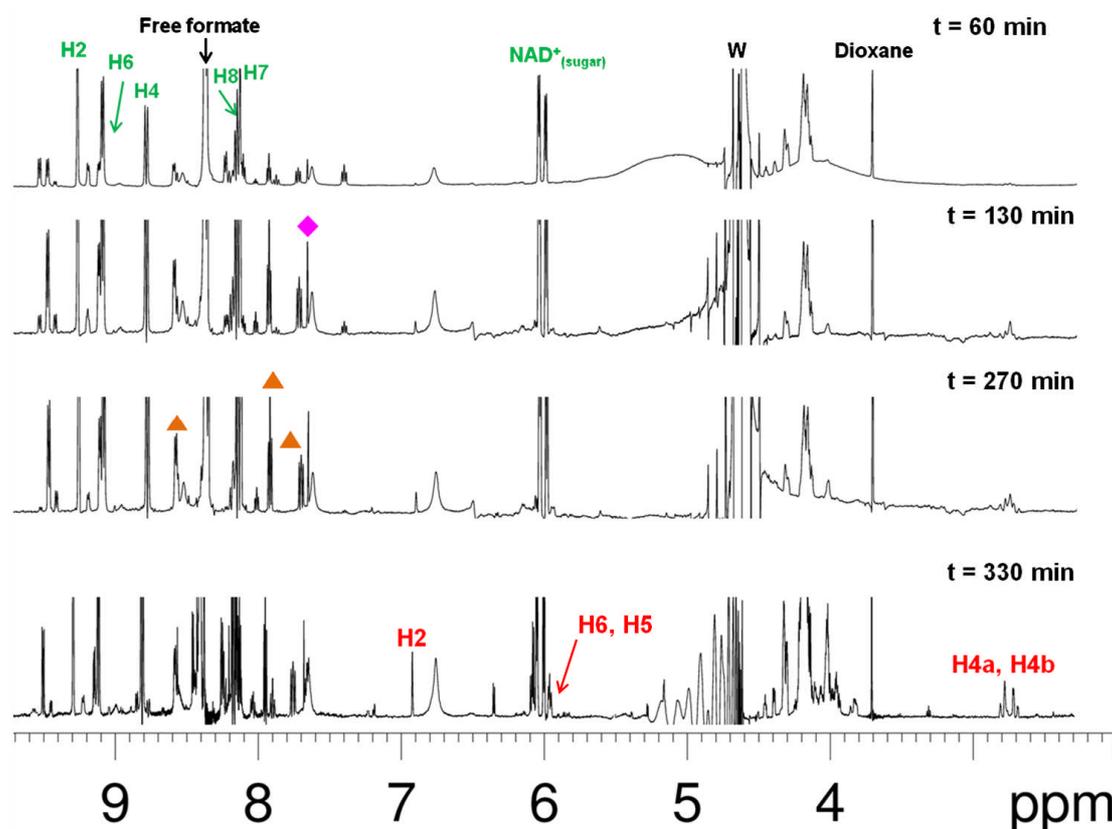
Figure 5.19. ^1H NMR spectra recorded during the aqueous photolysis (λ_{irr} = 300–400 nm) of a 300 mM solution (90% H_2O/10% D_2O) of [(η^6-hmb)Ru(bpm)(Py)]^{2+} (**13**) in the presence of NaHCO_2 and NAD^+ (molar ratios 1:25:1, respectively) at 310 K and pH* ≈ 5.8. ♦ **Pink** = [(η^6-hmb)Ru(bpm)(O_2CH)]^{+}. Free Py is indicated with **Orange** ▲. **NAD^+** is indicated in **dark green** and **1,4-NADH** in **red.**

An overall of *ca.* 300 min of photoirradiation with UVA (λ_{irr} = 300–400 nm) were needed to achieve full conversion of the original Py compound to the corresponding aqua adduct. During the first *ca.* 130 min of photoirradiation with UVA (λ_{irr} = 300−400 nm) some additional (simultaneous) changes in the ^{1}H NMR spectrum were noticed. These changes resemble to those observed for the reaction of the chlorido complex [(η^6-hmb)Ru(bpm)Cl]$^+$ (**3**) with NAD$^+$ after *ca.* 300 min. The changes point again to the relatively fast reduction of NAD$^+$ to 1,4-NADH, as indicated by a decrease in the intensity of the signals corresponding to free NAD$^+$ and the new peaks assignable to 1,4-NADH. The overall changes in the ^{1}H NMR spectra indicate that although the initial amount of NAD$^+$ is not fully consumed in this case (as opposed to the chlorido analogue), the reaction to generate 1,4-NADH is relatively faster. Furthermore, when a control solution of the pyridine Ru^{II} arene complex, NAD$^+$ and formate under the same conditions was kept in the dark (as a control), no reaction was observed. After *ca.* 300 min, the photoirradiation was suspended and the mixture was allowed to further react in the dark at 310 K. The resulting spectrum is shown in Figure 5.20. Within the next 300 min (and overall reaction time of *ca.* 660 min) the appearance of multiple low-intensity signals in the aromatic region was detected. The ^{1}H NMR spectra suggest again 1,6-NADH formation (as was also observed for the chlorido complexes **3** and **4**) but no evidence of Ru–H species (i.e. signals in the high field region of the spectrum) was detected over this period.
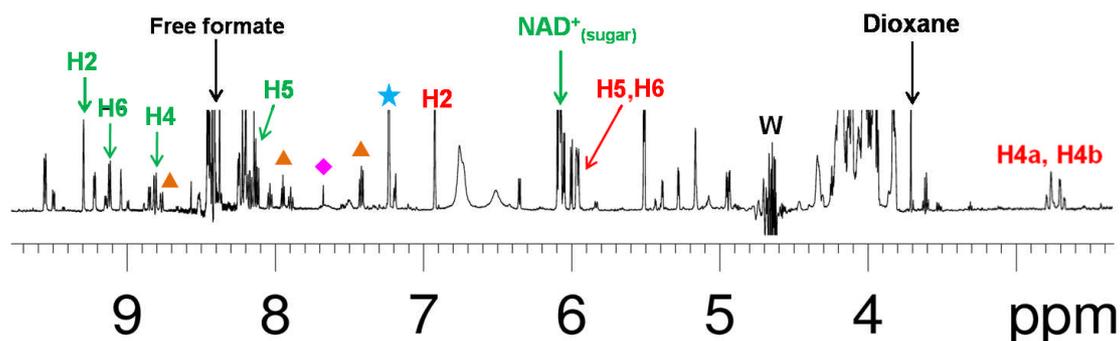
Figure 5.20. ^{1}H NMR spectra recorded *ca.* 660 min after aqueous photolysis (λ_{irr} = 300–400 nm and 330 min of photoirradiation) of a 300 mM solution (90% H$_2$O/10% D$_2$O) of [(η^6-hmb)Ru(bpm)(Py)]$^{2+}$ (**13**) in the presence of NaHCO$_2$ and NAD$^+$ (molar ratios 1:25:1, respectively) at 310 K and pH* ≈ 5.8. ♦ **Pink** = [(η^6-hmb)Ru(bpm)(O$_2$CH)]$^+$; ★ = 1,6-NADH. Free Py is indicated with **Orange ▲**. **NAD$^+$** is indicated in **dark green** and **1,4-NADH** in **red.**

5.3.8 Interactions of Ru^{II} Arene Complexes with 1,4-NADH

In order to explore the possibility of a hydride-transfer reaction from 1,4-NADH to selected Ru^{II} arene chlorido complexes, an equimolar amount of 1,4-NADH was added to an NMR tube containing a 300 mM solution of the halido Ru^{II} arene complexes **1**, **2**, **3**, and **9** in 90% H$_2$O/10% D$_2$O at room temperature. The pH* of the solutions prior to the addition of 1,4-NADH was 6.8–7.1; once added, the pH* of the solutions increased to 8.5–9.1. The ^{1}H NMR spectra of the resulting solutions were recorded at 310 K at various time intervals during 12 h. Figure 5.21 shows the progress of the reaction for complex **3** after 270 min. The appearance of a high-intensity sharp singlet in the high-field region of the spectrum (–7.44 ppm) within the first 15 min of reaction was noticed. It suggests that a fast hydride-transfer reaction from 1,4-NADH to the Ru^{II} arene complex **3** to generate a Ru–H species could be taking place. In the low-field region of the spectrum of [(η^6-hmb)Ru(bpm)Cl]$^+$ (**3**), the appearance of a new set of signals was also detected during the first 15 min of reaction. The new set of peaks is attributable to the formation of NAD$^+$ whose increasing concentration seems to be related to the decrease in intensity of the signals

of 1,4-NADH and the complete disappearance of the Ru–H signal after 270 min. During the course of the reaction, a slight decrease in the intensity of the signals for the corresponding aqua adducts of complexes **1**, **2**, **3**, and **9** was recorded. No further changes were observed after 12 h. Table 5.8 lists the time when the maximum intensity for the corresponding Ru–H species of the Ru^{II} arene complexes **1**, **2**, **3**, and **9** were detected as well as the chemical shift of the corresponding hydride peaks.
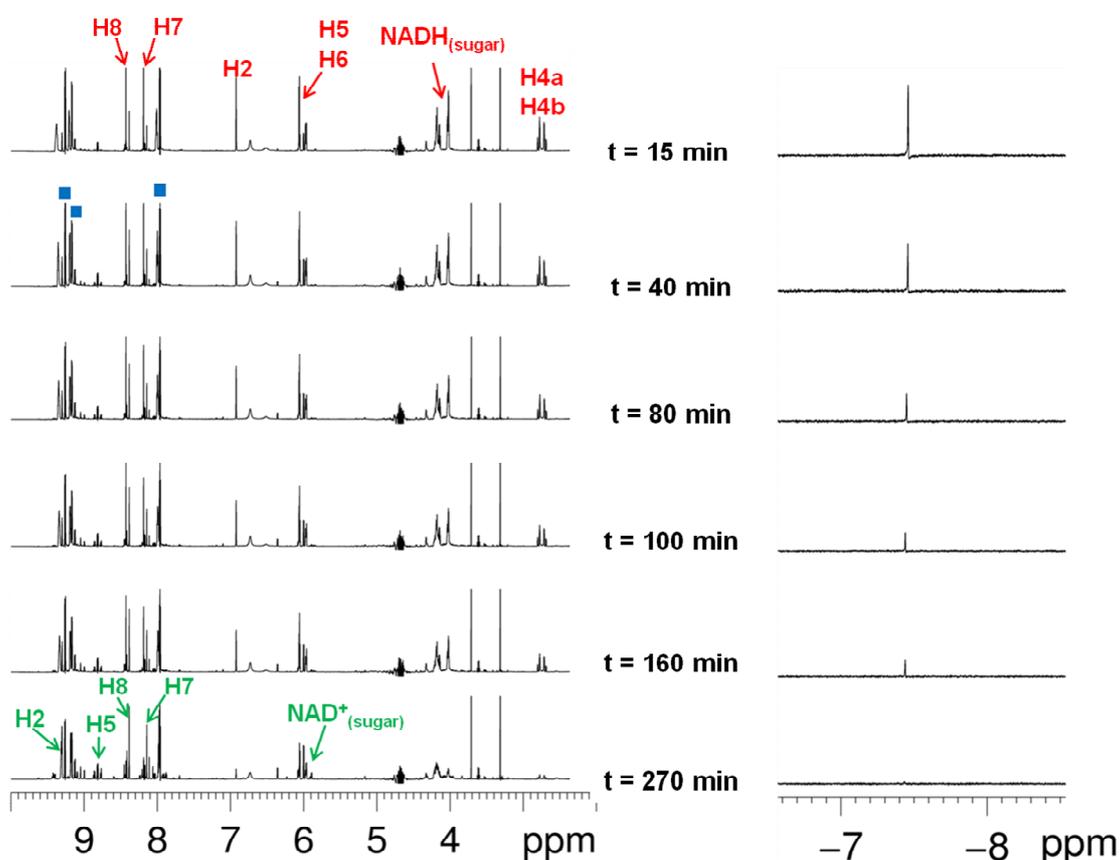
Figure 5.21. ^{1}H NMR spectra of a 300 mM solution (90% H$_2$O/10% D$_2$O) of [(η^6-hmb)Ru(bpm)Cl]$^+$ (**3**) with 1,4-NADH (molar ratios 1:1) at 310 K and pH* ≈ 8.7. **Blue** = [(η^6-hmb)Ru(bpm)(OH$_2$)]$^{2+}$; ■ = bpm. **NAD$^+$** is indicated in **dark green** and **1,4-NADH** in **red**.

Table 5.8. Time of detection (min) and chemical shift (ppm) of the signal associated with Ru–H species generated from the reaction of a 300 mM solution (90% H$_2$O/10% D$_2$O) of the [(η^6-arene)Ru(N,N')Cl]$^+$ complexes **1**, **2**, **3**, and **9** with 1,4-NADH (molar ratios 1:1) at 310 K and pH* ≈ 8.5–9.1.

Compound	Time (min)	Chemical shift (ppm)
(**1**) [(η^6-*p*-cym)Ru(bpm)Cl]$^+$	31	–6.13
(**2**) [(η^6-*p*-cym)Ru(phen)Cl]$^+$	34	–6.21
(**3**) [(η^6-hmb)Ru(bpm)Cl]$^+$	15	–7.44
(**9**) [(η^6-thn)Ru(bpm)Cl]$^+$	22	–6.61

5.3.9 Interactions of Ru^{II} Arene Complexes with 1,4-NADH upon UVA Photoirradiation

In order to explore the possibility of phototriggering the hydride-transfer from 1,4-NADH to a photoactivatable Ru^{II} arene pyridine complex with UVA photoirradiation (λ_{irr} = 300–400 nm) in aqueous solution, an equimolar amount of 1,4-NADH was added to an NMR tube containing a 300 mM solution of the Ru^{II} arene pyridine complex **13** in 90% H$_2$O/10% D$_2$O at room temperature. It was noticed that if the initial solution was placed under an UVA lamp, it emitted an intense blue colour which disappeared upon photoirradiation, Figure 5.22.
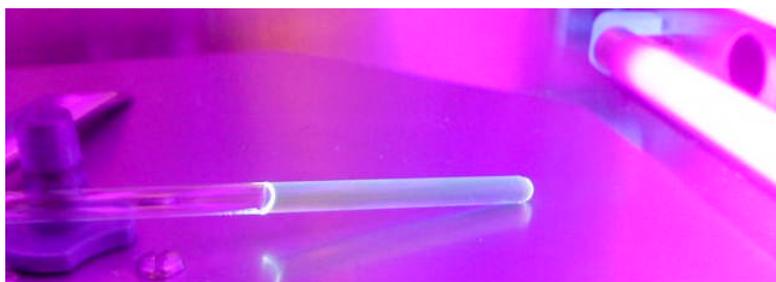
Figure 5.22. Blue-coloured emission of a 300 mM solution (90% H$_2$O/10% D$_2$O) of [(η^6-hmb)Ru(bpm)(Py)]$^{2+}$ (**13**) in the presence of 1,4-NADH (molar ratios 1:1) at 310 K and pH* ≈ 8.5 upon UVA photoirradiation (λ_{irr} = 300−400 nm).

The ^{1}H NMR spectra of the resulting solution were recorded at 310 K at various time intervals for 24 h. Figure 5.23 shows the progress of the reaction during the first 330 min. The spectra initially contained a set of peaks assigned to the original Ru−Py

complex, $[(\eta^6\text{-hmb})Ru(bpm)(Py)]^{2+}$ (**13**). Further photoirradiation with UVA (λ_{irr} = 300−400 nm) at 310 K produces a second set of peaks which increase in intensity as photoirradiation is maintained and are assigned to the correspondent aqua species $[(\eta^6\text{-hmb})Ru(bpm)(OH_2)]^{2+}$ (along with the peaks assigned to the released Py ligand) as it had been previously observed for this system (*vide supra* and within Chapter 4). During the first 120 min of photoirradiation with UVA some additional changes in the ^{1}H NMR spectrum were noticed. These changes point to the fast oxidation of 1,4-NADH to NAD$^+$, as indicated by a decrease in the intensity of the signals of free 1,4-NADH and the new peaks assignable to NAD$^+$.
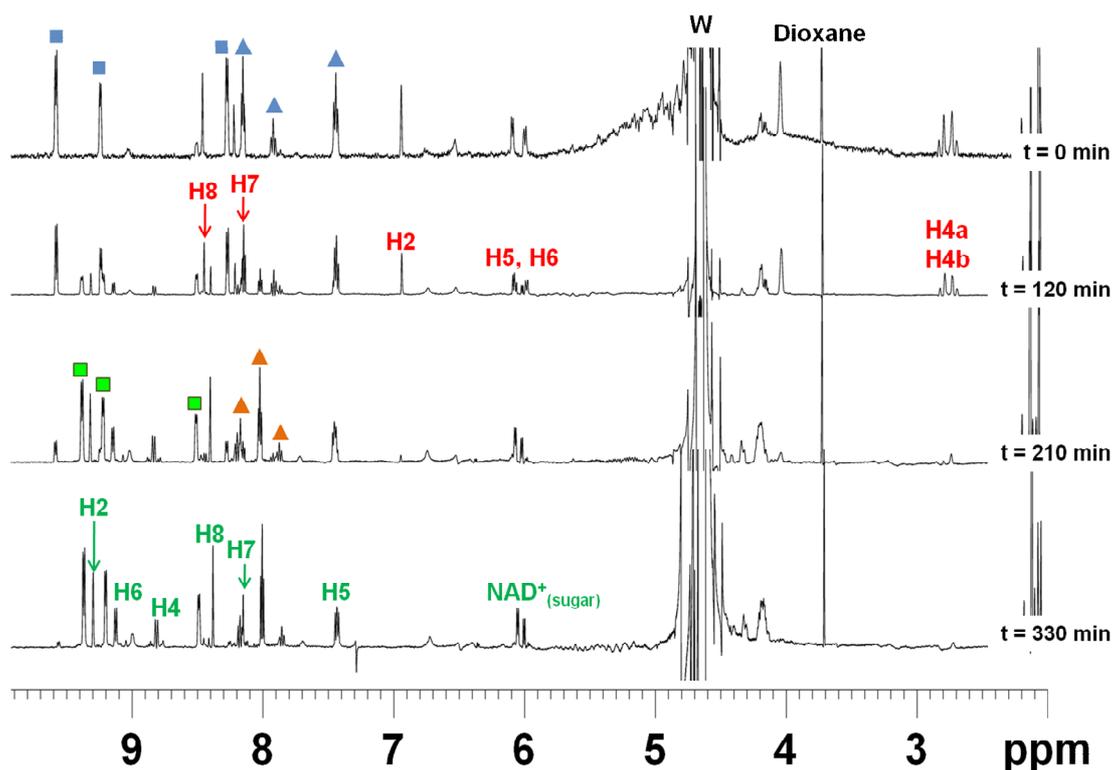
Figure 5.23. ^{1}H NMR spectra during the aqueous photolysis (λ_{irr} = 300–400 nm) of a 300 mM solution (90% H$_2$O/10% D$_2$O) of $[(\eta^6\text{-hmb})Ru(bpm)(Py)]^{2+}$ (**13**) in the presence of 1,4-NADH (molar ratios 1:1) at 310 K and pH* ≈ 8.5. **Blue** = $[(\eta^6\text{-hmb})Ru(bpm)Cl]^+$; **Bright Green** = $[(\eta^6\text{-hmb})Ru(bpm)(OH_2)]^{2+}$; ■ = bpm. Free Py is indicated with **Orange ▲**. **NAD$^+$** is indicated in **dark green** and **1,4-NADH** in **red**.

The overall changes in the ^{1}H NMR spectra indicate that the initial amount of 1,4-NADH is fully consumed to generate NAD$^+$ after *ca.* 330 min of photoirradiation. No changes in the amount of [(η^6-hmb)Ru(bpm)(OH$_2$)]$^{2+}$ initially generated by photoirradiation with UVA (λ_{irr} = 300−400 nm) were observed, nor the formation of Ru–H peaks in the high-field region of the spectrum. When a control mixture of the Ru^{II} arene pyridine complex **13** and 1,4-NADH under the same conditions was kept in the dark, no reaction was observed.

5.3.10 Qualitative Studies of 1,4-NADH with UVA Photoirradiation

In order to explore the qualitative photochemistry of 1,4-NADH, a 100 μM aqueous solution of 1,4-NADH was irradiated with UVA (λ_{irr} = 300−400 nm) during *ca.* 330 min at 310 K. The photoreaction was followed by UV-vis spectroscopy at different stages of photoirradiation. The resulting absorption spectrum is shown in Figure 5.24.
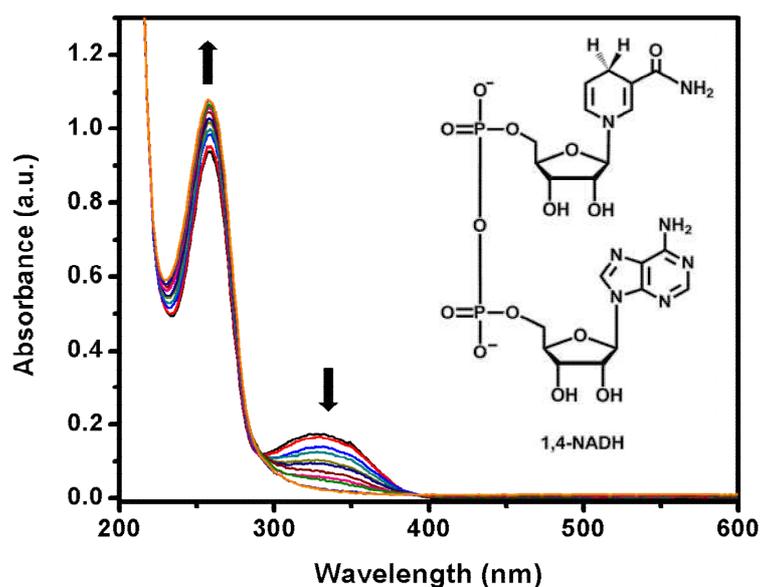
Figure 5.24. UV-vis absorption spectrum of the aqueous photolysis (λ_{irr} = 300–400 nm) of 1,4-NADH in aqueous solution (100 μM) at 310 K.

Photoirradiation of 1,4-NADH with UVA (λ_{irr} = 300–400 nm) produces noticeable changes in the shape of its UV-vis absorption spectrum. An important decrease on the 340 nm absorption band occurs simultaneously with an increase on the 260 nm high-energy band.

5.4 Discussion

5.4.1 Interactions of Ru^{II} Arene Complexes with Sodium Formate (NaHCO$_2$), NAD$^+$ and 1,4-NADH

The interaction of Ru^{II} arene chlorido complexes with an excess of sodium formate in aqueous solution at 310 K, showed that a very stable formate adduct can be formed. This adduct (Ru–O$_2$CH) is generated by the direct binding of formate to the Ru^{II} centre in the reactive aqua species (Ru–OH$_2$) formed *in situ via* the Ru–Cl bond hydrolysis (in complexes **1**, **2**, **3**, **4**, and **9**). This reactive aqua species presumably binds to the negatively charged oxygen in the carboxylate moiety (as has been previously suggested for similar formate and other carboxylate metal complexes).[11,24] The binding of formate to the Ru^{II} centre in these complexes was confirmed by the appearance of a sharp singlet at 7.66 ppm in the ^{1}H NMR spectrum (high-field shifted compared to free formate at 8.40 ppm under the same conditions; 310 K and pH* ≈ 6.9–7.2). This shifting has been previously observed for analogous Ru^{II} arene formato and acetato complexes[24,25,26] and could be attributed to the shielding effect exerted on the proton in the formato ligand upon coordination (of the carboxylate oxygen) to the metal centre. The formato complex [(η^6-*p*-cym)Ru(bpm)(O$_2$CH)]$^+$ (**16**) was synthesised, isolated and characterised; it was found to display a half-life of hydrolysis of 45 min to a relatively high extent (68.2%). As could be expected, no

hydrolysis reaction for complex **16** was observed in aqueous solution when an excess of formate (25 mol equiv) is also present in the solution. The Ru–O$_2$CH adducts of all of the complexes studied here, did not catalyse the reduction of the organic substrate acetone (10 mol equiv) at 310 K and pH* ≈ 6.9–7.2, suggesting that they display a high stability and inertness towards hydride-transfer to acetone under the experimental conditions tested. Previous studies have also demonstrated the occurrence of stable Ru^{II} arene formato complexes in solution and in the solid state[7,27] as well as non-arene octahedral Ru^{II} formato complexes.[28] Furthermore, the pH dependence of the catalytic activity towards reduction of aromatic ketones of analogous Ru^{II} arene complexes has been studied.[22] The optimum pH conditions were found to be *ca*. 4, which is close to the pK$_a$ of formic acid (3.77; at this pH value, formic acid and formate are in 1:1 equilibrium). Surprisingly, the conversion of NAD$^+$ into 1,4-NADH catalysed by the Ru^{II} arene complexes in the presence of sodium formate (25 mol equiv) in aqueous solution at 310 K was observed. The evidence suggests that a hydride-transfer reaction by the Ru^{II} arene formato complexes of **3** and **4**, occurs *via* the proposed mechanism (based in previously published work)[29,31,21] shown in Figure 5.25. The first step of the reaction shown in Figure 5.25(**A**), proceeds *via* the hydrolysis of the corresponding Ru–Cl bonds in complexes **3** and **4**, followed by a rapid binding of formate to the Ru^{II} centre in the Ru–OH$_2$ species. The binding generates remarkably stable Ru–O$_2$CH adducts (at pH* values *ca*. 7), Figure 5.25(**B**). When NAD$^+$ is added and the pH* value of the solution drops (to more acidic conditions), the following step in the reaction is believed to involve a β-hydrogen elimination.

This process is thought to proceed *via* ring-slippage of the arene (hmb in complex **3** and ind in complex **4**) characterised by a change from η^6- to η^4- coordination, as has been previously proposed for analogous complexes,[29] Figure 5.25(**C**).
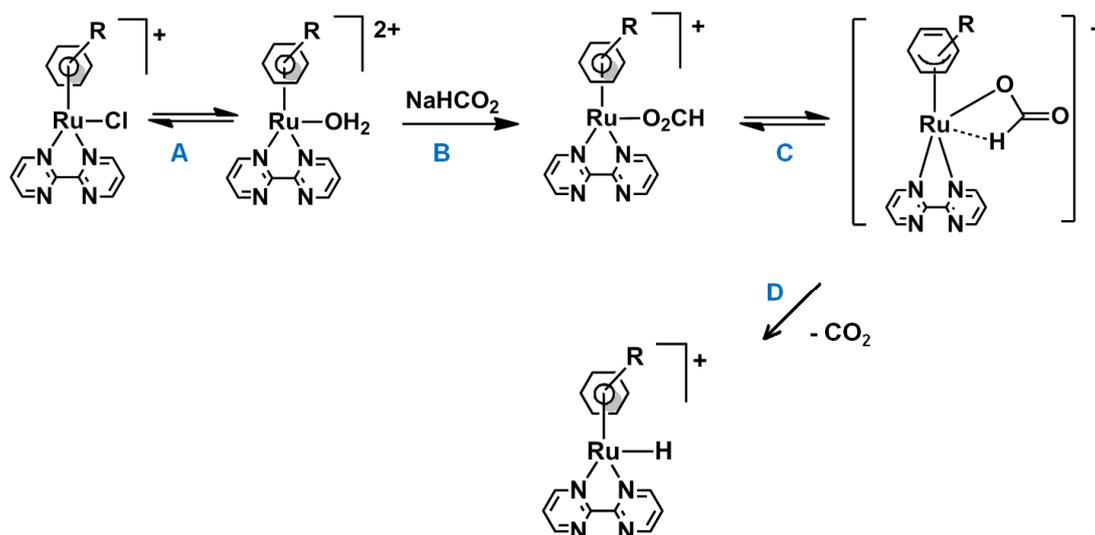
Figure 5.25. Proposed mechanism for the hydride-transfer reaction from HCO$_2$ to the Ru^{II} arene complexes [(η^6-hmb)Ru(bpm)Cl]$^+$ (**3**) and [(η^6-ind)Ru(bpm)Cl]$^+$ (**4**) *via* a ring slippage process. R represents hmb (**3**) or ind (**4**).

The final products in this step are the corresponding Ru–H species and CO$_2$, Figure 5.25(**D**). The formation of the Ru−H species is characterised by the appearance of sharp singlets in the high-field region of the ^{1}H NMR spectrum (between –7 and –8 ppm) as it has been observed in similar Ru^{II} arene hydride species.[19,30] The release of CO$_2$ could also be contributing to the observed decrease in pH*. The fact that the formation of the corresponding Ru–H species occurs after more than 11 h of reaction at 310 K for complexes **3** and **4** but not at all for the other Ru^{II} arene complexes [(η^6-*p*-cym)Ru(bpm)Cl]$^+$ (**2**) and [(η^6-thn)Ru(bpm)Cl]$^+$ (**9**), suggests that the hydride-transfer from formate to the Ru^{II} centre might be the slow rate-determining step. It is also believed that the hydride-transfer is highly dependent on the nature of the arene, being most facile with the relatively strongest electron-donor arenes (such as hmb and

ind). However, it is not clear at present whether this effect is mainly steric or electronic in nature, or both. The hypothesis on the rate-determining step has been tested previously[19] and the results of the experiments showed in the first place, that when NaHCO$_2$ was replaced by NaDCO$_2$ in the reaction of NAD$^+$ and the analogous Ru^{II} arene complex [(η^6-hmb)Ru(en)Cl]$^+$, a pronounced kinetic isotope effect was observed. Secondly, the turnover frequency of the reaction decreased in the order hmb > ind ≈ *p*-cym. Furthermore, in the Ru^{II} arene system herein studied, it was observed that once the corresponding Ru–H species are formed (after more than 11 h) then a fast hydride-transfer to NAD$^+$ takes place, until it is fully consumed. A plausible mechanism for the regioselective reduction of NAD$^+$ to 1,4-NADH has been previously suggested[29,31] for NAD$^+$-models. Based on those results, a proposed mechanism for the Ru^{II} arene complexes described herein is shown in Figure 5.26. It is believed that the amide functionality in NAD$^+$ could coordinate to the Ru^{II} arene complex,[18,31] Figure 5.26(**E**) through an open coordination site made available by the well documented ring-slippage mechanism[29,34] (also proposed for the hydride-transfer from formate to the Ru^{II} centre, Figure 5.25(**C**) or 5.26(**C**) *vide supra*). This mechanism includes the formation of a kinetically-favoured six-membered ring transition state. It is suggested that this intermediate further provides the driving force for the regioselective hydride-transfer at C4 of NAD$^+$, Figure 5.26(**F**); by an induced electronic effect of the bound carbonyl group, the C4 position might become a more electrophilic site towards hydride-transfer. This step also includes the reversion of the η^4- to η^6- coordination of the arene (hmb in **3** or ind in **4**), along with binding and hydride-transfer[31] or concerted binding with hydride-transfer.
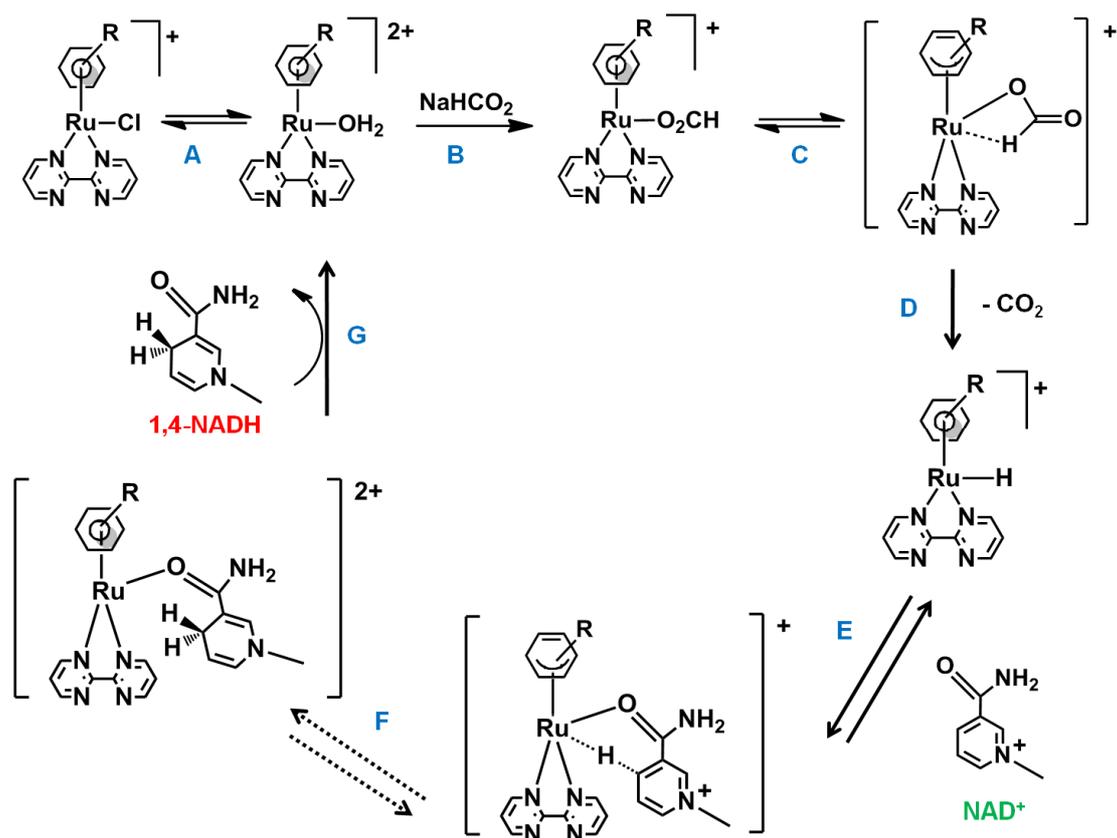
Figure 5.26. Proposed mechanism for the regioselective reduction of NAD$^+$ to 1,4-NADH by the Ru^{II} arene complexes [(η^6-hmb)Ru(bpm)Cl]$^+$ (**3**) and [(η^6-ind)Ru(bpm)Cl]$^+$ (**4**). R represents hmb (**3**) or ind (**4**).

It should also be noted that hydride-transfer (step **E** to **F** in Figure 5.26), could be a reversible process (*vide infra*). Finally, displacement of the 1,4-dihydro product by a H$_2$O molecule recycles the Ru^{II} arene aqua species completing the catalytic cycle, Figure 5.26(**G**). In the reduction process herein studied, 1,4-NADH is the major product of the reaction (especially at early stages), though the presence of 1,6-NADH was also detected by ^{1}H NMR (mainly towards the end of the reaction). This observation is in good agreement with a recent report that the kinetic product from the reduction of the NAD$^+$-model (1-benzylnicotinamide triflate) is the 1,4- rather than the 1,6-dihydro isomer.[18,29,31] This reduction is believed to occur *via* the rearrangement of the 1,4-dihydro isomer formed from the catalysed reduction of NAD$^+$ by the Rh^{III} complex [(Cp*)Rh(bpy)(OH$_2$)]$^{2+}$ where Cp* is

pentamethylcyclopentadienyl and bpy is 2,2'-bipyridine.[29,31] This rational could also be applied to explain the formation of 1,6-NADH in the case of the catalytic reduction of NAD$^+$ by the Ru^{II} arene systems herein discussed. On the other hand, if more NAD$^+$ is introduced into the Ru^{II} arene catalytic system, the cycle is restarted and then accumulation of 1,4-NADH is again observed (along with the regeneration of the signal for the Ru–H species of complexes **3** and **4** in the negative region of the ^{1}H NMR spectrum). In order to prove the feasibility of the occurrence of the reverse reaction in Figure 5.26 steps **E** to **F**, a separate experiment was performed. The interaction of the Ru^{II} arene complexes [(η^6-*p*-cym)Ru(bpm)Cl]$^+$ (**1**), [(η^6-*p*-cym)Ru(phen)Cl]$^+$ (**2**), [(η^6-hmb)Ru(bpm)Cl]$^+$ (**3**) or [(η^6-thn)Ru(bpm)Cl]$^+$ (**9**) with 1,4-NADH at 310 K and initial pH* $\approx$ 6.9–7.2 was followed by ^{1}H NMR spectroscopy. The ^{1}H NMR spectra of the reaction suggest that 1,4-NADH could be transferring a hydride anion to the corresponding Ru–OH$_2$ adducts (formed *in situ* by hydrolysis of the corresponding Ru–Cl bonds) to generate a detectable Ru–H species (sharp singlet between –6.10 and –7.50 ppm) and the observed accumulation of NAD$^+$. Reported examples of hydride-transfer from 1,4-NADH (as the hydride source) to metal complexes are (to the best of my knowledge) not known. The hydride-transfer from porphyrin NADH-analogues to a manganese^{IV}-oxo complex, [(TMP)Mn^{IV}(O)] where TMP = 5,10,15,20-tetrakis(2,4,6-trimethylphenyl) porphyrin, has been reported[32] and it was found to occur *via* disproportionation of [(TMP)Mn^{IV}(O)] to [(TMP)Mn^{III}]$^+$ and [(TMP)Mn^{V}(O)]$^+$ that acts as the hydride acceptor. Others have investigated the non-enzymatic oxidation of NADH by a large number of different quinones both theoretically and experimentally.[33] It was concluded that the smaller benzo- and naphtha-quinones are capable of oxidising NADH in aqueous solution, whereas the larger anthraquinone is not. The plausible

mechanisms for the oxidative conversion of 1,4-NADH to NAD$^+$ observed in the case

of the Ru^{II} hydride complexes studied herein might proceed according to the proposed

hydride-transfer scheme shown in Figure 5.27. The first step of the reaction shown in

Figure 5.27(**A**), proceeds *via* the hydrolysis of the corresponding Ru–Cl bonds,

followed by the plausible coordination of the amide functionality in 1,4-NADH to the

Ru^{II} arene complexes, most probably through direct displacement of the bound water

molecule, Figure 5.27(**B**).
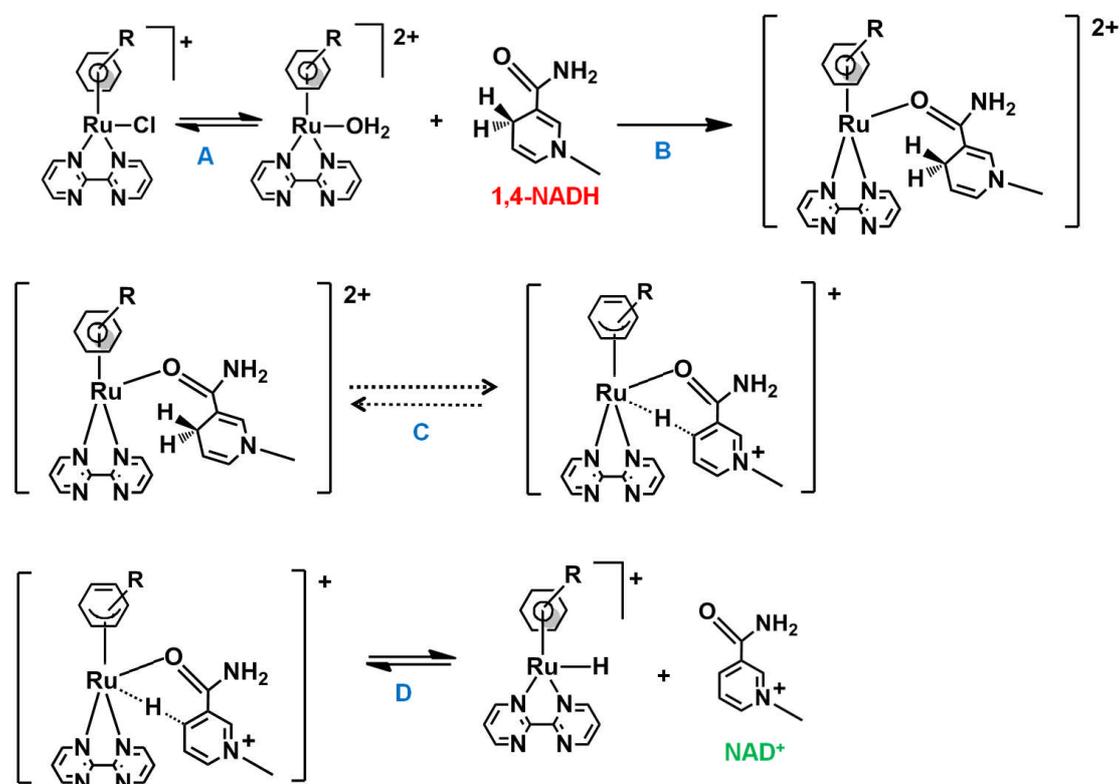
Figure 5.27. Proposed mechanism for the hydride-transfer reaction of 1,4-NADH to [(η^6-hmb)Ru(bpm)Cl]$^+$ (**3**).

The next step would involve the direct hydride-transfer from 1,4-NADH to the Ru^{II}

arene complex *via* the formation of the kinetically-favoured six-membered ring

transition state, Figure 5.27(**C**) (analogous to the one shown in Figure 5.26(**E**))

through a vacant coordination site which becomes available by the same ring-slippage

mechanism[29,34] (previously suggested *vide supra*). This step includes the reversion of the η^4- to η^6- coordination of the arene (*p*-cym in **1** and **2**, hmb in **3**, or thn in **9**), and finally the release of the NAD$^+$ product and generation of the Ru^{II} hydride species, Figure 5.27(**D**). The results of these experiments confirm that 1,4-NADH can indeed transfer a hydride anion to Ru^{II} arene complexes.

5.4.2 Interactions of Ru^{II} Arene Complexes with Sodium Formate (NaHCO$_2$), NAD$^+$ and 1,4-NADH upon UVA and Visible Light Photoirradiation

The reaction of the half-sandwich Ru^{II} arene pyridine complexes (**11**–**15**) with an excess of sodium formate (25 mol equiv) in aqueous solution at 310 K and pH* $\approx$ 6.8–7.1, showed that very stable Ru^{II} arene formate adducts (Ru–O$_2$CH) can be achieved exclusively upon photoirradiation with UVA (λ_{irr} = 300–400 nm) or visible (λ_{irr} = 400–660 nm) light. The corresponding adducts (Ru–O$_2$CH) are more quantitatively generated if UVA photoirradiation is used and they are not susceptible to photodecomposition. The binding of formate to the Ru^{II} centre thus generates identical species as those formed from the reaction of the Ru^{II} arene chlorido analogues. The corresponding Ru–O$_2$CH adducts formed in solution upon photoirradiation with UVA or visible light, display the same reactivity as those achieved by the direct reaction of the analogue chlorido species (*vide supra*), i.e. they did not catalyse the reduction of the organic substrate acetone (10 mol equiv) under the experimental conditions. The pH* value seems to be a determinant factor for the hydride-transfer to proceed (being optimal under acidic conditions, *vide supra*). As observed for the Ru^{II} chlorido analogues, the pyridine Ru^{II} arene complex [(η^6-hmb)Ru(bpm)(Py)]$^{2+}$ (**13**) was found to catalyse the conversion of NAD$^+$ into 1,4-NADH in aqueous solution at 310 K in the presence of an excess of sodium formate (molar ratios 1:1:25, respectively) exclusively upon photoirradiation with UVA (λ_{irr} =

300–400 nm) or visible light (λ_{irr} = 400–660 nm). When a control solution of the Ru^{II} arene pyridine complex **13**, along with NAD$^+$ and formate was kept in the dark, no reaction was observed. Figure 5.28 shows the proposed mechanism (based on published work[11,18,29,31] and on the results discussed above for the chlorido complexes; *vide supra*) for the phototriggered reduction of NAD$^+$ into 1,4-NADH catalysed by the Ru^{II} arene pyridine complex **13**. The first step in the regioselective reduction, involves the photolysis of the corresponding Ru–N$_{(Py)}$ bond in complex **13** (and the selective release of the Py ligand), Figure 5.28 (**A**) followed by an almost simultaneous binding of formate to the Ru^{II} centre in the Ru–OH$_2$ species formed *in situ* upon photoirradiation, Figure 5.28(**B**). The reduction reaction is assumed to proceed *via* the slow-rate hydride-transfer mechanism also proposed for the chlorido complexes **3** and **4** (*vide supra*, Figure 5.26). Two main differences between the Ru^{II} arene halido complexes (**3** and **4**) and the Ru^{II} arene pyridine complexes are observed. The first one is that the aqua adduct of these latter complexes is clearly achieved exclusively upon UVA or visible light photoirradiation. The second difference is that no Ru–H signal is detected despite the fact that the reduction to 1,4-NADH is indeed observed (by ^{1}H NMR spectroscopy). This could be due not only to the reduced generation of 1,4-NADH (which was proved to also contribute to the generation of Ru–H species, *vide supra*) but also due to the probable simultaneous photodegradation of 1,4-NADH to NAD$^+$ upon photoirradiation by UVA (λ_{irr} = 300–400 nm) as it has been recently suggested.[35] It is believed that NAD$^+$, adenosine 5'-diphosphoribose (ADPR) and a second compound, which may be nicotinamide (NA) are the photoproducts resulting from long-time exposures (2 days) of 1,4-NADH to UVA photoirradiation (λ_{irr} = 300–400 nm) in water and normal-atmosphere-oxygen conditions. In that report it was also observed that ADPR and NA emerge exclusively

in oxygen-poor conditions. Therefore, at higher oxygen concentrations and shorter photoirradiation periods (as the ones used for the Ru^{II} arene pyridine system), NAD$^+$ must be the only photoproduct although still as a minor species. Further evidence to support this hypothesis was obtained from the reaction of the Ru^{II} arene pyridine complex **13** with 1,4-NADH under UVA light photoirradiation, where the only photoproducts present in solution at the end of the reaction (after 330 min of photoirradiation) were found to be the Ru–OH$_2$ species, free Py, and NAD$^+$ (and no evidence of generation of Ru–H species). The observed loss of the intrinsic photoemission of 1,4-NADH whilst converted to NAD$^+$ upon photoirradiation is in good agreement with the reaction mechanism.
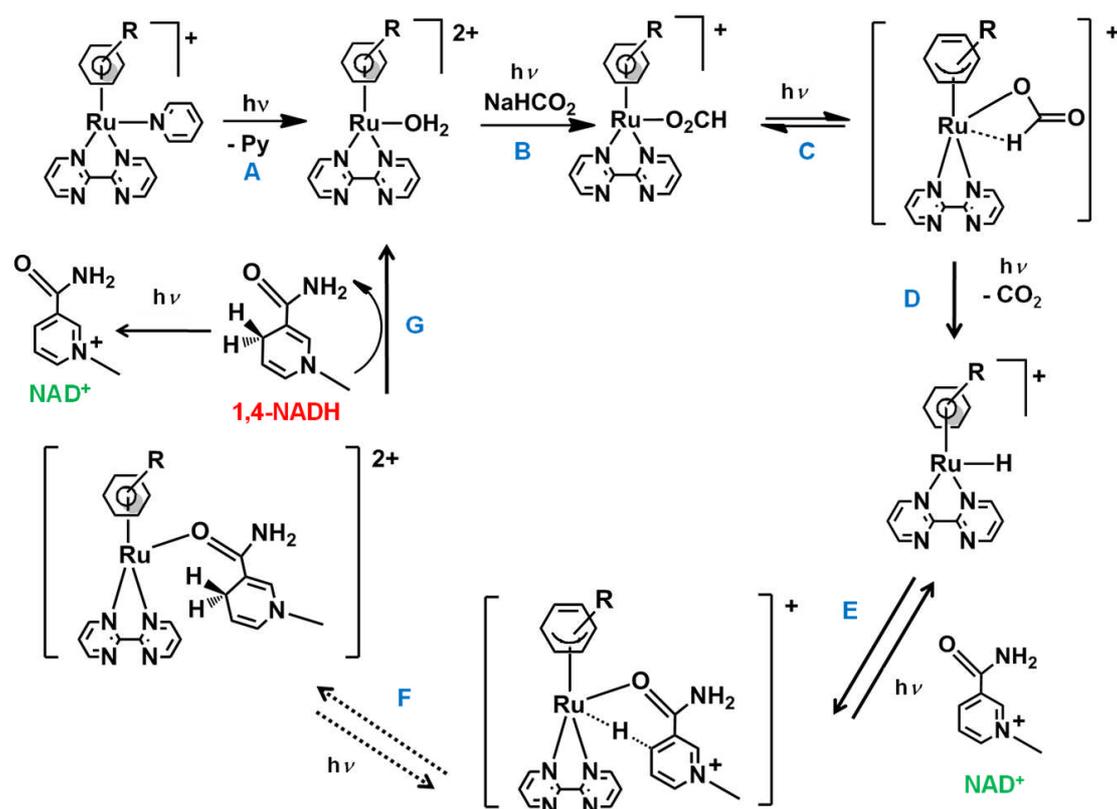
Figure 5.28. Proposed mechanism for the reaction of [(η^6-hmb)Ru(bpm)(Py)]$^{2+}$ (**13**), NaHCO$_2$ and NAD$^+$ upon photoirradiation by UVA (λ_{irr} = 300–400 nm). R represents hmb (**13**).

5.5 Summary

The interaction of Ru^{II} arene chlorido complexes with an excess of sodium formate (25 mol equiv) in aqueous solution at 310 K, showed that a formate adduct can be formed upon hydrolysis of the corresponding Ru−Cl bonds. The formate adduct thus produced is very stable in aqueous solution (pH* ≈ 7.0) and does not undergo hydrolysis provided that an excess of formate (25 mol equiv) is also present. It was observed that the isolated formato complex [(η^6-*p*-cym)Ru(bpm)(O$_2$CH)] (**16**) underwent hydrolysis in aqueous solution at 310 K with a half-life of 45 min and up to more than 65% extent. The same class of formate adducts can also be produced if a Ru^{II} arene pyridine complex is irradiated with UVA (λ$_{irr}$ = 300−400 nm) or visible light (λ$_{irr}$ = 400−660 nm) under the same conditions (310 K and pH* ≈ 7.0). This observation provides further evidence that such Ru^{II} arene formate complexes are also stable towards photoirradiation. None of the Ru^{II} arene formato adducts catalysed the reduction of acetone, suggesting a decreased reactivity for these complexes at biologically relevant pH* values. Four selected Ru^{II} arene complexes of the form [(η^6-arene)Ru(N,N')Cl][PF$_6$] where arene is *para*-cymene (*p*-cym, **1**), hexamethylbenzene (hmb, **3**), indane (ind, **4**) or thn (tehtrahydronaphtalene, **9**); and N,N' is 2,2'-bipyrimidine (bmp) were tested for hydride-transfer reactions. It was found that complexes **3** and **4** (but not **1** and **9**) can catalyse the regioselective reduction of NAD$^+$ in the presence of formate in water (25 mol excess) to form 1,4-NADH. The reaction occurs *via* the formation of a ^{1}H NMR detectable Ru−H (hydride) species. A second reduction product was also detected in latter stages of the reaction as a minor side-product, 1,6-NADH. The catalytic activity seems to be dependent on the arene with the hexamethylbenzene (hmb) complex **3**, showing the better activity by providing electronic stability during the formation of the Ru−H species and be

favoured at lower pH* values. It was also shown that the regioselective reduction of NAD$^+$ to NADH can be phototriggered by photoactivating a Ru^{II} arene pyridine complex, $[(\eta^6\text{-hmb})Ru(bpm)(Py)]^{2+}$ (**13**). In this case, no detectable ^{1}H NMR signals for Ru−H species were observed due to the reduced accumulation of 1,4-NADH (from NAD$^+$), which seems to be related to the formation of such hydride species. In this context, 1,4-NADH was proved for the first time (to the best of my knowledge) to participate in hydride-transfer reactions to Ru^{II} arene chlorido complexes to form a Ru−H species and NAD$^+$. When the reaction was repeated using a photoactivatable Ru^{II} arene pyridine complex using UVA photoirradiation, instead of the readily hydrolysable halido complex, the only photoproducts present in solution at the end of the reaction were the Ru–OH$_2$ species, free Py, and NAD$^+$ with no evidence for the generation of Ru–H species. This observation accounts for the simultaneous photodecomposition of 1,4-NADH upon photoirradiation which might explain its reduced accumulation (as a product).

5.6 References

[1]. Carrion, M. C.; Sepulveda, F.; Jalon, F. A.; Manzano, B. R.; Rodriguez, A. M. *Organometallics*, **2009**, *28*, 3822–3833.

[2]. Sandoval, C. A.; Bie, F.; Matsuoka, A.; Yamaguchi, Y.; Naka, H.; Li, Y.; Kato, K.; Utsumi, N.; Tsutsumi, K.; Ohkuma, T.; Murata, K.; Noyori, R. *Chem. Asian J.*, **2010**, *5*, 806–816.

[3]. Chaplin, A. B.; Dyson, P. J. *Organometallics*, **2007**, *26*, 4357–4360.

[4]. (a) Canivet, J.; Süss-Fink, G. *Green Chem.*, **2007**, *9*, 391–397; (b) Romain, C.; Gaillard, S.; Elmkaddem, M. K.; Toupet, L.; Fischmeister, Thomas, C. M.; Renaud, J.-L. *Organometallics*, **2010**, *29*, 1992–1995.

[5]. Herrmann, W. A; Kohlpaintner, C. W. *Angew. Chem., Int. Ed.*, **1993**, *32*, 1524–1544.

[6]. (a) Cornils, B.; Hermann, W. A. *Aqueous-Phase Organometallic Catalysis*, 2nd ed., Wiley-VCH, **2002**; (b) Lindstrom, U. M. *Chem. Rev.* **2002**, *102*, 2751–2772.

[7]. Himeda, Y.; Onozawa-Komatsuzaki, N.; Sugihara, H.; Arakawa, H.; Kasuga, K. *J. Mol. Cat. A-Chem.*, **2003**, *195*, 95–100.

[8]. (a) Casey, C. P.; Bikzhanova, G. A.; Cui, Q.; Guzei, I. A**.** *J. Am. Chem. Soc.*, **2005**, *127*, 14062–14071; (b) Zanotti-Gerosa, A.; Hems, W.; Groarke, M.; Hancock, F. *Platinum Metals Rev.*, **2005**, *49*, 158–165.

[9]. Soleimannejad, J.; Sisson, A.; White, C. *Inorg. Chim. Acta*, **2003**, *352*, 121–128

[10]. Davenport, A. J.; Davies, D. L.; Fawcett, J.; Russell, D. R. *Dalton Trans*., **2004**, 1481–1492.

[11]. (a) Ogo, S.; Makihara, N.; Watanabe, Y. *Organometallics*, **1999**, *18*, 5470–5474; (b) Ogo, S.; Uehara, K.; Abura, T.; Watanabe, Y.; Fukuzumi, S. *Organometallics*, **2004**, *23*, 3047–3052; (c) Ogo, S.; Abura, T.; Watanabe, Y. *Organometallics*, **2002**, *21*, 2964–2969.

[12]. Canivet, J., Karmazin-Brelot, L.; Süss-Fink, G., *J. Organomet. Chem.*, **2005**, *690*, 3202–3211.

[13]. Bassetti, M.; Centola, F.; Sémeril, D.; Bruneau, C.; Dixneuf, P. H. *Organometallics*, **2003**, *22*, 4459–4466.

[14]. Jan, D.; Delaude, L.; Simal, F.; Demonceau, A.; Noels, A. F. *J. Organomet. Chem.*, **2000**, *606*, 55–64.

[15]. (a) Lozano-Vila, A. M.; Monsaert, S.; Bajek, A.; Verpoort, F**.** *Chem. Rev.*, **2010**, *110*, 4865–4909; (b) Ung, T.; Hejl, A.; Grubbs, R. H.; Schrodi, Y. *Organometallics*, **2004**, *23*, 5399–5401; (c) Peris, E.; Crabtree, R. H. *Coord. Chem. Rev.* **2004**, *248*,

2239–2246.

[16]. (a) Grundwald, C.; Gevert, O.; Wolf, J.; Gonzales-Herrero, P.; Werner, H. *Organometallics*, **1996**, *15*, 1960–1962; (b) Drouin, S. D.; Yap, G. P. A.; Fogg, D. E. *Inorg. Chem.* **2000**, *39*, 5412–5414; (c) Nguyen, S. T.; Johnson, L. K.; Grubbs, R.; Ziller, J. W. *J. Am. Chem. Soc.* **1992**, *114*, 3974–3975.

[17]. (a) Lee, H. M.; Bianchini, C.; Jia, G.; Barbaro, P. *Organometallics*, **1999**, *18*, 1961–1966; (b) Toledo, J. C.; Neto, B. S. L.; Franco, D. W. *Coord. Chem. Rev.*, **2005**, *249*, 419–431; (c) Grela, K.; Harutyunyan, S.; Michrowska, A. *Angew. Chem. Int. Ed.*, **2002**, *41*, 4038–4040.

[18]. Steckhan, E.; Herrmann, S.; Ruppert, R.; Dietz, E.; Frede, M.; Spika, E. *Organometallics*, **1991**, *10*, 1568–1577.

[19]. Yan, Y. K.; Melchart, M.; Habtemariam, A.; Peacock, A. F. A.; Sadler, P. J. *J. Biol. Inorg. Chem.*, **2006**, *11*, 483–488.

[20]. Westerhausen, D.; Herrmann, S.; Hummel, W.; Steckhan, E. *Angew. Chem., Int. Ed. Engl.*, **1992**, *31*, 1529–1531.

[21]. Fernández, R.; Melchart, M.; Habtemariam, A.; Parsons, S.; Sadler, P. J. *Chem. Eur. J.*, **2004**, *10*, 5173–5179.

[22]. Govindaswamy, P.; Canivet, J.; Therrien, B.; Süss-Fink, G.; Štěpnička, P.; Ludvík, J. *J. Organomet. Chem.*, **2007**, *692*, 3664−3675.

[23]. Wang, F.; Habtemariam, A.; van der Geer, E. P. L.; Fernández, R.; Melchart, M.; Deeth, R. J.; Aird, R.; Guichard, S.; Fabbiani, F. P. A.; Lozano-Casal, P.; Oswald, I. D. H.; Jodrell, D. I.; Parsons, S.; Sadler, P. J. *Proc. Natl. Acad. Sci. U.S.A.*, **2005**, *102*, 18269–18274.

[24]. Koike, T.; Ikariya, T. *Adv. Synth. Catal.*, **2004**, *346*, 37–41.

[25]. (a) Crabtree, R. H.; Eisenstein, O.; Sini, G.; Peris, E. *J. Organomet. Chem.*,

1998, *567*, 7–11; (b) Peris, E. Jr.; Lee, J. C.; Crabtree, R. H. *J. Chem. Soc. Chem. Commun.*, **1994**, 2573–2574.

[26]. (a) Abdur-Rashid, K.; Clapham, S. E.; Hadzovic, A. J.; Harvey, N.; Lough, A. J.; Morris, R. H. *J. Am. Chem. Soc.*, **2002**, *124*, 15104–15118; (b) Fryzuk, M. D.; MacNeil, P. A.; Rettig, S. J. *J. Am. Chem. Soc.*, **1987**, *109*, 2803–2812.

[27]. Hayashi, H.; Ogo, S.; Abura, T.; Fukuzumi, S. *J. Am. Chem. Soc.*, **2003**, *125*, 14266–14267.

[28]. Whittlesey, M. K.; Perutz, R. N.; Moore, M. H. *Organometallics* **1996**, *15,* 5166–5169.

[29]. Lo, H. C.; Leiva, C.; Buriez, O.; Kerr, J. B.; Olmstead, M. M.; Fish, R. H. *Inorg. Chem.*, **2001**, *40*, 6705–6716.

[30]. de los Ríos, I.; Jiménez Tenorio, M.; Jiménez Tenorio, M. A.; Puerta, M. C.; Valerga, P. *J. Organomet. Chem.*, **1996**, *525*, 57–64.

[31]. Lo, H. C.; Leiva, C.; Buriez, O.; Kerr, J. B.; Olmstead, M. M.; Fish, R. H. *Angew. Chem. Int. Ed.*, **1999**, *38*, 1429–1432.

[32]. Fukuzumi,S.; Fujioka, N.; Kotani, H.; Ohkubo, K.; Lee, Y.-M.; Nam, W. *J. Am. Chem. Soc.*, **2009**, *131*, 17127–17134.

[33]. Scherbak, N.; Strid, A.; Eriksson, L. A. *Chem. Phys. Lett.*, **2005**, *414*, 243–247.

[34]. O'Connor, J. M.; Casey, C. P. *Chem. Rev.*, **1987**, *87*, 307–318; (b) Jones, W. D; Kuykendall, V. L.; Selmeczy, A. D. *Organometallics*, **1991**, *10*, 1577–1586.

[35]. Vitinius, U.; Schaffner, K.; Demuth, M.; Heibel, M.; Selbach, H. *Chem. Biodiv.*, **2004**, *1*, 1487–1497.

Chapter 6

Bifunctional Ru^{II} Arene Complexes
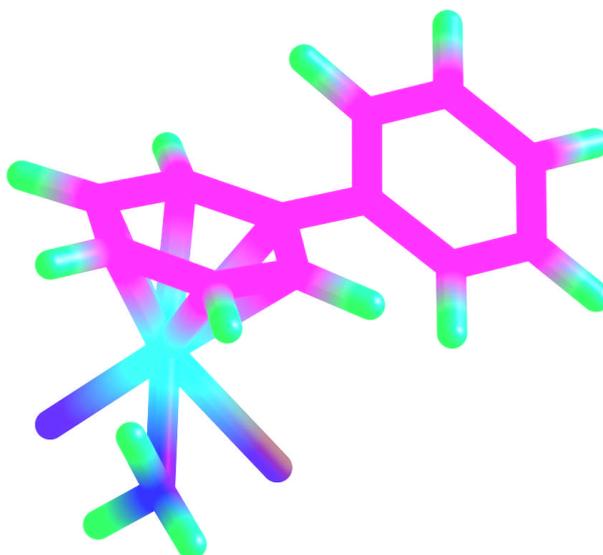
Chapter 6

Bifunctional Ru(II) Arene Complexes

6.1 Introduction

Soon after the discovery of cisplatin in the 1960s,[1,2,3] extensive studies of platinum ammine halide analogues led to a series of empirical rules governing the chemotherapeutic potential of this class of derivatives.[4] Specifically, it was then concluded that active compounds should: (1) be neutral, presumably to facilitate passive diffusion into cells; (2) have two leaving groups in a *cis-* configuration; (3) contain non-leaving groups with poor *trans-* labilising ability, similar to that of NH_3 or organic amines; and (4) have leaving groups with a window of lability centred on the chlorido ligand. Several recent studies have focused on applying analogous structure-activity relationships (SARs) to other metal complexes for anticancer drug design.[5] Half-sandwich Ru^{II} arene complexes of the general formula $[(\eta^6\text{-}$ arene$)Ru(X)(Y)(Z)]^{n+}$ where X and Y are two monodentate ligands or if linked, XY is a bidentate chelating ligand; and Z is a leaving group have recently been shown to be potential anticancer drugs.[6] Their primary geometry has been extensively used as a template to build cisplatin constitutional analogues which would ideally retain the biological activity. The first reported synthesis and structural characterisation of an organometallic Ru^{II} complex with similarity to cisplatin, bearing two ammonia ligands and one chloride $[(\eta^6\text{-benzene})Ru(NH_3)_2Cl][PF_6]$,[7,8] appeared thirty years ago but involved mainly studies of its photochemical properties. More recently, the synthesis and properties of a novel Ru^{II} arene complex namely $[(\eta^6\text{-}p\text{-cym})Ru(NH_3)_2Cl]^+$ have been described,[9] finding that despite its constitutional similarity to cisplatin, the complex displays an IC_{50} value 500 times larger than that for the platinum drug under

the same conditions. It is probable that the lack of activity arises from its instability in aqueous (and organic) solutions. The synthesis of numerous Ru^{II} arene dichlorido complexes bearing N-donor ligands[10] (mainly but not restricted to N-pyridine based) and mixed donor ligands (such as phosphines)[11] have also been tried. They have been shown not only to display interesting biological activities[12] but also have found use in other areas of research, such as catalysts in organic synthesis.[13,14] Various approaches towards bifunctional Ru^{II} arene complexes have included the use of bulkier N-monodentate ligands or non N-based monodentate ligands such as paullone derivatives,[15] 1,3,5-triaza-7-phosphatricyclo[3.3.1.1]decane (pta),[16] pyr(id)ones,[17] as well as biologically active groups such as staurosporine[18] or tyrphostin[19] derivatives. Drawn from several studies with platinum anticancer compounds,[20,27a] it seems that the presence of an H-bond donor atom may be a desirable feature in the design of bifunctional Ru^{II} arene complexes in order to, for example, aim for intrastrand cross-linking on DNA in a similar fashion to cisplatin.[21] In this respect, monodentate NH$_2$R ligands have been used.[22,23] However, the evidence suggests that the coordinated N-donor group can undergo ligand substitution reactions in solution and complexes such as [(η^6-mesitylene)Ru(NH$_2$R$_2$)Cl$_2$] where R = ethyl or butyl, decompose in solution.[24] In this work, the synthesis and structural characterisation of the first known examples (to the best of my knowledge) of neutral water soluble organometallic Ru^{II} complexes which possess constitutional similarity to cisplatin in the solid state and display similar behaviour in aqueous solution is described. It is also discussed how these complexes can readily bind to nucleobases in a similar fashion to that observed for cisplatin. The potential as cytotoxic agents for the neutral Ru^{II} arene complexes was also explored by means of cancer cell growth inhibition assays (IC$_{50}$ values).

6.2 Experimental Section

6.2.1 Materials

RuCl$_3$·3H$_2$O was acquired from Precious Metals Online (PMO Pty Ltd) and used as received. N,N'-dimethylbenzylamine (dmba) and NH$_4$PF$_6$ were obtained from Aldrich. The Ru^{II} arene precursor dimers [(η^6-*p*-cym)RuCl$_2$]$_2$ and [(η^6-bip)RuCl$_2$]$_2$ where arene is *para*-cymene (*p*-cym) or biphenyl (bip), were prepared following literature methods[25] as described in Chapter 2. The solvents used for UV-vis absorption spectroscopy were dry methanol (reagent grade) and deionised water. For NMR spectroscopy the solvents used were acetone-d_6, chloroform-d_3, methanol-d_4 and D$_2$O purchased from Aldrich unless otherwise stated. All chemicals were used without further purification.

6.2.2 Preparation of Dichlorido Ru^{II} Arene Complexes

Neutral complexes of the form [(η^6-arene)Ru(NH$_3$)Cl$_2$] where arene is *p*-cym or bip were synthesised using a similar procedure. A suspension of the appropriate Ru^{II} arene dimer [(η^6-arene)RuCl$_2$]$_2$, N,N'-dimethylbenzylamine (dmba) and NH$_4$PF$_6$ in 10 mL of dry MeOH (reagent grade) was stirred at room temperature under N$_2$ atmosphere for 18 h. The clear orange solution that formed was evaporated and the resulting solid was redissolved in the minimal amount of MeOH and left standing at 277 K for 5 h. The precipitate that formed was filtered off and washed with portions of Et$_2$O/MeOH and dried overnight in vacuum resulting in a microcrystalline product. Details of the amounts of reactants, colour changes, and nature of the products for the individual reactions are described below, as well as any variations in the synthetic procedure.

[(η^6-*p*-cym)Ru(NH$_3$)Cl$_2$] (1). [(η^6-*p*-cym)RuCl$_2$]$_2$ (0.10 g, 0.16 mmol), N,N'-dimethylbenzylamine (dmba) (0.05 mL, 0.32 mmol) and NH$_4$PF$_6$ (0.05 g, 0.32 mmol)

in dry MeOH; the solution turned from brick red to orange; bright orange crystals obtained; yield 68% (0.04 g, 0.11 mmol). Suitable crystals for X-ray diffraction were grown from a saturated dichloromethane solution at room temperature. Elemental Analysis calc. for $C_{19}H_{31}Cl_2N_2PRu$ %C: 37.76, %H: 5.17, %N: 4.63; found %C: 37.72, % H: 5.04, %N: 4.21. ESI-MS: calc for $C_{10}H_{19}Cl_2NRu$ {[M]–[H$^+$]}$^+$ *m/z* 324.2, found *m/z* 324.0. ^{1}H NMR ((CD$_3$)$_2$CO, 500 MHz) δ_H: 1.30 (6H, d; *J* = 7.50), 2. 20 (3H, s), 5.36 (2H, d, *J* = 6.25), 5.58 (2H, d, *J* = 6.25).

[(η^6-bip)Ru(NH$_3$)Cl$_2$] (2). [(η^6-bip)RuCl$_2$]$_2$ (0.10 g, 0.16 mmol), N,N'-dimethylbenzylamine (dmba) (0.049 mL, 0.32 mmol) and NH$_4$PF$_6$ (0.05 g, 0.32 mmol) in dry MeOH; the solution turned from brick red to orange; bright orange crystals obtained; yield 66% (0.04 g, 0.11 mmol). Suitable crystals for X-ray diffraction were grown from a saturated acetonitrile solution at room temperature. Elemental Analysis calc. for $C_{12}H_{15}Cl_2NORu$ %C: 39.90, %H: 4.19, %N: 3.88; found %C: 39.83, %H: 4.32, %N: 4.43. ESI-MS: calc for $C_{12}H_{14}Cl_2NRu$ {[M]–[H$^+$]}$^+$ *m/z* 344.2, found *m/z* 343.9. ^{1}H NMR ((CD$_3$)$_2$CO, 500 MHz) δ_H: 5.77 (1H, t, *J* = 5.63), 5.93 (2H, t, *J* = 5.63), 6.03 (2H, t, *J* = 5.63), 6.12 (2H, d, *J* = 6.25), 6.24 (1H, d, *J* = 6.25).

6.3   Results

6.3.1   Synthesis and Characterisation

The reaction of [(η^6-arene)RuCl$_2$]$_2$ where the arene is *p*-cym or bip, with two mol equiv of N,N'-dimethylbenzylamine (dmba) and 2 mol equivalents of NH$_4$PF$_6$ in dry MeOH under N$_2$ atmosphere at room temperature, afforded the neutral compounds [(η^6-*p*-cym)Ru(NH$_3$)Cl$_2$] (**1**) and [(η^6-bip)Ru(NH$_3$)Cl$_2$] (**2**) in good yields (68% and 66%, respectively), Figure 6.1. Both complexes were fully characterised by 1D and

2D ^{1}H NMR methods as well as elemental analysis, ESI-MS, and X-ray crystallography.
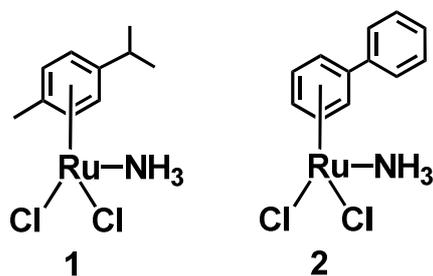
Figure 6.1. Structures of the neutral complexes studied in this work.

Compared to the corresponding parent dimers, the ^{1}H NMR resonances for both arenes in the Ru^{II} complexes are high-field-shifted by *ca.* 1 ppm. Figure 6.2 shows the ^{1}H NMR spectrum of complex [(η^6-*p*-cym)Ru(NH$_3$)Cl$_2$] (**1**) in acetone-*d$_6$* solution as a generic example.
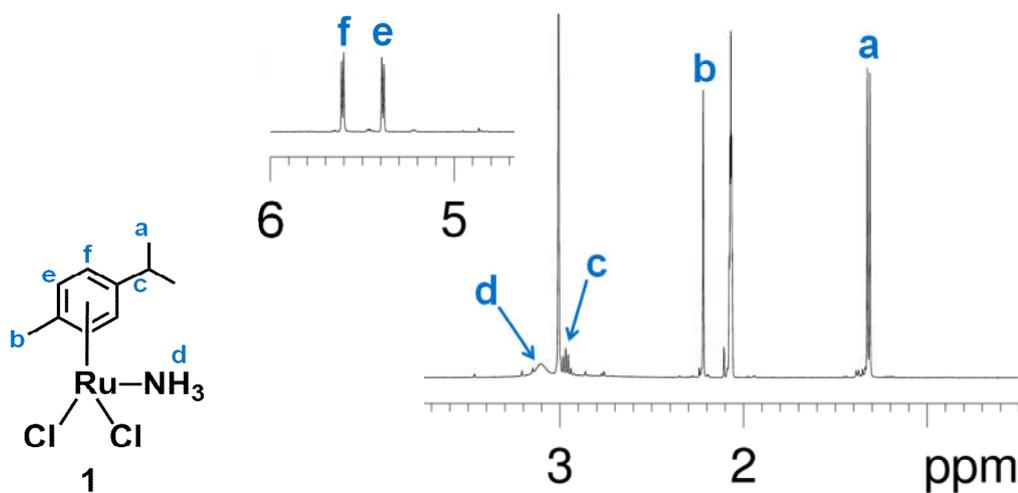
Figure 6.2. ^{1}H NMR spectrum of [(η^6-*p*-cym)Ru(NH$_3$)Cl$_2$] (**1**) in acetone-*d$_6$* solution.

6.3.2   X-ray Crystal Structures

Suitable crystals for X-ray diffraction of complexes **1** and **2** were grown from a saturated dichloromethane or acetonitrile solution at room temperature, respectively. Selected bond lengths and angles are given in Table 6.1, the structures with numbering schemes are shown in Figure 6.3 and the crystallographic data are listed in

Table A.6.1. The neutral Ru^{II} arene complexes adopt the familiar pseudo-octahedral three-legged piano stool geometry common to all other Ru^{II} arene structures[6,26] with the Ru centre π-bonded to the arene ligand (*p*-cym in **1** and bip in **2**), coordinated to one ammonia nitrogen, and to two chlorine atoms which constitute the three legs of the piano stool. The unit cell of the Ru^{II} arene complex **1** was found to contain the N,N'-dimethylbenzylammonium hexafluorophosphate ionic pair, (dmba–H)(PF$_6$).

Table 6.1. Selected bond lengths (Å) and angles (°) for [(η^6-*p*-cym)Ru(NH$_3$)Cl$_2$] (dmba–H)(PF$_6$) (**1**) and [(η^6-bip)Ru(NH$_3$)Cl$_2$] (**2**).

Bond length/angle	(**1**)	(**2**)
Ru(1)–arene$_{(centroid)}$	1.657	1.670
Ru(1)–Cl(1)	2.427(2)	2.4284(8)
Ru(1)–Cl(2)	2.421(2)	2.4246(9)
Ru(1)–N(1)	2.116(8)	2.135(3)
N(1)–Ru(1)–Cl(1)	83.80(2)	84.29(8)
N(1)–Ru(1)–Cl(2)	84.30(2)	84.73(8)
Cl(2)–Ru(1)–Cl(1)	85.11(8)	85.26(3)
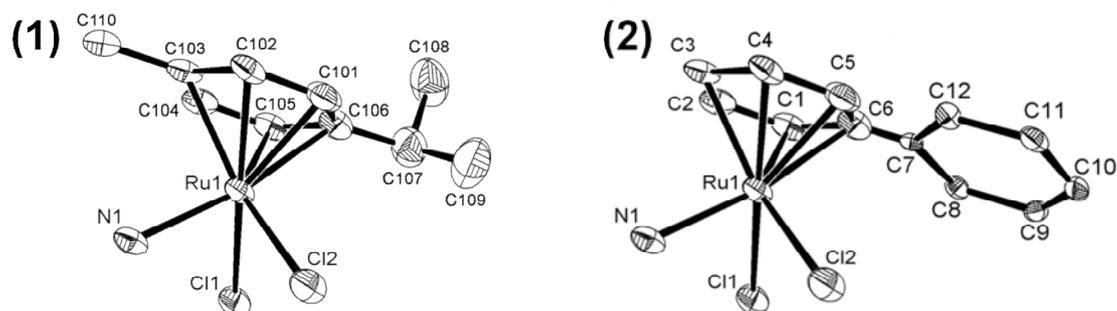
Figure 6.3. X-ray structure of the neutral Ru^{II} arene complexes [(η^6-*p*-cym)Ru(NH$_3$)Cl$_2$] (**1**) and [(η^6-bip)Ru(NH$_3$)Cl$_2$] (**2**). Thermal ellipsoids show 50% probability. The hydrogen atoms have been omitted for clarity.

The Ru–Cl and the Ru–N bond lengths in the two new neutral Ru^{II} arene complexes are almost the same (~2.42 and ~2.13 Å). The Ru–*p*-cym$_{(centroid)}$ distance (as measured from Mercury version 2.2.) in complex **1** is slightly shorter than the one found for the bip analogue **2**. The Ru^{II} arene molecules in the unit cell of complex **1** are closely related through an extended intermolecular H-bond network to the ionic pair (dmba–

H)(PF$_6$), Figure 6.4. The values for the hydrogen bonds range from 2.396 Å for the (N–H)$_{Ru}$···F bond up to 2.780 Å for the N–H···Cl. Selected H-bond lengths and angles not described herein are shown in Table A.6.2.
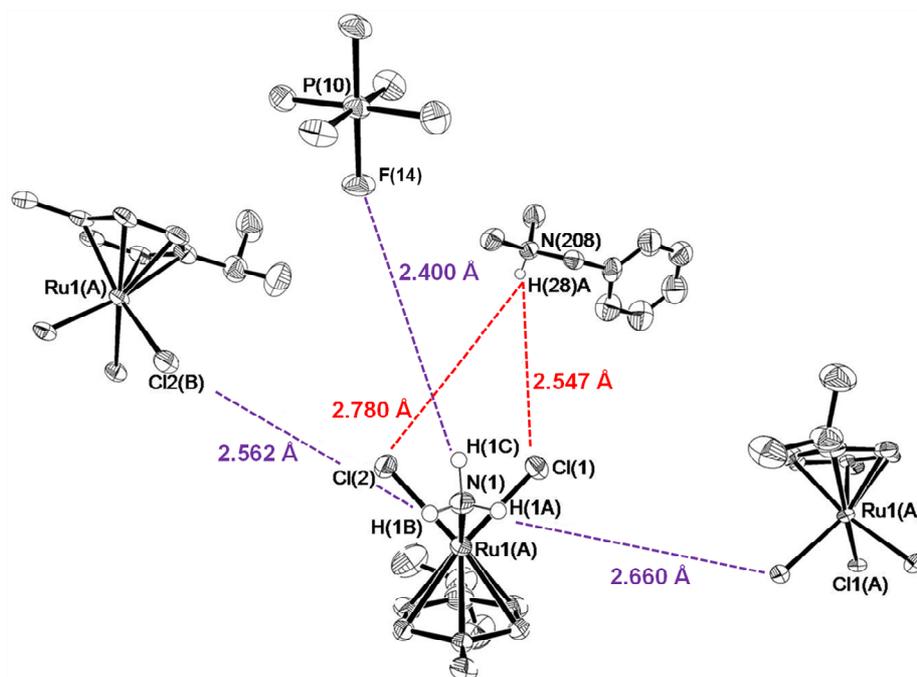
Figure 6.4. H-bond interactions for one Ru^{II} arene complex in the X-ray crystal structure of [(η^6-p-cym)Ru(NH$_3$)Cl$_2$] (**1**). Atoms not involved in the specified interactions were omitted for clarity.

For the N,N'-dimethylbenzylammonium cation, (dmba–H)$^+$ in the unit cell of complex **1**, a weak π-π interaction between two adjacent benzyl rings (bz) was found with a bz$_{(centroid)}$–bz$_{(centroid)}$ distance of 3.920 Å, Figure 6.5 (main feature). The mean planes distance between the two bz rings involved in the interaction is 3.440 Å. The space-filling model of (dmba–H)$^+$ (inset in Figure 6.5), shows the presence of the aromatic stacking where the shortest atomic contact C(204)···C(205) is 3.495 Å and the angle between the mean planes defined by the bz rings is 0°.
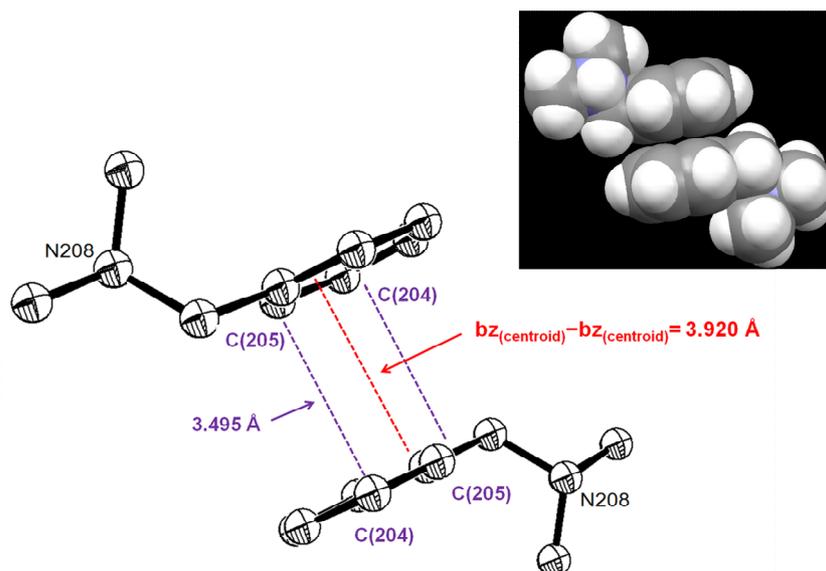
Figure 6.5. Intermolecular π-π stacking interaction between two molecules of N,N'-dimethylbenzylammonium cation through the bz rings in the crystal packing of [(η^6-*p*-cym)Ru(NH$_3$)Cl$_2$] (**1**). Inset: Spacefilling model showing the π-π stacking interaction.

Complex [(η^6-bip)Ru(NH$_3$)Cl$_2$] (**2**) was found to pair in the unit cell *via* H-bonding interactions between two of the ammonia protons and the chlorido ligands, Figure 6.6. The bond lengths for each N−H···Cl bond are 2.606 and 2.668 Å and the angles are 144.38 and 139.44°, respectively. Selected H-bond lengths and angles not described herein are shown in Table A.6.3. Complex [(η^6-bip)Ru(NH$_3$)Cl$_2$] (**2**) lays back-to-back with an adjacent complex, pairing in an intermolecular π-π stacking interaction. The mean planes involving the uncoordinated phenyl (ph) rings in the bip arene are parallel, Figure 6.7. The spacefilling model of complex **2** (inset in Figure 6.7) shows the presence of the aromatic stacking with the shortest atomic contact C(8)···C(10) being 3.587 Å and a ph$_{(centroid)}$−ph$_{(centroid)}$ distance of 3.687 Å. The uncoordinated ph ring is tilted 41.06º relative to the main plane defined by the Ru−ph$_{(bound)}$.
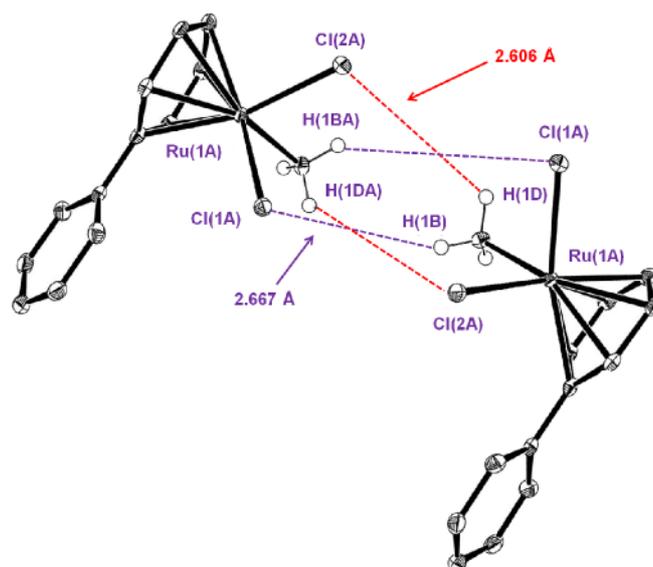
Figure 6.6. X-ray crystal structure of $[(\eta^6\text{-bip})Ru(NH_3)Cl_2]$ (**2**) showing N−H···Cl contacts.
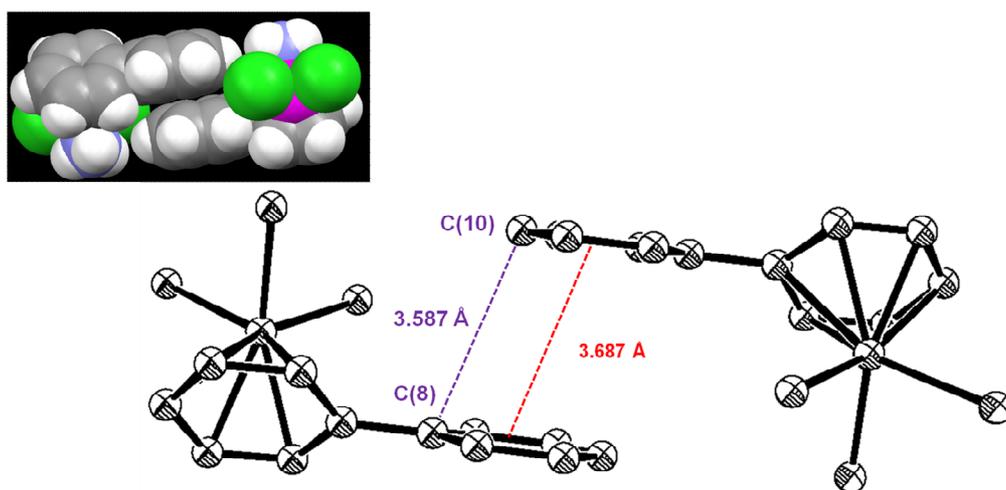
Figure 6.7. X-ray crystal structure of $[(\eta^6\text{-bip})Ru(NH_3)Cl_2]$ (**2**) showing a π-π stacking interaction between two uncoordinated bip rings in neighbouring molecules. Inset: Space-filling model showing the π-π stacking interaction.

6.3.3 Aqueous Solution Chemistry

The hydrolysis of the neutral Ru^{II} arene complexes **1** and **2** was studied at 310 K over 8−14 h. The nature of the hydrolysis products and equilibria of the individual reactions were verified by either ^{1}H NMR spectroscopy or ESI-MS. The time dependence of the increase in concentration of aqua adducts or decrease in concentration of halido species was followed using UV-vis spectroscopy.

6.3.3.1 Hydrolysis Equilibria

In order to characterise the products of hydrolysis and determine the extent of the reactions, freshly-made 100 μM (5% MeOD-d_4/95% D$_2$O) solutions of complexes **1** and **2** were allowed to equilibrate for 24 h at 310 K and then were studied at the same temperature using ^{1}H NMR spectroscopy. Figure 6.8 shows the ^{1}H NMR spectrum of complex **1** at 310 K followed over time in the aliphatic region for the CH$_{3(iso\text{-propyl})}$ protons on the *p*-cym ring (seen as a doublet). The ^{1}H NMR spectra of complexes **1** and **2** initially contained one major set of peaks (dichlorido species) and then a second and third set of peaks increased in intensity over time. The new sets of peaks are believed to correspond to the mono- and di-aqua adducts, $[(\eta^6\text{-}$ arene)Ru(NH$_3$)(OH$_2$)Cl]$^+$ and $[(\eta^6\text{-arene})$Ru(NH$_3$)(OH$_2$)$_2$]$^{2+}$. The mass-to-charge ratios obtained from ESI-MS spectra of the solutions after 24 h were consistent with the formation of the di-aqua complexes; Table 6.2 (observed as the base peaks of the spectra). For the complex $[(\eta^6\text{-bip})$Ru(NH$_3$)Cl$_2$] (**2**) an additional set of peaks was also observed in its ^{1}H NMR spectrum, for the product which had undergone arene loss during the aquation. Table 6.3 summarises the percentage of species detected at equilibrium by ^{1}H NMR after 24 h of reaction.
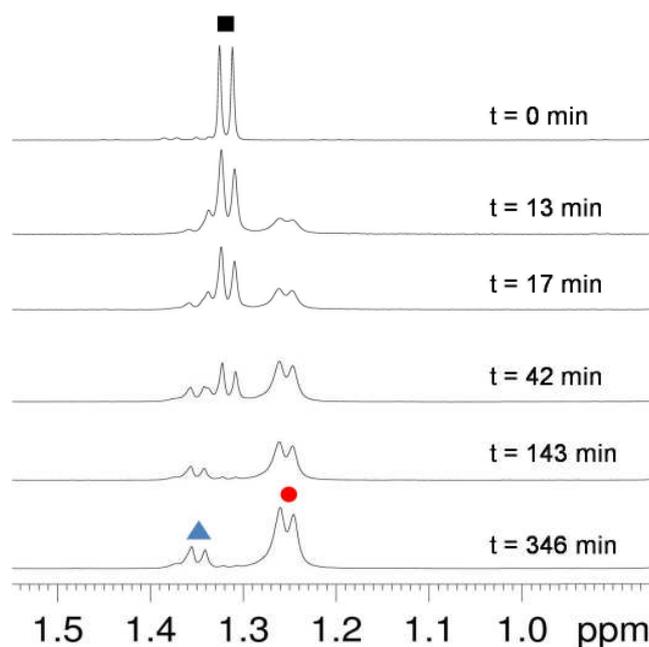
Figure 6.8. ^{1}H NMR spectrum in the aliphatic region of complex [(η^6-*p*-cym)Ru(NH$_3$)Cl$_2$] (**1**) in 5% MeOD-*d$_4$*/95% D$_2$O at 310 K recorded at different stages of aquation. ■ = [(η^6-*p*-cym)Ru(NH$_3$)(Cl)$_2$], ▲ = [(η^6-*p*-cym)Ru(NH$_3$)(OH$_2$)Cl]$^+$, ● = [(η^6-*p*-cym)Ru(NH$_3$)(OH$_2$)$_2$]$^{2+}$.

Table 6.2. Mass-to-charge ratios obtained from ESI-MS spectra for the products of hydrolysis of Ru^{II} arene complexes **1** and **2**.

	Observed peak [M]$^+$	Chemical formula Calc *m/z*	Found *m/z*
(**1**)	{[(η^6-*p*-cym)Ru(NH$_3$)(H$_2$O)$_2$]−[(H$^+$)]}$^+$	C$_{10}$H$_{20}$NO$_2$Ru 288.35	288.90
(**2**)	[{[(η^6-bip)Ru(NH$_3$)(H$_2$O)$_2$]−[(H$^+$)]}$^+$	C$_{12}$H$_{17}$NO$_2$Ru 308.34	308.90

Table 6.3. Percentage of species present at equilibrium after 24 h of the reaction in a 100 µM (5% MeOD-*d$_4$*/95% D$_2$O) solution at 310 K of complexes **1** and **2** followed by ^{1}H NMR.

		% Species		
Compound	Ru−X	Ru−OH$_2$	Ru−(OH$_2$)$_2$	Arene loss
(**1**) [(η^6-*p*-cym)Ru(NH$_3$)Cl$_2$]	3.1	20.8	76.1	0.0
(**2**) [(η^6-bip)Ru(NH$_3$)Cl$_2$]	~ 24.1^a	~ 2.2^a	~ 18.0^a	~ 55.7^a

^{a} Approximate value due to peak overlap

From Table 6.3, it can be seen that the *p*-cym complex **1**, undergoes mono- and dihydrolysis to a larger extent than complex **2**. Changing the arene from *p*-cym (**1**) to bip (**2**) greatly modifies the stability of the complex in aqueous solution at 310 K.

6.3.3.2   Kinetics of Hydrolysis

Dissolution of compounds **1** and **2** in 5% MeOH/95% H$_2$O at 310 K gave rise to ligand substitution reactions at the Ru^{II} centre as indicated by the concomitant changes in UV-Vis absorption bands. The time evolution spectra for the two Ru^{II} arene complexes at 310 K are shown in Figure 6.9. The initial electronic absorption spectrum of aqueous [(η^6-*p*-cym)Ru(NH$_3$)Cl$_2$] (**1**) at 310 K exhibits peaks with maxima at *ca.* 255 nm, 320 nm and 410 nm. The highest energy absorption band increases in intensity while the lower energy band decreases. The band centred at *ca.* 320 nm disappears upon hydrolysis. In the case of [(η^6-bip)Ru(NH$_3$)Cl$_2$] (**2**) in aqueous solution, the initial electronic absorption spectrum at 310 K exhibits peaks with maxima at *ca.* 255 nm and 274 nm which increase only slightly in intensity over a period of *ca.* 6 h. There is no indication of an isosbestic point in the corresponding UV-vis spectra in either case.
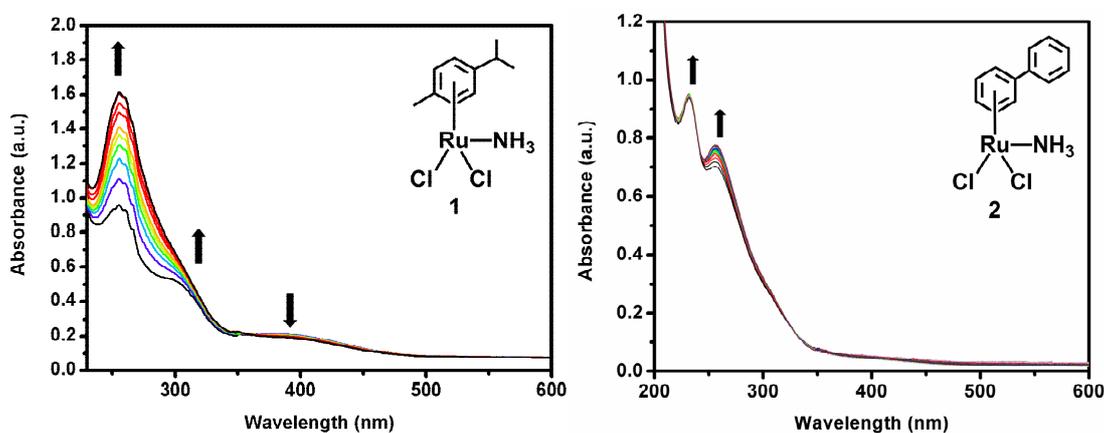
Figure 6.9. Time evolution of the hydrolysis reaction for 100 µM (5% MeOH/95% H$_2$O) solutions of complexes **1** and **2** at 310 K followed by UV-vis spectroscopy.

The decrease in absorbance at 255 nm followed over time for complexes **1** and **2** in 100 µM (5% MeOH/95% H$_2$O) at 310 K is shown in Figure 6.10. Both complexes display biexponential dependence as shown by the fit to the data. The rate constants

for complex **2** were determined over the period of time before the onset of arene loss (at ~160 min detected by ^{1}H NMR). The corresponding rate constants and half-life values are listed in Table 6.4. It can be seen that the bip complex **2** hydrolyses slower than the *p*-cym analogue complex **1**. The first hydrolysis rate is *ca.* 1 time slower for the bip complex (**2**). The second aquation rates are within the same range for both complexes.
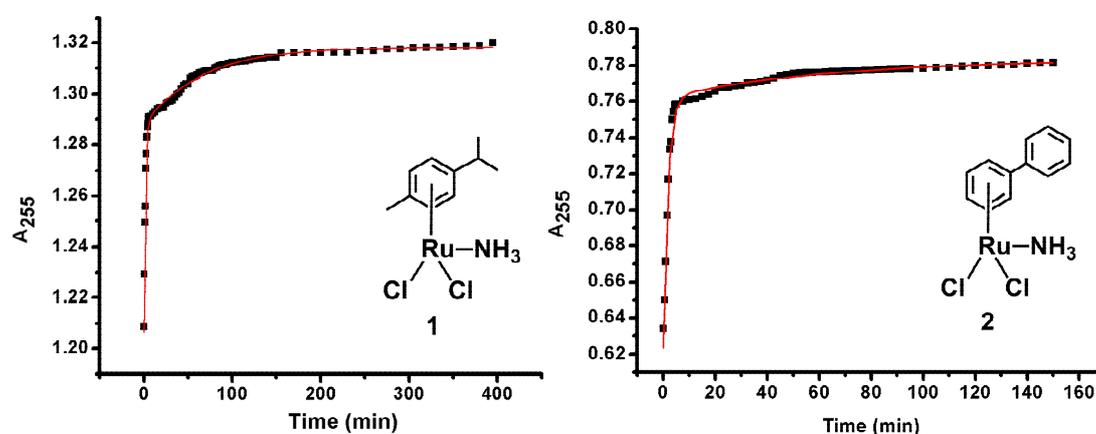
Figure 6.10. Dependence of the absorbance at 255 nm over *ca.* 7 h during aquation of 100 μM (5% MeOH/95% H$_2$O) solutions of [(η^6-*p*-cym)Ru(NH$_3$)Cl$_2$] (**1**) and over *ca.* 160 min of [(η^6-bip)Ru(NH$_3$)Cl$_2$] (**2**) at 310 K.

Table 6.4. Hydrolysis data for complexes **1** and **2** determined by UV-vis spectroscopy as 100 μM (5% MeOH/95% H$_2$O) solutions.

	(**1**)	(**2**)
First Aquation		
$k_1 \times 10^{-3}$ (min^{-1})^{a,b}	720.0 ± 21.8	555.0 ± 27.2
$(t_{1/2})_1$ (min)	1.0	1.2
Second Aquation		
$k_2 \times 10^{-3}$ (min^{-1})^{a,c}	15.2 ± 0.7	15.9 ± 5.8
$(t_{1/2})_2$ (min)	45.7	43.6

^{a} The errors quoted are fitting errors
^{b,c} The rate constants for complex **2** were determined over the period of time before the onset of arene loss (at *ca.* 160 min detected by ^{1}H NMR)

6.3.4 Interactions with Nucleobases

Attempts were made to prepare 9-EtG adducts of complexes **1** and **2**. The interactions were studied by means of multidimensional ^{1}H NMR spectroscopy and the nature of the products verified by ESI-MS. An equimolar amount of 9-EtG was added to an NMR tube containing a 100 μM solution of **1** or **2** in 5% MeOD-d_4/95% D$_2$O at 31O K, the reaction was then followed for *ca.* 6 h. The reactions occur *via* the *in situ* formation of the corresponding reactive aqua adducts (mono- and di-) for each complex upon hydrolysis. The binding is assumed to be through the *N7* position as has been previously observed for similar Ru^{II} arene guanine adducts.[27,28] Peaks assigned to the bound 9-EtG-*N7* in all complexes are shifted to low field in comparison to those of free 9-EtG under the same conditions (H8 peak of free 9-EtG appears at 8.1 ppm). For both complexes, it was observed that after *ca.* 10 min of reaction a second and third set of singlets low-field-shifted and with increased intensity appeared. These peaks are presumably related to the mono- and dinucleobase adducts. The H8 peak in the mono-guanine adduct of complex **1**, [(η^6-*p*-cym)Ru(NH$_3$)(9-EtG-*N7*)Cl]$^+$ (**1-EtG**), has a chemical shift of 8.20 ppm (*versus* 8.08 ppm for free 9-EtG under the same conditions). The second singlet, tentatively assigned to the di-guanine adduct [(η^6-*p*-cym)Ru(NH$_3$)(9-EtG-*N7*)$_2$]$^{2+}$ (**1-EtG$_2$**) has a chemical shift of 8.40 ppm, Figure 6.11(A). During this same time period another signal was detected around 8.15 ppm which might correspond either to a tris-9-EtG-*N7* adduct (formed upon hydrolysis of the NH$_3$ bond) or to the formation of 9-EtG-*N3*-bound adducts; no further attempts to characterise it were made. An analogous behaviour was observed for complex **2**, for which the H8 peak in the mono-guanine adduct [(η^6-bip)Ru(NH$_3$)(9-EtG-*N7*)Cl]$^+$ (**2-EtG**) has a chemical shift of 8.20 ppm (*versus* 8.08 ppm for free 9-EtG under the same conditions). The second singlet

tentatively assigned to the di-guanine adduct $[(\eta^6\text{-bip})\text{Ru}(\text{NH}_3)(9\text{-EtG-}N7)_2]^{2+}$ (**2-EtG$_2$**) has a chemical shift of 8.34 ppm, Figure 6.11(B). Several other peaks in the same region were also observed for the reaction of complex **2** with 9-EtG. These signals may correspond to the species that underwent arene loss over time and no further attempts were made to characterise them.
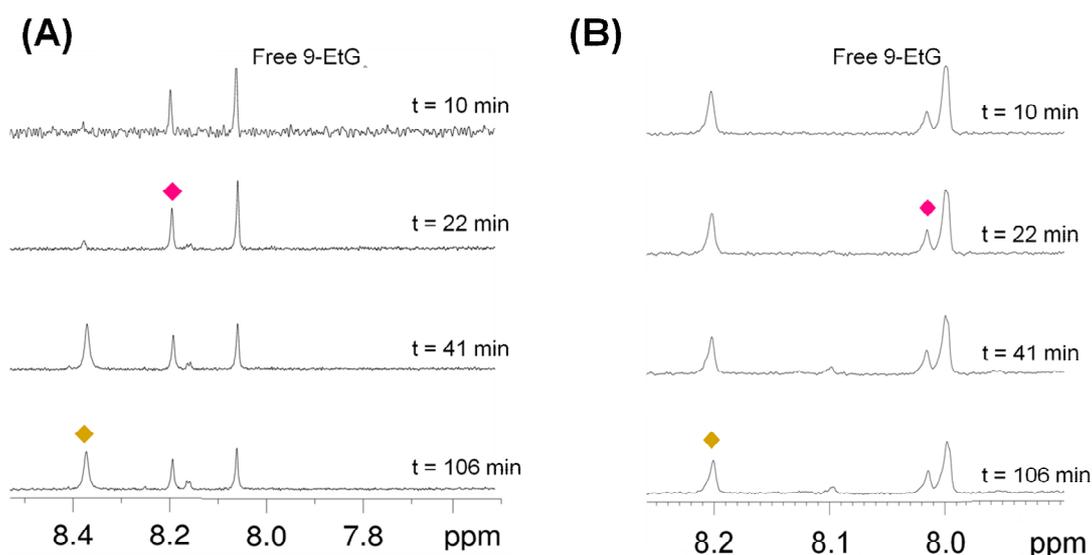
Figure 6.11. Time dependence ^{1}H NMR spectra of (A) complex $[(\eta^6\text{-}p\text{-}$cym)Ru(NH$_3$)Cl$_2$] (**1**) and (B) $[(\eta^6\text{-bip})\text{Ru}(\text{NH}_3)\text{Cl}_2]$ (**2**) in 5% MeOD-d_4/95% D$_2$O at 310 K in the presence of 9-EtG. ♦ **Magenta** = $[(\eta^6\text{-}p\text{-}$cym)Ru(NH$_3$)(9-EtG-$N7$)Cl]$^+$ (**1-EtG**)/$[(\eta^6\text{-bip})\text{Ru}(\text{NH}_3)(9\text{-EtG-}N7)\text{Cl}]^+$ (**2-EtG**); ♦ **Yellow** = $[(\eta^6\text{-}p\text{-}$cym)Ru(NH$_3$)(9-EtG-$N7$)$_2$]$^{2+}$ (**1-EtG$_2$**)/$[(\eta^6\text{-bip})\text{Ru}(\text{NH}_3)(9\text{-EtG-}N7)_2]^{2+}$ (**2-EtG$_2$**).

Table 6.5 lists the percentage of species detected after 24 h for the reaction of complexes **1** and **2** (before the onset of arene loss for the bip complex) with 9-EtG. As it can be seen, after 106 min, complex **1** had reacted with 9-EtG to form 20.4% of the corresponding mono-guanine adduct $[(\eta^6\text{-}p\text{-}$cym)Ru(NH$_3$)(9-EtG-$N7$)Cl]$^+$ (**1-EtG**) and 53.0% of the di-guanine adduct $[(\eta^6\text{-}p\text{-}$cym)Ru(NH$_3$)(9-EtG-$N7$)$_2$]$^{2+}$ (**1-EtG$_2$**). In the case of complex **2**, after 56 min it had reacted with 9-EtG to form 4.8% of the corresponding mono-guanine adduct $[(\eta^6\text{-bip})\text{Ru}(\text{NH}_3)(9\text{-EtG-}N7)\text{Cl}]^+$ (**2-EtG**) and

32.0% of the di-guanine adduct $[(\eta^6\text{-bip})Ru(NH_3)(9\text{-EtG-}N7)_2]^{2+}$ (**2-EtG$_2$**). The mass-to-charge ratios obtained from ESI-MS data were used to characterise some of the guanine adducts, Table 6.6.

Table 6.5. Time dependence of nucleobase adduct formation for Ru^{II} arene complexes **1** and **2** determined by ^{1}H NMR spectroscopy.

Compound	Time (min)	% Mono- (9-EtG-*N7*) adduct	% Di- (9-EtG-*N7*) adduct
(**1**) $[(\eta^6\text{-}p\text{-cym})Ru(NH_3)Cl_2]$	106^a	20.4	53.0
	1440	20.4	53.0
(**2**) $[(\eta^6\text{-bip})Ru(NH_3)Cl_2]$	~ 160^{b,c}	~ 4.8^{b,c}	~ 32.3^{b,c}
	1440	ND	ND

^{a} Time needed to reach equilibrium
^{b} Time before the onset of arene loss
^{c} Approximate value due to peak overlap
ND Not determined

Table 6.6. Mass-to-charge ratios obtained from ESI-MS spectra for the products of 9-EtG interactions of Ru^{II} arene complexes **1** and **2**.

	Observed peak $[M]^{n+}$	Chemical formula Calc *m/z*	Found *m/z*
(**1**)	$\{[(\eta^6\text{-}p\text{-cym})Ru(9\text{-EtG-}N7)(H_2O)_2]^{2+}\text{--}[H^+]\}^+$	$C_{17}H_{27}N_5O_3Ru$ 450.50	450.06
	$\{[(\eta^6\text{-}p\text{-cym})Ru(9\text{-EtG-}N7)]^{2+}$	$C_{17}H_{23}N_5ORu$ 207.23	207.54
(**2**)	$\{[(\eta^6\text{-bip})Ru(9\text{-EtG-}N7)(H_2O)_2]^{2+}\text{--}[H^+]\}^+$	$C_{19}H_{22}N_5O_3Ru$ 469.50	469.03
	$[(\eta^6\text{-bip})Ru(9\text{-EtG-}N7)Cl]^+$	$C_{16}H_{19}ClN_5ORu$ 469.91	470.03
	$[(\eta^6\text{-bip})Ru(9\text{-EtG-}N7)]^{2+}$	$C_{19}H_{18}N_5ORu$ 217.23	217.53
(**1**) (**2**)	$\{[Ru(9\text{-EtG-}N7)_2]^{2+}\text{--}[H^+]\}^+$	$C_{14}H_{17}N_{10}O_2Ru$ 458.43	458.09

6.3.5 Cancer Cell Growth Inhibition (IC$_{50}$ values)

The IC$_{50}$ values for the neutral Ru^{II} arene complexes **1** and **2** against the A2780 human ovarian cancer cell line were determined and are listed in Table 6.7.

Table 6.7. IC$_{50}$ values for Ru^{II} arene complexes **1** and **2** against the A2780 human ovarian cancer cell line.

Compound	IC$_{50}$ μM
(**1**) [(η^6-*p*-cym)Ru(NH$_3$)Cl$_2$]	> 100
(**2**) [(η^6-bip)Ru(NH$_3$)Cl$_2$]	> 100
Cisplatin	0.5

The neutral complexes **1** and **2** were found to be inactive against the A2780 human ovarian cancer cell line up to the maximum concentration tested (100 μM).

6.4 Discussion

Two new Ru^{II} arene complexes of the type [(η^6-arene)Ru(NH$_3$)Cl$_2$] where arene is *p*-cym (**1**) or bip (**2**), showing structural similarity to cisplatin were synthesised and fully characterised, including analysis of their X-ray crystal structures. In order to explore their potential as cytotoxic agents, the aquation process, the model nucleobase binding, and the IC$_{50}$ values were investigated.

6.4.1 Synthesis and Characterisation

In this work, the synthesis of the first known examples (to the best of my knowledge) of neutral Ru^{II} arene complexes of the type [(η^6-arene)Ru(NH$_3$)Cl$_2$] with structural similarity to cisplatin, was achieved by reacting the appropriate [(η^6-arene)RuCl$_2$]$_2$ dimer with two mol equiv of N,N-dimethylbenzylamine (dmba) and two mol equiv of NH$_4$PF$_6$ in dry MeOH under N$_2$ atmosphere at room temperature. The two neutral compounds [(η^6-*p*-cym)Ru(NH$_3$)Cl$_2$] (**1**) and [(η^6-bip)Ru(NH$_3$)Cl$_2$] (**2**) were afforded in good yields (68% and 66%, respectively). The first known examples of transition metal complexes of the form [(η^6-benzene)M(NH$_3$)$_2$Cl][PF$_6$] (where M = Ru or Os) were reported over thirty years ago[8] and their synthetic approach was rather complicated and in most of the cases gave mixtures of products. It involved reacting

the $[(\eta^6\text{-benzene})M(Cl)_2]_2$ dimer in concentrated aqueous ammonia in methanol, followed by the addition of a saturated aqueous NH_4PF_6 solution used to precipitate the complexes as the corresponding PF_6 salts. In the alternative synthetic approach used in this work, the first step in the synthesis is believed to involve the fast acid-base reaction between N,N'-dimethylbenzylamine (dmba) which acts as the Brönsted-Lowry base and the ammonium cation (NH_4^+) which is the Brönsted-Lowry proton donor, to form equimolar amounts of ammonia (NH_3) *in situ* which then react with the Ru^{II} arene dimer to afford complexes **1** and **2**. A similar reaction mechanism has also been suggested for the synthesis of the cationic complex $[(\eta^6\text{-}p\text{-cym})Ru(NH_3)_2Cl]^+$.[9] In organic chemistry, ammonia is known to act as a nucleophile in substitution reactions.[29] NH_3 can act as a ligand in transition metal complexes since it is a pure σ-donor and shows intermediate hard-soft behaviour.[30] The presence of the N,N'-dimethylammonium ion (dma-H)$^+$ in solution was detected by ^{1}H NMR spectroscopy (($CD_3)_2CO$, 500 MHz δ_H ppm: 3.01 (6H, s), 4.50 (2H, s), 7.50 (3H, m), 7.66 (2H, m)) thus providing further evidence to support the proposed mechanism. Furthermore, the nature of the solvent appears to play an important role in the quality of the products, since the syntheses carried out in CH_3CN and CH_2Cl_2 also afforded complexes **1** and **2** but in lower yields (less than 40% in both cases). This observation suggests that the reaction might proceed by a nucleophilic substitution pathway. The intermediate species generated upon the nucleophilic attack of NH_3 on the Ru^{II} centre might be considerably better stabilised by the interactions with a medium polarity-index solvent such as methanol (5.1) compared to either a more polar solvent as CH_3CN (5.8) or less polar such as CH_2Cl_2 (3.1).[29,31]

6.4.2   X-ray Crystal Structures

The molecular structures of complexes **1** and **2** were determined by single crystal X-ray diffraction. Suitable crystals were grown from a saturated dichloromethane solution at room temperature for complex **1** and from a saturated solution of acetonitrile at room temperature for complex **2**. In both cases the complexes adopt the familiar pseudo-octahedral three-legged piano stool geometry. The (dma-H)(PF$_6$) ionic pair was found in the crystal packing of the Ru^{II} arene complex **1**. The corresponding Ru–arene$_{(centroid)}$ distances in **1** and **2** (1.657 and 1.670 Å, respectively) are considerably shorter (~0.02−0.05 Å) than those found in related complexes where the Ru^{II} centre is bound to an aromatic XY-chelating ligand (XY are N, O, or S).[32] This could be a consequence of the lack of π-orbitals on the NH$_3$ group (as opposed to aromatic N,N'-chelating ligands) making the aromatic arenes the only π-acceptor ligands coordinated to the Ru^{II} centre, thus strengthening the π-bond. The Ru−Cl distances are not affected by a change of arene but are slightly longer than those found in related structures where N belongs to a pyridine ring.[33] The corresponding Ru−NH$_3$ bond lengths in complexes **1** and **2** (2.116(8) and 2.135(3) Å, respectively) are within the range found in similar complexes such as [(η^6-*p*-cym)Ru(NH$_3$)$_2$Cl]$^+$,[9] where the distances are 2.1504(15) and 2.1425(15) Å, but are slightly larger than the ones found in analogous complexes where the nitrogen donor atom belongs to a pyridine derivative.[9,33] A significant number of H-bond interactions were found throughout the corresponding unit cells of the Ru^{II} arene complexes **1** and **2**, where mainly the NH$_3$ groups (as H-bond donor groups) are involved. This feature is particularly interesting since it is known that the activity of platinum am(m)ine anticancer compounds depends on the presence of hydrogen-bond donor NH groups.[28] Similarly, the critical role of having N–H donor atoms within bidentate chelating

ligands in Ru^{II} arene complexes for controlling and promoting interactions with model DNA nucleobases, has been also demonstrated for $\{(\eta^6\text{-arene})Ru(en)\}^{2+}$ derivatives (en is ethylenediamine), for which a strong preference towards guanine derivatives has been established.[27] This site-selectivity appears to be controlled by the NH$_2$ groups of the en ligand, which can form strong hydrogen bonds with the C6O carbonyl group of guanine bases. Thus, the presence of a H-bond donor (such as NH$_3$ groups) may be an important feature in the future design of bifunctional Ru^{II} arene complexes such as **1** and **2**. Furthermore, the X-ray crystal structures of compounds **1** and **2** also show an increased number of intra and/or intermolecular π-π stacking interactions, a common feature observed in similar Ru^{II} complexes containing extended aromatic rings.[34] The (dmab–H)(PF$_6$) ionic pair in the crystal packing of **1** actively participates to H-bond and stacking interactions in the solid state. Amongst the latter interactions, an interesting π-π stacking was observed between molecules of the cation (dmab–H)$^+$. The phenomenon of stacking among positively charged π-rich systems despite strong electrostatic repulsion, has been theoretically and experimentally studied.[35] This type of non-bonding interaction, symbolised by (+)–(π)/(+) –(π) accounts for pairing of basic amino acid side chains such as arginines and histidines in proteins. In the case of complex **2**, an intermolecular π-π stacking interaction was observed through both of the phenyl rings in the bip arene with a ph$_{(centroid)}$–ph$_{(centroid)}$ distance of 3.687 Å, indicative of an effective stacking.[36]

6.4.3   Aqueous Solution Chemistry

The hydrolysis of complexes **1** and **2** at 310 K was studied using UV-vis spectroscopy. The extent of the reaction and the nature of the products were verified by ^{1}H NMR spectroscopy or ESI-MS. The decrease in absorbance at 225 nm with time for **1** and **2** in 5% MeOH/95% H$_2$O displayed a bi-exponential dependence, as

shown by the fit to the data. Related mononuclear Ru^{II} arene complexes undergo a monoexponential decrease in absorbance because of loss of a chloride and substitution by water.[37] In complexes **1** and **2**, there are two chlorido ligands that can be substituted by water. The absence of a clear isosbestic point in their UV-vis absorption spectra correlates to biexponential kinetics. The loss of the first chlorido ligand would be expected to be faster than the substitution of the second because of the formation of increased positive charge on the molecules whilst going from [M] $\rightarrow$ [M]$^+$ $\rightarrow$ [M]$^{2+}$. This is true for both complexes **1** and **2**, where the first hydrolysis rate (k_1) of complex **1** is not only *ca.* 48 times faster than the second (k_2) but *ca.* 1.5 times faster than k_1 for the bip complex **2** ($k_1 = 555.0 \times 10^{-3}$ min^{-1}). The donation of electron density to the Ru^{II} centre by the *p*-cym ring in **1** (and to a lesser extent by the bip arene in **2**) decreases the positive charge on the metal centre making it more favourable for the first chlorido ligand to leave thus speeding up the hydrolysis reaction. This could also account for the faster first-hydrolysis rate for complex **1** compared to that of complex **2**. On the other hand, the already increased destabilisation of complex **2** brought about by the hydrolysis of the first chlorido ligand along with the poor electron-donating properties of the bip arene (compared to *p*-cym in complex **1**) might account for the observed arene loss, a phenomenon which has been previously reported for other Ru^{II} bip complexes containing phenylazopyridines as π-acceptor ligands.[32b]

6.4.4   Interactions with Nucleobases

DNA is a potential target for transition metal anticancer complexes.[38] For this reason, reactions of complexes **1** and **2** with 9-EtG as a model nucleobase were investigated in aqueous solution at 310 K. Both complexes react relatively rapidly with *N7* of 9-EtG (less than 2 h to reach equilibrium in both cases) and to a moderate extent, to

form what is believed to be mono- and di-guanine adducts upon hydrolysis. A similar profile of reactivity has been found for cisplatin, which by having two available reactive sites can bind to its target site DNA in a bifunctional manner, forming intra- and inter-strand crosslinks.[39,40,41] Furthermore, coordination to two guanine bases has also been demonstrated for the fragment $\{\eta^6$-benzene)Ru$\}^{2+}$.[42] Overall, the reactions of complex **1** with 9-EtG take longer to reach equilibrium compared to those of complex **2**, but are more quantitative. Around 20% and 50% of the mono- and di-guanine adducts of complex **1**, respectively were formed after 106 min of reaction whereas complex **2** forms only little amounts of the mono-guanine adduct (less than 5%) and around 30% of the di-guanine adduct before the onset of arene loss (*ca.* 160 min). It is possible that a larger extent of guanine-substitution could occur in the case of complex **2** after *ca.* 160 min (as detected by ^{1}H NMR) given that three vacant positions are generated. On the other hand, in all the 9-EtG (both the mono- and the di-guanine) adducts of complexes **1** and **2**, the ^{1}H NMR peaks corresponding to H8 are shifted to lower field relative to free 9-EtG under the same conditions from a minimum of *ca.* 0.02 ppm for the mono-guanine adduct of complex **2** $[(\eta^6$-bip)Ru(NH$_3$)(9-EtG-*N7*)Cl]$^+$ (**2-EtG**), up to a maximum of *ca.* 0.4 ppm for the di-guanine adduct of complex **1** $[(\eta^6$-*p*-cym)Ru(NH$_3$)(9-EtG-*N7*)$_2$]$^{2+}$ (**1-EtG$_2$**). Metallation at the *N7* site of purine bases usually produces a low field shift of the H8 resonance by about 0.3–1 ppm.[43] This same behaviour has been previously observed for en Ru^{II} and Os^{II} arene complexes.[44]

6.4.5 Cancer Cell Growth Inhibition (IC$_{50}$)

None of the neutral complexes of the type $[(\eta^6$-arene)Ru(NH$_3$)Cl$_2$] containing either *p*-cym (**1**) or bip (**2**) were cytotoxic against the A2780 human ovarian cancer cell line up to the maximum concentration tested (100 μM). It is known that metal

coordination complexes can undergo ligand substitution reactions with components of the media in which they are dissolved.[45] In the case of complexes **1** and **2**, the diminished anticancer activity could be due to their tendency to hydrolyse in aqueous solution and therefore become inactivated by the components in the media even before reaching the cell or by other biomolecules once within the cell. This same hypothesis of inactivation has been previously suggested for complexes of the type [(η^6-*p*-cym)Ru(X)(Y)Z] where X, Y or Z are monodentate ligands such as halides, acetonitrile or isonicotinamide.[6] Further studies are needed to account for the reduced anticancer potency of complexes **1** and **2**.

6.5 Summary

In this Chapter it has been shown that neutral half-sandwich Ru^{II} constitutional analogues of cisplatin can be synthesised by the reaction of N,N'-dimethylbenzylamine, NH_4PF_6 and the corresponding Ru^{II} arene dimer. These analogues display extensive H-bond interactions in the solid state (as cisplatin does) through the NH_3 and Cl ligands. The biexponential hydrolysis rates of complexes [(η^6-arene)Ru(NH$_3$)Cl$_2$] **1** (*p*-cym) and **2** (bip), vary over many orders of magnitude; from half-lives of minutes (*ca.* 1 min for the first aquation of complex [(η^6-*p*-cym)Ru(NH$_3$)Cl$_2$] (**1**)) to hours (*ca.* 1 h for the second aquation of complex [(η^6-bip)Ru(NH$_3$)Cl$_2$] (**2**)) at 310 K. The possibility of using these complexes as anticancer agents was investigated by exploring their interactions with the model nucleobase 9-EtG in aqueous solution. Both complexes were found to readily form mono- and di-guanine adducts upon hydrolysis, which equilibrate in solution after 106 min (complex **1**) and 56 min (complex **2**). The reaction of complex **1** is slower but more quantitative. Hydrolysis is known to be a mechanism to provide a pathway for

cytotoxicity.[6] However, none of the neutral complexes were cytotoxic against the A2780 human ovarian cancer cell line up to the maximum concentration tested (100 μM). It is assumed that the reduced potency could arise from the inactivation of their aqua adducts by the components in the media even before reaching the cell or by other biomolecules within the cell. Further studies are needed to account for their reduced cytotoxicity.

6.6　References

[1]. Rosenberg, B.; Camp, L. V. *Nature*, **1965**, *205*, 698–699.

[2]. Rosenberg, B.; Camp, L. V.; Trosko, J. E.; Mansour, V. H. *Nature*, **1969**, *222*, 385–386.

[3]. Rosenberg, B.; Camp, L. V. *Cancer Res.*, **1970**, *30*, 1799–1802.

[4]. Cleare, M. J.; Hoeschele, J. D. *Bioinorg. Chem.*, **1973**, *2*, 187−210.

[5]. (a) Wang, X.; Guo, Z. *Dalton Trans.*, **2008**, *12*, 1521−1532; (b) Paraskar, A. S.; Soni, S.; Chin, K. T.; Chaudhuri, P.; Muto, K. W.; Berkowitz, J.; Handlogten, M. W.; Alves, N. J.; Bilgicer, B.; Dinulescu, D. M.; Mashelkar, R. A.; Sengupta, S. *Proc. Natl. Acad. Sci. U. S. A.*, **2010**, *107*, 12435−12440; (c) Zhao, G.; Lin, H. *Curr. Med. Chem.: Anti-Cancer Agents*, **2005**, *5*, 137−147.

[6]. (a) Morris, R. E.; Aird, R. E.; del Socorro Murdoch, P.; Chen, H.; Cummings, J.; Hughes, N. D.; Parsons, S.; Parkin, A.; Boyd, G.; Jodrell, D. I.; Sadler, P. J. *J. Med. Chem.*, **2001**, *44*, 3616−3621; (b) Chen, H.; Parkinson, J. A.; Parsons, S.; Coxall, R. A.; Gould, R. O.; Sadler, P. J. *J. Am. Chem. Soc.*, **2002**, *124*, 3064−3082

[7]. Gould, R. O.; Jones, C. L.; Robertson, D. R.; Stephenson, T. A. *Cryst. Struct. Comm.*, **1978**, *7*, 27−32.

[8]. (a) Robertson, D. R.; Stephenson, T. A.; Arthur, T. *J. Organomet. Chem.*, **1978**, *162*, 121–136; (b) Weber,W.; Ford, P. C. *Inorg. Chem.*, **1986**, *25*, 1088–1092; (c) Hung, Y.; W.-J., Kung; Taube, H. *Inorg. Chem.*, **1981**, *20*, 457–463.

[9]. Grguric-Sipka, S.; Stepanenko, I. N.; Lazic, J. M.; Bartel, C.; Jakupec, M. A.; Arion, V. B.; Keppler, B. K. *Dalton Trans.*, **2009**, 3334–3339.

[10]. (a) Bobka, R.; Roedel, J. N.; Neumann, B.; Krinninger, C.; Mayer, P.; Wunderlich, S.; Penger, A.; Lorenz, I.-P. *Z. Anorg. Allg. Chem.*, **2007**, *633*, 1985–1994; (b) Wallace, K. J.; Daari, R.; Belcher, W. J.; Abouderbala, L. O.; Boutelle, M. G.; Steed, J. W. *J. Organomet. Chem.*, **2003**, *666*, 63–74; (c) Dickson, S. J.; Paterson, M. J.; Willans, C. E.; Anderson, K. M.; Steed, J. W. *Chem. Eur. J.*, **2008**, *14*, 7296–7305.

[11]. (a) Govindaswamy, P.; Mozharivskyj, Y. A.; Kollipara, M. R. *Polyhedron*, **2004**, *23*, 3115–3123; (b) Singh, S. K.; Joshi, S.; Singh, A. R.; Saxena, J. K.; Pandey, D. Y. *Inorg. Chem.*, **2007**, *46*, 10869–10876.

[12]. (a) Ang, W. H.; De Luca, A.; Chapuis-Bernasconi, C.; Juillerat-Jeanneret, L.; Lo Bello, M.; Dyson, P. J. *Chem. Med. Chem.*, **2007**, *2*, 1799–1806; (b) Vock, C. A.; Ang, W. H.; Scolaro, C.; Phillips, A. D.; Lagopoulos, L.; Juillerat-Jeanneret, L.; Sava, G.; Scopelliti, R.; Dyson, P. J. *J. Med. Chem.*, **2007**, *50*, 2166–2175.

[13]. (a) Demonceau, A.; Stumpf, A. W.; Saive, E.; Noels, A. F. *Macromolecules*, **1997**, *30*, 3127–3130; (b) Delaude, L.; Demonceau, A.; Noels, A. F. *Curr. Org. Chem.*, **2006**, *10*, 203–215.

[14]. (a) Quebatte, L.; Solari, E.; Scopelliti, R.; Severin, K. *Organometallics*, **2005**, *24*, 1404–1406; (b) Sauvage, X.; Borguet, Y.; Noels, A. F.; Delaude, L.; Demonceau, A. *Adv. Synth. Catal.*, **2007**, *349*, 255–265.

[15]. Schmid, W. F.; John, R. O.; Arion, V. B.; Jakupec, M. A.; Keppler, B. K.

Organometallics, **2007**, *26*, 6643–6652.

[16]. Scolaro, C.; Bergamo, A.; Brescacin, L.; Delfino, R.; Cocchietto, M.; Laurenczy, G.; Geldbach, T. J.; Sava, G.; Dyson, P. J. *J. Med. Chem.*, **2005**, *48*, 4161–4171.

[17]. (a) Mendoza-Ferri, M. G.; Hartinger, C. G.; Nazarov, A. A.; Eichinger, R. E.; Jakupec, M. A.; Severin, K.; Keppler, B. K. *Organometallics*, **2009**, *28*, 6260–6265; (b) Kandioller, W.; Hartinger, C. G.; Nazarov, A. A.; Bartel, C.; Skocic, M.; Jakupec, M. A.; Arion, V. B.; Keppler, B. K. *Chem.–Eur. J.*, **2009**, *15*, 12283–12291; (c) Mendoza-Ferri, M. G.; Hartinger, C. G.; Mendoza, M. A.; Groessl, M.; Egger, A. E.; Eichinger, R. E.; Mangrum, J. B.; Farrell, N. P.; Maruszak, M.; Bednarski, P. J.; Klein, F.; Jakupec, M. A.; Nazarov, A. A.; Severin, K.; Keppler, B. K. *J. Med. Chem.*, **2009**, *52*, 916–925.

[18]. Maksomiska, J.; Williams, D. S.; Atilla-Gokcumen, G. E.; Smalley, K. S. M.; Carroll, P. J.; Webster, R. D.; Filippakopoulos, P.; Knapp, S.; Herlyn, M.; Meggers, E. *Chem. Eur. J.*, **2008**, *14*, 4816–4822.

[19]. Biersack, B.; Zoldakova, M.; Effenberger, K.; Schobert, R. *Eur. J. Med. Chem.*, **2010**, *45*, 1972–1975.

[20]. Sherman, S. E.; Lippard, S. J. *Chem. Rev.*, **1987**, *87*, 1153–1181

[21]. (a) Kostova, I. *Recent Pat. Anti-Cancer Drug Discovery*, **2006**, *1*, 1–22; (b) McGowan, G.; Parsons, S.; Sadler, P. J *Inorg. Chem.*, **2005**, *44*, 7459–7467.

[22]. Sheldrick, W. S.; Heeb, S. *Inorg. Chim. Acta*, **1990**, *168*, 93−100.

[23]. Bates, R. S.; Begley, M. J.; Wright, A. H. *Polyhedron*, **1990**, *9*, 1113−1118.

[24]. Carter, L.; Davies, D. L.; Fawcett, J.; Russell, D. R. *Polyhedron*, **1993**, *12*, 1123−1128.

[25]. (a) Bennet, M. A.; Smith, A. K. *J. Chem. Soc.*, *Dalton Trans.*, **1974**, 233−241;

(b) Govindaswamy, P.; Canivet, J.; Therrien, B.; Süss-Fink, G.; Štěpnička, P.; Ludvík, J. *J. Organomet. Chem.*, **2007**, *692*, 3664−3675; (c) Zelonka, R. A.; Baird, M. C. *J. Organomet. Chem.*, **1972**, *35*, C43−C46.

[26]. (a) Morrison, E. C.; Palmer, C. A.; Tocher, D. A. *J. Organomet. Chem.*, **1988**, *349*, 405–411; (b) Lahuerta, P.; Latorre, J.; Sanau, M.; Cotton, F. A.; Schwotzer, W. *Polyhedron*, **1988**, *7*, 1311−1316; (c) Elsegood, M. R. J.; Tocher, D. A. *J. Organomet. Chem.*, **1988**, *356*, C29−C31.

[27]. (a) Fernández, R.; Melchart, M.; Habtemariam, A.; Parsons, S.; Sadler, P. J. *Chem. Eur. J.*, **2004**, *10*, 5173–5179, (b) Dorcier, A., Dyson, P. J., Gossens, C.; Rothlisberger, U.; Scopelliti, R.; Tavernelli, I. *Organometallics*, **2005**, *24*, 2114−2123.

[28]. Reedijk, J. *Chem. Rev.*, **1999**, *99*, 2499−2510.

[29]. McMurry, J. *Organic Chemistry*, Brooks/Cole Thomson Learning, 5th. ed., **2000**, Pacific Groove, CA, U. S. A., p 860.

[30]. Shriver, D. F.; Atkins, P. W. *Inorganic Chemistry*, Oxford University Press, Oxford, **2002**, p 167.

[31]. Values taken from: (a) http://murov.info/orgsolvents.htm; (b) http://www.chemical-ecology.net/java/solvents.htm

[32]. (a) Bugarcic, T.; Habtemariam, A.; Stepankova, J.; Heringova, P.; Kasparkova, J.; Deeth, R. J.; Johnstone, R. D. L.; Prescimone, A.; Parkin, A.; Parsons, S.; Brabec, V.; Sadler, P. J. *Inorg. Chem.*, **2008**, *47*, 11470−11486.; (b) Dougan, S. J.; Melchart, M.; Habtemariam, A.; Parsons, S.; Sadler, P. J. *Inorg. Chem.*, **2006**, *45*, 10882−10894.

[33]. (a) Gupta, D. K.; Sahay, A. N.; Pandey, D. S.; Jha, N. K.; Sharma, P.; Espinosa, G.; Cabrera, A.; Puerta, M. C.; Valerga, P. *J. Organomet. Chem.*, **1998**, *568*, 13–20;

(b) Aronson, R.; Elsegood, M. R. J.; Steed, J. W.; Tocher, D. A. *Polyhedron*, **1991**, *15*, 1727−1732; (c) Singh, S. K.; Joshi, S.; Singh, A. R.; Saxena, J. K.; Pandey, D. S. *Inorg. Chem.*, **2007**, *46*, 10869−10876.

[34]. (a) van Rijt, S. H.; Hebden, A. J.; Amaresekera, T.; Deeth, R. J.; Clarkson, G. J.; Parsons, S.; McGowan, P.; Sadler, P. J. *J. Med. Chem.*, **2009**, *52*, 7753–7764; (b) Bugarcic, T.; Nováková, O.; Halámiková, A.; Zerzánková, L.; Vrána, O.; Kašpárková, J.; Habtemariam, A.; Parsons, S.; Sadler P. J.; Brabec, V. *J. Med. Chem.*, **2008**, *51*, 5310–5319.

[35]. Bruisine, E.; De Villiers, K.; Egan, T. J.; Biot, C. *J. Am. Chem. Soc.*, **2006**, *128*, 12122–12128.

[36]. Janiak, C. *J. Chem. Soc., Dalton Trans.*, **2000**, 3885–3896.

[37]. Wang, F.; Chen, H.; Parsons, S.; Oswald, I. D. H.; Davidson, J. E.; Sadler, P. J. *Chem. Eur. J.*, **2003**, *9*, 5810–5820.

[38]. Zhang, C. X.; Lippard, S. J. *Curr. Opin. Chem. Biol.*, **2003**, *7*, 481–489.

[39]. Jamieson, E. R.; Lippard, S. J. *Chem. Rev.*, **1999**, *99*, 2467–2498.

[40]. Brabec, B.; Kašpárková, J. *Metal Compounds in Cancer Chemotherapy*, **2005**, 187–218.

[41]. Wang, D.; Lippard, S. J. *Nature Rev. Drug Discovery*, **2005**, *4*, 307–320.

[42]. Korn, S.; Sheldrick, W. S. *J. Chem. Soc., Dalton Trans.*, **1997**, 2191–2199.

[43]. Scheller, K. H.; Scheller-Krattiger, V.; Martin, R. B. *J. Am. Chem. Soc.*, **1981**, *103*, 6833–6839.

[44]. Peacock, A. F. A.; Habtemariam, A.; Fernández, R.; Walland, V.; Fabbiani Francesca, P. A.; Parsons, S.; Aird, R. E.; Jodrell, D. I.; Sadler P. J. *J. Am. Chem. Soc.*, **2006**, *128*, 1739–1748.

[45]. Ronconi, L.; Sadler, P. J. *Coord. Chem. Rev.*, **2007**, *251*, 1633–1648.

Chapter 7

Future Work and

Perspectives

Chapter 7
Future Work and Perspectives

This Chapter deals with potential new areas of investigation that could be opened up based on the results in the previous chapters. Furthermore, it also discusses the experiments, discoveries, and observations made along the lines of the major work presented in this thesis which were not further developed but are together an important body of information worth of further study.

7.1 Hydrophobicity, Cancer Cell Growth Inhibition, Cell Uptake, and Cell Distribution

In Chapter 3 it was shown how the systematic variation of the different ligands surrounding the Ru^{II} centre in complexes of the type $[(\eta^6\text{-arene})Ru(N,N')X]^+$ can lead not only to significant changes in the chemical reactivity in relation to hydrolysis but also in the interaction with biologically relevant molecules such as nucleobases and DNA. The cytotoxic activity seems to be also highly dependent on the nature of the N,N' chelating ligand as demonstrated by the half-sandwich Ru^{II} arene complexes containing 1,10-phenanthroline (phen) and 4,7-diphenyl-1,10-phenanthroline (bathophen) which were found to be highly potent towards A2780 human ovarian cancer cells. Remarkably potent is the bathophen derivative (IC_{50} value of 0.5 μM). Preliminary DNA binding studies also showed that in addition to phen, complexes with 2,2'-bipyrimidine (bpm) can also bind to DNA. It is then concluded that further studies are needed to identify the mechanism that inactivates some of the complexes suppressing the cytotoxic activity up to the maximum concentration tested (100 μM). Partition coefficient (Log P) values could be thus determined; they give a measure of

how hydrophilic or hydrophobic a compound is and this information has been used to establish a relationship between hydrophobicity, cell uptake, and anticancer activity for some Pt^{II} and Pt^{IV} complexes[1,2] as well as for other metallo-anticancer drugs.[3,4,5] An extended set of experiments with CT-DNA in cell-free media (such as DNA transcription by RNA polymerase *in vitro*, DNA melting temperature, circular and linear dichroism, or quenching of EtBr fluorescence) could also be carried out in order to establish in more detail the mode in which these complexes interact with DNA. On the other hand, low IC_{50} values (in the range of *ca.* 9.0–25.0 μM) were determined for some of the photoactivatable Ru^{II} arene complexes with pyridine or pyridine-derivative ligands introduced in Chapter 4. Since these complexes do not hydrolyse spontaneously, there is the possibility that the intact cations might exert a cytotoxic effect by mechanisms which could include, for example, modification of mitochondrial membrane permeability. Cell-uptake studies and Log P value determination could be useful tools in an attempt to elucidate their mechanism of cytotoxicity.

7.2 Studies of Ru^{II} Arene Halido Complexes with Antileukaemic Thiopurine Drugs

An interesting approach to the design of metal-based drugs is the preparation of complexes with active chemotherapeutic agents as ligands to obtain a synergistic effect.[6] The drug 6-mercaptopurine (MP) is a well-known clinical agent for therapy of human leukemias and its 6-thioguanine (TG) analogue(s) are active against some types of human cancers.[7] They belong to the family of drugs known as *antimetabolites*[8] which inhibit the use of a metabolite.[9] Such *antimetabolites* are often similar in structure to the metabolite that they interfere with, Figure 7.1, such as the

antifolates that interfere with the action of folic acid. These compounds are used in chemotherapy for cancer given that their presence can have toxic effects on cells, such as halting cell growth and cell division.[10] MP is also used as an immunosuppressive drug in transplant surgery[11] and most recently has been shown to impair HIV replication. The incorporation of MP into DNA is known to be an essential step for its cytotoxic activity. However, the structural effects of the MP substitution on duplex DNA have not been fully characterised.[12]
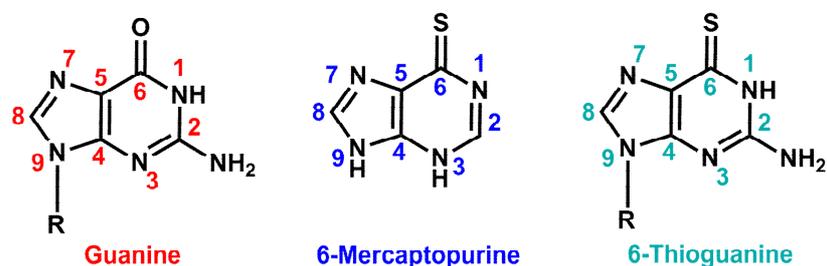
Figure 7.1. Structures of the DNA nucelobase guanine (G) and the *antimetabolites* 6-mercaptopurine (MP) and 6-thioguanine (TG). R represents the phosphate deoxyribose backbone.

The Ru^{II} arene complex $[(\eta^6\text{-}p\text{-cym})Ru(MP)(Cl)][PF_6]$ (**14**) introduced in Chapter 3, might be one of the few examples of piano-stool complexes which incorporate MP as the chelating ligand. A new family of complexes derived from $[(\eta^6\text{-}p\text{-cym})Ru(MP)(Cl)][PF_6]$ (**14**) could be studied, paying special attention to the investigation of their interactions with DNA as well as the overall chemical reactivity.

7.3 Synthesis of Photoactivatable Dinuclear Ru^{II} Arene Pyridine Complexes

Given that the photochemical studies on the mononuclear Ru^{II} arene complexes bearing pyridine or pyridine-derivatives studied in Chapter 4, showed that light activation can be used to phototrigger binding of these potential anticancer agents to

nucleobases and to DNA, the incorporation of a second Ru^{II} centre into the basic

scaffold of the molecule (using the unbound N,N' atoms in the bpm chelating ligand)

would in principle generate a new family of dinuclear Ru^{II} arene complexes such as

the *prototype* shown in Figure 7.2(A).
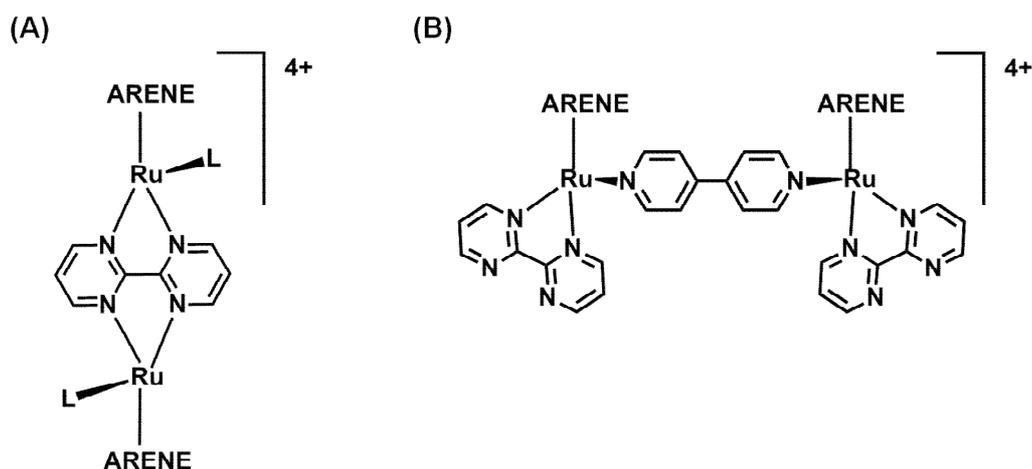
Figure 7.2. Structures of potential photoactivatable dinuclear Ru^{II} arene complexes where L is a pyridine or a pyridine-derivative ligand.

It has been previously reported that the dinuclear Ru^{II} indane complex $[\{(\eta^6\text{-}$ ind)Ru(Cl)$\}_2(\mu\text{-}2,3\text{-}dpp)_2][PF_6]_2$,[13] undergoes photoinduced arene loss in aqueous

media and in the presence of CT-DNA, producing novel types of DNA cross-links

that can not be readily achieved by chemical reactions alone. What is more, having

two metal centers (M^{n+}, where $M_1^{n+} = M_2^{n+}$ or $M_1^{n+} \neq M_2^{n+}$) in the same molecule

linked by an electron-rich (poly)pyridyl chelating ligand dramatically changes the

photochemical reactivity of complexes and therefore their potential applications.[14,15,16]

It is thus possible that by photoreleasing two L ligands from the dinuclear Ru^{II} arene

complex (depicted in Figure 7.2(A)), cell-lethal bifunctional lesions on DNA could be

generated. The formation of dinuclear Ru^{II} arene complexes could also be achieved by

carefully selecting the bridging ligand to incorporate it into the basic scaffold. The

two metal centres could be linked not only through the N,N'-chelating but also

through the monodentate ligand so as to generate structures as that shown in Figure 7.2(B). Those Ru^{II} arene dinuclear complexes would display high positive charges which could in turn improve and enhance their interactions with DNA, both with or without irradiation.

7.4 Photorelease of Biologically Active Molecules

From the structure-photoactivity relationship done for the Ru^{II} arene pyridine and pyridine-derivative complexes studied in Chapter 4, it is clear that the synthesis and photochemical behaviour of this family of complexes is exceptionally rich. A more detailed study could therefore be directed towards the potential role that the released ligand might have in the media where the photoactivation is actually happening. Coordination of a bioactive molecule to the Ru^{II} centre in these systems and its eventual photorelease could be coupled to biological assays where the activity of the bioactive molecule (once free) could be tested. This strategy could also be used to photorelease the biologically relevant molecule from the Ru^{II} centre into a specific compartment of the cell or be used as a probe through specific quenching/enhancement of fluorescence if the ligand is bound/free. Along this line, preliminary results from a collaboration with Miss Flavia Barragán from the Universitat de Barcelona in Spain, show that we were able to couple a biologically active polypeptide to the $\{(\eta^6\text{-}p\text{-cym})Ru(bpm)\}^{2+}$ fragment and proved its further specific photorelease using UVA irradiation in a similar fashion as the pyridine or pyridine-derivative ligands do.

7.5 Bio-inspired Hydride-Transfer Reactions of Ru^{II} Arene Complexes

In Chapter 5, it was proved for the first time (to the best of my knowledge) that 1,4-NADH can participate in hydride-transfer reactions to Ru^{II} arene chlorido complexes forming Ru−H species plus NAD$^+$. This reaction is of importance since it mimics the function of NADH in cells. The bio-inspired hydride-transfer is currently being explored towards the reduction of biologically relevant substrates. We are using sodium pyruvate as the substrate, aiming to mimic the function of the enzyme lactate dehydrogenase which catalyses the interconversion of pyruvate and lactate with concomitant interconversion of 1,4-NADH and NAD$^+$,[17] Figure 7.3.
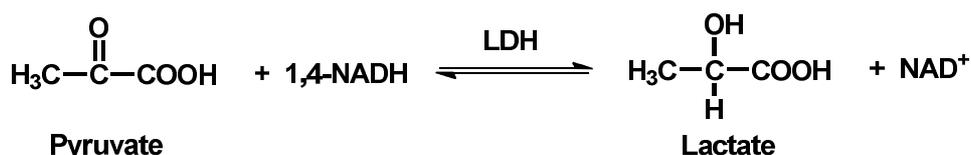
Figure 7.3. Catalytic reaction of the enzyme lactate dehydrogenase (LDH).

7.6 References

[1]. Hall, M. D.; Amjadi, S.; Zhang, M.; Beale, P. J.; Hambley, T. W. *J. Inorg. Biochem.*, **2004**, *98*, 16414−1627.

[2]. Oldfield, S. P.; Hall, M. D.; Platts, J. A. *J. Med. Chem.*, **2007**, *50*, 5227−5237.

[3]. Barbieri, R. *Inorg. Chim. Acta*, **1992**, *191*, 253−259.

[4]. Mendoza-Ferri, M.-G.; Hartinger, C. G.; Eichinger, R. E.; Stolyarova, N.; Severin, K.; Jakupec, M. A.; Nazarov, A. A.; Keppler, B. K. *Organometallics*, **2008**, *27*, 2405−2407.

[5]. van Rijt, S. H.; Mukherjee, A.; Pizarro, A.; Sadler, P. J. *J. Med. Chem.*, **2010**; 53, 840−849.

[6]. Chen, Y.; Lin, F.-T.; Shepherd, R. E. *Inorg. Chem.*, **1997**, *36*, 818−826.

[7]. (a) Zubrod, C. J. *Life Sci.*, **1974**, *14*, 809−818; (b) Williams, D. R. *Chem. Rev.*, **1972**, *72*, 203−213; (c) Wood, H. B., Jr. *Cancer Chemother. Rep.*, *Part 3*, **1971**, *2*, 9−22; (d) Hansch, C.; Sammes, P. G.; Taylor, J. B.; Emmett, J. C.; Kennewell, P. D.; Ramsden, C. A. (Eds.) *Comprehensive Medicinal Chemistry*, Pergamon Press, Oxford, **1990**.

[8]. Vora, A.; Mitchell, C. D.; Lennard, L.; Eden, T.; Kinsey, S. E.; Lilleyman, J.; Richards, S. M. *The Lancet*, **2006**, *368*, 1339−1348.

[9]. Smith, A. L. *Oxford Dictionary of Biochemistry and Molecular Biology*, Oxford, Oxford University Press, **1997**, p 43.

[10]. Peters, G. J.; van der Wilt, C. L.; van Moorsel, C. J.; Kroep, J. R.; Bergman, A. M.; Ackland, S. P. *Pharmacol. Ther.*, **2000**, *87*, 227–53.

[11]. Elion, C. B.; Bieber, S.; Hitchings, G. H. *Ann. N.Y. Sci.*, **1954**, *60*, 297−303.

[12]. Bohon, J.; de los Santos, C. R. *Nucleic Acids Res.*, **2003**, *31*, 1331−1338.

[13]. Magennis, S. W.; Habtemariam, A.; Novakova, O.; Henry, J. B.; Meier, S.; Parsons, S.; Oswald, I. D. H.; Brabec, V.; Sadler, P. J. *Inorg. Chem.*, **2007**, *46*, 5059−5068.

[14]. Gonzalez, V.; Wilson, T.; Kurihara, I.; Imai, A.; Thomas, J. A.; Otsuki, J. *Chem. Commun.*, **2008**, 1868−1870.

[15]. Schmitt, F.; Govindaswamy, P.; Süss-Fink, G.; Ang, W. H.; Dyson, P. J.; Juillerat-Jeanneret, L.; Therrien, B. *J. Med. Chem.*, **2008**, *51*, 1811−1816.

[16]. Schatzschneider, U. *Eur. J. Inorg. Chem.*, **2010**, 1451–1467.

[17]. (a) Walker, J. E. *Q. Rev. Biophys.*, **1992**, *25*, 253–324; (b) Yagi, T.; Yagi-Matsuno, A. *Biochemistry*, **2003**, *42*, 2266–2274; (c) Hirst, J. *Biochem. Soc. Trans.*, **2005**, *33*, 525–529; (d) Sazanov, L. A., *Biochemistry*, **2007**, *46*, 2275–2288.

Courses Attended

1. MOAC (Molecular Organisation and Assembly in Cells, University of Warwick) course on Biophysical Techniques and Instrumentation Design, November **2007**.

2. Postgraduate Award in Introduction to Academic and Professional Practice for Postgraduates who Teach, University of Warwick, November **2007**.

3. IAMBEC (Instrumental and Analytical Methods in Chemistry, University of Warwick) course on Chromatography, February **2008**.

4. Graduate School Skills Programme, University of Warwick training sessions, September **2007**–June **2009**.

    - Presenting to an Academic Audience

    - Organising References using EndNote Web

    - Paragraph Construction: Elements and Transition

    - Understanding Academic Writing and the Main Types of Postgraduate Writing

    - Engaging the Reader: Writing Text that is Interesting to Read; Coherence and Unity

    - Science Communication

    - Writing for Publication

    - Women PhDs

    - Speed Reading

5. RSC (Royal Society of Chemistry) Research Lectures held at the University of Warwick. **2007**–**2010**.

Conferences and Meetings Attended

1. COST D39 Meeting Metallo-drug Design and Action, Birmingham (U.K.), October **2007**.

2. Protein NMR Seminar at the University of Warwick, November **2007**.

3. Körber Project Meeting on Photonic Crystal Fibres in Biomedicine and Sensing at the University of Warwick, University of Bath, and Edinburgh University, June **2008**–December **2009**. *Oral Presentation*.

4. University of Warwick Chemistry Postgraduate Symposium, June **2009**. *Poster presentation*.

5. University of Warwick Chemistry Postgraduate Symposium, June **2010**. *Oral presentation and Talk Second prize awarded*.

6. Universitá degli Studi di Torino, Dipartimento di Chimica IFM (Chimica Inorganica, Chimica Fisica, Chimica dei Materiali), Turin, Italy, June **2010**. *Oral Presentation*.

7. 10th European Biological Inorganic Chemistry Conference EUROBIC, Thessaloniki (Greece), June **2010**. *Poster presentation*.

8. COST D39 Meeting "Metallo-drug design and Action", Thessaloniki (Greece), June **2010**.

Research Stays

1. Visiting Researcher in the laboratory of Prof Viktor Brabec at the Academy of Sciences of the Czech Republic, Brno as part of COST Action D39, November–December **2009**.

Chapter 3
Appendix

A.3.1.   *Computational details: Mechanism of Hydrolysis*

The Slater Type Orbital (STO) basis set comprised a triple-ζ plus 5p orbital set (TZP) on Ru with double-ζ plus polarisation (DZP) on all other atoms (ADF BASIS key: type DZP). Default convergence criteria were applied for SCF and cartesian geometry optimisations. For optimisations in internal coordinates, in particular TS searches, the angle threshold was set to 1.5° (default = 0.5 °). This criterion was relaxed due to the long bond lengths at the transition states, which make it harder to define torsional terms accurately. The same problem occurs for reactant and product species because the respective entering and leaving groups are included in the calculation, and their relatively weak interaction with the rest of the complex again leads to less well defined torsional terms. However, the energetic consequences of relaxing the angle constraints are negligible. The Amsterdam Density Functional (ADF) program reported a single negative eigenvalue in the Hessian matrix for all transition state optimisations. A representative TS was confirmed as a first order saddle point with frequency calculations as described earlier. The conductor-like screening model (COSMO) as implemented in ADF was used to simulate the aqueous environment with $\varepsilon = 78.4$, probe radius = 1.9 Å, and the ND parameter which controls integration accuracy set to 4 (default 3). The atomic radii (Å) used were Ru = 1.950, O = 1.517, C = 1.700, N = 1.608, H = 1.350, Cl = 1.725, Br = 1.850, and I = 1.967.

Table A.3.1. Crystallographic data for $[(\eta^6\text{-}p\text{-cym})\text{Ru(bpm)I}][\text{PF}_6]$ (**3**), $[(\eta^6\text{-bip})\text{Ru(bpm)Cl}][\text{PF}_6]$ (**4**), $[(\eta^6\text{-bip})\text{Ru(bpm)I}][\text{PF}_6]$ (**6**), $[(\eta^6\text{-etbz})\text{Ru(bpm)Cl}][\text{PF}_6]$ (**7**), and $[(\eta^6\text{-}p\text{-cym})\text{Ru(bpm)(9-EtG-}N7)][\text{PF}_6]_2$ (**15**)

	3	**4**	**6**	**7**	**15**
Formula	$C_{18}H_{20}F_6IN_4PRu$	$C_{20}H_{16}F_6ClN_4PRu$	$C_{20}H_{16}F_6IN_4PRu$	$C_{17}H_{16}ClF_6N_4O_2PRu$	$C_{25}H_{31}F_{12}N_9O_2P_2Ru$
Molar Mass	665.32	593.86	685.31	589.83	880.60
Crystal system	monoclinic	monoclinic	monoclinic	monoclinic	Orthorhombic
Crystal Size/mm^3	0.20 x 0.20 x 0.08	0.50 x 0.10 x 0.02	0.20 x 0.20 x 0.20	0.30 x 0.10 x 0.01	0.60 x 0.16 x 0.16
Space group	P2(1)	P2(1)/n	P2(1)/n	P2(1)/c	Pbca
Crystal	Orange/block	Orange/block	Orange/block	Brown/block	Red block
a/ Å	8.4028(5)	12.4224(10)	12.3617(2)	11.4826(5)	19.4807(2)
b/ Å	11.4784(4)	12.361(3)	12.1203(2)	b = 24.1735(7)	16.83500(10)
c/ Å	11.7850(11)	15.0821(6)	15.4384(3)	c = 7.1171(3)	19.85560(10)
α/deg	104.362(8)	90	90	90	90
β/deg	90	106.376(5)	107.858(2)	93.836(4)	90
γ/deg	90	90	90	90	90
Z	2	4		4	8
R [F>4σ (F)]	0.0194	0.0326	0.0205	0.0382	0.0290
Rw$_b$	0.0428	0.0934	0.0505	0.0526	0.0746
GOF^c	1.032	1.079	1.080	0.756	1.057
$\Delta\rho$ max and min/eÅ^{-3}	+0.389, –0.470	+0.821, –0.572	+1.637, –0.695	+0.697, –0.649	+0.796, –0.742

Table A.3.2. H-Bonding in the X-Ray crystal structures of $[(\eta^6\text{-}p\text{-cym})Ru(bpm)I][PF_6]$ (**3**), $[(\eta^6\text{-bip})Ru(bpm)Cl][PF_6]$ (**4**), $[(\eta^6\text{-bip})Ru(bpm)I][PF_6]$ (**6**), and $[(\eta^6\text{-etbz})Ru(bpm)Cl][PF_6]$(**7**)

Compound	D	H	A	D-H (Å)	H...A (Å)	D...A (Å)	D-H-A (°)
3	C(13)	H(13A)	F(12)	0.98	2.68	3.268(3)	118.7
	C(13)	H(13A)	F(14)	0.98	2.65	3.395(3)	133.1
	C(4)	H(4A)	F(16)	0.93	2.49	3.339(4)	151.3[a]
	C(11)	H(11A)	F(12)	0.93	2.64	3.553(3)	168.2[b]
	C(16)	H(16A)	F(11)	0.98	2.37	3.337(3)	167.1[c]
4	C(3)	H(3A)	F(6)	0.93	2.31	3.213(6)	164.7[d]
	C(3)	H(3A)	F(3)	0.93	2.84	3.353(8)	116.3[d]
	C(4)	H(4A)	F(3)	0.93	2.96	3.440(8)	113.3[d]
	C(14)	H(14A)	N(5)	0.98	2.46	3.355(4)	151.1[e]
	C(20)	H(20A)	F(5)	0.93	2.65	3.327(6)	129.7[f]
	C(15)	H(15A)	N(12)	0.98	2.56	3.512(4)	162.9[g]
	C(17)	H(17A)	F(2)	0.98	2.34	3.157(5)	140.0[h]
	C(24)	H(24A)	F(4)	0.93	2.66	3.508(8)	151.6[h]
	C(20)	H(20A)	F(4)	0.93	2.88	3.509(9)	125.6[i]
6	C(2)	H(2A)	F(15)	0.95	2.43	3.2907(19)	150.8
	C(13)	H(9A)	F(13)	0.95	2.49	3.0685(19)	119.3[j]
	C(4)	H(9A)	I(1)	0.95	2.98	3.8021(16)	145.1[k]
	C(11)	H(10A)	F(15)	0.95	2.57	3.477(2)	168.2[l]
7	C(17)	H(17A)	Cl(1)	1.00	2.52	3.411(4)	147.6[m]
	C(9)	H(9A)	F(6)	0.95	2.47	3.088(5)	122.2[n]
	C(15)	H(15A)	F(3)	1.00	2.42	3.115(5)	125.8[o]
	C(3)	H(3A)	F(2)	0.95	2.44	3.213(4)	138.1[p]

Symmetry operators used to generate equivalent atoms involved in these contacts:
[a] [x+1, y+1, z]; [b] [x+1, y, z]; [c] [x, y+1, z]; [d] [2–x, –y, –z]; [e] [x–1/2, 1/2–y, 1/2+z]; [f] [x–1/2, 1/2–y, z–1/2]; [g] [3/2–x, y–1/2, 1/2–z]; [h] [5/2–x, y–1/2, 1/2–z]; [i] [2–x, 1–y, –z]; [j] [x–1/2, 1/2–y, 1/2+z]; [k] [x–1/2, 1/2–y, z–1/2]; [l] [3/2–x, y–1/2, 1/2–z]; [m] [5/2–x, y–1/2, 1/2–z]; [n] [2–x, 1–y, –z]; [o] [–x, –y, 1–z]; [p] [x, 1/2–y, 1/2+z]; [q] [x–1, y, z]; [r] [x–1, y, 1+z].

Chapter 4

Appendix

Table A.4.1. Crystallographic data of [(η^6-p-cym)Ru(bpm)(4-MePy)][PF$_6$]$_2$ (**2**), [(η^6-p-cym)Ru(bpm)(4-BzPy)][PF$_6$]$_2$ (**6**), [(η^6-p-cym)Ru(bpm)(trz)][PF$_6$]$_2$ (**7**), [(η^6-p-cym)Ru(phen)(Py)][PF$_6$]$_2$ (**10**), [(η^6-ind)Ru(biPy)(Py)][PF$_6$]$_2$ (**13**).

	2	6	7	10	13
Formula	C$_{24}$H$_{27}$F$_{12}$N$_5$P$_2$Ru	C$_{30}$H$_{27}$F$_{12}$N$_5$P$_2$Ru	C$_{21}$H$_{27}$F$_{12}$N$_7$OP$_2$Ru	C$_{33}$H$_{39}$F$_{12}$N$_3$O$_2$P$_2$Ru	C$_{24}$H$_{23}$F$_{12}$N$_3$P$_2$Ru
Molar Mass	776.52	848.58	784.51	900.68	744.46
Crystal system	Monoclinic	Monoclinic	Monoclinic	Monoclinic	Monoclinic
Crystal size/mm^3	0.40 x 0.20 x 0.10	0.40 x 0.20 x 0.08	0.40 x 0.40 x 0.10	0.30 x 0.20 x 0.15	0.30 x 0.20 x 0.20
Space group	P2(1)/n	C2/c	P2(1)/c	P2(1)/c	P2(1)/c
Crystal		Green block	Yellow block	Yellow block	Yellow block
a/ Å	10.7691(14)	37.0577(9)	15.5359(2)	11.90151(12)	11.3406(2)
b/ Å	23.718(3)	8.6964(2)	11.15838(17)	18.89949(16)	19.5778(3)
c/ Å	12.0221(14)	20.0783(5)	16.4506(2)	16.67645(19)	12.3483(3)
α/deg	90	90	90	90	90
β/deg	106.688(12)°	95.974(2)	96.4121(13)	103.1051(10)	107.0675(19)
γ/deg	90	90	90	90	90
Z	4	8	4	4	4
R [F>4σ (F)][a]	0.0446	0.0349	0.0307	0.0309	0.0283
Rw$_b$	0.1101	0.0877	0.0829	0.0792	0.0732
GOF^c	1.051	0.984	1.062	1.075	1.065
Δρ max and min/eÅ^{-3}	+0.637, -0.982	+1.046, -0.546	+1.840, -0.774	+0.996, -0.663	+1.168, -0.707

Table A.4.2. H-Bonding in the X-Ray crystal structures of $[(\eta^6\text{-p-cym})Ru(bpm)(4\text{-BzPy})][PF_6]_2$ (**6**), $[(\eta^6\text{-p-cym})Ru(bpm)(trz)][PF_6]_2$ (**7**), and $[(\eta^6\text{-p-cym})Ru(phen)(Py)][PF_6]_2$ (**10**).

	D	H	A	D-H (Å)	H...A (Å)	D...A (Å)	D-H-A (°)
6	C(11)	H(11A)	F(12)	0.95	2.39	3.281(3)	155.9
	C(2)	H(2A)	F(24)	0.95	2.43	3.352(3)	162.9[a]
	C(14)	H(14A)	F(21)	0.95	2.42	3.287(3)	151.8[b]
7	N(16)	H(16)	O(100a)[c]	0.898(18)	1.91(2)	2.728(5)	151(3)
	N(16)	H(16)	O(200b)[d]	0.898(18)	1.89(2)	2.737(7)	156(3)
	C(2)	H(2A)	F(16)	0.95	2.43	3.208(3)	138.4
	C(4)	H(4A)	F(21)	0.95	2.42	3.200(3)	139.2
	C(17)	H(17A)	F(16)	0.95	2.46	3.233(3)	138.4
10	C(2)	H(2A)	F(23A)	0.95	2.31	3.200(8)	156.7
	C(2)	H(2A)	F(23)	0.95	2.44	3.130(2)	128.9
	C(2)	H(2A)	F(26A)	0.95	2.40	3.076(7)	128.2
	C(3)	H(3A)	F(21A)	0.95	2.51	3.179(13)	127.2
	C(4)	H(4A)	F(25)	0.95	2.38	3.317(2)	169.3[c]
	C(4)	H(4A)	F(25A)	0.95	2.24	3.163(11)	164.8[d]
	C(16)	H(16A)	F(26A)	0.95	2.47	3.329(7)	151.1
	C(22)	H(22A)	O(102)	1.00	2.28	3.199(2)	152.8

Symmetry operators used to generate equivalent atoms involved in these contacts:
[a] [x, y+1, z]; [b] [1-x, 1-y, 1-z]; [c,d] [x, 1/2-y, 1/2+z]

Figure A.4.1. Selected orbitals (isovalue 0.02) for complexes **1**–**6** and **8**–**16** in the ground state optimised geometry.

HOMO	LUMO	LUMO+1	LUMO+2	LUMO+3

HOMO	LUMO	LUMO+1	LUMO+2	LUMO+3
9				
10				
11				
12				
13				
14				
15				

16
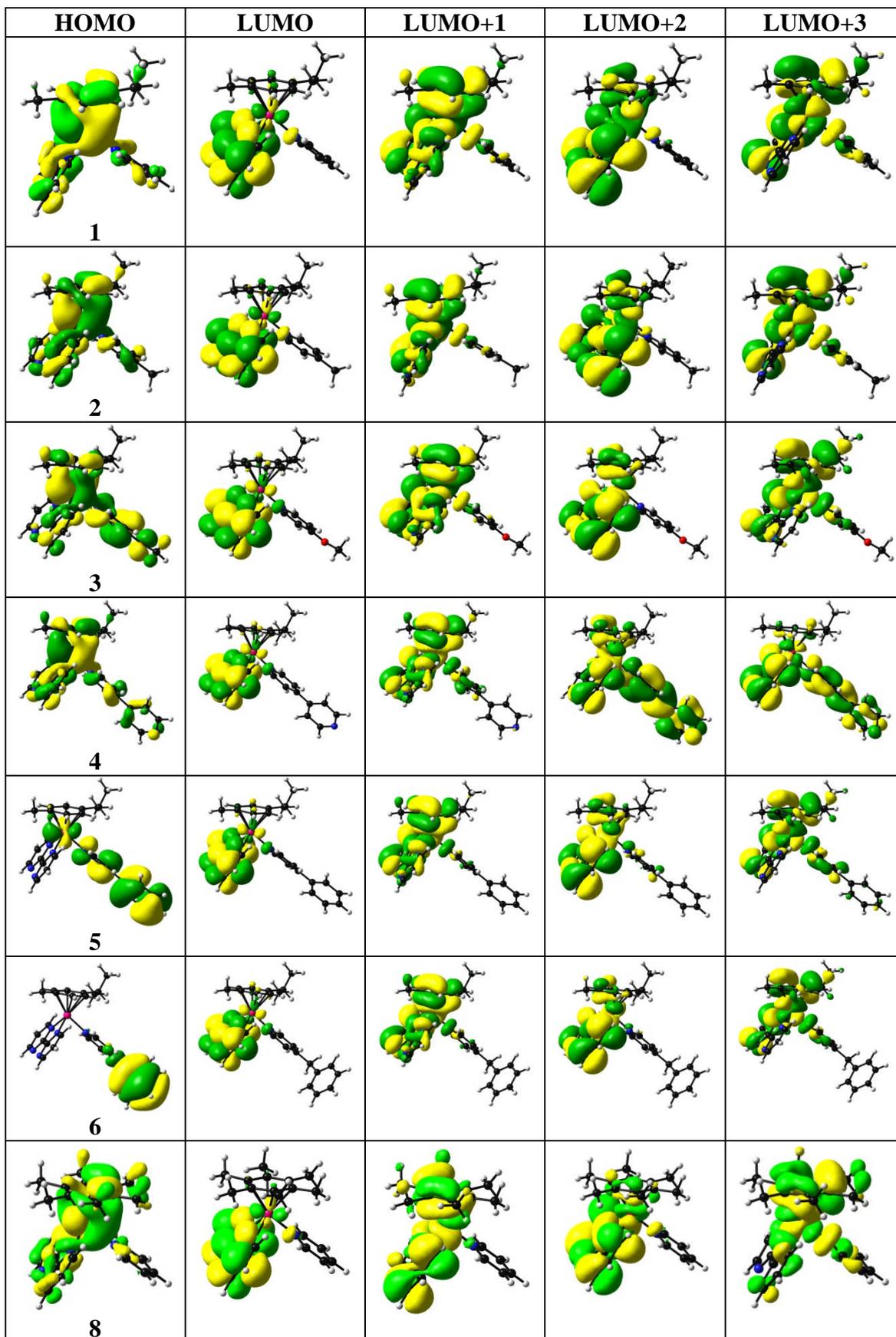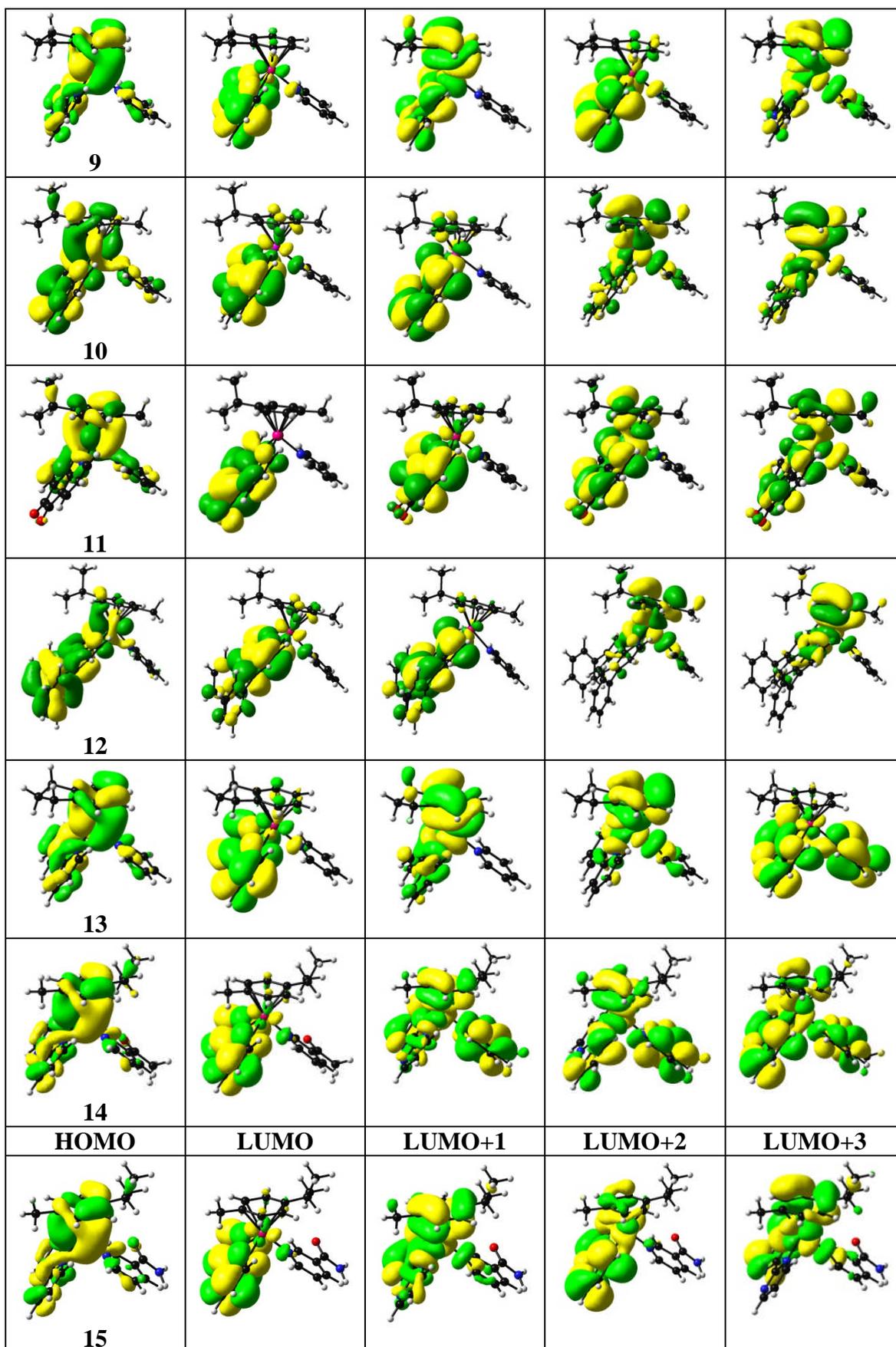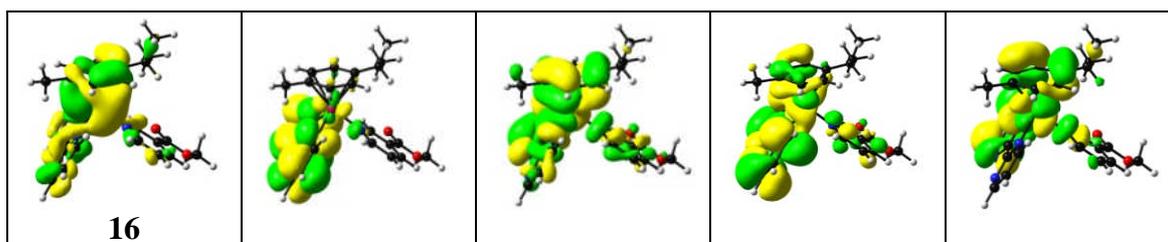
Figure A.4.2. Selected orbitals (isovalue 0.02) and spin density surface (isovalue 0.0004) for complexes **1**–**6** and **8**–**16** in the lowest-lying triplet optimised geometry.

	Lowest-SOMO	Highest-SOMO	Spin Density Surface
1			
2			
3			
4			
5			
6			

	Lowest-SOMO	Highest-SOMO	Spin Density Surface
8			
9			
10			
11			
12			
13			
14			

15			
16			
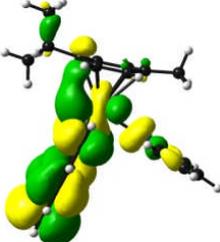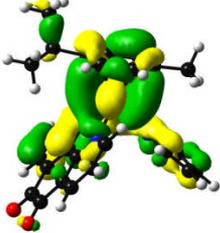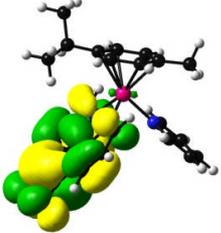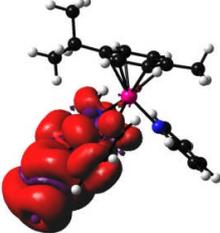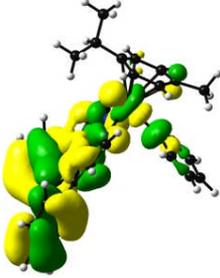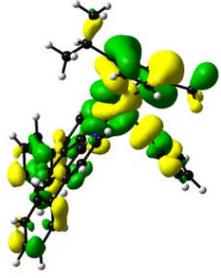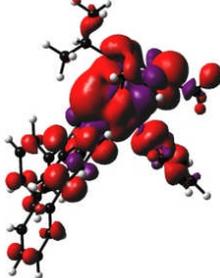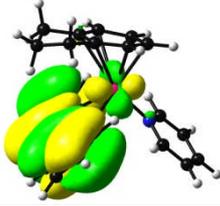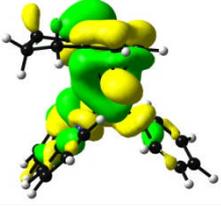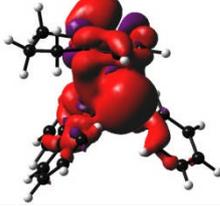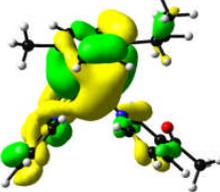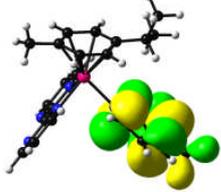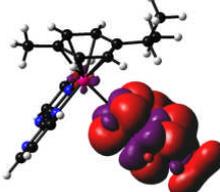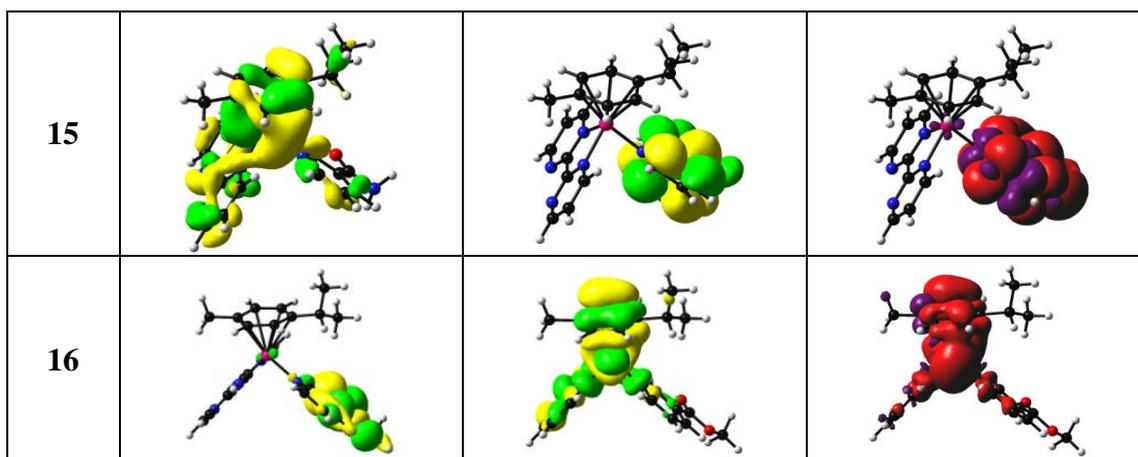
Table A.4.3. Selected TD-DFT singlet transitions for complex **1**.

	Energy (eV)	Wavelength (nm)	Oscillator Strength	Major contributions
1	2.8012	443	0.0024	HOMO→L+1 (46%) HOMO→L+3 (20%)
2	3.011	412	0.0059	H-2→L+3 (15%) H-1→L+3 (34%)
3	3.0392	408	0.001	H-1→L+1 (21%) H-1→L+3 (13%) HOMO→L+1 (12%) HOMO→L+2 (10%) HOMO→L+3 (14%) HOMO→L+4 (12%)
4	3.1191	398	0.001	H-2→L+1 (32%) H-2→L+2 (10%) H-2→L+4 (13%) H-1→L+1 (14%)
5	3.1993	387	0.0027	HOMO→LUMO (75%)
6	3.3581	369	0.0365	H-1→LUMO (79%)
8	3.6553	339	0.0148	H-2→LUMO (41%) H-2→L+3 (16%)
9	3.7767	328	0.0108	H-2→LUMO (48%) H-2→L+3 (-25%)
13	4.1763	297	0.0804	H-1→L+2 (13%) HOMO→L+4 (54%)
14	4.2527	291	0.0081	H-3→LUMO (16%) H-1→L+4 (59%)
16	4.4026	281	0.0051	H-7→LUMO (29%) H-6→LUMO (61%)
17	4.5092	275	0.0076	H-2→L+2 (19%) HOMO→L+5 (68%)
18	4.5221	274	0.0085	H-2→L+1 (10%) H-2→L+2 (43%) H-2→L+3 (10%) HOMO→L+5 (23%)

24	4.782	259	0.0807	H-5→LUMO (12%)
				H-3→L+1 (13%)
				H-1→L+6 (12%)
				H-1→L+7 (18%)
26	4.8081	258	0.1692	H-5→LUMO (18%)
				H-1→L+6 (11%)
				H-1→L+7 (18%)

Figure A.4.3. Selected Electron Difference Density Maps (EDDMs) of singlet excited state transitions of **1** in H_2O (light violet indicates a decrease in electron density, while purple indicates an increase).
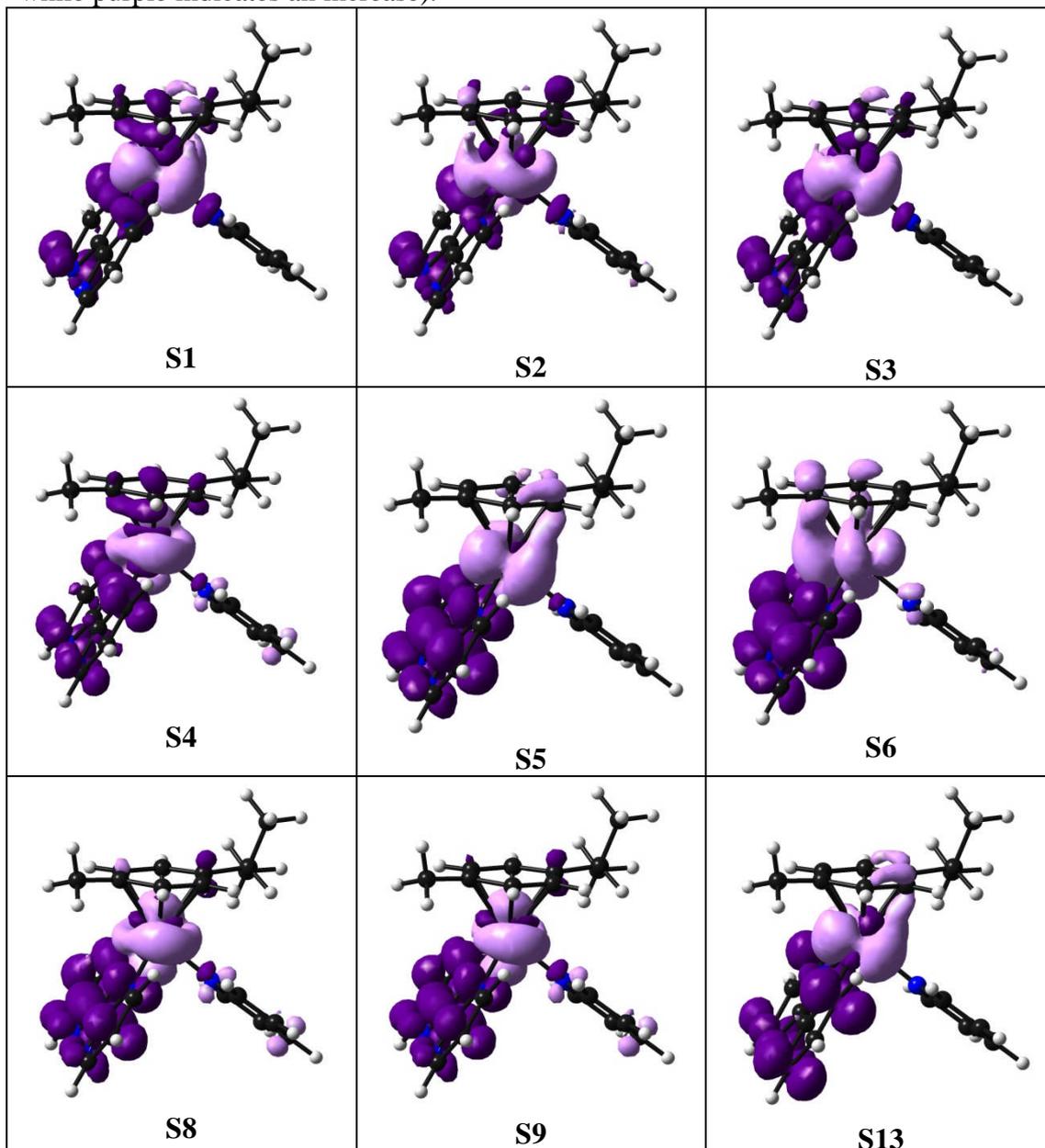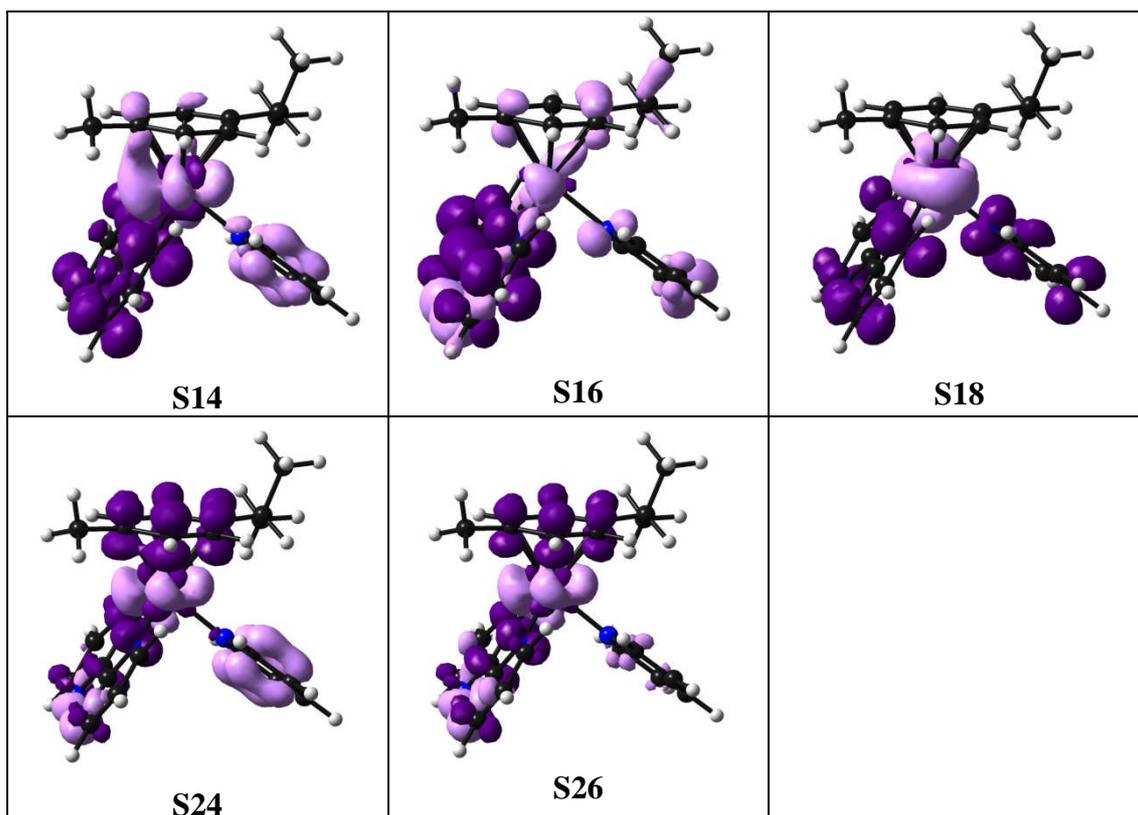
Table A.4.4. Selected TD-DFT singlet transitions for complex **2**.

	Energy (eV)	Wavelength (nm)	Oscillator Strength	Major contributions
1	2.805	442	0.0026	HOMO→L+1 (47%) HOMO→L+3 (20%)
2	3.011	412	0.0065	H-2→L+3 (10%) H-1→LUMO (10%) H-1→L+3 (46%)
3	3.046	407	0.0004	H-1→L+1 (18%) HOMO→L+1 (10%) HOMO→L+2 (11%) HOMO→L+3 (17%) HOMO→L+4 (15%)
4	3.125	397	0.0011	H-2→L+1 (28%) H-2→L+2 (11%) H-2→L+4 (14%) H-1→L+1 (12%) HOMO→LUMO (11%)
5	3.190	389	0.0036	HOMO→LUMO (68%)
6	3.340	371	0.0377	H-1→LUMO (77%)
8	3.636	341	0.0144	H-2→LUMO (57%) H-2→L+3 (10%)
13	4.161	298	0.0718	HOMO→L+2 (10%) HOMO→L+4 (56%)
21	4.683	264	0.0696	H-6→LUMO (36%) H-5→LUMO (29%)

24	4.738	262	0.0603	H-1→L+5 (64%)
25	4.780	259	0.0618	H-3→L+1 (35%)
				H-1→L+7 (15%)
27	4.803	258	0.2022	H-5→LUMO (19%)
				H-1→L+7 (13%)
31	5.054	245	0.0409	H-6→L+1 (12%)
				H-4→L+1 (12%)
				H-1→L+7 (12%)
35	5.160	240	0.0507	H-4→L+3 (15%)
				H-2→L+5 (49%)
41	5.279	235	0.0395	H-5→L+2 (28%)
				H-4→L+2 (16%)
45	5.387	230	0.0236	H-1→L+8 (38%)
				HOMO→L+8 (24%)

Figure A.4.4. Selected Electron Difference Density Maps (EDDMS) of singlet excited state transitions of **2** in H_2O (light violet indicates a decrease in electron density, while purple indicates an increase).
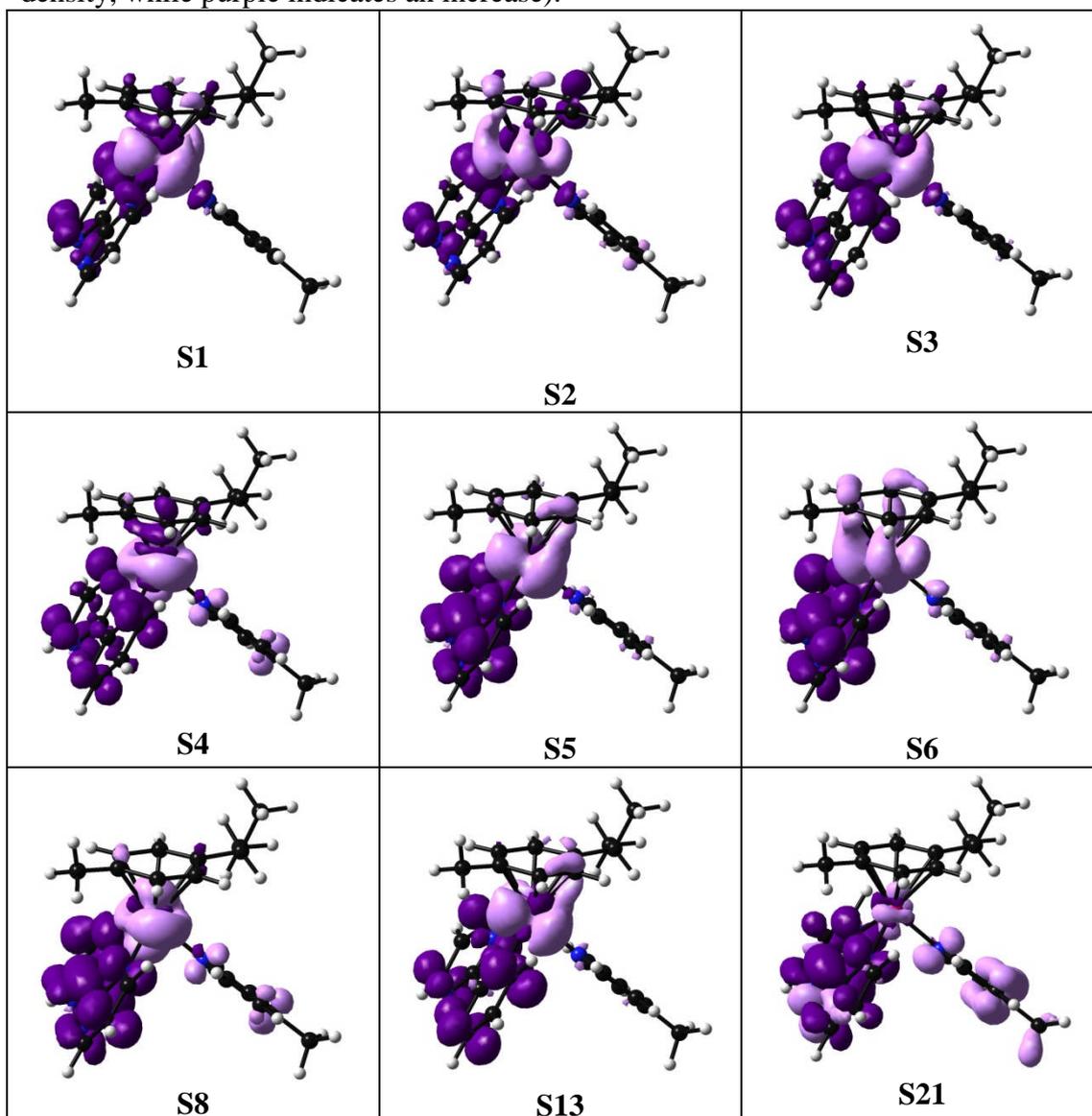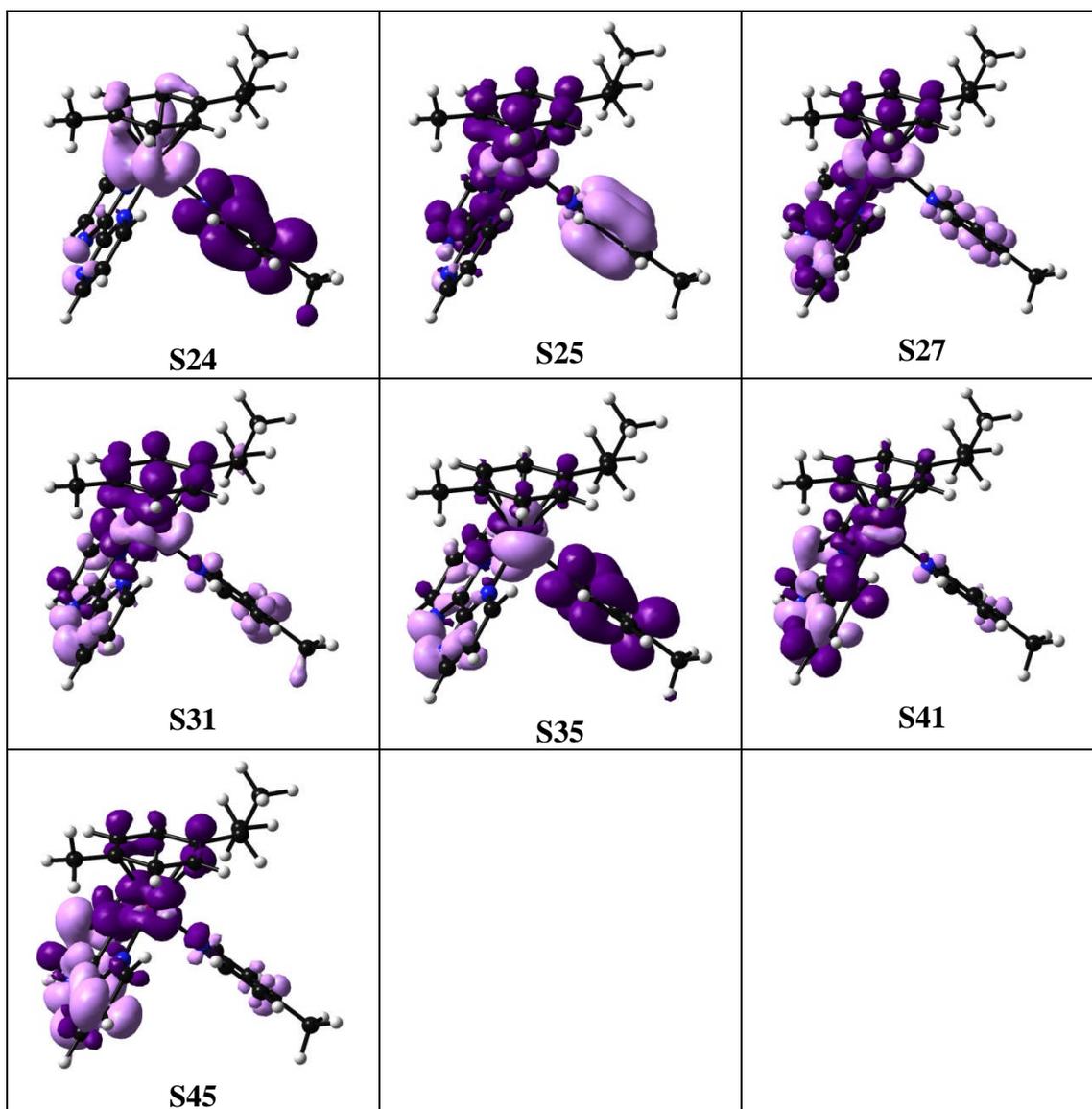
**Table A.4.5.** Selected TD-DFT singlet transitions for complex **3**.

	Energy (eV)	Wavelength (nm)	Oscillator Strength	Major contributions
1	2.795	444	0.0034	H-1→L+3 (12%) HOMO→L+1 (38%) HOMO→L+3 (14%)
2	2.992	414	0.0069	H-1→L+3 (40%) HOMO→L+3 (14%)
3	3.036	408	0.0004	H-1→L+1 (21%) H-1→L+2 (11%) H-1→L+4 (11%) HOMO→LUMO (12%) HOMO→L+3 (11%)
4	3.124	397	0.0013	H-2→L+1 (27%) H-2→L+2 (13%) H-2→L+4 (12%)

5	3.159	393	0.007	H-1→LUMO (22%)
				HOMO→LUMO (44%)
6	3.297	376	0.0349	H-1→LUMO (52%)
				HOMO→LUMO (23%)
12	4.046	306	0.0126	H-1→L+1 (18%)
				H-1→L+2 (50%)
13	4.085	304	0.0126	H-3→LUMO (24%)
				HOMO→L+4 (42%)
14	4.144	299	0.0298	H-3→LUMO (47%)
				HOMO→L+4 (22%)
15	4.206	295	0.0569	H-3→LUMO (13%)
				H-1→L+3 (11%)
				H-1→L+4 (53%)
26	4.784	259	0.2235	H-6→LUMO (38%)
31	4.964	250	0.0457	H-1→L+5 (36%)
				H-1→L+6 (10%)
				HOMO→L+5 (11%)
				HOMO→L+7 (14%)
34	5.059	245	0.0423	H-3→L+4 (11%)
				H-2→L+6 (16%)
				H-1→L+5 (13%)
35	5.079	244	0.0469	H-4→L+2 (15%)
				H-3→L+4 (26%)
47	5.407	229	0.1952	H-2→L+5 (45%)
				H-1→L+8 (21%)

Figure A.4.5. Selected Electron Difference Density Maps (EDDMS) of singlet excited state transitions of **3** in H_2O (light violet indicates a decrease in electron density, while purple indicates an increase).
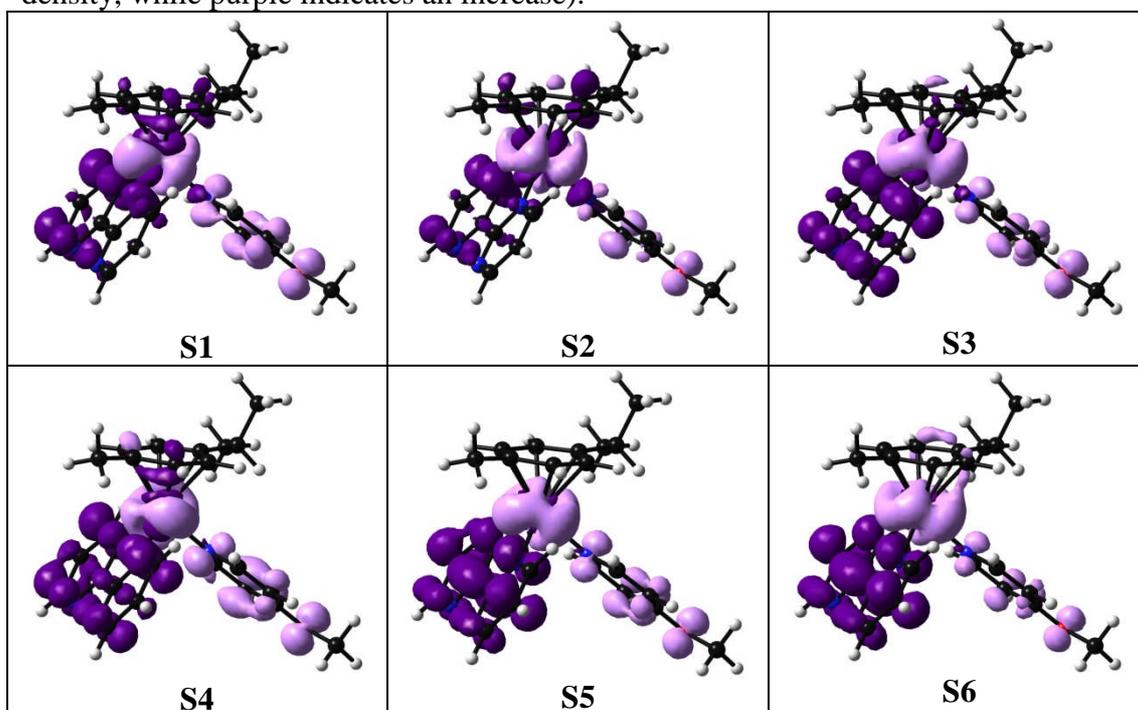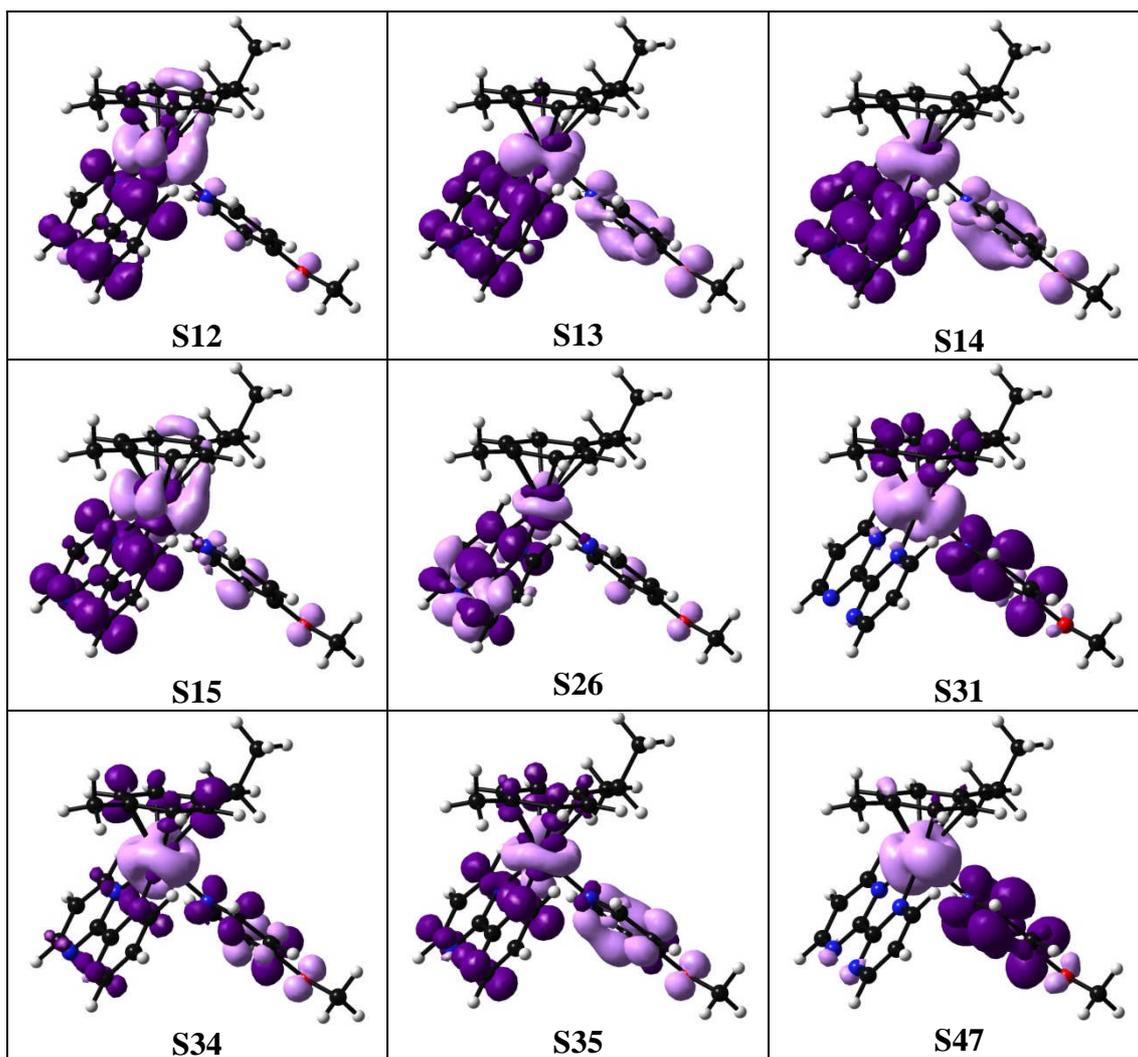
Table A.4.6. Selected TD-DFT singlet transitions for complex **4**.

	Energy (eV)	Wavelength (nm)	Oscillator Strength	Major contributions
1	2.808	442	0.0029	HOMO→L+1 (54%)
2	3.016	411	0.0071	H-1→LUMO (10%) H-1→L+4 (38%)
3	3.050	407	0.0005	H-1→L+1 (21%) HOMO→L+2 (12%) HOMO→L+4 (21%) HOMO→L+5 (10%)
4	3.133	396	0.0011	H-5→L+1 (10%) H-4→L+1 (23%)
5	3.210	386	0.0042	HOMO→LUMO (68%)
6	3.359	369	0.0362	H-1→LUMO (68%)
8	3.625	342	0.0105	H-5→LUMO (11%) H-4→LUMO (46%)
13	4.008	309	0.0064	H-8→LUMO (15%) H-7→LUMO (43%) HOMO→L+2 (13%) HOMO→L+3 (10%)

21	4.355	285	0.0009	H-6→LUMO (91%)
24	4.466	278	0.0405	H-4→L+1 (14%)
				H-4→L+2 (24%)
				H-4→L+3 (32%)
25	4.541	273	0.1679	H-4→L+2 (35%)
				H-4→L+3 (19%)
				H-4→L+5 (15%)
27	4.564	272	0.003	HOMO→L+6 (49%)
				HOMO→L+7 (32%)
31	4.674	265	0.0019	H-2→L+3 (24%)
				H-2→L+4 (69%)
35	4.744	261	0.065	H-5→L+1 (20%)
				H-4→L+1 (16%)
41	4.873	254	0.0385	H-6→L+1 (17%)
				H-5→L+2 (35%)
45	4.966	250	0.1434	H-5→L+2 (22%)
				H-5→L+4 (44%)
				H-4→L+4 (10%)

Figure A.4.6. Selected Electron Difference Density Maps (EDDMS) of singlet excited state transitions of **4** in H_2O (light violet indicates a decrease in electron density, while purple indicates an increase).
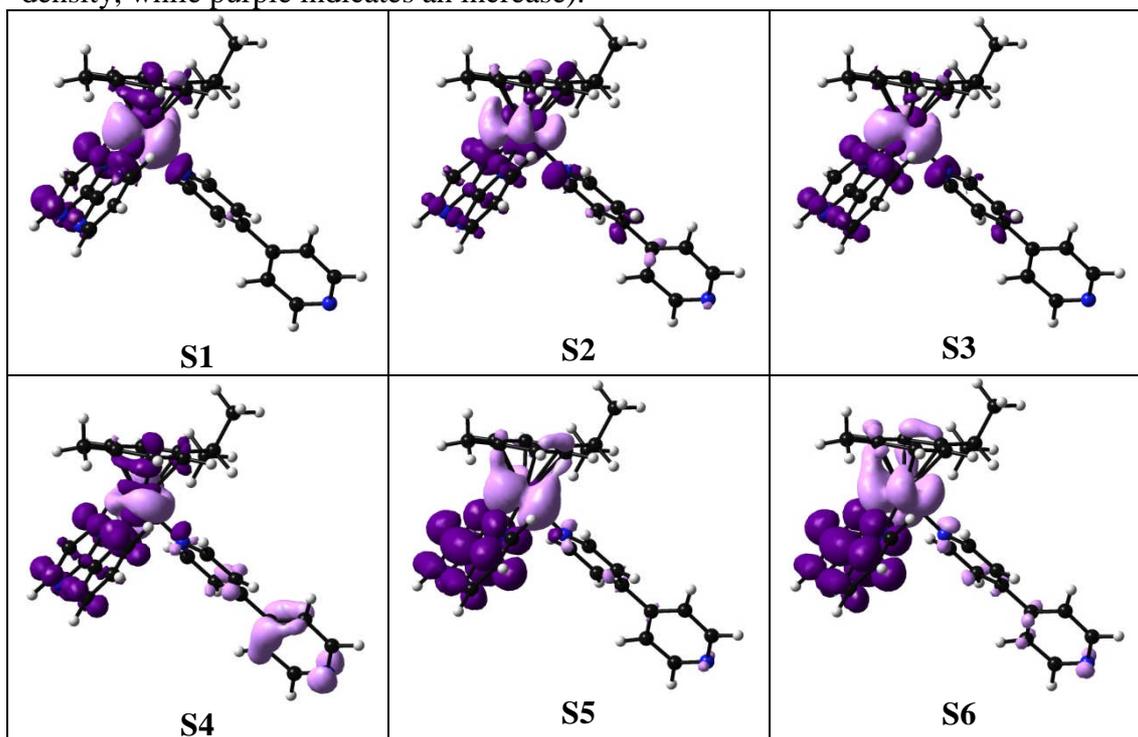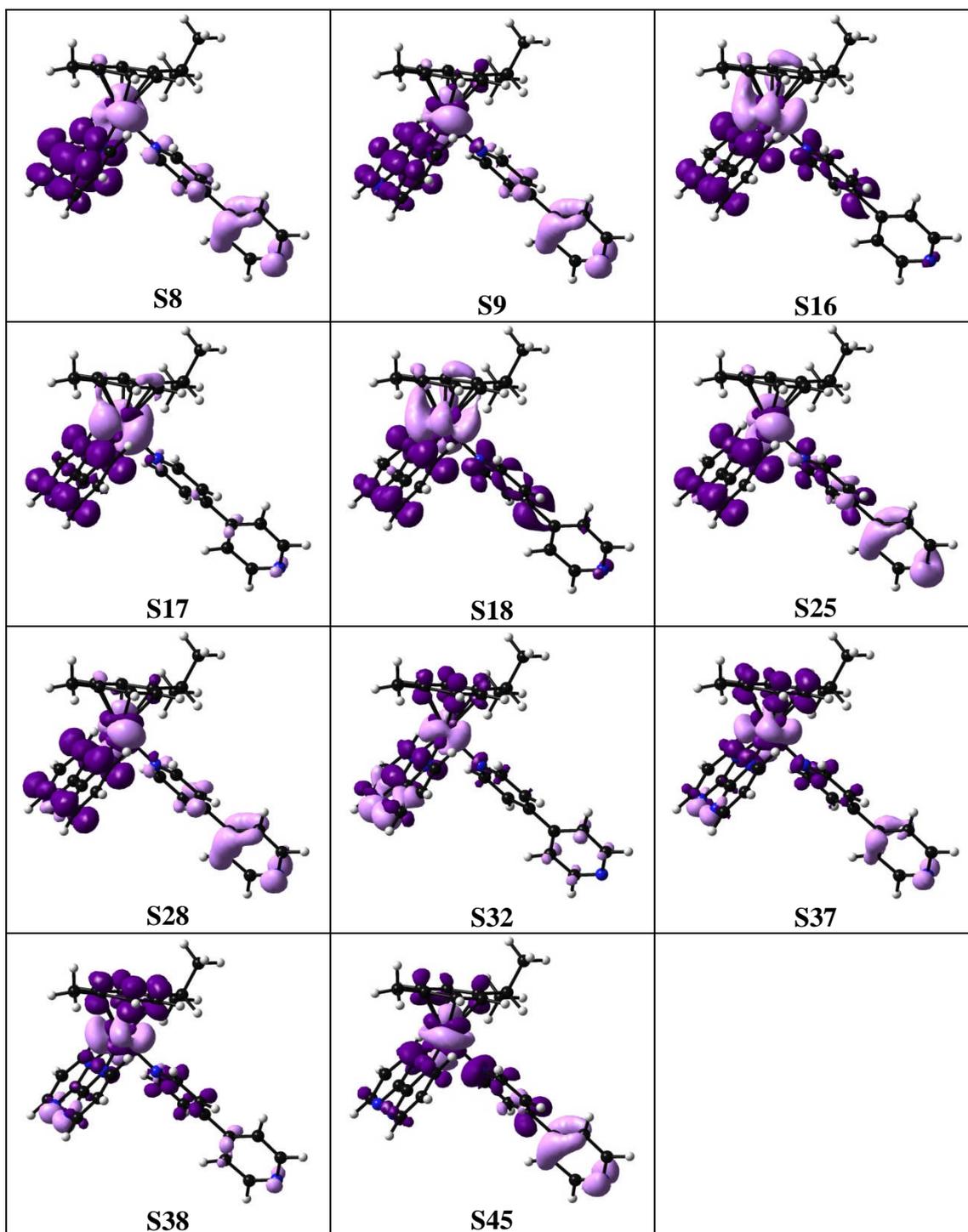
Table A.4.7. Selected TD-DFT singlet transitions for complex **5**.

	Energy (eV)	Wavelength (nm)	Oscillator Strength	Major contributions
1	2.812	441	0.0036	H-3→L+1 (10%) H-2→L+1 (26%) H-2→L+3 (20%) HOMO→L+1 (12%)

2	3.006	413	0.0097	H-4→L+3 (10%) H-3→L+3 (25%) HOMO→LUMO (10%) HOMO→L+3 (11%)
3	3.049	407	0.0003	H-2→L+1 (18%) H-2→L+2 (12%) H-2→L+4 (16%)
4	3.134	396	0.0018	H-4→L+1 (21%) H-3→L+1 (21%) H-2→LUMO (13%)
5	3.160	392	0.0105	H-4→L+1 (10%) H-2→LUMO (22%) HOMO→LUMO (35%)
6	3.253	381	0.0111	H-2→LUMO (40%) HOMO→LUMO (-30%)
7	3.410	364	0.0121	H-4→LUMO (11%) H-3→LUMO (71%) HOMO→LUMO (10%)
10	3.717	334	0.0152	H-4→L+3 (25%) H-3→L+3 (17%)
11	3.830	324	0.0257	H-4→LUMO (73%)
12	3.903	318	0.0130	H-2→L+2 (11%) HOMO→L+1 (18%) HOMO→L+2 (46%)
16	4.103	302	0.2253	H-3→L+1 (-13%) HOMO→L+1 (12%) HOMO→L+3 (33%) HOMO→L+4 (16%)
17	4.144	299	0.2741	H-2→L+4 (16%) HOMO→L+5 (37%)
18	4.184	296	0.1807	H-3→L+2 (10%) H-2→L+3 (10%) H-2→L+4 (22%) HOMO→L+5 (27%)
22	4.303	288	0.0496	H-2→L+5 (64%) H-1→L+5 (13%)
23	4.324	287	0.0186	H-2→L+5 (11%) H-1→L+2 (18%) H-1→L+3 (13%) H-1→L+4 (14%) H-1→L+5 (28%)
35	4.712	263	0.1104	H-7→LUMO (27%) H-6→L+2 (23%)
39	4.839	256	0.0814	H-6→L+2 (10%) H-4→L+4 (12%)
40	4.869	255	0.0334	H-5→L+5 (15%) HOMO→L+8 (42%)
47	5.128	242	0.0341	H-7→L+1 (26%) H-6→L+1 (38%)

48	5.184	239	0.0121	H-7→L+1 (30%)
				H-7→L+2 (12%)
				H-6→L+3 (33%)

Figure A.4.7. Selected Electron Difference Density Maps (EDDMS) of singlet excited state transitions of **5** in H_2O (light violet indicates a decrease in electron density, while purple indicates an increase).
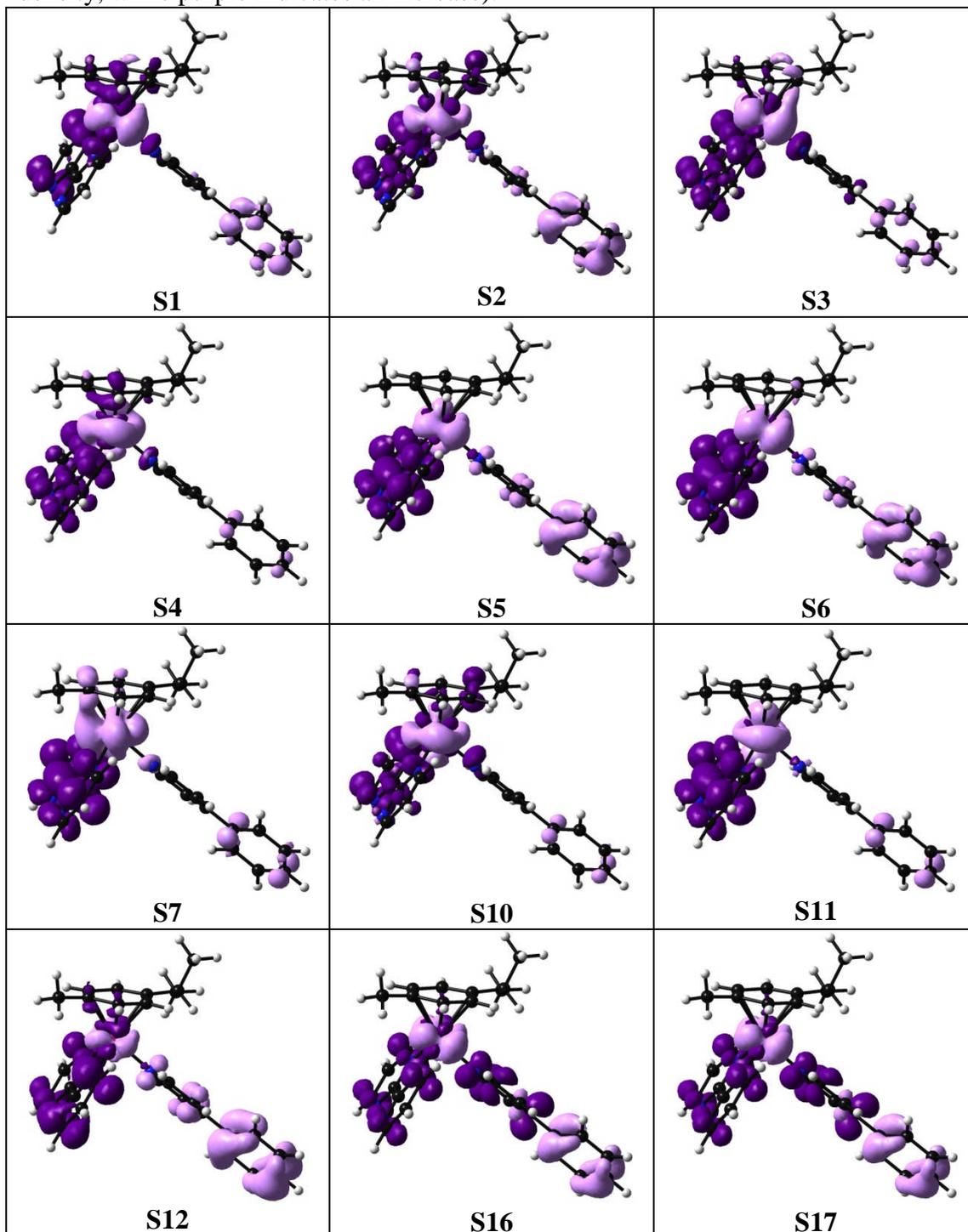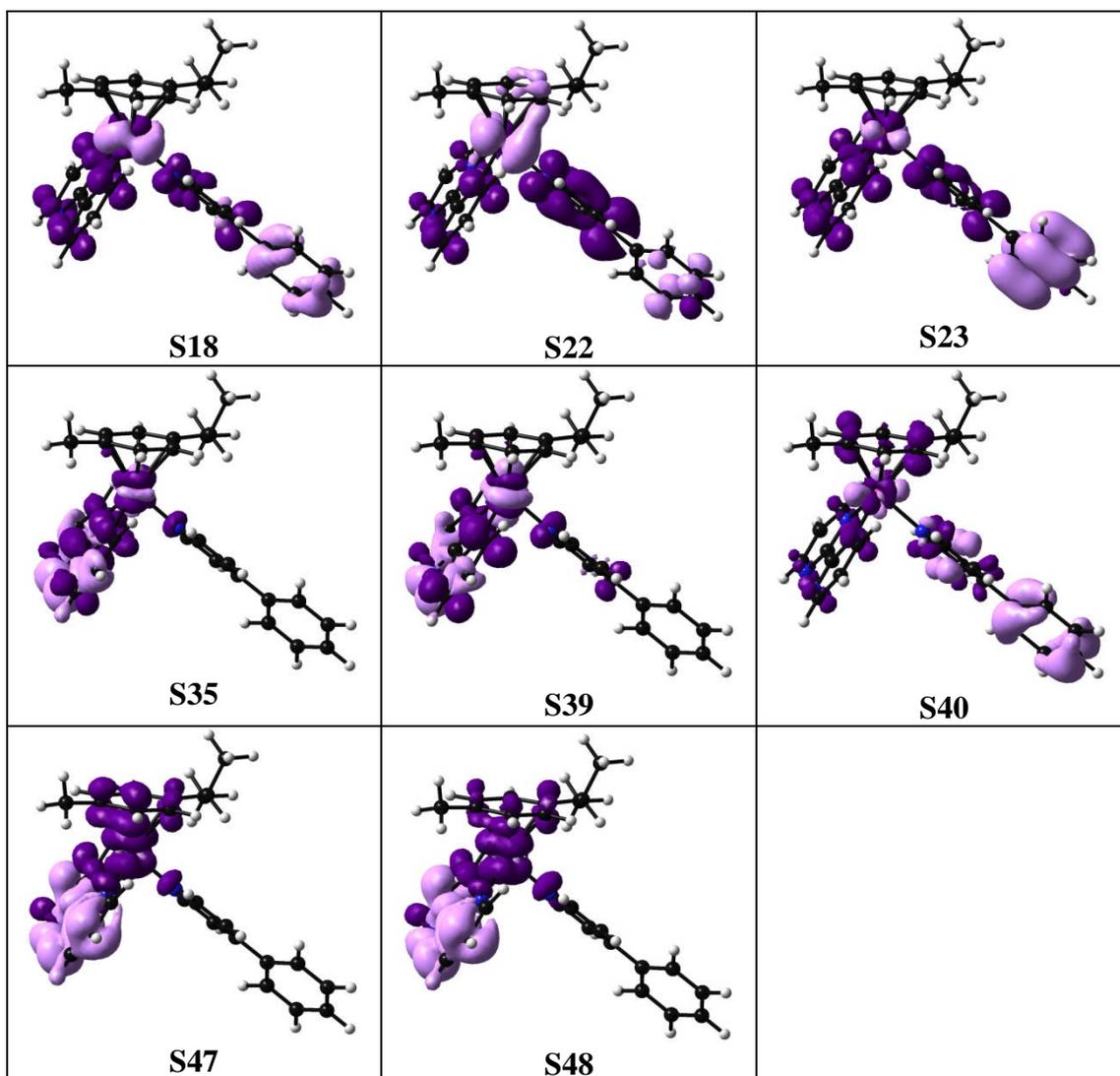
Table A.4.8. Selected TD-DFT singlet transitions for complex **6**.

	Energy (eV)	Wavelength (nm)	Oscillator Strength	Major contributions
1	2.816	440	0.0026	H-2→L+1 (40%) H-2→L+3 (24%)
2	3.018	411	0.0052	H-4→L+3 (14%) H-3→L+3 (31%)
3	3.051	406	0.0021	H-3→L+1 (19%) H-3→L+3 (22%) H-2→L+1 (11%) H-2→L+3 (10%) H-2→L+4 (11%)
4	3.131	396	0.001	H-4→L+1 (31%) H-4→L+2 (11%) H-4→L+4 (13%) H-3→L+1 (11%) H-2→LUMO (12%)
5	3.188	389	0.0028	H-2→LUMO (69%)

6	3.314	374	0.0081	H-3→LUMO (14%)
				HOMO→LUMO (80%)
10	3.648	340	0.014	H-4→LUMO (60%)
				H-4→L+3 (10%)
19	4.158	298	0.0512	H-2→L+4 (42%)
				H-1→L+2 (23%)
20	4.184	296	0.0191	H-1→L+2 (66%)
30	4.572	271	0.0196	H-2→L+5 (46%)
				H-1→L+5 (20%)
33	4.680	265	0.0574	H-8→LUMO (41%)
				H-7→LUMO (28%)
36	4.748	261	0.0645	H-3→L+5 (77%)
37	4.781	259	0.0913	H-7→LUMO (12%)
				H-5→L+1 (18%)
				H-3→L+7 (18%)
39	4.809	258	0.1779	H-7→LUMO (16%)
				H-5→L+1 (14%)
				H-3→L+7 (15%)

Figure A.4.8. Selected Electron Difference Density Maps (EDDMS) of singlet excited state transitions of **6** in H_2O (light violet indicates a decrease in electron density, while purple indicates an increase).

S10 **S19** **S20**

S30 **S33** **S36**

S37 **S39**
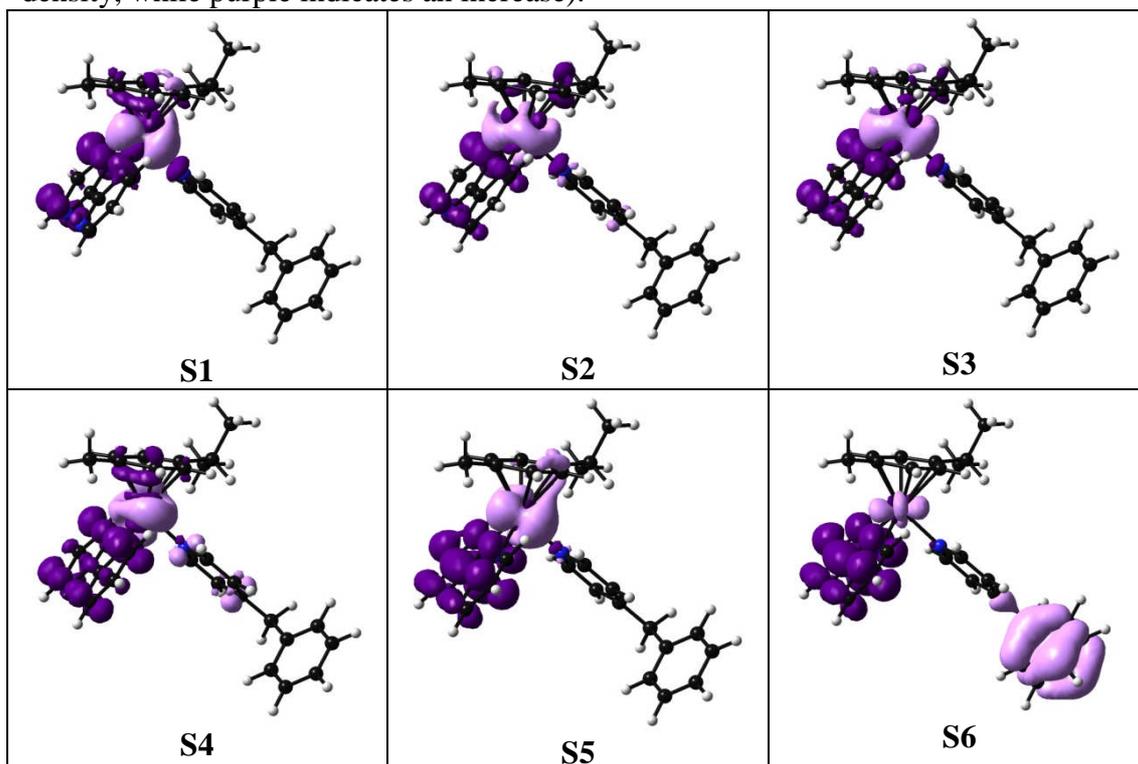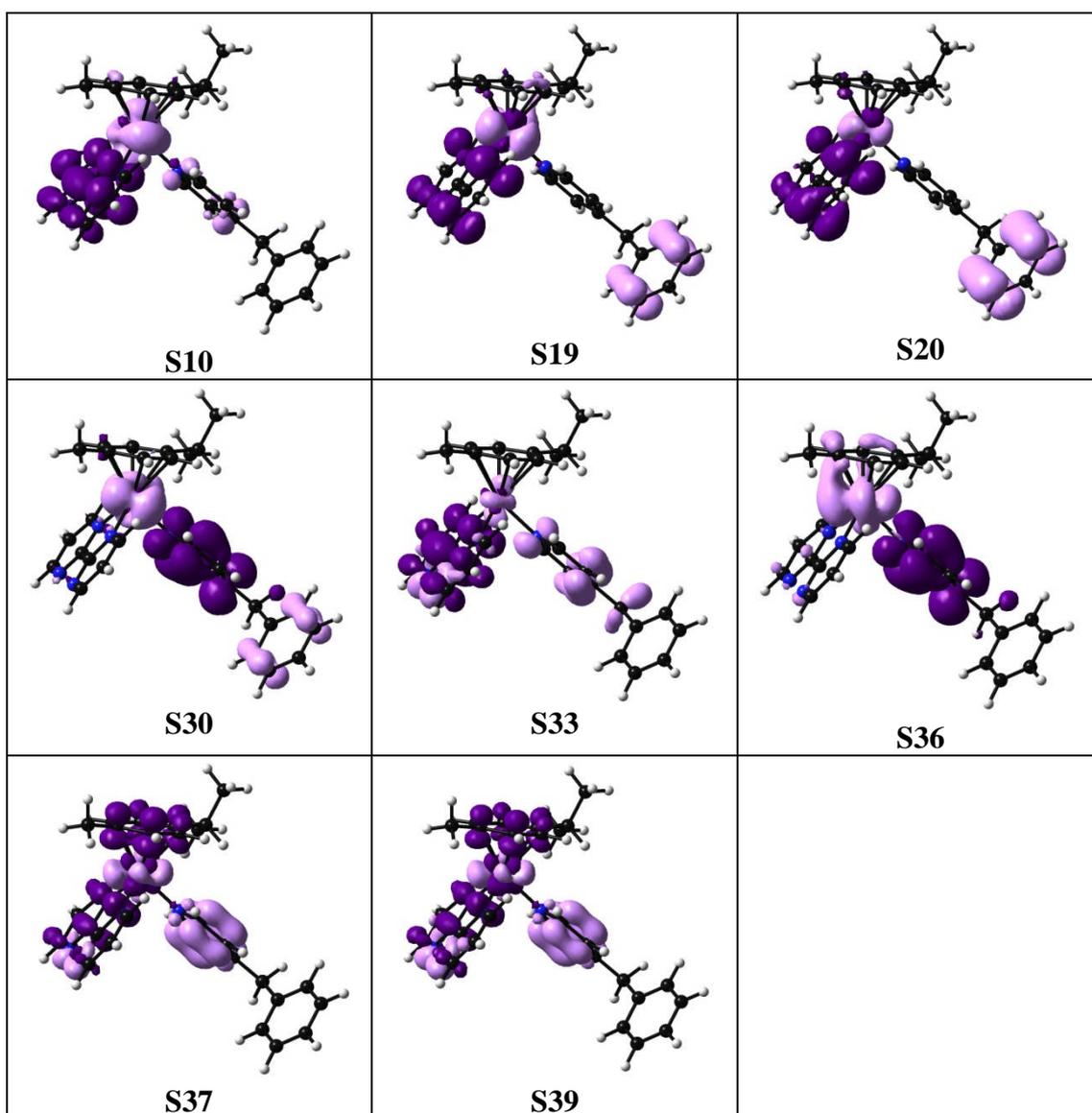
Table A.4.9. Selected TD-DFT singlet transitions for complex **8.**

	Energy (eV)	Wavelength (nm)	Oscillator Strength	Major contributions
1	2.7755	447	0.0001	H-1→L+1 (31%) HOMO→L+3 (39%)
2	2.921	424	0.0047	H-2→L+3 (13%) HOMO→L+1 (53%) HOMO→L+4 (15%)
3	2.9731	417	0.0084	H-1→LUMO (17%) H-1→L+3 (63%)
4	2.9943	414	0.0014	H-2→L+1 (33%) H-2→L+4 (10%) H-1→L+1 (10%) HOMO→LUMO (20%)
5	3.1016	400	0.0007	H-2→L+1 (11%) HOMO→LUMO (69%)

6	3.1883	389	0.0336	H-1→LUMO (76%)
				H-1→L+3 (11%)
8	3.5911	345	0.0145	H-2→LUMO (60%)
				H-2→L+3 (15%)
11	3.9289	316	0.0219	H-1→L+2 (80%)
13	4.0588	305	0.0608	HOMO→L+1 (15%)
				HOMO→L+4 (70%)
19	4.515	275	0.041	H-1→L+5 (92%)
22	4.6621	266	0.0478	H-5→LUMO (16%)
				H-4→L+2 (37%)
25	4.7523	261	0.1927	H-5→LUMO (34%)
				H-4→LUMO (11%)
29	4.9126	252	0.0675	H-8→LUMO (80%)
33	5.0238	247		H-2→L+5 (78%)

Figure A.4.9. Selected Electron Difference Density Maps (EDDMS) of singlet excited state transitions of **8** in H$_2$O (light violet indicates a decrease in electron density, while purple indicates an increase).

S19

S22

S25

S29

S33
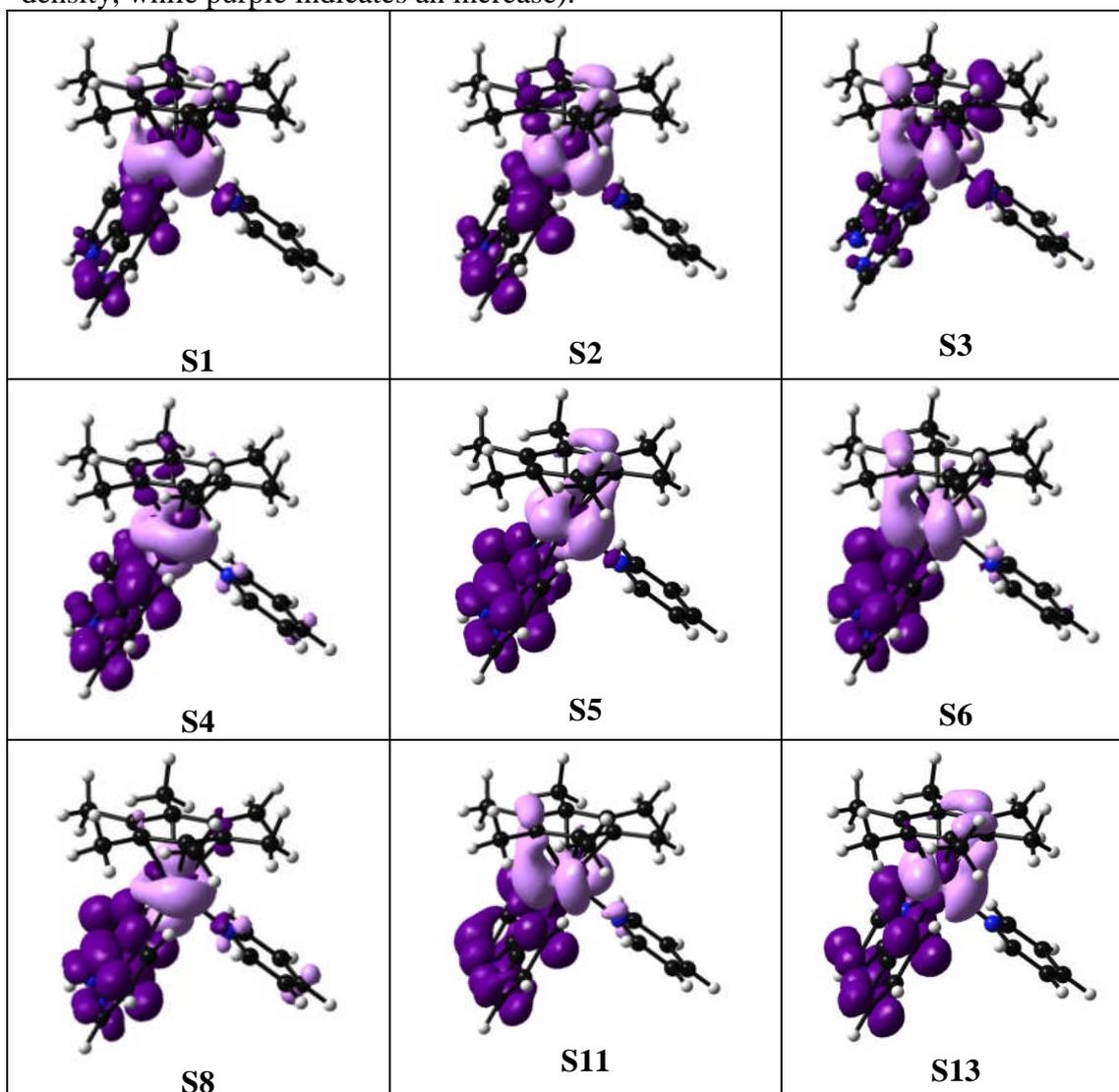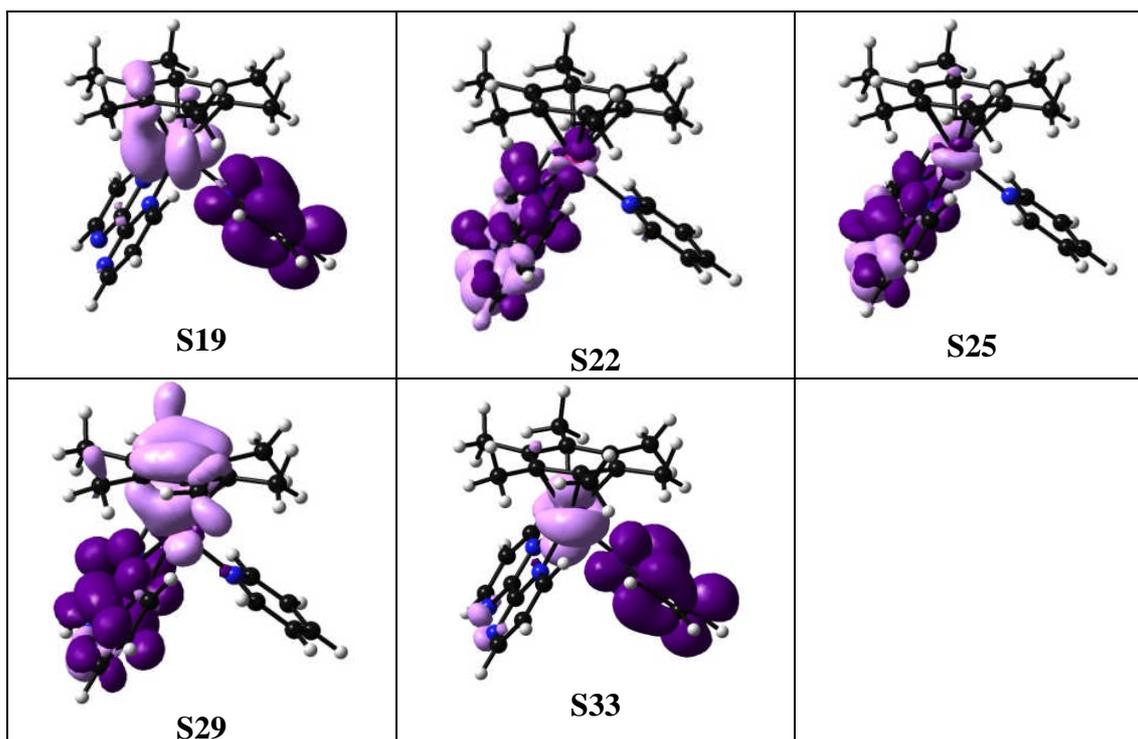
Table A.4.10. Selected TD-DFT singlet transitions for complex **9.**

	Energy (eV)	Wavelength (nm)	Oscillator Strength	Major contributions
1	2.8495	435	0.0001	H-1→L+1 (27%) HOMO→L+3 (49%)
2	2.9861	415	0.0035	H-2→L+3 (20%) HOMO→L+1 (52%), HOMO→L+4 (11%)
3	3.0497	407	0.007	H-1→LUMO (12%) H-1→L+3 (61%)
4	3.0855	402	0.0007	H-2→L+1 (45%) H-2→L+4 (11%) H-1→L+1 (16%) HOMO→LUMO (10%)
5	3.1763	390	0.0003	HOMO→LUMO (79%)
6	3.2844	377	0.0354	H-1→LUMO (79%)
8	3.6332	341	0.0155	H-2→LUMO (58%) H-2→L+3 (14%)
9	3.7455	331	0.0091	H-2→LUMO (33%) H-2→L+3 (42%)
12	4.0577	306	0.0171	H-1→L+2 (86%)
13	4.1827	296	0.0593	HOMO→L+1 (16%) HOMO→L+4 (71%)
21	4.6442	267	0.0609	H-1→L+5 (87%)
22	4.7063	263	0.0824	H-5→LUMO (21%) H-4→L+2 (41%)

24	4.7992	258	0.2569	H-5→LUMO (37%) H-4→L+2 (12%) H-2→L+4 (11%)
26	4.8184	257	0.023	H-7→L+2 (19%) H-4→L+1 (18%) H-4→L+4 (24%) H-3→L+1 (18%)
32	5.1137	242	0.0577	H-5→L+1 (11%) H-4→L+1 (17%) H-2→L+5 (53%)
33	5.1331	241	0.0401	H-5→L+1 (45%) H-4→L+1 (14%) H-2→L+5 (22%)

Figure A.4.10. Selected Electron Difference Density Maps (EDDMS) of singlet excited state transitions of **9** in H_2O (light violet indicates a decrease in electron density, while purple indicates an increase).
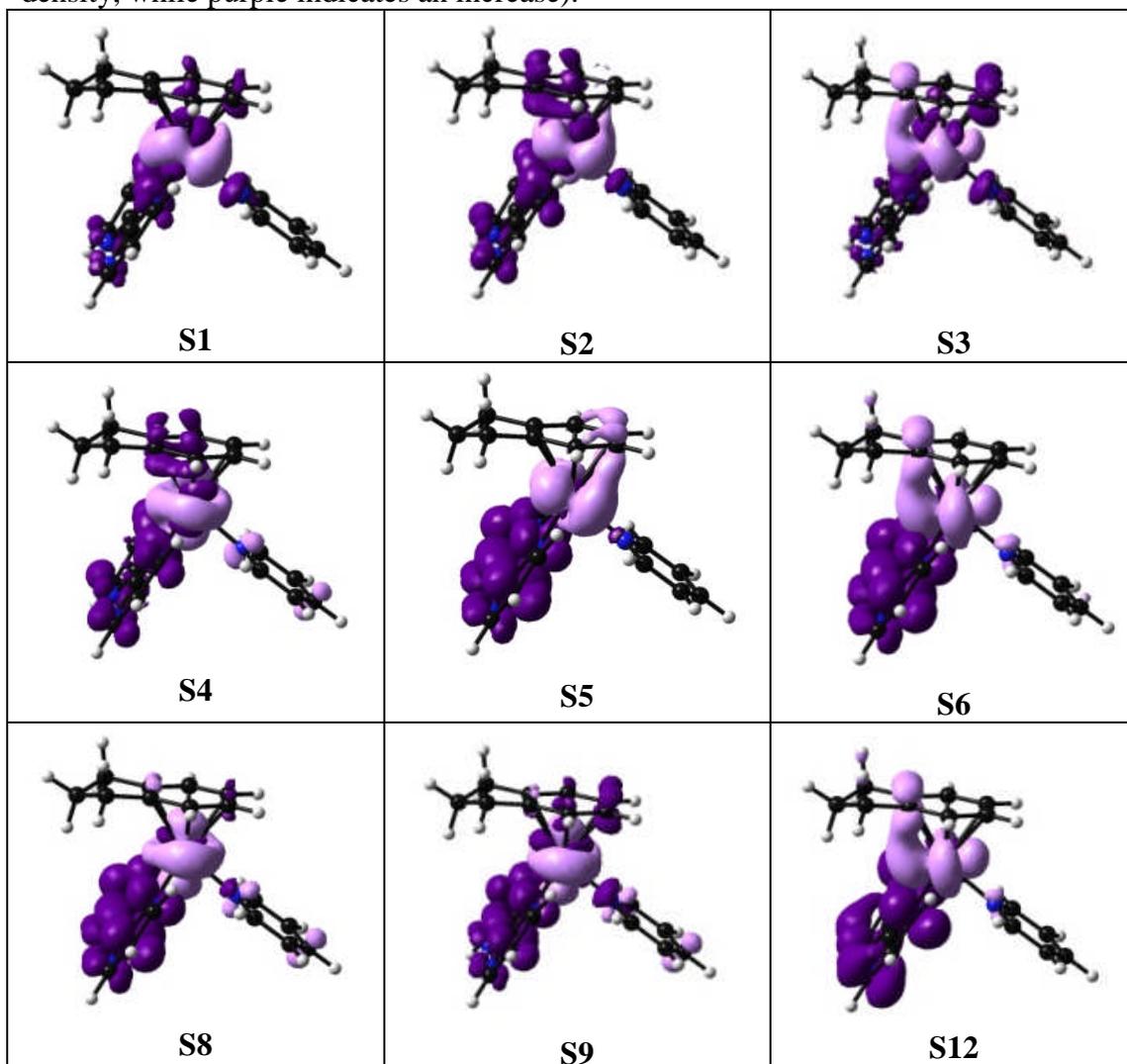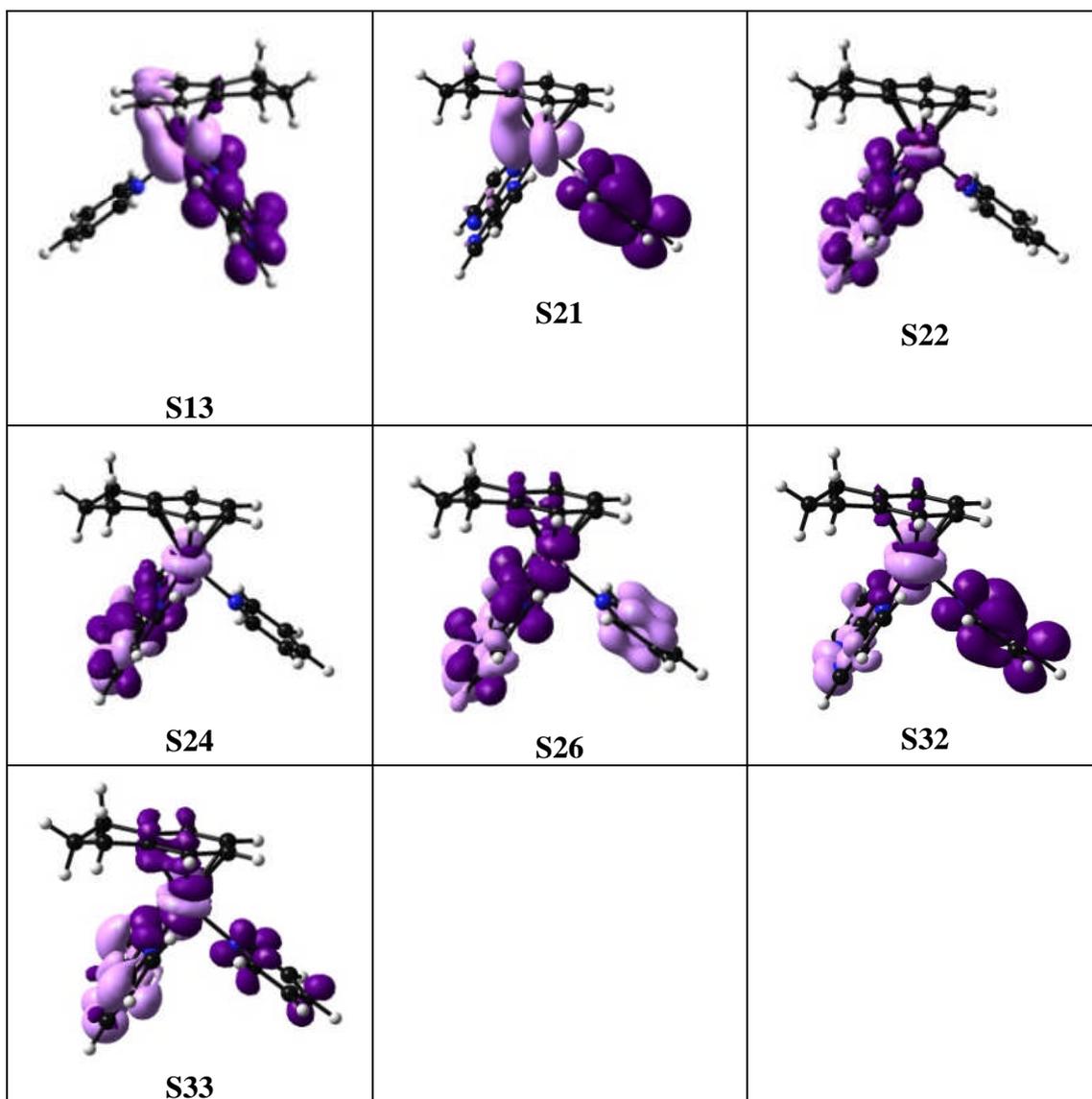
Table A.4.11. Selected TD-DFT singlet transitions for the complex **10.**

	Energy (eV)	Wavelength (nm)	Oscillator Strength	Major contributions
1	2.8322	438	0.0022	H-1→L+2 (27%) HOMO→L+2 (36%)
2	3.0001	413	0.0056	H-3→L+2 (15%) H-1→L+3 (24%) HOMO→L+2 (19%)
3	3.0682	404	0.0006	H-1→L+2 (15%) H-1→L+3 (32%) HOMO→L+3 (17%)
4	3.1602	392	0.0006	H-3→L+2 (14%) H-3→L+3 (24%) H-2→L+2 (14%) H-2→L+3 (21%)
5	3.4519	359	0.005	H-1→LUMO (45%) HOMO→LUMO (21%)

6	3.5525	349	0.039	HOMO→LUMO (48%)
				HOMO→L+3 (15%)
10	3.8892	319	0.0246	H-4→LUMO (10%)
				H-1→L+1 (12%)
				HOMO→L+1 (52%)
11	3.9674	312	0.0516	H-2→LUMO (40%)
				H-1→L+1 (28%)
17	4.4767	277	0.0335	H-3→L+3 (24%)
				H-2→L+3 (32%)
				HOMO→L+3 (11%)
20	4.5894	270	0.1062	H-4→L+1 (58%)
31	5.0741	244	0.1122	H-1→L+5 (27%)
				H-1→L+7 (10%)
				HOMO→L+5 (18%)
36	5.1776	239	0.0433	H-3→L+4 (41%)
				HOMO→L+8 (24%)
38	5.2235	237	0.018	H-6→LUMO (38%)
				H-3→L+4 (10%)
				H-1→L+8 (27%)

Figure A.4.11. Selected Electron Difference Density Maps (EDDMS) of singlet excited state transitions of **10** in H_2O (light violet indicates a decrease in electron density, while purple indicates an increase).
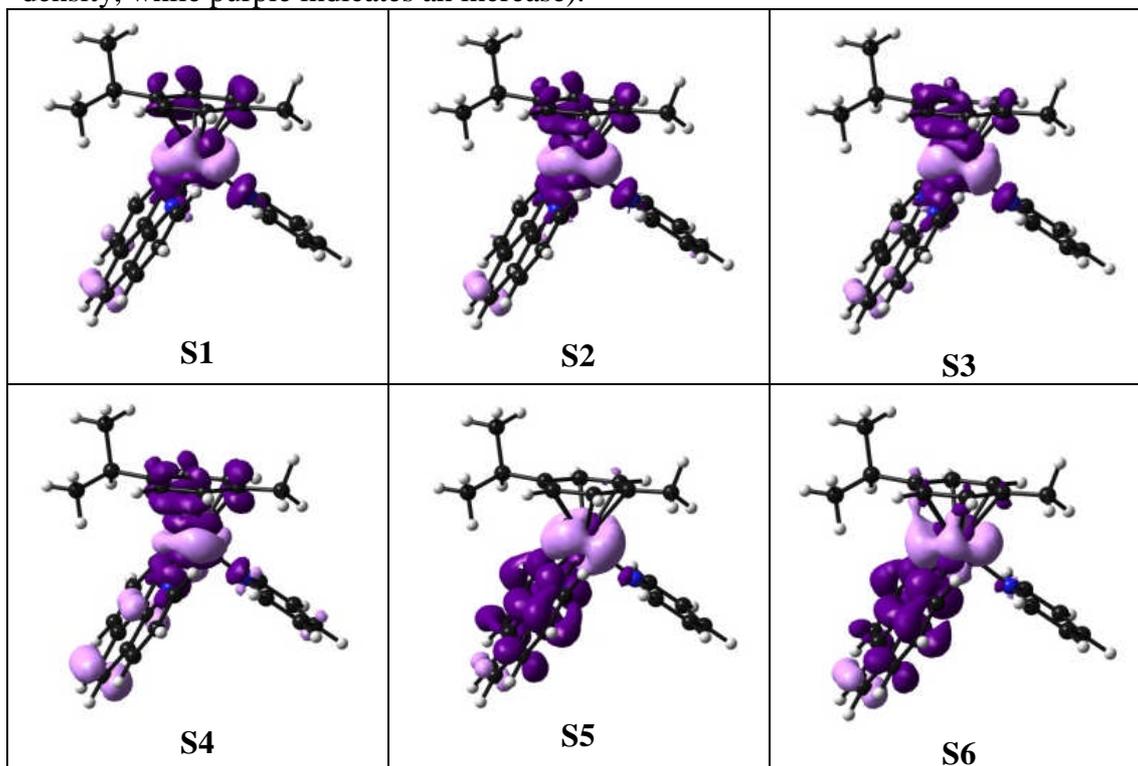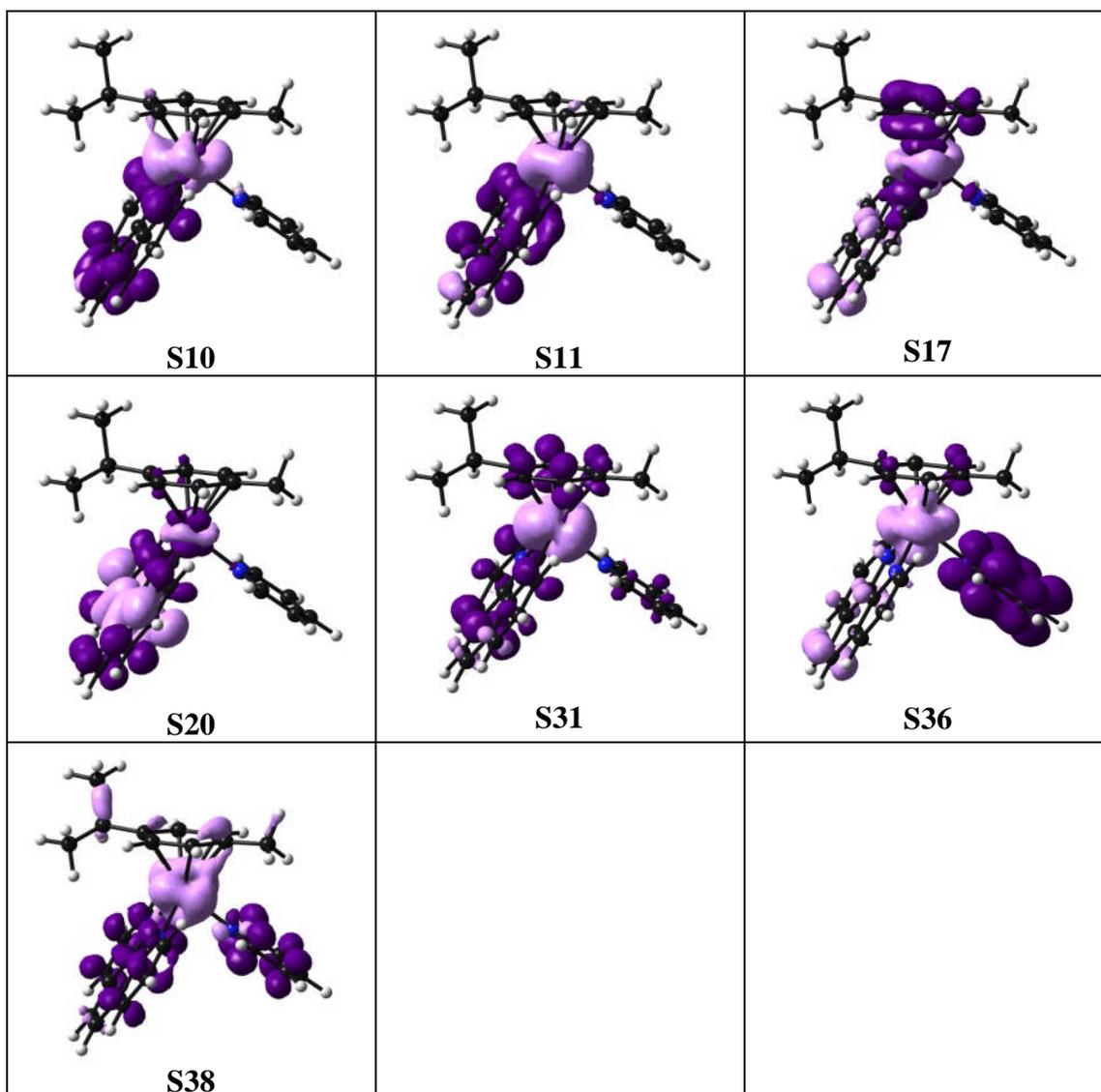
Table A.4.12. Selected TD-DFT singlet transitions for complex **11**.

	Energy (eV)	Wavelength (nm)	Oscillator Strength	Major contributions
1	2.3311	532	0.0003	H-3→LUMO (53%) H-2→LUMO (34%)
2	2.5061	495	0.0047	HOMO→LUMO (91%)
3	2.5935	478	0.0111	H-1→LUMO (88%)
4	2.794	444	0.0023	HOMO→L+2 (24%) HOMO→L+3 (48%)
5	2.9878	415	0.0056	H-2→L+3 (14%) H-1→L+3 (34%) H-1→L+4 (23%)
6	3.0142	411	0.0011	H-1→L+2 (15%) H-1→L+3 (-18%) HOMO→L+2 (12%) HOMO→L+4 (37%)
7	3.0709	403	0.0022	H-3→LUMO (36%) H-2→LUMO (57%)

8	3.088	401	0.0011	H-3→L+4 (10%)
				H-2→L+2 (20%)
				H-2→L+4 (26%)
9	3.2634	380	0.0283	H-4→LUMO (96%)
11	3.4415	360	0.0489	H-1→L+1 (75%)
15	3.6711	338	0.0134	H-3→L+3 (11%)
				H-2→L+3 (31%)
				H-1→L+3 (11%)
16	3.8365	323	0.0144	H-2→L+1 (81%)
18	4.0291	308	0.0237	H-3→L+1 (15%)
				HOMO→L+2 (28%)
				HOMO→L+4 (24%)
19	4.08	304	0.0383	H-1→L+2 (33%)
				H-1→L+3 (14%)
				H-1→L+4 (28%)
21	4.2723	290	0.1035	H-9→LUMO (16%)
				H-4→L+1 (55%)
24	4.448	279	0.0249	H-7→LUMO (77%)
29	4.6692	265	0.1369	H-9→LUMO (34%)
				H-4→L+1 (18%)
				H-4→L+2 (14%)
33	4.7978	258	0.0715	H-10→LUMO (46%)
				H-4→L+2 (13%)
				H-4→L+3 (18%)
				H-4→L+4 (14%)
42	5.0545	245	0.067	H-3→L+5 (13%)
				H-2→L+5 (72%)
47	5.1855	239	0.2698	H-13→LUMO (21%)
				H-4→L+4 (16%)

Figure A.4.12. Selected Electron Difference Density Maps (EDDMS) of singlet excited state transitions of **11** in H_2O (light violet indicates a decrease in electron density, while purple indicates an increase).

S4

S5

S6

S7

S8

S9

S11

S15

S16

S18

S19

S21
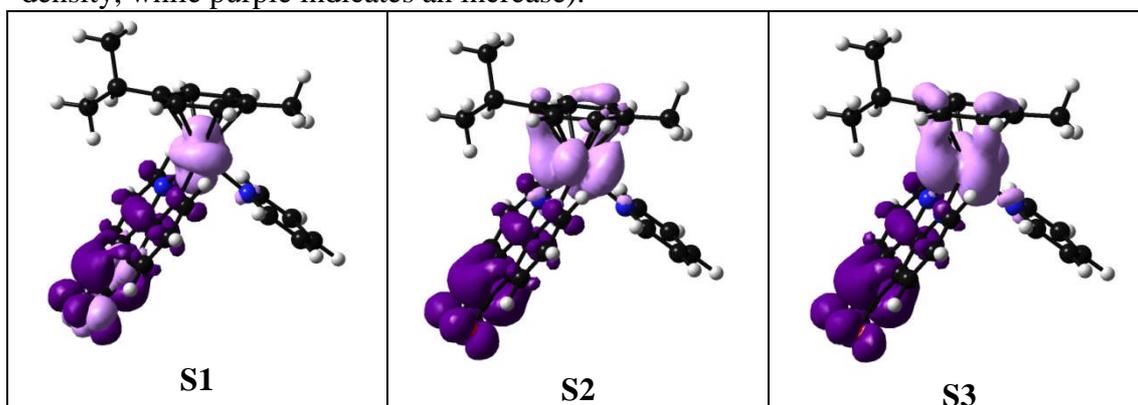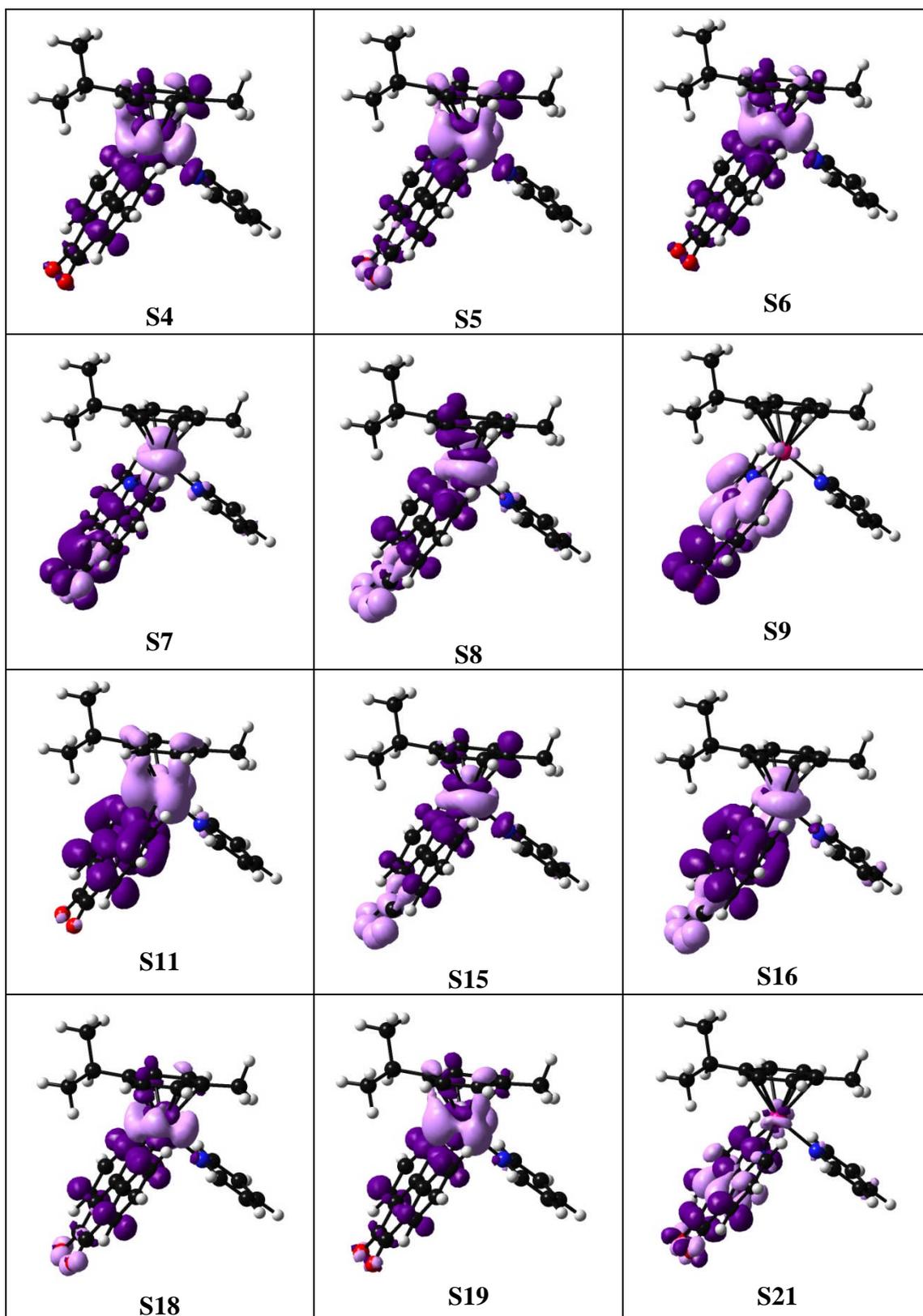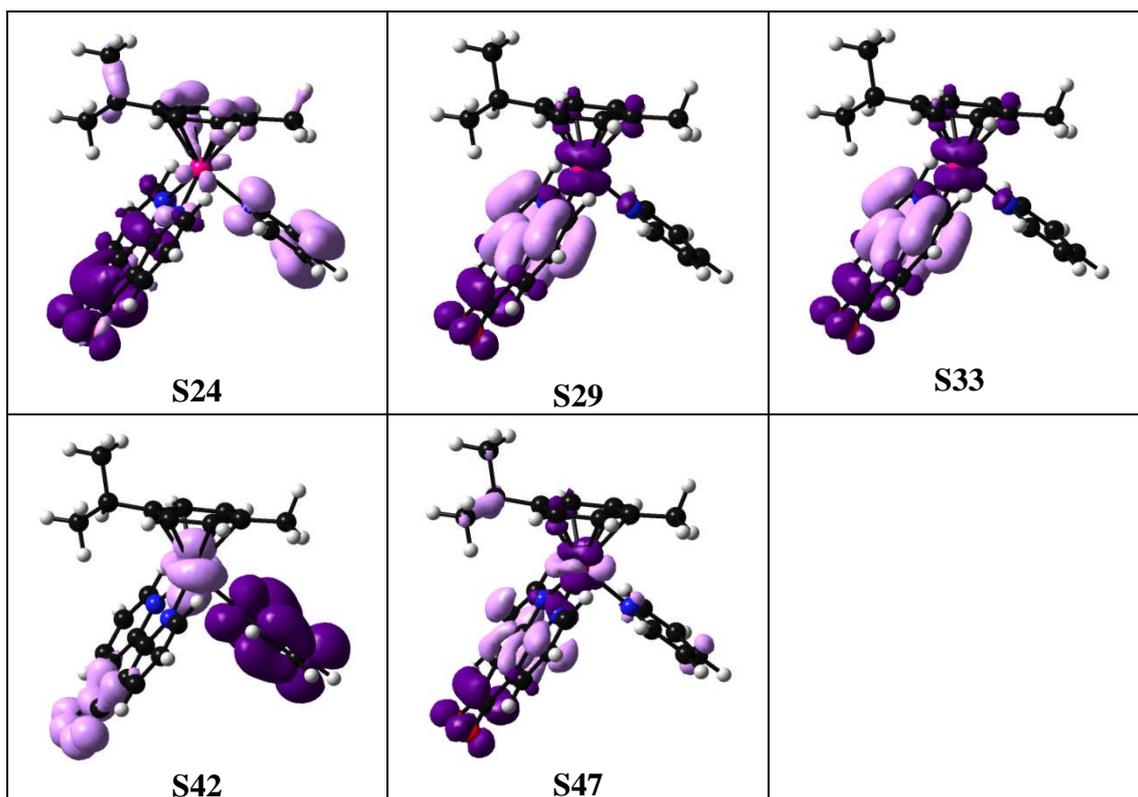
Table A.4.13. Selected TD-DFT singlet transitions for complex **12.**

	Energy (eV)	Wavelength (nm)	Oscillator Strength	Major contributions
1	2.804	437	0.0036	H-2→L+2 (17%) H-1→L+2 (33%) HOMO→L+2 (12%)
2	2.975	417	0.0188	H-5→L+2 (-10%) HOMO→LUMO (10%) HOMO→L+2 (19%) HOMO→L+3 (12%)
3	3.091	401	0.0005	H-5→L+2 (10%) H-2→L+3 (17%) H-1→L+3 (39%)
4	3.204	387	0.0027	H-7→L+2 (10%) H-7→L+3 (19%) H-6→L+3 (15%) H-5→L+2 (10%) H-5→L+3 (18%)
5	3.297	376	0.1807	HOMO→LUMO (72%)
6	3.371	368	0.0557	H-1→LUMO (58%)
7	3.470	357	0.2038	H-1→LUMO (10%) HOMO→L+1 (60%)
8	3.555	349	0.134	H-1→L+2 (10%) HOMO→L+1 (20%) HOMO→L+3 (26%)
10	3.680	337	0.2484	H-1→L+1 (75%)

12	3.845	322	0.0536	H-2→LUMO (71%)
				H-1→LUMO (10%)
15	3.981	311	0.0438	H-5→L+1 (67%)
				H-2→L+1 (18%)
16	4.021	308	0.0933	H-7→LUMO (13%)
				H-5→L+1 (19%)
				H-2→L+1 (57%)
23	4.272	290	0.1456	H-8→LUMO (43%)
				H-6→L+1 (44%)
30	4.506	275	0.0876	H-8→LUMO (10%)
				H-6→L+1 (13%)
				H-2→L+3 (30%)
				H-1→L+3 (17%)
31	4.523	274	0.1308	H-8→LUMO (19%)
				H-6→L+1 (17%)
				H-2→L+3 (17%)
				H-1→L+3 (11%)
44	4.895	253	0.0922	H-1→L+5 (31%)
				HOMO→L+7 (14%)
46	4.930	251	0.105	H-8→L+2 (10%)
				H-1→L+5 (17%)
				HOMO→L+7 (12%)

Figure A.4.13. Selected Electron Difference Density Maps (EDDMS) of singlet excited state transitions of **12** in H_2O (light violet indicates a decrease in electron density, while purple indicates an increase).

S7

S8

S10

S12

S15

S16

S23

S30

S31

S44

S46
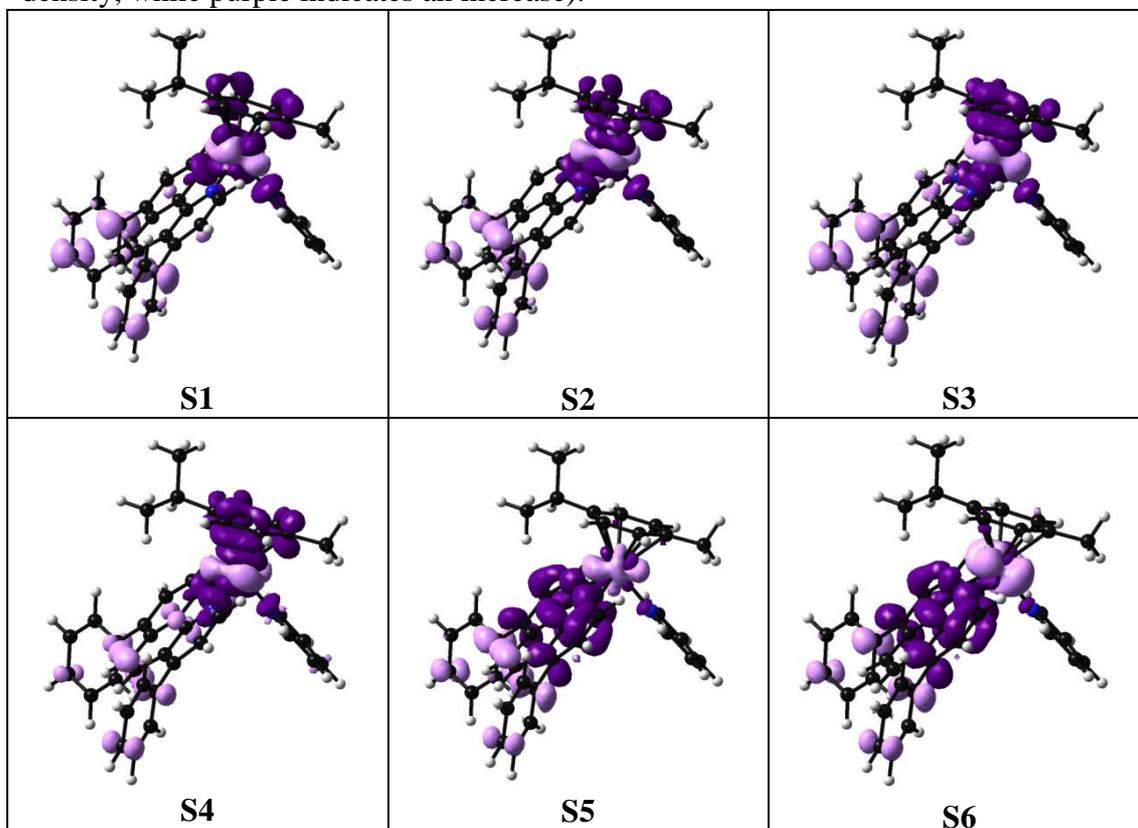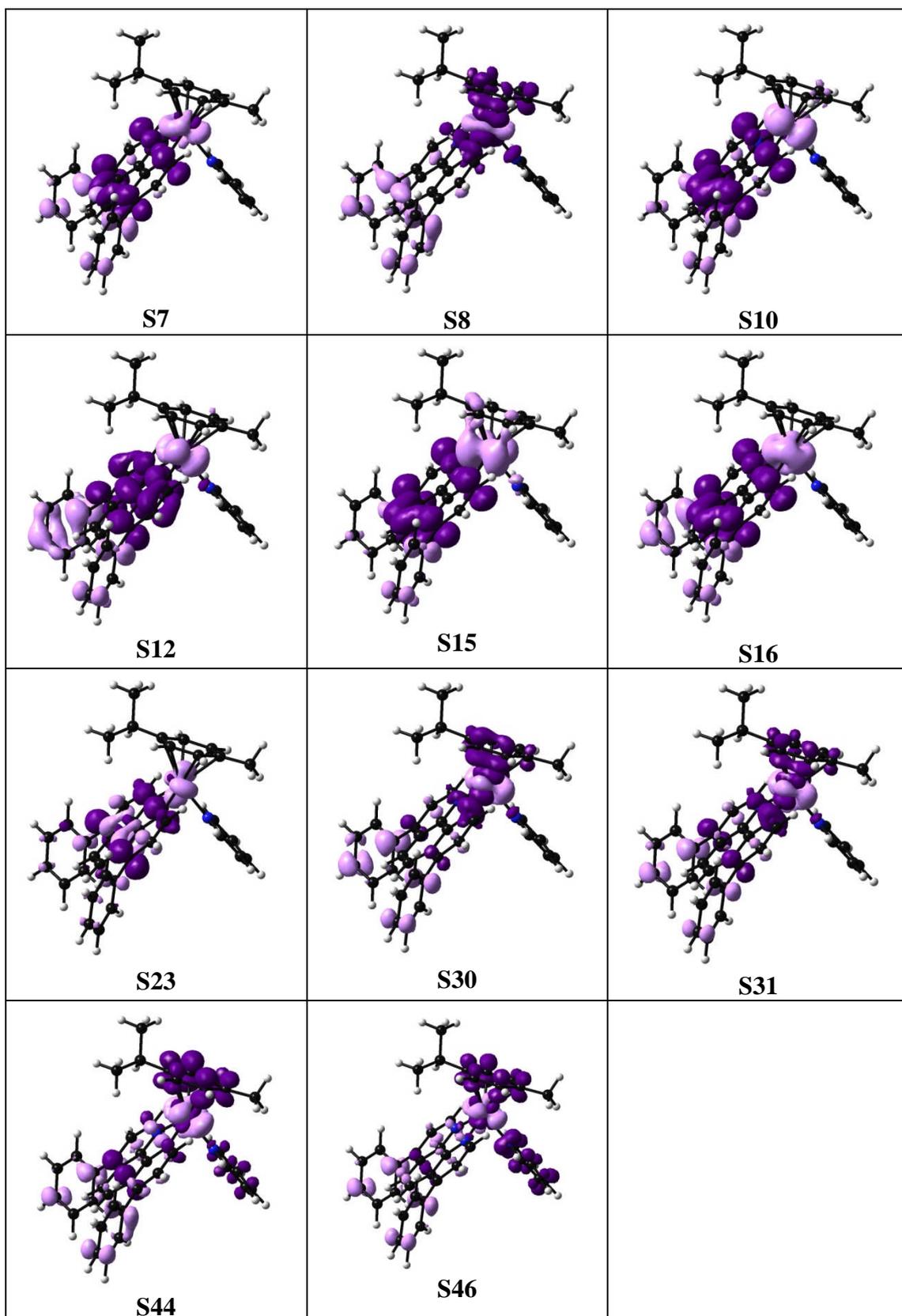
Table A.4.14. Selected TD-DFT singlet transitions for complex **13.**

	Energy (eV)	Wavelength (nm)	Oscillator Strength	Major contributions
1	2.8627	433	0.0002	H-1→L+1 (29%) HOMO→L+2 (56%)
2	3.0012	413	0.0055	H-2→L+2 (24%) H-1→L+2 (29%) HOMO→L+1 (31%)
3	3.059	403	0.0005	H-1→L+2 (45%) HOMO→L+1 (40%)
4	3.1387	395.	0.0005	H-2→L+1 (67%) H-1→L+1 (15%)
5	3.3872	366.	0.0001	HOMO→LUMO (84%)
6	3.5106	353	0.052	H-1→LUMO (79%)
7	3.5528	349	0.0005	H-2→L+1 (16%) H-1→L+1 (35%) HOMO→L+2 (25%)
8	3.6943	336	0.0151	H-2→L+2 (45%) H-1→L+2 (-12%)
10	4.2028	295	0.1902	H-3→LUMO (70%) HOMO→L+3 (12%)
13	4.4738	277	0.0486	H-1→L+3 (87%)
14	4.5377	273	0.0189	H-3→L+1 (88%)
15	4.542	273	0.0439	H-1→L+5 (13%) HOMO→L+3 (11%) HOMO→L+4 (67%)
17	4.5811	270	0.0691	HOMO→L+5 (62%)
19	4.6267	267	0.0314	H-3→L+2 (45%) H-1→L+5 (36%)
21	4.6733	265	0.0942	H-3→L+2 (49%) H-1→L+5 (18%)
22	4.8071	257	0.0783	H-1→L+5 (20%) H-1→L+7 (37%) H-1→L+8 (32%)
23	4.928	251	0.0369	H-2→L+3 (84%)

Figure A.4.14. Selected Electron Difference Density Maps (EDDMS) of singlet excited state transitions of 13 in H_2O (light violet indicates a decrease in electron density, while purple indicates an increase).

S4

S5

S6

S7

S8

S10

S13

S14

S15

S17

S19

S21

S22

S23
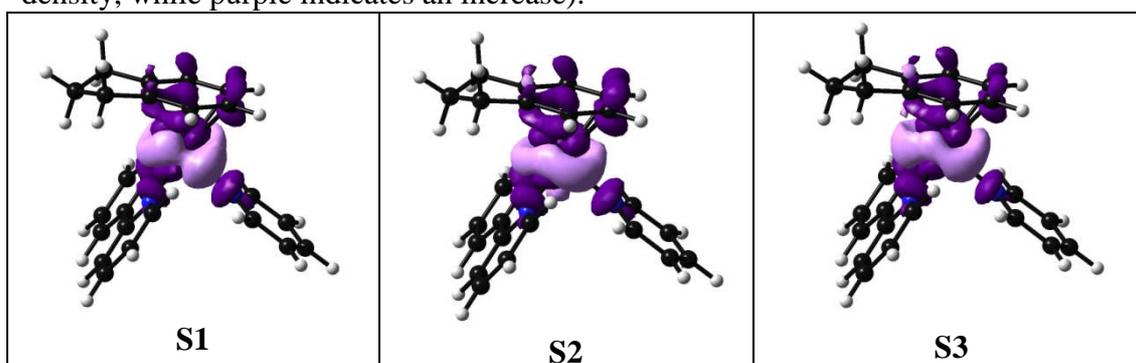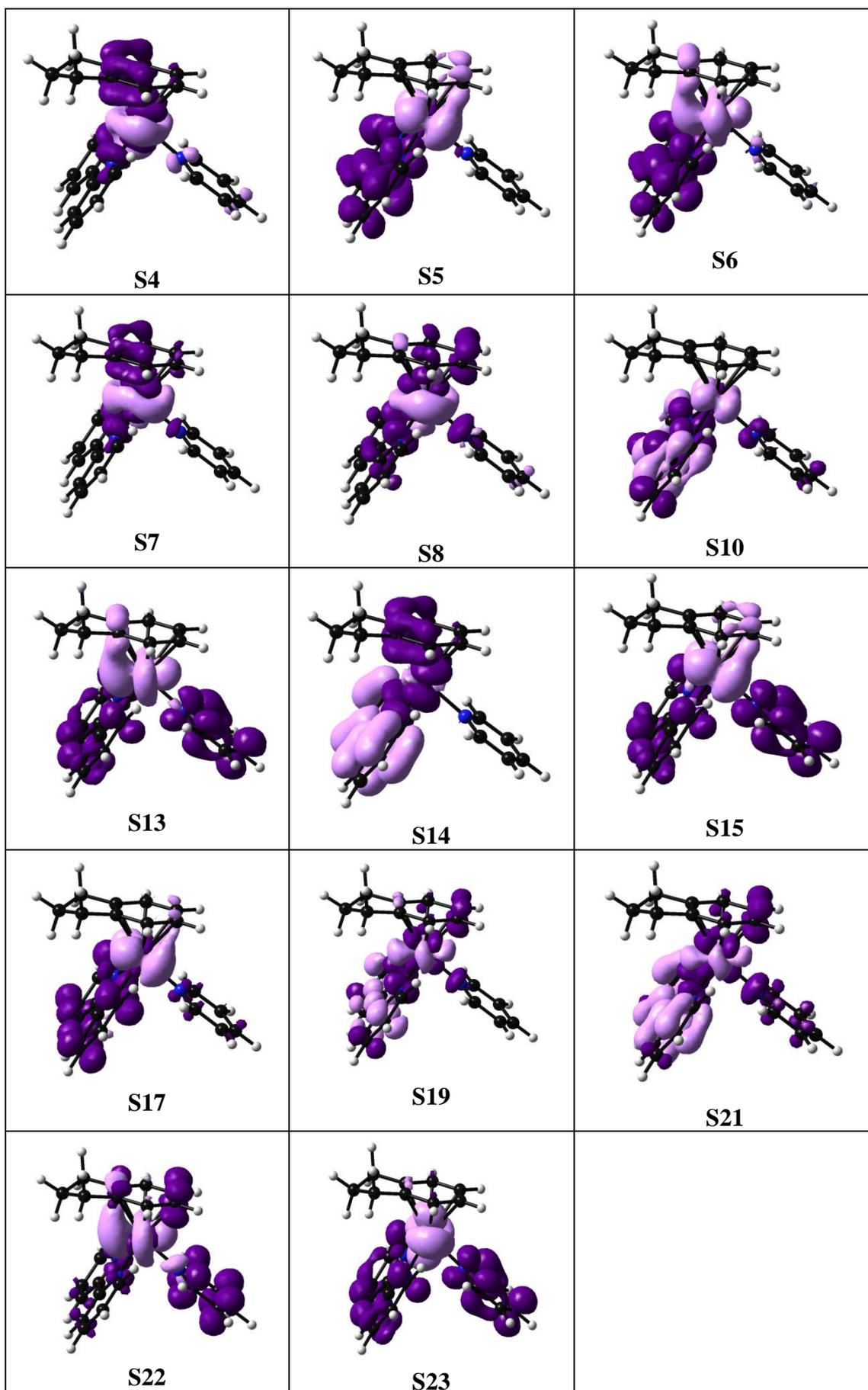
Table A.4.15. Selected TD-DFT singlet transitions for complex **14.**

	Energy (eV)	Wavelength (nm)	Oscillator Strength	Major contributions
1	2.8085	441	0.0027	HOMO→L+1 (24%) HOMO→L+2 (18%) HOMO→L+4 (16%)
2	3.0189	410	0.0047	H-3→L+4 (11%) H-1→L+4 (13%)
3	3.0515	406	0.0026	H-1→L+1 (11%) H-1→L+4 (21%)
4	3.134	395	0.001	H-3→L+1 (17%) H-3→L+2 (25%) H-3→L+5 (10%) H-1→L+2 (10%)
5	3.2201	385	0.0022	HOMO→LUMO (79%)
6	3.3888	366	0.0322	H-1→LUMO (78%)
8	3.6698	338	0.0141	H-3→LUMO (29%) H-3→L+4 (14%)
10	3.8035	326	0.014	H-3→LUMO (47%) H-3→L+4 (16%)
14	4.0852	303	303.5	HOMO→L+1 (10%) HOMO→L+2 (13%) HOMO→L+3 (54%) HOMO→L+4 (17%)
16	4.1931	296	0.0755	HOMO→L+5 (55%)
17	4.2395	292	0.011	H-1→L+1 (12%) H-1→L+2 (10%) H-1→L+3 (51%) H-1→L+4 (11%)
27	4.6589	266	0.0233	H-3→L+2 (20%) H-3→L+3 (10%) H-2→L+1 (11%)
28	4.7063	263	0.0909	H-6→LUMO (16%) H-2→L+4 (19%)
29	4.7211	262	0.0298	H-2→L+4 (40%)
32	4.8006	258	0.1406	H-6→LUMO (21%) H-2→L+6 (12%)
33	4.8199	257	0.0706	H-2→L+6 (51%)
34	4.8357	256	0.0321	H-7→L+3 (10%) H-5→L+5 (22%)

Figure A.4.15. Selected Electron Difference Density Maps (EDDMS) of singlet excited state transitions of **14** in H_2O (light violet indicates a decrease in electron density, while purple indicates an increase).
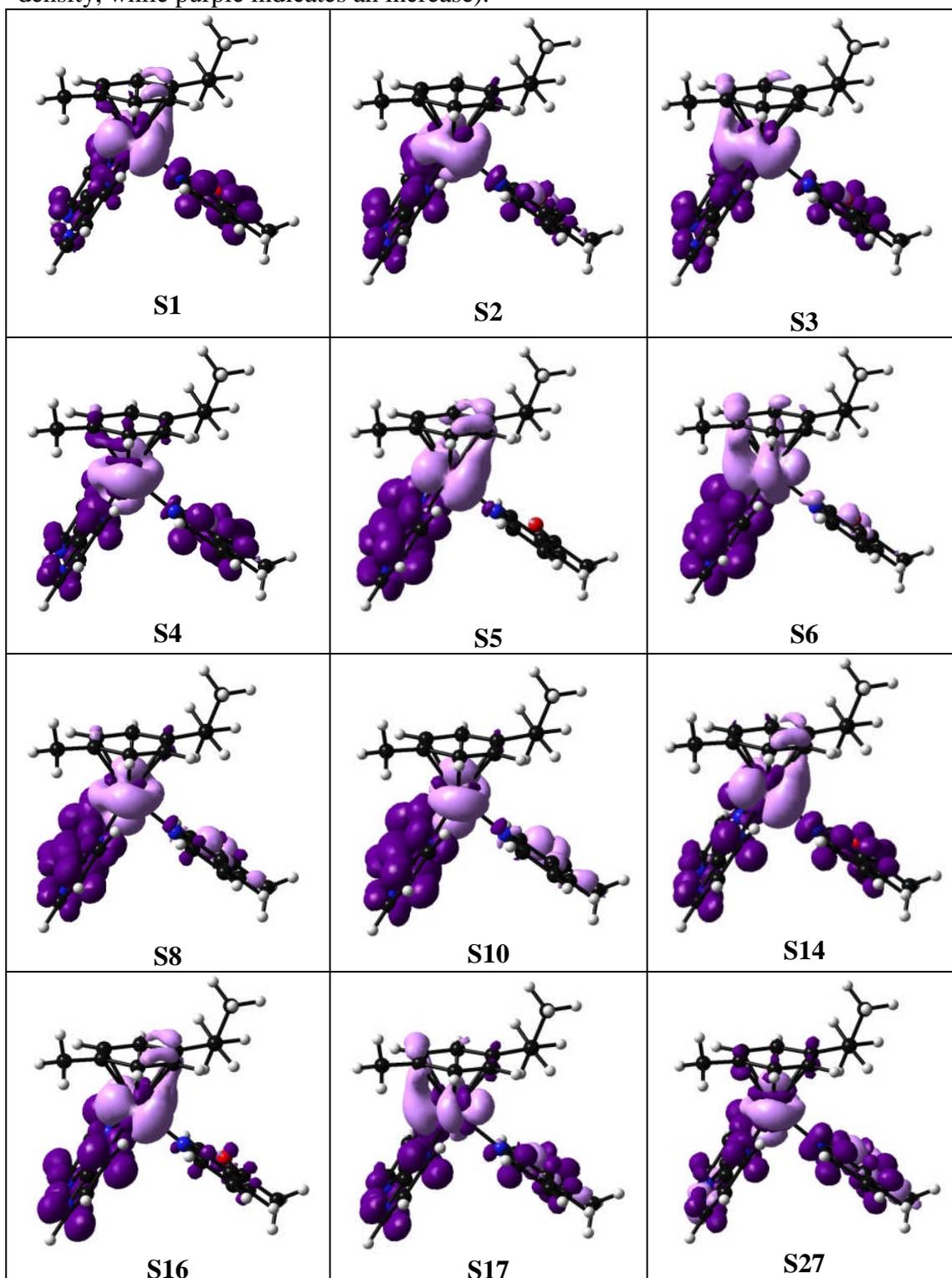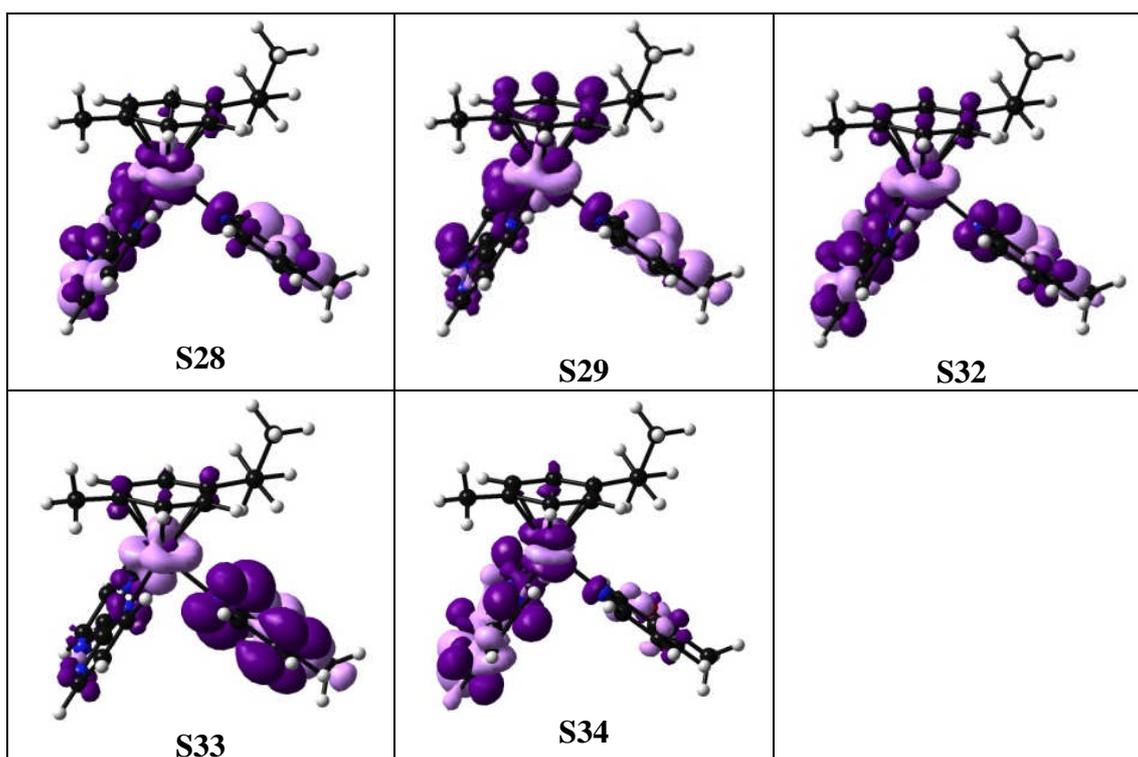
Table A.4.16. Selected TD-DFT singlet transitions for complex **15**.

	Energy (eV)	Wavelength (nm)	Oscillator Strength	Major contributions
1	2.8057	442	0.003	HOMO→L+1 (46%) HOMO→L+3 (17%)
2	3.016	411	0.0064	H-3→L+3 (11%) H-1→L+3 (33%)
3	3.0451	407	0.0011	H-1→L+1 (-14%) H-1→L+3 (10%) HOMO→L+2 (11%) HOMO→L+3 (19%) HOMO→L+4 (14%)
4	3.129	396	0.0011	H-3→L+1 (28%) H-3→L+2 (11%) H-3→L+4 (12%) H-1→L+1 (15%)
5	3.2064	387	0.0033	HOMO→LUMO (77%)
6	3.3661	368	0.0322	H-1→LUMO (78%)
8	3.6559	33	0.0158	H-3→LUMO (33%) H-3→L+3 (15%)
9	3.7803	328	0.0121	H-3→LUMO (35%) H-3→L+3 (22%) H-2→LUMO (12%)
14	4.1678	297	0.0271	H-4→LUMO (56%) HOMO→L+4 (19%)
15	4.1811	296	0.0553	H-4→LUMO (40%) HOMO→L+4 (30%)

21	4.4963	275	0.0251	H-2→L+5 (29%)
				H-1→L+5 (46%)
22	4.5159	274	0.0145	H-3→L+1 (11%)
				H-3→L+2 (43%)
				H-2→L+2 (13%)
29	4.7111	263	0.0761	H-7→LUMO (18%)
				H-6→L+2 (22%)
31	4.7919	258	0.1191	H-7→LUMO (15%)
				HOMO→L+6 (15%)
				HOMO→L+8 (15%)
32	4.8056	258	0.1008	H-7→LUMO (16%)
				HOMO→L+6 (15%)

Figure A.4.16. Selected Electron Difference Density Maps (EDDMS) of singlet excited state transitions of **15** in H$_2$O (light violet indicates a decrease in electron density, while purple indicates an increase).
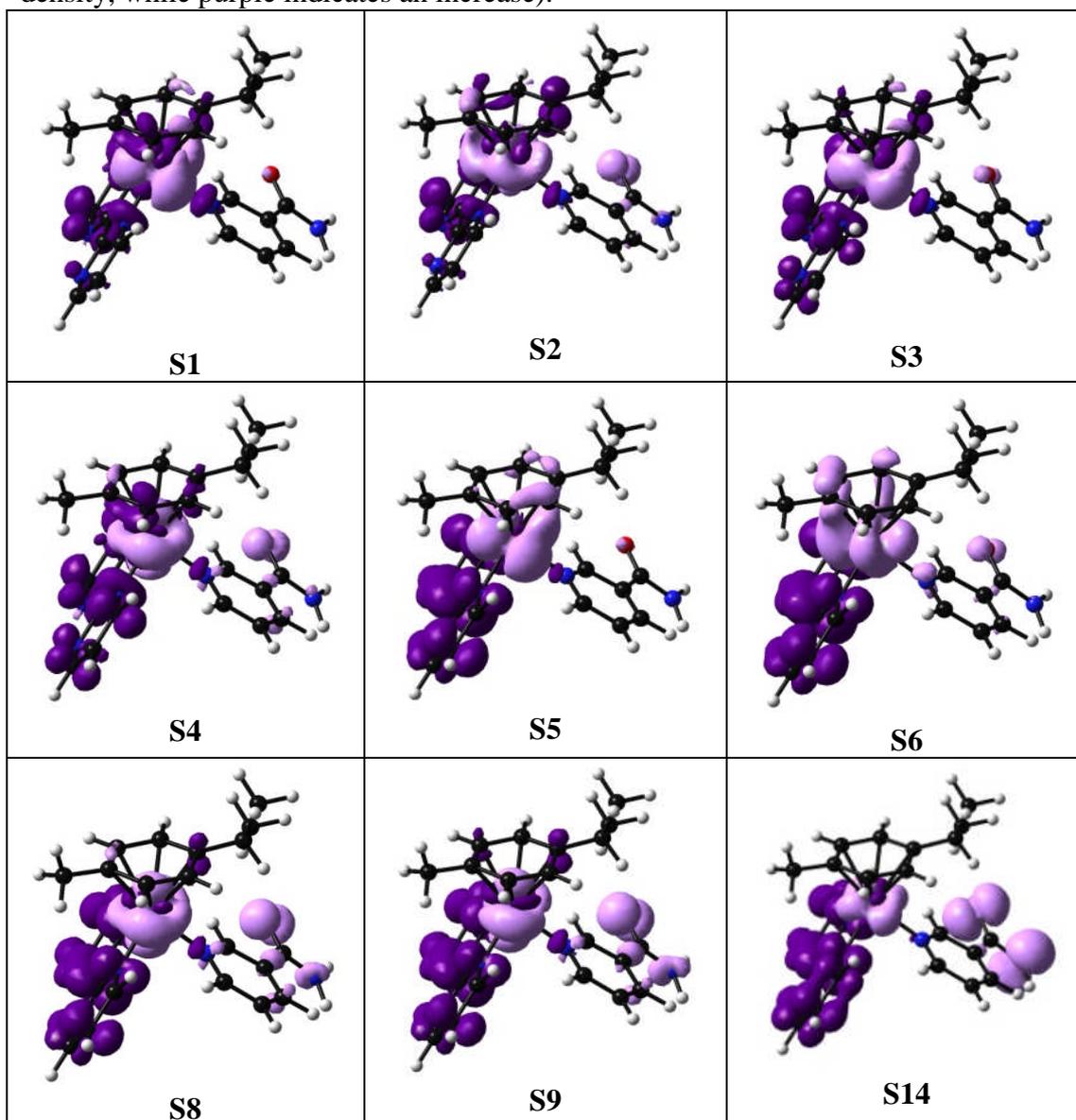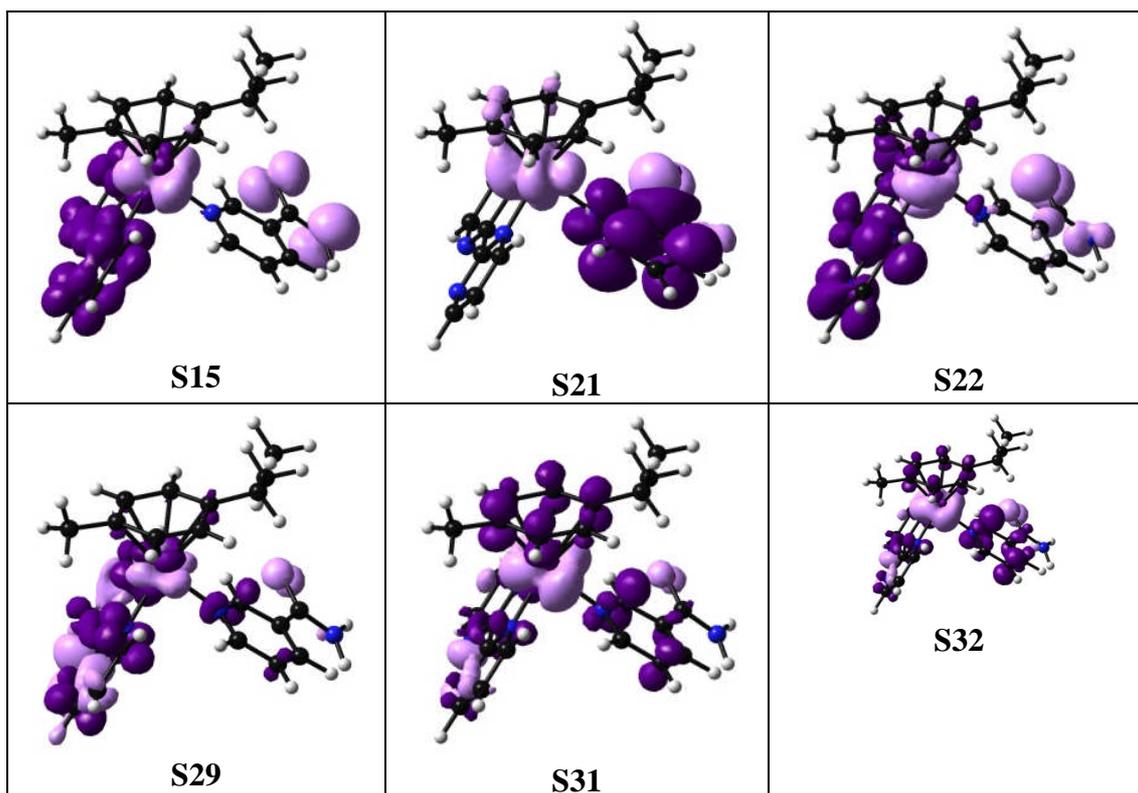
Table A.4.17. Selected TD-DFT singlet transitions for complex **16**.

	Energy (eV)	Wavelength (nm)	Oscillator Strength	Major contributions
1	2.811	441	0.0026	HOMO→L+1 (44%) HOMO→L+3 (20%)
2	3.0236	410	0.0056	H-2→L+3 (16%) H-1→L+3 (28%)
3	3.0522	406	0.0014	H-1→L+1 (19%) H-1→L+3 (17%) HOMO→L+2 (12%) HOMO→L+3 (14%) HOMO→L+5 (11%)
4	3.1366	395	0.0011	H-2→L+1 (28%) H-2→L+2 (15%) H-2→L+5 (12%) H-1→L+1 (14%)
5	3.2249	384	0.0026	HOMO→LUMO (78%)
6	3.3919	365	0.0325	H-1→LUMO (78%)
8	3.6686	337	0.0142	H-2→LUMO (31%) H-2→L+3 (19%)
9	3.8035	325	0.0138	H-2→LUMO (57%) H-2→L+3 (21%)
13	4.1977	295	0.0675	HOMO→L+4 (24%) HOMO→L+5 (41%)
14	4.2014	295	0.0277	HOMO→L+4 (68%) HOMO→L+5 (10%)
16	4.3552	284	0.0189	H-1→L+4 (93%)

24	4.6829	264	0.0196	H-1→L+6 (61%)
25	4.7108	263	0.0811	H-6→LUMO (20%)
				H-5→L+2 (12%)
28	4.8029	258	0.1504	H-6→LUMO (20%)
				H-2→L+4 (17%)
				H-2→L+5 (11%)
29	4.8098	258	0.0953	H-4→L+4 (12%)
				H-2→L+4 (27%)
30	4.8364	256	0.0468	H-7→L+2 (12%)
				H-5→L+2 (10%)
				H-5→L+5 (19%)

Figure A.4.17. Selected Electron Difference Density Maps (EDDMS) of singlet excited state transitions of **16** in H_2O (light violet indicates a decrease in electron density, while purple indicates an increase).

|	S14	S16	S24
	S25	S28	S29
	S30		
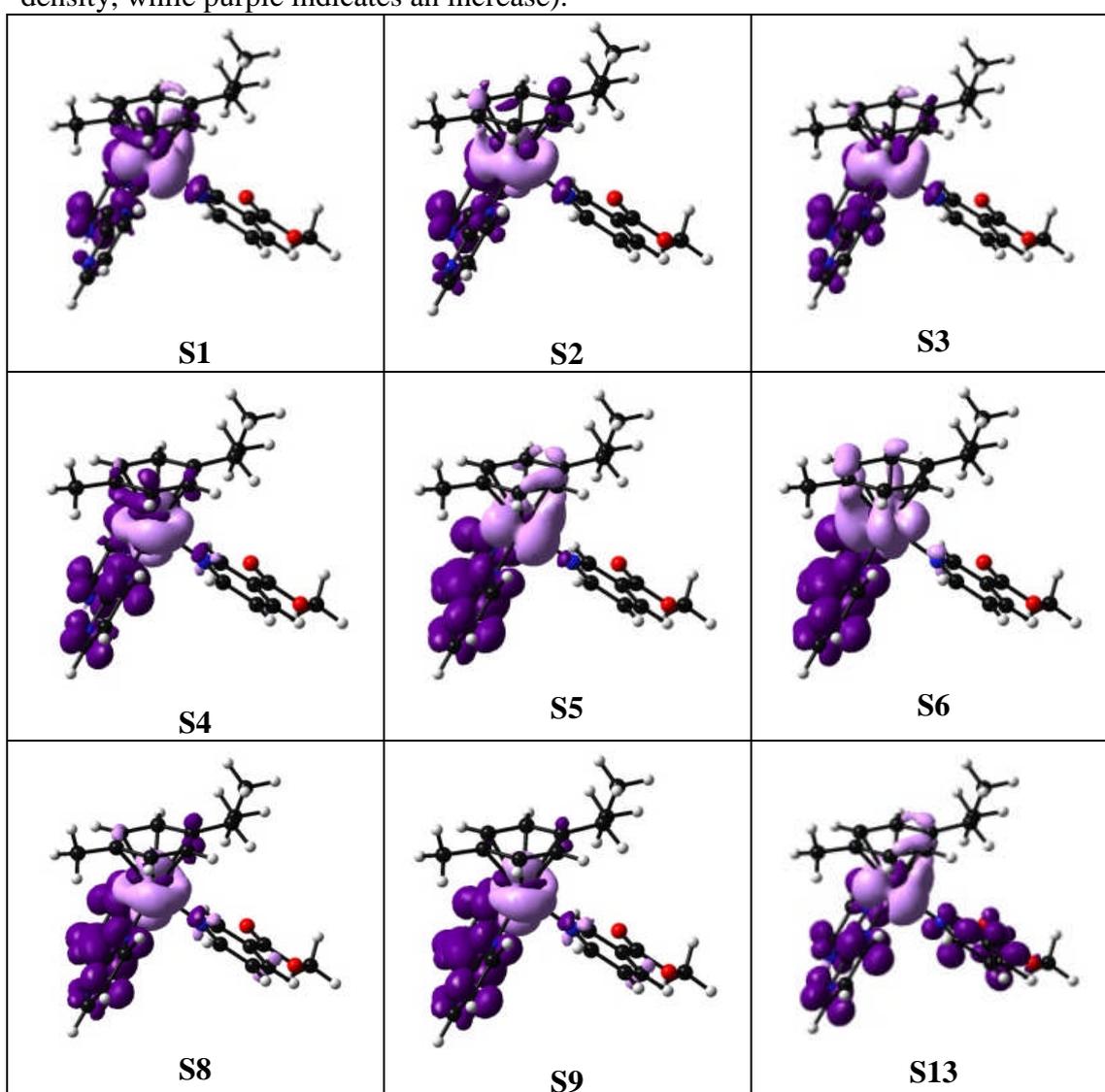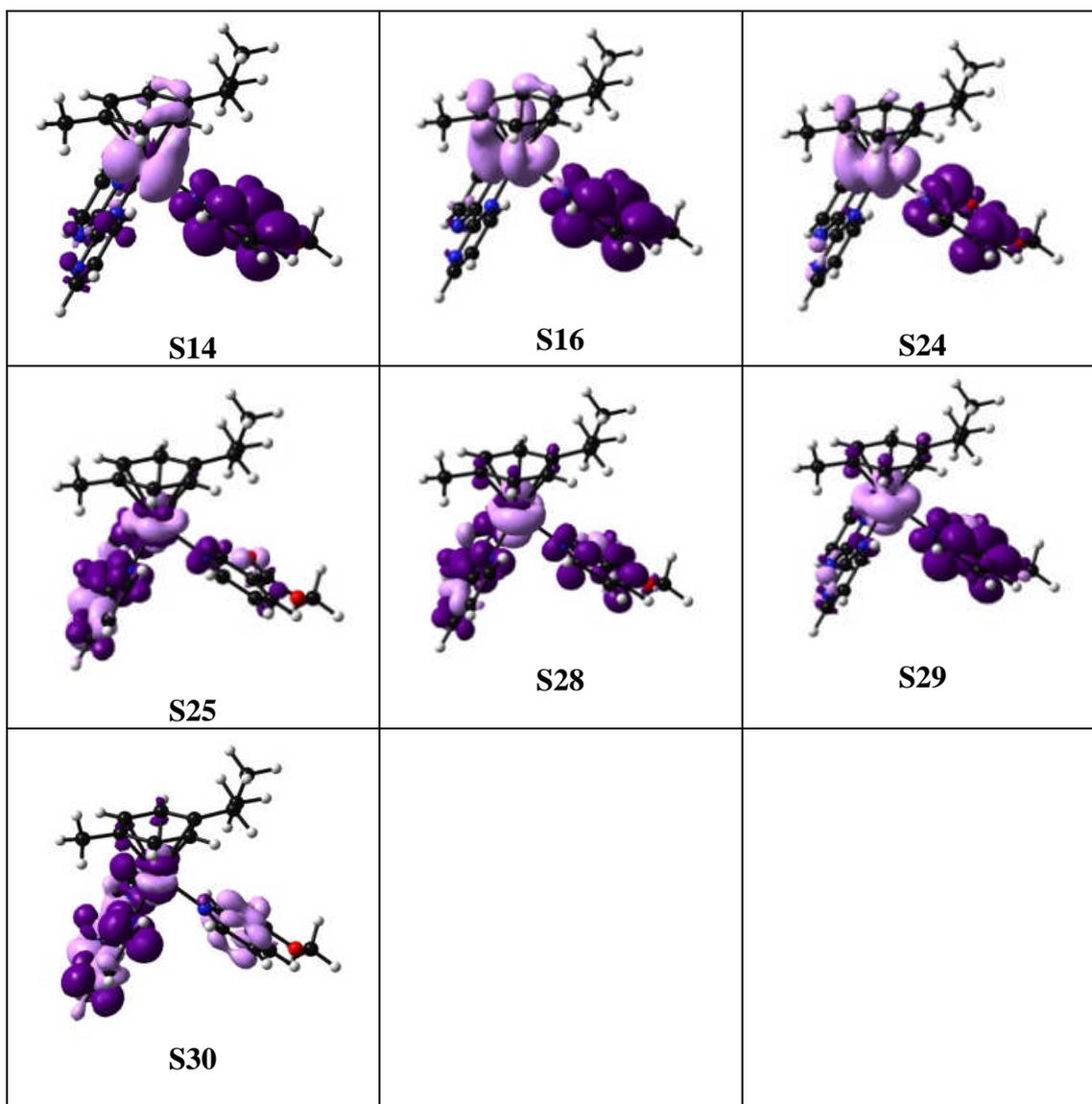
Table A.4.18. Selected TD-DFT triplet transitions for the complex **1** in the ground state optimised geometry.

	Energy (eV)	Wavelength (nm)	Oscillator Strength	Major contributions
1	2.252	550	0.0	HOMO→L+1 (74%) HOMO→L+3 (21%)
2	2.4005	516	0.0	HOMO→L+2 (17%) HOMO→L+3 (45%) HOMO→L+4 (23%)
3	2.4861	498	0.0	H-1→L+1 (69%) H-1→L+3 (19%)
4	2.5342	489	0.0	H-2→L+1 (13%) H-1→L+2 (12%) H-1→L+3 (48%) H-1→L+4 (16%)

5	2.7133	456	0.0	H-2→L+1 (58%)
				H-2→L+2 (10%)
				H-2→L+4 (14%)
6	2.8504	434	0.0	H-2→L+3 (69%)
7	2.9257	423	0.0	H-5→LUMO (18%)
				HOMO→LUMO (71%)
8	3.1334	395	0.0	H-1→LUMO (86%)

Figure A.4.18. Selected Electron Difference Density Maps (EDDMS) of triplet excited state transitions of **1** in H_2O (pink indicates a decrease in electron density, while red indicates an increase). Calculations were performed using the ground state optimised geometry.
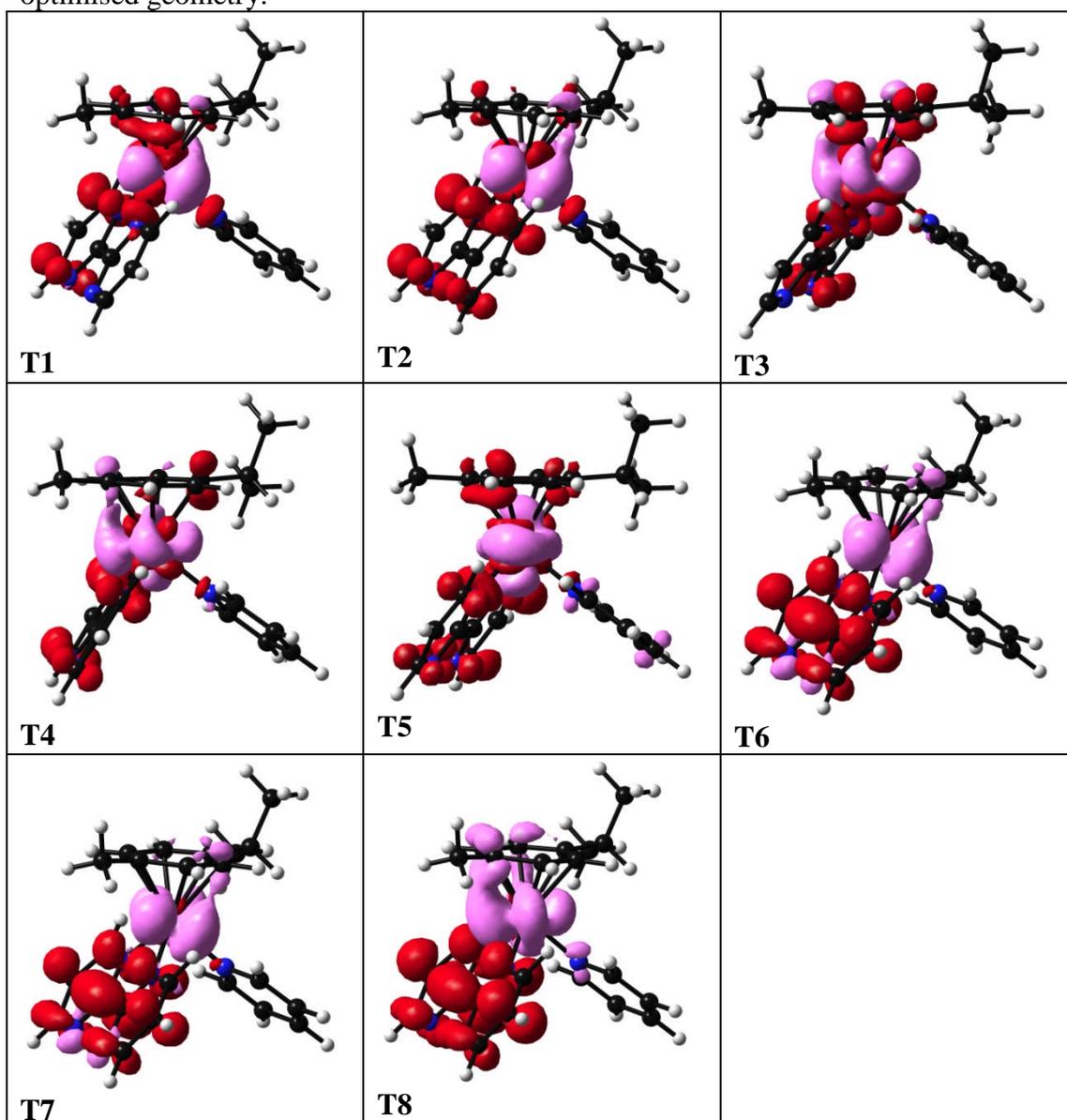
Table A.4.19. Selected TD-DFT triplet transitions for the complex **2** in the ground state optimised geometry.

	Energy (eV)	Wavelength (nm)	Oscillator Strength	Major contributions
1	2.260	549	0.0	HOMO→L+1 (72%) HOMO→L+3 (22%)
2	2.414	513	0.0	HOMO→L+2 (14%) HOMO→L+3 (41%) HOMO→L+4 (24%)
3	2.492	498	0.0	H-1→L+1 (64%) H-1→L+3 (26%)
4	2.537	489	0.0	H-2→L+1 (13%) H-1→L+2 (10%) H-1→L+3 (39%) H-1→L+4 (18%) HOMO→L+3 (10%)
5	2.712	457	0.0	H-2→L+1 (50%) H-2→L+2 (-11%) H-2→L+4 (-15%)
6	2.856	434	0.0	H-2→L+3 (67%)
7	2.920	425	0.0	H-5→LUMO (16%) HOMO→LUMO (67%)
8	3.108	399	0.0	H-1→LUMO (80%) HOMO→LUMO (-10%)

Figure A.4.19. Selected Electron Difference Density Maps (EDDMS) of triplet excited state transitions of **2** in H_2O (pink indicates a decrease in electron density, while red indicates an increase). Calculations were performed using the ground state optimised geometry.
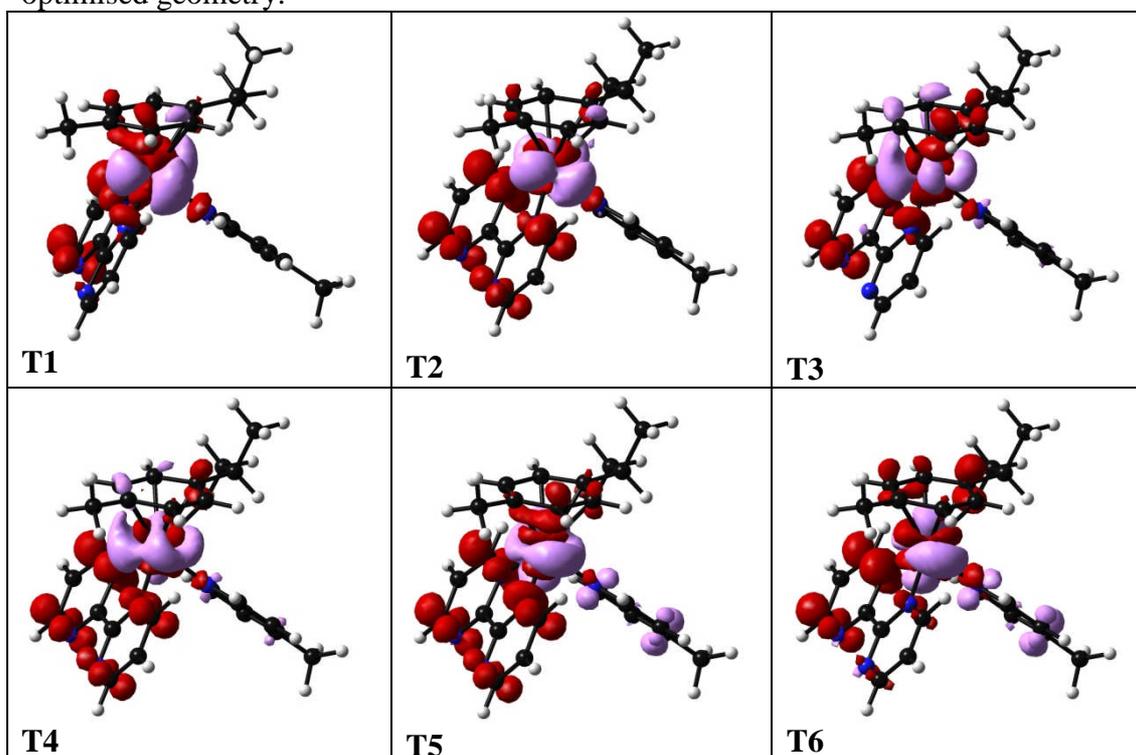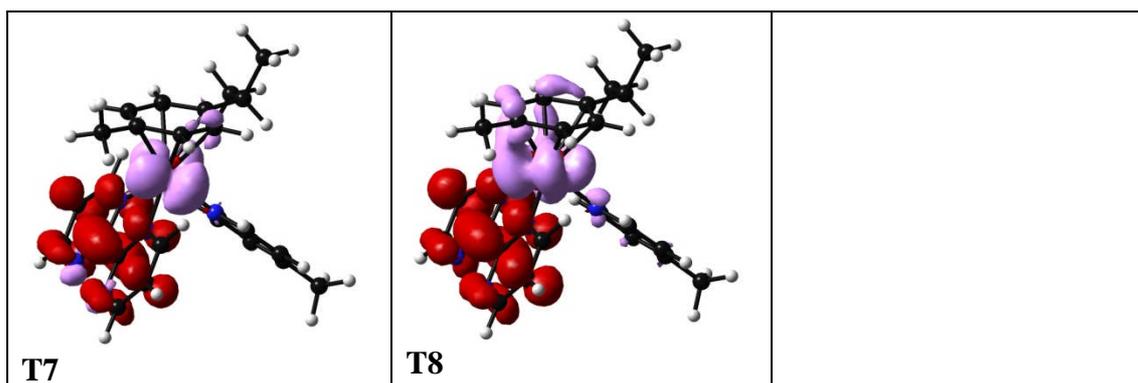
Table A.4.20. Selected TD-DFT triplet transitions for complex **3** in the ground state optimised geometry.

	Energy (eV)	Wavelength (nm)	Oscillator Strength	Major contributions
1	2.252	551	0.0	H-1→L+1 (13%) H-1→L+3 (11%) HOMO→L+1 (45%) HOMO→L+2 (11%) HOMO→L+3 (13%)
2	2.407	515	0.0	H-1→L+2 (12%) H-1→L+3 (30%) H-1→L+4 (23%) HOMO→L+3 (17%)
3	2.499	496	0.0	H-1→L+1 (33%) H-1→L+3 (32%)
4	2.531	490	0.0	H-2→L+1 (12%) H-2→L+4 (11%) HOMO→L+3 (27%)
5	2.678	463	0.0	H-3→L+1 (20%) H-3→L+2 (10%) H-2→L+1 (17%)
6	2.859	434	0.0	H-3→L+3 (25%) H-2→L+3 (48%)
7	2.905	427	0.0	H-6→LUMO (16%) H-1→LUMO (37%) HOMO→LUMO (36%)
8	3.056	406	0.0	H-1→LUMO (38%) HOMO→LUMO (46%)

Figure A.4.20. Selected Electron Difference Density Maps (EDDMS) of triplet excited state transitions of **3** in H_2O (pink indicates a decrease in electron density, while red indicates an increase). Calculations were performed using the ground state optimised geometry.
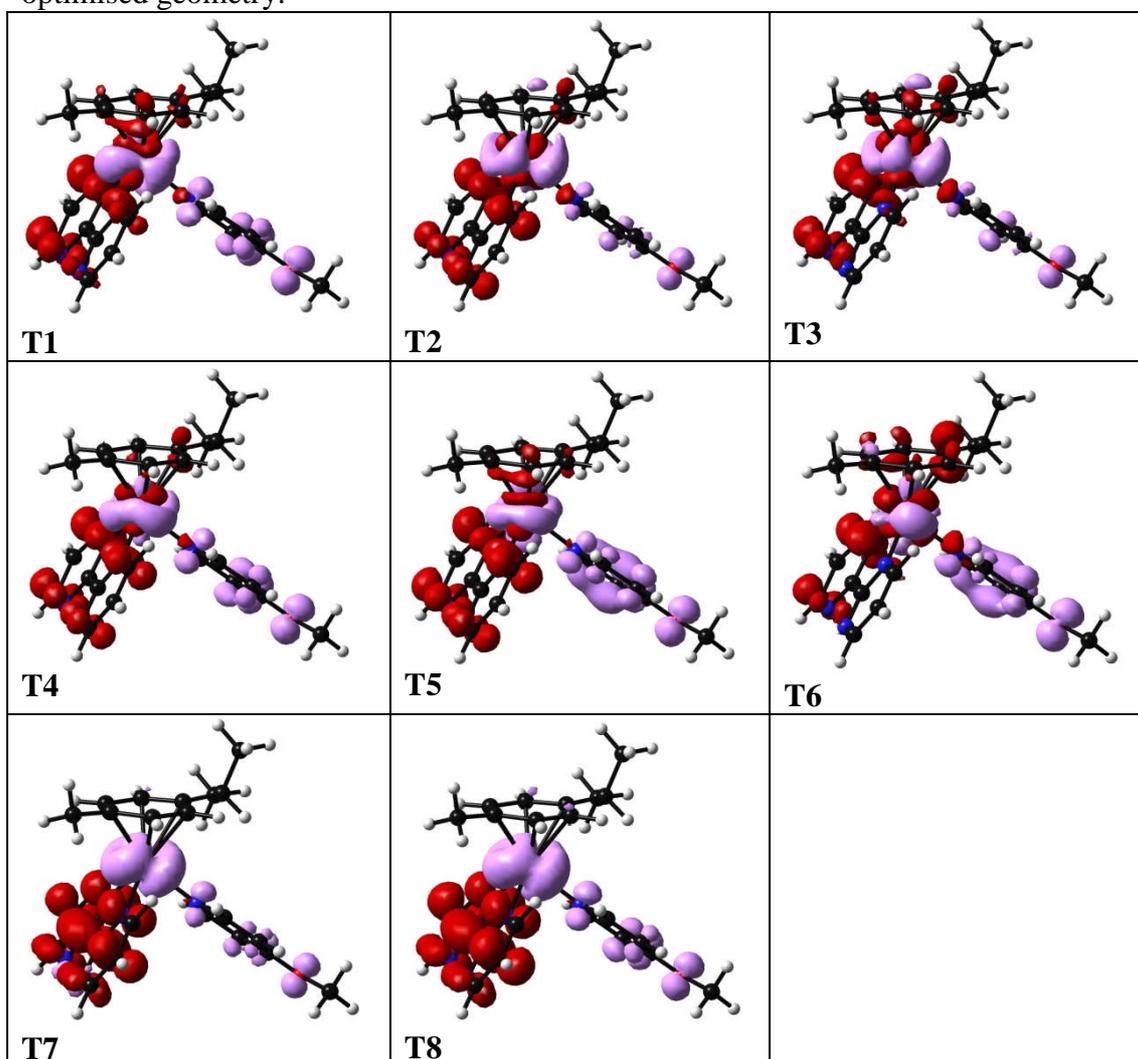

Table A.4.21. Selected TD-DFT triplet transitions for complex **4** in the ground state optimised geometry.

	Energy (eV)	Wavelength (nm)	Oscillator Strength	Major contributions
1	2.608	475	0.0	H-1→L+2 (10%) H-1→L+4 (12%) HOMO→L+1 (12%) HOMO→L+2 (14%) HOMO→L+4 (15%) HOMO→L+5 (11%)
2	2.770	448	0.0	H-1→L+1 (16%) HOMO→LUMO (17%) HOMO→L+1 (28%) HOMO→L+4 (11%)

3	2.955	420	0.0	H-8→LUMO (21%) H-1→LUMO (24%) HOMO→LUMO (46%)
4	3.171	391	0.0	H-1→LUMO (43%) HOMO→LUMO (12%) HOMO→L+1 (10%)
5	3.253	381	0.0	H-4→L+4 (11%) H-1→L+2 (20%) HOMO→L+2 (17%)
6	3.319	374	0.0	H-4→L+2 (17%) H-1→LUMO (11%) H-1→L+4 (14%) HOMO→L+4 (12%)
7	3.450	359	0.0	H-8→LUMO (29%) H-7→LUMO (41%) HOMO→LUMO (12%)
8	3.574	347	0.0	H-5→LUMO (16%) H-4→LUMO (52%)

Figure A.4.21. Selected Electron Difference Density Maps (EDDMS) of triplet excited state transitions of **4** in H_2O (pink indicates a decrease in electron density, while red indicates an increase). Calculations were performed using the ground state optimised geometry.
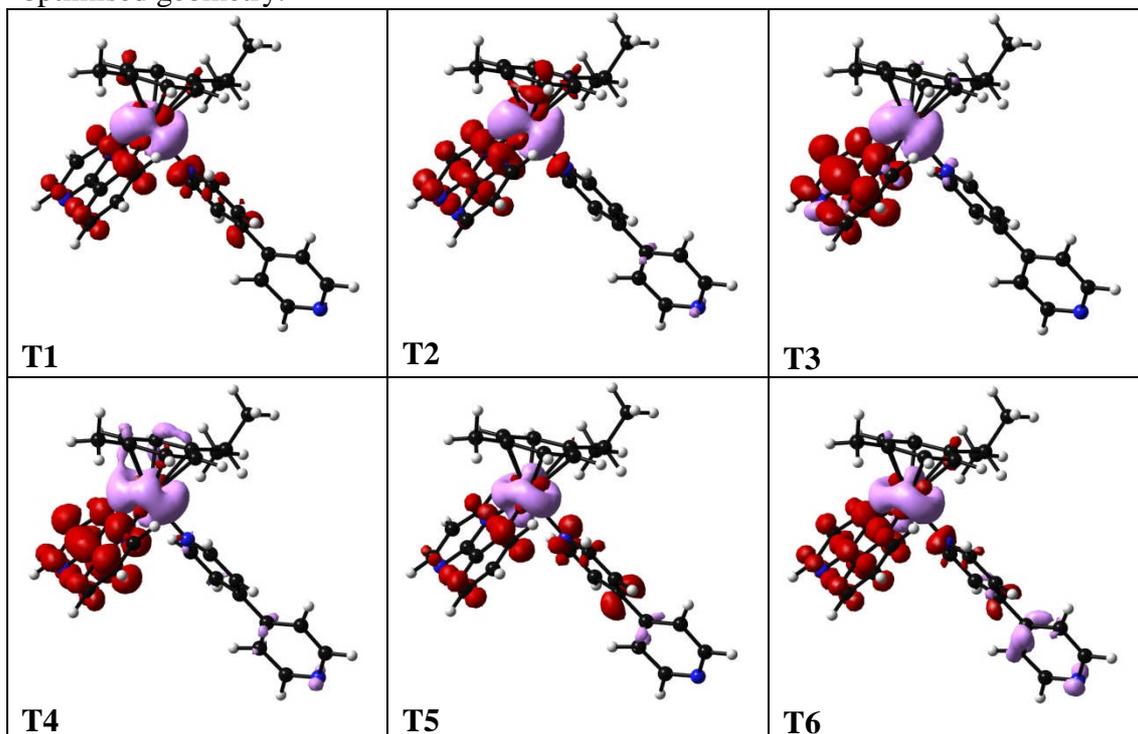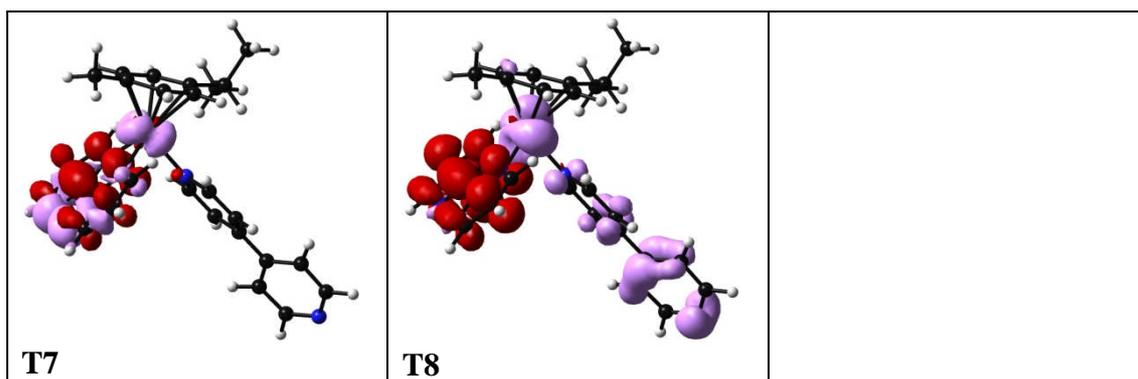
Table A.4.22. Selected TD-DFT triplet transitions for complex **5** in the ground state optimised geometry.

	Energy (eV)	Wavelength (nm)	Oscillator Strength	Major contributions
1	2.584	480	0.0	H-2→L+1 (25%) H-2→L+2 (17%) H-2→L+3 (14%) H-2→L+4 (22%)
2	2.756	450	0.0	H-3→L+1 (18%) H-3→L+3 (12%) HOMO→LUMO (11%) HOMO→L+1 (12%) HOMO→L+3 (11%)
3	2.940	422	0.0	H-7→LUMO (19%) H-2→LUMO (64%)
4	3.023	410	0.0	HOMO→LUMO (10%) HOMO→L+4 (23%) HOMO→L+5 (52%)
5	3.102	400	0.0	H-3→LUMO (26%) H-3→L+1 (10%) HOMO→LUMO (30%)
6	3.260	380	0.0	H-4→L+1 (11%) H-3→L+1 (13%) H-3→L+2 (12%) H-3→L+3 (12%) HOMO→LUMO (13%)
7	3.363	369	0.0	H-3→LUMO (56%) HOMO→LUMO (28%)
8	3.446	360	0.0	H-7→LUMO (29%) H-6→LUMO (38%) H-2→LUMO (17%)

Figure A.4.22. Selected Electron Difference Density Maps (EDDMS) of triplet excited state transitions of **5** in H_2O (pink indicates a decrease in electron density, while red indicates an increase). Calculations were performed using the ground state optimised geometry.
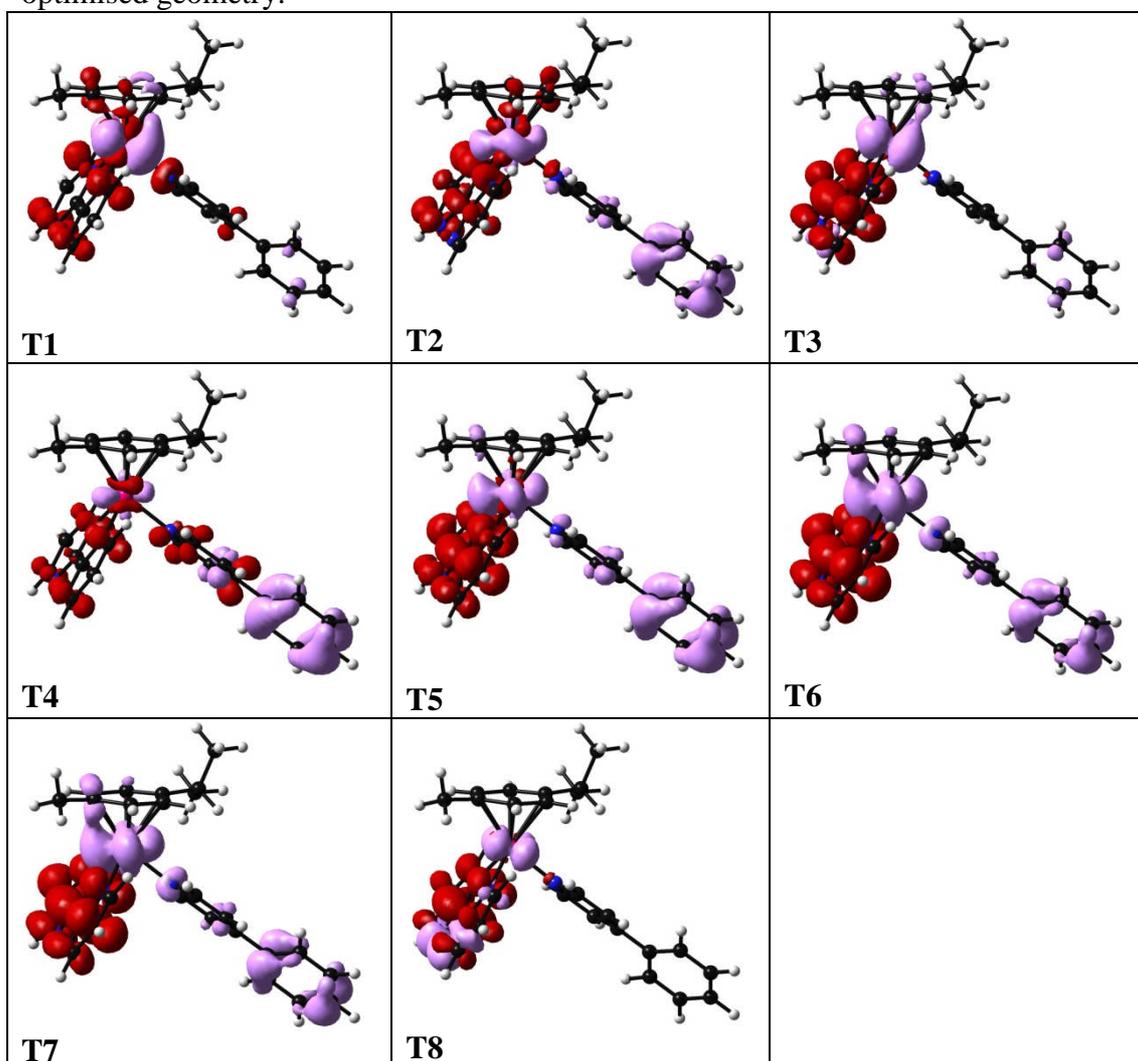

Table A.4.23. Selected TD-DFT triplet transitions for complex **6** in the ground state optimised geometry.

	Energy (eV)	Wavelength (nm)	Oscillator Strength	Major contributions
1	2.526	491	0.0	H-4→L+1 (12%) H-3→L+1 (18%) H-3→L+3 (13%) H-2→L+3 (29%) H-2→L+4 (13%)
2	2.908	426	0.0	H-7→LUMO (15%) H-3→LUMO (10%) H-2→LUMO (66%)
3	3.110	399	0.0	H-3→LUMO (65%) H-2→LUMO (12%)
4	3.158	393	0.0	H-2→L+1 (43%) H-2→L+2 (11%)

5	3.269	379	0.0	H-3→L+1 (12%)
				H-3→L+2 (10%)
6	3.322	373	0.0	HOMO→LUMO (85%)
7	3.332	372	0.0	H-3→L+3 (22%)
				H-2→L+3 (10%)
				HOMO→LUMO (13%)
8	3.447	360	0.0	H-1→LUMO (92%)

Figure A.4.23. Selected Electron Difference Density Maps (EDDMS) of triplet excited state transitions of **6** in H$_2$O (pink indicates a decrease in electron density, while red indicates an increase). Calculations were performed using the ground state optimised geometry.
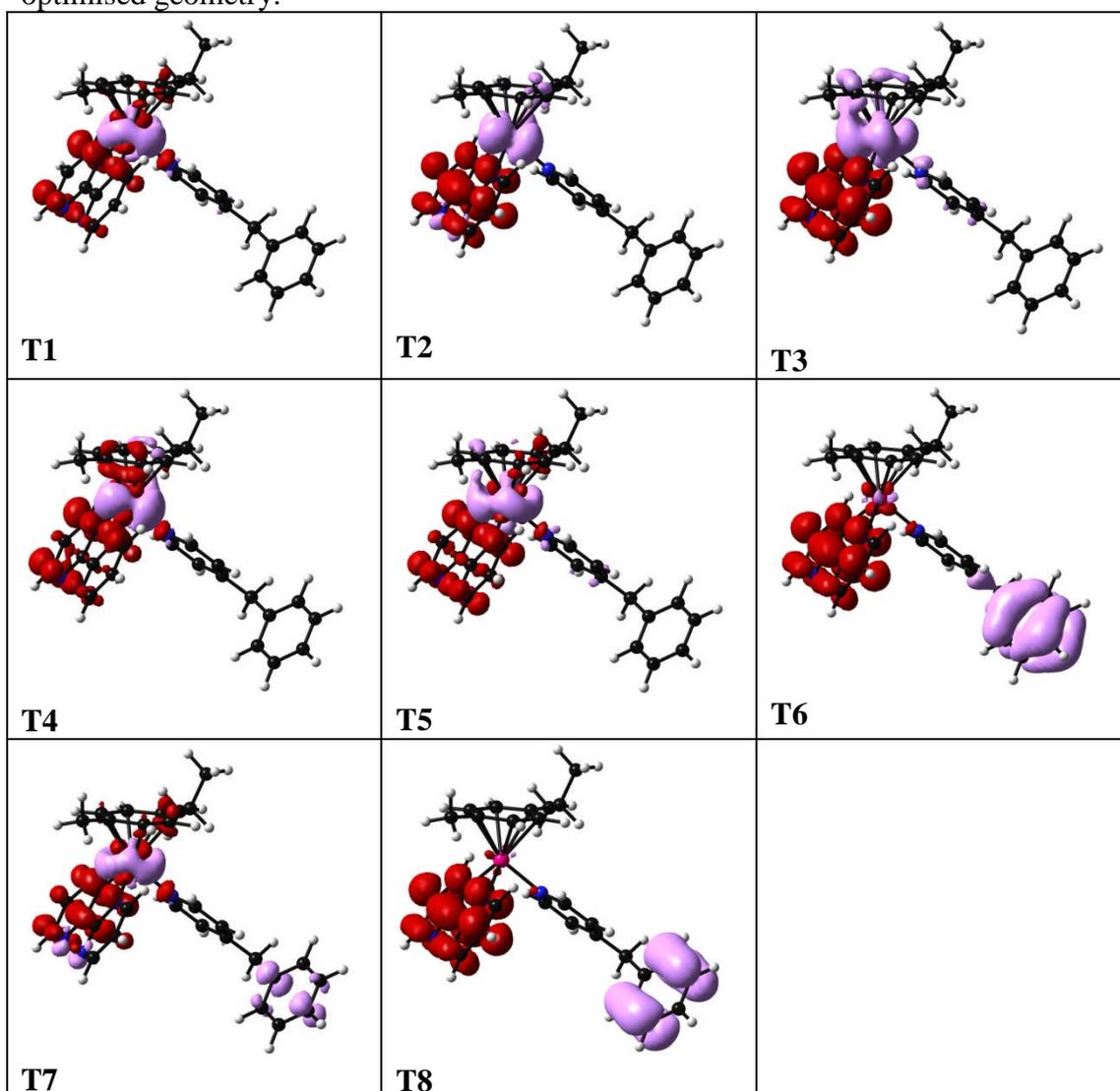
Table A.4.24. Selected TD-DFT triplet transitions for complex **8** in the ground state optimised geometry.

	Energy (eV)	Wavelength (nm)	Oscillator Strength	Major contributions
1	2.3186	534	0.0	HOMO→L+1 (71%) HOMO→L+4 (22%)
2	2.458	504	0.0	H-2→L+1 (28%) H-2→L+4 (10%) H-1→L+1 (44%) H-1→L+4 (14%)
3	2.8788	430	0.0	H-5→LUMO (15%) HOMO→LUMO (82%)
4	2.9615	418	0.0	H-1→LUMO (92%)
5	3.3209	373	0.0	H-1→L+3 (70%)
6	3.3873	366	0.0	H-5→LUMO (33%) H-4→LUMO (34%) HOMO→LUMO (12%) HOMO→L+3 (12%)
7	3.5108	353	0.0	H-2→LUMO (13%) HOMO→L+3 (50%)
8	3.5178	352	0.0	H-2→LUMO (69%)

Figure A.4.24. Selected Electron Difference Density Maps (EDDMS) of triplet excited state transitions of **8** in H_2O (pink indicates a decrease in electron density, while red indicates an increase). Calculations were performed using the ground state optimised geometry.

T7

T8
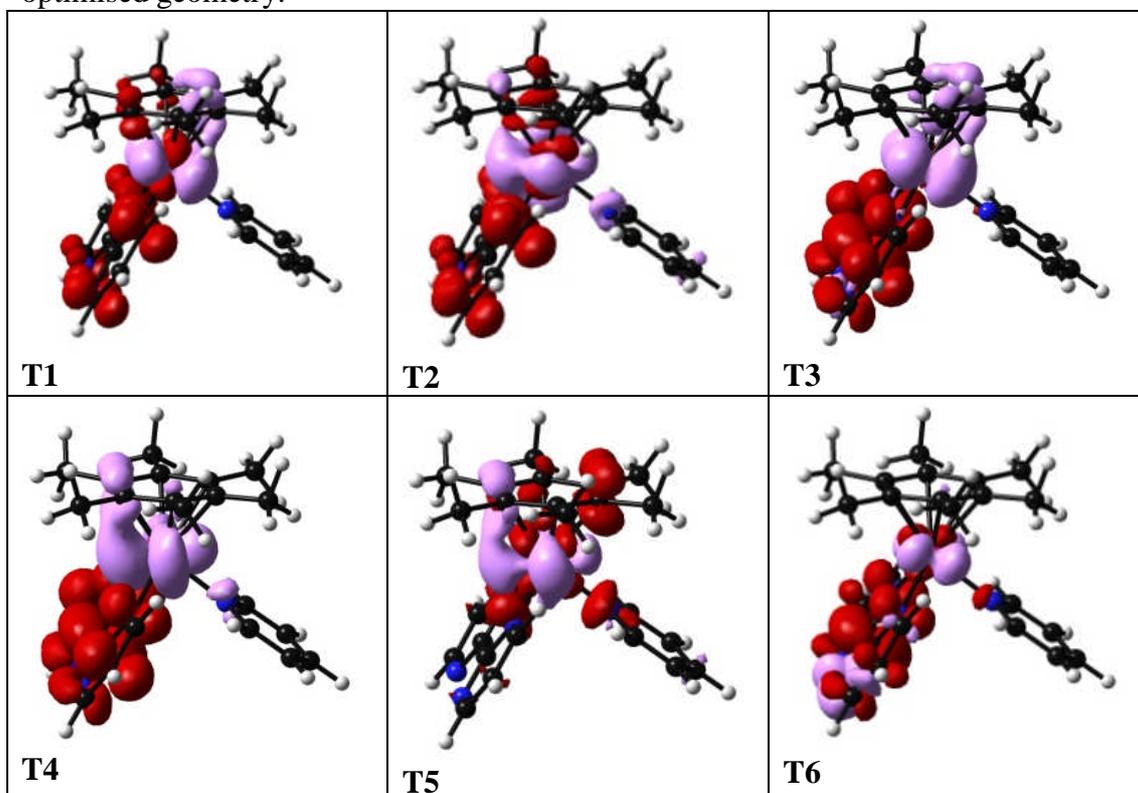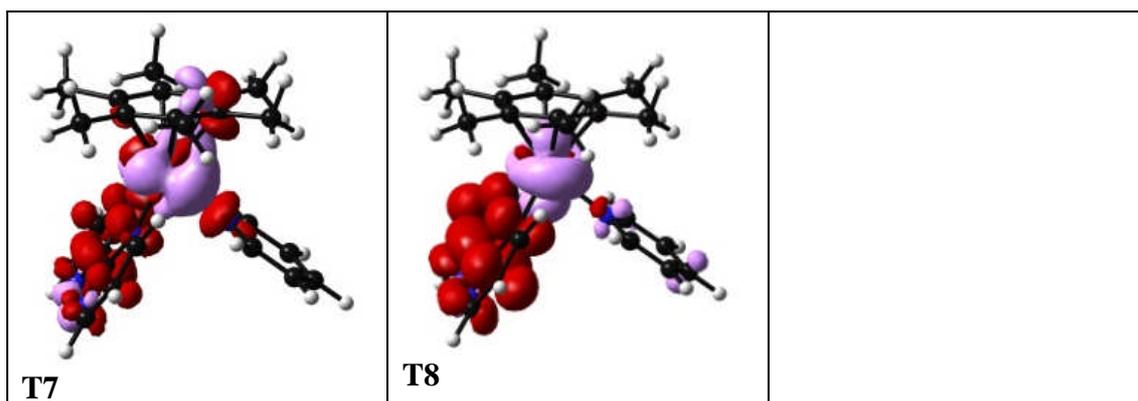
Table A.4.25. Selected TD-DFT triplet transitions for complex **9** in the ground state optimised geometry.

	Energy (eV)	Wavelength (nm)	Oscillator Strength	Major contributions
1	2.3213	534	0.0	H-1→L+1 (21%) HOMO→L+3 (77%)
2	2.3465	528	0.0	HOMO→L+1 (75%), HOMO→L+4 (19%)
3	2.4829	499	0.0	H-2→L+1 (14%) H-1→L+1 (53%) H-1→L+4 (13%) HOMO→L+3 (18%)
4	2.5264	490	0.0	H-1→L+3 (89%)
5	2.7131	456	0.0	H-2→L+1 (67%) H-2→L+4 (18%) H-1→L+1 (12%)
6	2.8455	435	0.0	H-2→L+3 (82%)
7	2.9069	426	0.0	H-5→LUMO (18%) HOMO→LUMO (76%)
8	3.0666	404	0.0	H-1→LUMO (93%)

Figure A.4.25. Selected Electron Difference Density Maps (EDDMS) of triplet excited state transitions of **9** in H_2O (pink indicates a decrease in electron density, while red indicates an increase). Calculations were performed using the ground state optimised geometry.


T1

T2

T3

T4	**T5**	**T6**
T7	**T8**	
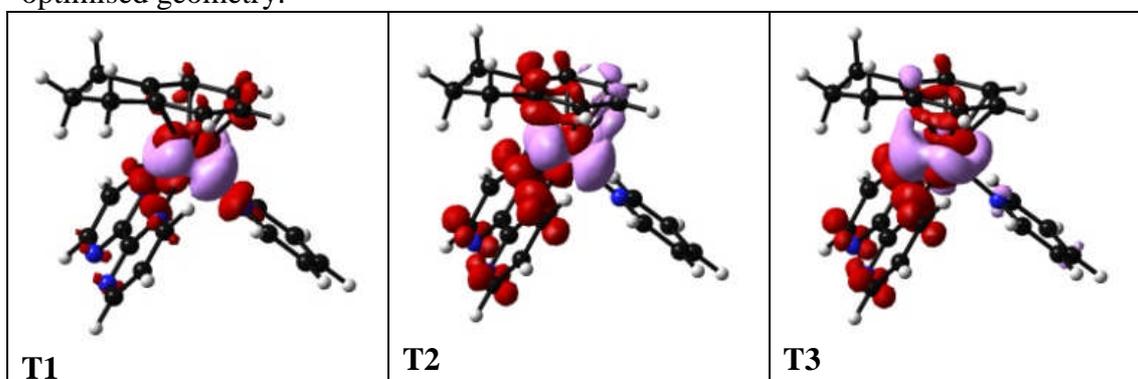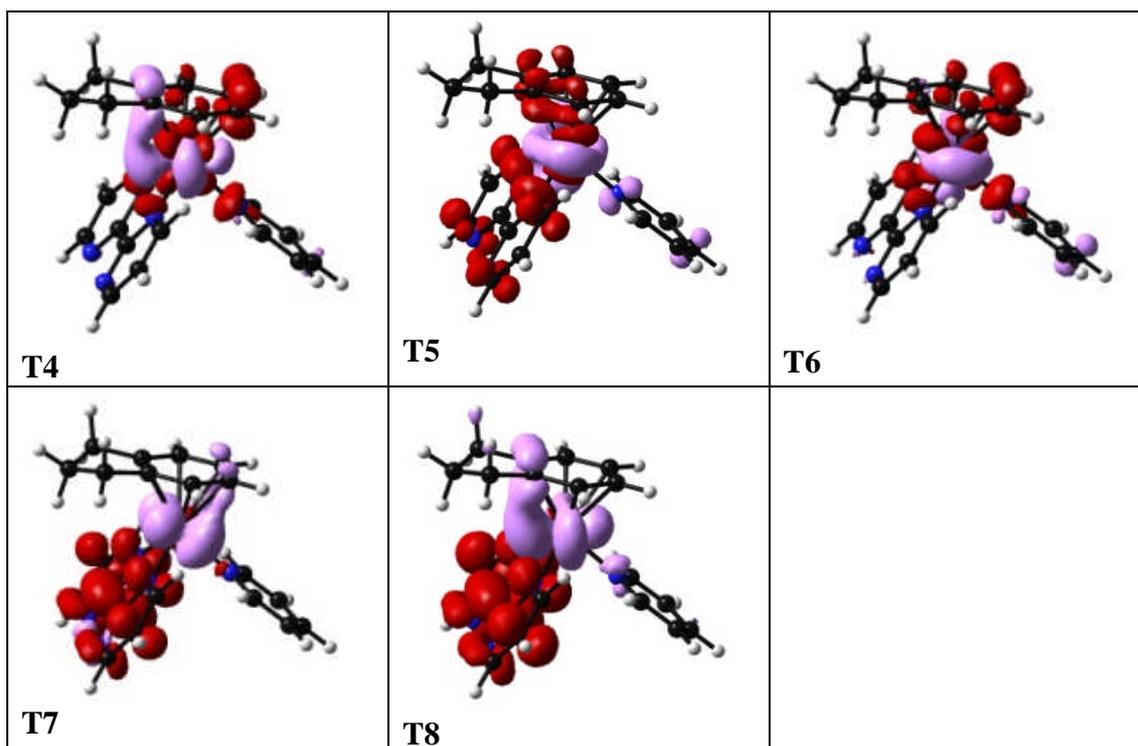
Table A.4.26. Selected TD-DFT triplet transitions for complex **10** in the ground state optimised geometry.

	Energy (eV)	Wavelength (nm)	Oscillator Strength	Major contributions
1	2.2809	543	0.0	H-1→L+2 (51%) HOMO→L+2 (40%)
2	2.4267	511	0.0	H-1→L+3 (80%) HOMO→L+3 (11%)
3	2.5013	496	0.0	H-2→L+2 (18%) H-1→L+2 (30%) HOMO→L+2 (32%) HOMO→L+3 (10%)
4	2.5628	484	0.0	H-2→L+3 (32%) HOMO→L+3 (34%)
5	2.7302	454	0.0	H-3→L+2 (37%) H-3→L+3 (20%) HOMO→L+1 (12%) HOMO→L+3 (10%)
6	2.7846	445	0.0	H-4→LUMO (11%) H-2→L+1 (20%) H-1→LUMO (13%) HOMO→L+1 (33%)
7	2.8337	438	0.0	H-3→L+2 (16%) H-3→L+3 (46%) H-2→L+2 (10%) H-2→L+3 (16%)

8	3.0311	409	0.0	H-2→LUMO (11%) H-1→LUMO (10%), HOMO→LUMO (74%)

Figure A.4.26. Selected Electron Difference Density Maps (EDDMS) of triplet excited state transitions of **10** in H$_2$O (pink indicates a decrease in electron density, while red indicates an increase). Calculations were performed using the ground state optimised geometry.
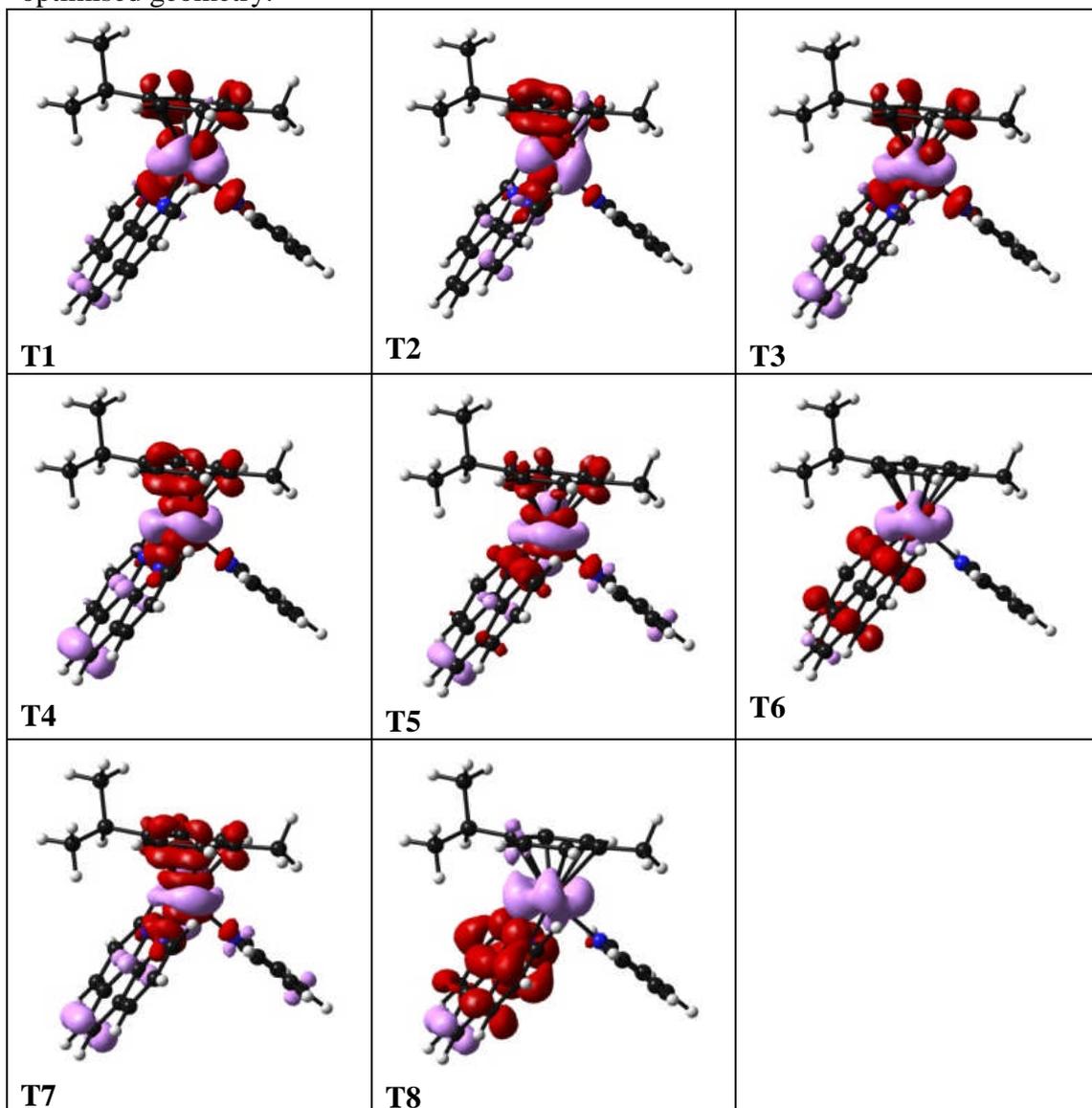

Table A.4.27. Selected TD-DFT triplet transitions for complex **11** in the ground state optimised geometry.

	Energy (eV)	Wavelength (nm)	Oscillator Strength	Major contributions
1	1.8474	671	0.0	H-3→LUMO (60%) H-2→LUMO (32%)
2	2.2446	552	0.0	HOMO->L+2 (-26%) HOMO->L+3 (54%)

3	2.3575	526	0.0	H-4→LUMO (20%)
				HOMO→LUMO (18%)
				HOMO→L+2 (14%)
				HOMO→L+4 (27%)
4	2.3832	520	0.0	H-4→LUMO (30%)
				HOMO→LUMO (12%)
				HOMO→L+4 (22%)
5	2.4432	507	0.0	H-1→LUMO (19%)
				H-1→L+2 (11%)
				H-1→L+3 (50%)
6	2.4697	502	0.0	H-1→L+2 (18%)
				H-1→L+4 (29%)
7	2.5169	493	0.0	H-4→LUMO (14%)
				H-1→L+3 (12%)
				HOMO→LUMO (41%)
8	2.5582	485	0.0	H-4→LUMO (14%)
				H-1→LUMO (57%)
				HOMO→LUMO (11%)

Figure A.4.27. Selected Electron Difference Density Maps (EDDMS) of triplet excited state transitions of **11** in H_2O (pink indicates a decrease in electron density, while red indicates an increase). Calculations were performed using the ground state optimised geometry.
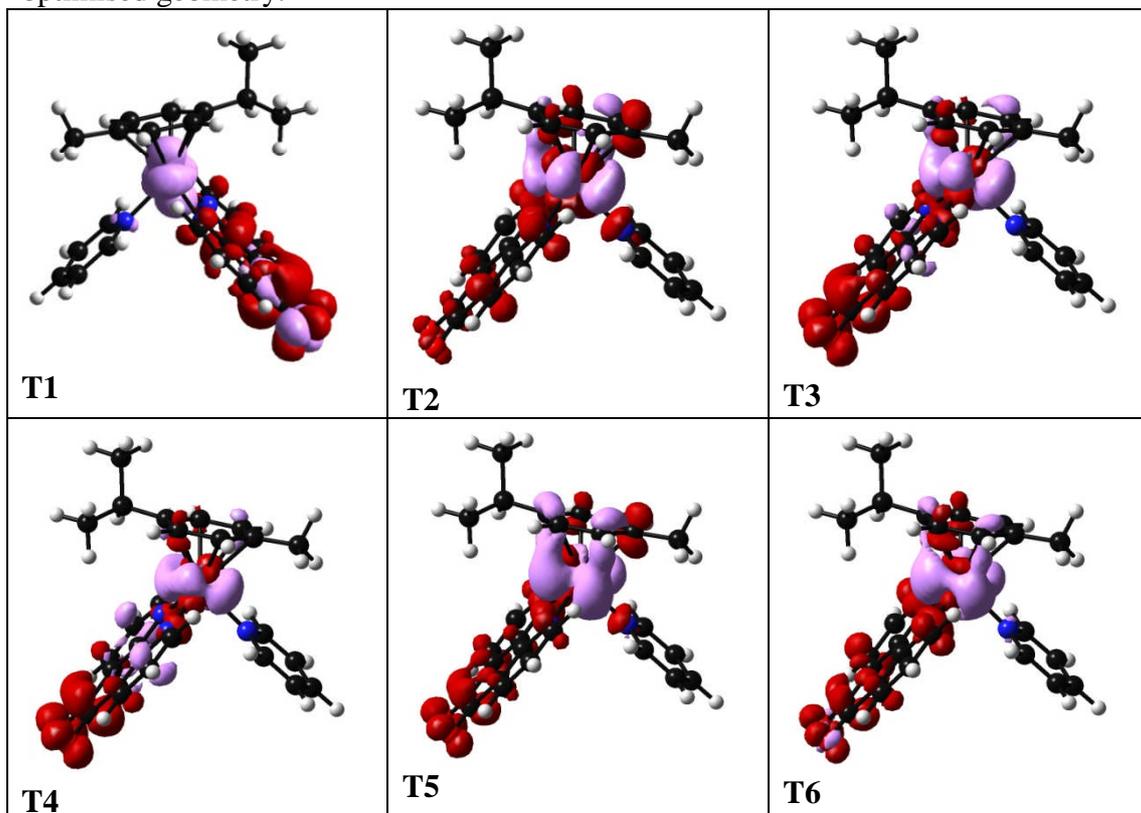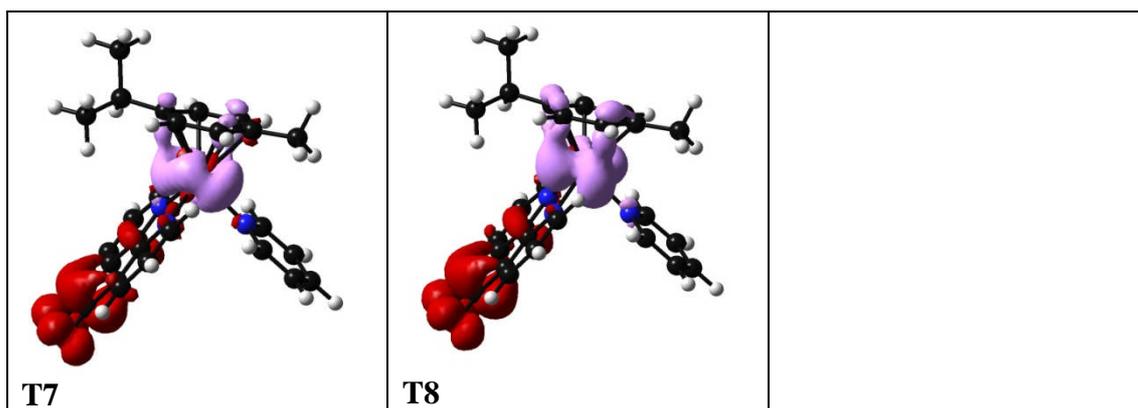
Table A.4.28. Selected TD-DFT triplet transitions for complex **12** in the ground state optimised geometry.

	Energy (eV)	Wavelength (nm)	Oscillator Strength	Major contributions
1	2.420	512	0.0	H-2→L+2 (22%) H-1→L+2 (39%) H-1→L+3 (16%)
2	2.572	482	0.0	H-1→LUMO (21%) HOMO→L+1 (71%)
3	2.678	463	0.0	HOMO→LUMO (93%)
4	2.752	451	0.0	H-7→L+3 (12%) H-6→L+3 (12%) H-5→L+2 (14%) H-5→L+3 (28%)
5	3.068	404	0.0	H-7→L+2 (10%) H-5→LUMO (10%) HOMO→L+2 (30%)
6	3.148	394	0.0	H-1→LUMO (62%) HOMO→L+1 (18%)
7	3.374	367	0.0	H-6→LUMO (11%) H-1→L+1 (50%)
8	3.414	363	0.0	H-6→L+1 (13%) H-2→LUMO (46%)

Figure A.4.28. Selected Electron Difference Density Maps (EDDMS) of triplet excited state transitions of **12** in H_2O (pink indicates a decrease in electron density, while red indicates an increase). Calculations were performed using the ground state optimised geometry.
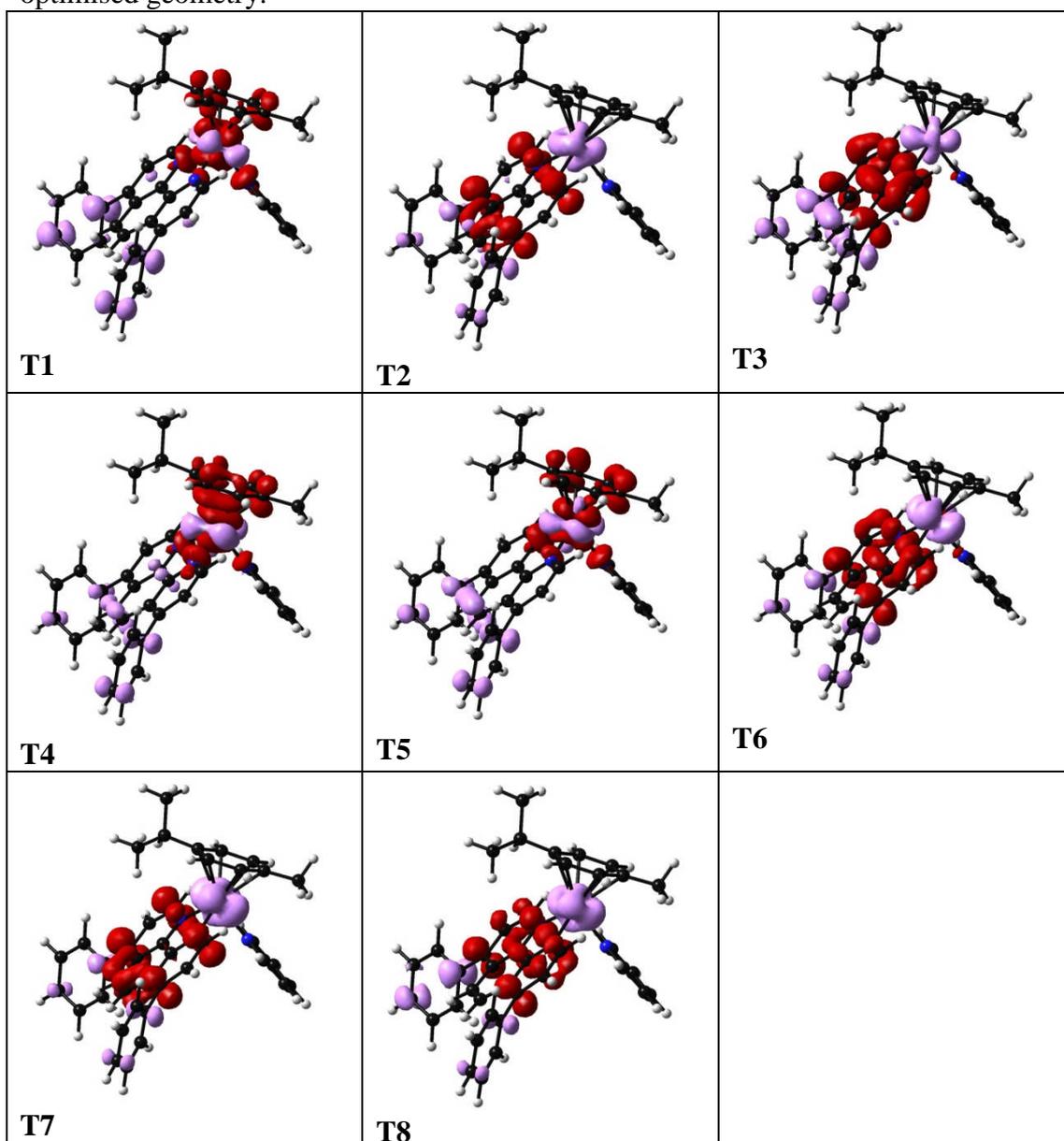

Table A.4.29. Selected TD-DFT triplet transitions for complex **13** in the ground state optimised geometry.

	Energy (eV)	Wavelength (nm)	Oscillator Strength	Major contributions
1	2.3241	533	0.0	H-1→L+1 (14%) HOMO→L+2 (75%)
2	2.3936	518	0.0	HOMO→L+1 (96%)
3	2.5138	493	0.0	H-1→L+2 (95%)
4	2.5283	490	0.0	H-2→L+1 (19%) H-1→L+1 (68%) HOMO→L+2 (10%)

5	2.7465	451	0.0	H-2→L+1 (79%)
				H-1→L+1 (17%)
6	2.8335	437	0.0	H-2→L+2 (96%)
7	2.9429	421	0.0	H-3→LUMO (47%)
				HOMO→LUMO (43%)
8	3.2487	381	0.0	H-1→LUMO (89%)

Figure A.4.29. Selected Electron Difference Density Maps (EDDMS) of triplet excited state transitions of **13** in H_2O (pink indicates a decrease in electron density, while red indicates an increase). Calculations were performed using the ground state optimised geometry.
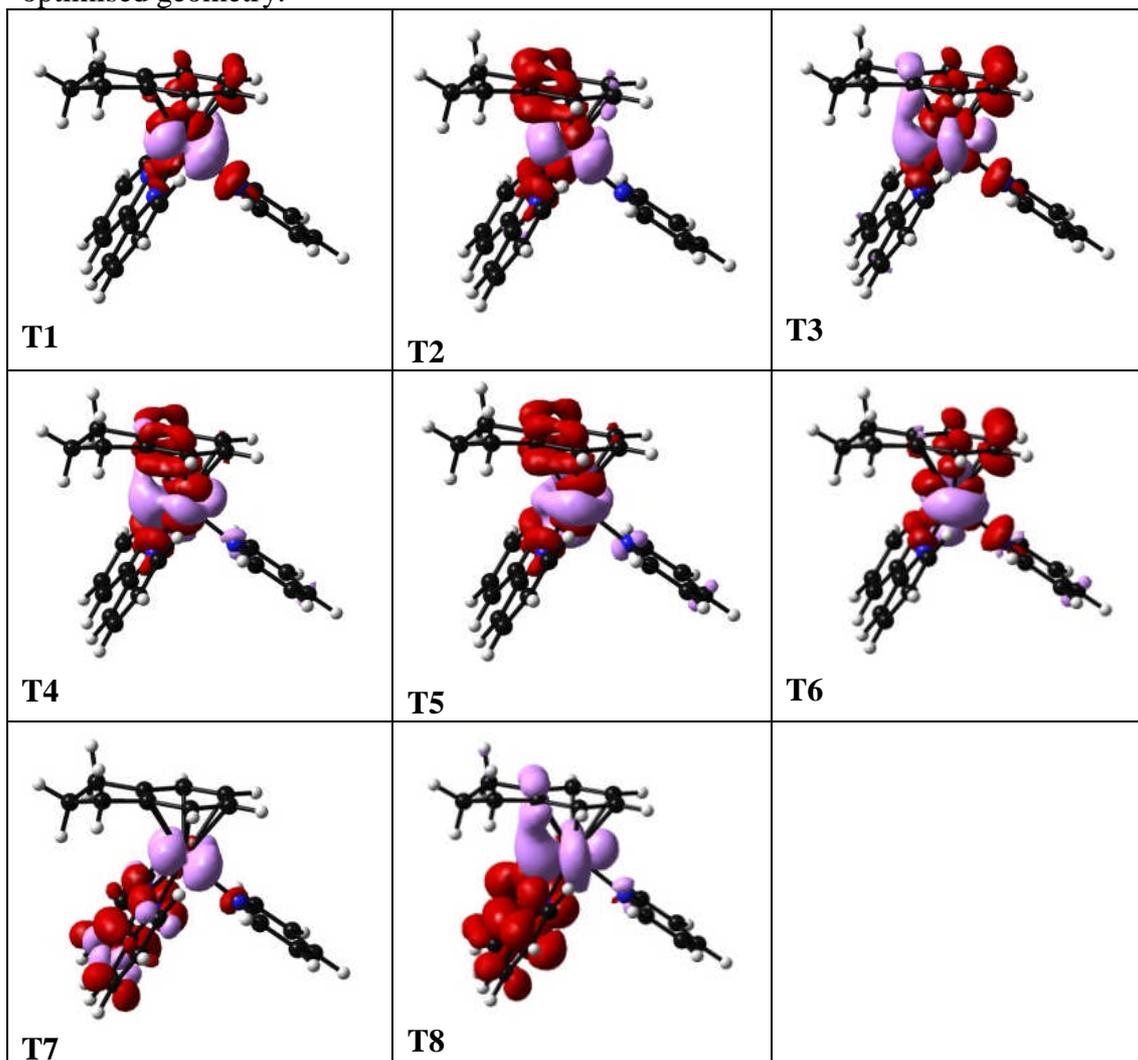
Table A.4.30. Selected TD-DFT triplet transitions for complex **14** in the ground state optimised geometry.

	Energy (eV)	Wavelength (nm)	Oscillator Strength	Major contributions
1	2.2499	551	0.0	HOMO→L+1 (40%) HOMO→L+2 (37%) HOMO→L+4 (16%)
2	2.4019	516	0.0	HOMO→L+2 (13%) HOMO→L+3 (22%) HOMO→L+4 (39%) HOMO→L+5 (22%)
3	2.5073	494	0.0	H-1→L+1 (37%) H-1→L+2 (33%) H-1→L+4 (15%)
4	2.5521	485	0.0	H-3→L+2 (10%) H-1→L+3 (18%) H-1→L+4 (34%) H-1→L+5 (16%)
5	2.7267	454	0.0	H-3→L+1 (28%) H-3→L+2 (35%)
6	2.856	434	0.0	H-3→L+3 (23%) H-3→L+4 (50%)
7	2.9384	422	0.0	H-6→LUMO (20%) HOMO→LUMO (71%)
8	3.1766	390	0.0	H-1→LUMO (85%)

Figure A.4.30. Selected Electron Difference Density Maps (EDDMS) of triplet excited state transitions of **14** in H_2O (pink indicates a decrease in electron density, while red indicates an increase). Calculations were performed using the ground state optimised geometry.
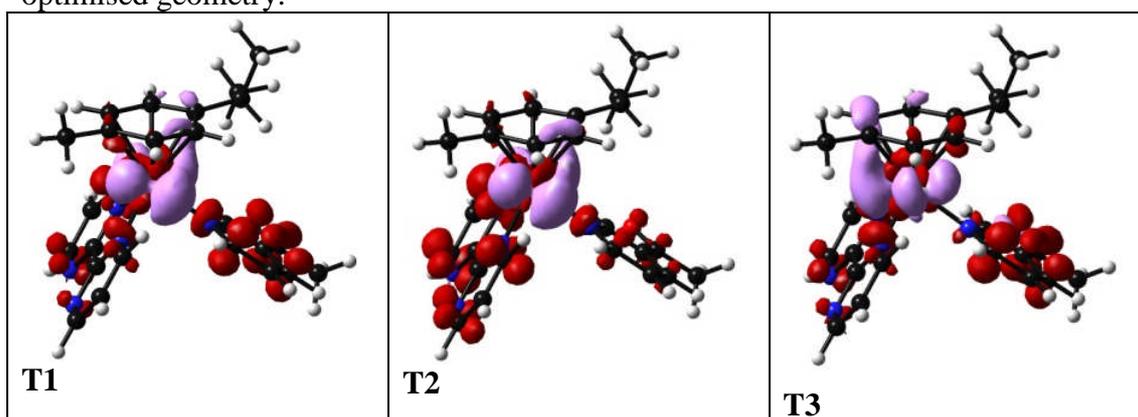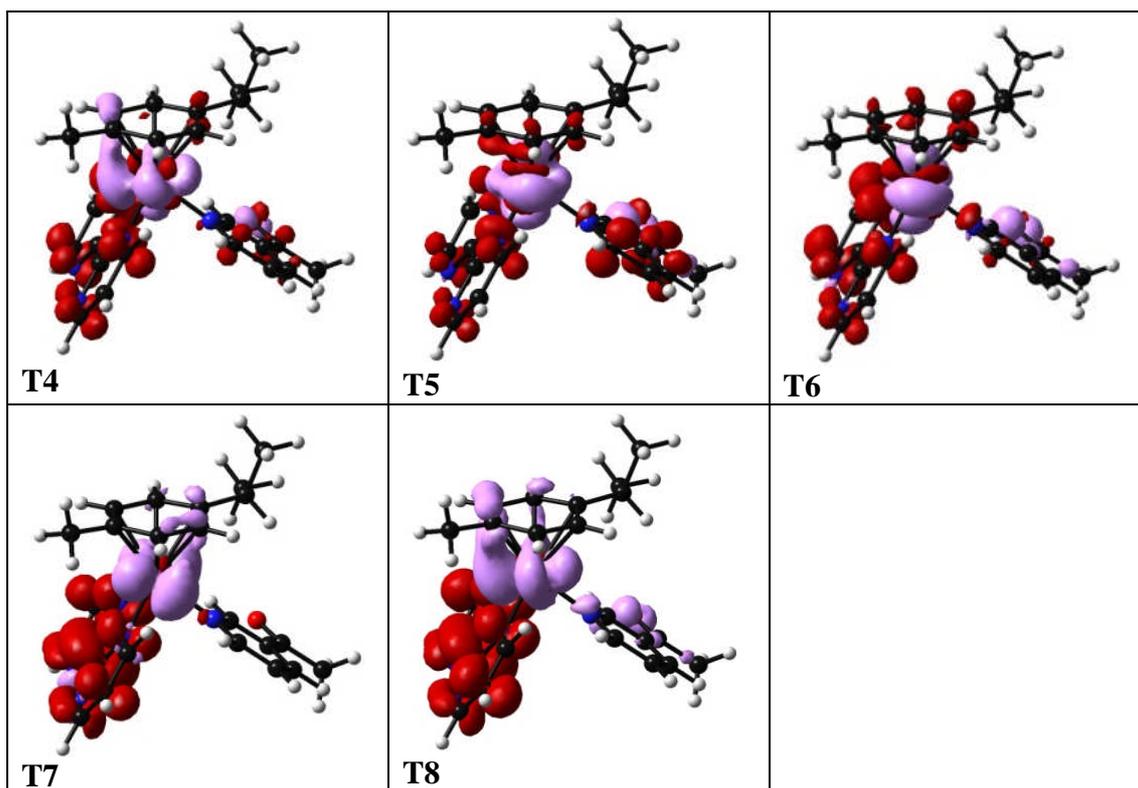
Table A.4.31. Selected TD-DFT triplet transitions for the complex **15** in the ground state optimised geometry.

	Energy (eV)	Wavelength (nm)	Oscillator Strength	Major contributions
1	2.2514	550	0.0	HOMO→L+1 (73%) HOMO→L+3 (17%)
2	2.4071	515	0.0	HOMO→L+2 (16%) HOMO→L+3 (52%) HOMO→L+4 (25%)
3	2.5023	495	0.0	H-1→L+1 (65%) H-1→L+3 (21%)
4	2.5446	487	0.0	H-3→L+1 (14%) H-1→L+2 (12%) H-1→L+3 (42%) H-1→L+4 (19%)
5	2.7166	456	0.0	H-3→L+1 (47%) H-3→L+2 (11%) H-3→L+4 (11%)
6	2.8511	434	0.0	H-3→L+3 (61%)
7	2.9292	423	0.0	H-7→LUMO (19%) HOMO→LUMO (71%)
8	3.1479	393	0.0	H-1→LUMO (84%)

Figure A.4.31. Selected Electron Difference Density Maps (EDDMS) of triplet excited state transitions of **15** in H_2O (pink indicates a decrease in electron density, while red indicates an increase). Calculations were performed using the ground state optimised geometry.
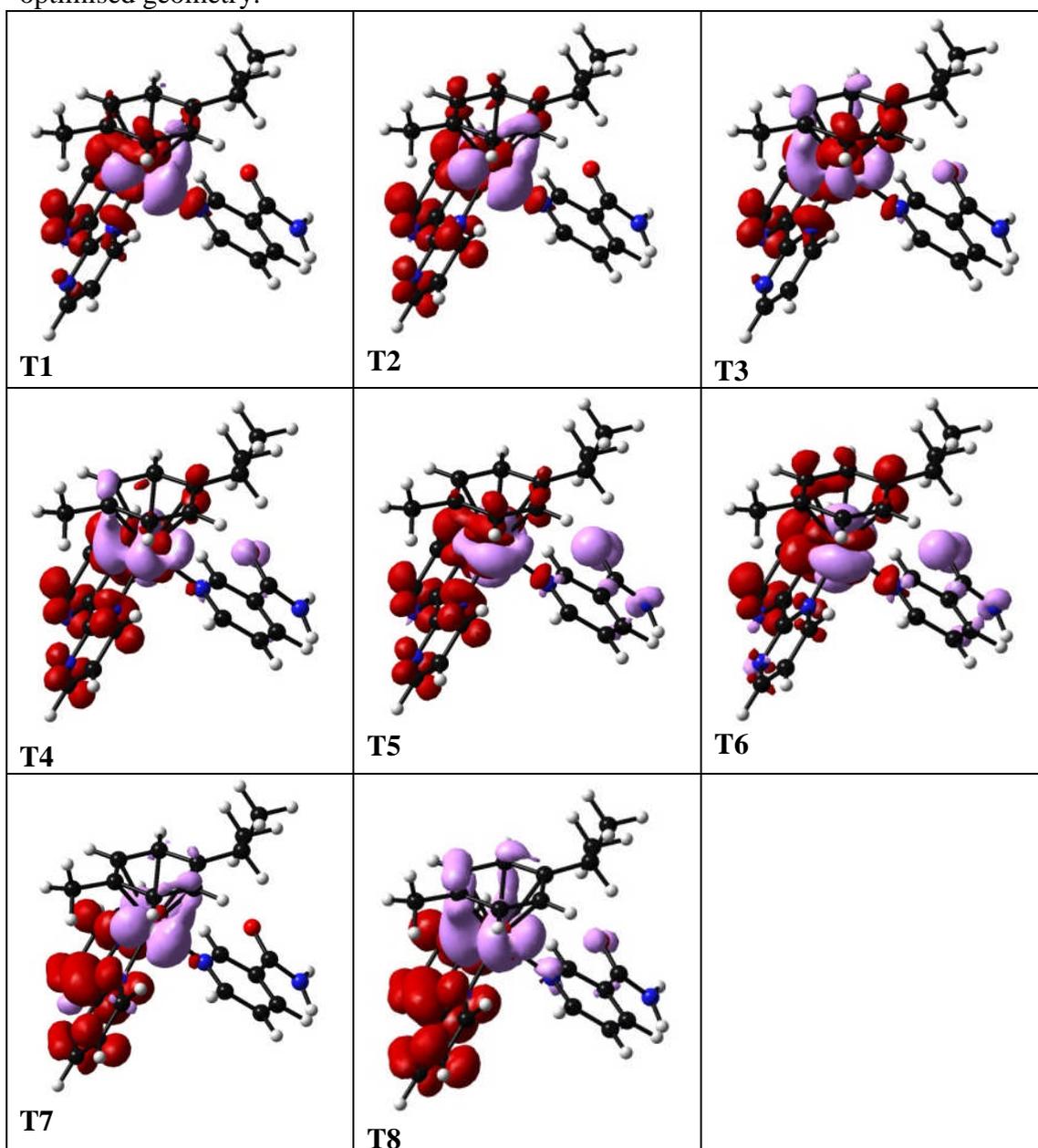
**Table A.4.32.** Selected TD-DFT triplet transitions for complex **16** in the ground state optimised geometry.

	Energy (eV)	Wavelength (nm)	Oscillator Strength	Major contributions
1	2.4952	497	0.0	HOMO→L+1 (18%) HOMO→L+2 (23%) HOMO→L+3 (23%) HOMO→L+5 (21%)
2	2.8055	442	0.0	HOMO→L+1 (35%) HOMO→L+3 (32%)

3	2.9418	421	0.0	H-6→LUMO (20%) HOMO→LUMO (67%)
4	3.0719	403	0.0	H-1→LUMO (24%) H-1→L+1 (28%)
5	3.2275	384	0.0	H-1→LUMO (64%)
6	3.4668	357	0.0	H-6→LUMO (27%) H-5→LUMO (32%) H-3→LUMO (11%) HOMO→LUMO (17%)
7	3.552	349	0.0	H-1→L+1 (21%) H-1→L+3 (41%)
8	3.6313	341	0.0	H-2→LUMO (78%)

Figure A.4.32. Selected Electron Difference Density Maps (EDDMS) of triplet excited state transitions of **16** in H_2O (pink indicates a decrease in electron density, while red indicates an increase). Calculations were performed using the ground state optimised geometry.
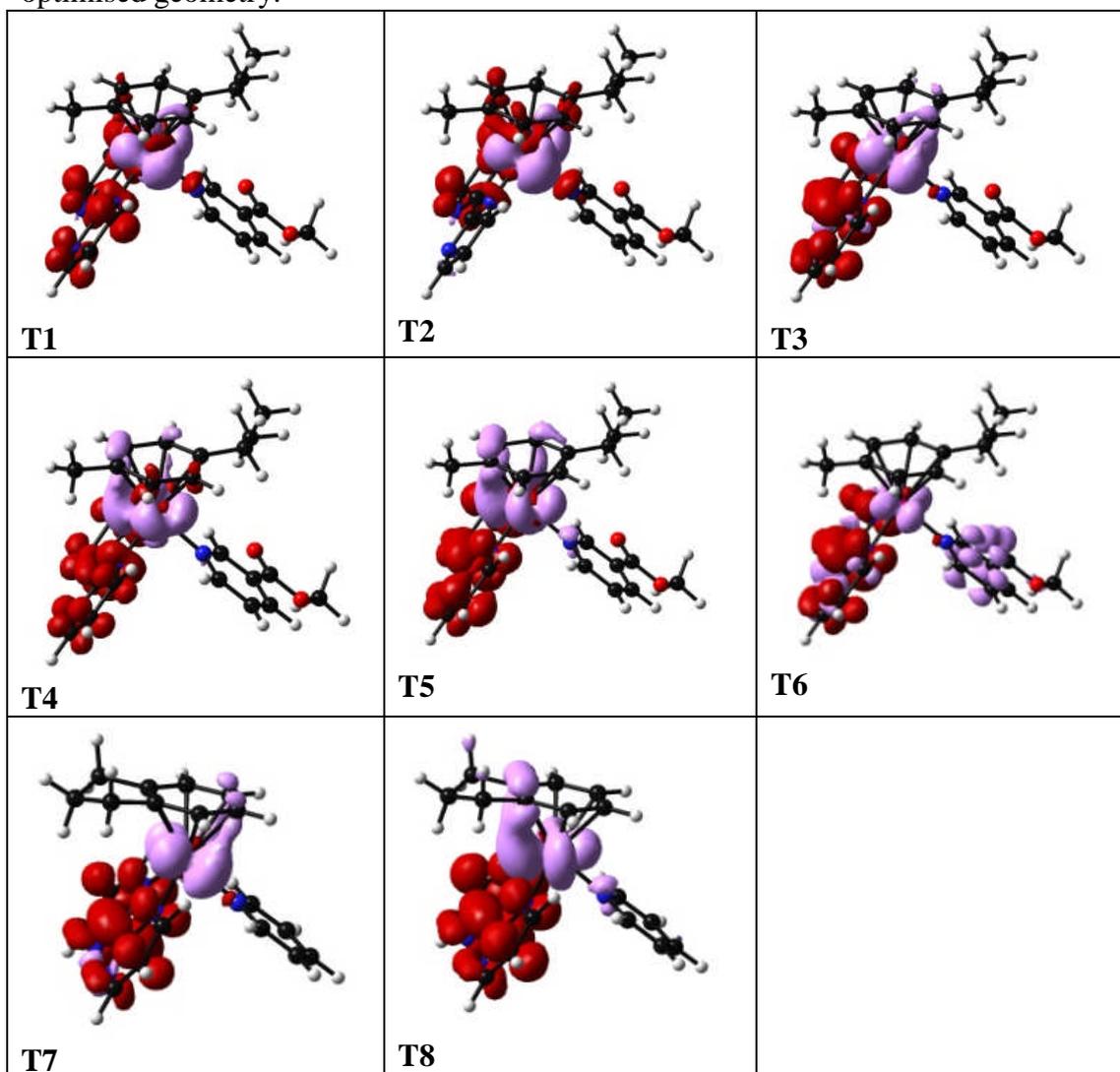
Table A.4.33. Selected TD-DFT triplet transitions for complex **1** in the lowest-lying triplet state optimised geometry.

	Energy (eV)	Wavelength (nm)	Oscillator Strength	Major contributions
1	0.6484	1912	0.0	H-1→LUMO (67%) HOMO→LUMO (32%)
2	0.8057	1538	0.0	H-1→LUMO (35%) HOMO→LUMO (64%)
3	1.0691	1159	0.0	H-2→LUMO (98%)
4	1.8923	655	0.0	HOMO→L+2 (97%)
5	2.1397	579	0.0	H-1→L+2 (99%)
6	2.4765	500	0.0	H-2→L+2 (96%)
7	2.9304	423	0.0	H-5→L+1 (16%) HOMO→L+1 (83%)
8	3.2859	377	0.0	H-1→L+1 (86%)

The energy values of the triplet transitions in the Table are calculated relatively to the energy of the lowest-lying geometry computed with multiplicity equal to 1 (singlet). To calculate the relative energy of these triplet states with respect to the ground state, 0.97 eV must be added.

Figure A.4.33. Selected Electron Difference Density Maps (EDDMS) of triplet excited state transitions of **1** in H_2O (pink indicates a decrease in electron density, while red indicates an increase). Calculations were performed using the lowest-lying triplet state optimised geometry.
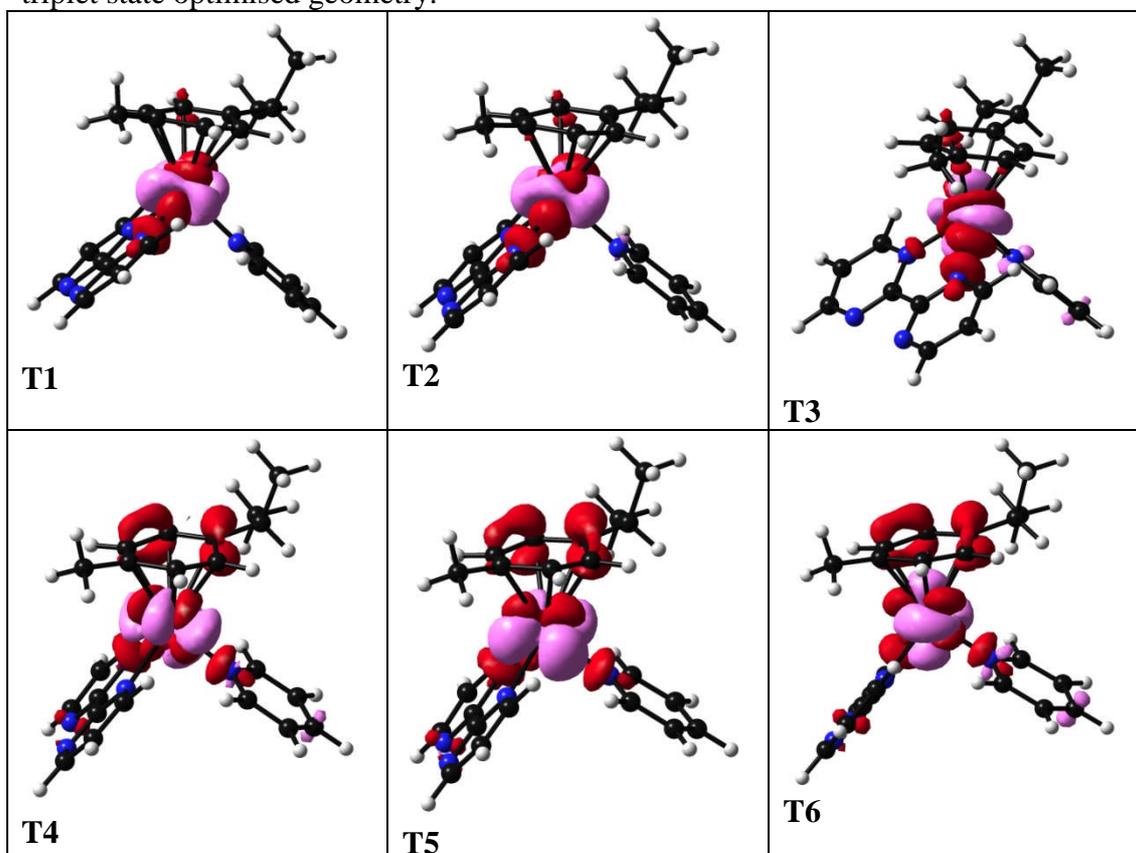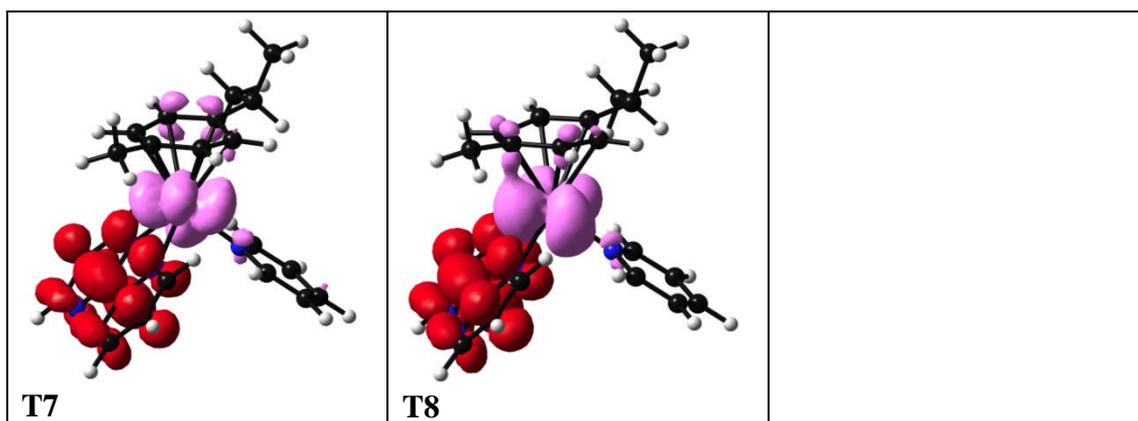
Table A.4.34. Selected TD-DFT triplet transitions for complex **2** in the lowest-lying triplet state optimised geometry

	Energy (eV)	Wavelength (nm)	Oscillator Strength	Major contributions
1	0.2814	4406	0.0	HOMO→LUMO (100%)
2	0.8864	1399	0.0	H-1→LUMO (100%)
3	1.055	1175	0.0	H-2→LUMO (100%)
4	1.664	745	0.0	HOMO→L+2 (39%) HOMO→L+3 (61%)
5	2.288	542	0.0	H-1→L+2 (39%) H-1→L+3 (61%)
6	2.421	512	0.0	H-2→L+2 (38%) H-2→L+3 (62%)
7	2.592	478	0.0	HOMO→L+1 (95%)
8	3.147	394	0.0	H-5→L+1 (24%) H-2→L+1 (13%) H-1→L+1 (53%)

The energy values of the triplet transitions in the Table are calculated relatively to the energy of the lowest-lying geometry computed with multiplicity equal to 1 (singlet). To calculate the relative energy of these triplet states with respect to the ground state, 1.09 eV must be added.

Figure A.4.34. Selected Electron Difference Density Maps (EDDMS) of triplet excited state transitions of **2** in H_2O (pink indicates a decrease in electron density, while red indicates an increase). Calculations were performed using the lowest-lying triplet state optimised geometry.
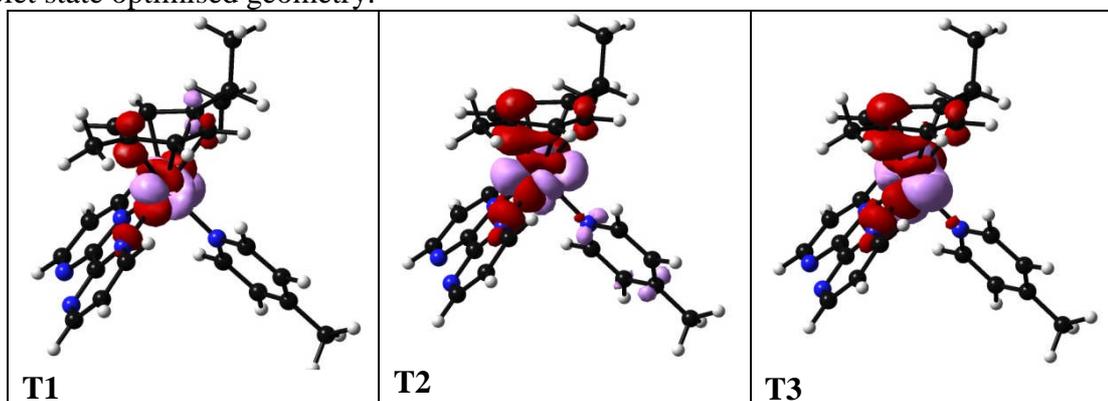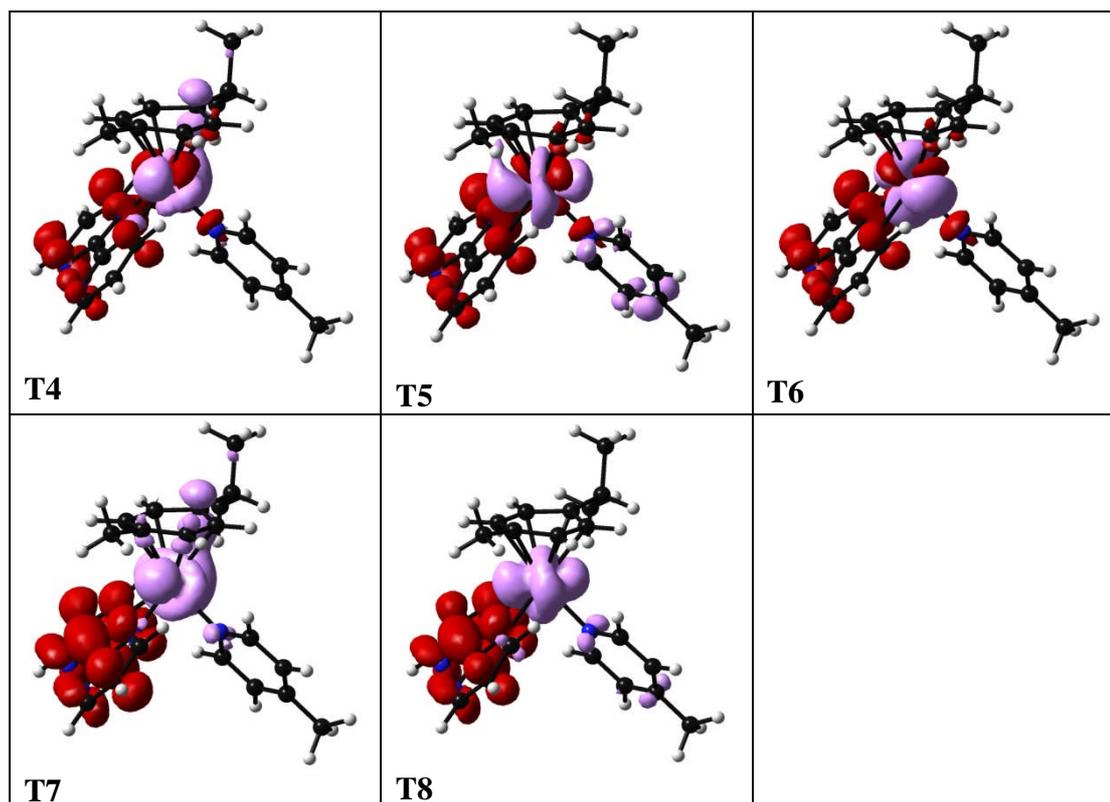
Table A.4.35. Selected TD-DFT triplet transitions for complex **3** in the lowest-lying triplet state optimised geometry.

	Energy (eV)	Wavelength (nm)	Oscillator Strength	Major contributions
1	-0.301	-4119	0.0	HOMO→LUMO (100%)
2	0.901	1376	0.0	H-3→LUMO (15%) H-1→LUMO (85%)
3	1.087	1140	0.0	H-2→LUMO (100%)
4	1.594	778	0.0	HOMO→L+2 (9%) HOMO→L+3 (91%)
5	2.358	526	0.0	H-2→L+3 (28%) H-1→L+3 (68%)
6	2.397	517	0.0	H-3→L+3 (10%) H-2→L+3 (72%) H-1→L+3 (18%)
7	2.451	506	0.0	HOMO→L+1 (97%)
8	3.114	398	0.0	H-3→LUMO (71%) H-1→LUMO (15%)

The energy values of the triplet transitions in the Table are calculated relatively to the energy of the lowest-lying geometry computed with multiplicity equal to 1 (singlet). To calculate the relative energy of these triplet states with respect to the ground state, 1.12 eV must be added.

Figure A.4.35. Selected Electron Difference Density Maps (EDDMS) of triplet excited state transitions of **3** in H_2O (pink indicates a decrease in electron density, while red indicates an increase). Calculations were performed using the lowest-lying triplet state optimised geometry.
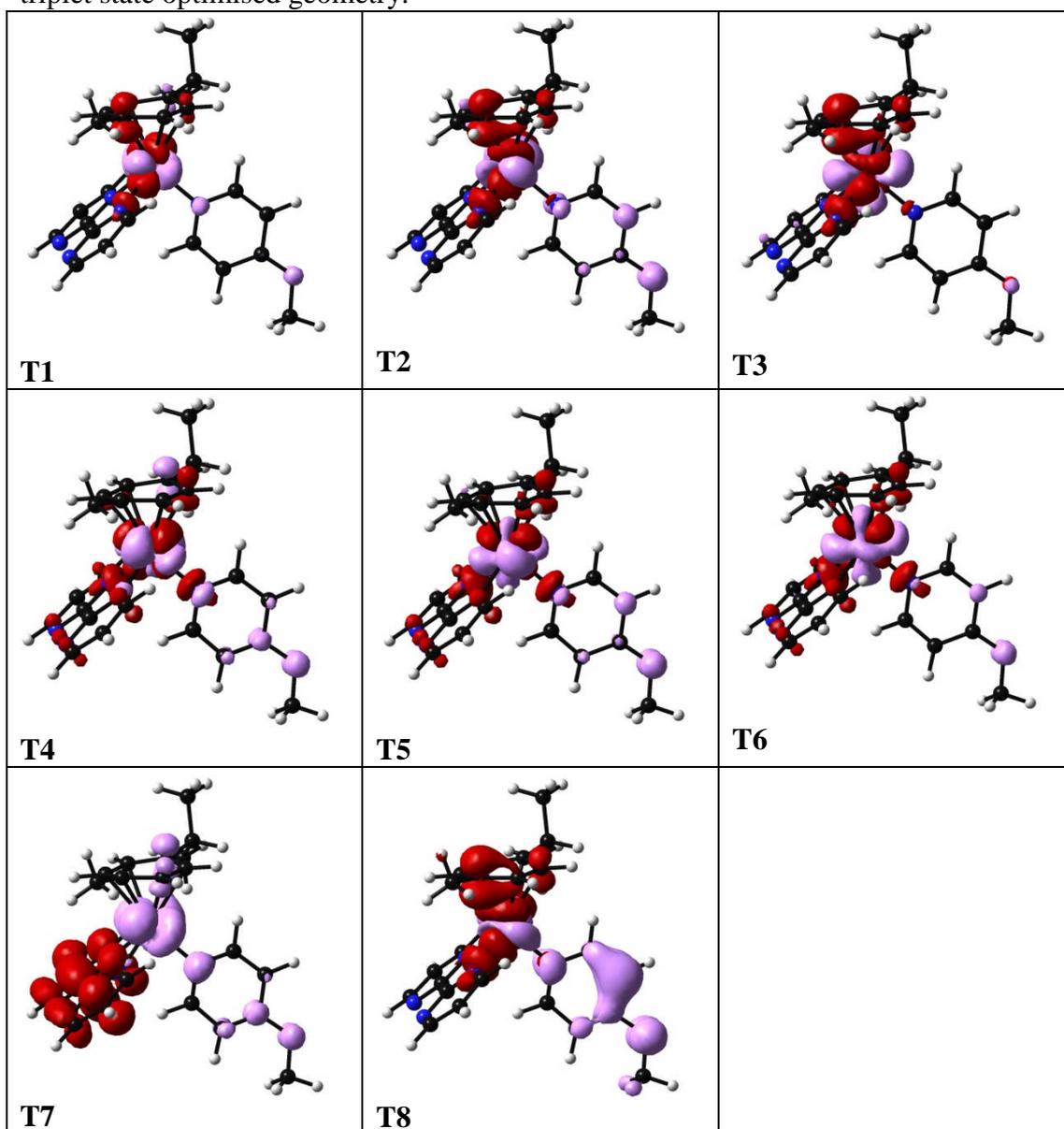
Table A.4.36. Selected TD-DFT triplet transitions for complex **4** in the lowest-lying triplet state optimised geometry.

	Energy (eV)	Wavelength (nm)	Oscillator Strength	Major contributions
1	0.861	1440	0.0	HOMO→LUMO (70%)
2	1.334	929	0.0	H-4→LUMO (85%) HOMO→L+2 (13%) HOMO→L+4 (10%)
3	2.003	619	0.0	H-2→LUMO (56%)
4	2.486	499	0.0	H-4→LUMO (11%) HOMO→L+1 (14%) HOMO→L+2 (33%) HOMO→L+4 (13%)
5	2.592	478	0.0	HOMO→L+1 (81%)
6	2.792	444	0.0	H-4→L+2 (44%) H-4→L+4 (28%)
7	3.033	409	0.0	HOMO→L+2 (18%) HOMO→L+4 (47%)
8	3.161	392	0.0	H-1→LUMO (98%)

The energy values of the triplet transitions in the Table are calculated relatively to the energy of the lowest-lying geometry computed with multiplicity equal to 1 (singlet). To calculate the relative energy of these triplet states with respect to the ground state, 1.13 eV must be added.

Figure A.4.36. Selected Electron Difference Density Maps (EDDMS) of triplet excited state transitions of **4** in H_2O (pink indicates a decrease in electron density, while red indicates an increase). Calculations were performed using the lowest-lying triplet state optimised geometry.
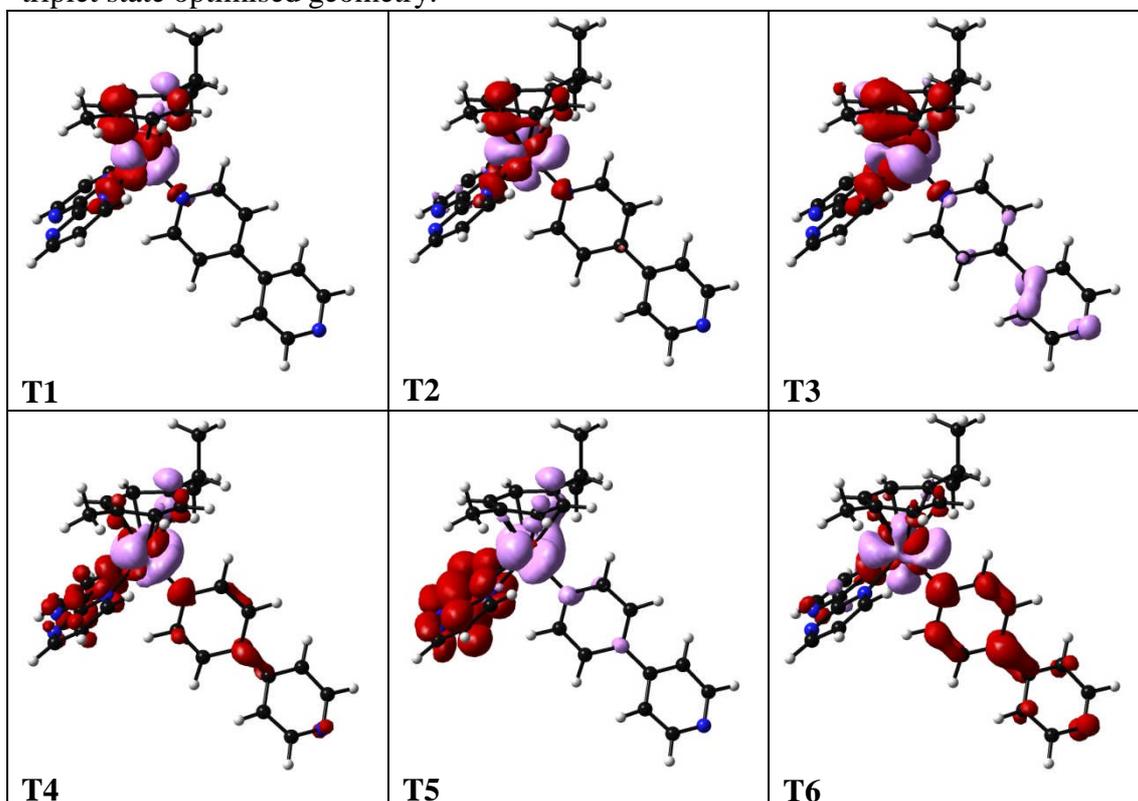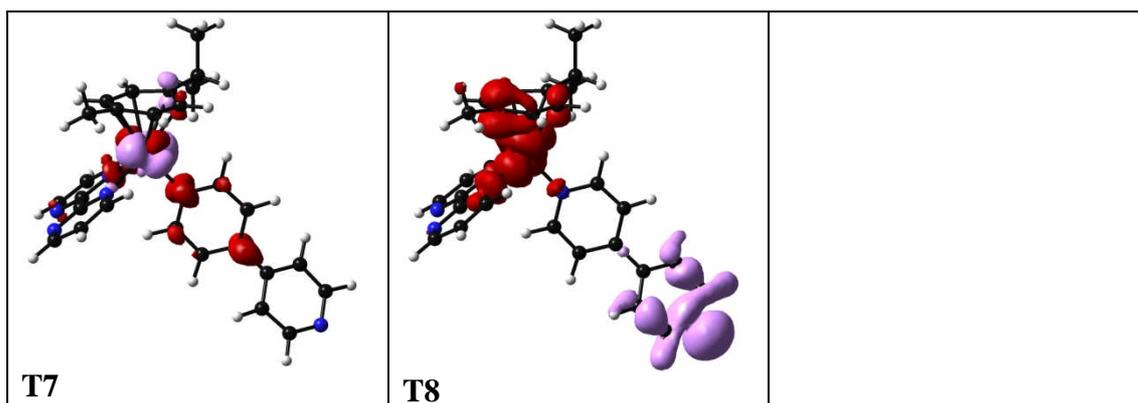
Table A.4.37. Selected TD-DFT triplet transitions for complex **5** in the lowest-lying triplet state optimised geometry.

	Energy (eV)	Wavelength (nm)	Oscillator Strength	Major contributions
1	0.945	1311	0.0	HOMO→LUMO (71%)
2	1.391	892	0.0	H-4→LUMO (69%) H-3→LUMO (15%) HOMO→L+3 (18%)
3	2.077	597	0.0	H-3→LUMO (49%) H-1→LUMO (13%)
4	2.485	499	0.0	H-1→LUMO (12%) HOMO→L+1 (51%) HOMO→L+3 (11%)
5	2.550	486	0.0	H-1→LUMO (20%) HOMO→L+1 (42%) HOMO→L+3 (15%)
6	2.717	456	0.0	H-4→LUMO (14%) H-1→LUMO (33%) HOMO→L+3 (13%)
7	2.915	425	0.0	H-1→L+4 (10%) H-1→L+5 (14%) HOMO→L+4 (34%) HOMO→L+5 (39%)
8	2.948	421	0.0	H-4→L+2 (10%) H-4→L+3 (42%) H-3→L+3 (10%)

The energy values of the triplet transitions in the Table are calculated relatively to the energy of the lowest-lying geometry computed with multiplicity equal to 1 (singlet). To calculate the relative energy of these triplet states with respect to the ground state, 1.14 eV must be added.

Figure A.4.37. Selected Electron Difference Density Maps (EDDMS) of triplet excited state transitions of **5** in H_2O (pink indicates a decrease in electron density, while red indicates an increase). Calculations were performed using the lowest-lying triplet state optimised geometry.
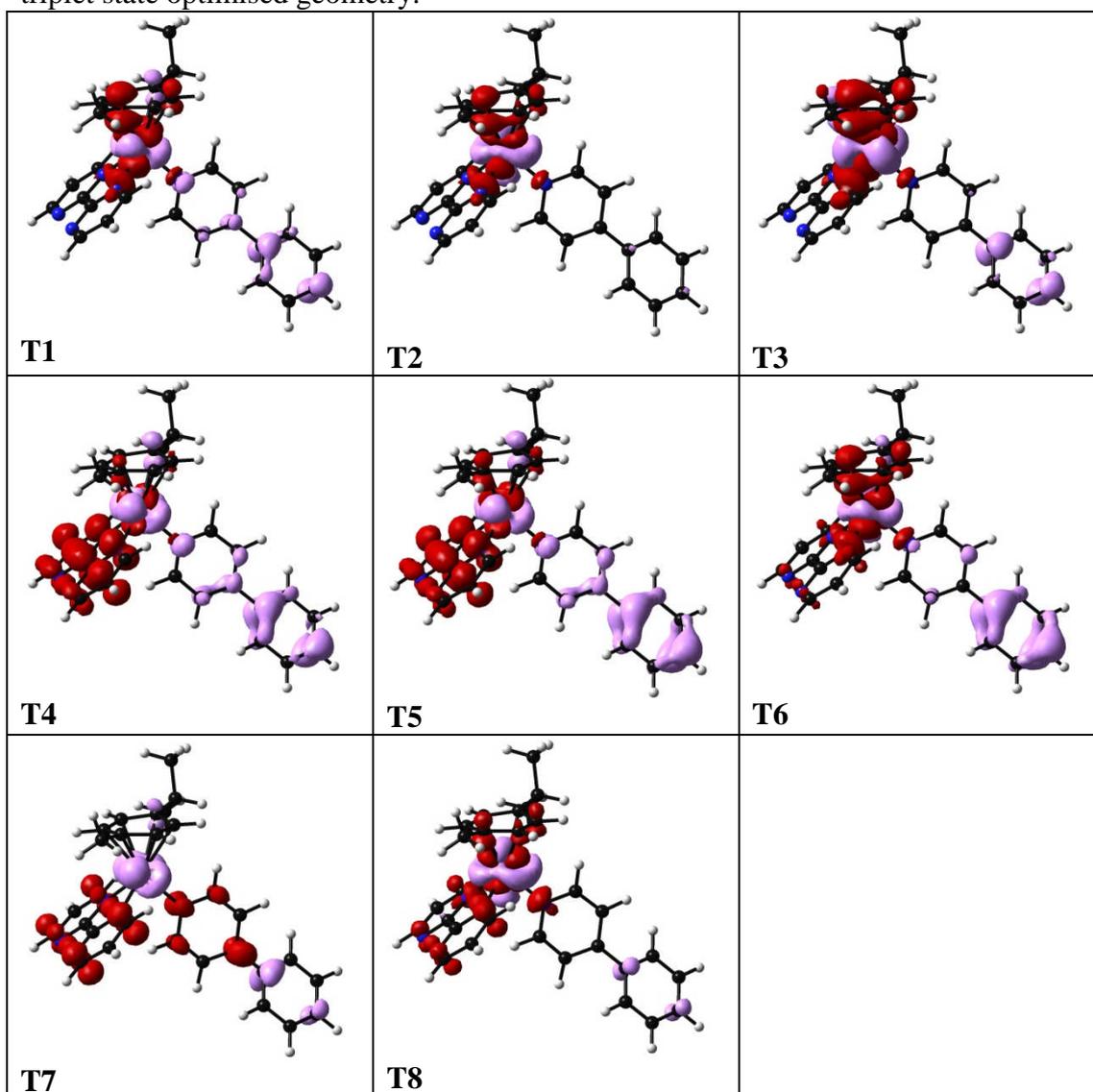

Table A.4.38. Selected TD-DFT triplet transitions for complex **6** in the lowest-lying triplet state optimised geometry.

	Energy (eV)	Wavelength (nm)	Oscillator Strength	Major contributions
1	1.036	1197	0.0	HOMO→LUMO (63%)
2	1.574	788	0.0	H-3→LUMO (76%)
3	2.049	605	0.0	H-4→LUMO (63%)
4	2.553	486	0.0	HOMO→L+1 (48%) HOMO→L+2 (13%) HOMO→L+3 (22%)
5	2.638	470	0.0	H-1→LUMO (97%)
6	2.680	463	0.0	HOMO→L+1 (46%) HOMO→L+3 (29%)
7	2.786	445	0.0	H-2→LUMO (99%)

8	3.198	388	0.0	H-7→L+1 (37%)
				H-4→L+1 (13%)
				H-3→L+1 (38%)

The energy values of the triplet transitions in the Table are calculated relatively to the energy of the lowest-lying geometry computed with multiplicity equal to 1 (singlet). To calculate the relative energy of these triplet states with respect to the ground state, 1.15 eV must be added.

Figure A.4.38. Selected Electron Difference Density Maps (EDDMS) of triplet excited state transitions of **6** in H_2O (pink indicates a decrease in electron density, while red indicates an increase). Calculations were performed using the lowest-lying triplet state optimised geometry.
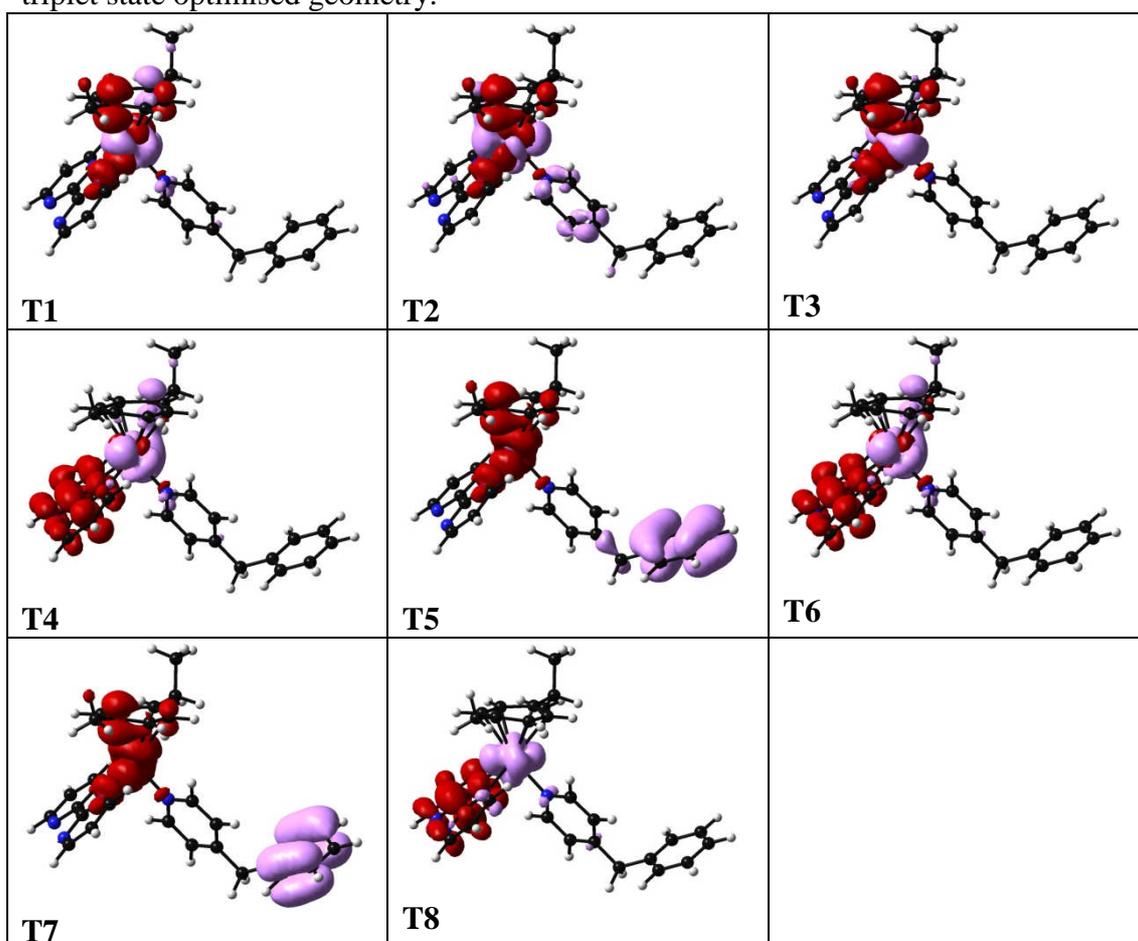

Table A.4.39. Selected TD-DFT triplet transitions for complex **8** in the lowest-lying triplet state optimised geometry.

	Energy (eV)	Wavelength (nm)	Oscillator Strength	Major contributions
1	0.3423	3622	0.0	HOMO→LUMO (97%)
2	1.3997	886	0.0	H-2→LUMO (77%)
				H-1→LUMO (22%)
3	2.1007	590	0.0	H-2→LUMO (15%)
				H-1→LUMO (51%)

4	2.489	498	0.0	HOMO→L+1 (44%)
				HOMO→L+3 (22%)
				HOMO→L+4 (16%)
5	2.664	465	0.0	HOMO→L+1 (53%)
				HOMO→L+3 (17%)
				HOMO→L+4 (16%)
6	3.193	388	0.0	H-5→L+1 (33%)
				H-2→L+1 (14%)
				H-1→L+1 (38%)
7	3.2822	378	0.0	H-8→LUMO (11%)
				H-7→LUMO (24%)
				H-4→LUMO (18%)
				HOMO→L+2 (14%)
				HOMO→L+6 (12%)
8	3.3501	370	0.0	H-1→L+1 (41%)
				HOMO→L+2 (33%)

The energy values of the triplet transitions in the Table are calculated relatively to the energy of the lowest-lying geometry computed with multiplicity equal to 1 (singlet). To calculate the relative energy of these triplet states with respect to the ground state, 1.00 eV must be added.

Figure A.4.39. Selected Electron Difference Density Maps (EDDMS) of triplet excited state transitions of **8** in H_2O (pink indicates a decrease in electron density, while red indicates an increase). Calculations were performed using the lowest-lying triplet state optimised geometry.

| T7 | T8 | |
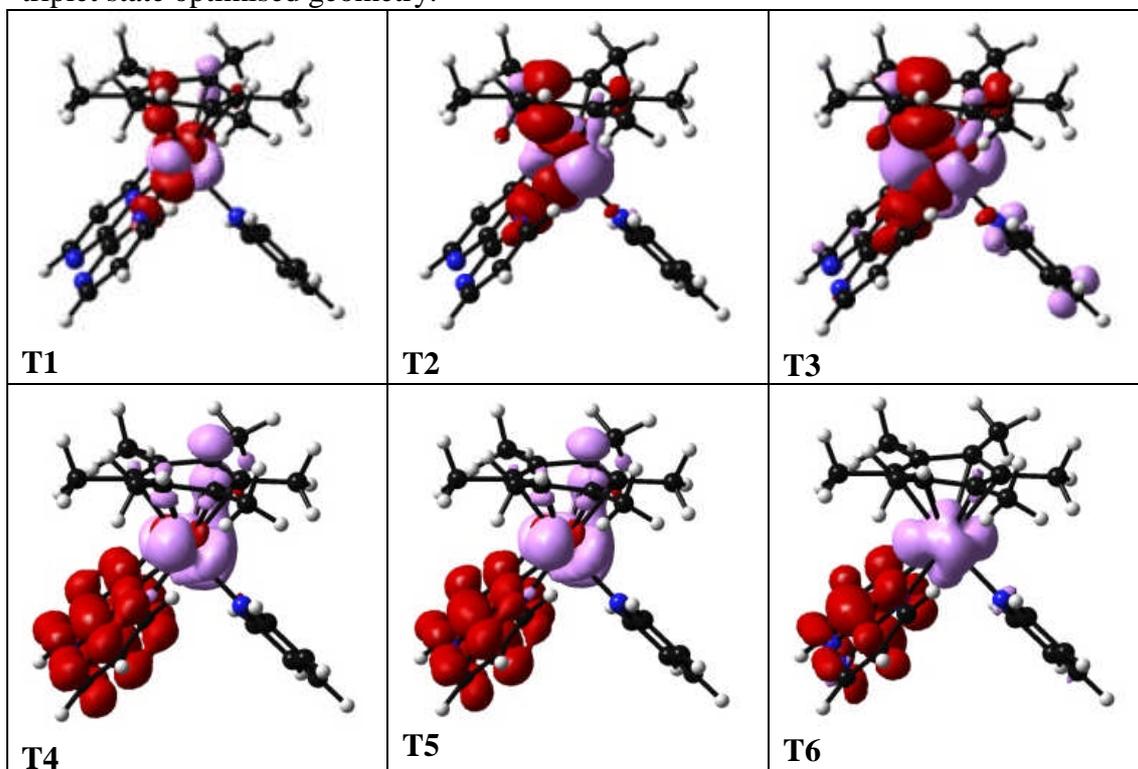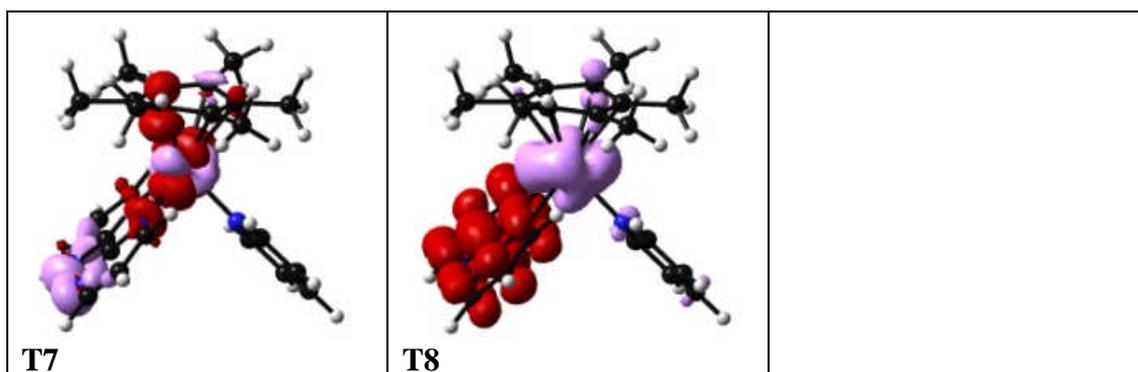
Table A.4.40. Selected TD-DFT triplet transitions for complex **9** in the lowest-lying triplet state optimised geometry.

	Energy (eV)	Wavelength (nm)	Oscillator Strength	Major contributions
1	-0.3525	-3517	0.0	HOMO→LUMO (97%)
2	0.7912	1567	0.0	H-2→LUMO (18%) H-1→LUMO (77%)
3	0.9384	1321	0.0	H-2→LUMO (80%) H-1→LUMO (17%)
4	1.4875	833	0.0	HOMO→L+2 (75%) HOMO→L+3 (13%)
5	2.0916	592	0.0	H-1→L+2 (82%) H-1→L+3 (14%)
6	2.2193	558	0.0	H-2→L+2 (84%) H-2→L+3 (14%)
7	2.5782	480	0.0	HOMO→L+1 (91%)
8	3.0924	400	0.0	H-5→L+1 (15%) H-2→L+1 (11%) H-1→L+1 (64%)

The energy values of the triplet transitions in the Table are calculated relatively to the energy of the lowest-lying geometry computed with multiplicity equal to 1 (singlet). To calculate the relative energy of these triplet states with respect to the ground state, 1.21 eV must be added.

Figure A.4.40. Selected Electron Difference Density Maps (EDDMS) of triplet excited state transitions of **9** in H_2O (pink indicates a decrease in electron density, while red indicates an increase). Calculations were performed using the lowest-lying triplet state optimised geometry.


| T1 | T2 | T3 |
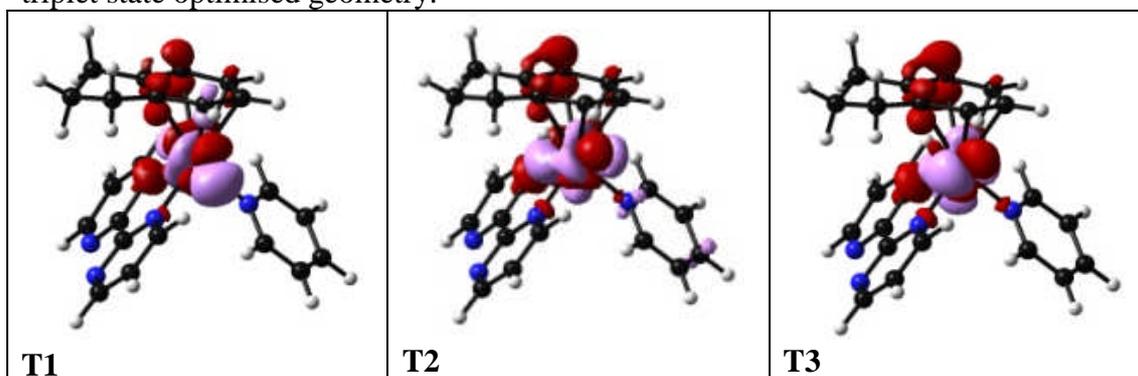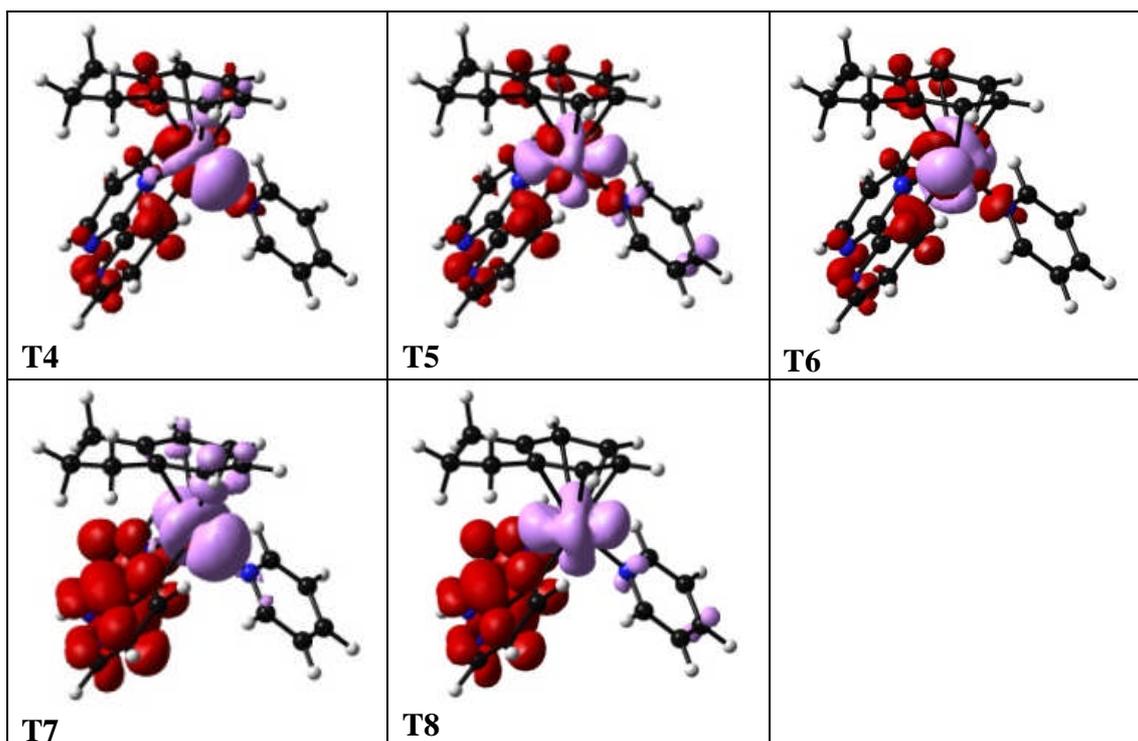
Table A.4.41. Selected TD-DFT triplet transitions for complex **10** in the lowest-lying triplet state optimised geometry.

	Energy (eV)	Wavelength (nm)	Oscillator Strength	Major contributions
1	0.1799	6890	0.0	HOMO→LUMO (98%)
2	0.874	1419	0.0	H-4→LUMO (6%) H-1→LUMO (93%)
3	1.1812	1050	0.0	H-3→LUMO (92%) H-2→LUMO (7%)
4	1.9618	632	0.0	HOMO→L+3 (99%)
5	2.4429	507	0.0	H-1→L+3 (98%)
6	2.5616	484	0.0	H-3→L+3 (99%)
7	2.7037	459	0.0	H-2→LUMO (33%) HOMO→L+1 (57%)
8	2.7351	453	0.0	H-2→L+2 (38%) H-1→L+1 (12%) HOMO→L+2 (34%)

The energy values of the triplet transitions in the Table are calculated relatively to the energy of the lowest-lying geometry computed with multiplicity equal to 1 (singlet). To calculate the relative energy of these triplet states with respect to the ground state, 1.00 eV must be added.

Figure A.4.41. Selected Electron Difference Density Maps (EDDMS) of triplet excited state transitions of **10** in H$_2$O (pink indicates a decrease in electron density, while red indicates an increase). Calculations were performed using the lowest-lying triplet state optimised geometry.
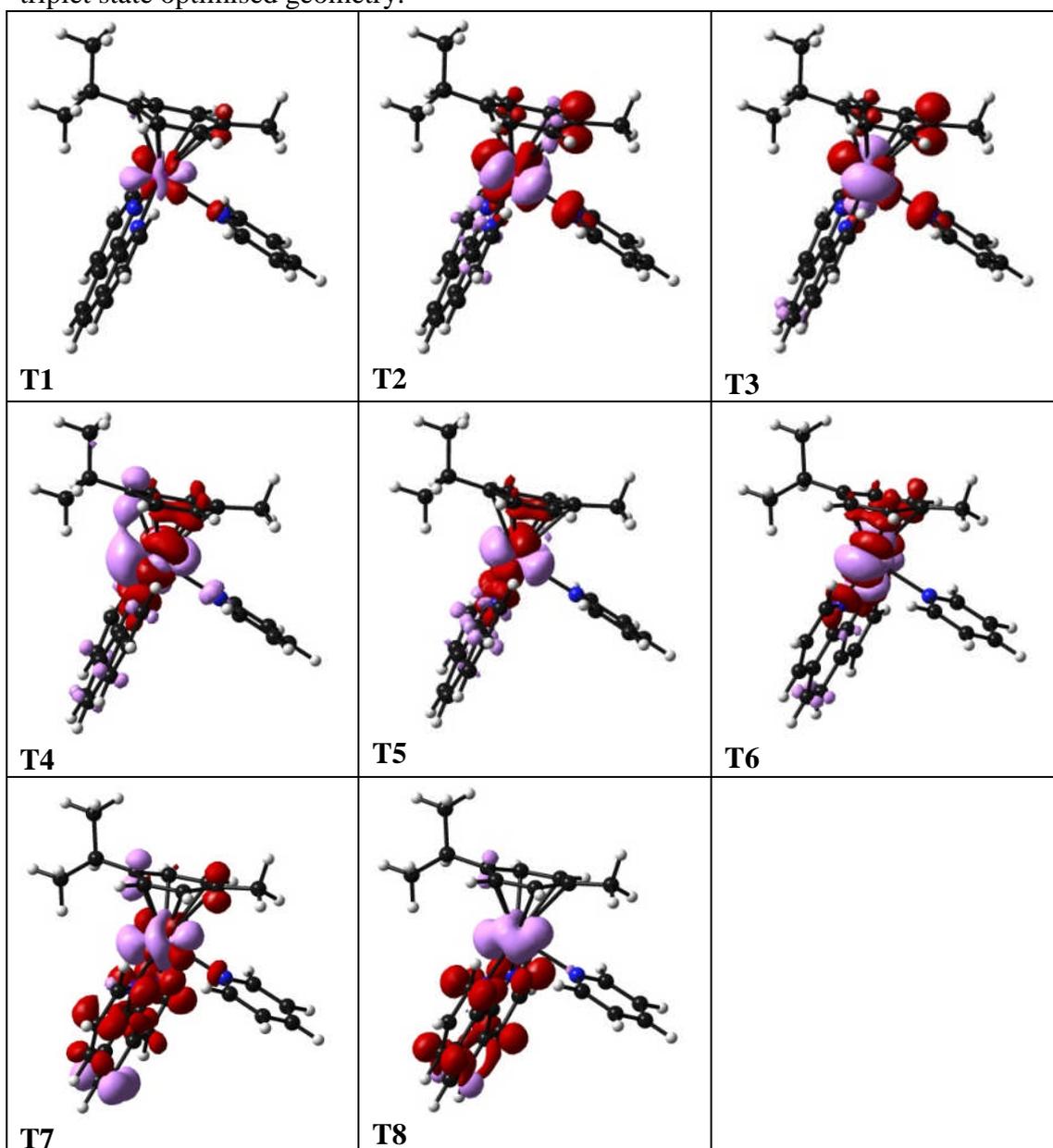

Table A.4.42. Selected TD-DFT triplet transitions for complex **11** in the lowest-lying triplet state optimised geometry.

	Energy (eV)	Wavelength (nm)	Oscillator Strength	Major contributions
1	1.689	733	0.0	H-3→LUMO (58%) H-2→LUMO (34%)
2	2.126	583	0.0	H-4→LUMO (64%) HOMO→LUMO (22%)
3	2.252	551	0.0	HOMO→LUMO (12%) HOMO→L+2 (11%) HOMO→L+3 (56%)

4	2.3187	535	0.0	H-1→LUMO (42%)
				HOMO→LUMO (34%)
5	2.357	526	0.0	H-4→LUMO (11%)
				H-1→LUMO (34%)
				HOMO→LUMO (18%)
				HOMO→L+4 (16%)
6	2.3949	518	0.0	H-1→L+4 (12%)
				HOMO→LUMO (10%)
				HOMO→L+4 (42%)
7	2.4764	500	0.0	H-1→L+2 (17%)
				H-1→L+3 (47%)
8	2.5051	495	0.0	H-1→L+3 (23%)
				H-1→L+4 (42%)

The energy values of the triplet transitions in the Table are calculated relatively to the energy of the lowest-lying geometry computed with multiplicity equal to 1 (singlet). To calculate the relative energy of these triplet states with respect to the ground state, 1.41 eV must be added.

Figure A.4.42. Selected Electron Difference Density Maps (EDDMS) of triplet excited state transitions of **11** in H_2O (pink indicates a decrease in electron density, while red indicates an increase). Calculations were performed using the lowest-lying triplet state optimised geometry.

T7 | **T8**
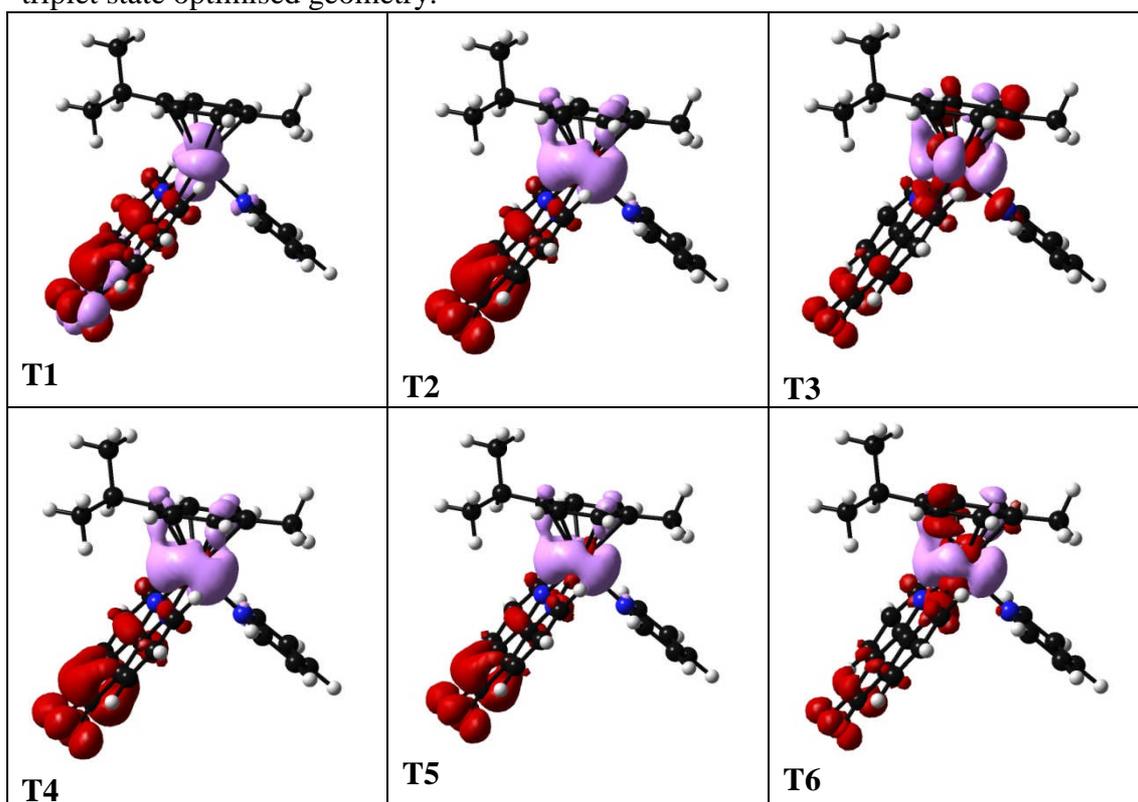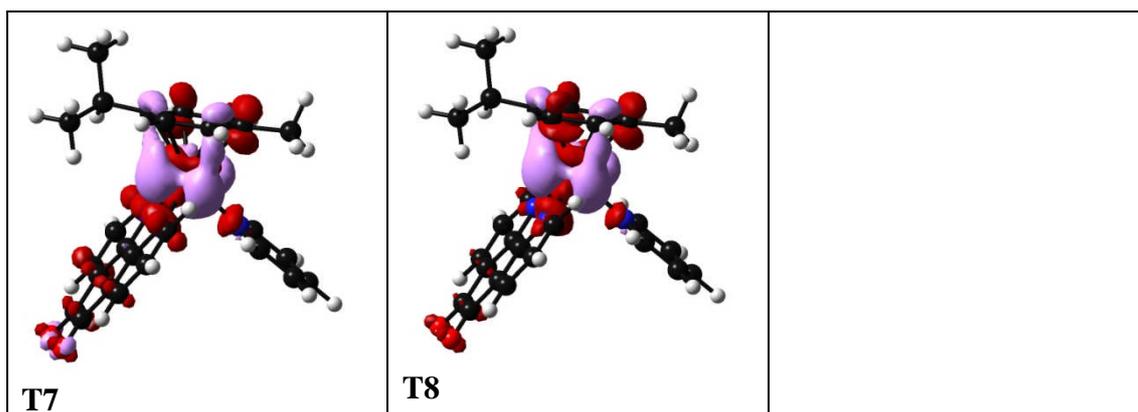
Table A.4.43. Selected TD-DFT triplet transitions for complex **12** in the lowest-lying triplet state optimised geometry.

	Energy (eV)	Wavelength (nm)	Oscillator Strength	Major contributions
1	0.859	1444	0.0	H-5→LUMO (66%) H-1→LUMO (24%)
2	1.363	909	0.0	HOMO→LUMO (59%)
3	2.377	522	0.0	H-6→LUMO (41%) H-2→LUMO (22%)
4	2.412	514	0.0	H-6→L+3 (63%) H-2→L+3 (17%) HOMO→L+3 (27%)
5	2.490	498	0.0	H-2→L+2 (13%) H-1→L+1 (20%) HOMO→L+2 (63%)
6	2.509	494	0.0	H-6→LUMO (26%) H-2→LUMO (25%) HOMO→L+1 (29%)
7	2.699	459	0.0	H-2→LUMO (32%) HOMO→L+1 (58%)
8	2.874	431	0.0	H-5→LUMO (34%) H-1→LUMO (41%) HOMO→L+2 (10%)

The energy values of the triplet transitions in the Table are calculated relatively to the energy of the lowest-lying geometry computed with multiplicity equal to 1 (singlet). To calculate the relative energy of these triplet states with respect to the ground state, 1.01 eV must be added.

Figure A.4.43. Selected Electron Difference Density Maps (EDDMS) of triplet excited state transitions of **12** in H_2O (pink indicates a decrease in electron density, while red indicates an increase). Calculations were performed using the lowest-lying triplet state optimised geometry.
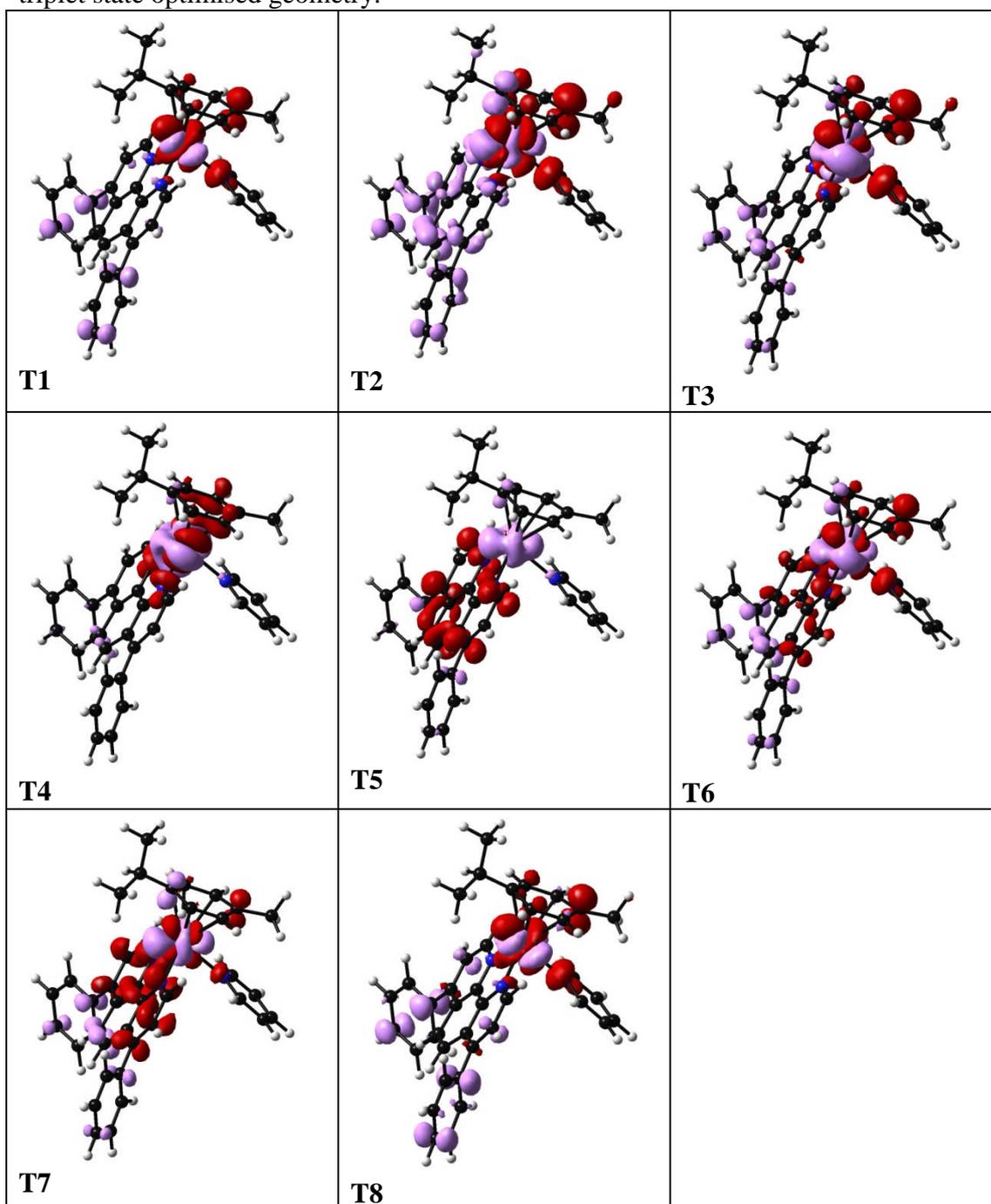
Table A.4.44. Selected TD-DFT triplet transitions for complex **13** in the lowest-lying triplet state optimised geometry.

	Energy (eV)	Wavelength (nm)	Oscillator Strength	Major contributions
1	-0.2468	-5024	0.0	HOMO→LUMO (99%)
2	0.9022	1374	0.0	H-2→LUMO (20%) H-1→LUMO (75%)

3	1.0014	1238	0.0	H-2→LUMO (73%)
				H-1→LUMO (18%)
4	1.5429	804	0.0	HOMO→L+1 (10%)
				HOMO→L+2 (83%)
5	2.1136	587	0.0	H-1→L+1 (11%)
				H-1→L+2 (86%)
6	2.2382	554	0.0	H-2→L+1 (10%)
				H-2→L+2 (81%),
7	2.8118	441	0.0	H-3→L+1 (12%)
				HOMO→L+1 (73%)
8	3.055	406	0.0	H-3→LUMO (80%)
				H-3→L+1 (11%)

The energy values of the triplet transitions in the Table are calculated relatively to the energy of the lowest-lying geometry computed with multiplicity equal to 1 (singlet). To calculate the relative energy of these triplet states with respect to the ground state, 1.12 eV must be added.

Figure A.4.44. Selected Electron Difference Density Maps (EDDMS) of triplet excited state transitions of **13** in H_2O (pink indicates a decrease in electron density, while red indicates an increase). Calculations were performed using the lowest-lying triplet state optimised geometry.
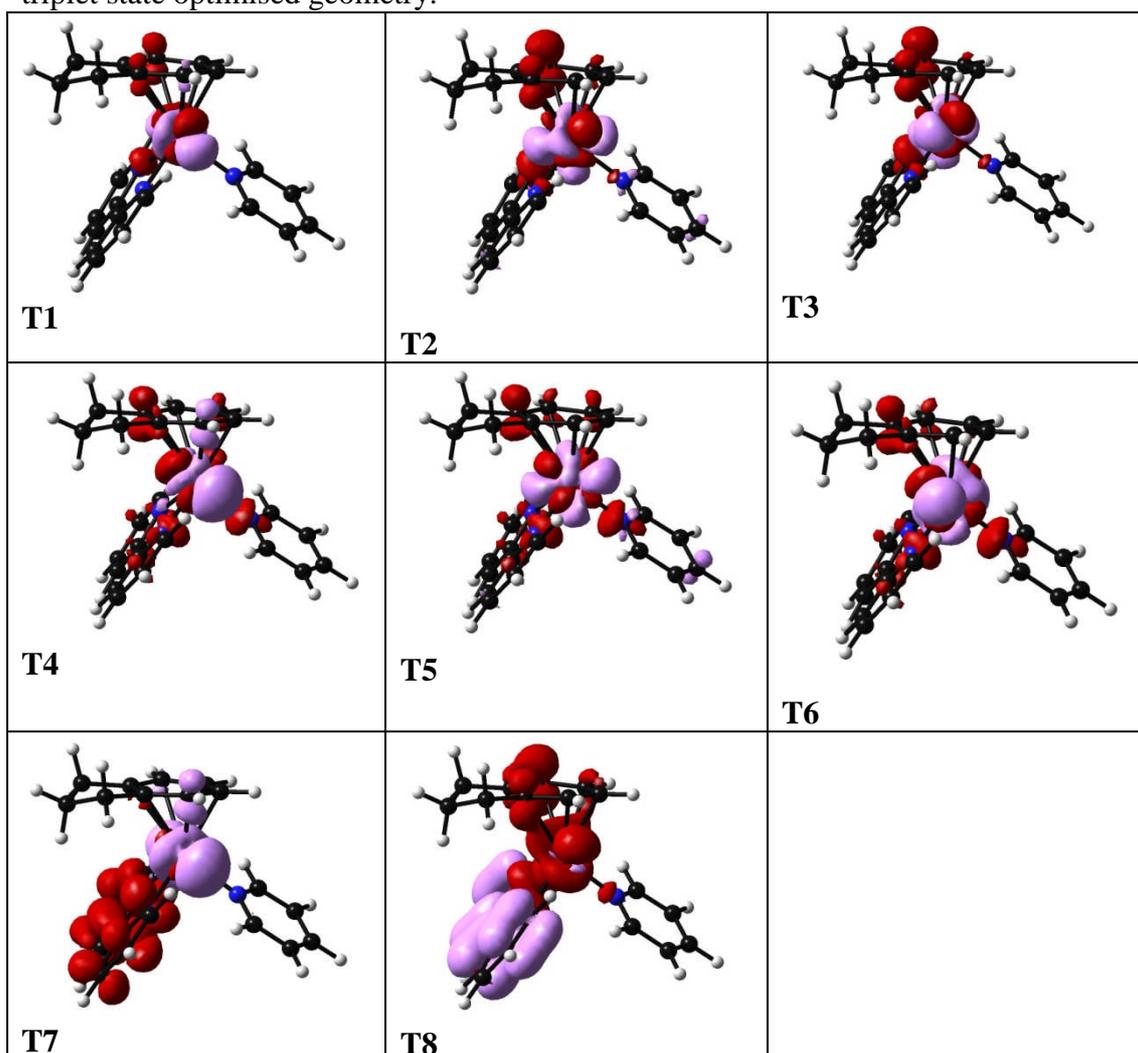
Table A.4.45. Selected TD-DFT triplet transitions for complex **14** in the lowest-lying triplet state optimised geometry.

	Energy (eV)	Wavelength (nm)	Oscillator Strength	Major contributions
1	2.2586	549	0.0	H-1→L+2 (13%) HOMO→L+2 (64%) HOMO→L+4 (15%)
2	2.4021	516	0.0	H-2→L+1 (34%) H-1→L+1 (59%)
3	2.4188	512	0.0	HOMO→L+3 (42%) HOMO→L+4 (23%) HOMO→L+5 (22%)
4	2.4932	498	0.0	H-2→L+2 (45%) H-2→L+4 (11%) H-1→L+2 (25%)
5	2.5525	486	0.0	H-3→L+2 (15%) H-2→L+3 (20%) H-2→L+4 (12%) H-2→L+5 (10%) H-1→L+3 (16%) H-1→L+4 (10%)
6	2.7481	451	0.0	H-3→L+2 (68%) H-3→L+5 (10%)
7	2.8323	438	0.0	H-4→L+1 (84%)
8	2.851	434	0.0	H-3→L+3 (35%) H-3→L+4 (40%) H-3→L+5 (11%)

The energy values of the triplet transitions in the Table are calculated relatively to the energy of the lowest-lying geometry computed with multiplicity equal to 1 (singlet). To calculate the relative energy of these triplet states with respect to the ground state, 0.52 eV must be added.

Figure A.4.45. Selected Electron Difference Density Maps (EDDMS) of triplet excited state transitions of **14** in H_2O (pink indicates a decrease in electron density, while red indicates an increase). Calculations were performed using the lowest-lying triplet state optimised geometry.
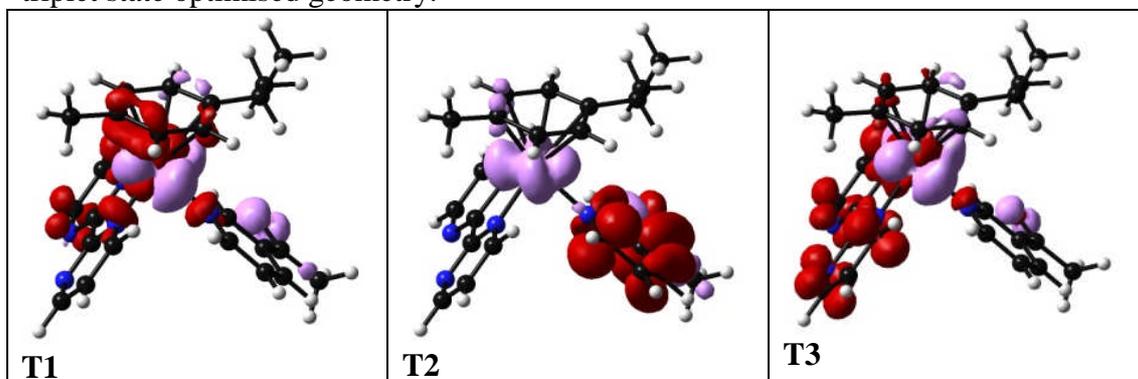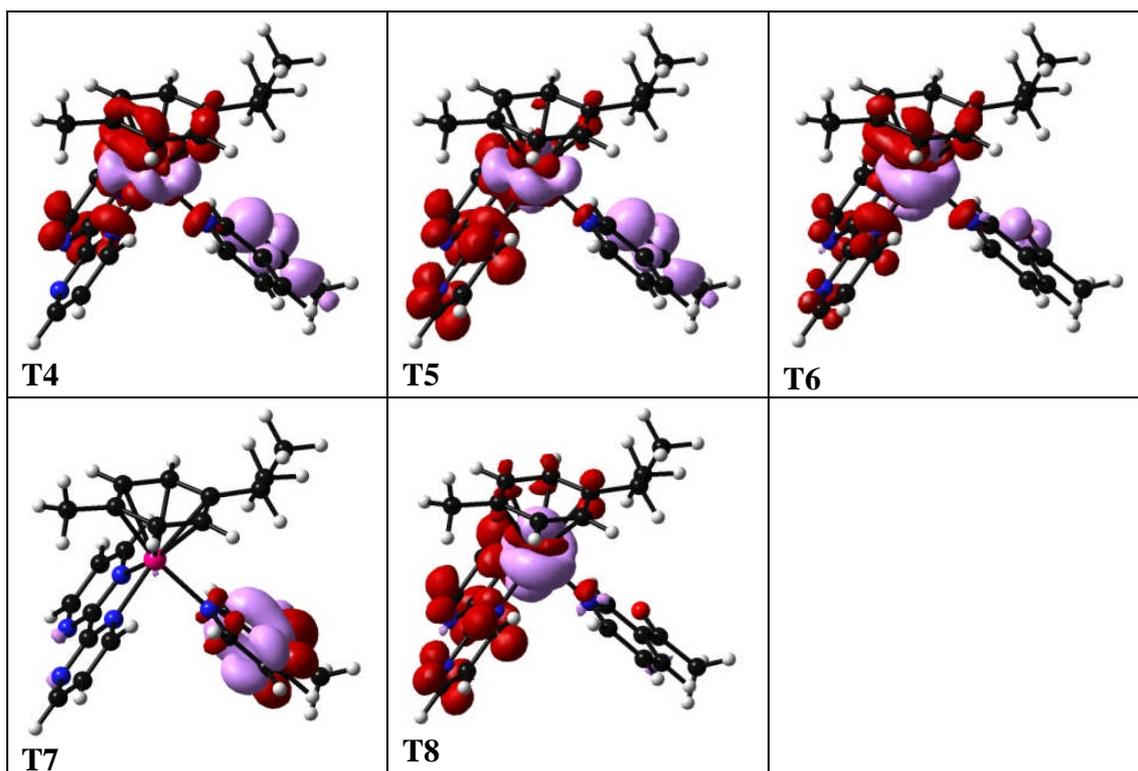
Table A.4.46. Selected TD-DFT triplet transitions for complex **15** in the lowest-lying triplet state optimised geometry.

	Energy (eV)	Wavelength (nm)	Oscillator Strength	Major contributions
1	1.4987	827	0.0	HOMO→L+1 (96%)
2	2.2646	547	0.0	H-1→L+2 (78%) H-1→L+4 (18%)
3	2.4261	511	0.0	H-1→L+3 (43%) H-1→L+4 (22%) H-1→L+5 (23%)
4	2.4351	509	0.0	HOMO→LUMO (92%)
5	2.4998	496	0.0	H-2→L+2 (73%) H-2→L+4 (20%)
6	2.5575	485	0.0	H-3→L+2 (14%) H-2→L+3 (36%) H-2→L+4 (19%) H-2→L+5 (18%)
7	2.755	450	0.0	H-3→L+2 (68%) H-3→L+5 (10%)
8	2.8224	439	0.0	H-4→L+1 (92%)

The energy values of the triplet transitions in the Table are calculated relatively to the energy of the lowest-lying geometry computed with multiplicity equal to 1 (singlet). To calculate the relative energy of these triplet states with respect to the ground state, 1.74 eV must be added.

Figure A.4.46. Selected Electron Difference Density Maps (EDDMS) of triplet excited state transitions of **15** in H_2O (pink indicates a decrease in electron density, while red indicates an increase). Calculations were performed using the lowest-lying triplet state optimised geometry.
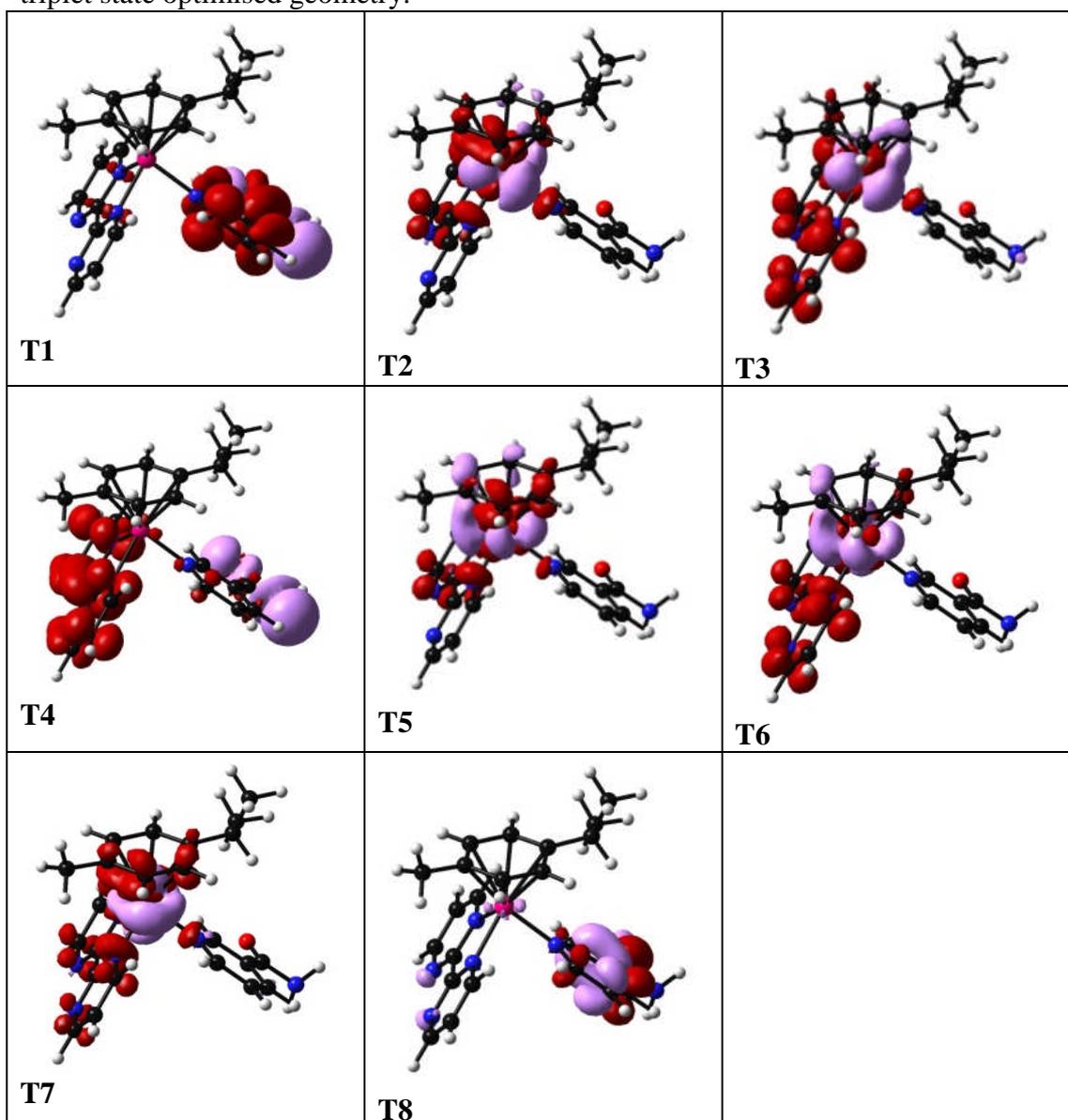

Table A.4.47. Selected TD-DFT triplet transitions for complex **16** in the lowest-lying triplet state optimised geometry.

	Energy (eV)	Wavelength (nm)	Oscillator Strength	Major contributions
1	-0.2687	-4615	0.0	HOMO→LUMO (91%)
2	2.0344	609	0.0	H-2→LUMO (48%) H-1→LUMO (20%)
3	2.3014	539	0.0	H-2→LUMO (18%) H-1→LUMO (42%)
4	2.3969	517	0.0	HOMO→L+2 (62%)
5	2.6641	465	0.0	HOMO→L+1 (91%)

6	2.7443	452	0.0	H-2→L+2 (11%)
				H-1→L+2 (57%)
7	3.2159	386	0.0	H-6→L+1 (52%)
				H-2→L+1 (11%)
				H-1→L+1 (27%)
8	3.3275	373	0.0	H-7→LUMO (19%)
				H-3→LUMO (43%)
				H-2→L+2 (10%)

The energy values of the triplet transitions in the Table are calculated relatively to the energy of the lowest-lying geometry computed with multiplicity equal to 1 (singlet). To calculate the relative energy of these triplet states with respect to the ground state, 1.25 eV must be added.

Figure A.4.47. Selected Electron Difference Density Maps (EDDMS) of triplet excited state transitions of **16** in H_2O (pink indicates a decrease in electron density, while red indicates an increase). Calculations were performed using the lowest-lying triplet state optimised geometry.
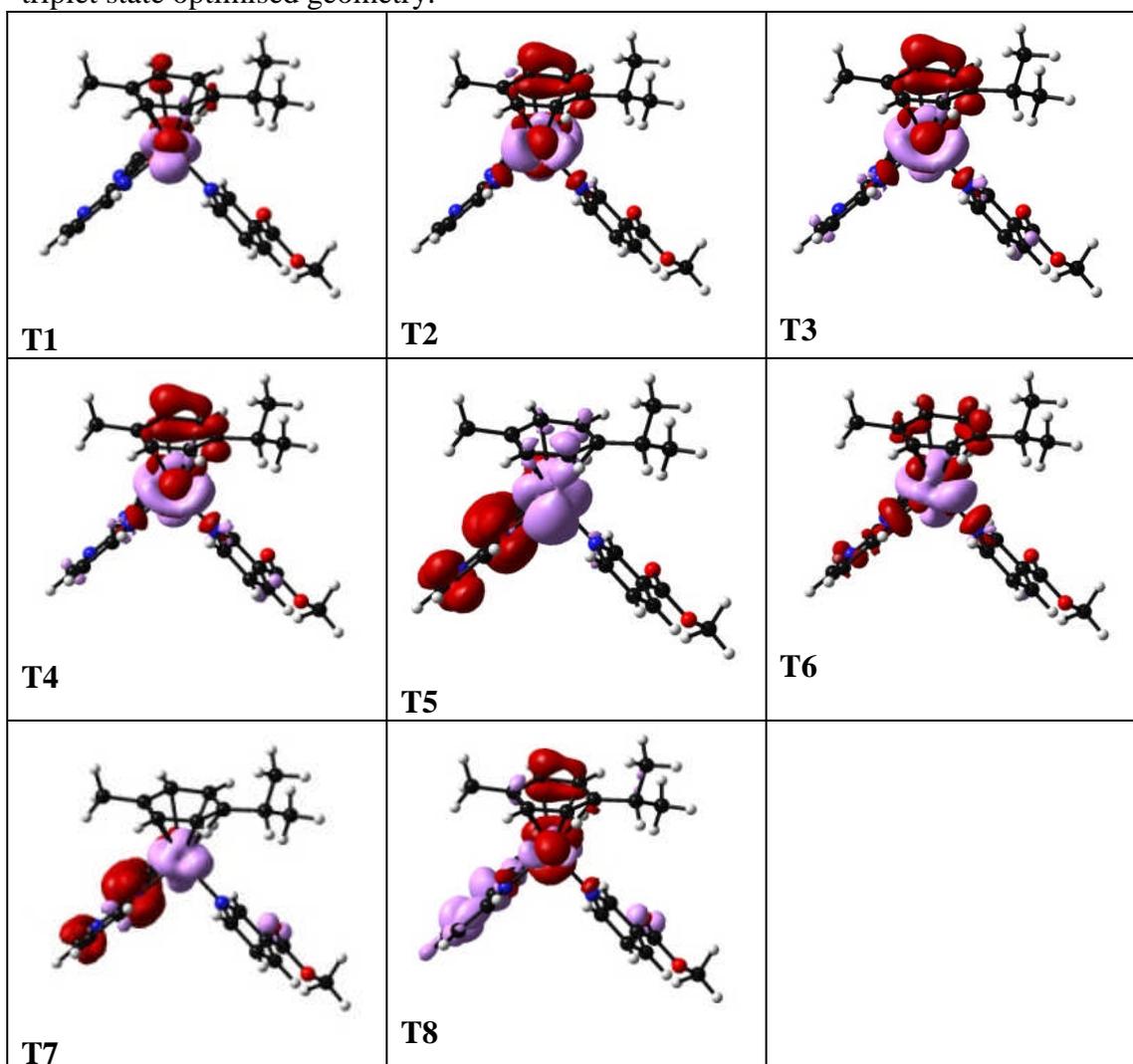
Table A.4.48. Changes in DNA Melting Temperature (Δt_m) by *irradiated* forms of complexes **1**, **4**, and **10** at different r_b values and ionic strengths $[ClO_4]^-$ (M).

Changes in DNA Melting Temperature (Δt_m) for complex **1**

r_b	$[ClO_4]^-$ (M)				
	0.01	0.06	0.11	0.21	0.22
0.000	0.00	0.00	0.00	0.00	0.00
0.021	2.10	-1.10	0.90	–	-1.20
0.042	2.15	-0.60	1.05	-0.10	0.10
0.046	4.90	0.1	1.20	–	0.10
0.050	0.80	0.00	0.80	0.90	–
0.030	1.50	–	–	–	–

Changes in DNA Melting Temperature (Δt_m) for complex **4**

r_b	$[ClO_4]^-$ (M)				
	0.01	0.06	0.11	0.21	0.22
0.000	0.00	0.00	0.00	0.00	0.00
0.021	4.10	2.00	3.20	–	0.70
0.042	0.40	-2.40	0.60	–	0.20
0.046	2.10	–	–	–	–
0.050	2.80	0.00	-0.40	–	-0.20
0.030	-0.60	1.50	-0.70	-2.10	–

Changes in DNA Melting Temperature (Δt_m) for complex **10**

| r_b	$[ClO_4]^-$ (M)				
	0.01	0.06	0.11	0.21	0.22
0.000	0.00	0.00	0.00	0.00	0.00
0.021	2.10	–	1.20	–	1.50
0.042	2.10	-0.30	1.30	–	1.00
0.046	2.10	0.20	1.0	–	-0.40
0.050	1.70	–	–	–	–
0.030	5.30	2.20	–	-2.10	-0.60
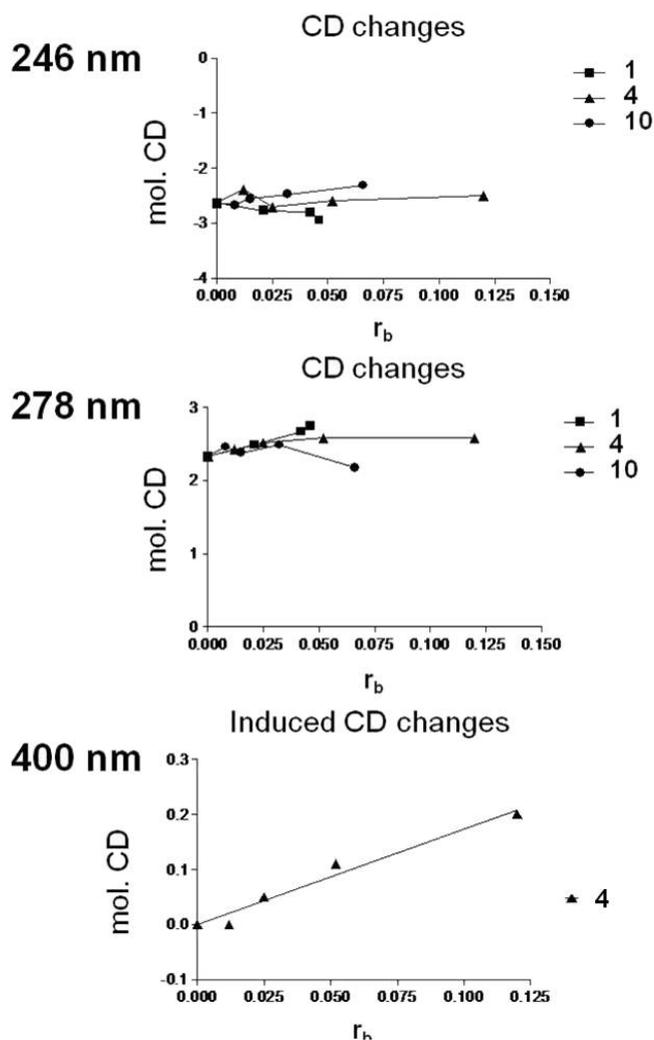
Figure A.4.48. The changes induced in CD spectra of CT-DNA modified by Ru^{II} arene complexes **1**, **4**, and **10** in their *irradiated* forms at different r_b values.
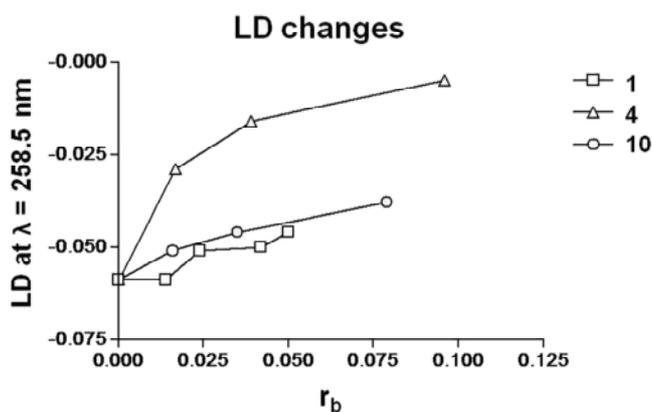

Figure A.4.49. The changes induced in LD spectra of CT-DNA modified by Ru^{II} arene complexes **1**, **4**, and **10** in their *irradiated* forms at different r_b values.

Chapter 6

Appendix

Table A.6.1 Crystallographic data for $[\eta^6\text{-}p\text{-cym})\text{Ru(NH}_3)\text{Cl}_2]$ (**1**) and $[\eta^6\text{-bip})\text{Ru(NH}_3)\text{Cl}_2]$ (**2**)

	1	2
Formula	$C_{19}H_{31}Cl_2F_6N_2PRu$	$C_{12}H_{13}Cl_2NRu$
Molar Mass	604.40	343.20
Crystal system	Yellow needle	Orange block.
Crystal size/mm^3	0.16 x 0.02 x 0.02	0.10 x 0.06 x 0.02
Space group	P-1	P-1
Crystal system	Triclinic	Triclinic
$a/$ Å	8.8456(7)	5.7821(3)
$b/$ Å	10.9737(9)	8.9621(4)
$c/$ Å	13.4054(12)	11.9292(6)
α/deg	110.456(4)	93.831(3)
β/deg	91.907(5)	101.256(2)
γ/deg	90.991(6)	105.661(3)
Z	2	2
R [F>4σ (F)]	0.0884	
Rw$_b$	0.1866	0.0664
GOF^c	1.123	1.060
Δρ max and min/eÅ^{-3}	1.102, –0.886	

Table A.6.2. Hydrogen bond lengths (Å) and angles (°) in $[\eta^6\text{-}p\text{-cym})\text{Ru(NH}_3)\text{Cl}_2]$ (**1**)

D	H	A	D–H (Å)	H···A (Å)	D···A (Å)	D–H–A (°)
N(208)	H(28A)	Cl(1)	0.85(2)	2.78(8)	3.407(9)	132(9)
N(208)	H(28A)	Cl(2)	0.85(2)	2.54(7)	3.279(9)	145(10)
N(1)	H(1A)	Cl(1)	0.85(2)	2.56(3)	3.392(9)	167(9)^a
N(1)	H(1C)	F(14)	0.85(2)	2.40(6)	3.142(9)	147(9)^a
N(1)	H(1B)	Cl(2)	0.85(2)	2.63(3)	3.460(9)	165(9)^b
C(110)	H(11B)	Cl(2)	0.98	2.67	3.626 (10)	165.6^b
C(110)	H(11A)	F(11)	0.98	2.43	3.351(11)	157.0^c
C(110)	H(11A)	F(15)	0.98	2.67	3.430(11)	137.2^c

Symmetry operators used to generate equivalent atoms involved in these contacts:
^{a} [–x+1, –y+1, –z+1]
^{b} [–x, –y+1, –z+1]
^{c} [1–x, –y, 1–z].

Table A.6.3. Hydrogen bond lengths (Å) and angles (°) in [η^6-bip)Ru(NH$_3$)Cl$_2$] (**2**)

| D	H	A	D–H (Å)	H···A (Å)	D···A (Å)	D–H–A (°)
N(1)	H(1B)	Cl(1)	0.910	2.667	3.410	139.42[a]
N(1)	H(1C)	Cl(1)	0.910	2.742	3.587	155.02[b]
N(1)	H(1D)	Cl(2)	0.910	2.606	3.388	144.41[c]

Symmetry operators used to generate equivalent atoms involved in these contacts:

[a] [–x+1, –y, –z+1]

[b] [x–1, y, z]

[c] [–x+1, –y, –z+1]

Chapter 3

Chapter 4

Chapter 5

1

2

3

4

5

6

7

8

9

10

11

12

13

14

15

16

Chapter 6

1

2